DESY–PROC–2009–02

Proceedings of the workshop

HERA and the LHC

workshop series on the implications of HERA for LHC physics

2006 - 2008, Hamburg - Geneva

Part 2

Editors: Hannes Jung, Albert De Roeck

Verlag Deutsches Elektronen-Synchrotron

Impressum

Proceedings of the workshop
HERA and the LHC
2nd workshop on the implications of HERA for LHC physics
2006 - 2008, Hamburg - Geneva

Conference homepage
`http://www.desy.de/~heralhc`

Online proceedings at
`http://www.desy.de/~heralhc/proceedings-2008/proceedings.html`

Editors:
Hannes Jung (DESY, U. Antwerp), Albert De Roeck (CERN, U. Antwerp)
March 2009
DESY-PROC-2009-02
ISBN 978-3-935702-32-4
ISSN 1435-8077

Published by
Verlag Deutsches Elektronen-Synchrotron
Notkestraße 85
22607 Hamburg
Germany

Organizing Committee:

H. Jung (DESY and U. Antwerp, chair), A. De Roeck (CERN and U. Antwerp, chair)
G. Altarelli (CERN), J. Blümlein (DESY), M. Botje (Nikhef), J. Butterworth (UCL), K. Eggert (CERN),
E. Gallo (INFN), T. Haas (DESY), R. Heuer (CERN), M. Klein (Liverpool), M. Mangano (CERN),
A. Morsch (CERN), G. Polesello (INFN/CERN), O. Schneider (EPFL), C. Vallee (CPPM)

Conveners:

part 1 Parton Density Functions:
M. Dittmar (ETH, Zürich, CMS), S. Forte (U. Milan), A. Glazov (DESY, H1), S. Moch (DESY)
Multi-jet final states and energy flows:
C. Gwenlan (UCL, ZEUS), L. Lönnblad (Lund), E. Rodrigues (LHCb), G. Zanderighi (CERN)
Contact persons: S. Banerjee (CMS), D. Traynor (H1)
Heavy quarks (charm and beauty):
M. Cacciari (Paris VI & VII.), A. Dainese (INFN, ALICE), A. Geiser (DESY, ZEUS), H. Spiesberger (U. Mainz)
Contact persons: K. Lipka (U. Hamburg, H1), Ulrich Uwer (CERN)
part 2 Diffraction:
M. Arneodo (U. Piemonte Orientale, Novara, INFN, CMS, ZEUS), M. Diehl (DESY), P. Newman (U. Birmingham, H1), V. A. Khoze (U. Durham)
Contact persons: A. Bruni (INFN, ZEUS), B. Cox (U. Manchester, ATLAS), R. Orava (U. Helsinki)
Cosmic Rays:
C. Diaconu (DESY, CPPM, H1), Ch. Kiesling (MPI Munich, H1), T. Pierog (FZ Karlsruhe),
Monte Carlos and Tools:
P. Bartalini (Taiwan, CMS), S.Chekanov (Argonne, ZEUS), F. Krauss (IPP Durham), S. Gieseke (U. Karlsruhe)

Advisory Committee:

G. Altarelli (CERN), J. Bartels (Hamburg), M. Della Negra (CERN), J. Ellis (CERN), J. Engelen (CERN),
G. Gustafson (Lund), G. Ingelman (Uppsala), P. Jenni (CERN), R. Klanner (DESY), M. Klein (DESY),
L. McLerran (BNL), T. Nakada (CERN), D. Schlatter (CERN), F. Schrempp (DESY),
J. Schukraft (CERN), J. Stirling (Durham), W.K. Tung (Michigan State), A. Wagner (DESY),
R. Yoshida (ANL)

Supported by:

Deutsches Elektronen-Synchroton DESY (Hamburg)
CERN (Geneva)

Contents

4 WG: Diffraction **395**

Working Group on Diffraction: Executive Summary **397**
M. Arneodo, M. Diehl, V.A. Khoze, P. Newman

Towards a Combined HERA Diffractive Deep Inelastic Scattering Measurement **401**
P. Newman, M. Ruspa

Diffractive Final States and Factorisation at HERA **412**
W. Słomiński, A. Valkárová

Leading Baryon Production at HERA **421**
W.B. Schmidke, A. Bunyatyan

Exclusive Vector Meson Production and Deeply Virtual Compton Scattering at HERA **427**
A. Bruni, X. Janssen, P. Marage

Exclusive Central Production and Diffractive W/Z Results from CDF II **440**
K. Goulianos, J. L. Pinfold

Survival probability in diffractive dijet photoproduction **448**
M. Klasen, G. Kramer

Fracture Functions at HERA and LHC **458**
F. A. Ceccopieri, L. Trentadue

Generalised parton distributions and exclusive vector meson production **464**
C. Nockles, T. Teubner

Dipole models and parton saturation in ep scattering **471**
L. Motyka, K. Golec-Biernat, G. Watt

Checking formalism for central exclusive production in the first LHC runs **482**
A.D. Martin, V.A. Khoze, M.G. Ryskin

Rapidity gap survival probability and total cross sections **488**
A.D. Martin, V.A. Khoze, M.G. Ryskin

Rapidity gap survival in central exclusive diffraction: Dynamical mechanisms and uncertainties **495**
M. Strikman, Ch. Weiss

Two-photon and photon-hadron interactions at the LHC **503**
J. Nystrand

Searching for the Odderon at HERA and the LHC **510**
C. Ewerz

Forward physics with CMS **516**
S. Erhan, S. Cerci, M. Grothe, J. Hollar, A. Vilela Pereira

Diffraction at TOTEM **527**
G. Antchev, P. Aspell V. Avati, M.G. Bagliesi, V. Berardi, M. Berretti, U. Bottigli, M. Bozzo, E. Brücken, A. Buzzo, F. Cafagna, M. Calicchio, M.G. Catanesi, P.L. Catastini, R. Cecchi, M.A. Ciocci, M. Deile, E. Dimovasili, K. Eggert, V. Eremin, F. Ferro, F. Garcia, S. Giani, V. Greco, J. Heino, T. Hildén, J. Kašpar, J. Kopal, V. Kundrát, K. Kurvinen, S. Lami, G. Latino, R. Lauhakangas, E. Lippmaa, M. Lokajíček, M. Lo Vetere, F. Lucas Rodriguez, M. Macrí, G. Magazzù, M. Meucci S. Minutoli, H. Niewiadomski, E. Noschis, G. Notarnicola, E. Oliveri, F. Oljemark, R. Orava, M. Oriunno, K. Österberg, P. Palazzi, E. Pedreschi, J. Petäjäjärvi, M. Quinto, E. Radermacher, E. Radicioni, F. Ravotti, G. Rella, E. Robutti, L. Ropelewski, G. Ruggiero, A. Rummel, H. Saarikko, G. Sanguinetti, A. Santroni, A. Scribano, G. Sette, W. Snoeys, F. Spinella, P. Squillacioti, A. Ster, C. Taylor, A. Trummal, N. Turini, J. Whitmore, J. Wu

The ALFA Detector and Physics Program **540**
K. Hiller, H. Stenzel

Diffractive Physics in ALICE **548**
R. Schicker

Physics with forward FP420/FP220 tagging systems **557**
P. Bussey, P. Van Mechelen

5 WG: Cosmic Rays, HERA and the LHC **566**

Introduction **567**
A. Bunyatyan, A. Cooper-Sarkar, C. Diaconu, R. Engel, C. Kiesling, K. Kutak, S. Ostapchenko, T. Pierog, T.C. Rogers, M.I. Strikman, T. Sako

Experimental results **582**

Model predictions for HERA, LHC and cosmic rays **611**

Summary **628**

6 WG: Monte Carlo and Tools **630**

Introduction to Monte Carlo models and Tools working group (WG5) **631**
P. Bartalini, S. Chekanov, S. Gieseke, F. Krauss

A multi-channel Poissonian model for multi-parton scatterings **635**
D. Treleani

Underlying events in Herwig++ **641**
M. Bähr, S. Gieseke, M. H. Seymour

Multiparton Interactions at HERA **646**
H. Jung, Ll. Marti, T. Namsoo, S. Osman

Modeling the underlying event: generating predictions for the LHC **656**
A. Moares

Measurement of the Underlying Event in Jet Topologies using Charged Particle and Momentum Densities **663**
F. Ambroglini, P. Bartalini, F. Bechtel, L. Fanò, R. Field

Double-Parton-Scattering in Photon-Three-Jet Final States at the LHC **670**
F. Bechtel

Underlying Event Studies with CASTOR in the CMS Experiment **675**
Z. Rúriková, A. Bunyatyan

Direct photon production at HERA, the Tevatron and the LHC **681**
R. E. Blair, S. Chekanov, G. Heinrich, A. Lipatov , N. Zotov

Propagation of Uncertainty in a Parton Shower **699**
Ph. Stephens, A. van Hameren

Perturbative description of inclusive single hadron production at HERA **710**
S. Albino

Nonperturbative corrections from an s-channel approach **716**
F. Hautmann

Single top production in the Wt mode with MC@NLO **721**
Ch. White

PYTHIA 8 Status Report **726**
T. Sjöstrand

THEPEG **Toolkit for High Energy Physics Event Generation** **733**
L. Lönnblad

CASCADE **737**
M. Deák, H. Jung, K. Kutak

`AlpGen` **and** `SHERPA` **in $Z/\gamma^* + jets$ at LHC** **740**
P. Lenzi

Generator comparison for top-pair production at CMS **747**
R. Chierici

Herwig++ Status Report **752**
M. Bähr, S. Gieseke, M.A. Gigg, D. Grellscheid, K. Hamilton, O. Latunde-Dada, S. Plätzer, P. Richardson, M.H. Seymour, A. Sherstnev, J. Tully, B.R. Webber

Forward Physics Monte Carlo (FPMC) **758**
M. Boonekamp,V. Juránek, O. Kepka, C. Royon

HEP data analysis using jHepWork and Java **763**
S. Chekanov

Tools for event generator tuning and validation **768**
A. Buckley

Prerequisites for the Validation of Experiment and Theory **774**
L. Sonnenschein

7 List of Authors **779**

8 List of Participants **783**

Chapter 4

Working Group Diffraction

Convenors:

M. Arneodo (U. Piemonte Orientale, Novara, INFN, CMS, ZEUS), M. Diehl (DESY), P. Newman (U. Birmingham, H1) V. A. Khoze (U. Durham)

Contactpersons: A. Bruni (INFN, ZEUS), B. Cox (ATLAS), R. Orava (U. Helsinki)

Working Group Members:

V. Andreev, M. Arneodo, J. Bartels, A. Bonato, K. Borras, A. Bruni, A. Bunyatyan, P. Bussey, F.A. Ceccopieri, S. Cerci, T. Coughlin, B. Cox, M. Diehl, S. Erhan, C. Ewerz, K. Golec-Biernat, K. Goulianos, M. Grothe, K. Hiller, J. Hollar, X. Janssen, M. Kapishin, J. Kaspar, V.A. Khoze, M. Klasen, G. Kramer, V. Kundrat, J. Łukasik, A. v. Manteuffel, P. Marage, U. Maor, I. Melzer-Pellman, A.D. Martin, L. Motyka, M. Mozer, P. Newman, H. Niewiadomski, C. Nockles, J. Nystrand, R. Orava, K. Österberg, A. Panagiotou, A. Pilkington, J.L. Pinfold, W. Plano, X. Rouby, C. Royon, M. Ruspa, P. Ryan, M.G. Ryskin, R. Schicker, F.-P. Schilling, W.B. Schmidke, G. Shaw, W. Słomiński, H. Stenzel, M. Strikman, M. Taševski, K. Terashi, T. Teubner, L. Trentadue, A. Valkárová, P. Van Mechelen, A. Vilela Pereira, G. Watt, S. Watts, C. Weiss, R. Wolf

Working Group on Diffraction: Executive Summary

M. Arneodo [a], *M. Diehl* [b], *V.A. Khoze* [c] *and P. Newman* [d]
[a] Università del Piemonte Orientale, I-28100 Novara, and INFN-Torino, I-10125 Torino, Italy
[b] Deutsches Elektronen-Synchroton DESY, 22603 Hamburg, Germany
[c] Institute for Particle Physics Phenomenology, University of Durham, DH1 3LE, UK
[d] School of Physics and Astronomy, University of Birmingham, B15 2TT, UK

Abstract
We give a brief overview of the topics covered in the working group on diffraction.

1 Introduction

From 2006 to 2008, the working group on diffraction had 74 individual presentations, documenting the considerable activity and progress in the field. This program covered a variety of topics: the presentation and assessment of new data from HERA and the Tevatron [1–5], developments in the theory of diffraction in ep and in pp or $p\bar{p}$ collisions [6–15], and the ongoing preparatory studies for measuring diffractive processes at the LHC [16–20]. Many presentations were related in one way or another to the prospect of seeing central exclusive production of the Higgs boson, $p + p \to p + H + p$, or of other new particles. Important progress has been made in this field since the first proceedings of the HERA/LHC workshop [21] appeared, both on the side of instrumentation at LHC and in the understanding of the relevant theory, with crucial input provided by new measurements from the H1, ZEUS, and CDF Collaborations. In the following we give a brief overview of the different topics presented in these proceedings and of their interrelation.

2 Diffraction from electron-proton to hadron-hadron collisions

A key result of the numerous studies of diffraction at HERA is that in the presence of a hard scale several diffractive channels can be understood in terms of a partonic description, which allows us to calculate important features of the process in perturbation theory. This concerns the inclusive cross section for diffractive deep inelastic scattering [1] as well as diffractive jet or heavy flavor production from a highly virtual photon [2, 9]. The increasingly precise HERA results for these channels are well described in terms of perturbatively calculated hard-scattering coefficients and of diffractive parton densities. The latter are a special case of fracture functions [6] and, just as the usual parton densities, have been fitted to data.

It has long been anticipated from theory and seen in data that such a simple factorized description is not valid in diffractive hadron-hadron collisions, and recent results from HERA and the Tevatron have corroborated this finding. Secondary interactions between partons of the colliding hadrons significantly decrease the fraction of events with large rapidity gaps, and it remains a challenge to quantitatively understand the dynamics of these interactions [7, 8] at the LHC. Let us recall that the associated physics is closely related to that of multiple parton interactions and hence of importance far beyond the context of diffractive final states [21]. Similar rescattering effects are also expected in ep collisions when the exchanged photon becomes quasi real, not

only for diffraction but also for events with an observed leading baryon [3]. The situation here seems, however, to be more complicated than initially thought due to the double nature of a real photon as a pointlike and a hadronic object. Based on the same data, the two contributions [2] and [9] to these proceedings draw conflicting conclusions about the magnitude of rescattering effects in diffractive photoproduction. The study of additional experimental observables, such as double differential distributions or certain ratios should help clarify the situation.

A wealth of information about high-energy dynamics can be gained from the detailed experimental studies of exclusive diffraction at HERA, notably of exclusive production of a vector meson or a real photon [4]. Precise data for such channels in particular provide good constraints on the generalized gluon distribution [10], which not only carries valuable information about proton structure at small momentum fractions but is also a key ingredient for calculating central exclusive production in pp or $p\bar{p}$ collisions. Ultraperipheral collisions at LHC offer the prospect to study exclusive diffraction initiated by a real photon at energies well beyond the HERA regime [11]. Suitable exclusive channels may also provide clear signals for odderon exchange, which, although naturally arising within the QCD picture of high-energy collisions, have been conspicuously absent from data so far [12].

Finally, the combined consideration of ep data for both inclusive and exclusive diffraction and for non-diffractive events remains maybe the best strategy for clarifying the importance of parton saturation at HERA, i.e., of non-linear dynamical effects due to high parton densities [13]. To understand such dynamics at the quantitative level remains one of the great challenges in high-energy QCD, and there is hope that the huge phase space available in pp collisions at LHC can be harnessed to shed further light on this physics. This remains an ambitious enterprise, requiring measurements at forward rapidities at the LHC [16] and further development of the theory [14].

3 Preparing for diffraction and forward physics at LHC

The opportunities for diffractive and forward measurements at LHC cover a wide area of physics, ranging from the determination of the elastic and total pp cross section at the highest energies yet achieved in the laboratory [17, 18] to the study of both electroweak and strong interactions in $\gamma\gamma$ and γp collisions [11, 16, 19, 20]. High hopes are put into the possibility to observe central exclusive production of new particles such as a light Higgs boson, with the prospect of the precise measurement of their mass, width, and quantum numbers in a very clean environment [20]. The theoretical description of the central exclusive production mechanism involves many difficult issues, and a milestone in testing our understanding of this mechanism has been the observation of exclusive dijet production by CDF [5]. Despite this success, one must keep in mind the uncertainties inherent in extrapolating dynamics from Tevatron to LHC energies, and a number of diffractive measurements have been proposed to validate the theory at an early stage of LHC running [15].

The forward instrumentation currently available at ATLAS, CMS and ALICE will allow a rich program to be carried out in forward and diffractive physics from the very beginning of the data taking. Feasibility studies performed by CMS [16] indicate that measurements of forward jets sensitive to the low-x PDFs of the proton are possible with the first 10 pb^{-1} of integrated luminosity. "Rediscovery" of hard diffraction at the LHC is possible within the first 10–100 pb^{-1},

via single-diffractive production of dijets and W bosons, as well as Υ photoproduction [16]. In addition, exclusive dilepton production can be used for the calibration of the forward detectors and for luminosity determination [16]. TOTEM [17] plans to measure central and single diffractive cross sections, as well as high-t elastic scattering and forward charged particle multiplicities with the first data. A more ambitious joint CMS-TOTEM physics program is foreseen [17] as soon as common CMS and TOTEM data taking is possible. TOTEM [17] and ATLAS [18] will also measure the total and elastic pp cross sections in dedicated runs with special beam optics. A diffractive physics program is also taking shape at ALICE [19], thanks to the particle-identification capability and good acceptance for low-p_T particles of the ALICE detector, along with the lack of pile-up at the ALICE interaction point.

ATLAS and CMS will also be able to carry out a forward and diffractive physics program at the highest LHC instantaneous luminosities if the AFP and FP420 programs are approved [20]. AFP aims at instrumenting with near-beam proton detectors the regions at ± 220 and ± 420 m from the ATLAS interaction point, while FP420 at CMS aims at instrumenting the ± 420 m region to complement existing proton detectors at TOTEM. These additions to ATLAS and CMS will permit the measurement of forward protons down to values of the fractional momentum loss of the proton of $\xi \simeq 0.002$.

In summary, the diffractive community is looking forward to the next years, when the final analysis of HERA data and a variety of measurements at LHC will hopefully teach us valuable lessons on the physics of the strong interaction and beyond.

References

[1] P. Newman and M. Ruspa, *Towards a combined HERA diffractive deep inelastic scattering measurement*, these proceedings.

[2] W. Słomiński and A. Valkárová, *Diffractive final states and factorization at HERA*, these proceedings.

[3] W.B. Schmidke and A. Bunyatyan, *Leading baryon production at HERA*, these proceedings.

[4] A. Bruni, X. Janssen and P. Marage, *Exclusive vector meson prdouction and deeply virtual Compton scattering at HERA*, these proceedings.

[5] K. Goulianos and J.L. Pinfold, *Exclusive central production and diffractive W/Z results from CDF II*, these proceedings.

[6] F.A. Ceccopieri and L. Trentadue, *Fracture functions at HERA and LHC*, these proceedings.

[7] A.D. Martin, V.A. Khoze and M.G. Ryskin, *Rapidity gap survival probability and total cross sections*, these proceedings.

[8] M. Strikman and C. Weiss, *Rapidity gap survival in central exclusive diffraction: Dynamic mechanisms and uncertainties*, these proceedings.

[9] M. Klasen and G. Kramer, *Survival probability in diffractive dijet production*, these proceedings.

[10] C. Nockles and T. Teubner, *Generalised parton distributions and exclusive vector meson production*, these proceedings.

[11] J. Nystrand, *Two-photon and photon-hadron interactions at the LHC*, these proceedings.

[12] C. Ewerz, *Searching for the odderon at HERA and the LHC*, these proceedings.

[13] L. Motyka, K. Golec-Biernat and G. Watt, *Dipole models and parton saturation in ep scattering*, these proceedings.

[14] J. Bartels, *Searching for saturation in pp scattering: the inclusive cross section in QCD*, presentation at this workshop, CERN, May 2008.

[15] A.D. Martin, V.A. Khoze and M.G. Ryskin, *Checking formalism for central exclusive production in the first LHC runs*, these proceedings.

[16] S. Erhan et al., *Forward physics with CMS*, these proceedings.

[17] G. Antchev et al., *Diffraction at TOTEM*, these proceedings.

[18] K. Hiller and H. Stenzel, *The ALFA detector and physics program*, these proceedings.

[19] R. Schicker, *Diffractive physics in ALICE*, these proceedings.

[20] P. Bussey and P. Van Mechelen, *Physics with forward FP420/FP220 tagging systems*, these proceedings.

[21] S. Alekhin et al., *HERA and the LHC – A workshop on the implications of HERA for LHC physics: Proceedings Parts A and B*, arXiv:hep-ph/0601012 and hep-ph/0601013.

Towards a Combined HERA Diffractive Deep Inelastic Scattering Measurement

Paul Newman [a], *Marta Ruspa* [b]
[a] School of Physics & Astronomy, University of Birmingham, B15 2TT, UK.
[b] Università del Piemonte Orientale, 28100 Novara, Italy.

Abstract
The diffractive dissociation of virtual photons, $\gamma^\star p \to Xp$, has been studied with the H1 and ZEUS detectors at HERA using various complementary techniques. Events have been selected by direct tagging of the outgoing proton or by requiring a large rapidity gap between the proton and the system X. The diffractive contribution has also been unfolded by decomposition of the inclusive hadronic final state invariant mass distribution. Here, detailed comparisons are made between diffractive cross section measurements obtained from the different methods and the two experiments, showing them to be consistent within the large uncertainties associated with the treatment of proton dissociation processes. First steps are taken towards the combination of the H1 and ZEUS results.

1 Introduction

In the single diffractive dissociation process in proton-proton scattering, $pp \to Xp$, at least one of the beam hadrons emerges intact from the collision, having lost only a small fraction of its energy and gained only a small transverse momentum. In the analogous process involving virtual photons, $\gamma^\star p \to Xp$ (figure 1) [1, 2], an exchanged photon of virtuality Q^2 dissociates through its interaction with the proton at a squared four momentum transfer t to produce a hadronic system X with mass M_X. The fractional longitudinal momentum loss of the proton during the interaction is denoted $x_{\mathbb{P}}$, while the fraction of this momentum carried by the struck quark is denoted β. These variables are related to Bjorken x by $x = \beta\, x_{\mathbb{P}}$.

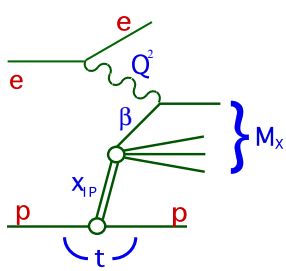

Fig. 1: Illustration of the kinematic variables describing the virtual photon dissociation process, $\gamma^\star p \to Xp$, in ep collisions.

Diffractive interactions are often discussed in the framework of Regge phenomenology [3] in terms of the exchange of a 'pomeron' with vacuum quantum numbers. This interpretation in terms of a universal exchange is experimentally supported by the 'proton vertex factorisation', which holds to good approximation over much of the accessible kinematic range at low $x_{\mathbb{P}}$, whereby the dependences on variables describing the soft interaction with the proton ($x_{\mathbb{P}}$, t) factorise from those related to the hard interaction with the virtual photon (β, Q^2). Similar reactions, in which sub-leading Reggeon and pion trajectories are exchanged, have a negligible cross section at the smallest $x_{\mathbb{P}}$ values.

Significant progress has been made in understanding diffraction in terms of QCD by studying virtual photon dissociation in deep inelastic ep scattering (DIS) at HERA (for a review see [4]). As well as being sensitive to novel features of parton dynamics in the high density, low x regime, diffractive DIS cross sections are used to extract diffractive parton density functions (DPDFs) [5–9], an essential ingredient in predicting many diffractive processes at the LHC and in estimating backgrounds to more exotic processes such as central exclusive Higgs production ($pp \to pHp$) [10].

Similarly to inclusive DIS, cross section measurements for the reaction $ep \to eXp$ are conventionally expressed in terms of the reduced diffractive cross section, $\sigma_r^{D(3)}$, which is related to the measured cross section by

$$\frac{\mathrm{d}\sigma^{ep\to eXp}}{\mathrm{d}\beta \mathrm{d}Q^2 \mathrm{d}x_{\mathbb{P}}} = \frac{4\pi\alpha^2}{\beta Q^4} \left[1 - y + \frac{y^2}{2}\right] \sigma_r^{D(3)}(\beta, Q^2, x_{\mathbb{P}}) \,. \tag{1}$$

At moderate inelasticities y, $\sigma_r^{D(3)}$ corresponds to the diffractive structure function $F_2^{D(3)}$ to good approximation. In this contribution, we tackle the technical issue of compatibility between different $\sigma_r^{D(3)}$ data sets through detailed comparisons between different measurements by the H1 and ZEUS collaborations and take the first steps towards a combined HERA data set.

2 Methods of selecting diffraction at HERA

Experimentally, diffractive ep scattering is characterised by the presence of a leading proton in the final state retaining most of the initial state proton energy, and by a lack of hadronic activity in the forward (outgoing proton) direction, such that the system X is cleanly separated and M_X may be measured in the central detector components. These signatures have been widely exploited at HERA to select diffractive events by tagging the outgoing proton in the H1 Forward Proton Spectrometer or the ZEUS Leading Proton Spectrometer (proton-tagging method [6, 11–14]) or by requiring the presence of a large gap in the rapidity distribution of hadronic final state particles in the forward region (LRG method [5, 8, 15, 16]). In a third approach (M_X method [16–19]), the inclusive DIS sample is decomposed into diffractive and non-diffractive contributions based on their characteristic dependences on M_X.

The kinematic coverages of the LRG and M_X methods are limited to $x_{\mathbb{P}} \lesssim 0.05$ by the need to contain the system X in the central detector components. These two methods are equivalent for $M_X \to 0$, but differences are to be expected at larger M_X, where the LRG method measures the full cross section from all sources at a given $(x_{\mathbb{P}}, \beta, Q^2)$ point, whereas the M_X method involves the subtraction of a 'non-diffractive' component. LPS and FPS data extend to $x_{\mathbb{P}} \sim 0.1$ and are therefore the most sensitive to non-leading contributions, including Reggeon and pion trajectory exchanges. Apart from the proton dissociation treatment in the H1 case (see section 4.2), the cross sections measured by the proton-tagging and LRG methods are equivalent.

The methods differ substantially in their dominant sources of systematic uncertainty. In the LRG and M_X methods, the largest uncertainties arise from the admixture of low mass leading baryon systems other than protons. These include proton excitations to low mass states as well as leading neutrons produced via charge exchange reactions. All such contributions are collectively referred to here as 'proton dissociation', $ep \to eXN$, with the baryon state N having mass M_N.

Proton dissociation processes cannot always be distinguished by the LRG and M_X methods from events in which the proton is scattered elastically. Conversely, low-$x_{I\!P}$ samples selected by the proton-tagging method have little or no proton dissociation background, but are subject to large uncertainties in the proton tagging efficiency, which is strongly dependent on the proton-beam optics. Proton spectrometers also allow a measurement of t, but the statistical precision is limited by their small acceptances.

Comparing the results from the three different methods is a powerful test of the control over the systematics of the measurements. At low $x_{I\!P}$, the ratio of results obtained by the LRG and M_X methods to those from the proton-tagging method can also be used to quantify the proton dissociation contributions in the former samples.

3 Data sets

A comprehensive comparison has been carried out between recent H1 and ZEUS measurements obtained with the three different methods. The data sets used are as follows.[1]

- Three data sets collected with the ZEUS detector in the years 1999 and 2000. Overlapping samples have been analysed with the ZEUS Leading Proton Spectrometer (termed **"ZEUS LPS"**, based on a luminosity of 32.6 pb^{-1}) [15], with the LRG method (**"ZEUS LRG"**, 62.2 pb^{-1}) [15] and with the M_X method, relying on the Forward Plug Calorimeter (**"ZEUS FPC I"**, 4.2 pb^{-1} [18] and **"ZEUS FPC II"**, 52.4 pb^{-1} [19]).
- A set of data collected with the H1 Forward Proton Spectrometer (**"H1 FPS"**, 28.4 pb^{-1}) [14] in the years 1999 and 2000.
- A set of data collected with the H1 detector in the years 1997, 1999 and 2000 and analysed with the LRG method (**"H1 LRG"**, 2.0 pb^{-1}, 10.6 pb^{-1} and 61.6 pb^{-1} for small, intermediate and large Q^2, respectively) [8].

The H1 LRG and FPS samples are statistically independent and are only weakly correlated through systematics. The three ZEUS samples also have different dominating systematics, but are not statistically independent. About 75% of events are common to both the ZEUS LRG and ZEUS FPC II data sets and 35% of the ZEUS LPS events are also contained in the ZEUS LRG sample.

4 Proton dissociation background and corrections

In proton dissociation processes at the lowest M_N, the dissociative system N often escapes entirely undetected into the forward beam-pipe. As M_N increases, it becomes more likely that dissociation products are detected in the instrumentation most sensitive to forward energy flow. The LRG and M_X methods therefore do not distinguish low M_N proton dissociation events from the case in which the proton is scattered elastically. Different cross-section definitions have been adopted, in which the proton dissociation contribution is either subtracted statistically, or else the quoted results are integrated over a specific range of M_N. Since understanding the proton dissociation contributions and the corresponding corrections is fundamental to comparisons between the different measurements, a detailed discussion is presented in the following.

[1] The comparisons here are restricted to published data and do not yet include the precise H1 LRG and M_X method results obtained from 1999-2004 running [16].

In both the ZEUS LPS and the H1 FPS analyses, the contribution from proton dissociation events is negligible at small $x_{I\!P} \lesssim 0.02$. At the largest $x_{I\!P}$ values, it becomes kinematically possible for the detected leading proton to be the result of a decay of an N^* or other proton excitation, the remaining decay products being unobserved. This background was estimated by ZEUS to contribute around 9% at $x_{I\!P} = 0.1$, using the PYTHIA Monte Carlo (MC) model [20]. In the H1 FPS analysis, using the RAPGAP [21] implementation of the DIFFVM proton dissociation model [22], it was estimated to reach 3% at $x_{I\!P} = 0.08$.

Proton dissociation contributions in the LRG and M_X methods can be controlled using dedicated proton dissociation simulations tuned in M_N regions where dissociating protons leave signals in the detectors, and extrapolated into the M_N regions where the dissociation products are typically not detected. In addition to this procedure, both H1 and ZEUS use standard simulations of non-diffractive processes to control the small migrations of very high M_N or $x_{I\!P}$ events into the measurement region, which occur due to inefficiencies of the forward detectors.

4.1 ZEUS LRG

In the recent ZEUS analysis, the PYTHIA simulation was tuned to proton dissociation signals. Two samples were selected by requiring activity either in the forward plug calorimeter (FPC) or at relatively low proton energy in the LPS. The samples thus include the low M_N region in which proton dissociation products are invisible to the central detector. The generated distributions were reweighted in M_N, M_X and Q^2 to best describe the energy distribution in the FPC ($E_{\rm FPC}$), and the scattered proton energy fraction distribution (x_L) in the LPS. Figures 2a and 2b show the comparison of the reweighted PYTHIA model with the two proton dissociation samples as a function of these variables. Also shown in figures 2c-e is the resulting estimate of the fraction of proton dissociation events in the LRG sample as a function of Q^2, β and $x_{I\!P}$. This fraction, obtained separately from the FPC and LPS samples, is constant at the level of 25%.

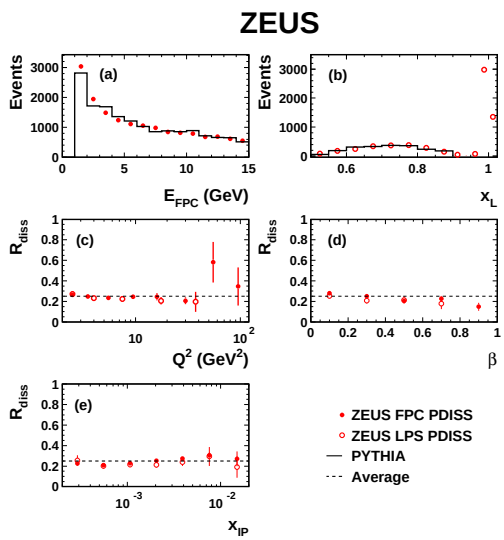

Fig. 2: (a) FPC energy and (b) LPS x_L distributions for ZEUS proton dissociation samples (see text), with data compared to the tuned PYTHIA model. (c-e) Extracted fractions of proton dissociation events in the ZEUS LRG sample as a function of Q^2, β and $x_{I\!P}$ after integration over the other variables [15].

The ratios of cross sections extracted from the ZEUS LPS and LRG data (the latter uncorrected for proton dissociation background), are shown in figure 3. There is no significant dependence on Q^2, $x_{I\!P}$ or β, illustrating the low $x_{I\!P}$ compatibility between the two methods. The ratio averages to $0.76 \pm 0.01({\rm stat.})^{+0.03}_{-0.02}({\rm syst.})^{+0.08}_{-0.05}({\rm norm.})$, the last error reflecting the normalisation uncertainty of the LPS data. The proton dissociation background fraction in the LRG data is thus $24 \pm 1({\rm stat.})^{+2}_{-3}({\rm syst.})^{+5}_{-8}({\rm norm.})$%, in agreement with the result of the MC

study, $25 \pm 1(\text{stat.}) \pm 3(\text{syst.})\%$ (figure 2). Unless stated otherwise, the ZEUS LRG data are corrected by this factor in the following and thus correspond exclusively to the truly proton-elastic process.

4.2 H1 LRG

The contribution from proton dissociation in the H1 LRG analysis is constrained through the DIFFVM MC [22] model, normalised using the response to large M_N events leaving signals in the forward and central detector components [8, 23].

The data are corrected using DIFFVM to $M_N < 1.6$ GeV. The H1 LRG data are then compared with the H1 FPS measurement, in order to extract the proton dissociation cross section with $M_N < 1.6$ GeV directly from the data. The ratio of the two measurements, after projection onto the Q^2, $x_{\mathbb{P}}$ and β axes, is shown in figure 4. There is no evidence for any dependence on any of the kinematic variables. as expected in the framework of proton vertex factorisation. The average value of the ratio is $1.23 \pm 0.03\ (\text{stat.}) \pm 0.16\ (\text{syst.})$, the largest uncertainty arising from the FPS efficiency. The result is in good agreement with the DIFFVM estimate of $1.15^{+0.15}_{-0.08}$. The data and DIFFVM ratios translate into proton dissociation background fractions of 19 % and 13 %, respectively, consistent within the uncertainties. The similarity between the proton dissociation fractions in the raw H1 and ZEUS LRG selections is to be expected given the similar forward detector acceptances of the two experiments.

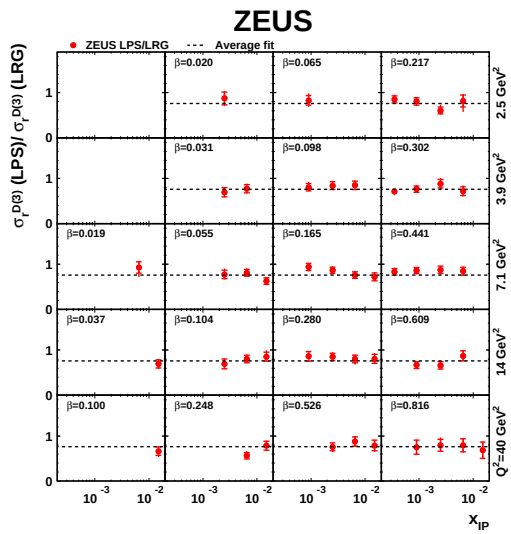

Fig. 3: The ratio of the ZEUS LPS measurement ($M_N = m_p$) to the ZEUS LRG measurement before subtraction of proton dissociation background [15]. The lines represent the average value of this ratio. An overall normalisation uncertainty of $^{+11}_{-8}\%$ is not included in the errors shown.

4.3 ZEUS FPC

The proton dissociation treatment is also critical in the M_X method, where the diffractive contribution is separated from the non-diffractive component in a fit to the inclusive $\ln M_X^2$ distribution. Proton dissociation events with sufficiently large M_N for dissociation products to reach the FPC and central detectors lead to a reconstructed M_X value which is larger than the actual photon dissociation mass. The resulting distortion of the $\ln M_X^2$ distribution affects the diffractive contribution extracted in the fit if corrections are not made. According to the SANG MC model, the N system contaminates the M_X reconstruction for $M_N > 2.3$ GeV on average [24], and events in this M_N range are therefore subtracted using SANG before the $\ln M_X^2$ distribution is decomposed. The upper M_N cut in the SANG sample is defined by $(M_N/W)^2 < 0.1$, which leads to a variation of the subtracted fraction of events with W, the centre-of-mass energy of the photon-proton system. This contrasts with the LRG method, where MC studies confirm that the rapidity

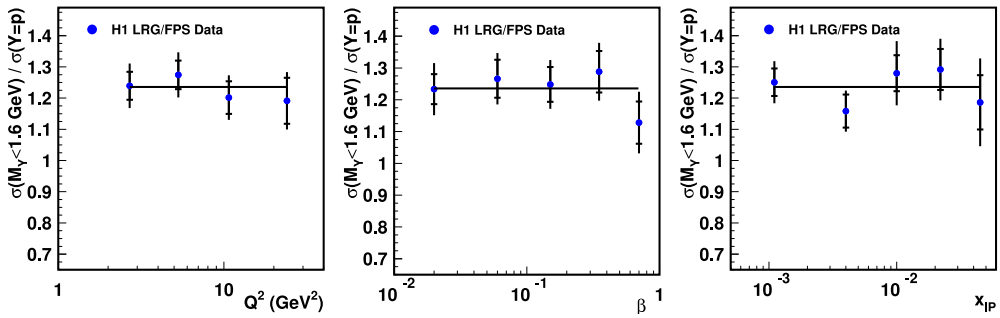

Fig. 4: The ratio of the H1 LRG measurement (corrected to $M_N < 1.6$ GeV) to the H1 FPS measurement ($M_N = m_p$), after integration over the variables not shown in each case [14]. The lines represent a fit to the data assuming no dependence on any of the variables. An overall normalisation uncertainty of 13% is not included in the errors shown.

gap requirement efficiently eliminates proton dissociation at large M_N, the remaining fractional low M_N contribution being independent of kinematics to good approximation (figures 3 and 4).

Despite these difficulties, there is acceptable agreement between the ZEUS FPC data and the ZEUS LRG measurement. A global fit comparing the normalisations of the two data sets (after correcting the LRG data to $M_N = m_p$) yields a normalisation factor of 0.83 ± 0.04 to be applied to the ZEUS FPC results. This factor is comaptible with with expectations for the residual proton dissociation contribution based on the MC studies in sections 4.1 and 4.2.

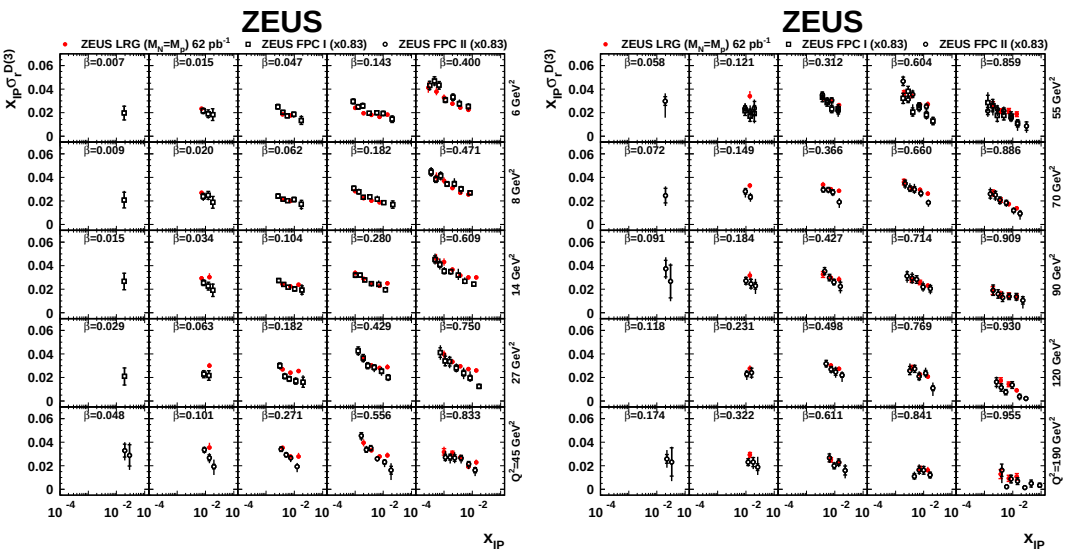

Fig. 5: Comparison between the ZEUS M_X method ('FPC I' and 'FPC II') and ZEUS LRG method data [15]. As explained in the text, the M_X method data are scaled by a constant factor of 0.83 to account for proton dissociation contributions with $M_N < 2.3$ GeV.

5 Cross section comparisons

Due to their differing M_N coverages, the $\sigma_r^{D(3)}$ measurements from the different data sets are not directly comparable. However, assuming the factorisation of the M_N dependence which is suggested in the data, varying the M_N range should introduce only global normalisation differences, which can be estimated using the proton dissociation simulations.

5.1 Comparison between LRG and M_X methods

ZEUS cross section measurements obtained with the LRG and M_X methods are compared in figure 5. The LRG data are corrected to $M_N = M_p$ as described in section 4.1 and the relative normalisation factor of 0.83 (section 4.3) is applied to the ZEUS FPC data to account for residual proton dissociation. The overall agreement between the two measurements is good, apart from some differences at large $x_{\mathbb{P}} \gtrsim 0.01$. The Q^2 dependence of the M_X method data is also slightly weaker than that of the LRG data.

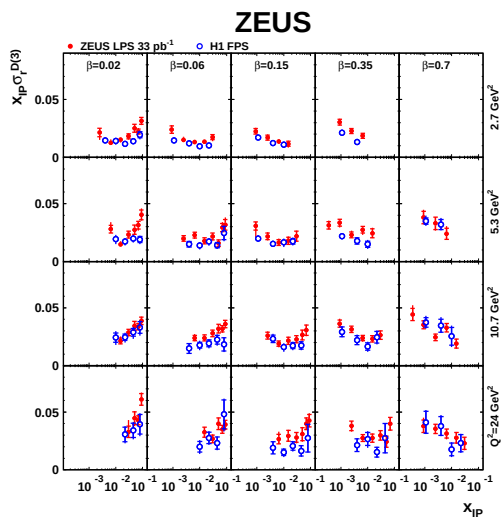

Fig. 6: Comparison between ZEUS LPS and H1 FPS measurements [15]. Normalisation uncertainties of $\pm 10\%$ (H1) and $^{+11\%}_{-7\%}$ (ZEUS) are not shown.

5.2 Comparison between ZEUS LPS and H1 FPS measurements

The ZEUS LPS and H1 FPS data are compared in figure 6. For this comparison, the ZEUS results are extracted at the same β and Q^2 values as H1 and are therefore not affected by extrapolation uncertainties. The shape agreement is satisfactory and the overall normalisation discrepancy of around 10% lies within the large combined normalisation uncertainty of around 14%.

5.3 Comparison between ZEUS and H1 LRG measurements

The ZEUS LRG data are extracted at the H1 β and $x_{\mathbb{P}}$ values, but at different Q^2 values. In order to match the $M_N < 1.6\,\text{GeV}$ range of the H1 data, a global factor of 0.91 ± 0.07, estimated with PYTHIA, is applied to the ZEUS LRG data in place of the correction to an elastic proton cross section. After this procedure, the ZEUS data remain higher than those of H1 by 13% on average, as estimated with a global fit comparing the normalisations of the two data sets for $Q^2 > 6\,\text{GeV}^2$. This normalisation discrepancy is similar to that between the H1 FPS and the ZEUS LPS data sets. It is in line with the errors due to the 8% uncertainty on the proton dissociation correction in the ZEUS LRG data and the 7% combined relative normalisation uncertainty between the two LRG data sets.

In figure 7, the ZEUS results are scaled by a factor 0.91×0.87 (the factor $0.87 = 1 - 0.13$ normalising the ZEUS to the H1 data) and compared with the H1 LRG measurement. An

excellent agreement between the Q^2 dependences is revealed throughout most of the phase space. There are small deviations between the β dependences of the two measurements at the highest and lowest β values. The results of the 'H1 Fit B' NLO QCD DPDF fit to the H1 LRG data [8] is also shown. It gives a good description of the data at large Q^2. However, the extrapolation beyond the fitted region ($Q^2 \geq 8.5\ \mathrm{GeV}^2$) undershoots the precise new ZEUS low Q^2 LRG data, confirming the observation in [8] that a standard DGLAP fit to the lowest Q^2 data is problematic.

6 A First Combination of Data Sets

For easy future consumption at the LHC and elsewhere, it is desirable to combine the various H1 and ZEUS diffractive DIS measurements into a single easily digestible HERA data set. Here we take the first steps towards this goal, by making a simple error-weighted average of the H1 and ZEUS LRG data sets, ignoring correlations between the data points due to the systematic errors. LPS and M_X method data are not considered at this stage. For the purpose of this exercise, the ZEUS normalisation is fixed to that of H1 as described in section 5.3 and shown in figure 7. The normalisation of the combined data thus has an uncertainty beyond the 10% level. Combinations can only meaningfully be made where there is basic agreement between the different measurements. Since this is not always the case at the lowest $x_{\mathbb{P}}$ values, we restrict the averaging to the $x_{\mathbb{P}} = 0.003$ and $x_{\mathbb{P}} = 0.01$ data. The combinations are performed throughout the measured Q^2 range, including the $Q^2 < 8.5\ \mathrm{GeV}^2$ region, beyond the range of the 'H1 Fit B' parameterisation which is compared with the data.

To account for the differences between the Q^2 binning choices, H1 data points are adjusted to the ZEUS Q^2 bin centres by applying small correction factors calculated using the 'H1 Fit B' parameterisation. Where both collaborations then have measurements at a given $(Q^2, x_{\mathbb{P}}, \beta)$ point, a simple weighted average is taken, using the quadratic sum of statistical and systematic uncertainties for each experiment, excluding normalisation uncertainties.

The results of this averaging procedure are shown in figure 8. They are indicative of the sort of precision which is achievable through combinations, with many data points having errors at the $3 - 4\%$ level, excluding the normalisation uncertainty. At $x_{\mathbb{P}} = 0.01$ the combined data agree well with the 'H1 Fit B' DPDF results. At $x_{\mathbb{P}} = 0.003$ the Q^2 dependences are also in good agreement with the parameterisation in the β and Q^2 region of the fit, with the exception of the highest β value, where the average is pulled towards the more precise ZEUS data.

More sophisticated averaging methods may be used in the future, for example that [25] developed to perform similar combinations of inclusive HERA data, with a full systematic error treatment. No attempt has yet been made to extract DPDFs from the combined data. Based on the combined $\sigma_r^{D(3)}$ and its Q^2 dependence shown here, no significant conflict is expected with the quark or gluon densities of 'H1 Fit B' in the bulk of the phase space. However, small modifications are likely to be necessary to the quark densities at small and large β values.

7 Summary

H1 and ZEUS diffractive DIS data obtained by various methods with very different systematics have been compared in detail. All measurements are broadly consistent in the shapes of the distributions. The comparisons between proton tagging and LRG method data internally to the

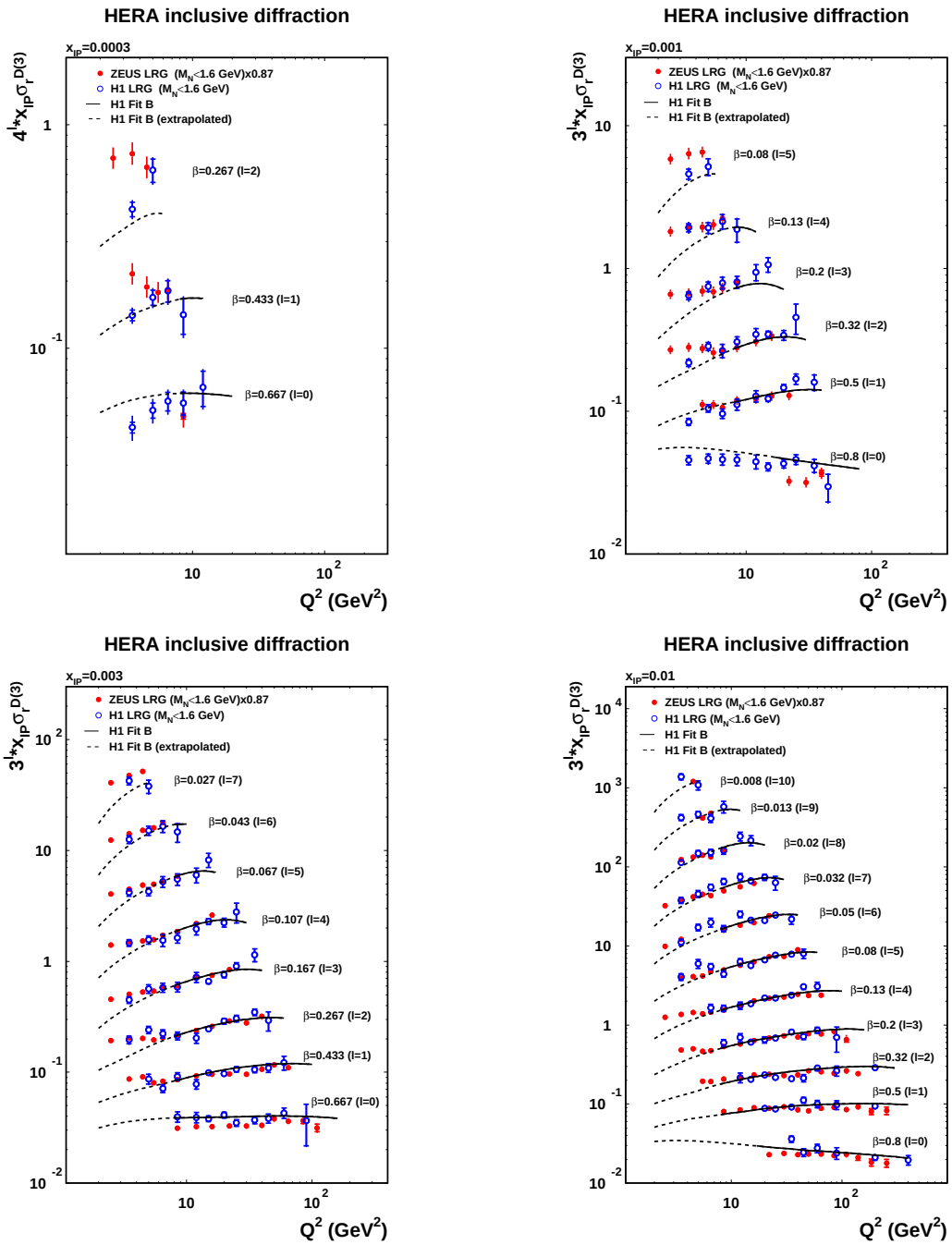

Fig. 7: Comparison between the H1 and ZEUS LRG measurements after correcting both data sets to $M_N < 1.6$ GeV and applying a further scale factor of 0.87 (corresponding to the average normalisation difference) to the ZEUS data. The measurements are compared with the results of the 'H1 Fit B' DPDF extraction, which was based on the H1 data shown. Further H1 data at $x_{\mathbb{P}} = 0.03$ are not shown.

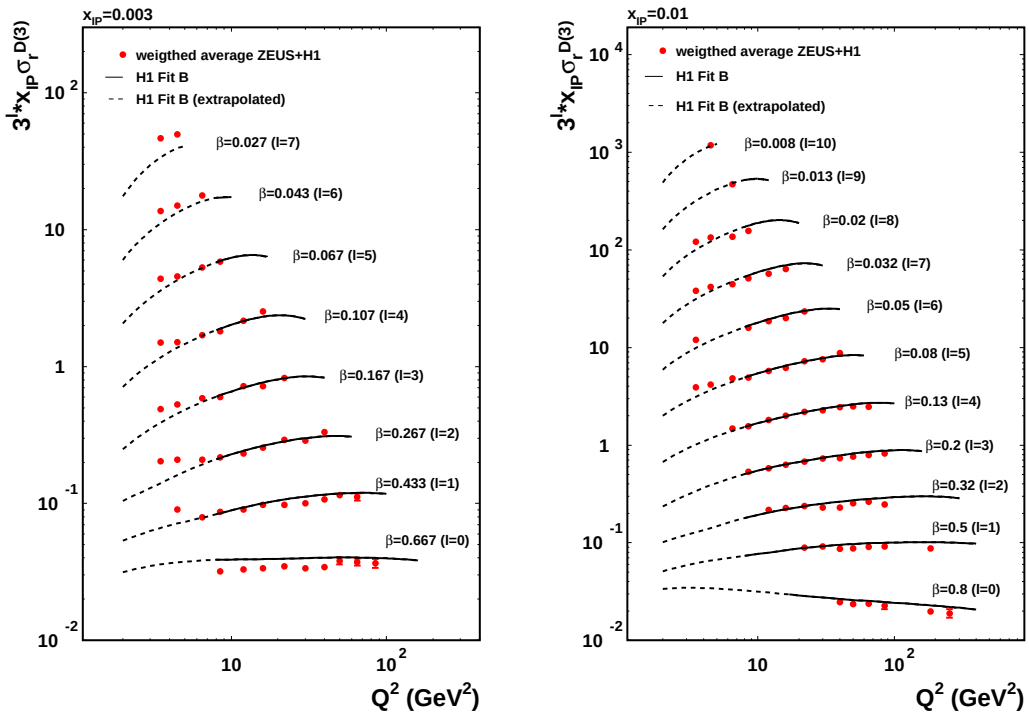

Fig. 8: Combination of the H1 and ZEUS LRG data following the procedure described in the text. The global normalisation is fixed to that of the H1 measurement, in order most easily to compare the data with the 'H1 Fit B' DPDF results.

two collaborations give compatible results on the proton dissociation contributions in the raw LRG selections. There is a global normalisation difference at the 13% level between the LRG measurements of the two experiments, which is a little beyond one standard deviation in the combined normalisation uncertainty. A similar difference is visible between the normalisations of the H1 and ZEUS proton tagged data.

A first step has been taken towards combining the two sets of LRG data, by arbitrarily fixing the normalisation to that of the H1 data set and ignoring correlations within the systematic uncertainties in obtaining weighted averages. The results hint at the precision which might be obtained in the future with a more complete procedure.

References

[1] ZEUS Collaboration, M. Derrick et al., Phys. Lett. **B 315**, 481 (1993).

[2] H1 Collaboration, T. Ahmed et al., Nucl. Phys. **B 429**, 477 (1994).

[3] P.D.B. Collins, *An Introduction to Regge Theory and High Energy Physics*. Cambridge University Press, Cambridge, 1977.

[4] M. Arneodo and M. Diehl, Procedings of the First HERA-LHC Workshop, eds. de Roeck, Jung, CERN-2005-014, hep-ph/0511047.

[5] H1 Collaboration, C. Adloff et al., Z. Phys. **C 76**, 613 (1997).

[6] ZEUS Collaboration, S. Chekanov et al., Eur. Phys. J. **C 38**, 43 (2004).

[7] A. Martin, M. Ryskin, G. Watt, Eur. Phys. J. **C 44**, 69 (2005).

[8] H1 Collaboration, A. Aktas et al., Eur. Phys. J. **C 48**, 715 (2006).

[9] H1 Collaboration, A. Aktas et al., JHEP 0710:042 (2007).

[10] FP420 R&D Collaboration, hep-ex/0806.0302 (2008).

[11] ZEUS Collaboration, J. Breitweg et al., Eur. Phys. J. **C 1**, 81 (1997).

[12] H1 Collaboration, C. Adloff et al., Eur. Phys. J. **C 6**, 587 (1999).

[13] ZEUS Collaboration, S. Chekanov et al., Eur. Phys. J. **C 25**, 169 (2002).

[14] H1 Collaboration, A. Aktas et al., Eur. Phys. J. **C 48**, 749 (2006).

[15] ZEUS Collaboration, S. Chekanov et al., DESY 08-175, submitted to Nucl. Phys. **B**.

[16] H1 Collaboration, H1prelim-06-014 (presented at DIS2006, E. Sauvan).

[17] ZEUS Collaboration, S. Chekanov et al., Eur. Phys. J. **C 25**, 69 (2002).

[18] ZEUS Collaboration, S. Chekanov et al., Nucl. Phys. **B 713**, 3 (2005).

[19] ZEUS Collaboration, S. Chekanov et al., Nucl. Phys. **B 800**, 1 (2008).

[20] T. Sjöstrand, L. Lönnblad and S. Mrenna, hep-ph/0108264 (2001).

[21] H. Jung, Comput. Phys. Commun. **86**, 147 (1995).

[22] B. List and A. Mastroberardino, Proceedings of the Workshop on MC Generators for HERA Physics, p. 396 (1999).

[23] C. Johnson, *Ph.D. Thesis, University of Birmingham*. 2002.

[24] H. Lim, *Ph.D. Thesis, The Graduate School, Kyungpook National University, Taegu (Republic of Korea)*. Unpublished, 2002.

[25] A. Glazov, Proceedings of DIS 2005, Madison, USA, eds Smith, Dasu, (AIP 2005).

Diffractive Final States and Factorisation at HERA

W. Słomiński[a] *and Alice Valkárová*[b]
[a]M. Smoluchowski Institute of Physics, Jagellonian University, Kraków,
[b]Institute of Particle and Nuclear Physics, Faculty of Mathematics and Physics, Charles University, Praha

Abstract
The recent experimental data from the H1 and ZEUS collaborations at HERA collider for diffractive dijet production and open charm production in deep inelastic scattering and photoproduction are presented and compared to next-to-leading order (NLO) QCD predictions. While good agreement is found for dijets in DIS and open charm production (D^*) in both DIS and photoproduction, the dijet photoproduction data for jets with low transverse energy $E_{\rm T}$ of the leading jet are clearly overestimated by NLO predictions. The indication of the dependence of the suppression factor on $E_{\rm T}$ was found. Within large errors the same amount of suppression was observed in both direct and resolved enhanced regions.

1 Factorisation and diffractive parton distribution functions

Diffractive electron-proton interactions studied with the HERA collider allow us to investigate the proton diffractive structure. In this type of interactions the proton remains intact or dissociates into a low-mass state, while the photon dissociates into a hadronic state X, $\gamma^* p \to X p'$. The final proton p' and the hadronic state X are separated by a large rapidity gap (LRG). [1] The diffractive exchange (Pomeron), with the vacuum quantum numbers, carries away a fraction $x_{I\!P}$ of the initial proton longitudinal momentum and has virtuality $t = (p - p')^2$. The Regge phenomenology tells us that for small $|t|$ the diffractive cross section drops exponentially with t which allows us to integrate over t to cope with experimental setup when the final proton is not tagged.

The actual beam particles are electrons or positrons which emit photons in a wide range of virtualities Q^2. In general, the cross sections depend on both the proton and the photon structure.

For a highly virtual photon, *i.e.* the one we can consider point-like, the factorisation theorem holds [2], stating that the cross section is given in terms of the universal diffractive parton distributions (DPDFs) and hard partonic cross sections. A generic formula reads

$$\frac{d\sigma^{\gamma^* p}}{dx_{I\!P}\, d\beta\, dQ^2} \propto \sum_{k=g,q,\bar{q}} f_k^{\mathrm{D}(3)}\left(x_{I\!P}, Q^2\right) \otimes \hat{\sigma}^{\gamma^* k}\,, \tag{1}$$

where $\otimes$ denotes the convolution and DPDFs $f_k^{\mathrm{D}(3)}\left(x_{I\!P}, z, Q^2\right)$ are integrated over t. In the leading log (LO) approximation Eq. (1) simplifies to

$$\frac{d\sigma^{\gamma^* p}}{dx_{I\!P}\, d\beta\, dQ^2} \propto \sum_q e_q^2\, f_q^{\mathrm{D}(3)}\left(x_{I\!P}, \beta, Q^2\right)\,, \tag{2}$$

[1]For the definition of kinematics and variables see *e.g.* G. Watt's talk [1].

yielding the parton-model interpretation of β being fractional momentum of the quark struck by γ^*.

The factorisation (1) holds for the inclusive as well as non-inclusive processes provided Q^2 is high enough for the photon to remain point-like and for the higher twist corrections to be neglected. Applied to the inclusive diffractive DIS it allows us to extract the proton DPDFs from the data. Both H1 and ZEUS collaborations performed such fits, assuming the Regge factorisation for DPDFs [3],

$$f_k^{\mathrm{D}(3)}\left(x_{I\!P}, z, Q^2\right) = f_{I\!P}(x_{I\!P}) f_k^{I\!P}\left(z, Q^2\right) \tag{3}$$

with the Pomeron flux $f_{I\!P}(x_{I\!P})$ taken from the Regge phenomenology. In actual fits a small contribution from a secondary Reggeon was also taken into account — for details see [4–7].

A more elaborate approach not assuming Regge factorisation and taking into account higher twists and perturbative Pomeron contributions is discussed in [1, 8].

With DPDFs at hand, we can study some semi-inclusive processes. The topics summarized in the following include dijet and open charm (D^*) production in both DIS and photoproduction (PHP) regimes. As already stated, if factorisation is not spoiled by higher twist contributions, it should work equally well for the above mentioned processes in the DIS regime. Thus one can extract the DPDFs from inclusive data only and use them to predict the dijet and D^* production cross sections. Comparison to the data provides us with the information on the quality of the fit and pQCD calculations. Another approach is to use inclusive as well as dijet and/or charm production data to extract DPDFs. The reason for using the semi-inclusive data is that the inclusive DIS is known to be mainly sensitive to the quark content of the proton, *cf.* (2). Gluons enter the cross section only via scaling violations and higher order QCD corrections, resulting in a quite high uncertainty in the extracted f_g [6]. Both dijet and charm production are directly sensitive to f_g and can be used to better establish the diffractive gluon distribution. A combined fit using inclusive and dijet data is discussed in detail in [7, 9–11], while the one using inclusive and D^* production data is presented in [5].

The photoproduction regime is qualitatively different. Here the photon is (nearly) real and reveals its hadronic structure. The γp interaction has components analogous to the hadron-hadron scattering, at LO ascribed to the 'resolved' photon. In this case there is no theoretical reason for the factorisation and experimentally it is known to be badly broken in the $p\bar{p}$ diffractive dijet production [12]. This factorisation breaking is phenomenologically understood in terms of the rescattering (screening) effects [13, 14], which lead to a suppression of the cross section calculated assuming that both proton and photon PDFs factorise.

In order to investigate the amount of this suppression the NLO QCD calculations using factorisation assumption are confronted with the experimental results. In general the observed suppression is much smaller than in the $p\bar{p}$ case, which qualitatively agrees with theoretical expectations [13, 14]. For a small suppression (up to ca. 50%, as observed at HERA) the accuracy of theoretical predictions becomes an important factor. The actual uncertainties can easily reach the order of the measured effect.

The uncertainty inherent in the perturbative QCD calculations, is the amount of higher order contributions. A common method to qualify it, is to look at the renormalisation/factorisation

scale dependence (there should be none in the complete result). As shown in the figures below this scale dependence is strong, telling us that the higher order corrections are important[2]. The only way to resolve this issue is to go to higher pQCD orders (NNLO,...). There are, however, other uncertainties which are not shown in the plots. Let us discuss them briefly.

The fits to the inclusive DIS data are performed using the Fixed Flavour Number Scheme (FFNS) with three massless quarks and heavy charm and bottom treated as massive particles, not partons. On the contrary, the NLO calculations of the dijet production cross section take all flavours massless, as in the Variable Flavour Number Scheme. The both flavour schemes differ in the heavy quarks treatment and in the amount of gluons.

Gluon content of the Pomeron is poorly established by a fit to the inclusive DIS data only and both dijet and open charm production are very sensitive to gluons. In photoproduction about 80% of the cross section comes from γg subprocesses [15]. This ambiguity is, of course, smaller in the case of combined fits [5, 9].

All the above mentioned uncertainties, present in the assumed model of Regge factorisation and non-perturbative Pomeron, should be kept in mind when looking at experimental data compared to the NLO QCD predictions.

For a discussion on theoretical aspects of diffractive dijet photoproduction see the contribution of M. Klasen and G. Kramer to these proceedings.

2 Diffractive Dijet Production

Diffractive dijet production in DIS was analysed by both H1 and ZEUS collaborations in [9, 16, 17] and presented in [10, 11, 15, 18–20]. The data was taken during the HERA running periods 1996/97 and 1999/00. The kinematic range of the photon virtuality was $4 < Q^2 < 80\ \mathrm{GeV}^2$ (H1) and $5 < Q^2 < 100\ \mathrm{GeV}^2$ (ZEUS). The photon-proton CMS energy W was above $100\ \mathrm{GeV}$. Diffractive events were selected with the help of criteria of large rapidity gap (LRG) and the jets were identified using the longitudinally invariant inclusive k_T cluster algorithm [21] in the Breit frame. The transverse energies for leading and subleading jets were required to be $E^*_{\mathrm{T}1} > 5\ \mathrm{GeV}$ ($E^*_{\mathrm{T}1} > 5.5\ \mathrm{GeV}$ in [9]) and $E^*_{\mathrm{T}2} > 4\ \mathrm{GeV}$.

The experimental results are compared to the NLO predictions obtained with the DISENT [22] and NLOJET++ [23] codes using several DPDFs. The cross sections vs. $x_{I\!P}$ and $E^*_{\mathrm{T}1}$ depicted in Figure 1, show that the NLO predictions agree within errors with the data. We can conclude that the QCD factorisation for diffractive dijets holds as expected. Note, however, that the ZEUS data tend to lie about (10–20)% below the NLO predictions.

The diffractive photoproduction (DPHP) of dijets was analysed by both H1 [16] and ZEUS [24] collaborations. The H1 experiment analysed the data with tagged electron in the running period 1996/97. The kinematic region was taken the same as for the DIS dijets (except $Q^2 < 0.01\ \mathrm{GeV}^2$) with the purpose to study the double ratio of photoproduction/DIS cross sections. The ZEUS analysis of dijets in DPHP covers somewhat different kinematic region, main difference being higher transverse energies of leading and subleading jets satisfying $E_{\mathrm{T}1} > 7.5\ \mathrm{GeV}$, $E_{\mathrm{T}2} > 6.5\ \mathrm{GeV}$. In both experiments the jets were identified using

[2] Note that very small or no scale dependence is not a proof that the result is correct.

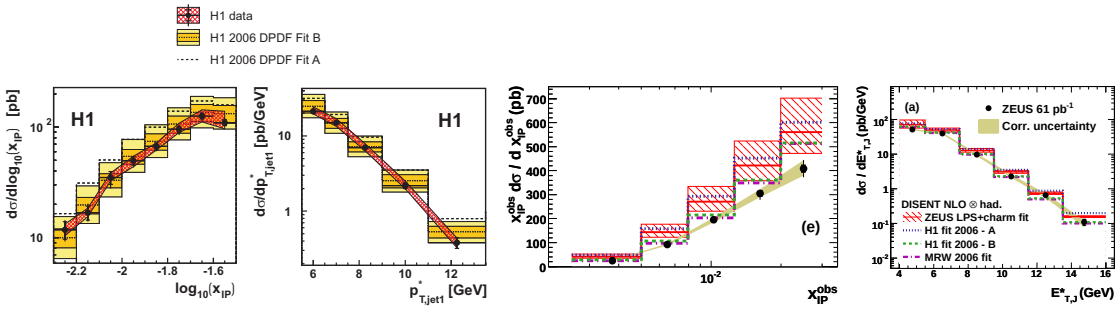

Fig. 1: Differential cross section for the diffractive production of dijets vs. $x_{I\!P}$ and E^*_{T1} as measured by H1 [9] (two left plots) and ZEUS [17] (two right plots). NLO predictions for several DPDFs parametrizations are also shown. The shaded bands show the uncertainty resulting from the variation of renormalization scale by factors 1/2 and 2.

the inclusive k_{T} cluster algorithm in the laboratory frame. For detailed discussion of the results see [10, 11, 15, 18, 19].

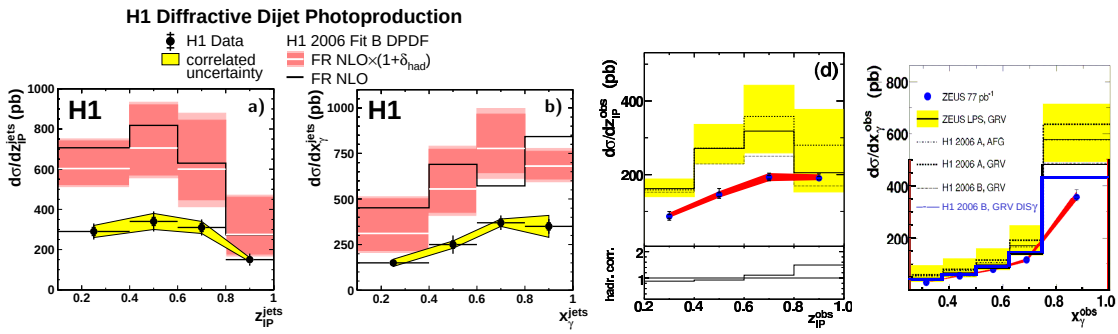

Fig. 2: Differential cross section for the diffractive photoproduction of dijets vs. $z_{I\!P}$ and x_γ as measured by H1 [16] (two left plots) and ZEUS [24] (two right plots). NLO predictions for several DPDFs parametrizations are also shown. The shaded bands show the uncertainty resulting from the variation of renormalization scale by factors 1/2 and 2.

The cross sections vs. $z_{I\!P}$ and x_γ are shown in Figure 2. The NLO QCD predictions were obtained using several DPDFs and photon PDFs parametrisations, and with two independent computer codes, one by Frixione and Ridolfi [25] and the other by Klasen and Kramer [26]. It was checked that both codes give the same results.

The H1 experiment observes a global suppression of NLO QCD predictions by factor 0.5. The ZEUS data are compatible with no suppression — the level of agreement with the NLO predictions is similar to the DIS case. However, 10–20% suppression is not excluded. Both experiments observe that the approach when only resolved photon part of the cross section is suppressed ($x_\gamma \lesssim 0.8$) is clearly disfavoured by data in contradiction with theoretical expectation of [14].

The difference between kinematic regions of both experiments lead us to a hypothesis that the suppression may depend on the E_{T} range of the jets [27]. Indeed, the cross section double ratio of data and NLO prediction for the diffractive PHP and DIS as a function of transverse

momentum E_{T} of the leading jet measured by H1, and the ratio of the ZEUS data cross section over the NLO predictions, indicate the rise with increasing E_{T}, as shown in Figure 3[3].

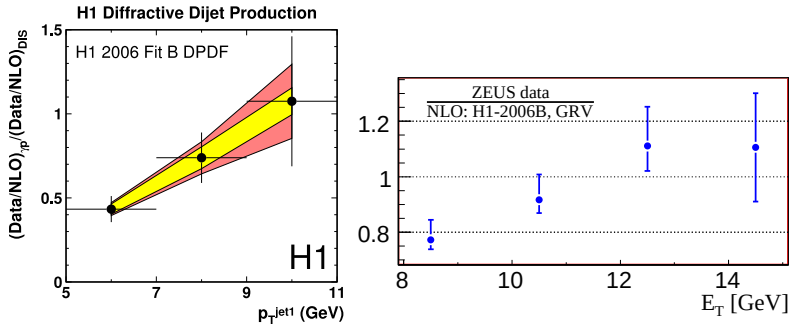

Fig. 3: Cross section double ratio of data to NLO prediction for photoproduction and DIS as a function of transverse momentum of the leading jet measured by H1 (left plot) and cross section ratio of data and NLO for the diffractive photoproduction of dijets vs. E_{T} of the leading jet as measured by ZEUS (right plot).

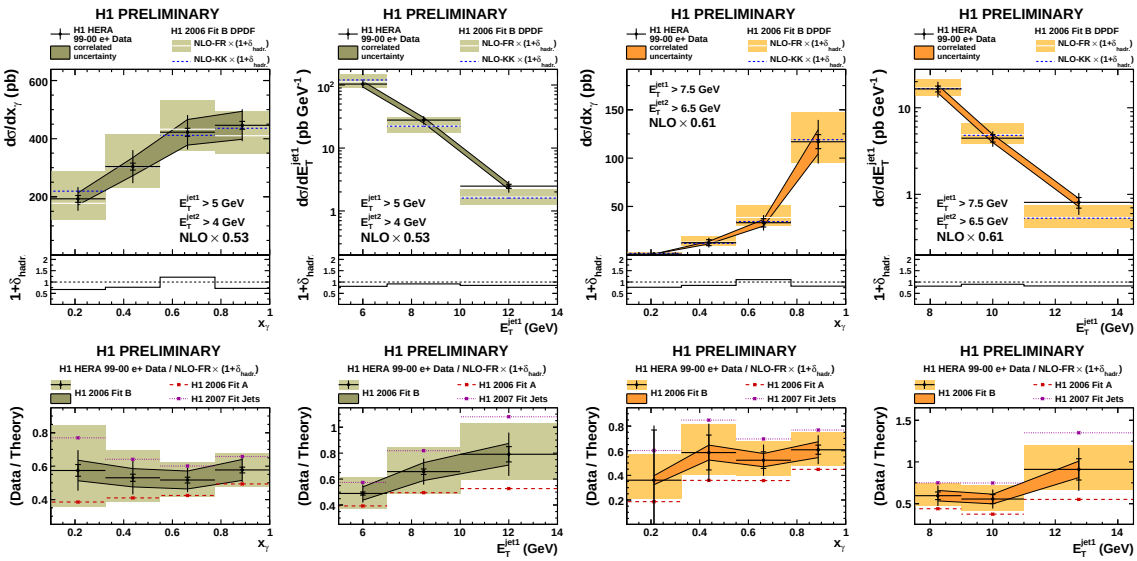

Fig. 4: Differential cross section for the diffractive photoproduction of dijets as a function of x_γ and E_{T1} for the lower E_{T} cut scenario (two left plots) and for the higher E_{T} cut scenario (two right plots), compared to NLO scaled calculations (upper plots). The lower plots show the corresponding ratios of the data to NLO calculated cross sections.

A detailed study of this issue was performed in the new H1 analysis of dijets in photoproduction [28]. The study was performed in two cut schemes. The first one identical to [16] with $E_{\mathrm{T1}} > 5$ GeV, to crosscheck results of previous analysis. The second one with all cuts as close as possible to the cuts used by ZEUS [24], $E_{\mathrm{T1}} > 7.5$ GeV, to check for a possible dependence of suppression on E_{T} of the jets. The results were compared to NLO calculations using three H1

[3] left plot derived from [16], thanks to S.Schaetzel

DPDFs — fits A,B and Jets. The best agreement of the shapes of measured cross sections was obtained with NLO predictions using fit B and scaled by factor 0.53 for low E_{T} cut scenario, and by factor 0.61 for high E_{T} cut scenario [28].

This measurement of the suppression factor together with the ZEUS results of 0.8–1 factor seem to support the idea of the E_{T}-dependent suppression.

As in the previous analyses no dependence of suppression on measured x_γ was observed, indicating that there is no evidence for the suppression of the resolved part only.

3 Open charm production in diffraction

Another semi-inclusive process analysed at HERA is the diffractive production of open charm observed in the reactions with D^* mesons production. Both DIS and PHP regimes have been studied and discussed during the workshop [18–20, 29, 30].

If QCD factorisation is fulfilled, NLO QCD calculations based on DPDFs measured in inclusive processes should be able to predict the production rates of such processes in shape and normalization.

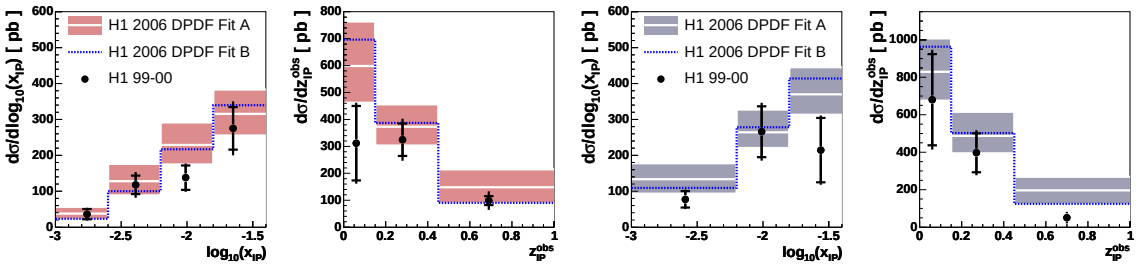

Fig. 5: Differential cross sections for diffractive D^* meson production as a function of $x_{I\!P}$ and $z_{I\!P}$ in DIS (two left plots) and photoproduction (two right plots).

The data from the HERA running period 1998–2000 were analysed by both H1 [31] and ZEUS [32] collaborations. The charm quark was tagged by the reconstruction of $D^{*\pm}(2010)$ meson in diffractive DIS and PHP regimes. H1 used also another method — based on the measurement of the displacement of tracks from primary vertex — to identify the D^* production in the sample of DIS events only.

The measurements were compared to the NLO QCD predictions using DPDFs from H1 and ZEUS fits. The calculations were performed using HVQDIS [33] for DIS and FMNR [34] for PHP. In Figure 5 the H1 results for the cross sections vs. $x_{I\!P}$ and $z_{I\!P}$ are shown. The recent ZEUS results for the diffractive $D^{*\pm}(2010)$ photoproduction are presented in Figure 6.

Within large errors a good agreement is observed, which supports the validity of QCD factorisation in both diffractive DIS and PHP. In particular no sizable suppression of the open charm photoproduction is seen, in contrast to the diffractive dijet case. A plausible explanation of this difference is that the resolved photon contribution to the D^* production is ca. 10% as compared to about 50% for the dijet diffractive PHP.

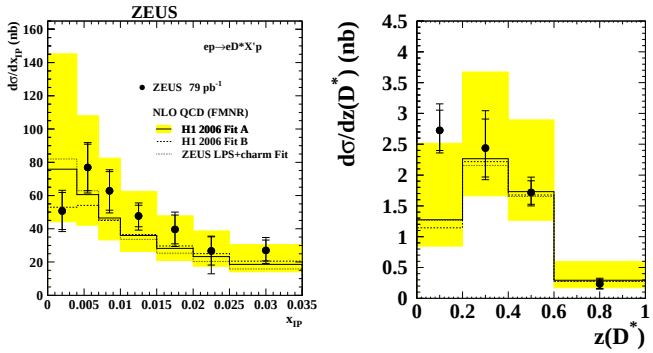

Fig. 6: Differential cross section for the diffractive photoproduction of $D^{*\pm}(2010)$ as a function of $x_{I\!P}$ and $z(D^*)$ compared to NLO predictions.

4 Summary

The factorisation issues were analyzed by H1 and ZEUS experiments studying the production of dijets and open charm in diffractive DIS and photoproduction. The factorisation was found to hold in the case of D^* production and dijet production in DIS. In dijet photoproduction factorisation breaking was observed. The indication was found that the suppression of the dijet photoproduction depends on the transverse momentum E_{T} of the leading jet. On the other hand, no dependence on measured x_γ was observed indicating the same order of suppression in the direct and resolved enhanced regions.

References

[1] G. Watt, *Theoretical uncertainties in diffractive parton densities*, in *2nd HERA and the LHC workshop*. 2006, available on `http://indico.cern.ch/conferenceDisplay.py?confId=1862`.

[2] J.C. Collins, Phys. Rev. **D57**, 3051 (1998). Erratum: *ibid.* **D61**, 019902 (2000).

[3] G. Ingelman and P.E. Schlein, Phys. Lett. **B152**, 256 (1985).

[4] H1 Coll., A. Aktas et al., Eur. Phys. J. **C48**, 715 (2006).

[5] ZEUS Coll., S. Chekanov et al., Eur. Phys. J. **C38**, 43 (2004).

[6] P. Newman, *H1 2006 diffractive parton densities*, in *3rd HERA and the LHC workshop*. 2007, available on `http://indico.cern.ch/conferenceDisplay.py?confId=11784`.

[7] M. Ruspa, *Inclusive diffraction in DIS*, in *4th HERA and the LHC workshop*. 2008, available on `http://indico.cern.ch/conferenceDisplay.py?confId=27458`.

[8] A.D. Martin, M.G. Ryskin and G. Watt, Eur. Phys. J. **C37**, 285 (2004).

[9] H1 Coll., A. Aktas et al., JHEP **10**, 042 (2007).

[10] M. Mozer, *Recent H1 results on jet production in diffractive DIS and photoproduction*, in *3rd HERA and the LHC workshop*. 2007, available on http://indico.cern.ch/conferenceDisplay.py?confId=11784.

[11] A. Valkarova, *Diffractive dijets at HERA*, in *4th HERA and the LHC workshop*. 2008, available on http://indico.cern.ch/conferenceDisplay.py?confId=27458.

[12] CDF Coll., A.A. Affolder et al., Phys. Rev. Lett. **84**, 5043 (2000).

[13] A. Bialas, Acta Phys. Polon. **B33**, 2635 (2002).

[14] A.B. Kaidalov, V.A. Khoze, A.D. Martin and M.G. Ryskin, Phys. Lett. **B567**, 61 (2003).

[15] W. Slominski, *Dijets in diffractive DIS and photoproduction*, in *XVI International Workshop on Deep Inelastic Scattering, DIS 2008*. April 2008, London, available on http://indico.cern.ch/conferenceDisplay.py?confId=24657. To be published in proceedings.

[16] H1 Coll., A. Aktas et al., Eur. Phys. J. **C51**, 549 (2007).

[17] ZEUS Coll., S. Chekanov et al., Eur. Phys. J. **C52**, 813 (2007).

[18] A. Bonato, *Diffractive final states at ZEUS*, in *2nd HERA and the LHC workshop*. 2006, available on http://indico.cern.ch/conferenceDisplay.py?confId=1862.

[19] R. Wolf, *Diffractive jets, charm and factorisation tests at H1*, in *2nd HERA and the LHC workshop*. 2006, available on http://indico.cern.ch/conferenceDisplay.py?confId=1862.

[20] I.-A. Melzer-Pellmann, *Diffractive dijet and D* production at ZEUS*, in *3rd HERA and the LHC workshop*. 2007, available on http://indico.cern.ch/conferenceDisplay.py?confId=11784.

[21] S.D. Ellis and D.E. Soper, Phys. Rev. **D48**, 3160 (1993).

[22] S. Catani and M.H. Seymour, Nucl. Phys. **B485**, 291 (1997). Erratum: *ibid.* **B510**, 503 (1998).

[23] Z. Nagy and Z. Trocsanyi, Phys. Rev. Lett. **87**, 082001 (2001).

[24] ZEUS Coll., S. Chekanov et al., Eur. Phys. J. **C55**, 177 (2008).

[25] S. Frixione, Z. Kunszt and A. Signer, Nucl. Phys. **B467**, 399 (1996).

[26] M. Klasen and G. Kramer, Eur. Phys. J. **C38**, 93 (2004).

[27] Y. Yamazaki, *Dijet production in diffractive DIS and photoproduction at ZEUS*, in *XV International Workshop on Deep Inelastic Scattering, DIS 2007*. 2007. Doi:10.3360/dis.2007.112.

[28] K. Cerny, *Dijets in diffractive photoproduction*, in *XVI International Workshop on Deep Inelastic Scattering, DIS 2008*. April 2008, London, available on `http://indico.cern.ch/conferenceDisplay.py?confId=24657`. To be published in proceedings.

[29] R. Wolf, *Diffractive open charm production at HERA*, in *3rd HERA and the LHC workshop*. 2007, available on `http://indico.cern.ch/conferenceDisplay.py?confId=11784`.

[30] A.W. Jung, *D* production in DIS and photoproduction at H1*, in *4th HERA and the LHC workshop*. 2008, available on `http://indico.cern.ch/conferenceDisplay.py?confId=27458`.

[31] H1 Coll., A. Aktas et al., Eur. Phys. J. **C50**, 1 (2007).

[32] ZEUS Coll., S. Chekanov et al., Nucl. Phys. **B672**, 3 (2003);
ZEUS Coll., S. Chekanov et al., Eur. Phys. J. **C51**, 301 (2007).

[33] B.W. Harris and J. Smith, Nucl. Phys. **B452**, 109 (1995);
L. Alvero, J.C. Collins and J.J. Whitmore, *Tests of factorization in diffractive charm production and double pomeron exchange*. Preprint hep-ph/9806340, 1998.

[34] S. Frixione, M.L. Mangano, P. Nason and G. Ridolfi, Phys. Lett. **B348**, 633 (1995);
S. Frixione, P. Nason and G. Ridolfi, Nucl. Phys. **B454**, 3 (1995).

Leading Baryon Production at HERA

William B. Schmidke[1] *and Armen Bunyatyan*[2] *(on behalf of the H1 and ZEUS collaborations)*
[1]MPI, Munich, [2]MPI, Heidelberg and Yerevan Physics Institute, Yerevan, Armenia

Abstract
Data from leading baryon production at HERA are presented and compared to models. Standard string fragmentation models alone do not describe the data; models including also baryon production via virtual meson exchange give a good description of the data. Exchange models accounting for absorption describe the Q^2 evolution of the data. In the exchange picture, leading neutron data are used to extract the pion structure function.

1 Introduction

Events with a baryon carrying a large fraction of the proton beam energy have been observed in ep scattering at HERA [1]. The dynamical mechanisms for their production are not completely understood. They may be the result of hadronization of the proton remnant, conserving baryon number in the final state. Exchange of virtual particles is also expected to contribute. In this picture, the target proton fluctuates into a virtual meson-baryon state. The virtual meson scatters with the projectile lepton, leaving the fast forward baryon in the final state. Leading neutron (LN) production occurs through the exchange of isovector particles, notably the π^+ meson. For leading proton (LP) production isoscalar exchange also contributes, including diffraction mediated by Pomeron exchange. In the exchange picture, the cross section for some process in ep scattering with e.g. LN production factorizes:

$$\sigma_{ep\to enX} = f_{\pi/p}(x_L, t) \cdot \sigma_{e\pi\to eX}.$$

Here $f_{\pi/p}$ is the flux of virtual pions in the proton, $x_L = E_n/E_p$ is the fraction of the proton beam energy carried by the neutron, and t is the virtuality of the exchanged pion.

The H1 and ZEUS experiments at HERA measured leading baryons in deep inelastic scattering and photoproduction events. Leading protons were measured with position sensitive detectors placed along the proton beam downstream of the interaction point. Leading neutrons were measured with lead-scintillator calorimeters at the zero-degree point after the proton beam was bent vertically; magnet apertures limited neutron detection to scattering angles less than 0.75 mrad.

2 Leading neutron production and models

Figure 1 shows the LN x_L distribution (left) and p_T^2 distributions in bins of x_L (right). The x_L distribution rises from lowest x_L because of the increasing p_T^2 range due to the angle limit, and then falls to zero at the kinematic limit $x_L = 1$. The p_T^2 distributions are well described by exponentials; thus the parameterization $d^2\sigma/dx_L dp_T^2 \propto a(x_L)\exp(-b(x_L)p_T^2)$ fully characterizes the two dimensional distribution.

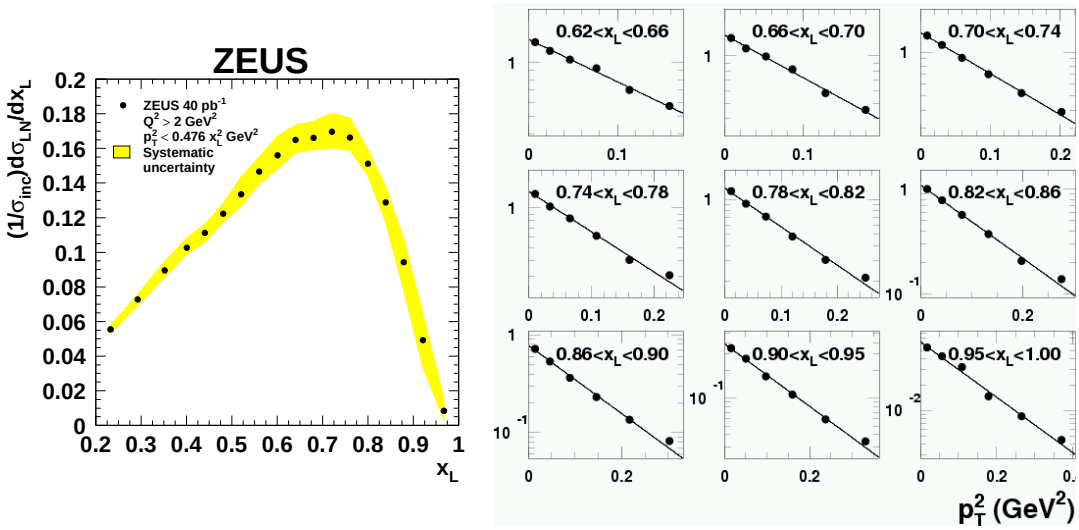

Fig. 1: Left: LN x_L distribution. Right: LN p_T^2 distributions in bins of x_L. The lines are the result of exponential fits.

The left side of Fig. 2 shows the LN x_L, intercept a and slope b distributions compared to several models. The standard fragmentation models implemented in RAPGAP and LEPTO do not describe the data, predicting too few neutrons, concentrated at lower x_L, and slopes too small and independent of x_L. The LEPTO model with soft color interactions gives a fair description of the x_L distribution and overall rate, but also fails to describe the slopes. The RAPGAP model mixing standard fragmentation and pion exchange gives a better description of the shape of the x_L distribution, and also predicts the rise of the slopes with x_L, although both with too high values. The right side of Fig. 2 shows the x_L distribution with an optimized mixture of standard fragmentation and pion exchange; the agreement with the data is very good.

3 Leading proton production and models

Figure 3 shows the x_L distribution for leading protons and neutrons in the same p_T range. If LP production proceeded only through isovector exchange, as LN production must, there should be half as many LP and LN. The data instead has approximately twice as many LP as LN. Thus, exchanges of particles with different isospins such as isoscalars must be invoked for LP production.

The left side of Fig. 4 shows a comparison of the LP x_L distributions and p_T^2 exponential slopes b to the DJANGOH and RAPGAP Monte Carlo models incorporating standard fragmentation or soft color interactions, none of which describe the data. The right side of Fig. 4 shows a comparison to a model including exchange of both isovector and isoscalar particles, including the Pomeron for diffraction [2]. These exchanges combine to give a good description of the the x_L distribution and slopes.

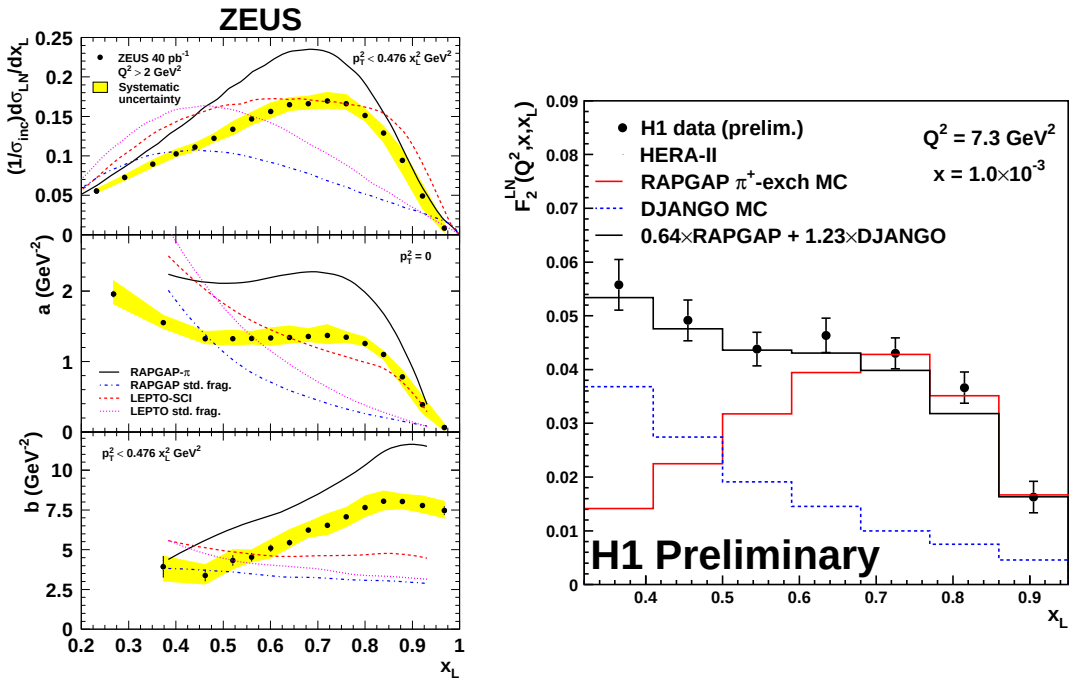

Fig. 2: Left: LN x_L, intercept and slope distributions compared to models. Right: LN x_L distribution with an optimized mixture of exchange and fragmentation models.

4 Absorption of leading neutrons

The evidence for particle exchange in leading baryon production motivates further investigation of the model. One refinement of the simple picture described in the introduction is absorption, or rescattering [3]. In this process, the virtual baryon also scatters with the projectile lepton. The baryon may migrate to lower x_L or higher p_T such that it is outside of the detector acceptance, resulting in a relative depletion of observed forward baryons. The probability of this should increase with the size of the exchanged photon. The size of the photon is inversely related to its virtuality Q^2, so the amount of absorption should increase with decreasing Q^2.

The left side of Fig. 5 shows the LN x_L spectra for photoproduction ($Q^2 \sim 0$) and three bins of increasing Q^2. The yield of LN increases monotonically with Q^2, in agreement with the expectation of the decrease of loss through absorption as Q^2 rises. The right side of Fig. 5 shows photoproduction data with two predictions from models of exchange with absorption [4]. The dashed curve model incorporates pion exchange with absorption, accounting also for the migration in x_L and p_T of the neutron. The solid curve model include the same effects, adding also exchange of ρ and a_2 mesons. Both models give a good description of the large depletion of LN in photoproduction relative to DIS seen in the left side of the figure.

5 Pion structure function

Analogous to the inclusive proton structure function $F_2(Q^2, x)$, one can define an LN tagged semi-inclusive structure function $F_2^{LN}(Q^2, x, x_L)$, including also the dependence on the LN

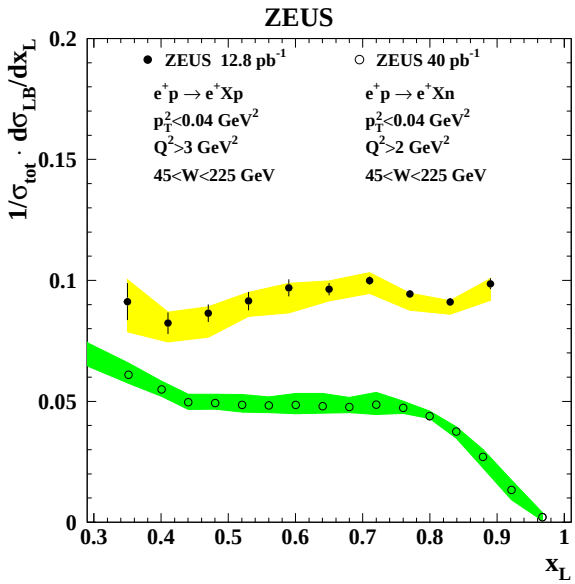

Fig. 3: LP and LN x_L distributions for $p_T^2 < 0.04$ GeV^2.

energy. The left side of Fig. 6 shows the ratios F_2^{LN}/F_2 as a function of Q^2 in bins of x and x_L. Here F_2^{LN} are the measured values from LN production in DIS and the values of F_2 are obtained from the H1-2000 parameterization [5]. For fixed x_L the ratios are almost flat for all (x, Q^2) implying that F_2^{LN} and F_2 have a similar (x, Q^2) behavior. This result suggests the validity of factorization, i.e. independence of the photon and the proton vertices. The statistical precision of the data precludes sensitivity to absorptive effects as discussed in the previous section.

Based on the assumption that at high x_L LN production is dominated by the pion exchange mechanism, the measurement of F_2^{LN} can provide important information about the pion structure. The quark and gluon distributions of the pion have previously been constrained using Drell–Yan and direct photon production data obtained by πp scattering experiments and are limited to high x values $x > 0.1$.

Using the measurement of $F_2^{LN(3)}$ for $0.68 < x_L < 0.77$, and the integral over t of the pion flux factor at the center of this x_L range, $\Gamma_\pi = \int f_{\pi/p}\, dt = 0.131$, one can estimate the pion structure function at low Bjorken–x. Assuming that the Regge model of leading neutron production is valid, the quantity $F_2^{LN(3)}/\Gamma_\pi$ can be associated to the structure function of the pion. The right side of Fig. 6 shows $F_2^{LN(3)}/\Gamma_\pi$ as a function of $\beta = x/(1 - x_L)$ for fixed values of Q^2. The results are consistent with a previous ZEUS measurement [6], where two extreme choices of the pion flux were used to extract F_2^π. The data are compared to predictions of parameterizations of the pion structure function [7]. The measurements are also compared to the H1-2000 parameterization of the proton structure function [5] which is multiplied by the factor 2/3 according to naive expectation based on the number of valence quarks in the pion and proton respectively. The distributions show a steep rise with decreasing β, in accordance with the

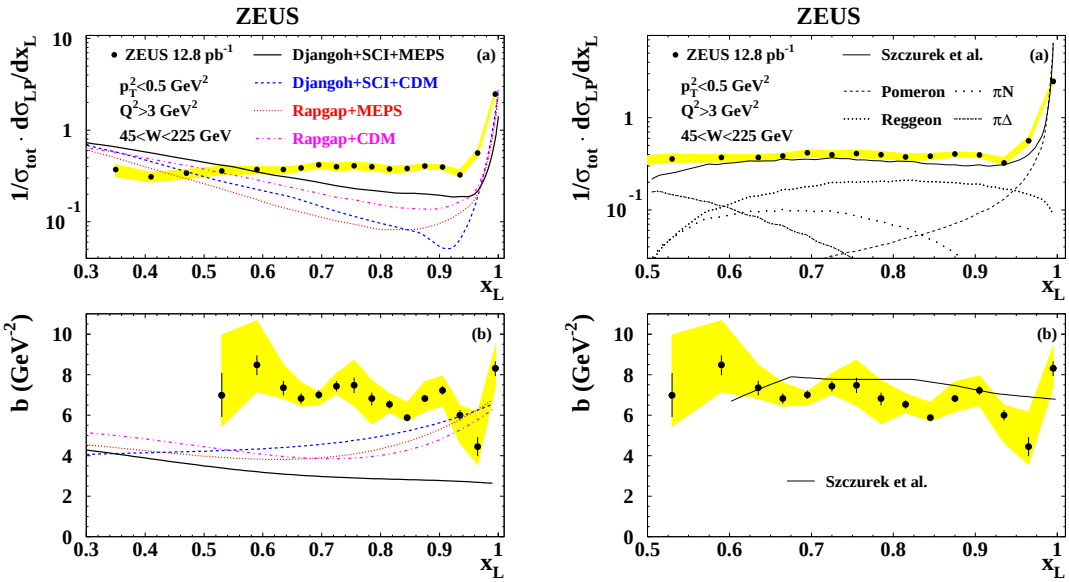

Fig. 4: Left: LP x_L distribution and exponential slopes compared to standard fragmentation models. Right: LP x_L distribution and exponential slopes compared to a model incorporating isoscalar and isovector exchanges.

pion and the proton structure function parameterizations. The scaled proton structure function gives the best description of the data. In absolute values, the presented data are slightly below the expectations, suggesting that additional phenomena, like absorption, may play a role.

References

[1] ZEUS Coll., S. Chekanov et al., Nucl. Phys. **B 776**, 1 (2007);
H1 Coll., contribution to ICHEP-08, H1prelim-08-111;
ZEUS Coll., *Leading proton production in deep inelastic scattering at HERA*, to be published;
and refernces cited therein.

[2] A. Szczurek, N.N. Nikolaev and J. Speth, Phys. Lett. **B 428**, 383 (1998).

[3] N.N. Nikolaev, J. Speth and B.G. Zakharov, Preprint KFA-IKP(TH)-1997-17 (hep-ph/9708290) (1997);
U. D'Alesio and H.J. Pirner, Eur. Phys. J. **A 7**, 109 (2000).

[4] V.A. Khoze, A.D. Martin and M.G. Ryskin, Eur. Phys. J. **C 48**, 797 (2006).

[5] H1 Coll., C. Adloff et al., Eur. Phys. J. **C 21**, 33 (2001).

[6] ZEUS Coll., S. Chekanov et al., Nucl. Phys. **B 637**, 3 (2002).

[7] P. Aurenche et al., Phys. Lett. **B 233**, 517 (1989);
M. Glück, E. Reya and I. Schienbein, Eur. Phys. J. **C 10**, 313 (1999).

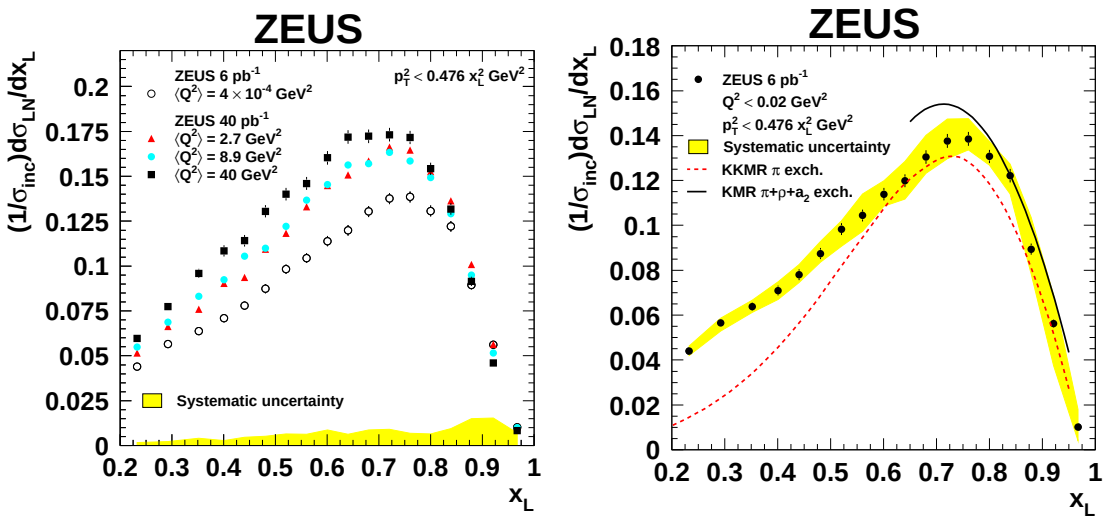

Fig. 5: Left: LN x_L distributions for photoproduction and three bins of Q^2 in DIS. Right: LN x_L distributions for photoproduction compared to exchange models including absorptive effects.

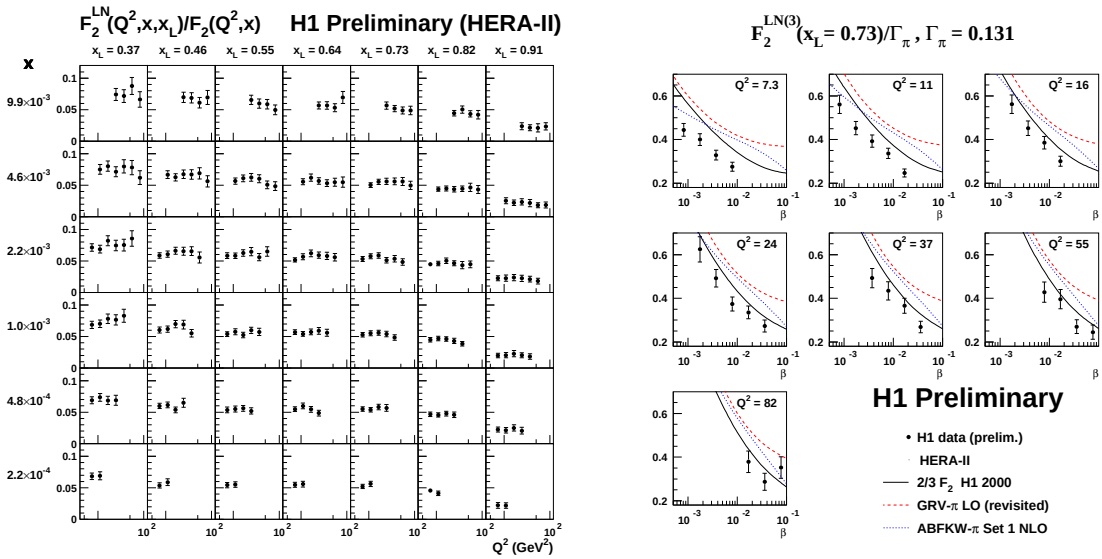

Fig. 6: Left: Ratio of semi-inclusive LN to inclusive structure functions as a function of Q^2 in bins of x and x_L. Right: Extracted pion structure function as a function of $\beta = x/(1 - x_L)$ in bins of Q^2. The curves are the proton structure function scaled by 2/3 and two parameterizations based on Drell-Yan and direct photon production data.

Exclusive Vector Meson Production and Deeply Virtual Compton Scattering at HERA

Alessia Bruni[1], *Xavier Janssen*[2], *Pierre Marage*[2]
[1] Istituto Nazionale di Fisica Nucleare, Via Irnerio 46, I-40126 Bologna, Italy
[2] Faculty of Science, Université Libre de Bruxelles, Bd. du Triomphe, B-1040 Brussels, Belgium

Abstract
Exclusive vector meson production and deeply virtual Compton scattering are ideally suited reactions for studying the structure of the proton and the transition from soft to hard processes. The main experimental data obtained at HERA are summarised and presented in the light of QCD approaches.

1 Introduction

The two processes which are the object of the present report, the exclusive production of a vector meson (VM) of mass M_V, $e+p \to e+VM+Y$, and deeply virtual Compton scattering (DVCS), $e+p \to e+\gamma+Y$, where Y is a proton (elastic scattering) or a diffractively excited system (proton dissociation), are characterised in Fig. 1. The kinematical variables are Q^2, the negative square of the photon four-momentum, W the photon-proton centre of mass energy ($W^2 \simeq Q^2\,(1/x-1)$, x being the Bjorken scaling variable) and t, the square of the four-momentum transfer at the proton vertex.

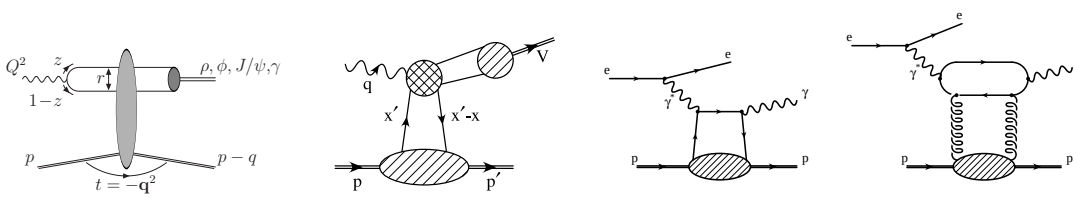

Fig. 1: (from left to right) Representative diagrams of a) low x dipole approach and b) GPD approach, for VM production; c) LO scattering and d) two gluon exchange, for the DVCS process.

The H1 and ZEUS collaborations at HERA have studied the elastic and proton dissociative production of ρ [1–4], ω [5], ϕ [3,6], J/ψ [7,8], $\psi(2s)$ [9] and Υ [10,11] mesons, and the DVCS process in the elastic channel [12, 13]. The measurements are performed in the low x, large W domain $10^{-4} \lesssim x \lesssim 10^{-2}$, $30 \leq W \leq 300$ GeV. They cover photoproduction ($Q^2 \simeq 0$), with $|t|$ values up to 30 GeV^2, and electroproduction in the deep inelastic (DIS) domain ($2 \leq Q^2 \leq 90\ \mathrm{GeV}^2$) with $|t| \lesssim 2\ \mathrm{GeV}^2$. The cross sections, expressed in terms of $\gamma^* p$ scattering, are measured differentially in Q^2, W and t. The measurement of angular distributions gives access to spin density matrix elements and polarised amplitudes.

1.1 Production mechanisms

Within the QCD formalism, two main complementary approaches are used to describe VM production and DVCS: dipole factorisation and collinear factorisation.

Dipole approach of VM production At high energy, i.e. small x, VM production can be described in the proton rest frame with three factorising contributions [14] (see Fig. 1a): the fluctuation of the virtual photon into a $q\bar{q}$ colour dipole, the elastic or proton dissociative dipole–proton scattering, and the $q\bar{q}$ recombination into the final state VM. The dipole–proton cross section is expected to be flavour independent and governed by the transverse size of the dipole. Light VM photoproduction is dominated by large dipoles, leading to large interaction cross sections with the incoming proton, similar to soft hadron–hadron interactions. In contrast, heavy VM production and large Q^2 processes are dominated by small dipoles, with smaller cross sections implied in QCD by colour transparency, the quark and the antiquark separated by a small distance tending to screen each other's colour.

The cross section for VM production can be computed at small x and for all Q^2 values through models [15–17] using universal dipole–proton cross sections measured in inclusive processes, possibly including saturation effects [18] (see also [19]). This formalism thus connects the inclusive and diffractive cross sections, also in the absence of a hard scale.

In the presence of a hard scale (large quark mass or Q), the dipole–proton scattering is modelled in perturbative QCD (pQCD) as the exchange of a colour singlet system consisting of a gluon pair (at lowest order) or a BFKL ladder (at leading logarithm approximation, LL $1/x$). At these approximations, the cross sections are proportional to the square of the gluon density $|xG(x)|^2$ in the proton [20]. The pQCD calculations [21–24] use k_t-unintegrated gluon distributions (see also [25]). The typical interaction scale is $\mu^2 \simeq z(1-z)(Q^2+M_V^2)$, where z is the fraction of the photon longitudinal momentum carried by the quark. For heavy VM (in the non-relativistic wave function (WF) approximation) and for light VM production from longitudinally polarised photons, $z \simeq 1/2$ and the cross sections are expected to scale with the variable $\mu^2 = (Q^2+M_V^2)/4$. In contrast, for light VM production by transversely polarised photons, contributions with $z \to 0,1$ result in the presence of large dipoles and the damping of the scale μ, thus introducing non-perturbative features even for non-small Q^2.

Collinear factorisation and GPD In a complementary approach (see Fig. 1b), a collinear factorisation theorem [26] has been proven in QCD for longitudinal amplitudes in the DIS domain, which does not require low x values. This allows separating contributions from different scales, a large scale at the photon vertex, provided by the photon virtuality Q (or the quark mass), and a small scale for the proton structure. The latter is described by Generalised Parton Distributions (GPD – see e.g. the reviews [27]), which take into account the distribution of transverse momenta of partons with respect to the proton direction and longitudinal momentum correlations between partons. They account for "off-diagonal" or "skewing" effects arising from the kinematic matching between the initial state (virtual) photon and the final state, VM or real photon for DVCS. GPD calculations have been performed for light VM electroproduction [28]. NLO corrections to light VM electroproduction and to heavy VM photoproduction have been computed [29].

DVCS Following collinear factorisation, the DVCS process is described at LO by Fig. 1c, where the virtual photon couples directly to a quark in the proton. QCD calculations at the scale $\mu^2 = Q^2$ involve GPD distributions [30, 31]. At higher order, two gluon exchange as in Fig. 1d gives also an important contribution at HERA. Joint fits to DVCS and inclusive structure functions data have been used to extract GPD distributions [32].

Large $|t|$ production Calculations for VM production at large $|t|$ have been performed both in a DGLAP and in a BFKL approach (see section 6).

1.2 Measurements at HERA

Vector mesons are identified by H1 and ZEUS via their decay to two oppositely charged particles $\rho \to \pi^+\pi^-$, $\phi \to K^+K^-$, $J/\psi \to e^+e^-, \mu^+\mu^-$ and $\Upsilon \to \mu^+\mu^-$. The kinematic variables are reconstructed from the scattered electron and decay particle measurements. Forward calorimeters and taggers at small angles are generally used to separate elastic and proton dissociative events. The scattered proton is also measured in forward proton spectrometers, with an acceptance of a few %, allowing the selection of a purely elastic sample and the direct measurement of the t variable.

VM production has been investigated mainly using the HERA I data, collected between 1992 and 2000 and corresponding to an integrated luminosity of $\simeq 150$ pb^{-1} for both collaborations. The integrated luminosity of 500 pb^{-1} collected at HERA II (2003-2007) has been analysed so far for DVCS [13] and Υ [11]. For HERA II, ZEUS has installed a microvertex detector but has removed the small angle detectors: the leading proton spectrometer and the forward and rear calorimeters, compromising the precise analysis of diffractive data. The HERA II analyses of H1 will benefit of the fast track trigger installed in 2002 and, for general diffraction studies, of the very forward proton spectrometer VFPS installed in 2003, which however has very limited acceptance for VM.

2 From soft to hard diffraction: t dependences and the size of the interaction

The t dependences of DVCS and VM production provide information on the size and the dynamics of the processes and on the scales relevant for the dominance of perturbative, hard effects. Whereas total cross sections (F_2 measurements) are related, through the optical theorem, to the scattering amplitudes in the forward direction, diffractive final states provide a unique opportunity to study the region of non-zero momentum transfer t. This gives indirect information on the variable conjugate to t, the transverse size of the interaction.

For $|t| \lesssim 1-2$ GeV^2, the $|t|$ distributions are exponentially falling with slopes b: $\mathrm{d}\sigma/\mathrm{dt} \propto \mathrm{e}^{-\mathrm{b}|\mathrm{t}|}$. In an optical model approach, the diffractive b slope is given by the convolution of the transverse sizes of the interacting objects: $b = b_{q\bar{q}} + b_Y + b_{I\!P}$, with contributions of the $q\bar{q}$ dipole, of the diffractively scattered system (the proton or the excited system Y) and of the exchange ("Pomeron") system. Neglecting effects related to differences in the WF, universal b slopes are thus expected for all VM with the same $q\bar{q}$ dipole sizes, i.e. with the same values of the scale $\mu^2 = (Q^2 + M_V^2)/4$. Conversely, elastic and proton dissociative slopes are expected to differ for all VM production at the same scale by the same amount, $b_p - b_Y$. Measurements of elastic and

proton dissociative b slopes for DVCS and VM production are presented in Fig. 2 as a function of the scale μ [1].

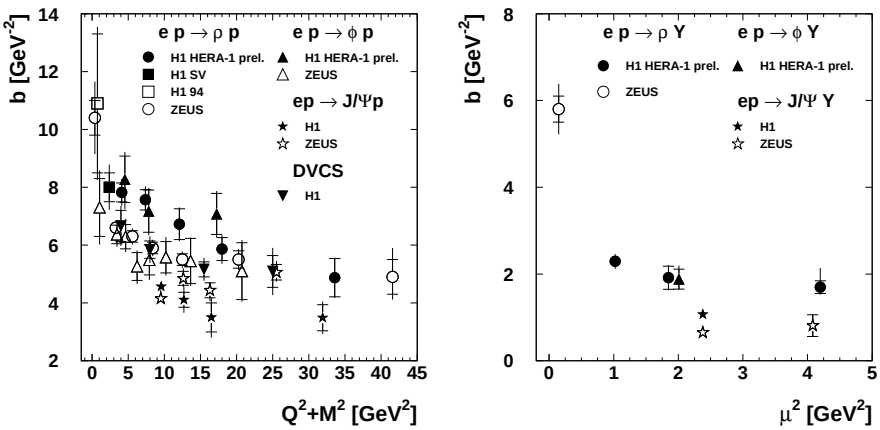

Fig. 2: Measurement of (left) the elastic and (right) the proton dissociative slopes b of the exponential t distributions, as a function of the scale $\mu^2 = (Q^2+M_V^2)/4$ for VM production and $\mu^2 = Q^2$ for DVCS.

For J/ψ elastic production, the b slope is $\lesssim 4.5$ GeV^{-2}, with no visible Q^2 dependence. This value may be related to the proton form factor [16]. For proton dissociation, the b slope is below 1 GeV^{-2}, putting an upper limit to the transverse size of the exchange (with the assumption that $b_Y \simeq 0$ for proton dissociation).

At variance with J/ψ production, which is understood as a hard process already in photoproduction, a strong decrease of b slopes for increasing values of $\mu^2 = (Q^2+M_V^2)/4$ is observed for light VM production, both in elastic and proton dissociative scattering. A similar scale dependence is observed for DVCS. This is consistent with a shrinkage of the size of the initial state object with increasing Q^2, i.e. in the VM case a shrinkage of the colour dipole. It should however be noted that, both in elastic and proton dissociative scatterings, b slopes for light VM remain larger than for J/ψ when compared at the same values of the scale $(Q^2+M_V^2)/4$ up to $\gtrsim 5$ GeV^2. The purely perturbative domain may thus require larger scale values.

3 From soft to hard diffraction: W dependences vs. mass and Q^2

Figure 3-left presents measurements as a function of W of the total photoproduction cross section and of the exclusive photoproduction cross sections of several VM; ρ electroproduction cross sections for several values of Q^2 are shown in Fig. 3-right. As expected for decreasing dipole sizes, the cross sections at fixed values of W decrease significantly with increasing VM mass or Q^2. In

[1] Differences between the H1 and ZEUS measurements for elastic scattering are due to differences in background subtraction. The major effect is due to the subtraction of ρ' production by H1, a contribution evaluated to be negligible by ZEUS. Another difference concerns the values used for the b slopes of the proton dissociative contamination.

addition, different reactions exhibit strongly different W dependences. The total photoproduction cross section and the photoproduction of light VM show weak energy dependences, typical of soft, hadron–hadron processes. In contrast, increasingly steep W dependences are observed with increasing mass or Q^2. In detail, the W dependences are investigated using a parameterisation inspired by Regge theory, in the form of a power law with a linear parameterisation of the effective trajectory

$$\sigma \propto W^{\delta}, \quad \delta = 4\,(\alpha_{I\!P} - 1), \quad \alpha_{I\!P}(t) = \alpha_{I\!P}(0) + \alpha' \cdot t. \tag{1}$$

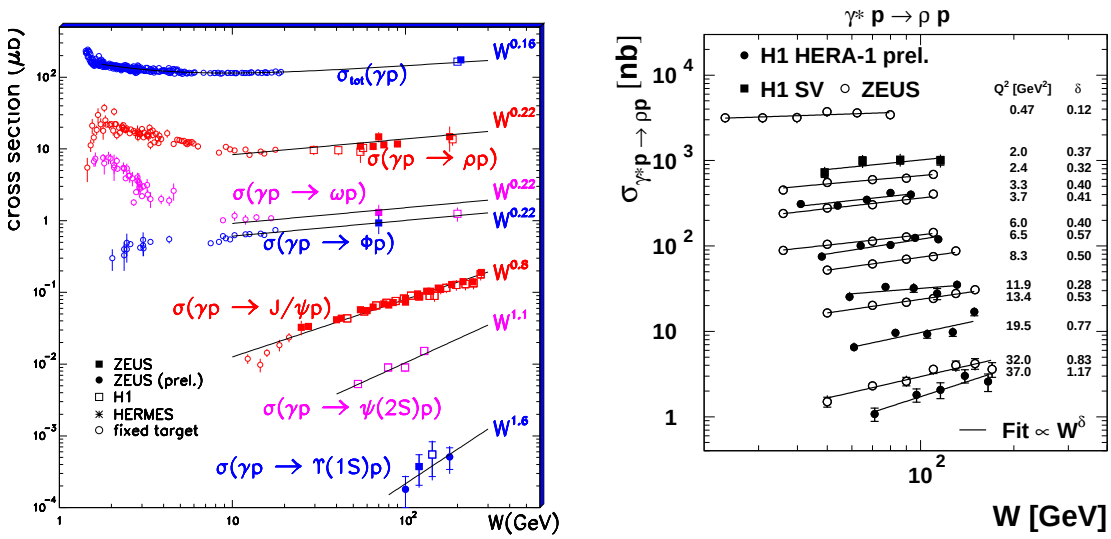

Fig. 3: W dependences of (left) total and VM photoproduction cross sections; (right) ρ electroproduction for several values of Q^2. The lines show fits to the form W^{δ}.

The intercept $\alpha_{I\!P}(0)$ of the effective trajectory quantifies the energy dependence of the reaction for $t = 0$. The evolution of $\alpha_{I\!P}(0)$ with μ^2 is shown in Fig. 4-left. Light VM production at small μ^2 gives values of $\alpha_{I\!P}(0) \lesssim 1.1$, similar to those measured for soft hadron–hadron interactions [33]. In contrast larger values, $\alpha_{I\!P}(0) \gtrsim 1.2$, are observed for DVCS, for light VM at large Q^2 and for heavy VM at all Q^2. This increase is related to the large parton densities in the proton at small x, which are resolved in the presence of a hard scale: the W dependences of the cross section is governed by the hard $x^{-\lambda}$ evolution of the gluon distribution, with $\lambda \simeq 0.2$ for $Q^2 \simeq M^2_{J/\psi}$. The W dependences of VM cross sections, measured for different Q^2 values, are reasonably well described by pQCD models (not shown). In detail these are however sensitive to assumptions on the imput gluon densities in the domain $10^{-4} \lesssim x \lesssim 10^{-2}$ which is poorly constrained by inclusive data [25, 34].

The slope α' in eq. (1) describes the correlation between the t and W dependences of the cross section. The measurement of the evolution with t of the δ exponent can be parameterised as a W dependence of the b slopes, with $b = b_0 + 4\alpha' \ln W/W_0$. In hadron–hadron scattering,

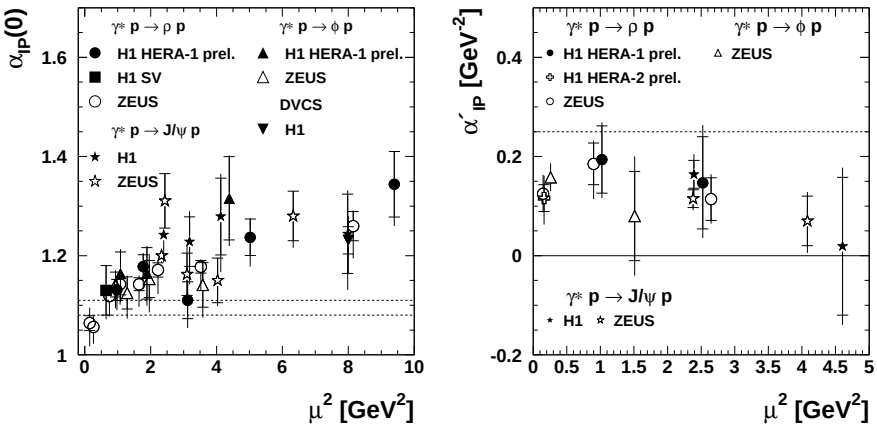

Fig. 4: Values of (left) the intercept $\alpha_{I\!P}(0)$ and (right) the slope α' of the effective Pomeron trajectory, obtained from fits of the W cross section dependences to the form $d\sigma/dt \propto W^{4(\alpha_{I\!P}(0)+\alpha' \cdot t-1)}$. The scales are $\mu^2 = Q^2$ for DVCS and $\mu^2 = (Q^2+M_V^2)/4$ for VM production. The dotted lines represent typical values for hadron–hadron scattering.

positive values of α' are measured, with $\alpha' \simeq 0.25$ GeV^{-2} [35]. This shrinkage of the diffractive peak indicates the expansion with energy of the size of the interacting system, i.e. the expansion of the gluon cloud in the periphery of the interaction. HERA measurements are presented in Fig. 4-right. The values of α' are positive and appear smaller than in hadron–hadron interactions, also for ρ photoproduction. This suggests a limited expansion of the systems considered here on the relevant interaction time scale. In a BFKL approach, α' is related to the average k_t of gluons around the ladder in their random walk, and is expected to be small [36].

4 Q^2 dependences in DVCS and VM production

The description of the Q^2 dependences of the cross sections is a challenge, in view of the presence of higher order corrections and of non-perturbative effects, especially for transverse VM production.

4.1 DVCS

The DVCS cross section depends on the proton GPD distributions. To investigate the dynamical effects due to QCD evolution, the Q^2 dependence has been measured and studied [13] as a function of the dimensionless scaled variable S,

$$S = \sqrt{\sigma_{DVCS}\, Q^4\, b(Q^2)\, /\, (1+\rho^2)},$$

which removes the effects of the photon propagator and of the Q^2 dependence of the b slope, and of the ratio R of the imaginary parts of the DVCS and DIS amplitudes,

$$R = \frac{\mathcal{I}mA(\gamma^* p \to \gamma p)_{t=0}}{\mathcal{I}mA(\gamma^* p \to \gamma^* p)_{t=0}} = 4\frac{\sqrt{\pi\, \sigma_{DVCS}\, b(Q^2)}}{\sigma_T(\gamma^* p \to X)}\, \sqrt{1+\rho^2},$$

with $\sigma_T(\gamma^* p \to X) = 4\pi^2 \alpha_{EM} F_T(x, Q^2)/Q^2$, $F_T = F_2 - F_L$ and $\rho = \mathcal{R}eA/\mathcal{I}mA$ determined from dispersion relations [31].

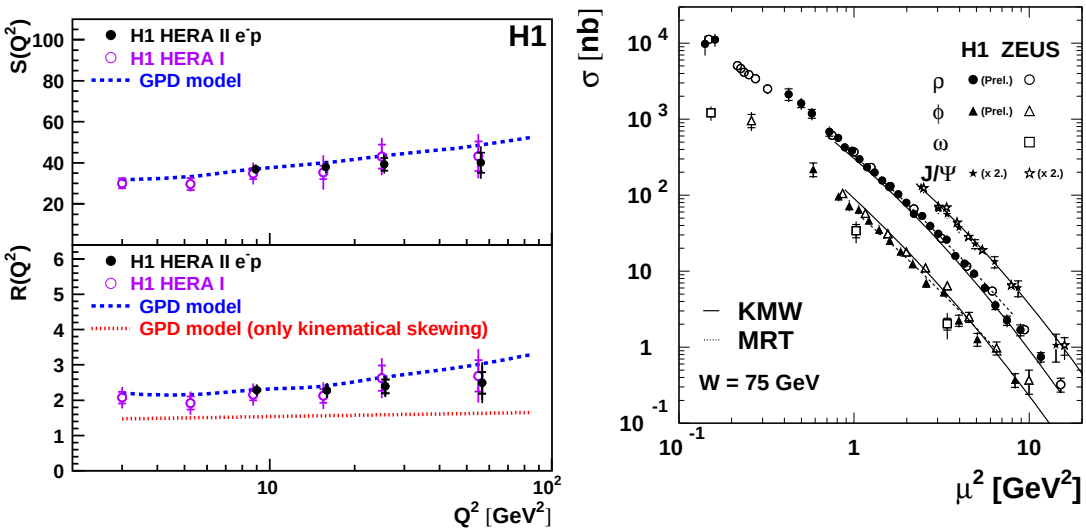

Fig. 5: (left) Q^2 dependences of the observables S and R for DVCS (see text); (right) ρ, ω, ϕ and J/ψ elastic production cross sections, as a function of the scale $\mu^2 = (Q^2 + M_V^2)/4$; for readability of the figure, the J/ψ cross sections have been multiplied by a factor 2. The curves are predictions of the KMW [16] and MRT [23] models.

Figure 5-upper-left shows a weak rise of S with Q^2, which is reasonably well described by the GPD model [30] using the CTEQ PDF parameterisation [37]. The large effect of skewing is visible in Fig. 5-lower-left, where the variable R takes values around 2, instead of 1 in the absence of skewing. GPD calculations [30] compare well with measurements, whereas the same figure shows that it is not sufficient to include only the kinematic contribution to skewing, and that the Q^2 evolution of the GPD must also be taken into account.

4.2 Vector mesons

The elastic production cross sections ρ, ω, ϕ and J/ψ are shown in Fig. 5-right, as a function of the scaling variable $(Q^2 + M_V^2)/4$ (for readability, the J/ψ cross sections have been multiplied by 2) [2]. It is striking that, whereas light VM and J/ψ production cross sections for the same value of Q^2 differ by orders of magnitude (see Fig. 3-left for $Q^2 = 0$), they are close when plotted as a function of the scaling variable $(Q^2 + M_V^2)/4$, up to the factors accounting for the VM charge

[2] Whereas the H1 and ZEUS measurements for ρ agree well, ϕ measurements of ZEUS are a factor 1.20 above H1. When an improved estimation of the proton-dissociation background, investigated for the latest ZEUS ρ production study [2], is used to subtract this background in their ϕ analysis, the cross section ratio of the two experiments is reduced to 1.06, which is within experimental errors.

content ($\rho : \phi : J/\psi = 9 : 2 : 8$) [3]. This supports the dipole approach of VM production at high energy.

The cross sections are roughly described by power laws $1/(Q^2{+}M_V^2)^n$, with $n \simeq 2.2{-}2.5$. The simple $n = 3$ dependence expected in a two-gluon approach for the dominant longitudinal cross sections is modified not only by an additional factor $1/Q^2$ in the transverse amplitudes, but also by the Q^2 dependence of the gluon distribution at small x, described by the DGLAP evolution equations. Calculations using the k_t-unintegrated gluon distribution model of MRT [23] or the GPD model [28] (not shown) give reasonable descriptions of the $(Q^2 + M_V^2)$ dependences. However, in detail, a good description necessitates the precise modelisation of the Q^2 dependence of the longitudinal to transverse cross section ratio R, with non-perturbative effects affecting σ_T. Dipole models using different saturation and WF parameterisations, e.g. the FSS [15], KMW [16] and DF [17] models, attempt at describing VM production over the full Q^2 range, including photoproduction, with reasonable success.

5 Matrix elements and σ_L/σ_T

Measurements of the VM production and decay angular distributions give access to spin density matrix elements, which are related to the helicity amplitudes $T_{\lambda_V \lambda_\gamma}$ [38]. Analyses of ρ, ϕ and J/ψ photo- and electroproduction indicate the dominance of the two s-channel helicity conserving (SCHC) amplitudes, the transverse T_{11} and the longitudinal T_{00} amplitudes, In the accessible Q^2 ranges, J/ψ production is mostly transverse, whereas for light VM electroproduction the longitudinal amplitude T_{00} dominates (see Fig. 6a and Fig. 7a). In ρ and ϕ electroproduction, a significant contribution of the transverse to longitudinal helicity flip amplitude T_{01} is observed. The amplitude ratio T_{01}/T_{00} decreases with Q^2 (Fig. 6b) and increases with $|t|$ (Fig. 6d), as expected (see e.g. [24]); the SCHC amplitude ratio T_{11}/T_{00} decreases with $|t|$ (Fig. 6c) .

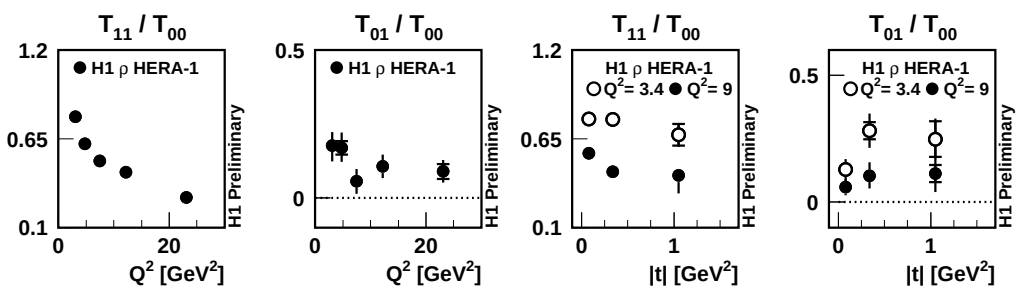

Fig. 6: Amplitude ratios T_{11}/T_{00} and T_{01}/T_{00} as a function of Q^2 and $|t|$ (for two bins in Q^2), for ρ electroproduction. The dotted lines represent the SCHC approximation.

Figure 7 presents measurements of the longitudinal to transverse cross ratio $R = \sigma_L/\sigma_T \simeq |T_{00}|^2/|T_{11}|^2$ (in the SCHC approximation). The behaviour $R \propto Q^2/M_V^2$ predicted for two-gluon exchange is qualitatively verified for all VM production, in fixed target and HERA ex-

[3] For detailed comparisons, modifications due to WF effects, as observed in VM electronic decay widths, may need to be taken into account.

periments. This is shown in Fig. 7-left, where R is plotted as a function of the scaled variable $Q^2 \cdot M_\rho^2/M_V^2$. However, the Q^2 dependence is tamed at large values of Q^2, a feature which is expected and relatively well described by pQCD based calculations, e.g. the GPD model [28], the k_t-unintegrated models [23, 24] or the dipole model [16].

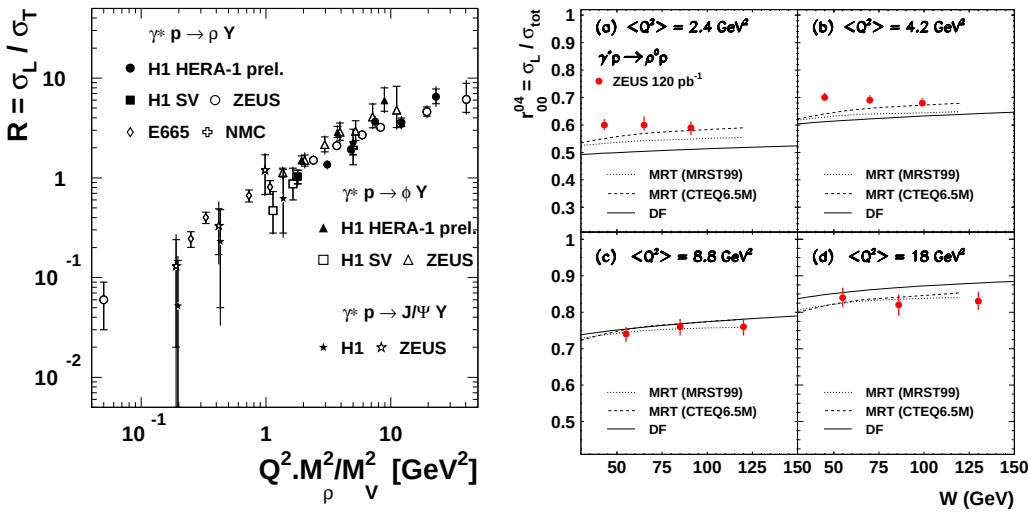

Fig. 7: Cross section ratio $R = \sigma_L/\sigma_T$ as a function of (left) the scaling variable $Q^2 \cdot M_\rho^2/M_V^2$ for different VM; (right) the centre of mass energy W in several Q^2 bins for ρ electroproduction, compared to model predictions.

The cross section ratio R for ρ electroproduction is also found to depend very significantly on the dipion mass $M_{\pi\pi}$ (not shown), in line with the Q^2/M_V^2 dependence if the relevant mass is the dipion mass rather than the nominal ρ resonance mass. Following the MRT model approach [23], this suggests a limited influence of the WF on VM production.

Figure 7-right shows that no strong dependence of R with W is observed. Since transverse amplitudes are expected to include significant contributions of large dipoles, with a soft energy dependence, this suggests that large dipoles are also present in longitudinal amplitudes, due to finite size effects, i.e. a smearing of z away from $z = 1/2$. On the other hand, in the domain $Q^2 \gtrsim 10 - 20\ \mathrm{GeV}^2$, no strong dependence of R with W is expected from models. It should also be noted that a significant phase difference is observed between the two dominant amplitudes, T_{00} and T_{11} [3]. This indicates a difference between the ratios of the real to imaginary parts of the forward amplitudes. Since these ratios are given by $\log 1/x$ derivatives of the amplitudes, the phase difference is an indication of different W dependences.

6 Large $|t|$; BFKL evolution

Large values of the momentum transfer $|t|$ provide a hard scale for diffractive processes in QCD, with the dominance of the proton dissociative channel for $|t| \gtrsim 1\ \mathrm{GeV}^2$. It should be noted that for large $|t|$ production, a hard scale is present at both ends of the exchanged gluon ladder. No

strong k_t ordering is thus expected, which is typical for BFKL evolutions for sufficiently high $|t|$ values. This is at variance with large Q^2 VM production at low $|t|$, where a large scale is present at the upper (photon) end of the ladder and a small scale at the proton end, implying that these processes are expected to be described by DGLAP evolutions, with strong k_t ordering along the ladder.

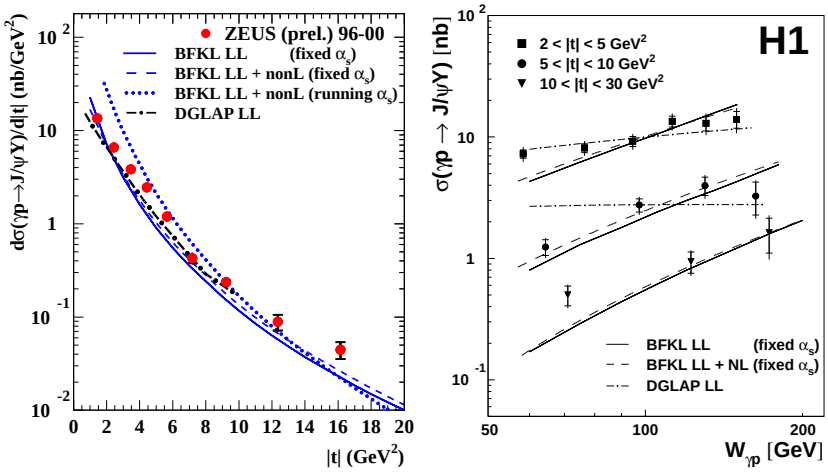

Fig. 8: t (left) and W (right) dependences of J/ψ production with $|t| > 2$ GeV^2, with comparisons to pQCD model predictions.

For $|t|$ larger than a few GeV^2, the t dependences of the cross sections follow power laws, both for ρ [4] and J/ψ [8] photoproduction. As shown by Fig. 8-left, they are well described by pQCD calculations based on the BFKL equations with fixed α_s [39]; predictions using the DGLAP evolution [40] also describe the J/ψ data for $|t| \lesssim m_\psi^2$. BFKL calculations describe the W evolution (Fig. 8-right), at variance with DGLAP, but do not describe well the spin density matrix elements. For ρ, ϕ and J/ψ photoproduction with $|t| \gtrsim 2$ GeV^2, the slope α' of the effective Regge trajectory tends to be slightly negative, but are compatible with 0.

7 Conclusions

In conclusion, studies of VM production and DVCS at HERA provide a rich and varied field for the understanding of QCD and the testing of perturbative calculations over a large kinematical domain, covering the transition from the non-perturbative to the perturbative domain. Whereas soft diffraction, similar to hadronic interactions, dominates light VM photoproduction, typical features of hard diffraction, in particular hard W dependences, show up with the developments of hard scales provided by Q^2, the quark mass or $|t|$. The size of the interaction is accessed through the t dependences. Calculations based on pQCD, notably using k_t-unintegrated gluon distributions and GPD approaches, and predictions based on models invoking universal dipole–proton cross sections describe the data relatively well. The measurement of spin density matrix

elements gives a detailed access to the polarisation amplitudes, which is also understood in QCD. Large $|t|$ VM production supports BFKL calculations.

Acknowledgements

It is a pleasure to thank the numerous colleagues from H1 and ZEUS who contributed to the extraction of the beautiful data presented here, and to thank the theorist teams whose efforts led to a continuous increase in the understanding of diffraction in terms of QCD, the theory of strong interactions. Special thanks are due to L. Motyka, T. Teubner and G. Watt for providing calculations used for the present review and to J.-R. Cudell and L. Favart for useful discussions and comments. It is also a pleasure to thank the organisors of the HERA-LHC Workshop for the lively discussions and the pleasant atmosphere of the workshop.

References

[1] H1 Coll., S. Aid et al., Nucl. Phys. **B 463**, 3 (1996);
ZEUS Coll., M. Derrick et al., Z. Phys. **C 73**, 253 (1997);
ZEUS Coll., J. Breitweg et al., Eur. Phys. J. **C 2**, 247 (1998);
H1 Coll., "A new Measurement of Exclusive ρ^0 Meson Photoproduction at HERA", XIV Int. Workshop on DIS, Tsukuba, Japan (2006);
ZEUS Coll., J. Breitweg et al., Eur. Phys. J. **C 6**, 603 (1999);
ZEUS Coll., J. Breitweg et al., Eur. Phys. J. **C 12**, 393 (2000);
H1 Coll., C. Adloff et al., Eur. Phys. J. **C 13**, 371 (2000);
H1 Coll., C. Adloff et al., Phys. Lett. **B 539**, 25 (2002).

[2] ZEUS Coll., S. Chekanov et al., PMC Phys. **A 1**, 6 (2007).

[3] H1 Coll., X. Janssen, "Diffractive ρ and ϕ production in DIS", XVI Int. Workshop on DIS, London, UK (2008);
H1 Coll., "Diffractive electroproduction of ρ and ϕ mesons at HERA", to be publ.

[4] ZEUS Coll., S. Chekanov et al., Eur. Phys. J. **C 26**, 389 (2003);
H1 Coll., A. Aktas et al., Phys. Lett. **B 638**, 422 (2006).

[5] ZEUS Coll., M. Derrick et al., Z. Phys. **C 73**, 73 (1996);
ZEUS Coll., J. Breitweg et al., Phys. Lett. **B 487**, 273 (2000).

[6] ZEUS Coll., M. Derrick et al., Phys. Lett. **B 377**, 259 (1996);
H1 Coll., C. Adloff et al., Phys. Lett. **B 483**, 360 (2000);
ZEUS Coll., S. Chekanov et al., Nucl. Phys. **B 718**, 3 (2005).

[7] ZEUS Coll., S. Chekanov et al., Eur. Phys. J. **C 24**, 345 (2002);
ZEUS Coll., S. Chekanov et al., Nucl. Phys. **B 695**, 3 (2004);
H1 Coll., A. Aktas et al., Eur. Phys. J. **C 46**, 585 (2006).

[8] H1 Coll., A. Aktas et al., Phys. Lett. **B 568**, 205 (2003);
ZEUS Coll., "Diffractive photoproduction of J/ψ mesons with large momentum transfer at HERA", subm. to XXXIII ICHEP, Moscow (2006).

[9] H1 Coll., C. Adloff et al., Phys. Lett. **B 541**, 251 (2002).

[10] ZEUS Coll., J. Breitweg et al., Phys. Lett. **B 437**, 432 (1998);
H1 Coll., C. Adloff et al., Phys. Lett. **B 483**, 23 (2000).

[11] ZEUS Coll., " Exclusive photoproduction of Υ mesons at HERA", submitted to the 2007 EPS Conference, Manchester (2007).

[12] ZEUS Coll., S. Chekanov et al., Phys. Lett. **B 573**, 46 (2003);
H1 Coll., A. Aktas et al., Eur. Phys. J. **C 44**, 1 (2005).

[13] H1 Coll., F. D. Aaron et al., Phys. Lett. **B 659**, 796 (2008).

[14] A.H. Mueller, Nucl. Phys. **B 335**, 115 (1990);
N.N. Nikolaev and B.G. Zakharov, Z. Phys. **C 49**, 607 (1991).

[15] J.R. Forshaw, R. Sandapen and G. Shaw, Phys. Rev. **D 69**, 094013 (2004).

[16] H. Kowalski, L. Motyka and G. Watt, Phys. Rev. **D 74**, 074016 (2006).

[17] H.G. Dosch and E. Ferreira, Eur. Phys. J. **C 51**, 83 (2007).

[18] K.J. Golec-Biernat and M. Wusthoff, Phys. Rev. **D 59**, 014017 (1999);
K.J. Golec-Biernat and M. Wusthoff, Phys. Rev. **D 60**, 114023 (1999);
S. Munier, A.M. Stasto and A.H. Mueller, Nucl. Phys. **B 603**, 427 (2001);
E. Iancu, K. Itakura and S. Munier, Phys. Lett. **B 590**, 199 (2004).

[19] L. Motyka, these proceedings.

[20] M.G. Ryskin, Z. Phys. **C 57**, 89 (1993);
J.S. Brodsky et al., Phys. Rev. **D 50**, 3134 (1994).

[21] L. Frankfurt, W. Koepf and M. Strikman, Phys. Rev. **D 54**, 3194 (1996).

[22] I.P. Ivanov, N.N. Nikolaev and A.A. Savin, Phys. Part. Nucl. **37**, 1 (2006).

[23] A.D. Martin, M.G. Ryskin and T. Teubner, Phys. Rev. **D 55**, 4329 (1997).

[24] D. Yu. Ivanov and R. Kirschner, Phys. Rev. **D 58**, 114026 (1998).

[25] T. Teubner, these proceedings.

[26] J. Collins, L. Frankfurt and M. Strikman, Phys. Rev. **D 56**, 2982 (1997).

[27] M. Diehl, Phys. Rep. **388**, 41 (2003);
A.V. Belitsky and A.V. Radyushkin, Phys. Rep. **418**, 1 (2005).

[28] S.V. Goloskokov and P. Kroll, Eur. Phys. J. **C 53**, 367 (2008).

[29] D. Yu. Ivanov, L. Szymanowski and G. Krasnikov, JETP Lett. **80**, 226 (2004);
D. Yu. Ivanov, A. Schafer, L. Szymanowski and G. Krasnikov, Eur. Phys. J. **C 34**, 297 (2004);
D. Yu. Ivanov, Blois Conference on Forward Physics and QCD, Hamburg (2007).

[30] A. Freund, Phys. Rev. **D 68**, 096006 (2003).

[31] L. Favart and M. V. T. Machado, Eur. Phys. J. **C 29**, 365 (2003).

[32] K. Kumericki, D. Mueller and K. Passek-Kumericki, Nucl. Phys. **B 794**, 244 (2008).

[33] A. Donnachie and P.V. Landshoff, Phys. Lett. **B 296**, 227 (1992);
J.-R. Cudell, K. Kang and S. Kim, Phys. Lett. **B 395**, 311 (1997).

[34] A. D. Martin, C. Nockles, M. G. Ryskin and T. Teubner, Phys. Lett. **B 662**, 252 (2008).

[35] G.A. Jaroszkiewicz and P.V. Landshoff, Phys. Rev. **D 10**, 170 (1974).

[36] S. J. Brodsky et al., JETP Lett. **70**, 155 (1999).

[37] J. Pumplin et al., JHEP **07**, 012 (2002).

[38] K. Schilling and G. Wolf, Nucl. Phys. **B 61**, 381 (1973).

[39] R. Enberg, L. Motyka and G. Poludniowski, Eur. Phys. J. **C 26**, 219 (2002).

[40] E. Gotsman, E. Levin, U. Maor and E. Naftali, Phys. Lett. **B 532**, 37 (2002).

Exclusive Central Production and Diffractive W/Z Results from CDF II

Konstantin Goulianos[1] *and James L. Pinfold*[2]

[1]The Rockefeller University
1230 York Avenue, New York, NY 10065, USA

[2]The University of Alberta
Centre for Particle Physics, Edmonton, Alberta T6G2N6, CANADA

Abstract

We report recently published results on central exclusive production of di-jets and di-photons, and exclusive QED production of e^+e^- pairs. In addition, we discuss preliminary results on exclusive photoproduction of charmonium and bottomonium, exclusive QED production of $\mu^+\mu^-$ pairs, and single diffractive W/Z production. All the presented results were extracted from data collected by the CDF II detector from $p\bar{p}$ collisions at $\sqrt{s}$=1.96 TeV. The implications of these results for the Large Hadron Collider (LHC) are briefly examined.

1 Introduction

We present results obtained by CDF II at the Tevatron [1] in two broad areas: inclusive diffraction and exclusive production. The main goal of the Run II inclusive diffractive program of CDF has been to understand the QCD nature of the Pomeron [2] ($I\!P$) by measuring the diffractive structure function [3] $F^{D4}(Q^2, x_{Bj}, \xi, t)$, where ξ is the fractional momentum loss of the diffracted nucleon, for different diffractive production processes. In addition, the possibility of a composite Pomeron is being investigated by studies of very forward jets with a rapidity gap between the jets. Important results are the observation of a breakdown of QCD factorization in hard diffractive processes, expressed as a suppression by a factor of $\mathcal{O}(10)$ of the production cross section relative to theoretical expectations, and the breakdown of Regge factorization in soft diffraction by a factor of the same magnitude [3]. Combined, these two results support the hypothesis that

[1]The presented results are from the CDF diffractive and exclusive physics program of Run II. This program relies on a system of special forward detectors, which include: a Roman Pot Spectrometer (RPS) equipped with scintillation counters and a fiber tracker to detect and measure the angle and momentum of leading anti-protons, a system of Beam Shower Counters (BSCs) [1] covering the pseudorapidity range $5.5 < |\eta| < 7.5$ used to select diffractive events by identifying forward rapidity gaps and reducing non-diffractive background on the trigger level, and two very forward ($3.5 < |\eta| < 5.1$) MiniPlug (MP) calorimeters [2], designed to measure energy and lateral position of both electromagnetic and hadronic showers. The ability to measure the event energy flow in the very forward rapidity region is vital for the identification of diffractive events in the high luminosity environment of Run II.

[2]Diffractive reactions are characterized by the exchange of a spin 1 quark/gluon construct with the quantum numbers of the vacuum. In Regge theory, this exchange is the vacuum trajectory traditionally referred to as the Pomeron ($I\!P$). Because the exchange is colorless, a large region in pseudorapidity space is left empty of particles (this region is called a "rapidity gap"). In perturbative QCD, the lowest order prototype of the Pomeron is the color neutral system of two gluons.

the breakdown of factorization is due to a saturation of the rapidity gap formation probability by an exchange of a color-neutral construct of the underlying parton distribution function (PDF) of the proton [4]. Historically, such an exchange is referred to as the Pomeron. Renormalizing the "gap probability" to unity over all (ξ, t) phase space corrects for the unphysical effect of overlapping diffractive rapidity gaps and leads to agreement between theory and experiment (see [4]).

Central exclusive production in $p\bar{p}$ collisions is a process in which the p and $\bar{p}$ remain intact and an exclusive state X_{excl} is centrally produced: $p + \bar{p} \rightarrow p + X_{excl} + \bar{p}$. The primary motivation for studying exclusive physics at the Tevatron is to test the feasibility of using exclusive production to search for and study the Higgs boson as well search for other new physics at the LHC [5]. In leading order QCD, exclusive production occurs through gluon-gluon fusion, while an additional soft gluon screens the color charge allowing the protons to remain intact [6]. This mechanism, historically termed Double Pomeron Exchange (DPE), enables exclusive production of di-jets [3], $\gamma\gamma$ [7], and the χ_c° [8] at the Tevatron, whereas at the LHC, where central masses up to several hundred GeV are attainable, new central exclusive channels open up, as for example W^+W^- and Z^0Z^0. While the main effort at the LHC is directed toward searches for inclusively produced Higgs bosons, an intense interest is developing in exclusive Higgs production, $p + \bar{p} \rightarrow p + H + \bar{p}$. This production channel presents several advantages, as for example the production of clean events in an environment of suppressed QCD background for the main Higgs decay mode of $H \rightarrow b_{jet} + \bar{b}_{jet}$ due to the $J_z = 0$ selection rule [5]. Exclusive production can also occur through photoproduction ($I\!P$ - γ fusion), yielding charmonium and bottomonium. The same tagging technique can also be utilized to select γp, or γq and γg interactions at the LHC, for which the energy reach and the effective luminosity are higher than for $\gamma\gamma$ interactions.

Additionally, exclusive production of central lepton pairs, $\gamma\gamma \rightarrow l^+l^-$ ($l = e, \mu, \tau$), via two-photon exchange has been observed at CDF [9]. Tagging two-photon production offers a significant extension of the LHC physics program.[3] Particularly exciting is the possibility of detecting two-photon exclusive W^+W^-, Z^0Z^0, Higgs boson and new physics production at the LHC [10]. The deployment of forward proton detectors at 200 m and 420 m (FP420 project) from the interaction point of ATLAS and CMS, in order to exploit the above mentioned forward physics scenarios, is currently under consideration [11]. Two-photon exclusive production of lepton pairs will provide an excellent monitoring tool of the tagging efficiency and energy scale of the detectors of the FP420 project. These events can also be used for several systematic studies, including luminosity normalization and contributions from inelastic production or accidental tagging.

2 Central Exclusive Production

Exclusive production is hampered by expected low production rates [5]. As rate calculations are model dependent and generally involve non-perturbative suppression factors, it is sensible to calibrate them against processes involving the same suppression factors but have high enough production rates to be measurable at the Tevatron. The leading order diagrams relating to the

[3]The effective luminosity of high-energy $\gamma\gamma$ collisions reaches $\sim$1% of the pp luminosity, so that the standard detector techniques used for measuring very forward proton scattering should allow for a reliable extraction of $\gamma\gamma$ results.

exclusive central production processes discussed in this paper are summarized in Fig. 1.

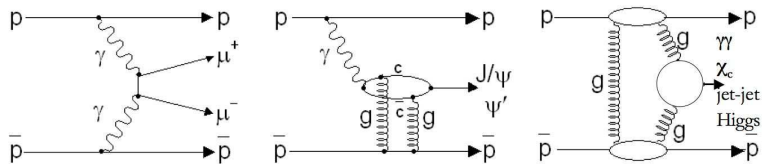

Fig. 1: Leading order diagrams for three types of exclusive process: $\gamma\gamma$ interactions (left), $\gamma I\!P$ fusion or photoproduction (middle), and gg t-channel color-singlet two-gluon exchange (right). Higgs boson production proceeds via the gg diagram.

2.1 Exclusive Di-jet Production

The process of exclusive di-jet production, which has been observed by CDF in Run II data [12], proceeds through the same mechanism as $\gamma\gamma$, χ_c°, and Higgs production, as shown in Fig. 1. The analysis strategy developed to search for exclusive di-jet production is based on measuring the di-jet mass fraction, R_{jj} , defined as the di-jet invariant mass M_{jj} divided by the total mass of the central system: $R_{jj} = M_{jj}/M_X$.[4] The POMWIG MC [13] generator along with a detector simulation are used to simulate the DPE di-jets. The signal from exclusive di-jets is expected to appear at high values of R_{jj}, smeared by resolution and gluon radiation effects. Events from the inclusive DPE production process $p + \bar{p} \rightarrow p$ + gap +[X + jj] + gap (the leading p is not observed in CDF II) are expected to contribute to the entire R_{jj} region. Any such events within the exclusive R_{jj} range contribute to background and must be subtracted when evaluating exclusive production rates.

The process of exclusive di-jet production is important for testing and/or calibrating models for exclusive Higgs production at the LHC. The CDF II collaboration has made the first observation of this process and the main final result is presented in Fig. 2. Details can be found in Ref. [12]. This result favours the model of Ref. [6], which is implemented in the MC simulation ExHuME [14].

2.2 Exclusive e^+e^- Production

The CDF II collaboration has reported the first observation of exclusive e^+e^- production in $p\bar{p}$ collisions [9] using 532 pb^{-1} $p\bar{p}$ data collected at $\sqrt{s} = 1.96$ TeV by CDF II at the Fermilab Tevatron. The definition of exclusivity used requires the absence of any particle signatures in the detector in the pseudorapidity region $|\eta| < 7.4$, except for an electron and a positron candidate each with transverse energy of $E_T \geq 5$ GeV and within the pseudorapidity $|\eta| \leq 2$. With these criteria, 16 events were observed. The dominant background is due to events with unobserved proton dissociation (1.6 ± 0.3 events). The total background expectation is 1.9 ± 0.3 events.

[4]The mass M_X is obtained from all calorimeter towers with energy above the thresholds used to calculate $\xi_{\bar{p}}^X$, while M_{jj} is calculated from calorimeter tower energies inside jet cones of R=0.7, where R=$\sqrt{\Delta\phi^2 + \Delta\eta^2}$. The exclusive signal is extracted by comparing the R_{jj} distribution shapes of DPE di-jet data and simulated di-jet events obtained from a Monte Carlo (MC) simulation that does not contain exclusive di-jet production.

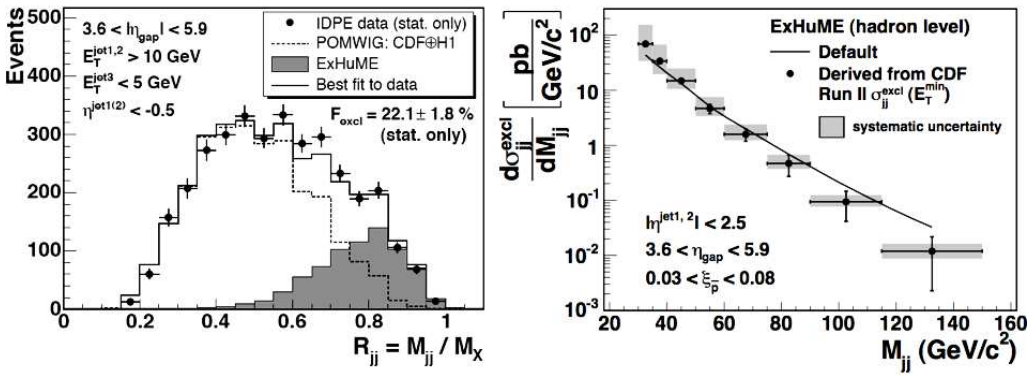

Fig. 2: (Left) The di-jet mass fraction in DPE data (points) and best fit (solid histogram) to a simulated di-jet mass fraction obtained from POMWIG MC events (dashed histogram) and ExHuME di-jet MC events (shaded histogram). (Right) The ExHuME [14] exclusive di-jet differential cross section at the hadron level vs. di-jet mass M_{jj} normalized to measured σ_{jj}^{excl} values. The curve is the cross section predicted by ExHuME.

The observed events are consistent in cross section and properties with the QED process $p\bar{p} \rightarrow p + (e^+e^-) + \bar{p}$ through two-photon exchange. The measured cross section is $1.6^{+0.5}_{-0.3}(stat) \pm 0.3(syst)$ pb. This agrees with the theoretical prediction of 1.71 ± 0.01 pb obtained using the LPAIR MC generator [15] and a GEANT based detector simulation, CDFSim [16]. Details on the observation of the exclusive e^+e^- signal are reported in reference [9].

2.3 Exclusive $\gamma\gamma$ Production

An exclusive $\gamma\gamma$ event can be produced via $gg \rightarrow \gamma\gamma$ (g = gluon) through a quark loop, with an additional "screening" gluon exchanged to cancel the color of the interacting gluons and so allow the leading hadrons to stay intact. This process is closely related [7, 17] to exclusive Higgs production at the LHC, $p\bar{p} \rightarrow p + H + \bar{p}$, where the production mechanism of the Higgs boson is gg-fusion through a top quark loop. These processes can also be described as resulting from DPE.

A search has been performed for exclusive $\gamma\gamma$ production in p-$\bar{p}$ collisions at $\sqrt{s} = 1.96$TeV, using 532 pb^{-1} of integrated luminosity data taken by CDF II at Fermilab. The event signature requires two electromagnetic showers, each with transverse energy $E_T \geq 5$ GeV and pseudorapidity $|\eta| \leq 1.0$, with no other particles detected. Three candidate events were observed. Each candidate can be interpreted as either a $\gamma\gamma$ or a $\pi^0\pi^0/\eta\eta$ final state with overlapping photons that satisfy the $\gamma\gamma$ selection criteria and thus form a background. The probability that processes other than these fluctuate to ≥ 3 events is 1.7×10^{-4}. Two events clearly favor the $\gamma\gamma$ hypothesis and the third event favors the $\pi^0\pi^0$ hypothesis. On the assumption that two of the three candidates are $\gamma\gamma$ events we obtain a cross section $\sigma(p\bar{p} \rightarrow p + \gamma\gamma + \bar{p}) = 90^{+120}_{-30}(stat) \pm 16(syst)$ fb, for $E_T \geq 5$ GeV and $|\eta| \leq 1.0$, compatible within the theoretical uncertainties with the prediction of 40 fb of Ref. [5]. A comparison between the predictions of the ExHuMe MC and the data shows good agreement both in normalization and in the shapes of the kinematic distributions.

Although two of the candidates are most likely to arise from $\gamma\gamma$ production, the $\pi^0\pi^0$ hypotheses cannot be excluded. A 95% C.L. upper limit is obtained on the exclusive $\gamma\gamma$ production cross section ($E_T \geq 5$ GeV, $|\eta| \leq 1.0$) of 410 fb, which is about ten times higher than the prediction of Ref. [7]. This result may be used to constrain calculations of exclusive Higgs boson production at the LHC. Additional CDF data, collected with a lower E_T threshold, are being analysed. Exclusive $\gamma\gamma$ production has not previously been observed in hadron-hadron collisions. This work is described in more detail in Ref. [18].

2.4 Exclusive $\mu^+\mu^-$ Production

Low Mass Exclusive $\mu^+\mu^-$ ***Production.*** The CDF II collaboration has performed a search for exclusive low mass $\mu^+\mu^-$ final states resulting from three processes: $\gamma\gamma \rightarrow$ non-resonant $\mu^+\mu^-$ "continuum" events, and $J/\psi \rightarrow \mu^+\mu^-$ & $\psi' \rightarrow \mu^+\mu^-$ events arising from $I\!P$ - γ fusion (photoproduction). In addition, evidence for exclusive χ_c° production was sought arising from the decay channel $\chi_c^\circ \rightarrow J/\psi(\rightarrow \mu^+\mu^-) + \gamma$. The invariant mass distribution of the exclusive di-muon events obtained from 1.48 fb^{-1} of data is shown in Fig. 3. The J/ψ and ψ' peaks can be clearly seen above the $\mu^+\mu^-$ continuum.[5] Continuum $\mu^+\mu^-$ production arises from $\gamma\gamma$

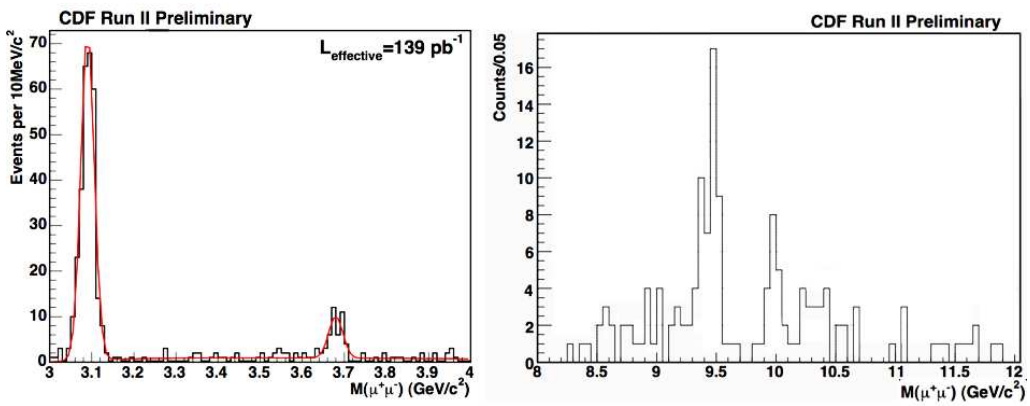

Fig. 3: (Left) The invariant mass distribution obtained from the exclusive $\mu^+\mu^-$ data; the J/ψ peak (left) and the smaller ψ' peak (right) can be clearly seen above the continuum of muon-pair production. (Right) The invariant mass distribution obtained from the exclusive higher mass $\mu^+\mu^-$ data: the Υ (1S) peak (middle-left) and the smaller Υ (2S) (middle) peaks can be clearly seen above the continuum, while he Υ (3S) peak (middle-right) is only barely discernible with these statistics.

interactions. These interactions are simulated by the LPAIR [15] and STARlight MCs [19]. Both give a very good description of the data in shape and in normalization. The events in the J/ψ and ψ' peak of Figure 3, from the process $p\bar{p} \rightarrow p + J/\psi(J/\psi') + \bar{p}$, are mainly produced via $I\!P$ - γ fusion. The STARLight MC is used to simulate the photoproduction of the J/ψ and the ψ'.

[5]The offline cuts applied to the muon-pair data are the same as those applied in the e^+e^- case: there should be no activity in the event in the region $|\eta| < 7.4$, and the final state must have two identified muons of $P_T > 1.4$ GeV/c within $|\eta| < 0.6$.

A J/ψ in the final state can arise from exclusive χ_c° production, $p\bar{p} \to p + (\chi_c^\circ) + \bar{p}$ with $\chi_c^\circ \to J/\psi(J/\psi \to \mu^+\mu^-) + \gamma$. The photon in the χ_c° decay is soft and consequently may not be reconstructed and form a "background" to exclusive J/ψ production via $I\!P$ - γ fusion. The χ_c° contributes to the exclusive J/ψ peak when the soft photon from its decay survives the exclusivity cut. By fitting the shapes of the E_T and $\Delta\phi$ distributions of the di-muon pair of the events in the J/ψ peak of the data with MC generated distributions of J/ψ from photoproduction and χ_c° production, CDF II estimates the χ_c° contribution to the exclusive J/ψ photoproduction peak to be $\approx 10\%$.

Higher Mass Exclusive $\mu^+\mu^-$ Production. The basis of the study of high exclusive muon pairs is somewhat different in that it does not rely on the "standard" exclusivity cuts applied to the low mass data. In this case, one looks for muon pairs that form a vertex with no additional tracks. It is also required that the muons be consistent with $\Delta\phi \approx 0$ and with P_T-sum approximately zero. For 890 pb^{-1} of data (2.3M events), with $\Delta\phi > 120^o$ and a P_T-sum of the two muon tracks less than 7 GeV/c, the mass plot shown in Fig. 3 was obtained. One can clearly discern the Υ(1S) and Υ(2) peaks in this plot. The high mass exclusive muon pair data, with enhanced statistics, is currently under study.

3 Diffractive W/Z Production

Studies of diffractively produced W/ Z boson are important for understanding the structure of the Pomeron. The production of intermediate vector bosons is due to the annihllation of quark-antiquark pairs and thus is a probe of the quark content of the Pomeron. In leading order, the W/Z is produced by a quark in the Pomeron, while production by a gluon is suppressed by a factor of α_S and can be distinguished from quark production by an associated jet [20]. Diffractive dijet production at the Tevatron was found to be suppressed by a factor of $\mathcal{O}(10)$ compared to expectations from the Diffractive Structure Function (DSF) extracted from diffractive deep inelastic scattering (DDIS) at the DESY ep Collider HERA. A more direct comparison could be made by measuring the DSF in diffractive W production at the Tevatron, which is dominated by a $q\bar{q}$ exchange, as in DDIS. In Run I, only the overall diffractive W fraction was measured by CDF [20]. In Run II, both the W and Z diffractive fractions and the DSF are measured.

The CDF Run II analysis is based on events with RPS tracking from a data sample of ~ 0.6 fb^{-1}. In addition to the W/Z selection requirements[6], a hit in the RPS trigger counters and a RPS reconstructed track with $0.03 < \xi < 0.1$ and $|t| < 1$ are required. A novel feature of the analysis is the determination of the full kinematics of the $W \to e\nu/\mu\nu$ decay using the neutrino E_T^ν obtained from the missing E_T, as usual, and η_ν from the formula $\xi^{\rm RPS} - \xi^{\rm cal} = (E_T/\sqrt{s})\exp[-\eta_\nu]$, where $\xi^{\rm cal} = \sum_{\rm towers}(E_T/\sqrt{s})\exp[-\eta]$. The extracted value of $M_W^{\rm exp} = 80.9 \pm 0.7$ GeV is in good agreement with the world average W mass of $M_W^{\rm PDG} = 80.403 \pm 0.029$ GeV [21]. After applying corrections accounting for the RPS acceptance, $A_{\rm RPS} \approx 80$ %, the trigger counter efficiency, $\epsilon_{\rm RPStrig} \approx 75$ %, the track reconstruction

[6]The CDF W/Z selection requirements are: $E_T^{e,\mu} > 25$ GeV, $40 < M_T^W < 120$ GeV, $66 < M^Z < 116$ GeV, and vertex z-coordinate $|z_{vtx}| < 60$ cm. In the W case, the requirement of $\xi^{\rm RPS} > \xi^{\rm CAL}$ is very effective in removing the overlap evemnts in the region of $\xi^{\rm CAL} < 0.1$, while a mass cut of $50 < M_W < 120$ GeV has the same effect. In the Z case, we use the $\xi^{\rm CAL}$ distribution of all Z events normalized to the RP-track distribution in the region of $-1 < \log\xi^{\rm CAL} < -0.4$ ($0.1 < \xi^{\rm CAL} < 0.4$) to obtain the ND background in the diffractive region of $\xi^{\rm CAL} < 0.1$.

efficiency, $\epsilon_{\rm RPStrk} \approx 87$ %, multiplying by 2 to include production by $p\bar{p} \to W/Z + p$, and correcting the ND event number for the effect of overlaps due to multiple interactions by multiplying by the factor $f_{1-\rm int} \approx 0.25$, the diffractive fraction of W/Z events was obtained as $R_{W/Z} = 2 \cdot N_{SD}/A_{\rm RPS}/\epsilon_{\rm RPStrig}/\epsilon_{\rm RPStrk}/(N_{\rm ND} \cdot f_{1-\rm int})$:

$$R_W(0.03 < \xi < 0.10,\ |t| < 0.1) = [0.97 \pm 0.05\ \text{(stat)} \pm 0.11\ \text{(syst)}]\% \quad (1)$$

$$R_Z(0.03 < \xi < 0.10,\ |t| < 0.1) = [0.85 \pm 0.20\ \text{(stat)} \pm 0.11\ \text{(syst)}]\% \quad (2)$$

The R_W value is consistent with the Run I result of $R_W(0.03 < \xi < 0.10,\ |t| < 0.1) = [0.97 \pm 0.47]$ obtained from the published value of $R^W(\xi < 0.1) = [0.15 \pm 0.51\ \text{(stat)} \pm 0.20\ \text{(syst)}]\%$ [20] multiplied by a factor of 0.85 that accounts for the reduced (ξ-t) range in Run II.

4 Conclusion

We present recent results on exclusive central prodction of di-jets, di-leptons, and di-photons reported by the CDF II collaboration, obtained from Run II data collected at the Tevatron $p\bar{p}$ collider at $\sqrt{s} = 1.96$ TeV. The results are compared with theoretical expectations, and implications for the possible observation of exclusive Higgs boson production and other interesting new physics processes at the Large Hadron Collider are discussed.

References

[1] M. Gallinaro (for the CDF Collaboration), arXiv:hep-ph/0407255, p. 1 (2004).

[2] K. Goulianos *et al.,* Nucl. Instrum. Meth. **A 518**, 42-44 (2004).

[3] T. Affolder *et al.,* Phys. Rev. Lett.. **84**, 5043 (2000).

[4] K. Goulianos, in Proceedings of *La Thuile 2004*, arXiv:hep-ph/0407035 .

[5] V. A. Khoze, A. Kaidalov, A. D. Martin, M. G. Ryskin, W. J. Stirling, World Scientific (Gribov Memorial Volume), arXiv:hep-ph/0507040, p. 1 (2005).

[6] V. A. Khoze, A. D. Martin, M. G. Ryskin, Eur. Phys. J. **C 14**, 525 (2000).

[7] V.A. Khoze, A.D. Martin, M.G. Ryskin, W.J. Stirling, Eur. Phys. J. **C 38**, 475 (2005).

[8] V.A. Khoze, A.D. Martin, M.G. Ryskin and W.J. Stirling, Eur. Phys. J. **C 35**, 211 (2004).

[9] A. Abulencia *et al.,* Phys.Rev.Lett. **98**, 112001 (2007).

[10] K. Piotrzkowski, Phys. Rev. **D 63**, 071502 (2001).

[11] M. Albrow *et al.,* arXiv:0806.0302 [hep-ex], FERMILAB-FN-0825-E, p. 1 (2008).

[12] T. Aaltonen *et al.,* Phys. Rev. **D 77**, 052004 (2008).

[13] B. Cox and J. Forshaw, Compu. Phys. Commun. **144**, 104 (2002).

[14] J. Monk and A. Pilkington, Comput. Phys. Commun. **175**, 232 (2006).

[15] S. P Baranov, O. Duenger, H. Shooshtari, J. A. M. Vermaseren, Hamburg 1991, in Proceedingsof *Physics at HERA* **3**, 1478 (1991).

[16] E. Gerchtein and M. Paulini, Computing in High Energy and Nuclear Physics, p. 1 (2003).

[17] M. Albrow *et al.*, arXiv:hep-ex/0511057, p. 1 (2005).

[18] T. Aaltonen *et al.*, Phys. Rev. Lett. **99**, 242002 (2007).

[19] S. Klein and J. Nystrand, Phys. Rev. **C 60**, 014903 (1999).

[20] K. Abe *et al.*, Phys. Rev. Lett. **78**, 2698 (1997).

[21] W.-M. Yao *et al.*, Journ. Phys. **G 33**, 1 (2006).

Survival probability in diffractive dijet photoproduction

Michael Klasen[1] *and Gustav Kramer*[2]
[1] Laboratoire de Physique Subatomique et de Cosmologie, Université Joseph Fourier / CNRS-IN2P3 / INPG, 53 Avenue des Martyrs, F-38026 Grenoble, France
[2] II. Institut für Theoretische Physik, Universität Hamburg, Luruper Chaussee 149, D-22761 Hamburg, Germany

Abstract
We confront the latest H1 and ZEUS data on diffractive dijet photoproduction with next-to-leading order QCD predictions in order to determine whether a rapidity gap survival probability of less than one is supported by the data. We find evidence for this hypothesis when assuming global factorization breaking for both the direct and resolved photon contributions, in which case the survival probability would have to be E_T^{jet}-dependent, and for the resolved or in addition the related direct initial-state singular contribution only, where it would be independent of E_T^{jet}.

1 Introduction

The central problem for hard diffractive scattering processes, characterized by a large rapidity gap in high-energy collisions, is whether they can be factorized into non-perturbative diffractive parton density functions (PDFs) of a colorless object (e.g. a pomeron) and perturbatively calculable partonic cross sections. This concept is believed to hold for the scattering of point-like electromagnetic probes off a hadronic target, such as deep-inelastic scattering (DIS) or direct photoproduction [1], but has been shown to fail for purely hadronic collisions [1, 2]. Factorization is thus expected to fail also in resolved photoproduction, where the photon first dissolves into partonic constituents, before these scatter off the hadronic target. The separation of the two types of photoproduction processes is, however, a leading order (LO) concept. At next-to-leading order (NLO) of perturbative QCD, they are closely connected by an initial-state (IS) singularity originating from the splitting $\gamma \to q\bar{q}$ (for a review see [3]), which may play a role in the way factorization breaks down in diffractive photoproduction [4]. The breaking of the resolved photoproduction component only leads to a dependence of the predicted cross section on the factorization scale M_γ [4]. Since this M_γ-dependence is unphysical, it must be remedied also for the factorization breaking of the resolved part of the cross section, e.g. by modifying the IS singular direct part. A proposal how to achieve this has been worked out in [4] and has been reviewed already in the proceedings of the workshop on *HERA and the LHC* of 2004-2005 [5] (see also [6]). Since from a theoretical point of view only the suppression of the resolved or in addition the IS singular direct component [4] is viable, it is an interesting question whether the diffractive dijet photoproduction data show breaking of the factorization, how large the suppression in comparison to no breaking will be, and whether the breaking occurs in all components or just in the resolved plus direct IS component. The value of the suppression factor or survival probability can then be compared to theoretical predictions [7] and to the survival probability

observed in jet production in $p\bar{p}$ collisions at the Tevatron [2] and will be of interest for similar diffractive processes at the LHC.

Since 2005 no further developments occurred on the theoretical side. On the experimental side, however, the final diffractive PDFs (DPDFs), which have been determined from the inclusive measurements of the diffractive structure function F_2^D by the H1 collaboration, have been published [8]. Also both collaborations at HERA, H1 and ZEUS, have now published their final experimental data of the cross sections for diffractive dijet photoproduction [9, 10]. Whereas H1 confirm in [9] their earlier findings based on the analysis of preliminary data and preliminary DPDFs, the authors of the ZEUS analysis [10] reached somewhat different conclusions from their analysis. Specifically, the H1 collaboration [9] obtained a global suppression of their measured cross sections as compared to the NLO calculations. In this comparison [9], the survival probability is R = 0.5, independent of the DPDFs fit used, i.e. fit A or B in Ref. [8]. In addition they concluded that the assumption that the direct cross section obeys factorization is strongly disfavored by their analysis. The ZEUS collaboration, on the other hand, concluded from their analysis [10], that, within the large uncertainties of the NLO calculations, their data are compatible with the QCD calculations, i.e. that no suppression would be present.

Due to these somewhat inconsistent results we made a new effort [11] to analyze the H1 [9] and the ZEUS [10] data, following more or less the same strategy as in our earlier work [12, 13] on the basis of the NLO program of [12, 13] and the new DPDFs sets of Ref. [8]. The H1 and the ZEUS dijet data cannot be compared directly, since they have different kinematic cuts. In particular, in the H1 measurements [9] $E_T^{jet1(2)} > 5$ (4) GeV and $x_{I\!P} < 0.03$, and in the ZEUS measurements [10] $E_T^{jet1(2}) > 7.5$ (6.5) GeV and $x_{I\!P} < 0.025$ (these and all other variables used in this review are defined in [11–13] and in the corresponding experimental contribution in these proceedings). It is clear that in order to establish a global suppression, i.e. an equal suppression of the direct and the resolved cross section, the absolute normalization and not so much the shape of the measured cross section is very important. This normalization depends on the applied kinematic cuts. Of course, the same cuts must be applied to the NLO cross section calculation. In case of a resolved suppression only, the suppression depends on the normalization of the cross sections, but also on the shape of some (in particular the x_γ^{obs}, E_T^{jet1}, M_{12}, and $\bar{\eta}^{jets}$) distributions, and will automatically be smaller at large E_T^{jet1} [3]. Distributions in $x_{I\!P}$ and y (or W) are not sensitive to the suppression mechanism. The distribution in $z_{I\!P}$, on the other hand, is sensitive to the functional behavior of the DPDFs, in particular of the gluon at large fractional momenta.

In the meantime, the H1 collaboration made an effort to put more light into the somewhat contradictory conclusions of the H1 [9] and ZEUS [10] collaborations by performing a new analysis of their data, now with increased luminosity, with the same kinematic cuts as in [9], i.e. the low-E_T^{jet1} cut, and the high-E_T^{jet1} cut as in the ZEUS analysis [10]. The results have been presented at DIS 2008 [14] and will be published soon. We have performed a new study of these H1 [14] and ZEUS data [10] to show more clearly the differences between the three data sets [15]. In this contribution we shall show a selection of these comparisons. The emphasis in these comparisons will be, how large the survival probability of the diffractive dijet cross section will be globally and whether the model with resolved suppression only will also describe the data in a satisfactory way. In section 2 we show the comparison with the H1 data [14] and in section

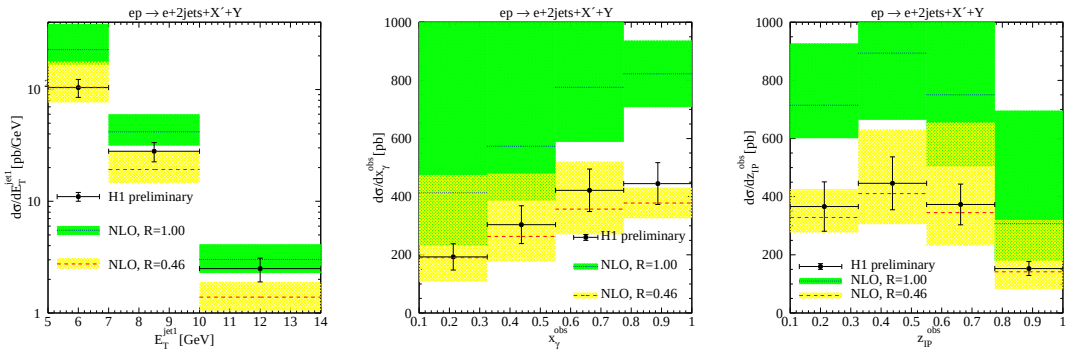

Fig. 1: Differential cross sections for diffractive dijet photoproduction as measured by H1 with low-E_T^{jet} cuts and compared to NLO QCD without ($R = 1$) and with ($R = 0.46$) global suppression (color online).

3 with the ZEUS data [10]. Section 4 contains our conclusions.

2 Comparison with recent H1 data

The recent H1 data for diffractive photoproduction of dijets [14] have several advantages as compared to the earlier H1 [9] and ZEUS [10] analyses. First, the integrated luminosity is three times higher than in the previous H1 analysis [9] comparable to the luminosity in the ZEUS analysis [10]. Second, H1 took data with low-E_T^{jet} and high-E_T^{jet} cuts, which allows for a comparison of [9] with [10]. The exact two kinematic ranges are given in [14]. The ranges for the low-E_T^{jet} cuts are as in the previous H1 analysis [9] and for the high-E_T^{jet} cuts are chosen as in the ZEUS analysis with two exceptions. In the ZEUS analysis the maximal cut on Q^2 is larger and the data are taken in an extended y-range. The definition of the various variables can be found in the H1 and ZEUS publications [9, 10]. Very important is the cut on $x_{I\!P}$. It is kept small in both analyses in order for the pomeron exchange to be dominant. In the experimental analysis as well as in the NLO calculations, jets are defined with the inclusive k_T-cluster algorithm [16, 17] in the laboratory frame. At least two jets are required with the respective cuts on E_T^{jet1} and E_T^{jet2}, where $E_T^{jet1(2)}$ refers to the jet with the largest (second largest) E_T^{jet}.

Before we confront the calculated cross sections with the experimental data, we correct them for hadronization effects. The hadronization corrections are calculated by means of the LO RAPGAP Monte Carlo generator. The factors for the transformation of jets made up of stable hadrons to parton jets were supplied by the H1 collaboration [14]. Our calculations are done with the 'H1 2006 fit B' [8] DPDFs, since they give smaller diffractive dijet cross sections than with the 'H1 2006 fit A'. We then take $n_f = 4$ with $\Lambda^{(4)}_{\overline{\rm MS}} = 0.347$ GeV, which corresponds to the value used in the DPDFs 'H1 2006 fit A, B' [8]. For the photon PDFs we have chosen the NLO GRV parameterization transformed to the $\overline{\rm MS}$ scheme [18].

As it is clear from the discussion of the various preliminary analyses of the H1 and ZEUS collaborations, there are two questions which we would like to answer from the comparison with the recent H1 and the ZEUS data. The first question is whether a suppression factor, which differs substantially from one, is needed to describe the data. The second question is whether the data

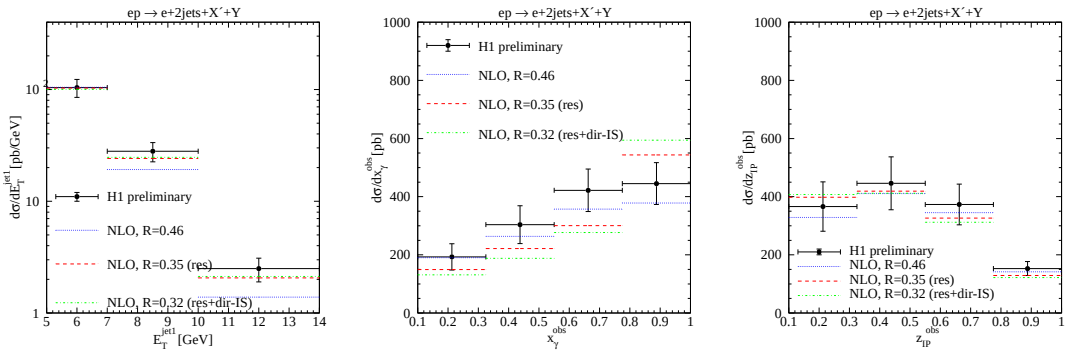

Fig. 2: Differential cross sections for diffractive dijet photoproduction as measured by H1 with low-E_T^{jet} cuts and compared to NLO QCD with global, resolved, and resolved/direct-IS suppression.

are also consistent with a suppression factor applied to the resolved cross section only. For both suppression models it is also of interest whether the resulting suppression factors are universal, i.e. whether they are independent of the kinematic variables of the process. To give an answer to these two questions we calculated first the cross sections with no suppression factor ($R = 1$ in the following figures) with a theoretical error obtained from varying the common scale of renormalization and factorization by factors of 0.5 and 2 around the default value (highest E_T^{jet}). In a second step we show the results for the same differential cross sections with a global suppression factor, adjusted to $d\sigma/dE_T^{jet1}$ at the smallest E_T^{jet1}-bin. As in the experimental analysis [14], we consider the differential cross sections in the variables x_γ^{obs}, $z_{I\!P}^{obs}$, $\log_{10}(x_{I\!P})$, E_T^{jet1}, M_X, M_{12}, $\overline{\eta}^{jets}$, $|\Delta\eta^{jets}|$ and W [15]. Here we show only a selection, i.e. the cross sections as a function of E_T^{jet1}, x_γ^{obs} and $z_{I\!P}^{obs}$. For the low-E_T^{jet} cuts, the resulting suppression factor is $R = 0.46 \pm 0.14$, which gives in the lowest E_T^{jet1}-bin a cross section equal to the experimental data point. The error comes from the combined experimental statistical and systematic error. The theoretical error due to the scale variation is taken into account when comparing to the three distributions. The results of this comparison are shown in Figs. 1a-c. With the exception of Fig. 1a , where the comparison of $d\sigma/dE_T^{jet1}$ is shown, the other two plots are such that the data points lie outside the error band based on the scale variation for the unsuppressed case. However, the predictions with suppression $R = 0.46$ agree nicely with the data inside the error bands from the scale variation. Most of the data points even agree with the $R = 0.46$ predictions inside the much smaller experimental errors. In $d\sigma/dE_T^{jet1}$ (see Fig. 1a) the predictions for the second and third bins lie outside the data points with their errors. For $R = 1$ and $R = 0.46$ this cross sections falls off stronger with increasing E_T^{jet1} than the data, the normalization being of course about two times larger for $R = 1$. In particular, the third data point agrees with the $R = 1$ prediction. This means that the suppression decreases with increasing E_T^{jet1} (see also Fig. 5 below). This behavior was already apparent when we analyzed the first preliminary H1 data [12,13]. Such a behavior points in the direction that a suppression of the resolved cross section only would give better agreement with the data, as we shall see below. The survival probability $R = 0.46 \pm 0.14$ agrees with the result in [14], which quotes $R = 0.51 \pm 0.01$ (stat.) $\pm$ 0.10 (syst.), determined by fitting the integrated cross section. From our comparison we conclude that the low-E_T^{jet} data show a global

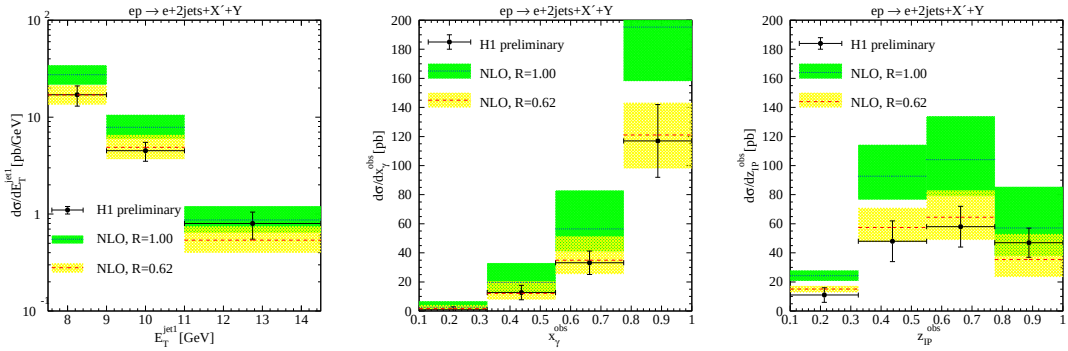

Fig. 3: Differential cross sections for diffractive dijet photoproduction as measured by H1 with high-E_T^{jet} cuts and compared to NLO QCD without ($R = 1$) and with ($R = 0.62$) global suppression (color online).

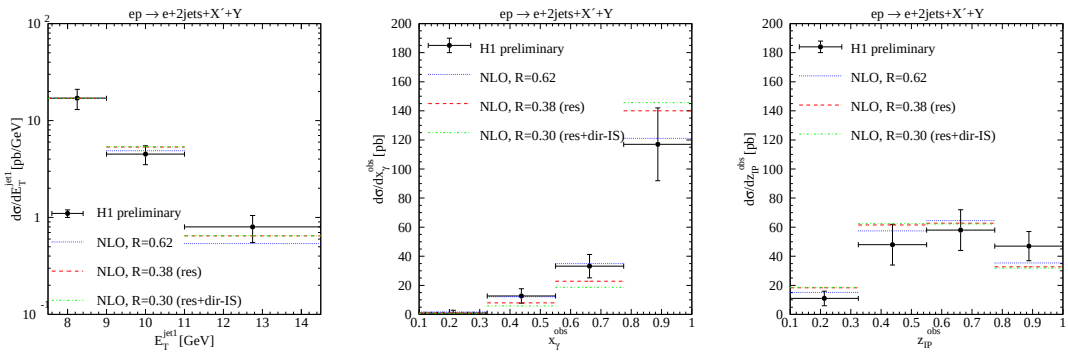

Fig. 4: Differential cross sections for diffractive dijet photoproduction as measured by H1 with high-E_T^{jet} cuts and compared to NLO QCD with global, resolved, and resolved/direct-IS suppression.

suppression of the order of two in complete agreement with the results [12, 13] and [9] based on earlier preliminary and final H1 data [9].

Next we want to answer the second question, whether the data could be consistent with a suppression of the resolved component only. For this purpose we have calculated the cross sections in two additional versions: (i) suppression of the resolved cross section and (ii) suppression of the resolved cross section plus the NLO direct part which depends on the factorization scale at the photon vertex [4]. The suppression factors needed for the two versions will, of course, be different. We determine them again by fitting the measured $d\sigma/dE_T^{jet1}$ for the lowest E_T^{jet1}-bin (see Fig. 2a). Then, the suppression factor for version (i) is $R = 0.35$ (denoted res in the figures), and for version (ii) it is $R = 0.32$ (denoted res+dir-IS). The results for $d\sigma/dE_T^{jet1}$, $d\sigma/dx_\gamma^{obs}$ and $d\sigma/dz_{I\!P}^{obs}$ are shown in Figs. 2a-c, while the six other distributions can be found in [15]. We also show the global (direct and resolved) suppression prediction with $R = 0.46$ already shown in Figs. 1a-c. For the cross section as a function of $z_{I\!P}^{obs}$, the agreement with the global suppression ($R = 0.46$) and the resolved suppression ($R = 0.35$ or $R = 0.32$) is comparable. For $d\sigma/dE_T^{jet1}$, the agreement improves considerably for the resolved suppression only

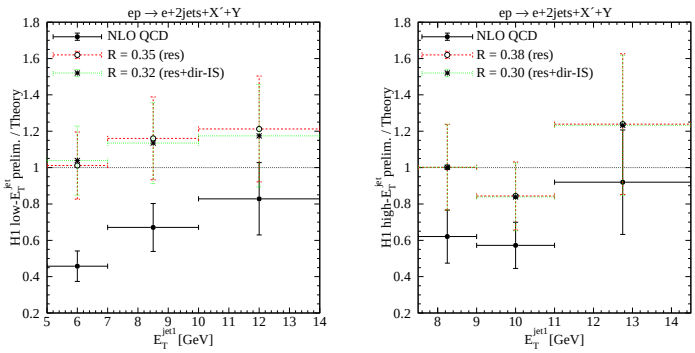

Fig. 5: Ratio of the E_T^{jet1}-distribution as measured by H1 with low-E_T^{jet} (left) and high-E_T^{jet} cuts (right) to the NLO QCD prediction without (full), with resolved-only (dashed), and with additional direct IS suppression (dotted).

(note the logarithmic scale in Fig. 2a). The global suppression factor could, of course, be E_T-dependent, although we see no theoretical reason for such a dependence. For $d\sigma/dx_\gamma^{obs}$, which is usually considered as the characteristic distribution for distinguishing global versus resolved suppression, the agreement with resolved suppression does not improve. Unfortunately, this cross section has the largest hadronic corrections of the order of $(25-30)\%$ [14]. Second, also for the usual photoproduction of dijets the comparison between data and theoretical results has similar problems in the large x_γ^{obs}-bin [19], although the E_T^{jet}-cut is much larger there. In total, we are tempted to conclude from the comparisons in Figs. 2a-c that the predictions with a resolved-only (or resolved+direct-IS) suppression are consistent with the new low-E_T^{jet} H1 data [14] and the survival probability is $R = 0.35$ (only resolved suppression) and $R = 0.32$ (resolved plus direct-IS suppression), respectively.

The same comparison of the high-E_T^{jet} data of H1 [14] with the various theoretical predictions is shown in the following figures. The global suppression factor is obtained again from a fit to the smallest E_T^{jet1}-bin. It is equal to $R = 0.62 \pm 0.16$, again in agreement with the H1 result $R = 0.62 \pm 0.03$ (stat.) $\pm$ 0.14 (syst.) [14]. The same cross sections as for the low-E_T^{jet} comparison are shown in Figs. 3a-c for the two cases $R = 1$ (no suppression) and $R = 0.62$ (global suppression), while the six others can again be found in [15]. As before with the exception of $d\sigma/dE_T^{jet1}$ and $d\sigma/dM_{12}$ (not shown), most of the data points lie outside the $R = 1$ results with their error bands and agree with the suppressed prediction with $R = 0.62$ inside the respective errors. However, compared to the results in Figs. 1a-c the distinction between the $R = 1$ band and the $R = 0.62$ band and the data is somewhat less pronounced, which is due to the larger suppression factor. We also tested the prediction for the resolved (resolved+direct-IS) suppression, which is shown in Figs. 4a-c. The suppression factor fitted to the smallest bin came out as $R = 0.38$ (res) and $R = 0.30$ (res+dir-IS), which are almost equal to the corresponding suppression factors derived from the low-E_T^{jet} data. In most of the comparisons it is hard to observe any preference for the global against the pure resolved (resolved plus direct-IS) suppression. We remark that the suppression factor for the global suppression is increased by 35%, if we go from the low-E_T^{jet} to the high-E_T^{jet} data, whereas for the resolved suppression this increase is only 9%. Under the assumption that the suppression factor should not depend on E_T^{jet1}, we would

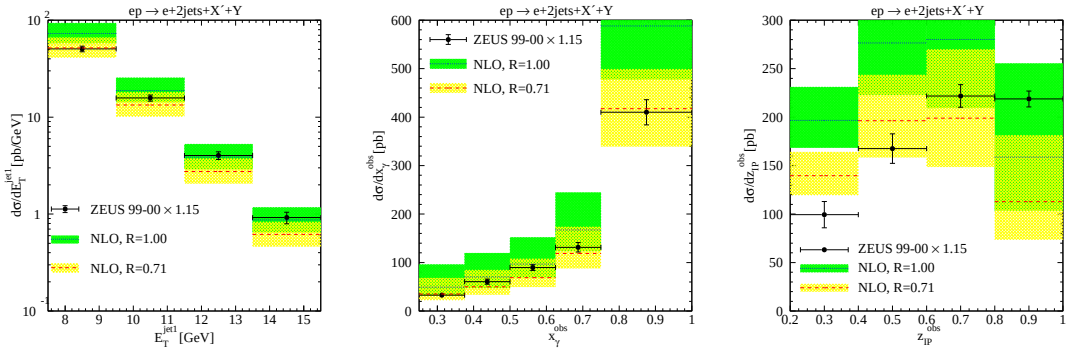

Fig. 6: Differential cross sections for diffractive dijet photoproduction as measured by ZEUS and compared to NLO QCD without ($R = 1$) and with ($R = 0.71$) global suppression (color online).

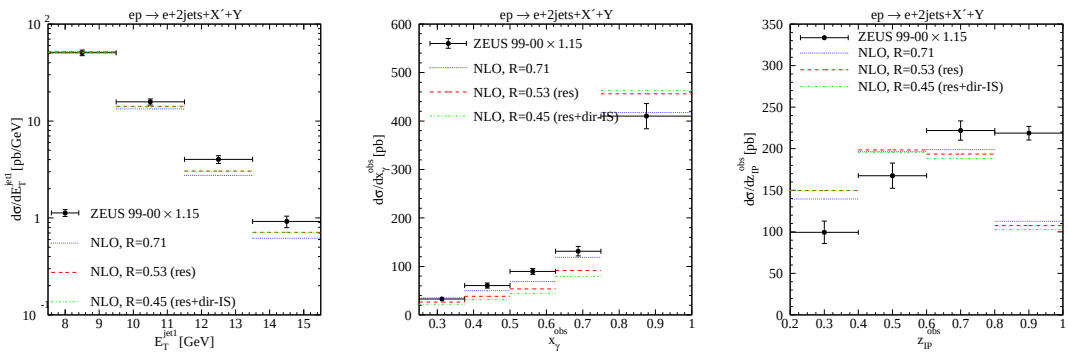

Fig. 7: Differential cross sections for diffractive dijet photoproduction as measured by ZEUS and compared to NLO QCD with global, resolved, and resolved/direct-IS suppression.

conclude that the resolved suppression would be preferred, as can also be seen from Fig. 5. A global suppression is definitely observed also in the high-E_T^{jet} data and the version with resolved suppression explains the data almost as well as with the global suppression.

In Fig. 5 we show the ratio of of the E_T^{jet1}-distribution as measured by H1 to the NLO QCD prediction without (full), with resolved-only (dashed), and with additional direct IS suppression (dotted). Within the experimental errors, obviously only the former, but not the latter are E_T^{jet}-dependent.

3 Comparison with ZEUS data

In this section we shall compare our predictions with the final analysis of the ZEUS data, which was published this year [10], in order to see whether they are consistent with the large-E_T^{jet} data of H1. The kinematic cuts [10] are almost the same as in the high-E_T^{jet} H1 measurements. The only major difference to the H1 cuts is the larger range in the variable y. Therefore the ZEUS cross sections will be larger than the corresponding H1 cross sections. The constraint on M_Y is

not explicitly given in the ZEUS publication [10]. They give the cross section for the case that the diffractive final state consists only of the proton. For this they correct their measured cross section by subtracting in all bins the estimated contribution of a proton-dissociative background of 16%. When comparing to the theoretical predictions they multiply the cross section with the factor 0.87 in order to correct for the proton-dissociative contributions, which are contained in the DPDFs 'H1 2006 fit A' and 'H1 2006 fit B' by requiring $M_Y < 1.6$ GeV. We do not follow this procedure. Instead we leave the theoretical cross sections unchanged, i.e. they contain a proton-dissociative contribution with $M_Y < 1.6$ GeV and multiply the ZEUS cross sections by 1.15 to include the proton-dissociative contribution. This means that the so multiplied ZEUS cross sections have the same proton dissociative contribution as is in the DPDF fits of H1 [8]. Since the ZEUS collaboration did measurements only for the high-E_T^{jet} cuts, $E_T^{jet1(2)} > 7.5$ (6.5) GeV, we can only compare to those. In this comparison we shall follow the same strategy as before. We first compared to the predictions with no suppression ($R = 1$) and then determine a suppression factor by fitting $d\sigma/dE_T^{jet1}$ to the smallest E_T^{jet1}-bin. Then we compared to the cross sections as a function of the seven observables x_γ^{obs}, $z_{I\!P}^{obs}$, $x_{I\!P}$, E_T^{jet1}, y, M_X and η^{jet1} instead of the nine variables in the H1 analysis. The distribution in y is equivalent to the W-distribution in [14]. The theoretical predictions for these differential cross sections with no suppression factor ($R = 1$) are shown in Figs. 6a-g of [11], together with their scale errors and compared to the ZEUS data points, and a selection is shown in Fig. 6. Except for the x_γ^{obs}- and E_T^{jet1}-distributions, most of the data points lie outside the theoretical error bands for $R = 1$. In particular, in Figs. 6b, c, e, f and g, most of the points lie outside. This means that most of the data points disagree with the unsuppressed prediction. Next, we determine the suppression factor from the measured $d\sigma/dE_T^{jet1}$ at the lowest E_T^{jet1}-bin, 7.5 GeV $< E_T^{jet1} < 9.5$ GeV, and obtain $R = 0.71$. This factor is larger by a factor of 1.15 than the suppression factor from the analysis of the high-E_T^{jet} data from H1. Curiously, this factor is exactly equal to the correction factor we had to apply to restore the dissociative proton contribution. Taking the total experimental error of $\pm 7\%$ from the experimental cross section $d\sigma/dE_T^{jet1}$ in the first bin into account, the ZEUS suppression factor is 0.71 ± 0.05 to be compared to 0.62 ± 0.14 in the H1 analysis [14], so that both suppression factors agree inside the experimental errors.

If we now check how the predictions for $R = 0.71$ compare to the data points inside the theoretical errors, we observe from Figs. 6a-g of Ref. [11] that, with the exception of $d\sigma/dz_{I\!P}^{obs}$ and $d\sigma/dE_T^{jet1}$, most of the data points agree with the predictions. This is quite consistent with the H1 analysis (see above) and leads to the conclusion that also the ZEUS data agree much better with the suppressed predictions than with the unsuppressed prediction. In particular, the global suppression factor agrees with the global suppression factor obtained from the analysis of the H1 data inside the experimental error.

Similarly as in the previous section we compared the ZEUS data also with the assumption that the suppression results only from the resolved cross section. Here, we consider again (i) only resolved suppression (res) and (ii) resolved plus direct suppression of the initial-state singular part (res+dir-IS). For these two models we obtain the suppression factors $R = 0.53$ and $R = 0.45$, respectively, where these suppression factors are again obtained by fitting the data point at the first bin of $d\sigma/dE_T^{jet1}$. The comparison to the global suppression with $R = 0.71$ and to the data is shown in Figs. 7a-g of [11] and a selection in Fig. 7. In general, we observe that the difference

between global suppression and resolved suppression is small, i.e. the data points agree with the resolved suppression as well as with the global suppression.

4 Conclusion

In conclusion, we found that most of the data points of diffractive dijet photoproduction in the latest H1 analyses with low- and high-E_T^{jet} cuts and in the final ZEUS analysis with the same high-E_T^{jet} cuts disagree with NLO QCD predictions within experimental and theoretical errors. When global factorization breaking is assumed in both the direct and resolved contributions, the resulting suppression factor would have to be E_T^{jet}-dependent, although we see no theoretical motivation for this assumption. Suppressing only the resolved or in addition the direct initial-state singular contribution by about a factor of three, as motivated by the proof of factorization in point-like photon-hadron scattering and predicted by absorptive models [7], the agreement between theory and data is at least as good as for global suppression, and no E_T^{jet}-dependence of the survival probability is needed.

References

[1] Collins, J.C., Phys. Rev. **D57**, 3051 (1998).

[2] Affolder, A.A. *et al.,* Phys. Rev. Lett. **84**, 5043 (2000).

[3] Klasen, M., Rev. Mod. Phys. **74**, 1221 (2002).

[4] Klasen, M. and Kramer, G., J. Phys. **G31**, 1391 (2005).

[5] Bruni, A., Klasen, M., Kramer, G., and Schaetzel, S. Prepared for the Workshop on the Implications of HERA for LHC Physics, CERN, Geneva, Switzerland, 26-27 Mar 2004.

[6] Klasen, M. and Kramer, G., AIP Conf. Proc. **792**, 444 (2005).

[7] Kaidalov, A.B., Khoze, V.A., Martin, A.D., and Ryskin, M.G., Phys. Lett. **B567**, 61 (2003).

[8] Aktas, A. *et al.,* Eur. Phys. J. **C48**, 715 (2006).

[9] Aktas, A. *et al.,* Eur. Phys. J. **C51**, 549 (2007).

[10] Chekanov, S. *et al.,* Eur. Phys. J. **C55**, 177 (2008).

[11] Klasen, M. and Kramer, G., Mod. Phys. Lett. **A23**, 1885 (2008).

[12] Klasen, M. and Kramer, G. Prepared for 12th Int. Workshop on Deep Inelastic Scattering, Strbske Pleso, Slovakia, 14-18 Apr 2004.

[13] Klasen, M. and Kramer, G., Eur. Phys. J. **C38**, 93 (2004).

[14] Aktas, A. *et al.* Prepared for 16th Int. Workshop on Deep Inelastic Scattering, London, England, 7-11 Apr 2008.

[15] Klasen, M. and Kramer, G. DESY 08-109, LPSC 08-113, to be published.

[16] Ellis, S.D. and Soper, D.E., Phys. Rev. **D48**, 3160 (1993).

[17] Catani, S., Dokshitzer, Y.L., Seymour, M.H., and Webber, B. R., Nucl. Phys. **B406**, 187 (1993).

[18] Glueck, M., Reya, E., and Vogt, A., Phys. Rev. **D46**, 1973 (1992).

[19] Aktas, A. *et al.*, Phys. Lett. **B639**, 21 (2006).

Fracture Functions at HERA and LHC

Federico Alberto Ceccopieri, Luca Trentadue
Dipartimento di Fisica, Universitá degli Studi di Parma
INFN Gruppo Collegato di Parma, Italy

Abstract
Developments of the fracture functions formalism in the context of DIS jet cross-sections and Semi-Inclusive Drell-Yan process at hadron colliders are briefly presented.

Fracture functions were introduced in Ref. [1] in order to give a QCD-based description of semi-inclusive Deep Inelastic Scattering in the target fragmentation region. The first analyses of HERA data [2] revealed a non-negligible contributions to the DIS cross-sections of events characterized by absence of hadronic activity in the remnant direction. Recent analyses of diffractive data collected by H1 and ZEUS collaborations have now confirmed substantial contributions of perturbative QCD effects in diffractive DIS cross-sections [3]. This experimental evidence strengthens the idea itself of fracture functions. These non-perturbative distributions, hereafter indicated by $M^i_{h/P}(x,z,Q^2)$, give the conditional probability of finding at a given scale Q^2 a parton i with momentum fraction x of the incoming hadron momentum P while a hadron h, with momentum fraction z, is detected in the target fragmentation region of P. In Ref. [4] it was shown within a fixed order $\mathcal{O}(\alpha_s)$ calculation that the additional collinear singularities occurring in the remnant direction can be properly renormalized only introducing fracture functions. An all-order proof of collinear and soft singularities factorization into $M^i_{h/P}(x,z,Q^2)$ was finally given in Refs. [5] and [6], respectively. This theoretical background offers the basis for an accurate analysis of diffractive data and the possibility to fully exploit factorization in order to extract diffractive parton distributions, *i.e.* fracture functions. In this brief contribution we will report on recent developments in this topic. In particular we will focus on the extension of fracture functions in the context of DIS jet cross-section and their possible applications to hadronic collisions.

As is well known, hadrons resulting from a hard interaction are often collimated in a definite portion of momentum space. Hadron jets are the highlighting signature of the dominant collinear branching of pQCD dynamics. For this reason jet cross-sections are the natural and, possibly, the most effective representation of hadronic final state. While jet cross-sections with a given, in general low, number of partons in the final state are calculable within pQCD, a description of the beam-jet in terms of pQCD is however precluded by its intrinsic soft and kinematical nature. It results from the fragmentation of the spectator partons of the hadron remnants plus, eventually, semi-hard radiation coming from the evolution of the active parton at low momentum transfer. Since at the forthcoming hadron collider topics as minimum bias and underlying event will play a central role and will probably plague the extraction of hard scattering events signals, we have proposed and introduced in Ref. [7] a new semi-inclusive jet-like distribution, here after indicated with $\mathcal{M}^i_{\triangleleft}(x,Q^2,z,t)$, referring to it as to a jet-like fracture function. $\mathcal{M}^i_{\triangleleft}(x,Q^2,z,t)$ expresses the probability of finding a parton i with fractional momentum x of the incoming

hadron and virtuality Q^2, while a cluster of hadrons h_i is detected in a portion of phase space $\mathcal{R}$ specified by two variables, z and t. The region $\mathcal{R}$ is limited by the constraint

$$\mathcal{R}: \quad t_i = -(P - h_i)^2 < t, \quad t_0 \leq t \ll Q^2 \,, \tag{1}$$

where the value of t is arbitrary chosen and can be conceived as the analogous of the clustering variable used in ordinary jet-algorithms. Once the clustering procedure is performed, the variable z is obtained by summing the fractional longitudinal momenta of all hadrons h_i satisfying the constraint in eq. (1):

$$z = \sum_i z_i, \quad h_i \in \mathcal{R} \,. \tag{2}$$

In analogy with the standard inclusive DIS, which makes use of parton distributions functions, we may write the beam-jet DIS cross-section as

$$\frac{1}{\sigma_{tot}} \frac{d\sigma^{\mathcal{R},jet}}{dx dQ^2 dz dt} \propto x \sum_{i=q,\bar{q}} e_i^2 \, \mathcal{M}^i_{\triangleleft}(x, Q^2, z, t) \,. \tag{3}$$

In this framework, the parton initiating the space-like cascade is specified by the initial state radiation itself, *i.e.* the closest in rapidity to the hadron remnant. It has a fractional momentum $1 - z$, where z is overall fractional momentum taken away by the hadrons with $t_i \leq t$ and has the highest allowed virtuality, t, according to strong ordering. When t is chosen in the perturbative region, as shown in Ref. [7], jet-like fracture functions obey a standard DGLAP evolution equations:

$$Q^2 \frac{\partial}{\partial Q^2} \mathcal{M}^i_{\triangleleft}(x, Q^2, z, t) = \frac{\alpha_s(Q^2)}{2\pi} \int_{\frac{x}{1-z}}^1 \frac{du}{u} \, P^i_j(u) \, \mathcal{M}^j_{\triangleleft}(x/u, Q^2, z, t) \,. \tag{4}$$

This equation describes how the virtual photon resolves the distributions $\mathcal{M}^i_{\triangleleft}$ when the virtuality of the latter is varied. In particular it resums potentially large collinear logarithms of the type $\alpha_s^n \log^n(Q^2/t)$. In real processes, strong t-ordering is only partially realized and one could in principle improve the theoretical description including higher order and coherence effects. As discussed in Ref. [7], the introduction of $\mathcal{M}^i_{\triangleleft}$ allows one to include the beam remnants jet in the perturbative treatment of DIS jet cross-sections. Moreover jet-like fracture functions could find applications also in hard diffractive processes. In events characterized by the absence of hadron activity in the remnant direction, this absence can be conceived as the *shadow* in the detector of the propagation of the exchanged object in the t-channel. The rapidity gap can then be considered as a *missing jet*. It can be defined in terms of a jet-like fracture functions specified by the value t of the measured particle at the edge of the gap, *i.e.* the one with the highest rapidity (a part from the proton itself). The study of *gap topology* might be important to investigate diffractive phenomena and jet-like fracture functions could be a useful tool in this context.

The knowledge acquired at HERA on Deep Inelastic process in the target fragmentation region is expected to be essential in the LHC diffractive physics program. Dedicated experiments as TOTEM will measure leading baryon production, while combined CMS-TOTEM measurements will trigger on a wide class of diffractive processes characterized by a large momentum

transfer [8]. The fundamental step in transporting information from diffractive Deep Inelastic Scattering at HERA to LHC is to assume factorization to hold in hard diffractive hadron-hadron reactions. The Tevatron analysis has put, however, serious doubts on such an hypothesis. A non universality of diffractive parton distributions, as extracted from diffractive DIS, emerged when these distributions were used to predict hard scattering events cross-sections [9]. In such a reactions, at variance with diffractive DIS where factorization has been shown to hold in Ref. [6], theoretical arguments has been given such that the detection of particle in the target fragmentation region leads to a factorization breaking effect [6, 10]. For this reasons our understanding of the dynamics of diffractive processes is strongly correlated with the understanding of factorization.

Hard diffractive processes can be approached with pQCD techniques and the Drell-Yan process plays indeed a central role in this context. In particular it is the only hadrons-induced process for which factorization has been shown to hold at soft and collinear level [11]. Furthermore QCD corrections to this process have been calculated for inclusive and differential distributions in such a way that it constitutes a fundamental testing process of QCD at the hadron collider. For this reasons we have performed in Ref. [12] a pQCD analysis of the Semi-Inclusive Drell-Yan process

$$P_1 + P_2 \to \gamma^* + h + X\,. \tag{5}$$

In eq. (5) P_1 and P_2 stands for the incoming hadrons, γ^* the virtual photon of invariant mass Q^2 and h the additional hadron measured in the final state. If Q^2 is large enough so that perturbation theory applies, the factorization property of the considered cross-section should depend on the region of phase space in which the final hadron h is detected. In particular, if h is produced at sufficiently high transverse momentum, $p^2_{h\perp}$, then the relative cross-sections can be predicted by pQCD. On the contrary, if h is produced at low $p^2_{h\perp}$ and thus detected in the target fragmentation region, arguments against factorization have been already given in Refs. [6, 10]. The formalism of fracture functions allows one to performed a next-to-leading order QCD analysis of the Semi-Inclusive Drell-Yan process without introducing unphysical scale in order to separate the dominant production mechanisms in each region of phase space. The first step in order to perform consistently such a calculation is to provide a parton model formula for the considered process. Since in zero-th order QCD initial state radiation is absent, we assume the hadron h is "non-perturbatively" produced in the target fragmentation region of P_1 ($\mathcal{R}_{T_1}$) or P_2 ($\mathcal{R}_{T_2}$) by means of a "bare" (in the renormalization sense) fracture function $M^i_{h/P}(x,z)$. In the following we will consider the differential cross-sections for producing a lepton pair of invariant mass $Q^2 \gg \Lambda^2_{QCD}$, accompanied by an additional hadron h with fractional energy $z = 2E_h/\sqrt{S}$ (defined in the hadronic center of mass frame) and integrated over its transverse momentum, $p^2_{h\perp}$. By defining the combination $M^h_q(x,z) = M^{h/P_1}_q(x,z) + M^{h/P_2}_q(x,z)$, the parton model formula for the semi-inclusive Drell-Yan cross-sections reads:

$$\frac{d\sigma^{DY}(\tau)}{dQ^2 dz} = \frac{4\pi\alpha^2}{9SQ^2}\int_\tau^{1-z}\frac{dx_1}{x_1}\int_{\frac{\tau}{x_1}}^1\frac{dx_2}{x_2}\sum_q e_q^2\Big[M^h_q(x_1,z)f_{\bar q}(x_2) + (x_1 \leftrightarrow x_2)\Big]\,\delta\Big(1-\frac{\tau}{x_1x_2}\Big)\,. \tag{6}$$

A pictorial representation of this formula is drawn in Fig. (1). In the following we will restrict ourselves to the discussion of NLO corrections to the $q\bar q$ channel. The corrections to eq. (6) have

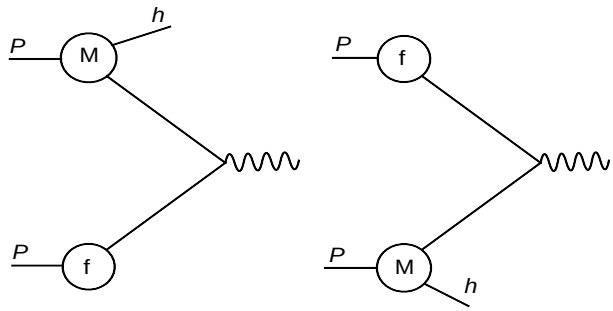

Fig. 1: A pictorial representation of the parton model formula for Semi-Inclusive Drell-Yan process, eq. (6).

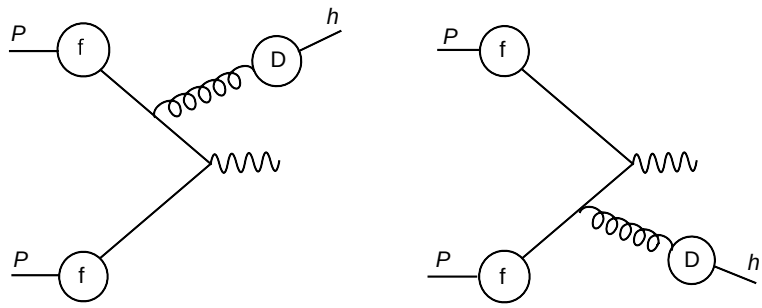

Fig. 2: A pictorial representation of the second term on r.h.s. in eq. (7). The observed hadron h results from the hadronization of initial state radiation (gluon).

the following formal structure

$$d\sigma_{q\bar{q}}^{DY,(1)} \;\simeq\; M_q^h \otimes f_{\bar{q}} \otimes \left[1 + \frac{\alpha_s}{2\pi} C_{q\bar{q}}\right] + \frac{\alpha_s}{2\pi} f_q \otimes f_{\bar{q}} \otimes D_g^h \otimes K_{q\bar{q}}^g \,, \tag{7}$$

where the symbol $\otimes$ stands for the convolution on the momentum fraction of the participating partons. The more involved part of the calculation does consist in evaluating next-to-leading order diagrams in which the final state parton hadronize into the observed hadron h. These diagrams are at the origin of the second term on the right hand side of eq. (7). An example of such a diagram is shown in Fig. (2). The coefficient functions $C_{q\bar{q}}$ and $K_{q\bar{q}}^g$ at this level still present poles due to collinear singularities. It is however possible to show, see Ref. [12] for details, that all collinear singularities can be subtracted from the coefficient functions by the same factorization procedure firstly used in Ref. [4] in the context of Deep Inelastic Scattering. We consider this result as a direct evidence of collinear factorization for the Semi-Inclusive Drell-Yan cross-sections. The present QCD-based calculation deals however only with standard soft gluon exchange between active partons but it is blind to soft gluon exchange between spectators. Since our findings support factorization at the collinear level, we implicitly confirm the general widespread idea indicating soft exchanges between spectators partons as responsible for factorization breaking in semi-inclusive hadronic collisions. When diffractive parton distribution, as obtained from HERA data, are used in the present calculation, the resulting predictions would

be valid only in the case that factorization hypothesis holds. As a consequence, any deviation observed in the data not accounted for by the present NLO calculation, could be interpreted as a manifestation of factorization breaking. A comparison with data would also establish whether a factorization breaking shows up only in a diffractive kinematic regime or if it manifests itself also in processes with a gapless final state containing, as well, a single hadron in the target fragmentation region. At the same time it would be interesting to study, within the proposed approach, light mesons production which is sensitive to the soft, high multiplicity, fragmentation process. For this reason, in Ref. [12], we address the Semi-Inclusive Drell-Yan process as a prototype of *factorization analyzer*. Since we expect that the factorizing properties of the cross-sections to be extremely sensible to the $p_{h\perp}^2$ of the measured hadron h, we guess that a more efficient observable in this context would be the triple-differential cross-sections:

$$\frac{d\sigma^{DY}}{dQ^2 dp_{h\perp}^2 dz}\,, \tag{8}$$

for which an analog of the present calculation is still not available. The possible identification of an intermediate scale or range of scales at which the factorization breaking effects start to manifest themselves would constitute an important insight into the dynamics of the factorization mechanism.

Let us conclude by listing some further possible developments of the formalism. The present work can be generalized to double hadron production. The evaluation of a double hadron production cross-section needs a full $\mathcal{O}(\alpha_s^2)$ QCD calculation. However, as discussed in Ref. [12], an approximate result could be obtained if one considers the production of two hadrons at low $p_{h\perp}^2$ observed in opposite fragmentation regions with respect to the incoming hadrons. In this case higher order corrections for this process should be the same as for inclusive Drell-Yan process, when the proper kinematics is taken into account. Finally we are thinking to a generalization of the present approach to include gluon initiated hard processes [13] whose relevance in diffractive Higgs production was first suggested in Ref. [14].

References

[1] L. Trentadue, G. Veneziano, Phys. Lett. **B 323**, 201 (1994) .

[2] ZEUS Collaboration, Phys. Lett. **B 315**, 481 (1993);
H1 Collaboration Nucl. Phys. **B 435**, 3 (1995) .

[3] S. Chekanov & al., ZEUS Collaboration, Nucl. Phys. **B 713**, 3 (2005);
A. Aktas & al., H1 Collaboration, Eur. Phys. J. **C 48**, 715 (2006) .

[4] D. Graudenz, Nucl. Phys. **B 432**, 351 (1994) .

[5] M. Grazzini, L. Trentadue, G. Veneziano, Nucl. Phys. **B 519**, 394 (1998) .

[6] J.C. Collins, Phys. Rev. **D 57**, 3051 (1998) .

[7] F.A. Ceccopieri, L. Trentadue, Phys. Lett. **B 665**, 15 (2007) .

[8] M. Albrow et al., CERN-LHCC-2006-039, CERN-LHCC-G-124, CERN-CMS-NOTE-2007-002 .

[9] CDF Collaboration, Phys. Rev. Lett. **84**, 5043 (2000) .

[10] J. C. Collins, L. Frankfurt, M. Strikman, Phys. Lett. **B 307**, 161 (1993); A. Berera, D. E. Soper, Phys. Rev. **D 50**, 4328 (1994) .

[11] W.W. Lindsay, D.A. Ross, C.T. Sachrajda, Phys. Lett. **B 117**, 105 (1982); Nucl. Phys. **B 214**, 61 (1983); Nucl. Phys. **B 222**, 189 (1983); J.C. Collins, D.E. Soper, G. Sterman, Phys. Lett. **B 134**, 263 (1984); Nucl. Phys. **B 261**, 104 (1985); G. T. Bodwin, Phys. Rev. **D 31**, 2616 (1985); Erratum-ibid. **D 34**, 3932 (1986) .

[12] F.A. Ceccopieri, L. Trentadue, Phys. Lett. **B 668**, 319 (2008) .

[13] S. Chekanov *et al.* [ZEUS Collaboration], Eur. Phys. J. C **52**, 813 (2007); A. Aktas *et al.* [H1 Collaboration], JHEP **0710**, 042 (2007); A. A. Affolder *et al.* [CDF Collaboration], Phys. Rev. Lett. **88**, 151802 (2002) .

[14] D. Graudenz, G. Veneziano, Phys. Lett. **B 365**, 302 (1996) .

Generalised parton distributions and exclusive vector meson production

C. Nockles and T. Teubner
Department of Mathematical Sciences, University of Liverpool, Liverpool L69 3BX, U.K.

Abstract
We briefly review recent developments in the description of exclusive vector meson production in terms of generalised parton distributions. The determination of the gluon distribution at small x from HERA data on diffractive J/ψ production is discussed.

1 Introduction

Contrary to normal DIS, processes like deeply virtual Compton scattering (DVCS) or the diffractive production of (di-) jets, heavy quarks or vector mesons (VMs), cannot be described accurately with the diagonal (normal) parton distribution functions (PDFs). This can be seen from Fig. 1, where the leading order diagram for DVCS (left) and J/ψ vector meson production (right figure) are shown. While DVCS is mainly testing the quark distribution, the amplitude for exclusive vector meson production is, to leading order, directly probing the gluon PDF. The momentum fractions x and x' of the two partons are in general different, resulting in a deviation from the diagonal limit for the distribution function of the respective parton. In this instance, a generalised parton distribution (GPD) must be used to describe the process.

Unlike the diagonal parton distributions, which represent a probability distribution, generalised distributions are defined by matrix elements of quark and gluon light-cone operators $\hat{\mathcal{O}}$ for different initial and final states of the proton, $\langle p'|\hat{\mathcal{O}}|p\rangle$. They encode richer information about the distribution of partons inside the hadron and have no direct probabilistic interpretation. One may express the parton momentum fractions in a GPD in a symmetric manner, with the introduction of a skewing parameter ξ and a symmetric $\tilde{x}$: $x = \tilde{x}-\xi$, $x' = \tilde{x}+\xi$. In the forward limit $\xi, t \to 0$, the generalised partons reduce to the conventional diagonal partons, where t is the square of the momentum transfer between initial and final protons. In the following we will briefly discuss

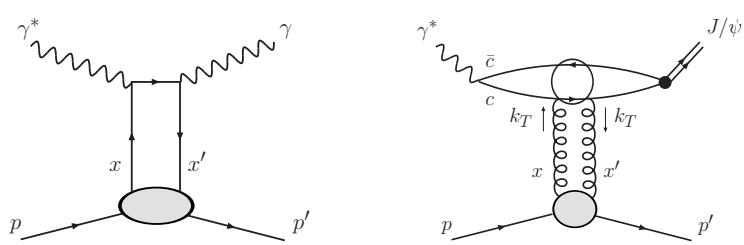

Fig. 1: Left: DVCS $\gamma^* p \to \gamma p'$ and right: elastic J/ψ production $\gamma^* p \to J\psi p'$. The two partons entering the scattering have different momentum fractions x, x'.

selected recent work on the prediction of diffractive production of vector mesons based on generalised parton distributions, both in the framework of collinear and k_T factorisation, and the determination of the small x gluon from diffractive J/ψ data in the latter framework.

2 Predictions for diffractive vector meson production

In the last years a lot of work has been done on dipole and saturation models. For a review of these topics in these proceedings we refer to [1]. Calculations in the framework of dipole cross sections often do not attempt at including the effect of non-forwardness. However, in [2] the skewedness is treated as in [3] discussed below.

2.1 Predictions based on collinear factorisation

Kroll and Goloskokov have described electroproduction of light vector mesons using collinear factorisation on the proton side [4–6]. In the limit of large photon virtuality Q^2 the production amplitude factorises into a perturbatively calculable hard scattering amplitude (coefficient function), a generalised PDF and the wave function of the VM. This is similar to DVCS, where the term 'handbag factorisation' is used which is particularly suitable in the case of initial quarks relevant at lower c.m. energies. The transverse momentum p_T of the quarks forming the vector meson is retained, and a corresponding meson light-cone wave function $\psi_{VM}(\tau, p_T)$ (with p_T the intrinsic transverse momentum and τ the fraction of the light-cone plus component of the meson's momentum carried by the quark) is used. In addition a Sudakov factor $\exp[-S(\tau, p_T, Q^2)]$ is applied at next-to-leading-logarithmic accuracy. This suppresses gluon radiation in the regime between a soft cut-off and a factorisation scale related to the quark-antiquark separation. Softer gluons are included in the VM wave function while harder ones are part of the hard, perturbative scattering amplitude. This so-called 'modified perturbative approach' cures the end-point singularities stemming from configurations with large transverse quark-antiquark separation which otherwise would prevent a prediction of the cross section for transversely polarised mesons. The generalised parton distributions are derived using the ansatz of double distributions following the work of Radyushkin [7] and using global PDFs as input for the diagonal limit.[1] The evolution is approximated by the evolution of the diagonal input. With their approach Kroll and Goloskokov find fair agreement with electroproduction data from COMPASS, HERMES, E665, ZEUS and H1, see [4–6] and Fig. 2 for an example of their longitudinal cross section predictions for ϕ and ρ electroproduction. The extension to contributions from transverse photons is discussed in [6].

While the approach of Kroll and Goloskokov is not restricted by the high energy approximation adopted in other calculations, the hard, perturbative scattering kernel used in [4–6] is leading order (LO) only. Next-to-leading order (NLO) corrections in the framework of collinear factorisation have been calculated by Ivanov et al. [8] and were found to be large generally. In their recent work Diehl and Kugler [9] have made use of these results to further study the impact

[1] Double distributions offer a way to parameterise the hadronic matrix elements defining generalised distributions [7]. They are defined through Fourier transforms of these matrix elements. Such double distributions guarantee the required symmetry properties and the polynomiality (Nth moments of GPDs are Nth degree polynomials in the skewing parameter ξ) of the derived generalised distributions. However their physical interpretation is different (and maybe less apparent) as they are not directly dependent on ξ.

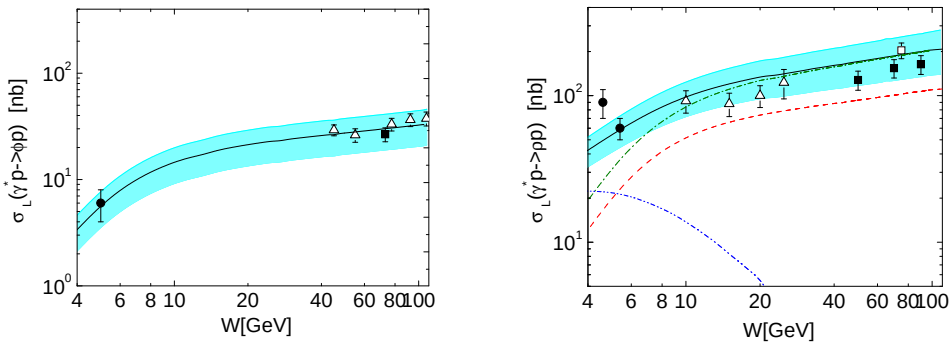

Fig. 2: Predictions from [5] for the longitudinal cross section of ϕ electroproduction for $Q^2 = 3.8\,\mathrm{GeV}^2$ (left) and ρ electroproduction for $Q^2 = 4\,\mathrm{GeV}^2$ (right). ϕ production data are from HERMES (solid circle), ZEUS (open triangles) and H1 (solid square), and ρ production data are from HERMES (solid circles), E665 (open triangles), ZEUS (open square) and H1 (solid square), see [5] for references. The dashed (dash-dotted) line represents the gluon (gluon+sea) contribution. The dash-dot-dotted line represents the sum of the interference between the valance and (gluon+sea) contributions and the valance contribution. The solid line is the sum of all contributions.

of the NLO corrections to exclusive meson production. They use collinear factorisation, neglecting the transverse momenta of the partons entering the hard scattering both on the proton and on the meson side. For the evolution of the generalised partons they use the leading order evolution code of Vinnikov [10] which uses an optimised fourth order Runge-Kutta method to solve the LO kernels as given in [11]. The input GPDs are again estimated via the double distribution method, and with diagonal input from the global PDF fit CTEQ6M [12]. Diehl and Kugler observe large NLO corrections leading to a strong suppression of the LO result in the small x regime, but no gain from LO to NLO in the stability w.r.t. the scale variation. In Fig. 3 this is shown for the case of ρ electroproduction in different kinematic regimes. Unfortunately such large corrections, which can partly be traced back to BFKL type logarithms (see [13] for first predictions including resummation effects), limit the applicability of the fixed-order collinear approach to describe data for elastic VM production.

2.2 Vector meson production in k_T factorization

Traditionally, k_T (or 'high energy') factorisation has been introduced for the description of heavy quark production in the high energy regime. Recently it has also been applied to various other processes including Higgs production at hadron colliders. Martin et al. have used it for the calculation of diffractive production of light and heavy vector mesons at HERA [14, 15]. The relevant amplitude is shown in Fig. 1 (right diagram). Their predictions involve the integration over the transverse momentum k_T of the exchanged gluons, so the input parton distributions need to be unintegrated w.r.t. k_T. This involves the application of a Sudakov factor, see [15] for details. Additional contributions from the real part of the amplitude are calculated based on dispersive methods. This approach goes beyond the leading $\log Q^2$ approximation while also capturing certain contributions beyond the leading high energy (BFKL) limit. Of course NLO corrections also arise from additional loops, for example gluonic one-loop corrections to the

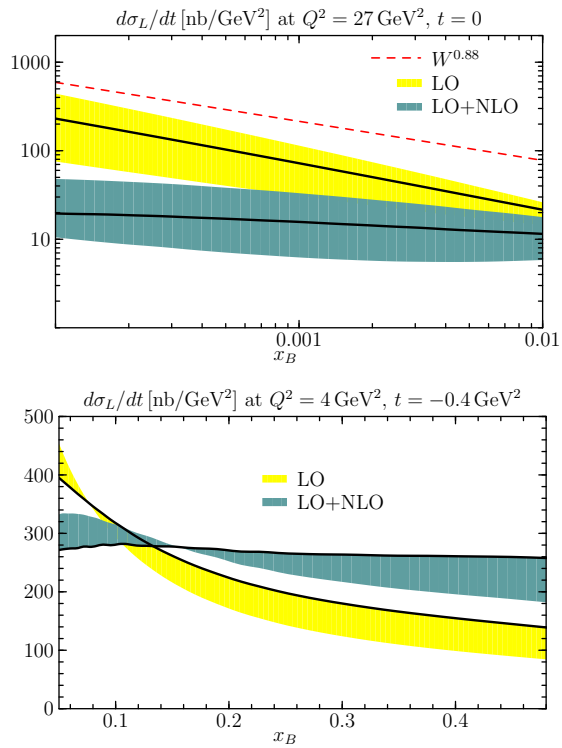

Fig. 3: Longitudinal cross section predictions for ρ electroproduction from [9] for Q^2, t and x as indicated on the plots. The bands are generated from the ranges $Q/2 < \mu < 2Q$ (left) and $2 < \mu < 4\,\mathrm{GeV}^2$ (right), where μ is the renormalisation and factorisation scale. The solid lines correspond to $\mu = Q$. The dashed line in the left panel shows the power-law behaviour $\sigma \propto W^{0.88}$ (with arbitrary normalisation) obtained from a fit by the ZEUS Collaboration to data in the range $x_B = 0.001 \ldots 0.005$.

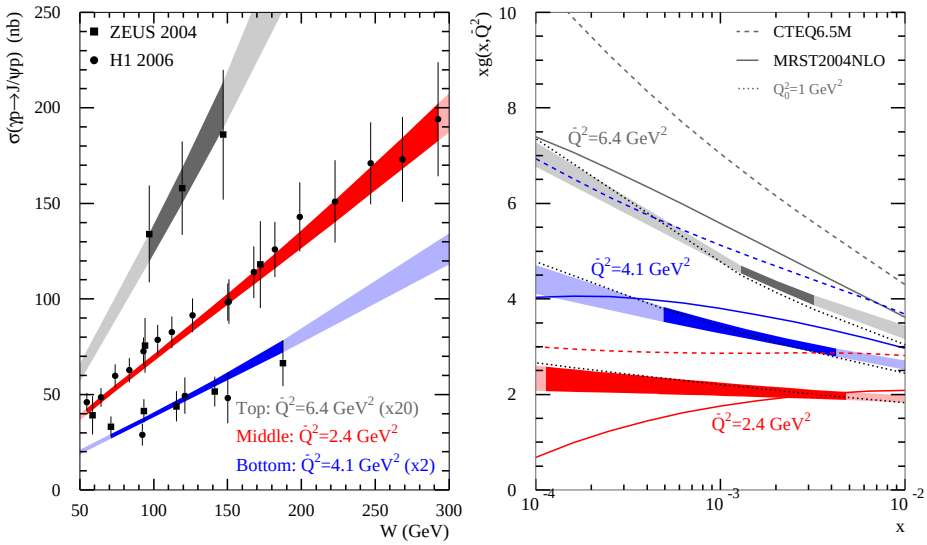

Fig. 4: 'NLO' fit of elastic J/ψ data from HERA [19] as done in [3]. Left: cross section compared to some of the H1 and ZEUS data for three different values of the effective scale $\bar{Q}^2 = (Q^2 + M_{J/\psi}^2)/(W^2 + M_{J/\psi}^2)$. Right: Fitted diagonal gluon compared to global gluons for scales as indicated. The width of the bands displays the uncertainty of the cross section predictions and the fitted gluon, whereas darker shaded areas indicate the region of available data.

two-gluon quark-antiquark vertex, or when the two gluon system couples via a quark loop to the proton. While such quark contributions are suppressed in the high energy regime, the former class of corrections leads to a genuine K factor which was calculated by Ivanov et al. [8] in collinear factorisation but which is not known in the case of k_T factorisation. Work is in progress to calculate these corrections.

Skewing corrections are taken into account via the Shuvaev transform [16] which, in the case of small x and ξ, allows to calculate the GPDs from the forward PDFs.[2] In this regime, with the assumption of a pure power behaviour of the diagonal PDF $\sim x^{-\lambda}$, the skewing correction is well approximated by a simple factor, $R = \frac{2^{2\lambda+3}}{\sqrt{\pi}} \frac{\Gamma(\lambda+5/2)}{\Gamma(\lambda+3+p)}$ ($p = 1$ for gluons, 0 for quarks), which only depends on the anomalous dimension λ.

3 Determination of the gluon from diffractive J/ψ data

While a good description of many data from HERA and other experiments has been achieved, the predictions show a large dependence on the gluon parametrisations used as input, in the regime of small x and semi-hard scales where they are only poorly known. However, Martin et al. have turned the game around and used their theoretical approach as described above together with exclusive J/ψ data from HERA [19] to determine the gluon distribution in the small x and low-scale regime [3]. Note that whereas in [14, 15] VM production was described via parton-hadron

[2]The use of the Shuvaev transform has become subject of some criticism [17], but see [18] for the justification of its applicability in the regime under consideration here.

duality by integrating over open quark-antiquark production in a suitably chosen mass regime, for the gluon fits in [3] the non-relativistic limit for the J/ψ wave function was adopted. While this is a sufficient approximation w.r.t. the other theoretical and experimental uncertainties, it also allows for the prediction of the normalisation which is not well controlled in the parton-hadron duality approach. With the use of a simple three-parameter ansatz for the gluon, $xg(x,\mu^2) = Nx^{-\lambda}$, with $\lambda = a + b\,\ln\ln(\mu^2/\Lambda^2_{\rm QCD})$, a fit (with $\chi^2_{\rm min}/d.o.f. = 0.8$) gives the results $N = 1.55\pm0.18$, $a = -0.50\pm0.06$, $b = 0.46\pm0.03$. In Fig. 4, both the results for the emerging cross section predictions (left) and the fitted gluon distribution (right panel) are shown for different scales and compared to the gluon PDFs of global fits from CTEQ [20] and MRST [21].

4 Conclusions

We have briefly reviewed recent work on the description of exclusive vector meson production in ep collisions based on generalised parton distributions. While it has been known for a long time that this process is particulary interesting due to its quadratic sensitivity on the input partons, the complexity of the full amplitudes makes systematic higher order predictions difficult. Different approaches as presented above have been discussed at the recent HERA-LHC workshops. Clearly we have gained a much better understanding of exclusive VM production, though the quantitative predictions have not yet achieved the desired accuracy. Nevertheless, a lot of progress has been made in predicting these processes and first results on extracting the gluon at small x from HERA data have been reported. The situation will be even more complicated at the LHC, and with the wider kinematic range accessible, the future will be very interesting.

References

[1] L. Motyka, K. Golec-Biernat and G. Watt, in these proceedings.

[2] H. Kowalski, L. Motyka and G. Watt, Phys. Rev. **D 74**, 074016 (2006).

[3] A.D. Martin, C.J. Nockles, M.G. Ryskin and T. Teubner, Phys. Lett. **B 662**, 252 (2008).

[4] S.V. Goloskokov and P. Kroll, Eur. Phys. J. **C 42**, 281 (2005).

[5] S.V. Goloskokov and P. Kroll, Eur. Phys. J. **C 50**, 829 (2007).

[6] S.V. Goloskokov and P. Kroll, Eur. Phys. J. **C 53**, 367 (2008).

[7] A.V. Radyushkin, Phys. Lett. **B 449**, 81 (1999);
I.V. Musatov and A.V. Radyushkin, Phys. Rev. **D 61**, 074027 (2000).

[8] D.Yu. Ivanov, L. Szymanowski and G. Krasnikov, JETP Lett. **80**, 226 (2004);
D.Yu. Ivanov, A. Schäfer, L. Szymanowski and G. Krasnikov, Eur. Phys. J. **C 34**, 297 (2004);
D.Yu. Ivanov, M.I. Kotsky and A. Papa, Eur. Phys. J. **C 38**, 195 (2004).

[9] M. Diehl and W. Kugler, Eur. Phys. J. **C 52**, 933 (2007).

[10] A.V. Vinnikov, *Code for prompt numerical computation of the leading order gpd evolution*. Preprint arXiv:hep-ph/0604248.

[11] J. Blümlein, B. Geyer and D. Robaschik, Nucl. Phys. **B 560**, 283 (1999).

[12] CTEQ Collaboration, J. Pumplin et al., JHEP **0207**, 012 (2002).

[13] D.Yu. Ivanov, *Exclusive vector meson electroproduction*. Preprint arXiv:0712.3193 [hep-ph].

[14] A.D. Martin, M.G. Ryskin and T. Teubner, Phys. Lett. **B 454**, 339 (1999).

[15] A.D. Martin, M.G. Ryskin and T. Teubner, Phys. Rev. **D 62**, 014022 (2000).

[16] A. Shuvaev, Phys. Rev. **D 60**, 116005 (1999);
A.G. Shuvaev, K.J. Golec-Biernat, A.D. Martin and M.G. Ryskin, Phys. Rev. **D 60**, 014015 (1999).

[17] M. Diehl and W. Kugler, Phys. Lett. **B 660**, 202 (2008).

[18] A.D. Martin, C.J. Nockles, M.G. Ryskin, A.G. Shuvaev and T. Teubner. To appear.

[19] H1 Collaboration, A. Aktas et al., Eur. Phys. J. **C 46**, 585 (2006);
ZEUS Collaboration, S. Chekanov et al., Nucl. Phys. **B 695**, 3 (2004);
ZEUS Collaboration, J. Breitweg et al., Z. Phys. **C 75**, 215 (1997);
ZEUS Collaboration, J. Breitweg et al., Eur. Phys. J. **C 6**, 603 (1999).

[20] CTEQ Collaboration, W.-K. Tung et al., JHEP **0702**, 053 (2007).

[21] A.D. Martin, R.G. Roberts, W.J. Stirling and R.S. Thorne, Phys. Lett. **B 604**, 61 (2004).

Dipole models and parton saturation in ep scattering

L. Motyka[1,2]*, K. Golec-Biernat*[3,4] *and G. Watt*[5]
[1] II Institute for Theoretical Physics, Luruper Chaussee 149, 22761 Hamburg, Germany
[2] Institute of Physics, Jagellonian University, Reymonta 4, 30-059 Kraków, Poland
[3] Institute of Nuclear Physics, Polish Academy of Sciences, Kraków, Poland
[4] Institute of Physics, University of Rzeszów, Rzeszów, Poland
[5] Department of Physics & Astronomy, University College London, WC1E 6BT, UK

Abstract
In this contribution we briefly review the current status of the dipole models and parton saturation on the basis of results presented at the HERA–LHC workshops in the years 2006–2008. The problem of foundations of the dipole models is addressed within the QCD formalism. Some limitations of the models and open problems are pointed out. Furthermore, we review and compare the currently used dipole models and summarise the applications to describe various sets of HERA data. Finally we outline some of the theoretical approaches to the problem of multiple scattering and saturation.

1 Introduction

Dipole models [1–3] represent a QCD motivated framework that has been successfully applied to describe a variety of gluon mediated scattering cross sections at high energies. In particular, they provide a transparent and intuitive picture of scattering processes. Their main strength is a combination of universality, simplicity and efficiency. The dipole models are capable of simultaneously describing all F_2, F_L and heavy quark production ep data at small x, the inclusive diffractive data, the bulk of measurements for exclusive diffractive vector meson production, deeply virtual Compton scattering (DVCS), and even nuclear shadowing [4–13]. This unified description is achieved using only a few parameters with a transparent physical meaning, such as the normalisation of the gluon distribution at a low scale, the quark mass or the proton size. At the same time, the dipole models provide a phenomenological insight into important aspects of high energy scattering, like the relative importance of multiple scattering or higher twist contributions. This importance may be quantified in terms of a *saturation scale*, Q_S, the scale of the process at which the unitarity corrections become large [4]. Up to now, the dipole models applied to HERA data offer one of the most convincing arguments for the dependence of this scale on the scattering energy and provide one of the best quantitative estimates of the saturation scale [4–6, 11, 12]. This shows the complementarity of dipole models to the rigorous framework of collinear factorisation, within which the description of multiple scattering, although possible in principle, is quite inefficient. It is not only very demanding from the technical side (for instance, even the basis of twist-four operators is not fully understood yet), but it would also require introducing a set of new unknown functions parameterising the expectation values of higher twist operators at the low (input) scale. In dipole models this problem is bypassed by simply fitting the (implicitly) resummed multiple scattering cross section together with the nonperturbative contribution with constraints imposed by the unitarity of the scattering matrix.

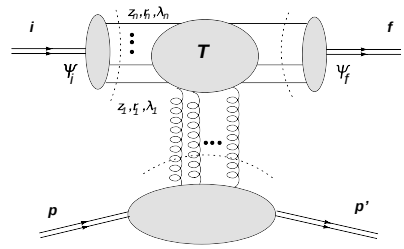

Fig. 1: High energy scattering in the dipole representation.

2 Foundations and limitations of dipole models

Let us consider a $2 \to 2$ scattering amplitude of $i + p \to f + p$, where the strongly interacting projectile i hits a hadronic target p and undergoes a transition to a state f, while the target scatters elastically. At HERA the projectile is always a virtual photon, γ^*, with a four-momentum q and virtuality $q^2 = -Q^2$, and the target is a proton, with initial momentum p and final momentum p'. The final states considered are virtual and real photon states, vector meson states and diffractive states. The states i and f carry a typical scale $\bar{Q}^2$; for $i = f = \gamma^*(Q^2)$, $\bar{Q}^2 = Q^2$. The invariant collision energy $s = (p+q)^2$ is assumed to be large, $s \gg \bar{Q}^2$ and $s \gg |t|$, where $t = (p-p')^2$ is the momentum transfer. We shall also use the variable $x = \bar{Q}^2/s$, that reduces to the Bjorken x for the case of deeply inelastic scattering (DIS).

The key idea behind dipole models is a separation (factorisation) of a high energy scattering amplitude, $\mathcal{A}^{i\,p\to f\,p}$, into an initial ($\Psi_i$) and final ($\Psi_f$) state wave function of the projectile i and the outgoing state f, and a (diagonal) universal scattering amplitude of a multi-parton Fock state, $\mathcal{F}_n$, off a target p; see Fig. 1. The scattering operator, T, is assumed to be diagonal in the basis of states that consist of a definite number of partons, n, with fixed longitudinal momentum fractions, z_k ($k = 1, \ldots, n$), of the projectile, definite helicities, λ_k, and transverse positions, $\boldsymbol{r}_k$. One may write symbolically (see e.g. [14]):

$$\mathcal{A}^{i\,p\to f\,p} = \sum_{\mathrm{n},\mathcal{F}_\mathrm{n},\{\lambda_\mathrm{k}\}} \int [\mathrm{d}^{2n}\boldsymbol{r}_k] \int [\mathrm{d}^{\mathrm{n}} z_k]\; \Psi_f^*(n, \{z_k, \boldsymbol{r}_k, \lambda_k\})\; T(\mathcal{F}_n)\; \Psi_i(n, \{z_k, \boldsymbol{r}_k, \lambda_k\}). \quad (1)$$

In most practical applications one takes into account only the lowest Fock states, composed of a quark–antiquark ($q\bar{q}$) pair and, possibly, one additional gluon ($q\bar{q}g$). In the limit of a large number of colours, $N_c \to \infty$, flavourless scattering states, i and f, may be represented as a collection of colour dipoles [2]. For the simplest case of $q\bar{q}$ scattering, the intermediate state $\mathcal{F}_2$ is defined by the quark and antiquark helicities, the longitudinal momentum fraction, z, of the projectile carried by the quark, the dipole vector, $\boldsymbol{r} = \boldsymbol{r}_2 - \boldsymbol{r}_1$, and the impact parameter vector, $\boldsymbol{b} = z\boldsymbol{r}_1 + (1-z)\boldsymbol{r}_2$. It is convenient to define the imaginary part of the dipole scattering amplitude (assuming independence of the azimuthal angles), $\mathcal{N}(x, \boldsymbol{r}, \boldsymbol{b}) \equiv \mathrm{Im}\, T(\mathcal{F}_2),$ and the b-dependent dipole–target cross-section

$$\frac{\mathrm{d}\sigma_{q\bar{q}}}{\mathrm{d}^2\boldsymbol{b}} = 2\,\mathcal{N}(x, r, b). \quad (2)$$

The picture encoded in (1) may be motivated within perturbative QCD. In the high energy limit of QCD [15, 16], the dominant contribution to scattering amplitudes comes from vector boson (gluon) exchanges, that lead to cross-sections constant with energy (modulo quantum corrections that may generate an additional enhancement). For each spin-1/2 fermion (quark) exchange in the t-channel the amplitude is power suppressed by a factor of $1/s^{1/2}$. In consequence, the high energy scattering amplitude may be factorised into the amplitude describing slow (in the target frame) gluon fields and the amplitude of fast parton fields of the projectile moving in the gluon field of the target. This is, in fact, the basic assumption of the k_T- (high energy) factorisation [16, 17]. In the high energy limit, the vertex describing the coupling of the fast s-channel parton (quark or gluon) to a gluon exchanged in the t-channel is *eikonal*: the large light-cone component of the longitudinal parton momentum and the parton helicity are conserved. Also, up to subleading terms in the collision energy, the fast parton does not change its transverse position in the scattering process. These properties of high energy amplitudes in QCD were used to derive the dipole model for hard processes. In more detail, the scattering amplitudes in the dipole model follow from the QCD scattering amplitudes obtained within the k_T-factorisation scheme, in the high energy limit and at the leading logarithmic (LL) $\ln(1/x)$ approximation [1].

The fact that the QCD dipole model follows from the k_T-factorisation approximation implies that the model, up to subleading terms in $1/s$, is also consistent with the leading order (LO) collinear approximation [17]. In addition, as in the case of the k_T-factorisation framework, the dipole model incorporates an exact treatment of the quark transverse momentum in the box diagram. These kinematic effects, when analysed within the collinear approximations, manifest themselves as higher order corrections to the coefficient functions [17]. Although the implicit resummation of the collinear higher order terms in the dipole model is only partial, it should still be viewed as an improvement of the LO collinear approximation.

Practical use of dipole models is not restricted to hard processes, where precise predictions can be obtained within the collinear factorisation framework. On the contrary, one of the most successful applications of the dipole model (the saturation model [4]) provides an efficient and simple description of the transition from the perturbative single scattering regime (the colour transparency regime) to the multiple scattering regime as a function of the process scale and scattering energy (or $\bar{Q}^2$ and x). In this transition region scattering amplitudes are expected to receive contributions both of the nonperturbative nature and from perturbatively calculable multiple scattering effects. The nonperturbative effects in high energy scattering are currently not computable with theoretical methods and have to be modelled. The multiple scattering effects enter the scattering amplitudes e.g. as higher twist contributions [18][1], that are suppressed by inverse powers of the hard scale, $\bar{Q}^2$, and additional powers of α_s. Nevertheless, the higher twist effects may be quite sizable at small x and at moderately large $\bar{Q}^2$ [18]. This originates from a rapid growth of the multi-gluon density with decreasing x: assuming the large N_c limit, the n-gluon density evolves approximately as the single gluon density to power n [19, 20]. Thus, at decreasing x the multiple scattering effects are increasingly enhanced and may eventually become competitive with the single scattering contribution.

Thus far we discussed the dipole model from the perspective of perturbative QCD. An interesting attempt to provide foundations of the model in a general (i.e. non-perturbative) frame-

[1] Multiple scattering effects that occur at low scales are absorbed into the input gluon density at the initial scale.

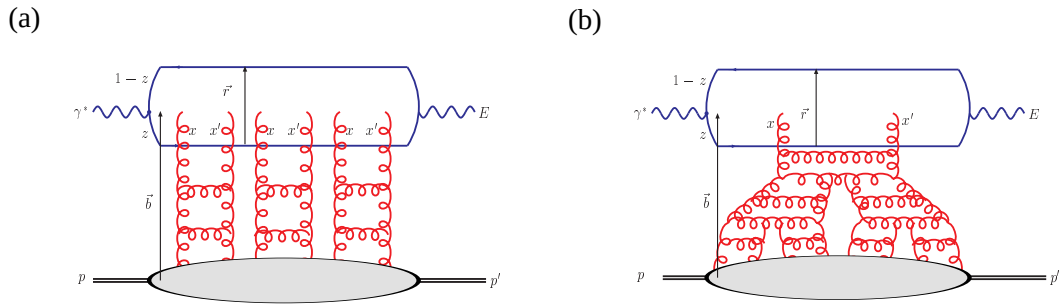

Fig. 2: The $\gamma^* p$ scattering amplitude with unitarisation achieved via (a) *eikonal* diagrams or (b) *fan* diagrams. For exclusive diffractive processes, such as vector meson production ($E = V = \Upsilon, J/\psi, \phi, \rho$) or DVCS ($E = \gamma$), we have $x' \ll x \ll 1$ and $t = (p - p')^2$. For inclusive DIS, we have $E = \gamma^*$, $x = x' \ll 1$ and $p = p'$.

work was recently put forward [21, 22]. The scattering amplitudes were written in terms of skeleton diagrams and the QCD path-integral. Approximations and assumptions necessary to recover the dipole model amplitudes were identified. To a large extent the conclusions from that analysis confirm those obtained within the perturbative framework: the dipole model accuracy is not theoretically guaranteed when higher twist and higher order corrections are large. An interesting point raised in Refs. [22, 23] is the dependence of the dipole cross section, $\sigma_{q\bar{q}}$, on the dipole–target collision energy, $\sqrt{s}$. In most models one assumes that $\sigma_{q\bar{q}}$ depends on s through $x = \bar{Q}^2/s$. The scale, however, is part of the wave functions and it is not obvious that the dipole cross section should depend on $\bar{Q}^2$ rather than on the dipole variables, like e.g. the dipole scale, $1/r^2$. Interestingly, assuming the dependence of $\sigma_{q\bar{q}}$ on a combined variable $s\,r^2$ was shown to create some tension between the HERA data on F_2 and F_L and the dipole model, irrespective of the detailed functional form of $\sigma_{q\bar{q}}$. Some insight may be gained from inspecting the issue in the k_T-factorisation approach. Then, the energy dependence enters through x_g of the gluon, that essentially depends on the external state virtuality, the scattered quarks' transverse momenta and the distribution of the quark longitudinal momentum. So, the proposed replacement of $\bar{Q}^2$ by $1/r^2$ might be somewhat oversimplified. On the other hand, within the LL$(1/x)$ approximation the standard choice of $x_g \simeq \bar{Q}^2/s$ is justified. To sum up, the choice of the optimal dimensionless variable that would carry the energy dependence of the dipole cross-section remains an open and interesting problem.

3 Phenomenology of dipole models

Implementations of multiple scattering in colour dipole models are based on two main approaches, that adopt different approximations. The Glauber–Mueller (GM) *eikonal* approach [24] is used in the family of models that evolved from the Golec-Biernat–Wüsthoff (GBW) model [4]. One assumes in this approach that multiple colour dipole scatters are independent of each other, see Fig. 2a. This assumption may be supported (although it was not yet explicitly derived) with properties of the collinear evolution of quasi-partonic operators describing the multi-gluon density in the proton, and in the large N_c limit [18–20]. Assuming in addition a factorised b-dependence of the gluon distribution, one postulates the dipole–proton scattering amplitude of

the form:

$$\mathcal{N}(x,r,b) = 1 - \exp\left(-\frac{\pi^2}{2N_c} r^2 \alpha_s(\mu^2)\, xg(x,\mu^2)\, T(b)\right), \tag{3}$$

where the scale $\mu^2 = C/r^2 + \mu_0^2$ with $\mu_0 \sim 1$ GeV. HERA data on exclusive vector meson production imply a Gaussian form of the proton shape in the transverse plane, $T(b)$, with $\sqrt{\langle b^2 \rangle} = 0.56$ fm. The corresponding quantity determined from the proton charge radius (0.87 fm) is somewhat larger, $\sqrt{\langle b^2 \rangle} = 0.66$ fm, implying that gluons are more concentrated in the centre of the proton than quarks. The form (3) is denoted by the "b-Sat" model [6, 11]. It can be considered to be an improvement on a previous model [5] where $T(b) \propto \Theta(R_p - b)$ was assumed, and also on the original GBW model [4] where additionally the scale dependence of the gluon distribution was neglected, that is, $xg(x,\mu^2) \propto x^{-\lambda}$ was assumed for a fixed power $\lambda \sim 0.3$. Note that in the GBW model large saturation effects were needed to get from the hard Pomeron behaviour ($\sim r^2\, x^{-0.3}$) at small dipole sizes to soft Pomeron behaviour ($\sim x^{-0.1}$) at large dipole sizes. On the other hand, in Refs. [5, 6, 11] this transition can alternatively be achieved with DGLAP evolution, therefore saturation effects are correspondingly smaller.

In the alternative approach one exploits solutions of the Balitsky–Kovchegov (BK) equation [25]. It was derived for scattering of a small colour dipole off a large nucleus, composed of A nucleons. The LL BK equation rigorously resums contributions of BFKL Pomeron *fan* diagrams (Fig. 2b), that are leading in A, $1/N_c$ and in the $\ln 1/x$ approximation (properties of solutions of the next-to-LL BK equation are not known yet and so cannot be used in the dipole models). A colour glass condensate (CGC) dipole model parameterisation [8] was constructed from an approximate solution of the BK equation:

$$\mathcal{N}(x,r,b) = T(b)\mathcal{N}(x,r) \,=\, \Theta(R_p - b) \begin{cases} \mathcal{N}_0 \left(\frac{rQ_s}{2}\right)^{2\left(\gamma_s + \frac{\ln(2/rQ_s)}{9.9\lambda \ln(1/x)}\right)} & : \quad rQ_s \le 2 \\ 1 - \mathrm{e}^{-A \ln^2(BrQ_s)} & : \quad rQ_s > 2 \end{cases}, \tag{4}$$

where $Q_s = (x_0/x)^{\lambda/2}$ is a saturation scale.[2] The original analysis [8] neglected the charm quark contribution to F_2. The inclusion of charm was later found [11] to significantly lower the saturation scale when the anomalous dimension γ_s was fixed at the LO BFKL value of 0.63. By letting γ_s go free, a solution was subsequently found with $\gamma_s = 0.74$ which included heavy quarks but had a large saturation scale [9]. (This model has been modified to include a t dependence in the saturation scale allowing the description of exclusive diffractive processes [10].) However, the HERA data do not show a strong preference for the solution with $\gamma_s = 0.74$, and a secondary solution with $\gamma_s = 0.61$ and a much smaller saturation scale also describes the data well [12]. The CGC model (4) assumes a factorised b dependence which is not supported by HERA diffractive data, where one finds a significantly non-zero effective Pomeron slope $\alpha'_{\mathbb{P}}$, indicating correlation between the b and x dependence of the dipole scattering amplitude. A more realistic impact parameter dependence was included by introducing a Gaussian b dependence into the saturation scale Q_s, denoted by the "b-CGC" model [11, 12]. It was not possible to obtain a good fit to HERA data with a fixed $\gamma_s = 0.63$ [11], but on freeing this parameter, a good fit was obtained

[2] In what follows we shall use Q_s (with a lower-case s) to denote the saturation scale defined in a model-dependent way.

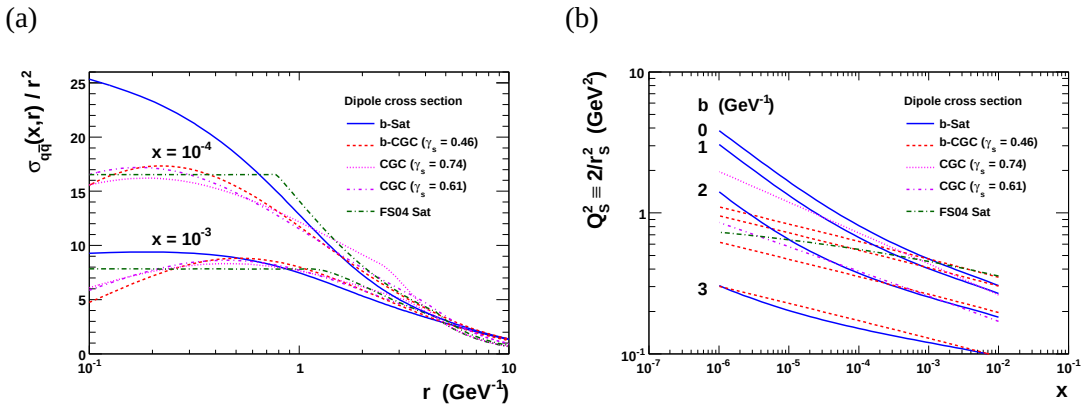

Fig. 3: (a) The b-integrated dipole–proton cross sections divided by r^2 and (b) the saturation scale $Q_S^2 \equiv 2/r_S^2$.

with a value of $\gamma_s = 0.46$ [12], close to the value of $\gamma_s \simeq 0.44$ obtained from numerical solution of the BK equation [26]. However, the value of $\lambda = 0.119$ obtained from the "b-CGC" fit [12] is lower than the perturbatively calculated value of $\lambda \sim 0.3$ [27].

In both the approaches to unitarisation one neglects multi-gluon correlations in the target. Thus, the key difference between the eikonal and the BK approaches is that in the latter one resums the leading logarithms of $1/x$ while in the former one aims at keeping a reasonable representation of leading logarithms of $\bar{Q}^2$. Both dipole model realisations have built in saturation of the black disc limit of the colour dipole scattering amplitude. This means that the absolute value of the T-matrix elements tends to unity for large dipoles or as $x \to 0$. It is curious that the choice of approximation has a striking consequence in how the unitarity (the black disc) limit is approached. In the GM case unitarisation happens because of cancellations between contributions of non-saturating multiple gluon exchanges, while in the BK case multiple scattering effects are contained in the single gluon density that saturates at a certain small value of x. These differences in the mechanism of unitarisation do not affect, however, the crucial qualitative feature of the dipole cross-section: the transition from a power-like growth with decreasing x in the colour transparency regime to a flat (possibly $\sim \ln(1/x)$) behaviour in the black disc limit. Thus, the necessary modelling of the dipole cross section for large dipole sizes is strongly constrained.

A third type of parameterisation for the dipole cross section does not assume any mechanism for unitarisation. It is a two-component Regge model (FS04 Sat) [7], which uses hard Pomeron behaviour ($\sim r^2\, x^{-0.3}$) for small dipole sizes $r < r_0$ and soft Pomeron behaviour ($\sim x^{-0.1}$) for large dipole sizes $r > r_1$, with linear interpolation between the two regions. Again, a factorising impact parameter dependence is assumed. Saturation effects are modelled by allowing r_0 to move to lower values with decreasing x. This feature was found to be preferred by the HERA data, whereas the two-component Regge model with a fixed r_0 was disfavoured [7].

We compare the dipole model parameterisations in Fig. 3a, where the b-integrated dipole cross sections have been divided by the trivial factor r^2 in order to emphasise the differences at small r. We restrict attention to dipole model parameterisations which have been shown to give a good fit (with charm quarks included) to recent HERA inclusive structure function data, meaning a χ^2 per data point of ~ 1. This excludes, for example, the original GBW parameterisation [4]

and the unsaturated two-component Regge model [7]. All parameterisations shown in Fig. 3a are similar at intermediate dipole sizes where they are most constrained by HERA data. At very small dipole sizes the b-Sat model deviates from the other parameterisations, as it is the only one which incorporates explicit DGLAP evolution. The b-Sat model was found to be preferred over the b-CGC model for observables sensitive to relatively small dipole sizes [12]. There are also differences between the parameterisations in the approach to the unitarity limit at large dipole sizes. For example, the b-Sat and b-CGC dipole cross sections tend to a constant at large r only for a fixed b, but not when integrating over all impact parameters.

In order to compare the magnitude of unitarity corrections between various models it is customary to define a model-independent saturation scale Q_S^2, that is, the momentum scale at which the dipole–proton scattering amplitude $\mathcal{N}$ becomes sizable. There is no unique definition of Q_S^2 and various choices are used in the literature. We define the saturation scale $Q_S^2 \equiv 2/r_S^2$, where the saturation radius r_S is the dipole size where the scattering amplitude

$$\mathcal{N}(x, r_S[, b]) = 1 - \mathrm{e}^{-\frac{1}{2}} \simeq 0.4, \tag{5}$$

chosen to match the corresponding quantity, Q_s, in the GBW model [4]. Note that this "saturation scale" is still far from the unitarity limit where $\mathcal{N} = 1$. The model-independent saturation scale Q_S^2 is shown in Fig. 3b: it is generally less than 0.5 GeV^2 in the HERA kinematic regime for the most relevant impact parameters $b \sim$ 2–3 GeV^{-1} [11, 12]. It should be remembered, however, that any observable will depend on integration over a range of dipole sizes, therefore even at high Q^2 there will be some contribution from large dipole sizes $r > r_S$. Moreover, dipole models incorporating saturation fitted to HERA data may be extrapolated to very low x and to predict cross sections for nuclear collisions where the saturation scale is enhanced by $A^{1/3}$ [13]. In these situations, multi-Pomeron exchange may become important and extrapolation based on single-Pomeron exchange would be unreliable.

4 Theory outlook: saturation beyond the BK equation in a statistical picture

The BK equation describes unitarity corrections in the asymmetric configuration, when the target is extended and dense and the projectile is small and dilute. In a more symmetric situation, like $\gamma^*(Q^2)p$ scattering at low Q^2, the BK approximation is no longer sufficient. In the diagrammatic formulation, besides the fan diagram one should then take into account diagrams with closed Pomeron loops. To construct a fully reliable and practical theoretical treatment of this complex case has turned out to be a prohibitively difficult task so far. Fortunately, the key properties of solutions of the BK equation in the low momentum region follow from its universal features and do not rely on the details of the equation.

In the Kovchegov derivation of the BK equation [25] one uses the Mueller dipole cascade picture [2] of the small x QCD evolution. The equation expressed in terms of the dipole scattering amplitude, $N_{\boldsymbol{uv}}(Y) \equiv \mathcal{N}(x, \boldsymbol{r}, \boldsymbol{b})$, with $Y = \ln(1/x)$, reads

$$\frac{\partial N_{\boldsymbol{uv}}}{\partial Y} = \frac{\overline{\alpha}_s}{2\pi} \int \mathrm{d}^2\boldsymbol{w}\, \frac{(\boldsymbol{u}-\boldsymbol{v})^2}{(\boldsymbol{u}-\boldsymbol{w})^2(\boldsymbol{w}-\boldsymbol{v})^2} \left[N_{\boldsymbol{uw}} + N_{\boldsymbol{wv}} - N_{\boldsymbol{uv}} - N_{\boldsymbol{uw}} N_{\boldsymbol{wv}}\right] \tag{6}$$

where $\boldsymbol{u} = \boldsymbol{b} - \boldsymbol{r}/2$, and $\boldsymbol{v} = \boldsymbol{b} + \boldsymbol{r}/2$ (assuming z=1/2 in the definition of $\boldsymbol{b}$, cf. Sec. 2). The equation has two fixed points: the repulsive one, $N_{\boldsymbol{uv}} = 0$, from which the solution is

driven out by the linear term, and the attractive one, $N_{\boldsymbol{uv}} = 1$, where the linear and nonlinear term compensate each other. This scenario of linear growth of the amplitude tamed by non-linear rescattering effects is common to all existing approaches to the saturation phenomenon. In the uniform case, when N does not depend on the impact parameter, b, this combination of growth and nonlinearity was shown to lead to a *geometric scaling* property [28] of the solutions, $N_{\boldsymbol{uv}}(Y) = N(|\boldsymbol{u}-\boldsymbol{v}|^2 Q_s^2(Y))$ for $Y \gg 1$, irrespective of the initial conditions [29]. For the $\gamma^* p$ cross section, geometric scaling implies that $\sigma^{\gamma^* p}(x, Q^2) = \sigma^{\gamma^* p}(Q_s^2/Q^2)$, which was observed in HERA data [28].

Interestingly enough, the geometric scaling property of the BK equation does not depend on the details of either the linear or the non-linear term. Therefore the scaling is a robust and universal phenomenon. In particular, the BK equation belongs to the same universality class as a simpler and well understood Fisher–Kolmogorov–Petrovsky–Piscounov (FKPP) equation [29], $\partial_t u(x,t) = \partial^2_{xx} u + u - u^2$, where the rapidity is mapped onto the time t and the logarithm of the dipole size onto the real variable x. Employing this connection it was proved that, indeed, both the emergence of geometric scaling and the rapidity evolution of the saturation scale are universal phenomena and do not depend on the details of the BK equation, provided that the initial condition is uniform in the impact parameter space.

The statistical framework implied by the Mueller dipole model may also be used to provide some qualitative insight into the effect of "Pomeron loops" in the scattering amplitudes [30, 31]. This effect corresponds to a stochastic term added to the FKPP equation [31],

$$\partial_t u(x,t) = \partial^2_{xx} u + u - u^2 + \sqrt{u(1-u)}\,\eta \tag{7}$$

where η is the white noise. The origin of stochasticity can be traced back to the discreteness of the colour dipoles in the Mueller cascade model. The BK equation is derived in the mean field approximation when the density of colour dipoles in the projectile is large enough ($n \gg 1$) that statistical fluctuations in the number of dipoles can be neglected. In this case, $N_{\boldsymbol{uv}}$ is an averaged dipole scattering amplitude. At the edge of the dense regime of the dipole distribution, however, the dipole occupation number is small, $n \sim 1$, so the statistical fluctuations play an important rôle. It was realised in Ref. [30] and subsequently developed in Ref. [31] that these fluctuations get enhanced in the Y-evolution and affect the global properties of the amplitude. In this approach the saturation scale becomes a stochastic variable that fluctuates from one scattering event to another, with a lognormal distribution with the variance $\sigma^2 = DY$, where $D \sim \alpha_s/\ln^3(1/\alpha_s^2)$ [32]. The most important result of fluctuations is a new scaling of the physical amplitude, called *diffusive scaling* [31]. Namely, the dipole scattering amplitude $N_{\boldsymbol{uv}}(Y)$, should depend only on one variable, $\xi = (\ln(r^2) + \langle \ln Q_s^2 \rangle)/\sqrt{DY}$. Note that the factor $\sqrt{DY}$ in the denominator which spoils the geometric scaling is of the diffusive origin. A first attempt to trace the diffusive scaling in the HERA data on F_2 was presented in Ref. [33] with a negative result. This would suggest that Pomeron loops introduce only a small effect in the HERA data.

The results presented here neglect the impact parameter dependence of the scattering amplitudes, assuming that the high energy QCD evolution is local in the transverse coordinate space. Thus the local evolutions at different b's are uncorrelated. Recent numerical studies [34] suggest that this is a quite accurate picture of high energy scattering if the dipole size is significantly smaller than the target size.

Recently, an interesting attempt was made [35] to explicitly model the colour dipole cascade taking into account effects related to Pomeron loops. In more detail, subleading effects in the $1/N_c$ expansion were phenomenologically incorporated that lead to a possibility of colour dipole reconnections in the dipole wave function. The resulting dipole–dipole scattering amplitudes were shown to respect with good accuracy the symmetry between the target and the projectile, which does not hold in the absence of the colour reconnection. The approach employs Monte-Carlo methods and was shown to be quite successful in describing total cross-sections and many diffractive observables.

5 Concluding remarks

The dipole models applied to HERA data on inclusive and diffractive processes provide a successful unified description of most observables. These analyses provide significant evidence for sizable unitarity (rescattering) corrections to the single scattering approximation, that is used in the linear QCD evolution equations, in both DGLAP and BFKL. These corrections become strong below the saturation scale, $Q_S(x)$. The determination of the saturation scale within different dipole models yields consistently that $Q_S < 1$ GeV, over the HERA kinematic range. Q_S is found to increase with $1/x$, approximately as $Q_S^2(x) \sim (1/x)^{\lambda_S}$ with $\lambda_S \simeq 0.12-0.2$, depending on the model. Both these properties of Q_S suggest that the onset of perturbative saturation is probed at HERA, and that non-perturbative effects may still be significant around Q_S. Fortunately, the key results on the saturation phenomenon obtained within perturbative QCD are universal and should remain valid despite a possible non-perturbative contamination.

Acknowledgements

K. G.-B. and L. M. acknowledge a support of grant of Polish Ministry of Education No. N N202 249235. L. M. is supported by the DFG grant SFB 676. G. W. acknowledges the UK Science and Technology Facilities Council for the award of a Responsive Research Associate position.

References

[1] N. N. Nikolaev and B. G. Zakharov, Z. Phys. **C49**, 607 (1991);
N. N. Nikolaev and B. G. Zakharov, Z. Phys. **C53**, 331 (1992).

[2] A. H. Mueller, Nucl. Phys. **B415**, 373 (1994);
A. H. Mueller and B. Patel, Nucl. Phys. **B425**, 471 (1994).

[3] K. J. Golec-Biernat, *Review on parton saturation.*
Talk at the 4th HERA and the LHC workshop, CERN, 26–30 May 2008,
`http://indico.cern.ch/conferenceDisplay.py?confId=27458`.

[4] K. J. Golec-Biernat and M. Wüsthoff, Phys. Rev. **D59**, 014017 (1999);
K. J. Golec-Biernat and M. Wüsthoff, Phys. Rev. **D60**, 114023 (1999).

[5] J. Bartels, K. J. Golec-Biernat and H. Kowalski, Phys. Rev. **D66**, 014001 (2002);
K. J. Golec-Biernat and S. Sapeta, Phys. Rev. **D74**, 054032 (2006).

[6] H. Kowalski and D. Teaney, Phys. Rev. **D68**, 114005 (2003).

[7] J. R. Forshaw and G. Shaw, JHEP **12**, 052 (2004);
J. R. Forshaw, R. Sandapen and G. Shaw, JHEP **11**, 025 (2006);
G. Shaw, *Saturation and the colour dipole model*.
Talk at the 3rd HERA and the LHC workshop, DESY, 12–16 March 2007,
`http://indico.cern.ch/conferenceDisplay.py?confId=11784`.

[8] E. Iancu, K. Itakura and S. Munier, Phys. Lett. **B590**, 199 (2004).

[9] G. Soyez, Phys. Lett. **B655**, 32 (2007).

[10] C. Marquet, R. B. Peschanski and G. Soyez, Phys. Rev. **D76**, 034011 (2007).

[11] H. Kowalski, L. Motyka and G. Watt, Phys. Rev. **D74**, 074016 (2006).

[12] G. Watt and H. Kowalski, Phys. Rev. **D78**, 014016 (2008);
G. Watt, *Exclusive diffractive processes within the dipole picture*.
Talk at the 4th HERA and the LHC workshop, CERN, 26–30 May 2008,
`http://indico.cern.ch/conferenceDisplay.py?confId=27458`.

[13] H. Kowalski, T. Lappi and R. Venugopalan, Phys. Rev. Lett. **100**, 022303 (2008);
H. Kowalski, T. Lappi, C. Marquet and R. Venugopalan, `arXiv:0805.4071 [hep-ph]`.

[14] J. Bartels and L. Motyka, Eur. Phys. J. **C55**, 65 (2008).

[15] P. Lepage and S. Brodsky, Phys. Rev. **D22**, 2157 (1980).

[16] L. V. Gribov, E. M. Levin and M. G. Ryskin, Phys. Rept. **100**, 1 (1983).

[17] S. Catani, M. Ciafaloni and F. Hautmann, Nucl. Phys. **B366**, 135 (1991);
S. Catani and F. Hautmann, Nucl. Phys. **B427**, 475 (1994).

[18] J. Bartels, K. J. Golec-Biernat and K. Peters, Eur. Phys. J. **C17**, 121 (2000);
L. Motyka, *Higher twists from the saturation model*.
Talk at the 4th HERA and the LHC workshop, CERN, 26–30 May 2008,
`http://indico.cern.ch/conferenceDisplay.py?confId=27458`.

[19] A. P. Bukhvostov, G. V. Frolov, L. N. Lipatov and E. A. Kuraev, Nucl. Phys. **B258**, 601 (1985).

[20] J. Bartels and M. Ryskin, Z. Phys. **C60**, 751 (1993).

[21] C. Ewerz and O. Nachtmann, Annals Phys. **322**, 1635 (2007);
C. Ewerz and O. Nachtmann, Annals Phys. **322**, 1670 (2007).

[22] A. von Manteuffel, *Bounds on DIS observables from the colour dipole picture*.
Talk at the 3rd HERA and the LHC workshop, DESY, 12–16 March 2007,
`http://indico.cern.ch/conferenceDisplay.py?confId=11784`.

[23] C. Ewerz, A. von Manteuffel and O. Nachtmann, Phys. Rev. **D77**, 074022 (2008).

[24] R. J. Glauber, Phys. Rev. **99**, 1515 (1955);
A. H. Mueller, Nucl. Phys. **B335**, 115 (1990).

[25] I. Balitsky, Nucl. Phys. **B463**, 99 (1996);
Y. V. Kovchegov, Phys. Rev. **D60**, 034008 (1999);
Y. V. Kovchegov, Phys. Rev. **D61**, 074018 (2000).

[26] D. Boer, A. Utermann and E. Wessels, Phys. Rev. **D75**, 094022 (2007).

[27] D. N. Triantafyllopoulos, Nucl. Phys. **B648**, 293 (2003).

[28] A. M. Staśto, K. Golec-Biernat and J. Kwieciński, Phys. Rev. Lett. **86**, 596 (2001).

[29] S. Munier and R. Peschanski, Phys. Rev. Lett. **91**, 232001 (2003);
S. Munier and R. Peschanski, Phys. Rev. **D69**, 034008 (2004);
S. Munier and R. Peschanski, Phys. Rev. **D70**, 077503 (2004).

[30] A. H. Mueller and A. Shoshi, Nucl. Phys. **B692**, 175 (2004).

[31] S. Munier, Nucl. Phys. **A755**, 622 (2005);
E. Iancu, A. Mueller and S. Munier, Phys. Lett. **B606**, 342 (2005).

[32] C. Marquet, G. Soyez and Bo-Wen Xiao, Phys. Lett. **B639**, 635 (2006);
R. Enberg, K. Golec-Biernat and S. Munier, Phys. Rev. **D72**, 074021 (2005).

[33] E. Basso, M. B. Gay Ducati, E. G. de Oliveira and J. T. de Santana Amaral,
arXiv:0807.1556 [hep-ph].

[34] S. Munier, G. P. Salam, and G. Soyez, arXiv:0807.2870 [hep-ph].

[35] E. Avsar, G. Gustafson and L. Lönnblad, JHEP **07**, 062 (2005);
E. Avsar, G. Gustafson and L. Lönnblad, JHEP **01**, 012 (2007);
E. Avsar, G. Gustafson and L. Lönnblad, JHEP **12**, 012 (2007);
C. Flensburg, G. Gustafson and L. Lönnblad, arXiv:0807.0325 [hep-ph];
E. Avsar, *Small-x physics and an improved dipole model*.
Talk at the 3rd HERA and the LHC workshop, DESY, 12–16 March 2007,
http://indico.cern.ch/conferenceDisplay.py?confId=11784.

Checking formalism for central exclusive production in the first LHC runs

A.D. Martin, V.A. Khoze and M.G. Ryskin
Institute for Particle Physics Phenomenology, University of Durham, DH1 3LE, UK

Abstract

We discuss how the early LHC data runs can provide crucial tests of the formalism used to predict the cross sections of central exclusive production.

1 Introduction

The physics potential of forward proton tagging at the LHC has attracted much attention in the last years, for instance, [1–5]. The combined detection of both outgoing protons and the centrally produced system gives access to a unique rich programme of studies in QCD, electroweak and BSM physics. Importantly, these measurements will provide valuable information on the Higgs sector of MSSM and other popular BSM scenarios, see [6–9].

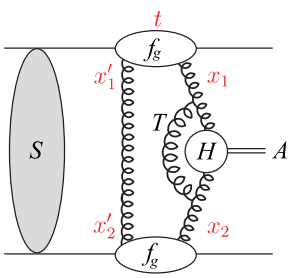

Fig. 1: A symbolic diagram for the CEP of a system A.

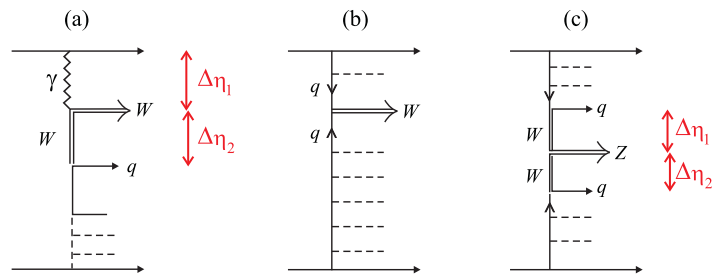

Fig. 2: (a) W production with 2 gaps, (b) Inclusive W production, (c) Z production with 2 gaps.

The theoretical formalism [10–12] for the description of a central exclusive production (CEP) process contains quite distinct parts, shown symbolically in Fig. 1. We first have to calculate the $gg \to A$ subprocess, H, convoluted with the gluon distributions f_g. Next, we must account for the QCD corrections which reflect the absence of additional radiation in the hard subprocess – that is, for the Sudakov factor T. Finally, we must enter soft physics to calculate the survival probability S^2 of the rapidity gaps (RG) .

The uncertainties of the CEP predictions are potentially not small. Therefore, it is important to perform checks using processes that will be accessible in the first LHC runs [13]. We first

consider measurements which do not rely on proton tagging and can be performed through the detection of RG.

The main uncertainties of the CEP predictions are associated with

(i) the probability S^2 that additional secondaries will not populate the gaps;

(ii) the probability to find the appropriate gluons, that are given by generalized, unintegrated distributions $f_g(x, x', Q_t^2)$;

(iii) the higher order QCD corrections to the hard subprocess, in particular, the Sudakov suppression;

(iv) the so-called semi-enhanced absorptive corrections (see [14, 15]) and other effects, which may violate the soft-hard factorization.

2 Gap survival factor S^2

Usually, the gap survival is calculated within a multichannel eikonal approach [16]. The probability S^2 of elastic pp rescattering, shown symbolically by S in Fig. 1 can be evaluated in a model independent way once the elastic cross section $d\sigma_{\rm el}/dt$ is measured at the LHC. However, there may be excited states between the blob S and the amplitude on the r.h.s of Fig. 1. The presence of such states enlarges absorption. To check experimentally the role of this effect, we need a process with a bare cross section that can be reliably calculated. Good candidates are the production of W or Z bosons with RGs [13]. In the case of 'W+gaps' production the main contribution comes from the diagram of Fig. 2(a) [17]. One gap, $\Delta\eta_1$, is associated with photon exchange, while the other, $\Delta\eta_2$, is associated with the W. In the early LHC data runs the ratio (W+gaps/W inclusive) will be measured first. This measurement is a useful check of the models for soft rescattering [13].

A good way to study the low impact parameter (b_t) region is to observe Z boson production via WW fusion, see Fig. 2(c). Here, both gaps originate from W-exchange, and the corresponding b_t region is similar to that for exclusive Higgs production. The expected Z+gaps cross section is of the order of 0.2 pb, and S^2=0.3 for $\Delta\eta_{1,2} > 3$ and for quark jets with $E_T > 50$ GeV [18].

3 Generalized, unintegrated gluon distribution f_g

The cross section for the CEP of a system A essentially has the form [10]

$$\sigma(pp \to p{+}A{+}p) \simeq \frac{S^2}{B^2}\left|\frac{\pi}{8}\int \frac{dQ_t^2}{Q_t^4}\, f_g(x_1, x_1', Q_t^2, \mu^2) f_g(x_2, x_2', Q_t^2, \mu^2)\right|^2 \hat{\sigma}(gg \to A). \quad (1)$$

Here the factor $1/B^2$ arises from the integration over the proton transverse momentum. Also, f_g denotes the generalized, unintegrated gluon distribution. In our case the distribution f_g can be obtained from the conventional gluon distribution, g, known from the global parton analyses. The main uncertainty here comes from the lack of knowledge of the integrated gluon distribution

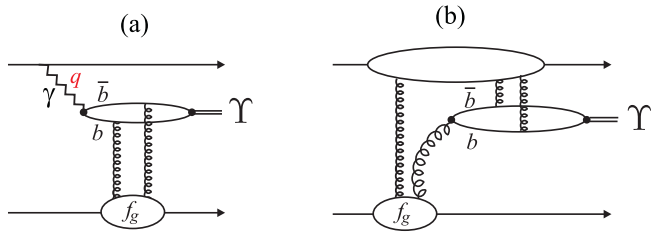

Fig. 3: Exclusive Υ production via (a) photon exchange, and (b) via odderon exchange.

$g(x,Q_t^2)$ at low x and small scales. For example, taking $Q_t^2 = 4\ \mathrm{GeV}^2$ we find [13] $xg = (3-3.8)$ for $x = 10^{-2}$ and $xg = (3.4-4.5)$ for $x = 10^{-3}$. These are big uncertainties bearing in mind that the CEP cross section depends on $(xg)^4$. To reduce the uncertainty associated with f_g we can measure exclusive Υ production. The process is shown in Fig. 3(a). The cross section for $\gamma p \to \Upsilon p$ is given in terms of the same unintegrated gluon distribution f_g that occurs in Fig. 1. There may be competition between production via photon exchange, Fig. 3(a), and via odderon exchange, see Fig. 3(b). A lowest-order calculation (e.g. [19]) indicates that the odderon process (b) may be comparable to the photon-initiated process (a). If the upper proton is tagged, it will be straightforward to separate the two mechanisms.

4 Three-jet events as a probe of the Sudakov factor

The search for the exclusive dijets at the Tevatron, $p\bar{p} \to p+jj+\bar{p}$, is performed [20] by plotting the cross section in terms of the variable $R_{jj} = M_{jj}/M_A$, where M_A is the mass of the whole central system. However, the R_{jj} distribution is smeared out by QCD radiation, hadronization, the jet algorithm and other experimental effects [20,21]. To weaken the smearing it was proposed in Ref. [21] to study the dijets in terms of a variable $R_j = 2E_T\ (\cosh\eta^*)/M_A$, where only the transverse energy and the rapidity η of the jet with the *largest* E_T enter. Here $\eta^* = \eta - y_A$, where y_A is the rapidity of the central system. Clearly, the largest E_T jet is less affected by the smearing. As shown in [13], it is sufficient to consider the emission of a third jet, when we take all three jets to lie in a specified rapidity interval $\delta\eta$. The cross section $d\sigma/dR_j$, as a function of R_j, for the production of a pair of high E_T dijets accompanied by a third jet is discussed in [13, 21]. It is shown that the measurements of the exclusive two- and three-jet cross sections *as a function of* E_T of the highest jet allow a detailed check of the Sudakov physics; with much more information coming from the $\delta\eta$ dependence study. A clear way to observe the Sudakov suppression is just to measure the E_T dependence of exclusive dijet production. On dimensional grounds we would expect $d\sigma/dE_T^2 \propto 1/E_T^4$. This behaviour is modified by the gluon anomalous dimension and by a stronger Sudakov suppression with increasing E_T. Already the existing CDF dijet data [20] exclude predictions which omit the Sudakov effect.

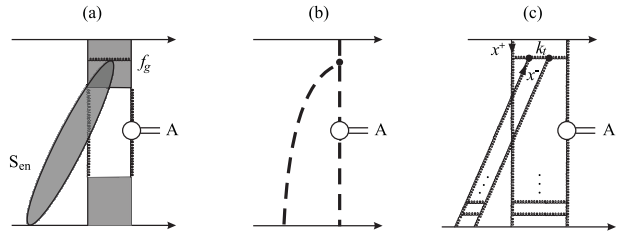

Fig. 4: (a) A typical enhanced diagram, where the shaded boxes denote f_g, and the soft rescattering is on an intermediate parton, giving rise to a survival factor $S_{\rm en}$; (b) and (c) are the Reggeon and QCD representations, respectively.

5 Soft-hard factorization: enhanced absorptive effects

The soft-hard factorization implied by Fig. 1 could be violated by the so-called enhanced Reggeon diagrams, see Fig. 4(a). The contribution of the first Pomeron loop, Fig. 4(b) was calculated in pQCD in Ref. [15]. A typical diagram is shown in Fig. 4(c). For LHC energies it was found that such effect may be numerically large. The reason is that the gluon density grows at low x and, for low k_t partons, approaches the saturation limit. However, as discussed in [13], the enhanced diagram should affect mainly the very beginning of the QCD evolution – the region that cannot be described perturbatively and which, in [11, 12], is already included phenomenologically.

Experimentally, we can study the role of semi-enhanced absorption by measuring the ratio R of diffractive event rate for W (or Υ or dijet) as compared to the inclusive process [13]. That is

$$R \;=\; \frac{\text{no. of } (A+\text{gap}) \text{ events}}{\text{no. of (inclusive } A) \text{ events}} \;=\; \frac{a^{\rm diff}(x_{I\!P},\beta,\mu^2)}{a^{\rm incl}(x=\beta x_{I\!P},\mu^2)}\,\langle S^2 S^2_{\rm en}\rangle_{\text{over } b_t}, \qquad (2)$$

where $a^{\rm incl}$ and $a^{\rm diff}$ are the parton densities determined from the global analyses of inclusive and diffractive DIS data, respectively. We can measure a double distribution $d^2\sigma^{\rm diff}/dx_{I\!P}dy_A$, and form the ratio R using the inclusive cross section, $d\sigma^{\rm incl}/dy_A$. If we neglect the enhanced absorption, it is quite straightforward to calculate the ratio R of (2). The results for a dijet case are shown by the dashed curves in Fig. 5 as a function of the rapidity y_A of the dijet system. The enhanced rescattering reduce the ratios and lead to steeper y_A distributions, as illustrated by the continuous curves. Perhaps the most informative probe of $S^2_{\rm en}$ is to observe the ratio R for dijet production in the region $E_T \sim 15-30$ GeV. For example, for $E_T \sim 15$ GeV we expect $S^2_{\rm en} \sim$ 0.25, 0.4 and 0.8 at $y_A = -2,\ 0$ and 2 respectively.

6 Conclusion

The addition of forward proton detectors to LHC experiments will add unique capabilities to the existing LHC experimental programme. For certain BSM scenarios, the tagged-proton mode may even be the discovery channel. There is also a rich QCD, electroweak, and more exotic physics, menu.

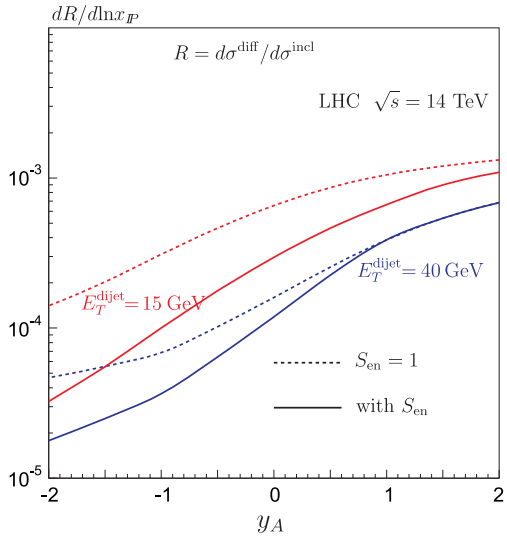

Fig. 5: The predictions of the ratio R of (2) for the production of a pair of high E_T jets.

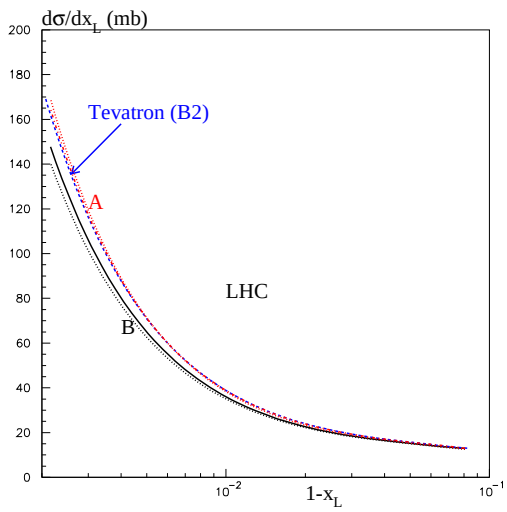

Fig. 6: The cross section $d\sigma_{\rm SD}/dx_L$ for single dissociation integrated over t at the LHC energy.

The uncertainties in the prediction of the CEP processes are potentially not small. Therefore, it is crucial to perform checks of the theoretical formalism using reactions that will be experimentally accessible in the first LHC runs [13].

Most of the measurements discussed above can be performed, without detecting the protons, by taking advantage of the relatively low luminosity in the early LHC runs. When the forward proton detectors are operating much more can be done. First, it is possible to measure directly the cross section $d^2\sigma_{\rm SD}/dtdM_X^2$ for single diffractive dissociation and also the cross section $d^2\sigma_{\rm DPE}/dy_1dy_2$ for soft central diffractive production. These measurements will strongly constrain the models used to describe diffractive processes and the effects of soft rescattering. The recent predictions can be found in [12]. For illustration we show in Fig. 6 the expectation for $d\sigma_{\rm SD}/dx_L$, see for details [12]. Next, a study of the transverse momentum distributions of both of the tagged protons, and the correlations between their momenta, is able to scan the proton optical density [17, 22].

References

[1] V.A. Khoze, A.D. Martin and M.G. Ryskin, *Eur. Phys. J.* **C23**, 311 (2002).

[2] A. De Roeck *et al.*, *Eur. Phys. J.* **C25**, 391(2002).

[3] J. Forshaw and A. Pilkington, *In *Hamburg 2007, Blois07, Forward physics and QCD* 130-136.*

[4] M. G. Albrow *et al.* [FP420 R and D Collaboration], arXiv:0806.0302 [hep-ex].

[5] P. J. Bussey, arXiv:0809.1335 [hep-ex].

[6] A.B. Kaidalov *et al.*, *Eur. Phys. J.* **C33**, 261 (2004).

[7] S. Heinemeyer *et al.*,*Eur. Phys. J.* **C53**, 231 (2008).

[8] B. Cox, F. Loebinger and A. Pilkington, JHEP **0710**, 090 (2007).

[9] J. R. Forshaw *et al.*, JHEP **0804**, 090 (2008).

[10] V.A. Khoze, A.D. Martin and M.G. Ryskin, *Eur. Phys. J.* **C14**, 525 (2000).

[11] V.A. Khoze, A.D. Martin and M.G. Ryskin, *Eur. Phys. J.* **C18**, 167 (2000).

[12] M.G. Ryskin, A.D. Martin and V.A. Khoze, *Eur. Phys. J.* **C54**, 199 (2008); E.G.S. Luna *et al.*,arXiv:0807.4115 [hep-ph].

[13] V.A. Khoze, A.D. Martin and M.G. Ryskin, Eur. Phys. J. C **55**, 363 (2008).

[14] A.B. Kaidalov et al., *Eur. Phys. J.* **C21**, 521 (2001).

[15] J. Bartels et al., Phys. Rev. **D73**, 093004 (2006).

[16] For a review see: E. Gotsman et al., arXiv:hep-ph/0511060.

[17] V.A. Khoze, A.D. Martin and M.G. Ryskin, *Eur. Phys. J.* **C24**, 459 (2002).

[18] V.A. Khoze et al., *Eur. Phys. J.* **C26**, 429 (2003).

[19] A. Bzdak et al., Phys. Rev. **D75**, 094023 (2007).

[20] T. Aaltonen *et al.* [CDF Run II Collaboration], Phys. Rev. D **77**, 052004 (2008).

[21] V.A. Khoze, A.D. Martin and M.G. Ryskin, *Eur. Phys. J.* **C48**, 467 (2006).

[22] V.A. Khoze, A.D. Martin and M.G. Ryskin, *Eur. Phys. J.***C24**, 581 (2002).

Rapidity gap survival probability and total cross sections

A.D. Martin, V.A. Khoze and M.G. Ryskin
Institute for Particle Physics Phenomenology, University of Durham, DH1 3LE, UK

Abstract
We discuss recent calculations of the survival probability of the large rapidity gaps in exclusive processes of the type $pp \to p + A + p$ at high energies. Absorptive or screening effects are important, and one consequence is that the total cross section at the LHC is predicted to be only about 90 mb.

At the LHC, the observation of an exclusive process of the type $pp \to p + A + p$, where a produced new heavy object A is separated from the outgoing protons by large rapidity gaps (LRG), will provide very good experimental conditions to study the properties of object A [1–3]. The process is sketched in Fig. 1. The case of $A = H \to b\bar{b}$ is particularly interesting. The cross is usually written in the form

$$\sigma \;\sim\; \frac{\langle S^2\rangle}{B^2}\left|N\int \frac{dQ_t^2}{Q_t^4} f_g(x_1,x_1',Q_t^2,\mu^2) f_g(x_2,x_2',Q_t^2,\mu^2)\right|^2 \tag{1}$$

where $B/2$ is the t-slope of the proton-Pomeron vertex, and the constant N is known in terms of the $A \to gg$ decay width. The amplitude-squared factor, $|...|^2$, can be calculated in perturbative QCD, since the dominant contribution to the integral comes from the region $\Lambda^2_{QCD} \ll Q_t^2 \ll M_A^2$, for the large values of M_A^2 of interest. The probability amplitudes, f_g, to find the appropriate pairs of t-channel gluons (x_1, x_1') and (x_2, x_2') of Fig. 1, are given by skewed unintegrated gluon densities at a hard scale $\mu \sim M_A/2$. To evaluate the cross section of such an exclusive processes it is important to know the probability, $\langle S^2\rangle$, that the LRG survive and will not be filled by secondaries from eikonal and enhanced rescattering effects. The main effect comes from the rescattering of soft partons, since they have the largest absorptive cross sections. Therefore, we need a realistic model to describe soft interactions at the LHC energy, and to predict the total cross section at LHC. The model must account for (i) elastic rescattering (with two protons in intermediate state), (ii) the probability of the low-mass proton excitations (with an intermediate proton replaced by the N(1400), N(1700), etc. resonances), and (iii) the screening corrections due to high-mass proton dissociation.

The effect of elastic rescattering may be evaluated in a model independent way once the elastic pp-amplitude is known. The effect of the low-mass dissociation is usually calculated in the framework of the Good-Walker formalism [4], that is, by introducing diffractive eigenstates, ϕ_i with $i = 1,..n$, which only undergo 'elastic' scattering. The resulting n-channel eikonal $\Omega_{ik}(s,b)$ depends on the energy and the impact parameter of the pp interaction. The parameters

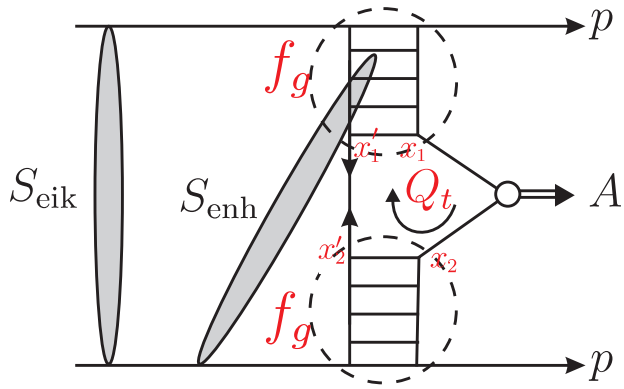

Fig. 1: The mechanism for the exclusive process $pp \to p + A + p$, with the eikonal and enhanced survival factors shown symbolically.

of the model are chosen to reproduce the available (fixed-target and CERN-ISR) data on the cross section of low-mass diffractive dissociation. Usually either a two- or three-channel eikonal is used. Finally, high-mass dissociation is described in terms of Reggeon diagram technique [5]. A symbolic representation of these soft scattering effects is shown in Fig. 2. The latest calculations along these lines are described in Refs. [6, 7]. In Ref. [6] the authors account only for the triple-Pomeron vertex, and, moreover, sum up only the specific subset[1] of multi-Pomeron diagrams that were considered in Ref. [8], which is called the MPSI approximation. In Ref. [7] all possible multi-Pomeron vertices were included under a reasonable assumption about the form of the $n \to m$ multi-Pomeron vertices, g_m^n. The assumption corresponds to the hypothesis that the screening of the s-channel parton c during the evolution is given by the usual absorption factor $\exp(-\Omega_{ic}(b) - \Omega_{ck}(b))$, where $\Omega_{ic}(b)$ ($\Omega_{ck}(b)$) is the value of the opacity of the beam (target) proton at impact parameter b with respect to the parton c.

Since the absorptive corrections increase with energy, the cross section grows more slowly than the simple power ($\sigma \propto s^{\Delta}$) parametrisation [9]. In spite of the fact that the models of [6] and [7] are quite different to each other, after the parameters are fixed to describe the data on the total, elastic and single dissociation cross sections ($\sigma_{\rm tot}$, $d\sigma_{\rm el}/dt$ and $d\sigma_{\rm SD}/dM^2$) within the CERN-ISR – Tevatron energy range, the latest versions of the Tel-Aviv and Durham models predict almost the same total cross section at the LHC, namely $\sigma_{\rm tot} \sim 90$ mb. Correspondingly, both models predict practically the same gap survival probability $\langle S^2_{\rm eik} \rangle \sim 0.02$ with respect to the eikonal (including the elastic and low-mass proton excitation) rescattering, for the exclusive production of a Higgs boson.

A more delicate problem is the absorptive correction to exclusive cross sections caused by the so-called enhanced diagrams, that is by the interaction with the intermediate partons, see

[1] For example, the third, but not the second, term on the right-hand side of the expression for $\Omega_{ik}/2$ in Fig. 2 is included; neither are multi-Pomeron terms, like the last term, included.

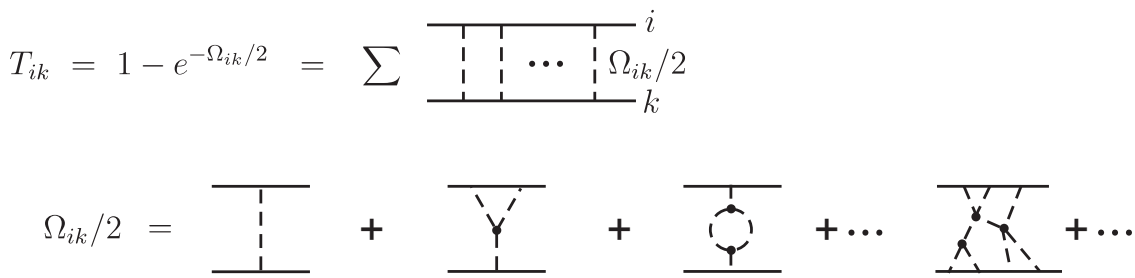

Fig. 2: The multi-channel eikonal form of the amplitude, where i, k are diffractive (Good-Walker) eigenstates. Low-mass proton dissociation is included by the differences of the Pomeron couplings to one or another Good-Walker state (i) in the first diagram, while the remaining (multi-Pomeron) diagrams on the right-hand side of the expression for $\Omega_{ik}/2$ include the high-mass dissociation.

Fig. 1. This rescattering violates 'soft-hard' factorisation, since the probability of such an interaction depends both on the transverse momentum and on the impact parameter of the intermediate parton.

The contribution of the first enhanced diagram was evaluated in [10] in the framework of the perturbative QCD. It turns out to be quite large. On the other hand, such an effect is not seen experimentally. The absorptive correction due to enhanced screening must increase with energy. This was not observed in the present data (see [11] for a more detailed discussion).

Several possible reasons are given below.

(a) We have to sum up the series of the multi-loop Pomeron diagrams. The higher-loop contributions partly compensate the correction caused by the first-loop graph.

(b) There should be a "threshold", since Pomeron vertices must be separated by a non-zero rapidity interval [12]. That is, at present energies, the kinematical space available for the position of a multi-Pomeron vertex in an enhanced diagram is small, and the enhanced contribution is much less than that obtained in leading logarithmic (LL) approximation.

(c) The factor $S^2_{\rm eik}$ already absorbs almost all the contribution from the center of the disk. The parton only survives eikonal rescattering on the periphery, that is at large b. On the other hand, on the periphery the parton density is rather small, and the probability of *enhanced* absorption is not large. This fact can be seen in Ref. [13]. There, the momentum, Q_s, below which we may approach saturation, was extracted from HERA data in the framework of the dipole model. Already at $b = 0.6$ fm the value of $Q_s^2 < 0.3$ GeV^2 for $x < 10^{-6}$. See also [14] where the value of Q_s was evaluated using LO DGLAP evolution.

Point (c) is relevant to the calculation of $S^2_{\rm enh}$ described in [6]. First, note that the b dependence of the beginning of 'saturation caused by enhanced graphs' is not accounted for in the MPSI approximation used in [6]. In this model, we have the same two-particle irreducible amplitude (which sums up the enhanced diagrams) at any value of b. Therefore, the enhanced

screening effect does not depend on the initial parton density at a particular impact parameter point b. For this reason the suppression due to enhanced screening corrections $\langle S^2_{\rm enh}\rangle = 0.063$ claimed in [6] is much too strong[2].

The survival factor $\langle S^2_{\rm enh}\rangle$ has also been calculated in the new version of the Durham model [16]. The model includes 3 components of the Pomeron, with the different transverse momenta k_t of the partons in each Pomeron component, in order to mimic BFKL diffusion in $\ln\ k_t$. In this way we obtain a more realistic estimate of the 'enhanced screening' in exclusive diffractive Higgs boson production at the LHC. The model predicts $\langle S^2_{\rm enh}\rangle \sim 1/3$. However the CDF data on exclusive $\gamma\gamma$ and χ_c production indicate that this suppression is not so strong.

Note, that comparing the values of the survival factors in this way is too simplistic. The problem is that, with enhanced screening on intermediate partons, we no longer have exact factorisation between the hard and soft parts of the process. Thus, before computing the effect of soft absorption we must fix what is included in the bare exclusive amplitude calculated in terms of perturbative QCD.

The first observation is that the bare amplitude is calculated as a convolution of two generalised (skewed) gluon distributions with the hard subprocess matrix element, see (1). These gluon distributions are determined from integrated gluon distributions of a global parton analysis of mainly deep inelastic scattering data. Now, the phenomenological integrated parton distributions already include the interactions of the intermediate partons with the parent proton. Thus calculations of $S_{\rm enh}$ should keep only contributions which embrace the hard matrix element of the type shown in Fig. 1.

The second observation is that the phenomenologically determined generalised gluon distributions, f_g, are usually taken at $p_t = 0$ and then the observed "total" cross section is calculated by integrating over p_t of the recoil protons assuming the an exponential behaviour $e^{-Bp_t^2}$; that is

$$\int dp_t^2\ e^{-Bp_t^2}\ =\ 1/B\ =\ \langle p_t^2\rangle. \tag{2}$$

However, the total soft absorptive effect changes the p_t distribution in comparison to that for the bare cross section determined from perturbative QCD. Thus the additional factor introduced by the soft interactions is not just the gap survival S^2, but rather the factor S^2/B^2 [17], which strictly speaking has the form $S^2\langle p_t^2\rangle^2$.

In order to compare determinations of the suppression due to absorptive effects we should compare only the values of the complete cross section for $pp \to p{+}A{+}p$. However a comparison is usually made by reducing the cross section to a factorized form. If this is done, as in (1), then

[2]Moreover, since the irreducible amplitude approaches saturation at some fixed energy (rapidity), independent of the value of b, the approximation gives $\sigma_{\rm tot}(s\to\infty)\to$ constant. On the other hand, a theory with an asymptotically constant cross section can only be self-consistent in the so-called 'weak coupling' regime for which the triple-Pomeron vertex vanishes for zero momentum transfer [15]. The vertex used in [6] does not vanish. This indicates that the MPSI approximation cannot be used at asymptotically high energies, and the region of its validity must be studied in more detail.

the Durham predictions for the survival factor to eikonal and enhanced screening of the exclusive production of a 120 GeV Higgs at the LHC are $\langle S^2\rangle = 0.008,\ 0.017, 0.030$ where enhanced sreening is only permitted outside a threshold rapidity gap $\Delta y = 0,\ 1.5,\ 2.3$ respectively. The values correspond to $B = 4\ \mathrm{GeV}^{-2}$.

Let us discuss the survival factors claimed by Frankfurt et al. [18]. They use another approach. Within the eikonal formalism, they account for elastic rescattering only. The possibility of proton diffractive excitation is included in terms of parton-parton correlations, for both low- and high-mass dissociation. At a qualitative level, it is possible to consider all the effects discussed above in terms of such a language. On the other hand, to the best of our knowledge, they did not describe the available data on $\sigma_{\rm tot},\ d\sigma_{\rm el}/dt,\ M^2 d\sigma_{\rm SD}/dM^2$. Also, the energy (i.e. $1/x$) dependence of the parton densities was evaluated using simple LO DGLAP evolution. This is grossly inadequate for the low values of x sampled, $x \sim 10^{-5}$. Thus, it is difficult to judge the accuracy of their numerical predictions. Moreover, part of the Sudakov-like suppression, which above was calculated using perturbative QCD, is here treated as parton correlations and included in the value of $S^2_{\rm enh}$.[3] Therefore, one cannot compare literally the predictions for the gap survival factors $S^2 = \langle S^2_{\rm eik}(b) S^2_{\rm enh}(b)\rangle$ given by [18] and by the Durham, Tel-Aviv and Petrov et al. [19] models[4]. The only possibility is to compare the predictions for the final exclusive cross section. Unfortunately, such a prediction is not available in [18].

Next, we comment on another recent calculation [20] along the lines of eq. (1). They claim very large uncertainties in the predictions arising mainly from the freedom in the choice of limits of integration in the Sudakov form factor which is embedded in f_g. However, this is not the case. In fact, the Sudakov factors have been calculated to *single* log accuracy. The collinear single logarithms are summed up using the DGLAP equation. To account for the 'soft' logarithms (corresponding to the emission of low energy gluons) the one-loop virtual correction to the $gg \to A$ vertex was calculated explicitly, and then the scale $\mu = 0.62\ M_A$ was chosen so that double log expression for the Sudakov form factor reproduces the result of the explicit calculation. Similarly, the lower limit $k_t^2 = Q_t^2$ was verified to give the one-loop result. It is sufficient to calculate just the one-loop correction since it is known that the effect of 'soft' gluon emission exponentiates. Thus double log expression, with $\mu = 0.62\ M_A$, gives the Sudakov factor to single log accuracy. Also the form used for f_g's in Ref. [20] contradicts the known leading $\log(1/x)$ asymptotic behaviour.

Finally, we discuss a very recent calculation [21] based on the dipole approach. A new development is that instead of using a multi-channel eikonal with a fixed number of diffractive eigenstates, the authors consider an explicit wave function of a fast hadron (proton, pion) and have a continuous integration over the size of the quark-quark dipoles. In this model the incoming

[3] In general, one may include the absence of QCD radiation in the large rapidity gap in the "soft" survival factors, but to make comparisons we must define precisely in which part of the calculation each effect is included. Note also that in [18] the DL expression for Sudakov T–factor is used, which grossly overestimates the suppression.

[4] The last group calculated S^2 within their own eikonal model and fitted the parameters in a Regge-type expression for f_g to describe HERA data. The final prediction is again rather close to that by the Durham group.

hadron wave function is approximated by a simple Gaussian. The parameters are fitted so as to describe the data on $\sigma_{\rm tot}, \sigma_{\rm el}$ and F_2 at low x. A shortcoming is that high-mass dissociation is calculated separately. Its contribution is not included in the proton dipole opacity $\Omega(r, b)$, for which a simplified asymptotic solution of the BFKL equation was used. Moreover, to calculate the gap survival probability, $S^2(b)$, the b dependence is considered, but the dependence of the "hard subprocess" cross section on the dipole size was not accounted for. That is, again, the correlation between the saturation momentum Q_s and b is lost. Nevertheless, the model confirms the observation that the energy dependence of S^2 is not too steep; S^2 at the LHC for central exclusive production is only reduced by a factor of about 2.5 to that at the Tevatron. Thus, Tevatron data serve as a reliable probe of the theoretical model predictions of these production rates.

In summary, we have briefly discussed various recent calculations of the exclusive process $pp \to p + A + p$ at high energy. The value of the cross section when $A = (H \to b\bar{b})$ is important for the feasibility of using tagged protons to study the Higgs sector via this process at the LHC. We have paid special attention to the survival factors of the large rapidity gaps. We see no reason to doubt the claimed value, or accuracy, of the existing predictions of the Durham model. Recall that these predictions have been checked in many places by comparing with the available experimental data on exclusive $\gamma\gamma$ and high E_T dijet production at the Tevatron and on exclusive diffractive J/ψ production at HERA (see [22, 23] for more details). Since all the factors, which enter the calculations, depend rather weakly (logarithmically) on the initial energy, there is no reason to expect that the model, which describes the data at the Tevatron energy, will be too far from reality at the LHC.

References

[1] V. A. Khoze, A. D. Martin and M. G. Ryskin, Eur. Phys. J. C **23**, 311 (2002).

[2] A. De Roeck, V. A. Khoze, A. D. Martin, R. Orava and M. G. Ryskin, Eur. Phys. J. C **25**, 391 (2002).

[3] V. A. Khoze, A. D. Martin and M. G. Ryskin, arXiv:0705.2314 [hep-ph].

[4] M.L. Good and W.D. Walker, Phys. Rev. **120** (1960) 1857.

[5] V.N. Gribov, Sov. Phys. JETP **26** (1968) 414.

[6] E. Gotsman, E. Levin, U. Maor and J. S. Miller, arXiv:0805.2799 [hep-ph].

[7] M. G. Ryskin, A. D. Martin and V. A. Khoze, Eur. Phys. J. C **54**, 199 (2008)

[8] A. H. Mueller and B. Patel, Nucl. Phys. **B425**, 471 (1994); A. H. Mueller and G. P. Salam, Nucl. Phys. **B475**, 293 (1996); G. P. Salam, Nucl. Phys. **B461**, 512 (1996); E. Iancu and A. H. Mueller, Nucl. Phys. **A730** (2004) 460, 494.

[9] A. Donnachie and P.V. Landshoff, Phys. Lett. **B296** 227 (1992).

[10] J. Bartels, S. Bondarenko, K. Kutak and L. Motyka, Phys. Rev. D **73**, 093004 (2006).

[11] V. A. Khoze, A. D. Martin and M. G. Ryskin, JHEP **0605**, 036 (2006).

[12] A. B. Kaidalov, V. A. Khoze, A. D. Martin and M. G. Ryskin, Eur. Phys. J. C **21**, 521 (2001).

[13] G. Watt, arXiv:0712.2670v1 [hep-ph]; arXiv:0807.4464 [hep-ph].

[14] T. Rogers, V. Guzey, M. Strikman and X. Zu, Phys. Rev. D **69**, 074011 (2004).

[15] V.N. Gribov and A.A. Migdal, Sov. J. Nucl.Phys. **8** (1969).

[16] M. G. Ryskin, A. D. Martin and V. A. Khoze, to be published.

[17] V. A. Khoze, A. D. Martin, M. G. Ryskin and W. J. Stirling, Eur. Phys. J. C **35**, 211 (2004).

[18] L. Frankfurt et al., arXiv:07102942; arXiv:0808.0182 [hep-ph].

[19] V. A. Petrov and R. A. Ryutin, J. Phys. G **35**, 065004 (2008), and references therein.

[20] J. R. Cudell, A. Dechambre, O. F. Hernandez and I. P. Ivanov, arXiv:0807.0600 [hep-ph].

[21] A. Kormilitzin and E. Levin, arXiv:0809.3886.

[22] V. A. Khoze et al., arXiv:hep-ph/0507040.

[23] V. A. Khoze, A. D. Martin and M. G. Ryskin, Eur. Phys. J. C **55**, 363 (2008).

Rapidity gap survival in central exclusive diffraction: Dynamical mechanisms and uncertainties*

Mark Strikman[a], *Christian Weiss*[b]
[a] Department of Physics, Pennsylvania State University, University Park, PA 16802, USA
[b] Theory Center, Jefferson Lab, Newport News, VA 23606, USA

Abstract
We summarize our understanding of the dynamical mechanisms governing rapidity gap survival in central exclusive diffraction, $pp \to p + H + p$ (H = high–mass system), and discuss the uncertainties in present estimates of the survival probability. The main suppression of diffractive scattering is due to inelastic soft spectator interactions at small pp impact parameters and can be described in a mean–field approximation (independent hard and soft interactions). Moderate extra suppression results from fluctuations of the partonic configurations of the colliding protons. At LHC energies absorptive interactions of hard spectator partons associated with the $gg \to H$ process reach the black–disk regime and cause substantial additional suppression, pushing the survival probability below 0.01.

1 Strong interaction dynamics in rapidity gap survival

Calculation of the cross section of central exclusive diffraction, $pp \to p + H + p$ (H = dijet, heavy quarkonium, Higgs boson, *etc*.) presents a major challenge for strong interaction physics. It involves treating the hard dynamics in the elementary $gg \to H$ subprocess, and calculating the probability that no other interactions leading to hadron production occur during the pp collision. The latter determines the suppression of diffractive relative to non-diffractive events with the same hard process, referred to as the rapidity gap survival (RGS) probability. In this article we summarize our understanding of the dynamical mechanisms determining the RGS probability, their phenomenological description, and the uncertainties in present numerical predictions.

RGS in central exclusive diffraction has extensively been discussed in an approach where soft interactions are modeled by eikonalized pomeron exchange; see Ref. [1] for a summary. More recently a partonic description was proposed, which allows for a model–independent formulation of the interplay of hard and soft interactions and reveals the essential role of the "transverse geometry" of the pp collision [2]. In the mean–field approximation, where hard and soft interactions are considered as independent aside from their common dependence on the impact parameter, we derived a simple "factorized" expression for the RGS probability, using closure of the partonic states to take into account inelastic diffractive intermediate states. The resulting RGS probability is smaller than in the models of Refs. [1, 3] without inelastic diffraction,

but comparable to the some of the versions of those models with multichannel diffraction. Our partonic description also permits us to go beyond the mean–field approximation and incorporate various types of correlations between the hard scattering process and spectator interactions. Here we discuss two such effects: (a) quantum fluctuations of the partonic configurations of the colliding protons, which somewhat reduce the survival probabilities at RHIC and Tevatron energies; (b) absorptive interactions of high-virtuality spectator partons ($k^2 \sim$ few GeV^2) associated with the hard scattering process, related to the onset of the black–disk regime (BDR) in hard interactions at LHC energies; this new effect substantially reduces the RGS probability compared to previously published estimates.

2 Soft spectator interactions in the mean–field approximation

A simple picture of RGS is obtained in the impact parameter representation. On one hand, to produce the heavy system H two hard gluons from each of the two protons need to collide in the same space–time point (actually, an area of transverse size $\sim 1/\langle k_T^2 \rangle$ in the hard process); because such gluons are concentrated around the transverse centers of the protons this is most likely when the protons collide at a small impact parameters, $b \lesssim 1$ fm. On the other hand, soft inelastic spectator interactions are strongest at small b and would favor collisions at $b \gg 1$ fm for diffractive scattering. These different preferences limit diffraction to an intermediate range of impact parameters and ensure that its cross section is substantially suppressed compared to non–diffractive scattering. More precisely, the RGS probability is given by [2]

$$S^2 \;=\; \int d^2b\; P_{\rm hard}(b)\; |1-\Gamma(b)|^2, \qquad\qquad b \equiv |\boldsymbol{b}|. \tag{1}$$

Here $P_{\rm hard}(b)$ is the probability for two gluons to collide at the same transverse point as a function of the pp impact parameter, given by the convolution of the transverse spatial distributions of the gluons in the colliding protons, normalized to $\int d^2b\; P_{\rm hard}(b) = 1$ (see Fig. 1a). The factor $|1-\Gamma(b)|^2$ is the probability for the two protons not to interact inelastically in a collision at the given impact parameter, calculable in terms of the profile function of the pp elastic amplitude, $\Gamma(b)$. Figure 1b shows the b–dependence of the two factors as well as their product, illustrating the interplay described above. While we have motivated Eq. (1) by probabilistic arguments, it actually can be derived (as well as the expression for the differential cross section) in the partonic description of Ref. [2] within the mean–field approximation, where one assumes no correlation between the presence of the gluons involved in the hard interaction (with the particular x) and the strength of the soft spectator interactions. In this approximation one can use closure to sum over the different diffractive intermediate states, and thus effectively include the contribution of inelastic diffraction.[1] The numerical values of the RGS probability obtained from Eq. (1) are of the order $S^2 \sim 0.03$ for $M_H = 100\,$GeV and $\sqrt{s} = 14\,$TeV; see Ref. [2] for details.

It is worthwhile to discuss the uncertainty in the numerical predictions for S^2 in the mean–field approximation, Eq. (1), resulting from our imperfect knowledge of the functions in the

[1] In principle there is also a contribution from excitation of a diffractive state by soft spectator interactions and subsequent transition back to the proton via the nondiagonal gluon GPD; however, it is strongly suppressed because the typical excitation masses in hard and soft diffraction are very different in the kinematics of Higgs production at the LHC ($10^{-8} \le x_{I\!P} \le 0.1$ for generic pp diffraction and $10^{-2} \le x_{I\!P} \le 0.1$ for the GPD); see Section IV C of Ref. [2].

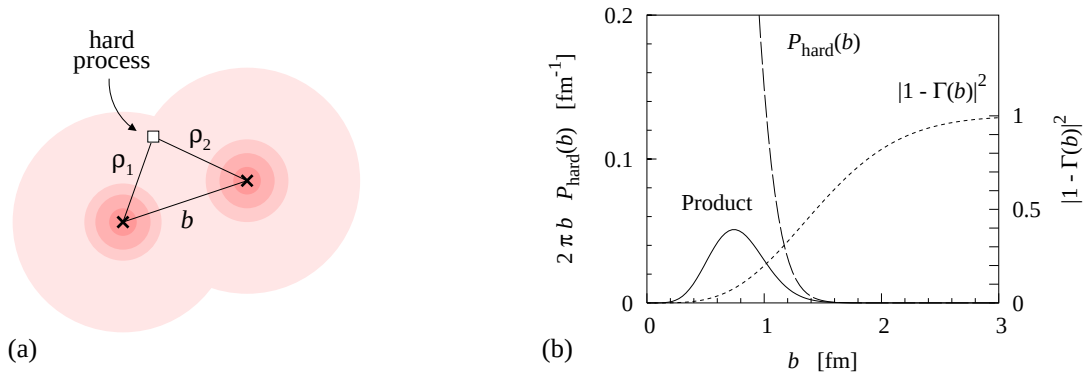

Fig. 1: (a) Transverse geometry of hard diffractive pp scattering. (b) RGS probability in the impact parameter representation *cf.* Eq. (1), for $\sqrt{s} = 14\,\text{TeV}, M_H \sim 100\,\text{GeV}$ [2]. Dashed line: Probability for hard scattering process $P_{\text{hard}}(b)$ (left vertical axis). Dotted line: Probability for no inelastic interactions between the protons, $|1 - \Gamma(b)|^2$ (right vertical axis). Solid line: Product $P_{\text{hard}}(b)|1 - \Gamma(b)|^2$ (left vertical axis). The RGS probability Eq. (1) is given by the area under this curve.

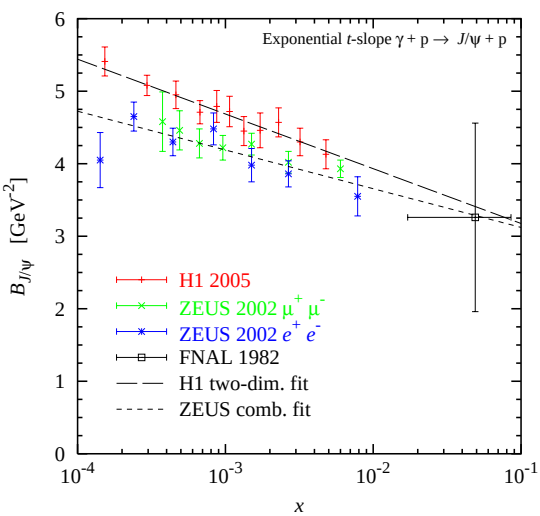

Fig. 2: The exponential t–slope, $B_{J/\psi}$, of exclusive J/ψ photoproduction, extracted from fits to the FNAL E401/E458 [4], HERA H1 [5], and ZEUS [6] data. The long–dashed and short–dashed lines represent fits to the x–dependence of the H1 and ZEUS t–slopes [5, 6], *cf.* Eq. (2). The t–slope of the gluon GPD, B_g, is obtained from $B_{J/\psi}$ after applying a small correction for the finite size of the J/ψ [7].

integrand. We first consider the transverse spatial distribution of gluons entering in $P_{\rm hard}(b)$. The latter is obtained as the Fourier transform of the t–dependence (more precisely, transverse momentum dependence) of the gluon generalized parton distribution (GPD) measured in hard exclusive vector meson production. Extensive studies at HERA have shown that exclusive J/ψ photoproduction, $\gamma p \to J/\psi + p$, provides an effective means for probing the t–dependence of the gluon GPD at small and intermediate x (a small correction for the finite transverse size of the J/ψ is applied) [7]. Figure 2 summarizes the results for the exponential t–slope of this process, $B_{J/\psi}$, from HERA H1 [5] and ZEUS [6] and the FNAL E401/E458 experiment [4], as well as fits to the x–dependence of the H1 and ZEUS results of the form (here $x = M_{c\bar{c}}^2/W^2$)

$$B_{J/\psi}(x) \;=\; B_{J/\psi}(x_0) \;+\; 2\alpha'_{J/\psi}\;\ln(x_0/x). \tag{2}$$

There is a systematic difference between the H1 and ZEUS results due to different analysis methods [5, 6]; however, the fits to both sets agree well with the FNAL point when extrapolated to larger x. In diffractive production of a system with $M_H = 100\,\text{GeV}$ at $\sqrt{s} = 14\,\text{TeV}$ at zero rapidity the gluons coupling to the heavy system H have momentum fractions $x_{1,2} = M_H/\sqrt{s} = 0.007$. Assuming exponential t–dependence of the gluon GPD, we can estimate the uncertainty in the transverse spatial distribution of gluons at such x by evaluating the fits to the HERA data within the error bands quoted for $B_{J/\psi}(x_0)$ and $\alpha'_{J/\psi}$ [5, 6]. We find a 15-20% uncertainty of $B_{J/\psi}$ at $x = 0.007$ in this way, translating into a 20–30% uncertainty in the mean–field RGS probability, Eq. (1). We note that there is at least a comparable uncertainty in S^2 from the uncertainty of the shape of the t–dependence; this is seen from Fig. 10 of Ref. [2], where the exponential is compared with a theoretically motivated dipole form which also describes the FNAL data. Altogether, we estimate that our imperfect knowledge of the spatial distribution of gluons results in an uncertainty of the mean–field result for S^2 by a factor ~ 2. Dedicated analysis of the remaining HERA exclusive data, and particularly precision measurements with a future electron–ion collider (EIC), could substantially improve our knowledge of the transverse spatial distribution of gluons.

We now turn to the uncertainty in S^2 arising from the pp elastic amplitude, $\Gamma(b)$. Most phenomenological analyses of pp elastic and total cross section data find that for TeV energies $|1 - \Gamma(b)| \leq 0.05$ at $b = 0$, corresponding to near–unit probability of inelastic interactions at small impact parameters (BDR). This is supported by theoretical studies in the QCD dipole model, which show that the large–x partons with virtualities of up to several GeV^2 experience "black" interactions with the small–x gluon field in the other proton when passing through the other proton at transverse distances $\rho \leq 0.5$fm, and receive transverse momenta $k_T \geq 1\,\text{GeV}$ (see Ref. [7] for a summary). At pp impact parameter $b = 0$ the chance that none of the leading partons in the protons receive such a kick is extremely small, implying that $|1 - \Gamma(b)| \sim 0$ [8]. For the RGS probability in the mean–field approximation, Eq. (1), the fact that $|1 - \Gamma(b)|^2$ is small at $b = 0$ is essential, as this eliminates the contribution from small b in the integral (see Fig. 1b) and stabilizes the numerical predictions. However, present theoretical arguments and data analysis cannot exclude a small non-zero value of $|1 - \Gamma(b)|$ at $b = 0$; a recent analysis finds $|1 - \Gamma(b)| \sim 0.1$ [9]. To investigate the potential implications for the RGS probability, we evaluate Eq. (1) with the Gaussian parametrization of $\Gamma(b)$ of Ref. [2], Eq. (12), but with $\Gamma(b = 0) = 1 - \epsilon$. We find that a value of $\epsilon = 0.1$, corresponding to $|1 - \Gamma(b)|^2 = 0.01$, increases

the mean–field result for S^2 by a factor ~ 1.8, indicating significant uncertainty of the mean–field result. However, as explained in Sec. 4 below, hard spectator interactions associated with the $gg \to H$ process lead to an additional suppression of diffraction at small b (not contained in the soft RGS probability), which mitigates the impact of this uncertainty on the overall diffractive cross section.

3 Fluctuations of parton densities and soft–interaction strength

Corrections to the mean–field picture of RGS arise from fluctuations of the interacting configurations in the colliding protons. This concept is known well in soft diffraction, where fluctuations of the strength of interaction between the colliding hadrons give rise to inelastic diffraction. In hard diffraction, one expects that also the gluon density fluctuates; *e.g.* because the color fields are screened in configurations of small size [10]. In fact, the variance of the gluon density fluctuations can be directly related to the ratio of inelastic and elastic diffraction in processes such as $\gamma_L^* + p \to$ "vector meson" $+ X$,

$$\omega_g \equiv \frac{\langle G^2 \rangle - \langle G \rangle^2}{\langle G \rangle^2} = \frac{d\sigma_{\rm inel}}{dt} \Big/ \left. \frac{d\sigma_{\rm el}}{dt} \right|_{t=0} . \tag{3}$$

The HERA data are consistent with the dynamical model estimate of $\omega_g \sim 0.15 - 0.2$ for $Q^2 = 3\,\mathrm{GeV}^2$ and $x \sim 10^{-4} - 10^{-3}$ [10]; unfortunately, the limited Q^2 range and the lack of dedicated studies do not allow for a more precise extraction of this fundamental quantity.

In central exclusive diffraction, correlated fluctuations of the soft–interaction strength and the gluon density lower the RGS probability, because small-size configurations which experience little absorption have a lower gluon density. This effect can be modeled by a generalization of the mean–field expression (1), in which both the gluon GPDs in $P_{\rm hard}$ and the profile function fluctuate as a function of an external parameter controlling the overall size of the configurations [10]. Numerical studies find a reduction of the RGS probability by a factor $\sim 0.82\,(0.74)$ for a system with mass $M_H = 100\,\mathrm{GeV}$ produced at zero rapidity at $\sqrt{s} = 2\,(14)\,\mathrm{TeV}$. The dynamical model used in this estimate does not include fluctuations of the gluon density at larger $x (\sim 0.05 - 0.1)$, which could increase the suppression.

We emphasize again that inelastic diffraction *per se* is included in the partonic approach of Ref. [2] through the closure of partonic states. The effect discussed in this section is specifically related to correlations between the fluctuations of the parton densities and the soft–interaction strength; in the limit of zero correlations (independent fluctuations) we recover the mean–field result described above [10].

4 Black–disk regime in hard spectator interactions

Substantial changes in the mechanism of diffractive scattering are brought about by the onset of the BDR in hard interactions at LHC energies, where even highly virtual partons ($k^2 \sim$ few GeV^2) with $x \gtrsim 10^{-2}$ experience "black" interactions with the small–x gluons in the other proton. This new effect modifies the amplitude of central exclusive diffraction in several ways: (a) absorption of the "parent" partons of the gluons attached to the high–mass system; (b) absorption of the hard gluons attached to the high–mass system; (c) absorption due to local interactions

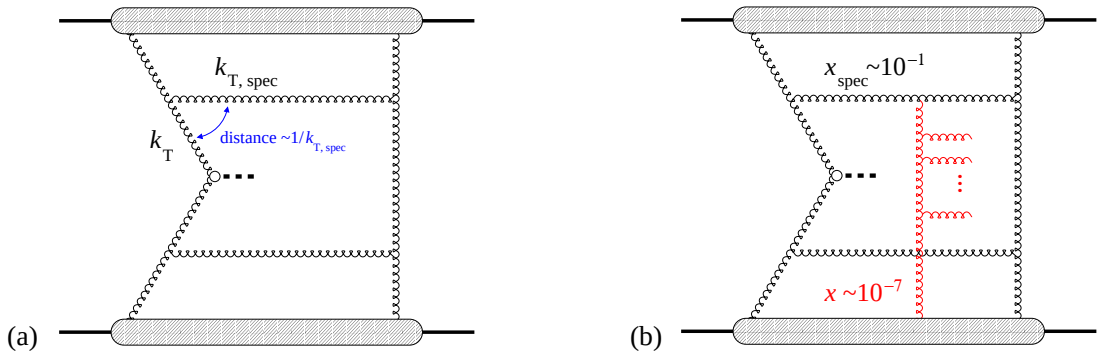

Fig. 3: (a) QCD evolution–induced correlation between hard partons. The transverse distance between the active parton and the spectator is $\sim 1/k_{T,\,\mathrm{spec}}$. (b) Absorptive interaction of the hard spectator with small–x gluons in the other proton.

within the partonic ladder. Such absorptive hard interactions cause additional suppression of diffractive scattering, not included in the traditional soft–interaction RGS probability [2]. Because of the generic nature of "black" interactions, we can estimate this effect by a certain modification of the mean–field picture in the impact parameter representation. Here we focus on mechanism (a) and show that it causes substantial suppression; the other mechanisms may result in further suppression.

According to Ref. [11] (and references therein) the dominant contribution to the hard amplitude of Higgs production at the LHC ($M_H = 100\,\mathrm{GeV}, x_{1,2} \sim 10^{-2}$) originates from gluons with transverse momenta of the order $k_T \sim 2\,\mathrm{GeV}$. Such gluons are typically generated by DGLAP evolution starting from the initial scale, Q_0^2, in which spectator partons, mostly gluons, are emitted (see Fig.3a). In the leading–log approximation $Q_0 \ll k_{T,\,\mathrm{spec}} \ll k_T$, and thus the transverse distance between the active and spectator parton is $\sim 1/k_{T,\,\mathrm{spec}} \ll R_{\mathrm{proton}}$, amounting to short–range correlations between partons. If the interactions of the spectator parton with the small–x gluons in the other proton become significant (see Fig.3b), the basic assumption of the mean–field approximation — that the spectator interactions are independent of the hard process — is violated, and the interactions of that parton need to be treated separately. Indeed, studies within the QCD dipole model show that at the LHC energy spectator gluons with $k_{T,\,\mathrm{spec}} \sim 1\,\mathrm{GeV}$ and $x_{\mathrm{spec}} \sim 10^{-1}$ "see" gluons with momentum fractions $x \sim 10^{-7}$ in the other proton, and are absorbed with near–unit probability if their impact parameters with the other proton are less than $\sim 1\,\mathrm{fm}$ [2].[2] For pp impact parameters $b < 1\,\mathrm{fm}$ about 90% of the strength in $P_{\mathrm{hard}}(b)$ comes from parton–proton impact parameters $\rho_{1,2} < 1\,\mathrm{fm}$ (*cf.* Fig. 1a), so that this effect practically eliminates diffraction at $b < 1\,\mathrm{fm}$. Since $b < 1\,\mathrm{fm}$ accounts for 2/3 of the cross section (see Fig. 1b), and the remaining contributions at $b > 1\,\mathrm{fm}$ are also reduced by absorption, we estimate that absorptive interactions of hard spectators in the BDR reduce the RGS probability at LHC to about 20% of its mean–field value. Much less suppression is expected

[2]The cross section of "gluonic" (88) dipoles is larger than that of the quark–antiquark ($\bar{3}3$) dipoles in $\gamma^* p$ scattering [12] by a factor $9/4$. A summary plot of the profile function for gluon–proton scattering is given in Fig. 13 of Ref. [7] (right y–axis). Note that $\Gamma^{\mathrm{gluon-proton}} = 0.5$ already corresponds to a significant absorption probability of $1 - |1 - \Gamma^{\mathrm{gluon-proton}}|^2 = 0.75$.

at the Tevatron energy, where hard spectator interactions only marginally reach the BDR.

In the above argument one must also allow for the possibility of trajectories with no gluon emission, which correspond to the Sudakov form factor–suppressed $\delta(1-x)$–term in the evolution kernel. While such trajectories are not affected by absorption, their contributions are small both because of the Sudakov suppression, and because they effectively probe the gluon density at a low scale, $Q_0^2 \sim 1\,\mathrm{GeV}^2$, where evolution–induced correlations between partons can be neglected. We estimate that the contribution of such trajectories to the cross section is suppressed compared to those with emissions by a factor $R = \left[S_G^2\, G(x,Q^2)/G(x,Q_0^2)\right]^2 \sim 1/10$, where $S_G^2 = \exp[-(3\alpha_s/\pi)\ln^2(Q^2/Q_0^2)]$ is the square of the Sudakov form factor, and $Q^2 \sim 4\,\mathrm{GeV}^2$. Their net contribution is thus comparable to that of the trajectories with emissions, because the latter are strongly suppressed by the absorption effect described above. Combining the two, we obtain an overall suppression by a factor of the order ~ 0.3. More accurate estimates would need to take into account fluctuations in the number of emissions; in particular, trajectories on which only one of the partons did not emit gluons are suppressed only by $\sqrt{R}$ and may make significant contributions.

The absorptive hard spectator interactions described here "push" diffractive pp scattering to even larger impact parameters than would be allowed by the soft spectator interactions included in the mean–field RGS probability, Eq. (1) (except for the Sudakov–suppressed contribution). One interesting consequence of this is that it makes the uncertainty in the mean–field prediction arising from $\Gamma(0) \neq 1$ (see Sec. 2) largely irrelevant, as the region of small impact parameters is now practically eliminated by the hard spectator interactions. Another consequence is that the final–state proton transverse momentum distribution is shifted to to smaller values; this could in principle be observed in p_T–dependent measurements of diffraction. We note that the estimates of hard spectator interactions reported here are based on the assumption that DGLAP evolution reasonably well describes the gluon density down to $x \sim 10^{-6}$; the details (but not the basic picture) may change if small–x resummation corrections were to significantly modify the gluon density at such values of x (see Ref. [13] and references therein).

5 Summary

The approach to the BDR in the interaction of hard spectator partons, caused by the increase of the gluon density at small x, has profound implications for central exclusive diffraction at LHC: *No saturation without disintegration!* The RGS probability is likely to be much smaller (by a factor of $\sim 1/3$ or less) than predicted by the mean–field approximation or corresponding models which neglect correlations of partons in the transverse plane. Diffractive scattering is relegated either to very large impact parameters ($b > 1\,\mathrm{fm}$) or to Sudakov–suppressed trajectories without gluon radiation. We estimate that the overall RGS probability at LHC is $S^2 < 0.01$. Extrapolation of the Tevatron results may be misleading because interactions of hard spectators are generally far from "black" at that energy. The new effects described here call for detailed MC–based studies of possible histories of the hard scattering process and their associated spectator interactions.

References

[1] Khoze, V. A. and Martin, A. D. and Ryskin, M. G., Eur. Phys. J. **C55**, 363 (2008).

[2] Frankfurt, L. and Hyde, C. E. and Strikman, M. and Weiss, C., Phys. Rev. **D75**, 054009 (2007).

[3] Gotsman, E. and Levin, E. and Maor, U. and Miller, J. S. (2008).

[4] Binkley, M. and others, Phys. Rev. Lett. **48**, 73 (1982).

[5] Aktas, A. and others, Eur. Phys. J. **C46**, 585 (2006).

[6] Chekanov, S. and others, Nucl. Phys. **B695**, 3 (2004).

[7] Frankfurt, L. and Strikman, M. and Weiss, C., Ann. Rev. Nucl. Part. Sci. **55**, 403 (2005).

[8] Frankfurt, L. and Strikman, M. and Zhalov, M., Phys. Lett. **B616**, 59 (2005).

[9] Luna, E. G. S. and Khoze, V. A. and Martin, A. D. and Ryskin, M. G. (2008).

[10] Frankfurt, L. and Strikman, M. and Treleani, D. and Weiss, C., Phys. Rev. Lett. **101**, 202003 (2008).

[11] Khoze, Valery A. and Martin, Alan D. and Ryskin, M. G., Eur. Phys. J. **C14**, 525 (2000).

[12] Rogers, T. and Guzey, V. and Strikman, M. and Zu, X., Phys. Rev. **D69**, 074011 (2004).

[13] Ciafaloni, M. and Colferai, D. and Salam, G. P. and Stasto, A. M., JHEP **08**, 046 (2007).

Two-photon and photon-hadron interactions at the LHC

Joakim Nystrand
Department of Physics and Technology,
University of Bergen, Bergen, Norway

Abstract
The possibilities to extend the results from HERA by using the strong flux of equivalent photons associated with the proton and nuclear beams at the LHC are reviewed.

1 Introduction

Much of the focus of this workshop has been on how the parton distribution functions determined at HERA will be an integral part of the interpretation of the results from the LHC. We wish to point out, however, that the LHC offers an opportunity to directly extend the results from HERA on photoproduction, by using the strong flux of photons associated with the proton and nuclear beams.

Charged particles moving with relativistic velocities are surrounded by a cloud of virtual photons. For point particles, the energy of the virtual photons can in principle be as high as the energy of the charged particle itself. For extended objects, like protons and nuclei, the maximum photon energy is highly suppressed for energies above a fraction of the charged particle's energy because of the form factor. At the extreme energies of the LHC, this is not a serious limitation, however, and it will be possible to probe photon-induced interactions at energies much higher than at HERA both in proton-proton and nucleus-nucleus collisions. Photon-induced interactions can be studied in ultra-peripheral collisions where the impact parameter is larger than the sum of the projectile radii and no hadronic interactions occur. This is illustrated in Fig. 1.

The photon-induced interactions can be divided into two categories: exclusive interactions, where a certain final state is produced, while both beam particles remain intact; and inclusive interactions, where a certain final state is produced but where the photon target breaks up and additional particles may be produced. Exclusive interactions include two-photon and photon-Pomeron interactions. Inclusive interactions include, but are not limited to, direct photon-parton interactions. These two types of processes will be discussed in the following two sections. For two longer reviews of photon interactions at hadron colliders, see [1, 2].

2 Exclusive Production

The study of photon-induced interactions at hadron colliders has so far focused mainly on exclusive production, where both protons or nuclei remain intact. The cross sections for exclusive production are normally lower than for the corresponding inclusive reaction channel. The advantage is, however, that the exclusive events have a much clearer event topology, with rapidity gaps on both sides of the produced state, which makes it easy to separate them from background and hadronic processes.

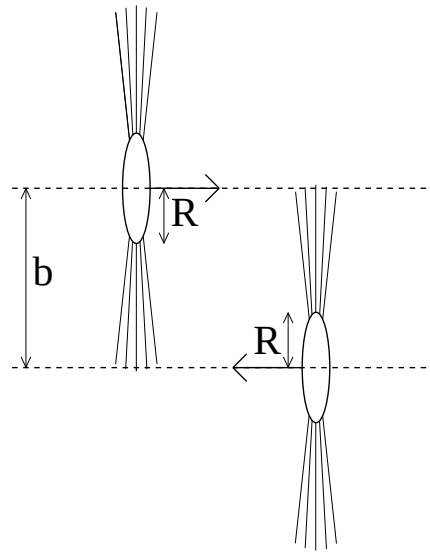

Fig. 1: An ultra-peripheral collision with impact parameter b much larger than the sum of the projectile radii, R. The solid lines indicate the Lorentz contracted electric fields.

The early theoretical studies of electromagnetic processes at hadron colliders were concentrated on two-photon interactions. It was later discovered that exclusive production of vector mesons through photon-Pomeron fusion had much larger cross sections [3]. Exclusive photoproduction of vector mesons and two-photon interactions will be discussed in the following two subsections. One should note, however, that exclusive production of vector mesons can occur also through the hadronic process Odderon-Pomeron fusion; this possibility has attracted an increased interest recently [4].

2.1 Photon-hadron interactions

According to the Vector Meson Dominance model, the bulk of the photon-hadron cross section can be explained by the photon first fluctuating to a vector meson, with the same quantum numbers as the photon. While in the vector meson state, the photon will interact hadronically with the target. This interaction can be elastic or inelastic. In elastic scattering enough momentum can be transferred for the virtual vector meson to become real; this is the basis for exclusive photoproduction of vector mesons.

The cross section for exclusive production of the lightest vector meson, ρ^0, is very high in collisions with heavy ions, such as Au or Pb, reaching 50% of the total inelastic hadronic cross sections at the energies of the LHC [3]. At the Relativistic Heavy-Ion Collider (RHIC), the measured exclusive ρ^0 cross section in Au+Au collisions at $\sqrt{s_{NN}} = 200$ GeV is 530$\pm$19(stat)$\pm$57(syst), roughly 10% of the total inelastic cross section [5].

The momentum transfer from each projectile is limited by the form factor, and the vector meson production is therefore typically centered around mid-rapidity; the exact shape of the

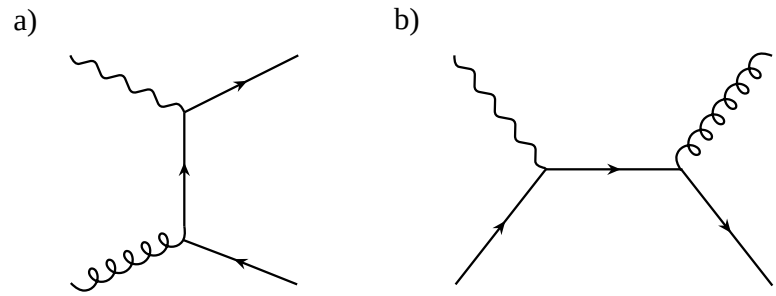

Fig. 2: Feynman diagrams for direct photoproduction of jets in ultra-peripheral collisions through photon-gluon fusion, $\gamma + g \rightarrow q + \overline{q}$, and the QCD Compton process, $\gamma + q \rightarrow g + q$. Direct photoproduction of heavy quarks is described by the diagram in a).

rapidity distribution varies somewhat with collision energy and vector meson mass.

Exclusive vector mesons have been studied by the STAR [5] and PHENIX [6] collaborations at RHIC, and by the CDF collaboration at the Tevatron [7].

The STAR collaboration at RHIC has studied exclusive photoproduction of ρ^0 mesons in Au+Au collisions at $\sqrt{s_{NN}} = 200$ GeV. The energy range probed by STAR, $7.6 \leq W_{\gamma p} \leq 20.6$ GeV, includes energies larger than have been studied in fixed target experiments with lepton beams on heavy nuclear targets. The measured cross sections are found to be in good agreement with models that include a Weizsäcker-Williams photon spectrum and Glauber-like models for the photonuclear cross section.

The PHENIX collaboration has studied exclusive production of J/Ψ in Au+Au collisions in coincidence with Coulomb break-up of at least one of the nuclei. Coulomb break-up means that an additional, soft photon is exchanged in the interaction, leading to the break up of the "target" nucleus. The J/Ψs have been studied around mid-rapidity in the e^+e^- decay channel.

The CDF collaboration has studied exclusive J/Ψ and Ψ' production in the $\mu^+\mu^-$ decay channel in $p\overline{p}$ collisions at the Tevatron [7]. CDF has also seen hints of Υ mesons.

The outlook for studying exclusive vector meson production at the LHC is promising. The rates are very high. The J/Ψ cross section, for example, increases by about a factor 100 from Au+Au collisions at RHIC to Pb+Pb collisions at the LHC. There are plans to study this reaction channel in both the CMS and ALICE experiments, in pp as well as in PbPb collisions.

2.2 Two-photon interactions

The cross section for two-photon production of lepton pairs scales as Z^4, where Z is the charge of the projectile. The total cross section for producing an e^+e^-–pair is several orders of magnitude larger than the total hadronic cross section in heavy-ion interactions at RHIC and the LHC. Most of these electrons/positrons are produced with very low invariant masses, however, and are emitted with small angles relative to the beam axis.

The pairs can be produced as free pairs or as bound-free pairs, where the electron (or the positron with anti-proton beams) binds to the beam particle. When a bound-free pair is produced, the rigidity of the capturing beam nucleus or proton changes and it is lost from the beam. This is the leading source of beam loss at high energy heavy-ion colliders such as RHIC and the LHC. Moreover, the projectile that has captured the electron will hit the wall of the beam pipe at a well-defined spot downstream from the interaction point. At the LHC, the resulting heat deposition could induce quenching of the superconducting magnets. The impact of copper ions with a captured electron about 140 m downstream from the interaction point has recently been observed at RHIC [8]. Bound-free pair production where the positron binds to the anti-proton has been used to observe anti-hydrogen at the Tevatron [9].

Free pair production has been studied in fixed target heavy-ion interactions, in Au+Au collisions at RHIC [6, 10], and, recently, by the CDF Collaboration in $p\overline{p}$ collisions at the Tevatron [11]. The results have generally been found to be in good agreement with lowest order perturbation theory. The limit on invariant mass used by the CDF Collaboration (> 10 GeV) is unfortunate, however, since it falls almost on top of the mass of the $\Upsilon(2S)$ meson. The yield from heavy vector mesons produced by photon-Pomeron fusion and decaying to di-lepton pairs is comparable or larger than the one from two-photon production over the relevant invariant mass range.

Two-photon production of mesons, e.g. at e^+e^- colliders, is a useful tool in meson spectroscopy. In principle, such studies could be performed also at hadron colliders, but backgrounds from coherent photonuclear interactions pose a problem. A two-photon "standard candle" like the $f_2(1270)$ is likely to be obscured by continuum production of $\pi^+\pi^-$ through photon-Pomeron fusion. No results on two-photon production of mesons at hadron colliders have been reported.

Finally, it has been suggested to search for the Higgs boson in two-photon interactions at the LHC. Despite the enhancement by a factor Z^4 in heavy-ion collisions, the cross section for a standard model Higgs with mass around 100 GeV appears too low, only about 10 pb in Pb+Pb collisions, corresponding to an event rate of only 10^{-9} s^{-1} [12]. With Ca beams the situation is a bit better because of the higher luminosity, but the event rate is not more than about 10^{-6} s^{-1}.

3 Inclusive Production

The bulk of the photonuclear particle production stems from events where the photon first fluctuates to a hadronic state, which then interact with the target nucleus or proton. Since the energy of the photon typically is much lower than that of the beam particle, these events resemble fixed target interactions. The photon can, however, also interact as a "bare" photon with one of the partons in the target nucleus or proton. The focus of this section will be on photon-parton interactions in nucleus-nucleus collisions. Direct processes that can be calculated using perturbative QCD include photoproduction of jets and heavy quarks. None of these processes have been investigated at RHIC or the Tevatron, but the prospects should be good at the LHC, particularly because of the strong increase in the cross sections with energy.

3.1 Photoproduction of jets

The Feynman diagrams for the two leading-order direct contributions to the jet yield, $\gamma + g \rightarrow q + \overline{q}$ and $\gamma + q \rightarrow g + g$, are shown in Fig. 2. The corresponding differential cross section can be written as a convolution of the equivalent photon flux with the parton distribution functions and the partonic cross sections

$$s^2 \frac{d^2\sigma}{dtdu} = 2 \int_{k_{min}}^{\infty} n(k) dk \int_{x_{2_{min}}}^{1} \frac{dx_2}{x_2} \left[\sum_{i=q,\overline{q},g} F_i(x_2, Q^2) s'^2 \frac{d^2\sigma_{\gamma i}}{dt'du'} \right] . \quad (1)$$

Here, $n(k)$ is the number of equivalent photons with energy k. $F_i(x_2, Q^2)$ is the parton density for parton i at scale Q^2 and x_2 is the Bjorken-x of the parton in the target nucleus. The unprimed Mandelstam variables, s, t, u, refer to the hadronic system, whereas the primed variables, s', t', u', refer to the partonic system. The minimum x_2 is given by $x_{2_{min}} = -u/(s+t)$ and k_{min} is the minimum photon energy needed to produce the final state.

The cross section for photonuclear jet production is high at the LHC. The cross section to produce a jet with $p_T > 50$ GeV/c and rapidity $|y| < 1$ in Pb+Pb collisions is for example larger than 1 μb [13]. As can be seen from Eq. 1, the jet cross section is sensitive to the nuclear parton distributions. Calculations show that nuclear shadowing (and anti-shadowing) affects the yield by up to 10%, while the differences between individual parameterizations of shadowing differ by a few percent. It has also been noted that there is a significant contribution to the jet yield from resolved interactions, where a parton in the target interacts with a parton in the resolved photon; the resolved contribution is expected to be the leading production mechanism in certain regions of phase space, particularly for low $p_T < 50$ GeV/c [13].

3.2 Photoproduction of heavy quarks

For the production of heavy quarks, only the diagram in Fig. 2 a) contributes. The production cross section is thus a less ambiguous probe of the proton or nuclear gluon distribution. The cross sections are very high at the LHC, as can be seen in Table 3.2 (from [14] with updated numbers from [1]). Calculations are shown for two different parameterizations of the nuclear gluon shadowing and without shadowing. Shadowing has an enhanced effect on the cross section for $c\overline{c}$ pairs, where lower values of x are probed. In Pb+Pb collisions, the two parameterizations correspond to reductions by 16% and 32%, respectively. For $b\overline{b}$ pairs, the effect of shadowing is smaller, 4% and 10% in the two cases.

The resolved contribution is smaller than for jet production. It is largest for $c\overline{c}$ pairs, but does not contribute more than 15-20 % to the total cross section.

The cross section for producing pairs of top quarks is too low for observation with the design LHC Pb+Pb luminosity. It might be possible with lighter ions or with protons.

4 Summary

The feasibility of studying at least a few reaction channels in ultra-peripheral collisions at collider energies has been shown by experiments at RHIC and the Tevatron. The measured cross sections have been found to be in general agreement with expectations, but the statistics have so far been

	flavor	σ [mb] No shadowing	σ [mb] EKS98	σ [mb] FGS
Ar+Ar	$c\overline{c}$	16.3	14.3	12.3
	$b\overline{b}$	0.073	0.070	0.066
Pb+Pb	$c\overline{c}$	1250	1050	850
	$b\overline{b}$	4.9	4.7	4.4

Table 1: Cross sections for $q\overline{q}$ photoproduction through direct photon-gluon fusion in Ar+Ar and Pb+Pb interactions at the LHC. The numbers in column 3 and 4 include nuclear gluon shadowing from the parameterizations by Eskola, Kolhinen, and Ruuskanen (EKS98) and Frankfurt, Guzey, and Strikman (FGS), respectively.

low. There are plans to study photon-induced processes in at least 3 of the 4 LHC experiments, although it is not the main focus of any of them. There is an overwhelming number of reaction channels that can be investigated at the LHC in "ordinary" hadronic interactions. Including photon-induced processes leads to an even greater number. It seems unlikely that all these will be investigated during the life-time of the LHC. It will be up to the experiments to judge which are the most interesting and to which the necessary trigger resources and bandwidths should be allocated. In this talk, we have tried to argue that at least some photon-induced processes should meet the criteria for feasibility and interest.

References

[1] A.J. Baltz et al., Phys. Rep. **458**, 1 (2008).

[2] C.A. Bertulani, S.R. Klein, J. Nystrand, Ann. Rev. Nucl. Part. Sci. **55**, 271 (2005).

[3] S.R. Klein, J. Nystrand, Phys. Rev. **C60**, 014903 (1999).

[4] A. Bzdak, L. Motyka, L. Szymanowski, J.R. Cuddel, Phys. Rev. **D75**, 094023 (2007).

[5] STAR Coll., B.I. Abelev et al., Phys. Rev. **C77**, 034910 (2008).

[6] PHENIX Coll., D. d'Enterria et al., *Coherent photoproduction of J/Psi and high-mass e+e- pairs in ultra-peripheral Au+Au collisions at sqrt(sNN) = 200 GeV* (unpublished). Nucl-ex/0601001.

[7] J. Pinfold, *presentation at this workshop*.

[8] R. Bruce et al., Phys. Rev. Lett. **99**, 144801 (2007).

[9] G. Blanford et al., Phys. Rev. Lett. **80**, 3037 (1998).

[10] STAR Coll., J. Adams et al., Phys. Rev. **C70**, 031902 (2004).

[11] CDF Coll., A. Abulencia et al., Phys. Rev. Lett. **98**, 112001 (2007).

[12] CMS Coll., G. Baur et al., Eur. Phys. J. **C32**, s69 (2003).

[13] M. Strikman, R. Vogt, S. White, Phys. Rev. Lett. **96**, 082001 (2006);
R. Vogt, *Jet Photoproduction in Peripheral Heavy-Ion Collisions* (unpublished). Hep-ph/0407298.

[14] S.R. Klein, J. Nystrand, R. Vogt, Phys. Rev. **C66**, 044906 (2002).

Searching for the Odderon at HERA and the LHC

Carlo Ewerz
Institut für Theoretische Physik, Universität Heidelberg
Philosophenweg 16, D-69120 Heidelberg, Germany

Abstract
We review the present status of the odderon, focusing in particular on searches at HERA and the prospects for finding the odderon in exclusive processes at the LHC.

1 The odderon

The odderon is the negative charge parity ($C=-1$) partner of the well-known pomeron. Therefore, it is the t-channel exchange that gives rise to the difference between a particle-particle scattering cross section and the corresponding particle-antiparticle cross section at high center-of-mass energy $\sqrt{s}$. The concept of the odderon was introduced and its existence conjectured in [1] in the context of Regge theory. It was subsequently realized that in QCD a colorless exchange in the t-channel with negative C-parity can be constructed from three gluons in a symmetric color state. In recent years considerable progress in understanding the odderon has been made in particular in perturbative QCD. The nonperturbative odderon, on the other hand, remains poorly understood.

In perturbative QCD the odderon is described by the Bartels-Kwieciński-Praszałowicz (BKP) equation [2] which resums the leading logarithms of $\sqrt{s}$, corresponding to the pairwise interaction of the three gluons exchanged in the t-channel. One finds that also compound states of more than three gluons with odderon quantum numbers can be constructed, which are also described by the BKP equation. The BKP equation exhibits interesting mathematical properties like conformal invariance in impact parameter space and holomorphic separability [3], and even turns out to be an integrable system [4]. Two explicit solutions to the BKP equation have been found, one with intercept $\alpha_{\mathbb{O}}=1$ [5] and one with a slightly smaller intercept [6], giving rise to a high-energy behavior of the cross section $\sim s^{\alpha_{\mathbb{O}}-1}$. The main difference of the two solutions lies in their different coupling to external particles rather than in their intercepts which for all practical purposes can be considered equal.

While the perturbative odderon is at least theoretically rather well understood, our picture of the odderon in the nonperturbative regime is not at all satisfying. The main reason is the lack of experimental data which does not even allow us to test models of nonperturbative odderon exchange. This is in strong contrast to the nonperturbative pomeron which is theoretically equally hard to describe, but for the pomeron a rather clear picture has emerged at least on the phenomenological level from the study of a variety of high energy scattering data.

In the following we discuss some aspects of the odderon which are particularly relevant for HERA and LHC. A detailed review of the odderon and further references can be found in [7].

2 Experimental evidence

It would seem natural to expect that odderon exchange is suppressed relative to pomeron (two-gluon) exchange only by a power of α_s due to the requirement to couple an additional gluon to the external particles. And at moderately low momenta α_s is not too small, such that – given the ubiquitous pomeron – one expects odderon exchange to appear in many processes. Surprisingly, the contrary is true.

So far the only experimental evidence for the odderon has been found in a small difference in the differential cross sections for elastic proton-proton and proton-antiproton scattering at $\sqrt{s} = 53\,\text{GeV}$. Figure 1 shows the data taken at the CERN ISR in the dip region around $t = -1.3\,\text{GeV}^2$. The proton-proton data have a dip-like structure, while the proton-antiproton data

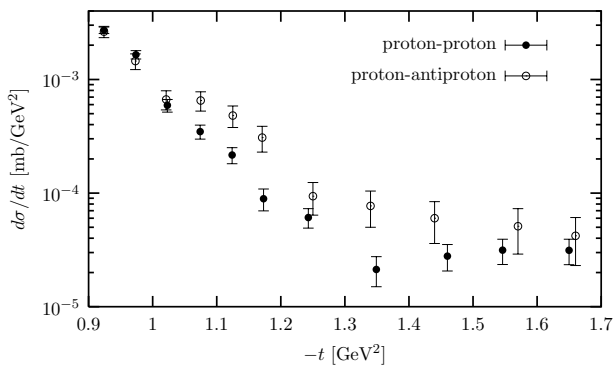

Fig. 1: Differential cross section for elastic pp and $p\bar{p}$ scattering in the dip region for $\sqrt{s} = 53\,\text{GeV}$; data from [8]

only level off at the same $|t|$. This difference between the two data sets can only be explained by invoking an odderon exchange. However, the difference relies on just a few data points with comparatively large error bars.

The data at various energies are well described by models that take into account the various relevant exchanges between the elastically scattering particles [9], [10]. Both of these models involve of the order of twenty parameters that need to be fitted. The structure in the region around $|t| = 1 - 2\,\text{GeV}^2$ is the result of a delicate interference between different contributions to the scattering amplitude including the odderon. Therefore it is rather difficult to extract the odderon contribution unambiguously. In fact it turns out that the two odderon contributions obtained in [9] and [10], respectively, are not fully compatible with each other [11] (see also [7]). In [12] it was shown that assuming a perturbative odderon (three gluon exchange) in the context of the model of [9] requires to choose a very small coupling of the odderon to the proton. This small coupling can be either due to a small relevant value of $\alpha_s \simeq 0.3$ or due to a small average distance of two of the constituent quarks in the proton corresponding to a diquark-like structure.

Unfortunately, $\sqrt{s} = 53\,\text{GeV}$ is the only energy for which data for both reactions are available. The comparison of data taken at different energies rather strongly relies on theoretical models. Given the large number of parameters in these models it is not possible to arrive at firm conclusions about the odderon on the basis of the presently available data.

3 Odderon searches at HERA

The cross section for elastic pp and $p\bar{p}$ scattering is a typical example in which the odderon exchange is only one of many contributions to the scattering amplitude. It was recently realized that the chances for a clean identification of the odderon should be better in exclusive processes in which the odderon is the only exchange (usually besides the well-understood photon) that can give rise to the final state to be studied. This strategy was chosen at HERA.

Searches for the odderon at HERA have concentrated on the exclusive diffractive production of pseudoscalar mesons ($M_{\rm PS}$) as depicted in Figure 2. In addition to that diagram only the exchange of a photon instead of the odderon is possible at high energies. (Similarly also tensor mesons can be produced only by odderon and photon exchange.) This process had been suggested in [13]. The photon exchange contribution is rather well understood and is expected

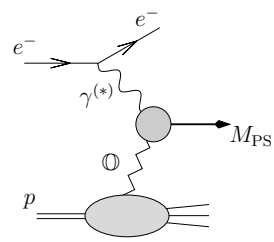

Fig. 2: Diffractive production of a pseudoscalar meson in ep scattering

to have a much steeper t-dependence than the odderon exchange.

The process which has been studied in most detail experimentally is the exclusive diffractive production of a single neutral pion, $\gamma^{(*)}p \to \pi^0 X$. Early theoretical considerations [14] had led to an estimate of the total photoproduction cross section for that process of $\sigma(\gamma p \to \pi^0 X) \simeq 300\,\text{nb}$, with a possible uncertainty of a factor of about two. The experimental search for that process, however, was not successful and resulted in an upper limit of $\sigma(\gamma p \to \pi^0 X) < 49\,\text{nb}$ [15], obviously ruling out the prediction of [14]. The smallness of the cross section is a striking result since of all processes at HERA in which hadrons are diffractively produced this is the one with the largest phase space. Therefore a strong suppression mechanism must be at work here. One possibility is again a potentially small coupling of the odderon to the proton. Further possible causes for the failure of the prediction of [14] were discussed in [16]. The most important among them is probably the suppression of pion production due to approximate chiral symmetry, as has been discussed in detail in [17]. In fact it turns out that the odderon contribution to the amplitude for diffractive single-pion production vanishes exactly in the chiral limit. This suppression had not been taken into account properly in [14].

Also searches for similar processes in which instead of the pion some other pseudoscalar or tensor meson is produced diffractively have been performed, although only on a preliminary basis [18]. Again, no evidence for the odderon was found. However, for these processes the experimental bounds are closer to the theoretical estimates of [14], and hence the situation is less clear.

4 Prospects for the LHC

At the LHC one can in analogy to the ISR try to look for the odderon in elastic pp scattering. The measured differential cross section can be compared to models which are fitted to the differential cross section at lower energies and extrapolated to LHC energies, see for example [19]. Although these models involve a large number of fit parameters and some uncertainty in the extrapolation to a new energy range it is argued in [19] that there is a chance to see evidence of the odderon. Also the spin dependence of elastic scattering is sensitive to the odderon and can be used to search for it, see [20]. In both cases the odderon is again one of several contributions to the scattering amplitude, which makes an unambiguous identification unlikely.

Recent proposals for odderon searches at the LHC (and analogously at the Tevatron) have therefore again focussed on exclusive processes in which the odderon is (except for the photon) the only contribution to the cross section. Here the mere observation of the process can already be sufficient to confirm odderon exchange. The most prominent of these exclusive processes at LHC is the double-diffractive production of a vector meson M_V in pomeron-odderon fusion, that is $p + p \to X + M_V + Y$ with the vector meson separated from the forward hadronic systems X and Y by rapidity gaps, see Figure 3. This process was first proposed and discussed in the

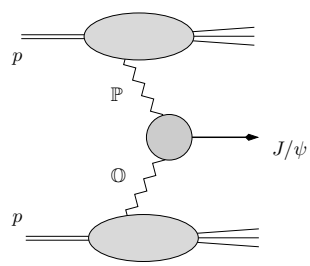

Fig. 3: Pomeron-odderon fusion mechanism for double-diffractive J/ψ production in $p\bar{p}$ scattering

framework of Regge theory in [21]. In particular heavy vector mesons, $M_V = J/\psi, \Upsilon$, are well suited for odderon searches since here the reggeon exchange contribution (in place of the odderon) is suppressed by Zweig's rule. (In the production of ϕ mesons that contribution could still be relevant – especially if the odderon contribution is small.) At the LHC in particular the ALICE detector appears to be best suited for the observation of centrally produced J/ψ or Υ mesons and can in addition identify rapidity gap events [22].

In [23] a detailed study of this process has been performed in perturbation theory. The leading perturbative diagram contains the fusion of two of the three gluons in the odderon with one from the two in the pomeron to the J/ψ or Υ, and an additional ('spectator') gluon exchange between the two protons. There are two important uncertainties in the calculation of this process. One is again the coupling of the odderon to the proton which might be small. The other main uncertainty is the survival probability for the rapidity gaps in the final state. Presently, a full understanding of the gap survival is still lacking. In hadronic collisions the gap survival is very different from ep scattering, and extrapolations from Tevatron energies to the LHC energy contain a considerable uncertainty. Depending on the assumptions about these uncertainties the expected

cross sections $d\sigma/dy|_{y=0}$ at mid-rapidity y for J/ψ production are between 0.3 and 4 nb at the LHC. For the Υ one expects 1.7 – 21 pb. One has to keep in mind that also photon instead of odderon exchange can give rise to the same final state. A possibility to separate the two contributions is to impose a cut on the squared transverse momentum p_T^2 of the vector meson. The photon dominates at small p_T^2 but then falls rapidly towards higher p_T^2. The odderon contribution does not fall so quickly and for the J/ψ dominates above $p_T^2 \simeq 0.3\,\mathrm{GeV}^2$.

It is possible that the negative result of all odderon searches to date is caused by a small coupling of the odderon to the proton. If that coupling is indeed so small also the process just described will not be observable at the LHC. A possibility to find the odderon nevertheless might then be to look for the production of two heavy vector mesons in triple-diffractive events, $p+p \to X + M_V + M_V + Y$ (with the $+$-signs indicating rapidity gaps), as suggested in [7]. This process is shown in Figure 4. For small odderon-proton coupling the right hand diagram can be neglected.

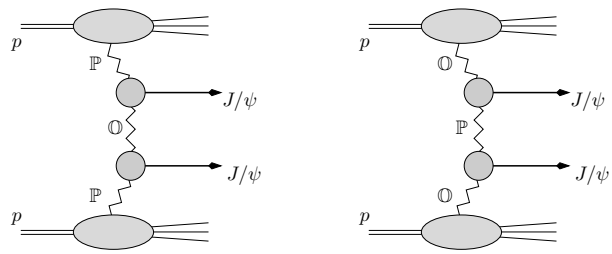

Fig. 4: Diagrams contributing to the triple-diffractive production of two J/ψ mesons in $p\bar{p}$ scattering

In the left hand diagram – which does not involve the $\mathbb{O}p$ coupling – the middle rapidity gap can only be produced by odderon (or photon) exchange and the mere observation of the process could finally establish the existence of the odderon.

5 Summary

The existence of the odderon is a firm prediction of perturbative QCD. But also in the nonperturbative regime we do not have good reasons to expect the absence of the odderon. A possible obstacle in finding it might be its potentially small coupling to the proton. As we have pointed out there are exclusive processes that can give a clear indication of the odderon at the LHC – including some which do not involve the potentially small odderon-proton coupling. If the odderon remains elusive also in these processes we might have to reconsider our picture of QCD at high energies.

References

[1] Lukaszuk, L. and Nicolescu, B., Nuovo Cim. Lett. **8**, 405 (1973);
Joynson, David and Leader, Elliot and Nicolescu, Basarab and Lopez, Cayetano, Nuovo Cim. **A30**, 345 (1975).

[2] Bartels, Jochen, Nucl. Phys. **B175**, 365 (1980);
Kwiecinski, J. and Praszalowicz, M., Phys. Lett. **B94**, 413 (1980).

[3] Lipatov, L. N., Phys. Lett. **B251**, 284 (1990).

[4] Lipatov, L. N. (1993);
Lipatov, L. N., JETP Lett. **59**, 596 (1994);
Faddeev, L. D. and Korchemsky, G. P., Phys. Lett. **B342**, 311 (1995).

[5] Bartels, Jochen and Lipatov, L. N. and Vacca, G. P., Phys. Lett. **B477**, 178 (2000).

[6] Janik, R. A. and Wosiek, J., Phys. Rev. Lett. **82**, 1092 (1999).

[7] Ewerz, Carlo (2003).

[8] Breakstone, A. and others, Phys. Rev. Lett. **54**, 2180 (1985).

[9] Donnachie, A. and Landshoff, P. V., Nucl. Phys. **B267**, 690 (1986).

[10] Gauron, Pierre and Nicolescu, Basarab and Leader, Elliot, Phys. Lett. **B238**, 406 (1990).

[11] Schatz, Volker (2003).

[12] Dosch, Hans Günter and Ewerz, Carlo and Schatz, Volker, Eur. Phys. J. **C24**, 561 (2002).

[13] Schäfer, A. and Mankiewicz, L. and Nachtmann, O. In Proc. of the Workshop *Physics at HERA*, DESY Hamburg 1991, vol. 1, p. 243;
Barakhovsky, V. V. and Zhitnitsky, I. R. and Shelkovenko, A. N., Phys. Lett. **B267**, 532 (1991);
Kilian, W. and Nachtmann, O., Eur. Phys. J. **C5**, 317 (1998).

[14] Berger, E. R. and others, Eur. Phys. J. **C9**, 491 (1999).

[15] Adloff, C. and others, Phys. Lett. **B544**, 35 (2002).

[16] Donnachie, A. and Dosch, H. G. and Nachtmann, O., Eur. Phys. J. **C45**, 771 (2006).

[17] Ewerz, Carlo and Nachtmann, Otto, Eur. Phys. J. **C49**, 685 (2007).

[18] Olsson, J. (2001).

[19] Avila, Regina and Gauron, Pierre and Nicolescu, Basarab, Eur. Phys. J. **C49**, 581 (2007).

[20] Trueman, T. L., Phys. Rev. **D77**, 054005 (2008).

[21] Schäfer, A. and Mankiewicz, L. and Nachtmann, O., Phys. Lett. **B272**, 419 (1991).

[22] Schicker, R. (2008).

[23] Bzdak, A. and Motyka, L. and Szymanowski, L. and Cudell, J. -R., Phys. Rev. **D75**, 094023 (2007).

Forward physics with CMS

Samim Erhan[1], *Salim Cerci*[2], *Monika Grothe*[3], *Jonathan Hollar*[4], *Antonio Vilela Pereira*[5]
on behalf of the CMS collaboration
[1]University of California, Los Angeles, Los Angeles, California, USA
[2]Cukurova University, Adana, Turkey
[3]University of Wisconsin, Madison, Wisconsin, USA
[4]Lawrence Livermore National Laboratory, Livermore, California, USA
[5]Universita di Torino e Sezione dell' INFN, Torino, Italy

Abstract
We describe several example analyses of the CMS forward physics program: A feasibility study for observing W production in single diffractive dissociation, the analysis of exclusive $\mu\mu$ production and the measurement of very low-x parton distributions and search for evidence of BFKL dynamics with forward jets.

1 Introduction

The CMS Experiment has a rich and broad forward physics program with measurements that can be realized from the start of the LHC [1–6]. The CMS detectors in the forward region allow an experimental program to be carried out that reaches beyond the traditional forward gap physics, such as soft and hard single diffraction and double Pomeron exchange physics, and also includes the study of $\gamma\gamma$ and γp interactions, energy and particle flow measurements relevant for understanding multi-parton interactions for tuning of Monte Carlo event generators, jet-gap-jet events to understand the origin of these event topologies, and forward jets and forward Drell-Yan processes at 14 TeV center-of-mass energies. Topics of soft and hard diffraction include but are not limited to:

1. Dependence of the diffractive cross sections on ξ, t and $\mathrm{M_x}$ as fundamental quantities of non-perturbative QCD.
2. Gap survival dynamics and multi-gap event topologies.
3. Production of jets, $W, \mathrm{J}/\psi, \mathrm{b}$ and t quarks, hard photons in hard diffraction.
4. Double Pomeron Exchange events as gluon factory.
5. Central exclusive Higgs boson production.
6. SUSY and other low mass exotics in exclusive processes.
7. Proton light cone studies.

CMS shares its interaction point (IP) with the TOTEM experiment [7]. The two experiments plan [8] to join their resources and use common trigger and data acquisition systems to increase their forward physics potential.

The studies presented in the following assume no event pile-up, i.e. are analyses to be carried out during the low pile-up, start-up phase of the LHC. In addition, CMS is studying a proposal to install tracking and time-of-flight detectors at 420 m from the IP [9], which has the

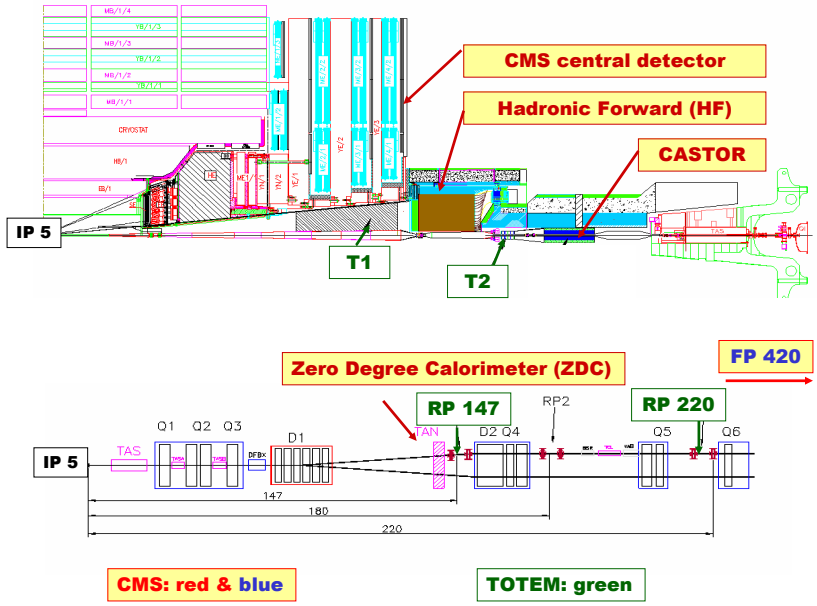

Fig. 1: Layout of the forward detectors around the CMS interaction point.

potential of adding discovery physics, notably central exclusive Higgs production, to the forward physics program of CMS.

For space limitations, in this paper, we describe only three processes as examples of the CMS forward physics program. After a brief description of the forward detector instrumentation around the CMS IP, section III covers a feasibility study on observing W production in single diffractive dissociation. The analysis of exclusive $\mu\mu$ production is discussed in Section IV and the possibility of measuring very low-x parton distributions and of looking for evidence of BFKL signatures with forward jets is described in Section V.

2 Forward detectors around the CMS interaction point

Forward physics at the LHC covers a wide range of diverse physics subjects that have in common that particles produced at small polar angles, θ, and hence large values of rapidity provide a defining characteristic. At the Large-Hadron-Collider (LHC), where proton-proton collisions occur at center-of-mass energies of 14 TeV, the maximal possible rapidity is $y_{max} = \ln \frac{\sqrt{s}}{m_\pi} \sim 11.5$. The central components of CMS are optimized for efficient detection of processes with large polar angles and hence high transverse momentum, p_T. They extend down to about $|\theta| = 1^\circ$ from the beam axis or $|\eta| = 5$, where $\eta = -\ln[\tan(\theta/2)]$ is the pseudorapidity. In the forward region, the central CMS components are complemented by several CMS [10] and TOTEM subdetectors with coverage beyond $|\eta| = 5$, see figure 1. TOTEM is an approved experiment at the LHC for precision measurements of the pp elastic and total cross sections. The combined CMS and TOTEM

apparatus comprises two suites of calorimeters with tracking detectors in front plus near-beam proton taggers. The CMS Hadron Forward (HF) calorimeter with the TOTEM telescope T1 in front covers the region $3 < |\eta| < 5$, the CMS CASTOR calorimeter with the TOTEM telescope T2 in front covers $5.2 < |\eta| < 6.6$. The CMS ZDC calorimeters are installed at the end of the straight LHC beam-line section, at a distance of ± 140 m from the IP. Near-beam proton taggers will be installed by TOTEM at ± 147 m and ± 220 m from the IP. The kinematic coverage of the combined CMS and TOTEM apparatus is unprecedented at a hadron collider. The CMS and TOTEM collaborations have described the considerable physics potential of joint data taking in a report to the LHCC [8]. Further near-beam proton taggers in combination with very fast timing detectors to be installed at ± 420 m from the IP (FP420) are in the proposal stage in CMS. FP420 would give access to possible discovery processes in forward physics at the LHC [9].

2.1 The CMS forward calorimeters HF, CASTOR, ZDC

The forward part of the hadron calorimeter, HF, is located 11.2 m from the interaction point. It consists of steel absorbers and embedded radiation hard quartz fibers, which provide a fast collection of Cherenkov light. Each HF module is constructed of 18 wedges in a nonprojective geometry with the quartz fibers running parallel to the beam axis along the length of the iron absorbers. Long (1.65 m) and short (1.43 m) quartz fibers are placed alternately with a separation of 5 mm. These fibers are bundled at the back of the detector and are read out separately with phototubes.

The CASTOR calorimeters are octagonal cylinders located at ~ 14 m from the IP. They are sampling calorimeters with tungsten plates as absorbers and fused silica quartz plates as active medium. The plates are inclined by 45° with respect to the beam axis. Particles passing through the quartz emit Cherenkov photons which are transmitted to photomultiplier tubes through aircore lightguides. The electromagnetic section is 22 radiation lengths X_0 deep with 2 tungsten-quartz sandwiches, the hadronic section consists of 12 tungsten-quartz sandwiches. The total depth is 10.3 interaction lengths λ_l. The calorimeters are read out segmented azimuthally in 16 segments and logitudinally in 14 segments. They do not have any segmentation in η. The CASTOR coverage of $5.2 < |\eta| < 6.6$ closes hermetically the CMS calorimetric pseudorapidity range over 13 units. Currently, funding is available only for a CASTOR calorimeter on one side of the IP. Installation is foreseen for 2009.

The CMS Zero Degree Calorimeters, ZDC, are located inside the TAN absorbers at the ends of the straight section of the LHC beamline, between the LHC beampipes, at ± 140 m distance on each side of the IP. They are very radiation-hard sampling calorimeters with tungsten plates as absorbers and as active medium quartz fibers read out via aircore light guides and photomultiplier tubes. The electromagnetic part, $19X_0$ deep, is segmented into 5 units horizontally, the hadronic part into 4 units in depth. The total depth is 6.5 λ_l. The ZDC calorimeters have 100% acceptance for neutral particles with $|\eta| > 8.4$ and can measure 50 GeV photons with an energy resolution of about 10%. The ZDC calorimeters are already installed and will be operational in 2009.

2.2 The TOTEM T1 and T2 telescopes

The TOTEM T1 telescope consists of two arms symmetrically installed around the CMS IP in the endcaps of the CMS magnet, right in front of the CMS HF calorimeters and with η coverage similar to HF. Each arm consists of 5 planes of Cathod Strip Chambers (CSC) which measure 3 projections per plane, resulting in a spatial resolution of 0.36 mm in the radial and 0.62 mm in the azimuthal coordinate in test beam measurements. The two arms of the TOTEM T2 telescope are mounted right in front of the CASTOR calorimeters, with similar η coverage. Each arm consists of 10 planes of 20 semi-circular modules of Gas Electron Multipliers (GEMs). The detector read-out is organized in strips and pads, a resolution of 115 μm for the radial coordinate and of 16 μrad in azimuthal angle were reached in prototype test beam measurements. A more detailed description can be found in [11].

2.3 Near-beam proton taggers

The LHC beamline with its magnets is essentially a spectrometer in which protons slightly off the beam momentum are bent sufficiently to be detectable by means of detectors inserted into the beam-pipe. At high luminosity at the LHC, proton tagging is the only means of detecting diffractive and γ mediated processes because areas of low or no hadronic activity in the detector are filled in by particles from overlaid pile-up events.

The TOTEM proton taggers at ± 220 m at nominal LHC optics have acceptance for scattered protons from the IP for $0.02 < \xi < 0.2$. Smaller values of ξ, $0.002 < \xi < 0.02$, can be achieved with proton taggers at ± 420 m. The FP420 proposal [9] foresees employing 3-D Silicon, an extremely radiation hard novel Silicon technology, for the proton taggers, and additional fast timing Cherenkov detectors for the rejection of protons from pile-up events. The proposal is currently under consideration in CMS. If approved, installation could proceed in 2010, after the LHC start-up.

Forward proton tagging capabilities enhance the physics potential of CMS. They would render possible a precise measurement of the mass and quantum numbers of the Higgs boson should it be discovered by traditional searches. They also augment the CMS discovery reach for Higgs production in the minimal supersymmetric extension (MSSM) of the Standard Model (SM) and for physics beyond the SM in γp and $\gamma\gamma$ interactions. The proposed FP420 detectors and their physics potential are discussed in [12].

3 Observation of single-diffractive W production with CMS: a feasibility study

The single-diffractive (SD) reaction $pp \to Xp$, where X includes a W boson (Fig. 2) is studied to demonstrate the feasibility of observing SD W production at CMS given an integrated effective luminosity for single interactions of 100 pb^{-1}. Only $W \to \mu\nu$ decay mode is considered in this analysis [2].

The analysis relies on the extended forward coverage of the CMS forward calorimeters, that cover the pseudo-rapidity range of $3 < |\eta| < 5$. Additional coverage at $-6.6 < \eta < -5.2$ is assumed by means of the CASTOR calorimeter.

Single diffractive W production was simulated by using the POMWIG generator [13], version v2.0 beta. For the diffractive PDFs and the Pomeron flux, the result of the NLO H1 2006

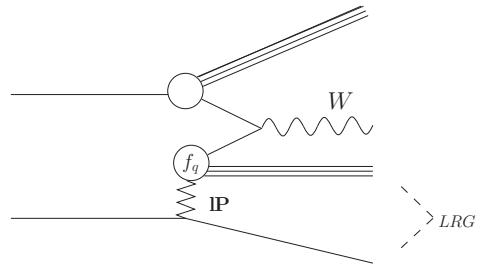

Fig. 2: Sketch of the single-diffractive reaction $pp \to Xp$ in which X includes a W boson. The symbol $I\!P$ indicates the exchange with the vacuum quantum numbers (Pomeron). The large rapidity gap (LRG) is also shown.

fit B [14] was used. A rapidity gap survival probability of 0.05, as predicted in Ref. [15], is assumed. For non-diffractive W production, the PYTHIA generator [16] was used. With the assumed numbers for the cross sections, the ratio of diffractive to inclusive yields is around 0.3%.

3.1 Event Selection and Observation of SD W Production

3.1.1 $W \to \mu\nu$ selection

The selection of the events with a candidate W decaying to $\mu\nu$ is the same as that used in Ref. [17]. Events with a candidate muon in the pseudo-rapidity range $|\eta| > 2.0$ and transverse momentum $p_T < 25$ GeV were rejected, as were events with at least two muons with $p_T > 20$ GeV. Muon isolation was imposed by requiring $\sum p_T < 3$ GeV in a cone with $\Delta R < 0.3$. The transverse mass was required to be $M_T > 50$ GeV. The contribution from top events containing muons was reduced by rejecting events with more than 3 jets with $E_T > 40$ GeV (selected with a cone algorithm with radius of 0.5) and requiring that the acoplanarity ($\zeta = \pi - \Delta\phi$) between the muon and the direction associated to $E_T^{\rm miss}$ be less than 1 rad. Approximately 2,400 SD W events and 600,000 non-diffractive W events per 100 pb^{-1} are expected to pass these cuts.

3.1.2 Diffractive selection and Evidence for SD W Production

Diffractive events have, on average, lower multiplicity both in the central region (lower underlying event activity) and in the hemisphere that contains the scattered proton, the so-called "gap side", than non-diffractive events.

The gap side was selected as that with lower energy sum in the HF. A cut was then placed on the multiplicity of tracks with $p_T > 900$ MeV and $|\eta| < 2$. For the events passing this cut, multiplicity distributions in the HF and CASTOR calorimeters in the gap side were studied, from which a diffractive sample can be extracted.

Figure 3 shows the HF tower multiplicity vs the CASTOR ϕ sector multiplicity for events with central track multiplicity $N_{\rm track} \leq 5$. Since CASTOR will be installed at first on the negative side of the interaction point, only events with the gap on that side (as determined with the procedure discussed above) were considered. The CMS software chain available for this study did not include simulation/reconstruction code for CASTOR; therefore, the multiplicity of generated hadrons with energy above a 10 GeV threshold in each of the CASTOR azimuthal

sectors was used.

The top left and top right plots show the distributions expected for the diffractive W events with generated gap in the positive and negative Z direction, respectively. The few events in the top left plot are those for which the gap-side determination was incorrect. The non-diffractive W events have on average higher multiplicities, as shown in the bottom left plot. Finally, the bottom right plot shows the sum of the POMWIG and PYTHIA distributions – this is the type of distribution expected from the data.

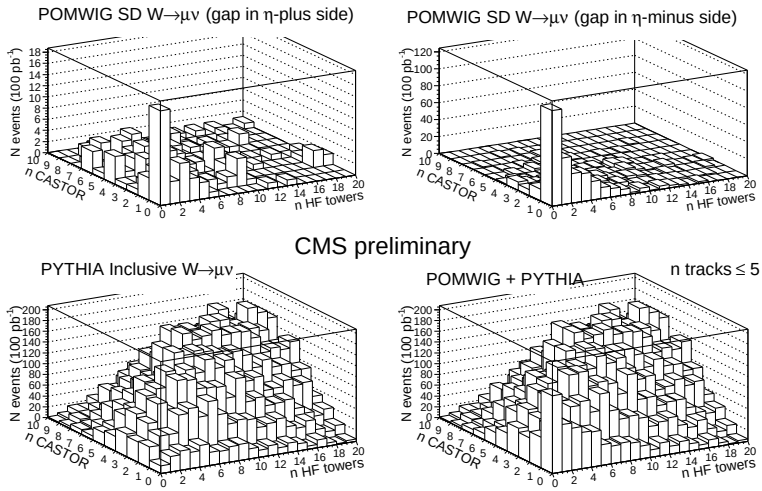

Fig. 3: HF tower multiplicity vs CASTOR sector multiplicity distribution for events with track multiplicity in the central tracker $N_{\rm track} \leq 5$.

A simple way to isolate a sample of diffractive events from these plots is to use the zero-multiplicity bins, where the diffractive events cluster and the non-diffractive background is small.

The HF plus CASTOR combination yields the best signal to background ratio. When an integrated effective luminosity for single interactions of 100 pb^{-1} becomes available, SD $W \to \mu\nu$ production can then be observed with $\mathcal{O}(100)$ signal events. The situation is even more favorable for SD dijet production where a recently completed study [3] arrives at $\mathcal{O}(300)$ SD dijet events per 10 pb^{-1} of integrated effective luminosity for single interactions. With an observation of a number of signal events of this size, it should be possible to exclude values of rapidity gap survival probability at the lower end of the spectrum of theoretical predictions. A method to establish that the observed population of the zero-multiplicity bins is indeed indicative of the presence of SD events in the data is described in [3]. The method is based on the observation that the size of the SD signal in the zero-multiplicity bins can be controlled in a predictable way when the cuts for enhancing the SD signal are modified.

The main background other than non-diffractive W production consists of SD W production with proton-dissociation, $pp \to XN$, where X contains a W boson and N is a low-mass state into which the proton has diffractively dissociated. A study of proton-dissociation has been carried out in Ref. [4], where it has been shown that about 50% of the proton-dissociative background can be rejected by vetoing events with activity in the CMS Zero Degree Calorimeter

(ZDC), which provides coverage for neutral particles for $|\eta| > 8.1$. The net effect is to enhance the diffractive signal in the zero multiplicity bin of Fig. 3 by about 30%.

4 Exclusive $\gamma\gamma \to \ell^+\ell^-$ and $\gamma p \to \Upsilon p \to \ell^+\ell^- p$

Exclusive dilepton production in pp collisions at CMS can occur through the processes $\gamma\gamma \to \ell^+\ell^-$ and $\gamma p \to \Upsilon p \to \ell^+\ell^- p$. The first is a QED process, making it an ideal sample for luminosity calibration at the LHC. The second will allow studies of vector meson photoproduction at energies significantly higher than previous experiments. Zero pileup is assumed for this study [4]. Both signal processes are characterized by the presence of two same-flavor opposite-sign leptons back-to-back in $\Delta\phi$, and with equal $|p_T|$. In the no-pileup startup scenario assumed here, the signal is also distinguished by having no calorimeter activity that is not associated with the leptons, and no charged tracks in addition to the two signal leptons. This exclusivity requirement is implemented by requiring that there be no more than 5 "extra" calorimeter towers with $E > 5$ GeV, where extra towers are defined as those separated from either of the lepton candidates by $\Delta R > 0.3$ in the $\eta - \phi$ plane. The track multiplicity is required to be < 3. The dominant inelastic photon-exchange background is reduced by requiring no activity in the CASTOR calorimeter (covering $5.2 < \eta < 6.6$) or the Zero Degree Calorimeter (covering $|\eta| > 8.2$). The residual background from non-photon exchange processes is estimated from an exponential fit to the sideband of the extra calorimeter towers distribution, resulting in a background estimate of approximately 39 events in 100 pb^{-1}, which is small compared to the inelastic background.

The expected $\gamma\gamma \to \mu^+\mu^-$ signal yields in 100 pb^{-1} are $N_{elastic}(\gamma\gamma \to \mu^+\mu^-) = 709 \pm 27$, and $N_{inelastic}(\gamma\gamma \to \mu^+\mu^-) = 223 \pm 15 \pm 42(model)$. Without the ZDC and Castor vetoes, the singly inelastic contribution would be significantly larger: $N_{inelastic}(\gamma\gamma \to \mu^+\mu^-) = 636 \pm 25 \pm 121(model)$. In the $\gamma\gamma \to e^+e^-$ channel, the expected yields are significantly smaller. After all trigger and selection criteria are applied the expected elastic signal yields in 100 pb^{-1} are: $N_{elastic}(\gamma\gamma \to e^+e^-) = 67 \pm 8$, and $N_{inelastic}(\gamma\gamma \to e^+e^-) = 31 \pm 6 \pm 6(model)$.

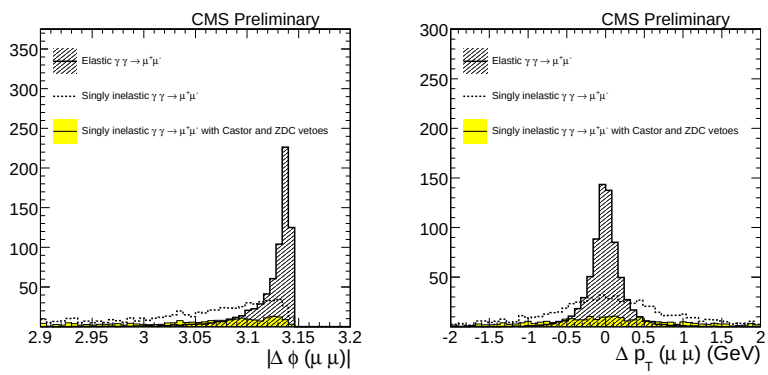

Fig. 4: Distributions of $|\Delta\phi(\mu^+\mu^-)|$ (left) and $|\Delta p_T(\mu^+\mu^-)|$ (right) for $\gamma\gamma \to \mu^+\mu^-$ events passing all selection requirements. The elastic signal is denoted by the open histogram, the inelastic background is shown with no CASTOR/ZDC vetos (dashed line), and with the veots described in the text (solid histogram).

Without the ZDC and Castor vetoes, the singly inelastic contribution would be: $N_{inelastic}(\gamma\gamma \rightarrow e^+e^-) = 82 \pm 9 \pm 15(model)$. The elastic $\gamma\gamma \rightarrow \mu^+\mu^-$ signal can be separated from the inelastic background for luminosity measurements using the $\Delta\phi$ and Δp_T distributions (Figure 4), while the Υ photoproduction signal can be further distinguished by performing a fit to the dimuon invariant mass distribution (Figure 5).

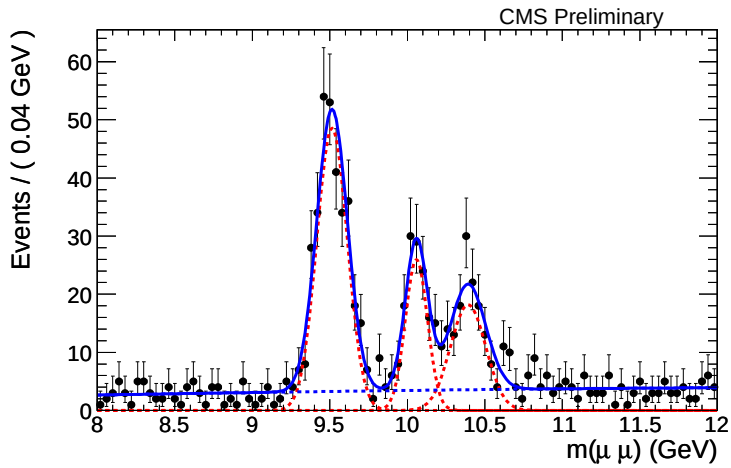

Fig. 5: Dimuon invariant mass in the range $8 < m(\mu^+\mu^-) < 12$ GeV. The lines show the result of a fit, where the dashed line is the Υ component, the dotted line is the two-photon continuum, and the solid line is the sum of the two.

We conclude that with $100pb^{-1}$ of integrated luminosity, a large sample of $\gamma\gamma \rightarrow \mu^+\mu^-$ and $\gamma p \rightarrow \Upsilon p \rightarrow \mu^+\mu^- p$ events can be triggered and reconstructed in the CMS detector, using a common selection for both samples. With minimal pileup these events can be cleanly distinguished from the dominant backgrounds. The Υ sample will allow measurements of cross-sections and production dynamics at significantly higher energies than previous experiments, while the $\gamma\gamma \rightarrow \ell^+\ell^-$ sample will serve as a calibration sample for luminosity studies.

5 Forward jets reconstruction in HF

5.1 Introduction

The parton distribution functions (PDFs) in the proton have been studied in detail in deep-inelastic-scattering (DIS) ep collisions at HERA [18]. For decreasing parton momentum fraction $x = p_{parton}/p_{hadron}$, the gluon density is observed to grow rapidly as $xg(x, Q^2) \propto x^{-\lambda(Q^2)}$, with $\lambda \approx 0.1$–0.3 rising logarithmically with Q^2. As long as the densities are not too high, this growth is described by the Dokshitzer-Gribov-Lipatov-Altarelli-Parisi (DGLAP) [19] or by the Balitski-Fadin-Kuraev-Lipatov (BFKL) [20] evolution equations which govern, respectively, parton radiation in Q^2 and x. Experimentally, direct information on the parton structure and evolution can be obtained in hadron-hadron collisions from the perturbative production of e.g. jets or prompt γ's, which are directly coupled to the parton-parton scattering vertex. The measurement of jets with transverse momentum $p_T \approx 20$ GeV in the CMS forward calorimeters (HF, $3 < |\eta| < 5$ and CASTOR, $5.1 < |\eta| < 6.6$) will allow one to probe x values as low as $x_2 \approx 10^{-5}$.

Figure 6 (right) shows the actual log($x_{1,2}$) distribution for two-parton scattering in p-p collisions at 14 TeV producing at least one jet above 20 GeV in the HF and CASTOR acceptances. Full detector simulation and reconstruction packages were used in obtaining these results.

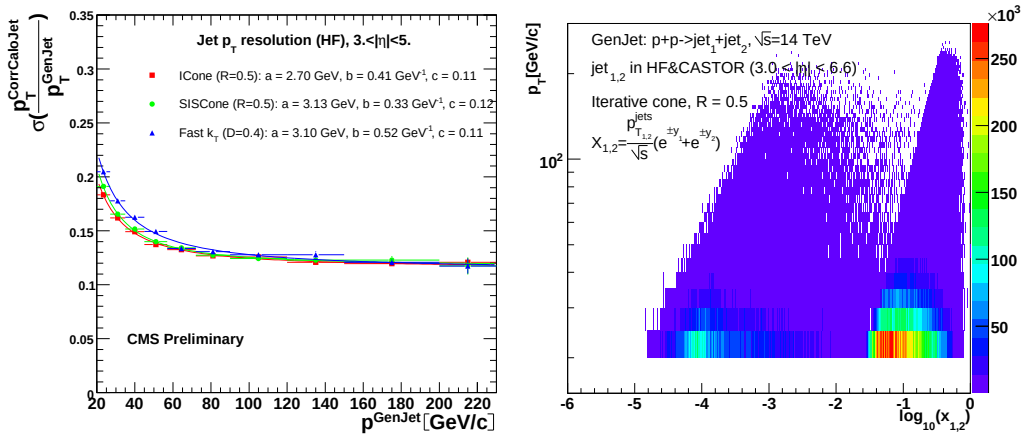

Fig. 6: Energy resolution as a function of p_T for the ICone, SISCone (with cone sizes $R = 0.5$) and FastKt ($D = 0.4$) algorithms for jets reconstructed in HF ($3. < |\eta| < 5.$). The resolutions are fitted to $f(p_T) = \sqrt{\left(\frac{a}{p_T^{gen}}\right)^2 + \left(\frac{b}{\sqrt{p_T^{gen}}}\right)^2 + c^2}$ with the parameters quoted in the legend (Left). Log($x_{1,2}$) distribution of two partons producing at least one jet above p_T = 20 GeV within HF ($3 < |\eta| < 5$) and CASTOR ($5.1 < |\eta| < 6.6$) in p-p collisions at $\sqrt{s}$ = 14 TeV (Right).

5.2 Forward jets reconstruction in HF

Jets in CMS are reconstructed at the generator- and calorimeter-level using 3 different jet algorithms [5]: iterative cone [10] with radius of $\mathcal{R} = 0.5$ in (η, ϕ), SISCone [22] ($\mathcal{R} = 0.5$), and the Fast-k_T [23] (E_{seed} = 3 GeV and E_{thres} = 20 GeV). The p_T resolutions for the three different algorithms are very similar: ∼18% at p_T ∼20 GeV decreasing to ∼12% for $p_T \gtrsim$100 GeV (Fig. 6, Left). The position (η, ϕ) resolutions (not shown here) for jets in HF are also very good: $\sigma_{\phi,\eta}$ = 0.045 at p_T = 20 GeV, improving to $\sigma_{\phi,\eta} \sim 0.02$ above 100 GeV.

5.3 Single inclusive jet p_T spectrum in HF

In this section, we present the reconstructed forward jet yields as a function of p_T for 1 pb^{-1} integrated luminosity. Figure 7 (left) shows reconstructed (and corrected for energy resolution smearing) single inclusive forward jet spectrum in HF in p-p collisions at 14 TeV for a total integrated luminosity of 1 pb^{-1} compared to fastNLO jet predictions [24] using various PDFs (MRST03 and CTEQ6.1M). Figure 7 (right) shows percent differences between the reconstructed forward jet p_T spectrum and two fastNLO predictions (CTEQ6.1M and MRST03 PDFs). The error bars include the statistical and the energy-resolution smearing errors. The solid curves indicate the propagated uncertainty due to the jet-energy scale (JES) error for "intermediate"

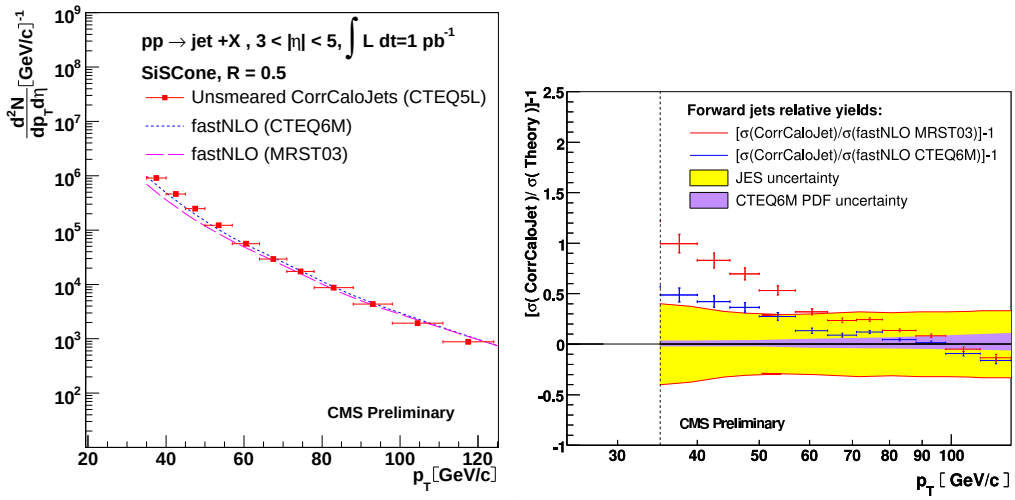

Fig. 7: Left: The forward jet yields for a total integrated luminosity of 1 pb^{-1}. Right: Percent differences between the reconstructed forward jet p_T spectrum and two fastNLO predictions (CTEQ6.1M and MRST03 PDFs). The solid curves indicate the propagated uncertainty due to the jet-energy scale (JES) error for "intermediate" 10% decreasing to a constant 5% for $p_T > 50$ GeV/c conditions.

(10% decreasing to a constant 5% for $p_T > 50$ GeV/c) conditions. If the JES can be improved below 10% (such as in the "intermediate" scenario considered), our measurement will be more sensitive to the underlying PDF. The main conclusion of this part of the study is that the use of the forward jet measurement in HF to constrain the proton PDFs in the low-x range will require careful studies of the HF jet calibration.

References

[1] CERN-LHCC-2006-021 (2006).

[2] CMS Collaboration, CMS PAS DIF-07-002 (2007).

[3] CMS Collaboration, CMS PAS FWD-08-002 (2008).

[4] CMS Collaboration, CMS PAS DIF-07-001 (2007).

[5] CMS Collaboration, CMS PAS FWD-08-001 (2008).

[6] M. Grothe, in proceedings of the workshop on high-energy photon collisions at the LHC, D. D'Enterria *et al.* (eds), CERN, Geneva, Switzerland, 2008.

[7] TOTEM Collaboration: Letter of Intent, CERN-LHCC 97-49; Technical Proposal, CERN-LHCC 99-7; Technical Design Report, CERN-LHCC-2004-002.

[8] M. Albrow *et al.* [CMS and TOTEM Collaborations], CERN/LHCC 2006-039/G-124.

[9] FP420 Collaboration, arXiv:0806.0302, [hep-ex].

[10] CMS Collaboration, CERN-LHCC-2006-001 (2006).

[11] TOTEM Collaboration, these proceedings.

[12] P. Bussey, these proceedings.

[13] B. E. Cox and J. R. Forshaw, Comput. Phys. Commun. **144** (2002) 104.

[14] A. Aktas *et al.*, [H1 Collaboration], Eur. Phys. J. C **48** (2006) 715.

[15] V. A. Khoze, A. D. Martin and M. G. Ryskin, Phys. Lett. B **643** (2006) 93.

[16] T. Sjostrand, S. Mrenna and P. Skands, JHEP **0605** (2006) 026.

[17] CMS Collaboration, CMS PAS EWK-07-002 (2007).

[18] M. Klein and R. Yoshida, arXiv:0805.3334 [hep-ex].

[19] V.N. Gribov and L.N. Lipatov, Sov. Journ. Nucl. Phys. **15** (1972) 438; G. Altarelli and G. Parisi, Nucl. Phys. **B126** (1977) 298; Yu. L. Dokshitzer, Sov. Phys. JETP **46** (1977) 641.

[20] L.N. Lipatov, Sov. J. Nucl. Phys. **23** (1976) 338; E.A. Kuraev, L.N. Lipatov and V.S. Fadin, Zh. Eksp. Teor. Fiz **72**, (1977) 3; I.I. Balitsky, L.N. Lipatov, Sov. J. Nucl. Phys. **28** (1978) 822.

[21] CMS Physics TDR, Volume 1, CERN-LHCC-2006-001, 2 February 2006

[22] G. P. Salam and G.Soyez, JHEP05 (2007) 086

[23] M.Cacciari and G. P. Salam, Phys. Lett. B **641** (2006) 57.

[24] T. Kluge, K. Rabbertz, M. Wobisch, arXiv:hep-ph/0609285; K. Rabbertz, private communication.

Diffraction at TOTEM

G. Antchev[1], *P. Aspell*[1], *V. Avati*[1,9], *M.G. Bagliesi*[5], *V. Berardi*[4], *M. Berretti*[5], *U. Bottigli*[5], *M. Bozzo*[2], *E. Brücken*[6], *A. Buzzo*[2], *F. Cafagna*[4], *M. Calicchio*[4], *M.G. Catanesi*[4], *P.L. Catastini*[5], *R. Cecchi*[5], *M.A. Ciocci*[5], *M. Deile*[1], *E. Dimovasili*[1,9], *K. Eggert*[9], *V. Eremin*[**], *F. Ferro*[2], *F. Garcia*[6], *S. Giani*[1], *V. Greco*[5], *J. Heino*[6], *T. Hildén*[6], *J. Kašpar*[1,7], *J. Kopal*[1,7], *V. Kundrát*[7], *K. Kurvinen*[6], *S. Lami*[5], *G. Latino*[5], *R. Lauhakangas*[6], *E. Lippmaa*[8], *M. Lokajíček*[7], *M. Lo Vetere*[2], *F. Lucas Rodriguez*[1], *M. Macrí*[2], *G. Magazzù*[5], *M. Meucci*[5], *S. Minutoli*[2], *H. Niewiadomski*[1,9], *E. Noschis*[1], *G. Notarnicola*[4], *E. Oliveri*[5], *F. Oljemark*[6], *R. Orava*[6], *M. Oriunno*[1], *K. Österberg*[6,‡], *P. Palazzi*[1], *E. Pedreschi*[5], *J. Petäjäjärvi*[6], *M. Quinto*[4], *E. Radermacher*[1], *E. Radicioni*[4], *F. Ravotti*[1], *G. Rella*[4], *E. Robutti*[2], *L. Ropelewski*[1], *G. Ruggiero*[1], *A. Rummel*[8], *H. Saarikko*[6], *G. Sanguinetti*[5], *A. Santroni*[2], *A. Scribano*[5], *G. Sette*[2], *W. Snoeys*[1], *F. Spinella*[5], *P. Squillacioti*[5], *A. Ster*[*], *C. Taylor*[3], *A. Trummal*[8], *N. Turini*[5], *J. Whitmore*[9], *J. Wu*[1]

[1]CERN, Genève, Switzerland,
[2]Università di Genova and Sezione INFN, Genova, Italy,
[3]Case Western Reserve University, Dept. of Physics, Cleveland, OH, USA,
[4]INFN Sezione di Bari and Politecnico di Bari, Bari, Italy,
[5]INFN Sezione di Pisa and Università di Siena, Italy,
[6]Helsinki Institute of Physics and Department of Physics, University of Helsinki, Finland,
[7]Institute of Physics of the Academy of Sciences of the Czech Republic, Praha, Czech Republic,
[8]National Institute of Chemical Physics and Biophysics NICPB, Tallinn, Estonia.
[9]Penn State University, Dept. of Physics, University Park, PA, USA.
[*]Individual participant from MTA KFKI RMKI, Budapest, Hungary.
[**]On leave from Ioffe Physico-Technical Institute, Polytechnicheskaya Str. 26, 194021 St-Petersburg, Russian Federation.

Abstract

The TOTEM experiment at the LHC measures the total proton-proton cross section with the luminosity-independent method and the elastic proton-proton cross-section over a wide $|t|$-range. It also performs a comprehensive study of diffraction, spanning from cross-section measurements of individual diffractive processes to the analysis of their event topologies. Hard diffraction will be studied in collaboration with CMS taking advantage of the large common rapidity coverage for charged and neutral particle detection and the large variety of trigger possibilities even at large luminosities. TOTEM will take data under all LHC beam conditions including standard high luminosity runs to maximize its physics reach. This contribution describes the main features of the TOTEM physics programme including measurements to be made in the early LHC runs. In addition, a novel scheme to extend the diffractive proton acceptance for high luminosity runs by installing proton detectors at IP3 is described.

[‡] corresponding author: Kenneth Österberg (kenneth.osterberg@helsinki.fi)

1 Introduction

The TOTEM experiment [1] is dedicated to the total proton-proton (pp) cross-section measurement using the luminosity-independent method, which requires a detailed measurement of the elastic scattering rate down to a squared four-momentum transfer of $-t \sim p^2\Theta^2 \sim 10^{-3}\,\mathrm{GeV}^2$ together with the measurements of the total inelastic and elastic rates. Furthermore, by studying elastic scattering with momentum transfers up to 10 GeV^2, and via a comprehensive study of diffractive processes – partly in cooperation with CMS [2], located at the same interaction point, TOTEM's physics programme aims at a deeper understanding of the proton structure. To perform these measurements, TOTEM requires a good acceptance for particles produced at small and even tiny angles with respect to the beams. TOTEM's coverage in the pseudo-rapidity range of $3.1 \leq |\eta| \leq 6.5$ ($\eta = -\ln\tan\frac{\theta}{2}$) on both sides of the interaction point (IP) is accomplished by two telescopes, T1 and T2 (Figure 1, top), for the detection of charged particles with emission angles between a few and about hundred milliradians. This is complemented by detectors in special movable beam-pipe insertions – so called Roman Pots (RP) – placed at about 147 m and 220 m from the IP, designed to detect elastically or diffractively scattered protons at merely a few millimeter from the beam center corresponding to emission angles down to a few microradians (Figure 1, bottom).

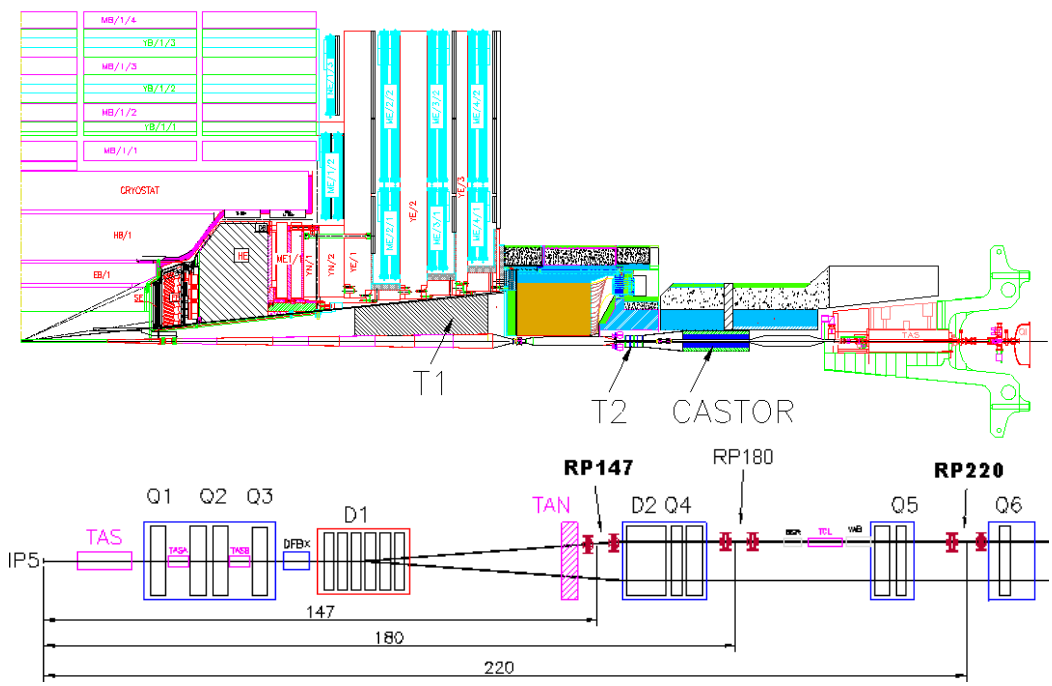

Fig. 1: Top: TOTEM forward telescopes T1 and T2 embedded in the CMS experiment together with the CMS forward calorimeter CASTOR. Bottom: LHC beam line on one side of interaction point IP5 and TOTEM Roman Pot stations at distances of about 147 m (RP147) and 220 m (RP220). RP180 at 180 m is another possible location but presently not equipped.

For the luminosity-independent total cross-section measurement, TOTEM has to reach the lowest possible $|t|$ values in elastic pp scattering. Elastically scattered protons close to the beam can be detected downstream on either side of the IP if the displacement at the detector location is large enough and if the beam divergence at the IP is small compared to the scattering angle. To achieve these conditions special LHC optics with high beta value at the IP (β^*) are required: the larger the β^*, the smaller the beam divergence ($\sim 1/\sqrt{\beta^*}$) will be. Two optics are proposed: an ultimate one with $\beta^* = 1540\,\mathrm{m}$ and another one, possibly foreseen for 2009, with $\beta^* = 90\,\mathrm{m}$. The latter uses the standard injection optics (β^* = 11 m) and beam conditions typical for early LHC running: zero degree crossing-angle and consequently at most 156 bunches together with a low number of protons per bunch.

The versatile physics programme of TOTEM requires different running scenarios that have to be adapted to the LHC commissioning and operation in the first years. A flexible trigger can be provided by the two telescopes and the Roman Pot detectors. TOTEM will take data under all optics conditions, adjusting the trigger schemes to the luminosity. The DAQ will allow trigger rates up to a few kHz without involving a higher level trigger. The high-β^* runs (Table 1) with 156 bunches, zero degree crossing-angle and maximum luminosity between 10^{29} and $10^{30}\,\mathrm{cm}^{-2}\mathrm{s}^{-1}$, will concentrate on low-$|t|$ elastic scattering, total cross-section, minimum bias physics and soft diffraction. A large fraction of forward protons will be detected even at the lowest ξ values. Low-β^* runs (Table 1) with more bunches and higher luminosity (10^{32} – $10^{34}\,\mathrm{cm}^{-2}\mathrm{s}^{-1}$) will be used for large-$|t|$ elastic scattering and diffractive studies with $\xi > 0.02$. Hard diffractive events come within reach. In addition, early low β^* runs will provide first opportunities for measurements of soft diffraction at LHC energies and for studies of forward charged multiplicity.

β^* [m]	k	$N/10^{11}$	$\mathcal{L}$ [$\mathrm{cm}^{-2}\mathrm{s}^{-1}$]	$\lvert t\rvert$-range [GeV^2] @ $\xi = 0$	ξ-range
1540	43 ÷ 156	0.6 ÷ 1.15	$10^{28} \div 2 \cdot 10^{29}$	0.002 ÷ 1.5	< 0.2
90	156	0.1 ÷ 1.15	$2 \cdot 10^{28} \div 3 \cdot 10^{30}$	0.03 ÷ 10	< 0.2
11	43 ÷ 2808	0.1 ÷ 1.15	$\sim 10^{30} \div 5 \cdot 10^{32}$	0.6 ÷ 8	0.02 ÷ 0.2
0.5 ÷ 3	43 ÷ 2808	0.1 ÷ 1.15	$\sim 10^{30} \div 10^{34}$	2 ÷ 10	0.02 ÷ 0.2

Table 1: Running scenarios at different LHC optics (k: number of bunches, N: number of particles per bunch, $\mathcal{L}$: estimated luminosity). The $|t|$ ranges for elastically scattered protons correspond to the $\geq 50\%$ combined RP147 and RP220 acceptance.

In the following, after a brief description of the TOTEM detectors and the principles of proton detection, the main features of the TOTEM physics programme will be given. This will be followed by a description of the early physics programme. Finally the novel idea of proton detection at IP3 will be presented. A detailed technical description of the TOTEM experiment can be found in Ref. [3].

2 TOTEM detectors and performance

2.1 Inelastic detectors

The measurement of the inelastic rate requires identification of all beam-beam events with detectors capable to trigger and reconstruct the interaction vertex. The main requirements of these

detectors are:

- to provide a fully inclusive trigger for minimum bias and diffractive events, with minimal losses at a level of a few percent of the inelastic rate;
- to enable the reconstruction of the primary vertex of an event, in order to disentangle beam-beam events from the background via a partial event reconstruction.

These requirements are fulfilled by the T1 telescope (centered at z = 9 m), consisting of Cathode Strip Chambers (CSC) and T2 telescope (centered at z = 13.5 m) exploiting Gas Electron Multipliers (GEM). The η coverage of T1 and T2 is $3.1 \leq |\eta| \leq 4.7$ and $5.3 \leq |\eta| \leq 6.5$, respectively. Each T1 telescope arm consists of five planes made up of six trapezoidal formed CSC's with a spatial resolution of $\sim$ 1 mm. Each T2 telescope arm consists of 20 semicircular shaped triple-GEM detectors with a spatial resolution of $\sim$ 100 μm in the radial direction and a inner radius that matches the beam-pipe. Ten aligned detectors mounted back-to-back are combined to form one T2 half arm on each side of the beam-pipe. For charged particles with momenta typical of particles produced within the detector acceptances in inelastic events, the particle η can be determined with a precision that increases with $|\eta|$ and is between 0.02 and 0.06 in T1 and between 0.04 and 0.1 in T2. The corresponding azimuthal angle resolution for both detectors is $\sim 1^o$. The magnetic field at the detector locations is too weak to allow for a momentum determination for the charged particles. The primary vertex can be reconstructed with a precision of $\sim$ 1.5 cm in the radial direction and $\sim$ 20 cm in the beam direction in presence of the CMS magnetic field. Vertex resolutions one order of magnitude better can be achieved running with the CMS magnetic field switched off.

2.2 Proton detectors

To measure elastically and diffractively scattered protons with high acceptance requires the reconstruction of the protons tracks by "trigger capable" detectors moved as close as $\sim$ 1 mm from the center of the outgoing beam. This is obtained with two RP stations installed, symmetrically on both sides of IP5, at a distance of $\sim$ 147 m and $\sim$ 220 m from IP5. These positions are given by an interplay between the development of the special TOTEM optics and the constraints given by the LHC accelerator elements. Each RP station is composed of two units at a distance of several meters. This large lever arm allows local track reconstruction and a fast trigger selection based on the track angle. Each unit consists of three pots, two approaching the beam vertically from the top and the bottom and one horizontally to complete the acceptance for diffractively scattered protons, in particular for the low β^* optics. Furthermore, the overlap of the detector acceptance in the horizontal and vertical pots is vital for the relative alignment of the three pots via common particle tracks. The position of the pots with respect to the beam is given by Beam Position Monitors mechanically fixed to all three pots in one unit. Each pot contains a stack of 10 planes of silicon strip "edgeless" detectors with half with their strips oriented at an angle of $+45^o$ and half at an angle of -45^o with respect to the edge facing the beam. These detectors, designed by TOTEM with the objective of reducing the insensitive area at the edge facing the beam to only a few tens of microns, have a spatial resolution of $\sim$ 20 μm. High efficiency up to the physical detector border is essential in view of maximizing the elastic and diffractive proton acceptances. For the same reason, the pots' stainless steel bottom foil that faces the beam has been reduced to a thickness of 150 μm.

2.3 Proton detection

The transverse displacement $(x(s), y(s))$ of an elastically or diffractively scattered proton at a distance s from the IP is related to its origin $(x^*, y^*, 0)$, scattering angles $\Theta^*_{x,y}$ and fractional momentum loss ξ (= $\Delta p/p$) value at the IP via the optical functions L and v, and the dispersion D:

$$x(s) = v_x(s) \cdot x^* + L_x(s) \cdot \Theta^*_x + \xi \cdot D(s) \quad \text{and} \quad y(s) = v_y(s) \cdot y^* + L_y(s) \cdot \Theta^*_y \quad (1)$$

L, v and D determining the explicit path of the proton through the LHC elements, depend mainly on the position along the beam line i.e. on all the elements traversed before reaching that position and their settings, which is a optics dependent repetition, and hence the RP acceptance for leading protons will depend on the optics. The allowed minimum distance of a RP to the beam center on one hand being proportional to the beam size ($(10-15)\cdot\sigma_{x(y)}(s)$) as well as constraints imposed by the beam-pipe or beam screen size on the other hand will determine the proton acceptance of a RP station.

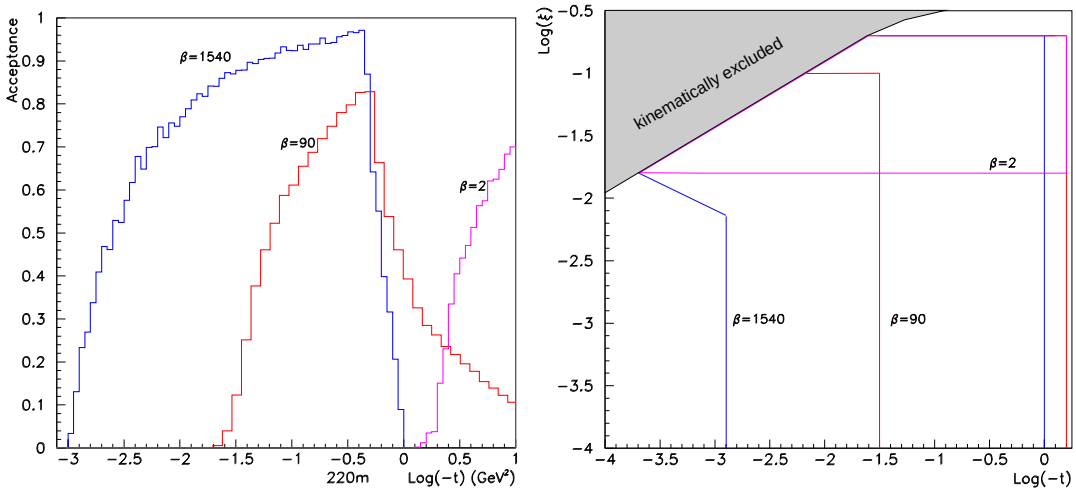

Fig. 2: Left: RP220 $\log_{10}|t|$ acceptance for elastically scattered protons at different optics configurations. Right: contour lines of 10 % acceptance for RP220 in $\log_{10}|t|$ and $\log_{10}\xi$ for diffractively scattered protons at different optics configurations.

The complementarity of the acceptances for different optics configurations is shown in Figure 2. The TOTEM-specific optics with $\beta^* = 1540\,\text{m}$ (blue graphs in Figure 2) is particularly optimized for accepting protons down to very low $|t|$-values. For the diffractive case all kinematically allowed values of ξ are accepted. With the $\beta^* = 90\,\text{m}$ optics (red graphs in Figure 2), diffractive scattered protons are still accepted independently of their ξ-value, but the t-acceptance is reduced compared to $\beta^* = 1540\,\text{m}$ optics. With the standard high luminosity optics (β^* = 0.5 $\div$ 3 m, magenta graphs in Figure 2) elastically scattered protons can only be detected at very large $|t|$ and diffractively scattered protons are accepted independently of their t value in the horizontal pots for ξ values above 2 %.

	β^* = 0.5 – 3 m	β^* = 90 m	β^* = 1540 m
$\sigma(\xi)$	0.001 ÷ 0.006	$\sim$ 0.0015 (w CMS vtx) $\sim$ 0.006 (w/o CMS vtx)	0.002 ÷ 0.006 ‡
$\sigma(t)$ [GeV^2]	(0.3÷0.45) $\sqrt{\lvert t\rvert}$	$\sigma(t_y) \sim 0.04\ \sqrt{\lvert t_y\rvert}$	$\sim 0.005\ \sqrt{\lvert t\rvert}$
$\sigma(M)$ [GeV] in central diffraction	(0.02 ÷ 0.05) M	$<$ 18 for R $>$ 0.6 (w CMS vtx) $<$ 80 for R $>$ 0.6 (w/o CMS vtx)	$\sim 20\ M^b$ ‡ b = 0.17 for R = 0.5 ÷ 1

Table 2: Summary of resolutions for the RP220 proton reconstruction at different optics configurations. "w CMS vtx" and "w/o CMS vtx" refers to whether vertex position information from CMS is available or not (relevant for β^* = 90 m), R = ξ_{lower}/ξ_{higher} to the momentum loss symmetry between the two outgoing protons and "‡" to reconstruction using also RP147.

The reconstruction of the proton kinematics is optics dependent. The main resolutions are given in Table 2. More details can be found in Ref. [4]. A feature of the β^* = 90 m optics is that $L_y \gg L_x$ and hence t_y is determined with almost an order of magnitude better precision than t_x. For central diffraction, the diffractive mass can be reconstructed from the ξ measurements of the two protons according to

$$M^2 = \xi_1\, \xi_2\, s\,. \tag{2}$$

The mass resolution for central diffractive events at different optics is also quoted in Table 2. If the scattering vertex is determined with high precision ($\sim 30\,\mu$m) with the CMS tracking detectors during common data taking, a substantial improvement in the ξ and M measurement is achieved at β^* = 90 m.

3 TOTEM physics programme

Given its unique coverage for charged particles at high rapidities, TOTEM is ideal for studies of forward phenomena, including elastic and diffractive scattering. Its main physics goals, precise measurements of the total cross-section and of elastic scattering over a large range in $|t|$, are of primary importance for distinguishing between different models of soft pp interactions. Furthermore, as energy flow and particle multiplicity of inelastic events peak in the forward region, the large rapidity coverage and proton detection on both sides allow the study of a wide range of processes in inelastic and diffractive interactions.

3.1 Elastic scattering and diffraction

Much of the interest in large-impact-parameter collisions centers on elastic scattering and soft inelastic diffraction. The differential cross-section of elastic pp interactions at 14 TeV, as predicted by different models [5–8], is given in Figure 3 (left). Increasing $|t|$ means looking deeper into the proton at smaller distances. Several $|t|$-regions with different behavior (at $\sqrt{s}$ = 14 TeV) can be distinguished:

- $|t| < 6.5 \cdot 10^{-4}\,\mathrm{GeV}^2$: The Coulomb region dominated by photon exchange: $d\sigma/dt \sim 1/t^2$.
- $10^{-3}\,\mathrm{GeV}^2 < |t| < 0.5\,\mathrm{GeV}^2$: The nuclear region, described in a simplified way by "single-Pomeron exchange": $d\sigma/dt \sim \mathrm{e}^{-B\,t}$, is crucial for the extrapolation of the differ-

ential counting-rate dN_{el}/dt to $t = 0$, needed for the luminosity-independent total cross-section measurement.

- $0.5\,\text{GeV}^2 < |t| < 1\,\text{GeV}^2$: A region exhibiting the diffractive structure of the proton.
- $|t| > 1\,\text{GeV}^2$: Domain of central elastic collisions, described by perturbative QCD, e.g. via triple-gluon exchange with a predicted cross-section $\propto |t|^{-8}$. The model dependence of the predictions being very pronounced in this region, measurements will test the validity of different models.

TOTEM will cover the full elastic $|t|$-range from 0.002 up to 10 GeV^2 by combining data from runs at several optics configurations as indicated in Figure 3 (left). With typical expected LHC machine cycle times of $10^4 - 10^5$ s, enough statistics at low $|t|$ values can be accumulated in one run. This statistics is also sufficient for track-based alignment of the RP detectors. The overlap between the acceptances of the different optics configurations will allow for cross-checks of the measurements.

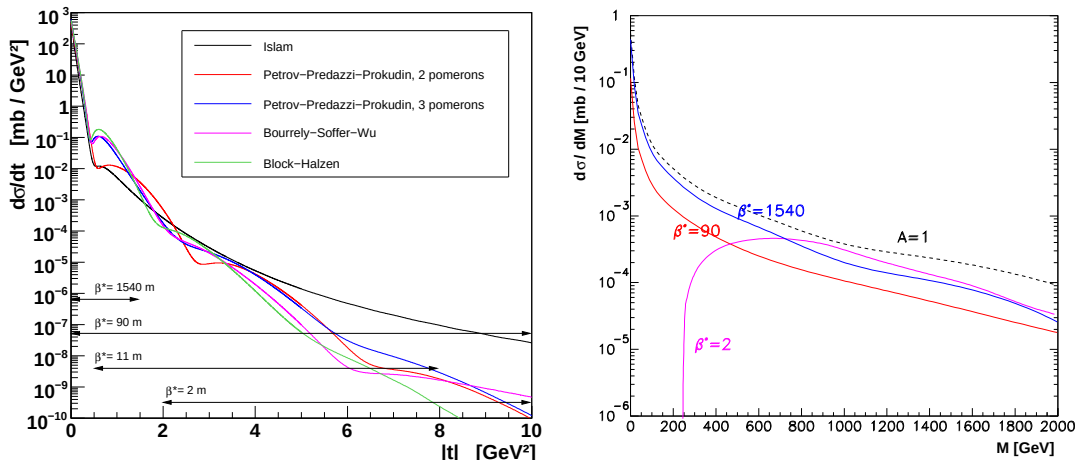

Fig. 3: Left: differential cross-section of elastic scattering at $\sqrt{s}$ = 14 TeV as predicted by various models together with the t-acceptance ranges of different optics configurations. Right: predicted differential cross-section of central diffraction at $\sqrt{s} = 14$ TeV with (solid) and without (dashed) taking the proton acceptance into account for different optics configurations.

Diffractive scattering comprises single diffraction, double diffraction, central diffraction (a.k.a. “double Pomeron exchange”), and higher order (“multi Pomeron”) processes, shown in Figure 4 with their cross-sections as measured at Tevatron [9–12] and as predicted for LHC [5–8, 13–15]. Together with elastic scattering these processes represent about 50 % of the total cross-section. Many details of these processes with close ties to proton structure and low-energy QCD are still poorly understood. Majority of diffractive events (Figure 4) exhibits intact (“leading”) protons in the final state, characterized by their t and ξ. For large β^* (see Figure 2, right) most of these protons can be detected in the RP detectors. Already at an early stage, TOTEM will be able to measure ξ-, t- and mass-distributions in soft central and single diffractive events. The full structure of diffractive events with one or more sizeable rapidity gap in the particle distribution

(Figure 4) will be optimally accessible when the detectors of CMS and TOTEM will be combined for common data taking with an unprecedented rapidity coverage, as discussed in [2].

Figure 3 (right) shows the predicted central diffractive mass distribution [15] together with the acceptance corrected distributions for three different optics. With high and intermediate β^* optics, all diffractive mass values are observable. For low β^* optics on the other hand, the acceptance starts at $\sim 250\,\text{GeV}$ but higher statistics for high masses will be collected due to the larger luminosity. By combining data from runs at low β^* with data from high or intermediate β^* runs, the differential cross-section as function of the central diffractive mass can be measured with good precision over the full mass range.

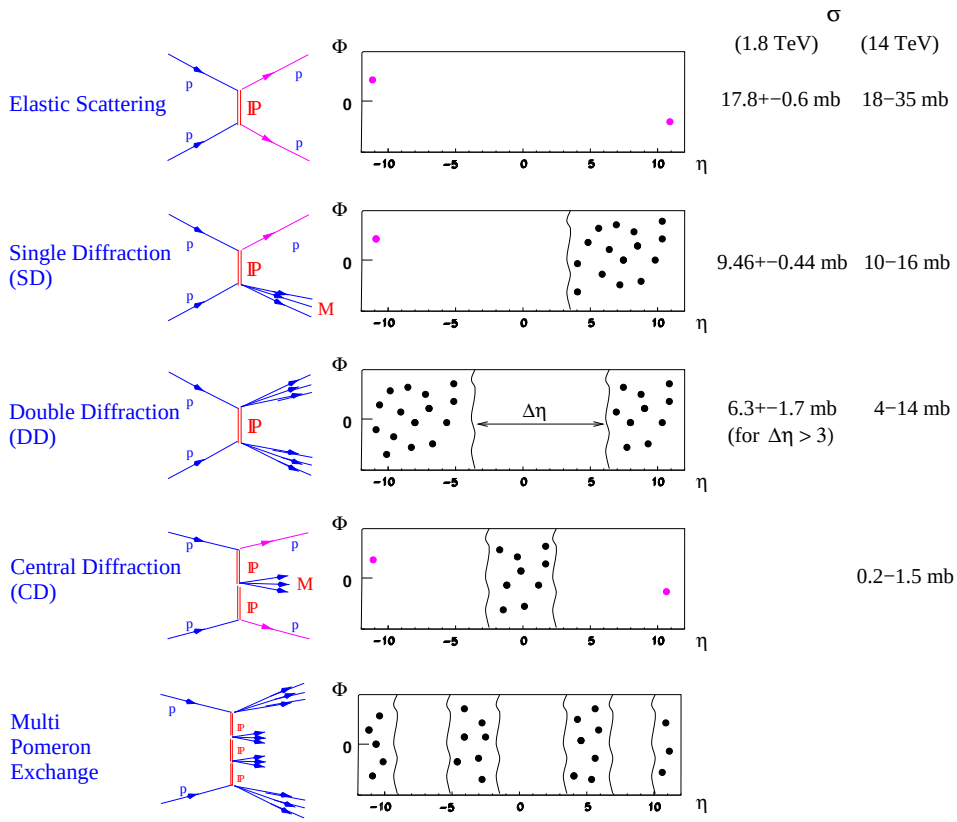

Fig. 4: Different classes of diffractive processes and their cross-sections as measured at Tevatron and as estimated for the LHC.

3.2 Total pp cross-section

The optical theorem relates the total pp cross-section σ_{tot} and the luminosity $\mathcal{L}$ to the differential elastic counting-rate dN_{el}/dt at $t = 0$ and the total elastic N_{el} and inelastic N_{inel} rates as:

$$\sigma_{tot} = \frac{16\pi}{1+\rho^2} \cdot \frac{dN_{el}/dt|_{t=0}}{N_{el}+N_{inel}} \qquad \text{and} \qquad \mathcal{L} = \frac{1+\rho^2}{16\pi} \cdot \frac{(N_{el}+N_{inel})^2}{dN_{el}/dt|_{t=0}} \,. \tag{3}$$

The parameter $\rho = \mathcal{R}[f_{el}(0)]/\mathcal{I}[f_{el}(0)]$, where $f_{el}(0)$ is the forward nuclear elastic amplitude, has to be taken from theoretical predictions. Since $\rho \sim 0.14$ enters only as a $1 + \rho^2$ term, its impact is small. The extrapolation of existing σ_{tot} measurements to LHC energies leaves a wide range for the expected value of σ_{tot} at LHC, typically between 85 and 120 mb, depending on the model used for the extrapolation. TOTEM aims at a 1 % σ_{tot} measurement. Hence the quantities to be measured are the following:

- the inelastic rate N_{inel} consisting of both non-diffractive minimum bias events and diffractive events, which can almost completely be measured by T1, T2 and the RP detectors;
- the total nuclear elastic rate N_{el} measured exclusively by the RP system;
- $dN_{el}/dt|_{t=0}$: the nuclear part of the elastic cross-section extrapolated to $t = 0$.

A summary of the uncertainties on σ_{tot} at different high β^* optics configurations is given in Table 3. Here only the main uncertainties are described. The extrapolation procedure and uncertainty estimates are described in more detailed in Ref. [3]. At β^* = 90 m, protons with $|t| > 0.03$ GeV^2 are observed, whereas $|t|_{min}$ = 10^{-3} GeV^2 at β^* = 1540 m, leading to a significantly smaller uncertainty contribution due to N_{el}, 0.1 % compared to 2 %, and to the extrapolation of dN_{el}/dt to $t = 0$, 0.2% compared to 4%.

Uncertainty	β^* = 90 m	β^* = 1540 m
Extrapolation of dN_{el}/dt to $t = 0$	$\pm$ 4 %	$\pm$ 0.2 %
Elastic rate N_{el}	$\pm$ 2 %	$\pm$ 0.1 %
Inelastic rate N_{inel}	$\pm$ 1 %	$\pm$ 0.8 %
ρ parameter	$\pm$ 1.2 %	$\pm$ 1.2 %
Total σ_{tot}	$\pm$ 4–5 %	$\pm$ 1–2 %

Table 3: Relative uncertainty on the total pp cross-section σ_{tot} measurement estimated at different high β^* optics configurations. Note that the total uncertainty takes into account the correlations between the uncertainties, notably the strong correlation between the extrapolation of the differential elastic counting-rate dN_{el}/dt to $t = 0$ and the elastic rate N_{el}.

The largest contribution to the uncertainty on σ_{tot} at β^* = 90 m comes from the extrapolation of dN_{el}/dt to $t = 0$; mainly due to systematics in the t-measurement from uncertainties in L and v (see Eq.1). This contribution will be reduced to 0.1 % at β^* = 1540 m requiring, however, an improved knowledge of L and v and a RP alignment precision of better than 50 μm. The dominating uncertainty, 0.2 %, will then be due to the model-dependent extrapolation procedure. For β^* = 1540 m, the largest contribution to the σ_{tot} uncertainty will most likely come from N_{inel}, mainly from trigger losses in single and double diffractive events. The lost events, corresponding to ~ 3 mb, have very low diffractive mass M (below ~ 10 GeV/c^2). As a consequence, all particles have pseudo-rapidities beyond the T2 acceptance and hence escape detection of the single arm trigger. To obtain the total inelastic rate, the fraction of events lost due to the incomplete angular coverage is estimated by extrapolating the reconstructed $1/M^2$ distribution. The uncertainty on N_{inel} after corrections is estimated to be 0.8 and 1 % for β^* = 1540 and 90 m optics, respectively. The uncertainty on the ρ parameter as estimated from lower energy measurement [16] gives a σ_{tot} uncertainty of 1.3 %. A reduction is expected when ρ

is measured at the LHC via the interference between Coulomb and nuclear contributions to the elastic scattering cross-section [17].

At an early stage in 2009 with non-optimal beams and β^* = 90 m, TOTEM will measure σ_{tot} ($\mathcal{L}$) with a 4–5 % (7 %) relative precision. After having understood the initial measurements and with improved beams at $\beta^* = 1540\,\mathrm{m}$, a final relative precision on σ_{tot} ($\mathcal{L}$) of 1 % (2%) should be achievable.

4 Early physics with TOTEM

The early runs at the LHC start will be characterized by low β^* beams with a reduced number of bunches and a lower number of protons per bunch. Under these conditions diffractive protons in the ξ range of 0.02 - 0.2 will be within the acceptance of RP220 giving TOTEM ample opportunities to make first soft diffractive studies. The early physics programme of TOTEM in stand-alone runs will concentrate on measurements of individual cross-sections and event topologies for the following processes:

- central diffractive events with diffractive masses between $\sim$ 250 GeV and $\sim$ 2.8 TeV;
- single diffractive events with diffractive masses between $\sim$ 2 TeV and $\sim$ 6 TeV;
- elastic scattering events with $|t|$ values between $\sim$ 2 GeV^2 and $\sim$ 10 GeV^2;
- forward charged particle multiplicity of inelastic pp events in the $3.1 \leq |\eta| \leq 6.5$ region.

The cross-sections for the above processes are large ($\gtrsim 5\ \mu$b) even if the TOTEM acceptance is included, with the exception of high-$|t|$ elastic scattering. As an example, the BSW model [6] predicts an integrated elastic cross-section of $\sim$ 60 nb for $|t| > 2$ GeV^2. This prediction, together with the predictions of Ref. [13–15], imply that for an integrated luminosity of $\sim$ 10 pb^{-1}, TOTEM would collect more than 10^7 central and 10^8 single diffractive events, together with $\sim 10^5$ high-$|t|$ elastic events allowing a first test of the validity of different models as discussed in section 3.1. The main background to diffractive events at low β^* is either due to two overlapping pp collisions, like e.g. two overlapping single diffractive events for central diffraction, or one pp collision overlapping with beam induced proton background. Hence the event purity will depend strongly on the average number of pp collisions per bunch crossing, which should be significantly smaller than one. The beam induced proton background not due to pp collisions in IP5 will be studied in bunch crossings where normal bunches meet "empty" bunches. The interest in the forward charged particle multiplicity is two-fold: first as a basic measurement of pp interaction at LHC energies and secondly as valuable input to the modeling of very high energy cosmic rays [2].

The installation schedule of the TOTEM detectors depends crucially on the CMS installation schedule as well as on the LHC commissioning schedule. The full experiment is planned to be installed for the 2009 LHC running. The focus in the early LHC runs will be to understand the performance of the detectors and other vital parts like trigger and data acquisition, especially the approach of the RP detectors to the beam. The feasibility and time scale of the early physics programme will critically depend on the LHC performance in terms of luminosity and beam induced background in the TOTEM detectors.

5 Diffractive proton detection at IP3

It has been suggested that the central exclusive diffractive process

$$p\,p \rightarrow p\,+\,X\,+\,p\,, \tag{4}$$

where a "+" denotes a rapidity gap, could complement the standard methods of searching and studying new particles ("X") at LHC, see e.g. Ref. [18]. The main advantage is that the mass of the centrally produced particle X can be reconstructed from the measured ξ values of the outgoing protons as shown in Eq. 2. Provided that the two ξ values can be determined with sufficient precision, peaks corresponding to particle resonances may appear in the reconstructed diffractive mass distribution independent of the particles' decay modes. These measurements should be performed with high luminosity optics since the cross-sections are expected to be small. The work presented here aims to find the best detector locations at LHC in terms of ξ acceptance and resolution for the proton measurement in central diffractive events.

The diffractive proton acceptance of near beam detectors is determined by the ratio D_x/σ_x between horizontal dispersion and beam width. With larger D_x the protons are deflected further away from the beam center, while the closest safe approach of a detector to the beam is given by a multiple – typically 10 to 15 – of σ_x. By construction, the LHC region where D_x and D_x/σ_x are maximized and hence the sensitivity to particle X, is the momentum cleaning insertion in IP3, where off-momentum beam protons are intercepted. The idea is to install proton detectors pairs with a lever arm of several tens of meters close to IP3 to detect diffractive protons in both beams just before they are absorbed by the momentum cleaning collimators. In addition to promising perspectives in diffraction, the placement of detectors in front of the collimators has advantages for accelerator diagnostics and protection. The technical aspects of placing proton detectors at IP3 is being worked out together with the LHC collimation group.

The proton acceptance and resolution of an experiment with detectors at the TOTEM RP220 location and at IP3 have been studied [19] by fully tracking the protons along the LHC ring with the MAD-X [20] program using standard LHC high luminosity β^* = 0.55 optics. The detector acceptance at IP3 for protons originating from diffractive scattering in IP5 is $0.0016 \leq \xi \leq 0.004$ and $0.0016 \leq \xi \leq 0.01$ for protons turning clockwise ("B1") and anticlockwise ("B2") in the LHC, respectively. This complements well the $0.02 \leq \xi \leq 0.20$ acceptance of RP220 for both beams. The IP3 acceptance for B1 protons is reduced since these protons have to pass through the aperture limiting betatron cleaning insertion at IP7. In case of central diffraction [15], this gives access to diffractive masses from 25 GeV to 2.8 TeV as shown in Fig. 5 (left). A ξ resolution $\leq 10^{-4}$ for protons detected at IP3 is obtained in the study implying that the resolution will be limited by the beam energy spread of $1.1 \cdot 10^{-4}$. Combined with protons detected at RP220, this leads to a relative mass resolution ranging between 1 and 5 % for central diffractive events over the whole mass range as shown in Fig. 5 (right). The mass resolution depends on the ratio ξ_1/ξ_2, where ξ_1 and ξ_2 are the ξ value of the clockwise and anticlockwise turning proton, respectively.

The protons detectors at IP3 would in fact see diffractive protons with similar acceptance from all LHC interaction points (IP) and could by measuring the difference of the proton arrival times determine at which IP the event occurred. This way the low mass central diffractive spectrum could be determined independently for each IP and be used as means of an inter-experimental luminosity calibration.

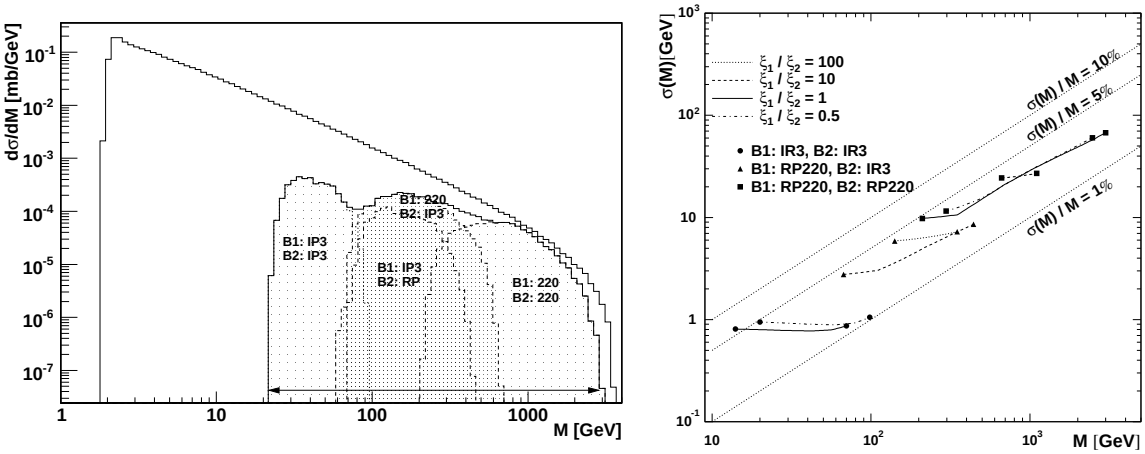

Fig. 5: Left: predicted diffractive mass distribution for central diffractive events with events indicated that have both protons within the acceptance of different combinations of the IP3 and RP220 detectors. Right: mass resolution for central diffractive events for some ξ_1/ξ_2 ratios. B1 and B2 refers to protons turning clockwise and anticlockwise, respectively, in the LHC.

6 Summary

The TOTEM physics program aims at a deeper understanding of the proton structure by measuring the total and elastic pp cross sections and by studying a comprehensive menu of diffractive processes. TOTEM will run under all LHC beam conditions to maximize the coverage of the studied processes. Special high β^* runs are needed for the total pp cross section measurement with the luminosity-independent method and for soft diffraction with large forward proton acceptances. At an early stage with non-optimal beams and an intermediate β^*, TOTEM will measure σ_{tot} with a 4–5 % precision. With improved understanding of the beams and $\beta^* = 1540\,\mathrm{m}$, a precision on σ_{tot} of 1% should be achievable. The measurement of elastic scattering in the range $10^{-3} < |t| < 10$ GeV^2 will allow to distinguish among a wide range of predictions according to current theoretical models. Early low β^* runs will provide first opportunities for measurements of soft diffraction for masses above $\sim$250 GeV and $\sim$2 TeV in central and single diffractive events, respectively, as well as studies of the forward charged multiplicity in inelastic pp events. Having proton detectors at IP3 would highly extend the diffractive mass acceptance of TOTEM for high luminosity runs giving e.g. a continuous mass acceptance from 25 GeV to 2.8 TeV for central diffractive events. Finally, hard diffraction as well as many forward physics subject will be studied in collaboration with CMS taking advantage of the unprecedented rapidity coverage for charged and neutral particles.

References

[1] TOTEM Coll., V. Berardi et al.: TOTEM: Technical Design Report CERN-LHCC-**2004-002;** addendum: CERN-LHCC-**2004-020** (2004).

[2] CMS and TOTEM diffractive and forward working group: Prospects for Diffractive and Forward Physics at the LHC, CERN-LHCC-**2006-039**, CMS Note-**2007/002,** TOTEM Note **06-5** (2006).

[3] TOTEM Coll., G. Anelli et al.: The TOTEM experiment at the CERN Large Hadron Collider, JINST **3**, S08007 (2008).

[4] H. Niewiadomski: Reconstruction of proton tracks in the TOTEM Roman Pot detectors at the LHC, PhD Thesis, University of Manchester, U.K. (2008).

[5] M. M. Islam, R. J. Luddy and A. V. Prokudin, Int. J. Mod. Phys. **A 21**, S08007 (2006).

[6] C. Bourrely, J. Soffer, and T. T. Wu, Eur. Phys. J. **C 28**, 97 (2003).

[7] V. A. Petrov, E. Predazzi and A. Prokudin, Eur. Phys. J. **C 28**, 525 (2003).

[8] M. M. Block, E. M. Gregores, F. Halzen and G. Pancheri, Phys. Rev. **D 60**, 054024 (1999).

[9] CDF Coll., F. Abe et al., Phys. Rev. D **50**, 5550 (1994).

[10] E811 Coll., C. Avila et al., Phys. Lett. B **445**, 419 (1999).

[11] CDF Coll., F. Abe et al., Phys. Rev. D **50**, 5535 (1994).

[12] CDF Coll., T. Affolder et al., Phys. Rev. Lett. **87**, 141802 (2001).

[13] M.G. Ryskin, A.D. Martin and V.A. Khoze, Eur. Phys. J. **C54**, 199 (2008).

[14] E. Gotsman, E. Levin, U. Maor and J.S. Miller, TAUP-2878-08; arXiv:0805.2799 [hep-ph] (2008).

[15] R. Engel: PHOJET manual (program version 1.05c, June 1996), available from: http://www-ik.fzk.de/∼engel/phojet.html (LHC predictions are based on program version 1.12).

[16] COMPETE Coll., J.R. Cudell et al., Phys. Rev. Lett. **89**, 201801 (2002).

[17] TOTEM Coll., G. Anelli et al.: TOTEM physics, Proceedings of 17th Rencontre de Blois: 11th International Conference on Elastic and Diffractive Scattering, Château de Blois, France (2005).

[18] V.A. Khoze, A.D. Martin and M.G. Ryskin, Eur. Phys. J. **C23**, 311 (2002).

[19] K. Eggert on behalf of TOTEM Coll.: TOTEM, a different LHC experiment, CERN seminar February 2008, http://indico.cern.ch/conferenceDisplay.py?confId=29356; paper in preparation.

[20] The MAD-X program, Methodical Accelerator Design, http://www.cern.ch/mad.

The ALFA Detector and Physics Program

K. Hiller [a], *H. Stenzel* [b]
[a] DESY Zeuthen, Platanenallee 6, D-15738 Zeuthen, Germany
[b] University of Giessen, II. Physikalisches Institut, Heinrich-Buff Ring 16, D-35444 Giessen, Germany

Abstract
The ALFA detector is dedicated to obtaining a precise absolute calibration for luminosity measurements at the ATLAS experiment. Fiber trackers are installed in Roman Pots at a distance of 240m from the interaction point on both sides of the detector. In special runs with high β^* optics the pots approach the beam to distances of order a millimeter, allowing elastically scattered protons to be detected at extremely small angles. Extracting the differential cross section in the corresponding Coulomb-Nuclear interference kinematic region as a function of the squared four-momentum transfer t leads to luminosity measurements with a precision of 3%.

1 Introduction

The luminosity relates event rates to cross sections - the main observable quantity of all accelerator-based experiments. Its value is defined by the machine parameters: beam currents, transverse beam widths and revolution frequency. A good measurement of the luminosity is required to ensure precise cross section measurements and to give fast feedback for beam tuning and monitoring for optimal operation of the LHC.

ATLAS follows a number of different approaches to measure the luminosity [1]. The first method is based on direct calculation based on the knowledge of LHC machine parameters. A precision of around 20% - 30% is envisaged at the LHC startup. After some years of dedicated machine studies, 5% accuracy seems to be the end point of this method. The second type of luminosity measurement involves counting the rate of a process with a well-known cross-section. For example, the production of lepton pairs via the QED two-photon process can be precisely calculated and used as in luminosity measurements. However the QED cross sections are small and resulting event rates are at the statistical limit, especially in the low luminosity phase. The QCD production of W and Z bosons is a more promising process with a large cross section and a clean signature. It is one of the best known QCD cross sections and the main uncertainty comes from the PDFs. Including the experimental uncertainties a total luminosity error of 10% seems feasible. The PDFs may become more contrained when LHC data are available and the luminosity error from this method might reach 5% after some years of LHC running.

The third method is related to the elastic proton scattering process. This rate is linked to the total interaction rate through the optical theorem and will provide several additional options to determine the luminosity. The standard approach combines the total interaction rate R_{tot} and

the forward elastic rate $R_{el}(t=0)$ via the optical theorem and determines the luminosity as

$$L = \frac{1}{16\pi} \frac{R_{tot}^2(1+\rho^2)}{dR_{el}/dt(t=0)} \; .$$

Here ρ is the ratio of the real to the imaginary part of the elastic forward scattering amplitude, which lies in the range 0.13-0.14 at LHC energies [2]. Small-angle elastic scattering has traditionally been used to get a handle on the luminosity calibration at hadron colliders via equation 1. This generally requires a precise knowledge of the inelastic rate over the full rapidity range, in contrast to the limited rapidity coverage of real detectors such as ATLAS. However, if very small scattering angles, corresponding to very small momentum transfers t, can be covered, the cross section becomes sensitive to the electromagnetic scattering. Via the precisely known Coulomb interaction, a calibration can then be performed without measurement of the inelastic rate. This option is pursued by the ATLAS collaboration, for which the ALFA detector [3] is currently under construction. In order to reach the Coulomb-Nuclear interference region where the electromagnetic and strong interaction amplitudes are of similar size, scattering angles of about 3.5 μrad must be covered, corresponding to $|t| = 0.00065$ GeV^2. To reach the Coulomb region is a very challenging task, since the tracking detectors have to be moved to a very close distance of about 1.5 mm from the circulating beams. If this can be managed, a luminosity error of 3% seems to be feasible.

Some details of tracking detectors in the Roman Pots, the Monte Carlo estimates for the luminosity determination and the present status of the main ALFA components are described in the next chapters. This can only be achieved with special beam optics with a very high β^*=2625m yielding a parallel-to-point focusing and a low normalised emittance $\epsilon_N = 1\mu$rad m. In addition, the detector has to be operated very close to the beam at a distance of about 1.5 mm, corresponding to 12 σ of the beam width. Dedicated runs are foreseen at low luminosity with these special beam conditions for measurement with ALFA, which can accumulate in 100 hours of beam time sufficient statistics to achieve a luminosity calibration with an accuracy of 3%, including systematic uncertainties [6].

2 The ALFA detector

Roman Pot stations equipped with two vertically movable Roman Pots housing the detectors will be installed in the LHC on both sides of the interaction point at a distance of 240 m. There will be two stations separated by 4 m on each side, thus in total 8 pots will be instrumented with ALFA detectors. Figure 1 shows an ALFA Roman Pot station in relation to the beampipe. Each unit consists of the Pots housing the detectors and the support and moving mechanics such as bellows, roller screws, motor drives, positioning sensors etc. To minimize the amount of material in front of the detectors the pots have thin 80μm windows. The interior of the Pot will be in a secondary vacuum of about 1 mbar to avoid deformations induced by the LHC primary vacuum. The 4m separation of the pairs of pots on either side of the interaction point ensures precise tracking. The positioning precision due to the Pot moving system is expected to be 10μm. The position of the Pot in respect to the circulating beam will be determined by LVDTs with a precision of $\pm$ 20μm. The Roman Pots are considered as machine elements and their movement is included in the LHC collimator control system.

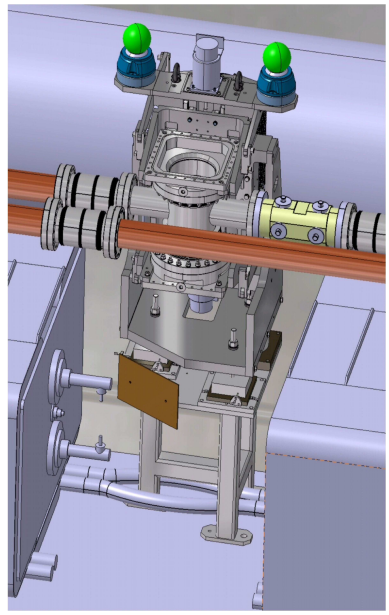

Fig. 1: Schematic drawing of the ALFA Roman Pot station.

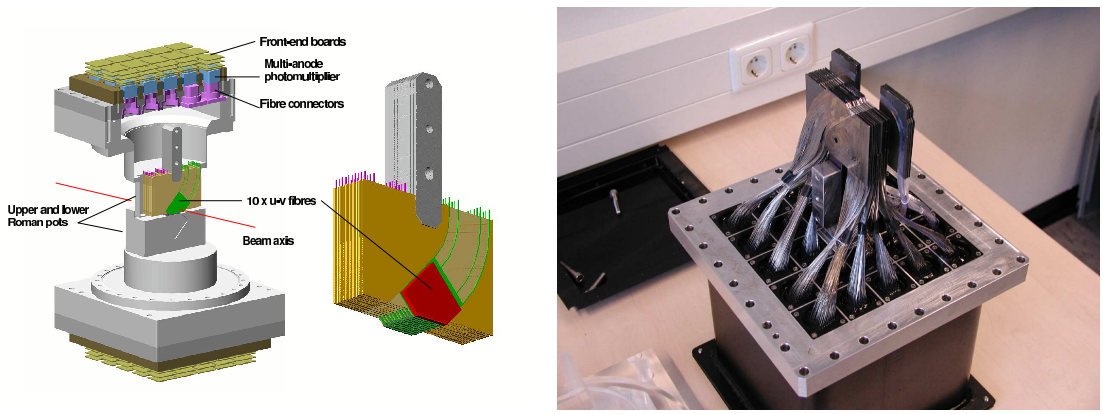

Fig. 2: Conceptual design of the ALFA tracker with multi-layer fiber detectors inserted and a photograph of a full-size prototype.

The design of the ALFA tracker is shown in Fig. 2. The tracking detectors are multi-layer scintillating fiber structures as illustrated in fig. 2. Layers of two times 64 KURARAY SCSF-78 single cladding fibers of square 0.5×0.5 mm^2 cross section are glued in stereo geometry on a Titanium substrate. Ten of such substrates, staggered by 71μm, are precisely assembled on a support structure. The ultimate resolution of such a detector arrangement is 14μm and in previous test beam measurements values of 25μm have been achieved [4, 5]. The spacing of the planes in beam direction is 2.5mm results in an inclination of the staggered fibers by 28mrad relative to the beam axis. Hence not to benefit from the staggering the detector axis should be

aligned with the beam axis with an precision around 3mrad.

As visible in fig. 2 the most fiber ends are cut at the lower edge under 45°. Apart from these cuts the fibers are aluminized to increase the light yield. For fibers with 90° ends the gain is about 75%, while for 45° ends about 50% of the light undergoes a reflection at the uncoated edge. The fibers are routed over 25cm distance to a connector flange. All 64 fibers of a plane are grouped into a 8×8 matrix to be coupled to the photo-cathode of the Multi Anode Photo-Multiplier Tube (MAPMT) Hamamatsu H7546B. This device has a gain around 10^6 at the maximum voltage of 1000V. The cross talk between adjacent channels is at the level of 2-3 %.

To ensure an exact positioning of the fiber detectors in respect to the LHC beam, which can vary from fill to fill, each Roman Pot is equipped with a pair of overlap detectors. These detectors move with the Pots and measure the relative vertical positions of the upper and lower tracking detectors. The measurement principle is the common tracking of halo particles in both overlap detectors. These detectors consist of 3 planes of 30 horizontally arranged fibers staggered by 166μm to each other. The achievable precision depends mainly on the statistics of accumulated halo tracks. A positioning precision of 10μm of the upper and lower detectors are needed to keep the contribution to the luminosity error below 2%. All 180 fibers of the overlap detectors in a Pot are read out by 3 MAPMTs H7546B.

Both main and overlap detectors are equipped with corresponding trigger counters which cover the active area. For the main detectors two trigger tiles of fast plastic scintillator BICRON BC-408 are used in coincidence. The overlap detectors are covered by a single trigger tile. The light signals from the scintillators are guided by bundles of clear 0.5mm round double cladding KURARAY fibers to the photo-multipliers. To amplify the trigger signals 4 single channels photo-multipliers R7401P with Bialkali photo-cathode or the new type R9880U with Super-Bialkali photo-cathode and enhanced quantum efficiency around 35% are foreseen.

A proton traversing a 0.5 mm scintillating fiber gives on average a light signal of 4 photo-electrons. The MAPMT H7546B with a typical gain of 0.5 - 1.0×10^6 leading therefore to signals charge of 0.3-0.6 pC at the amplifier input. The readout electronics is a stack of printed circuit boards, named PMF, located on top of each MAPMT. The MAPMT signals are fed into the MAROC2 readout chip, which performs amplification and shaping. The signals are compared to a threshold and the resulting digital data serially transmitted to the motherboard. The motherboard serialize the data from 23 PMF units and send them via an optical link to the central ATLAS data acquisition system.

3 The Measurement Principle

The detectors have to approach the circulating beams between 1 and 2mm distance, which requires well collimated beams under special optics. This optics at high β^* = 2625m and 90° phase advance yields a parallel-to-point focusing i.e. a linear relation between the track position in the fiber detectors and the scattering angle at the IP.

The expected detector performance was estimated by Monte Carlo simulation of elastic pp-scattering [6]. A modified version of PHYTIA6.4, to include the Coulomb-term and the real part of the nuclear elastic scattering amplitude, plus the beam transport program MADX were used for this purpose [7,8]. Accepted events are requested to fulfill the left-right trigger condition

and have a space point reconstructed in 4 fiber detectors. The resulting hit pattern in the ALFA fiber detectors is shown in fig. 3.

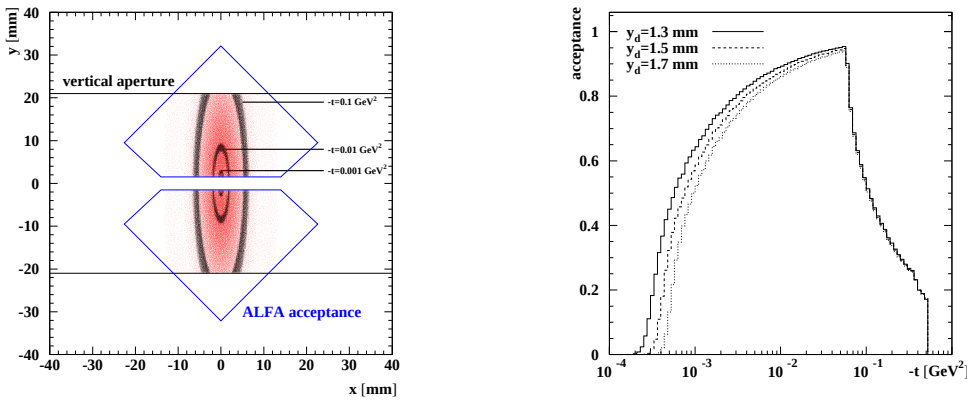

Fig. 3: Hit pattern of protons and acceptance in dependence on t.

Also shown in fig. 3 is the geometrical acceptance in dependence on t. The distance of closest approach to the beam centers is assumed between 10 and 20 σ_{beam}, depending on the halo conditions. For a distance of 1.5 mm about 67% of all events in the t-range 0.5 10^{-5} to 0.5 GeV^2 are accepted.

The absolute luminosity is obtained from a fit of the elastic scattering cross section formula to the reconstructed and corrected t-spectrum. Apart from the luminosity L, the nuclear slope b, the ratio of real and imaginary scattering amplitude ρ and the total cross section σ_{tot} are determined.

$$\frac{dN}{dt} = \pi L \left| -\frac{2\alpha}{|t|} + \frac{\sigma_{tot}}{4\pi}(i+\rho)e^{-b|t|/2} \right|^2$$

Out of 10 million generated elastic events 6.6 million with an acceptance above 50% are used for the luminosity fit. The simulated and reconstructed t-spectrum with a linear scale for the rate is shown in fig. 4. The large total cross section ensures the collection of enough events to keep the statistical error small. For 6.6 million events the statistical errors of the luminosity and the total cross section are 1.8% and 0.9%, respectively. Some systematic uncertainties which are not taken into account in the fit procedure are: the beam divergence and crossing angle at the IP $(0.3\%, 0.2\%)$, the uncertainties in the knowledge of the optical functions and phase advance to convert the hit points into a scattering angle at the IP $(0.6\%, 1.0\%)$, detector resolution and alignment $(0.3\%, 1.3\%)$, and finally statistical fluctuations in the background subtraction (1.2%). These values combined with the statistical error result in a total error of 3% [6].

Based on this Monte Carlo study about 100 hours running at a low luminosity of $1.0\times 10^{27} cm^{-2} s^{-1}$ are necessary to collect the used data sample [3].

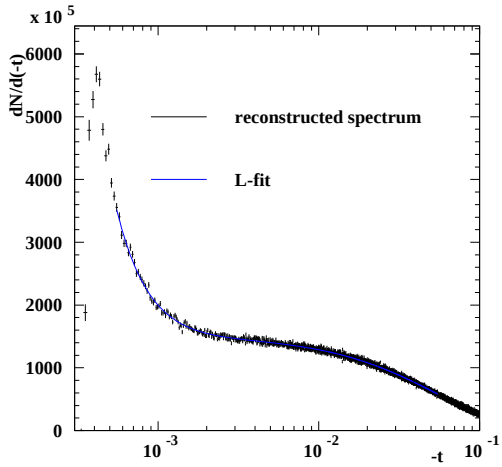

Fig. 4: Reconstructed t-spectrum for detectors placed at 1.5 mm distance.

4 The Status of ALFA Components

This chapter gives a brief review about the production status of the main components in summer 2008: the fiber detectors, the electronics, and the mechanics.

To enlarge the light yield and to reduce the optical cross talk all fibers are coated by a thin Aluminum layer. The gain is about 75% for fibers cutted by 90° and 50% for the 45° fibers. The far end of the fibers are coated by sputtering technology in LIP Lisbon, followed by the side coating via vacuum evaporation at CERN. All fibers for detector production can be ready at the end of 2008. The fibers are glued on precise Titanium substrates which were produced by electro-erosion in HU Berlin. These substrates have precision holes and edges to ensure the staggering of the fiber layers. This production step is finished and the 3D measurements confirmed an accuracy below 10μm. In the next step the fiber detectors are produced by capillary gluing at JLU Giessen. After that the assembling of the complete detector insert is performed, the routing of all fibers to the MAPMT connectors, the gluing and milling of the connectors. A prototype-1 detector has been produced for installation issues in the tight environment of the Roman pot. Another prototype-2 detector is ready for use in a test beam measurement in summer 2008. To benefit from the staggering all fiber positions are measured by microscope at DESY Hamburg. The fiber positions are described by straight lines, which are stored in a data base and used for the track reconstruction. The precise positioning is limited due to some inherent conditions: the RMS of the fiber diameter, defects from the Aluminum coating, the precision of approaching the edges due to dust particles and the bending force on the fibers, and more. In some substrates of the prototype-2 deviations of about 100μm from the nominal staggering have been observed. This results in a reduced resolution of 40μm, while 25μm has been measured in the 2006 test beam campaign for a detector with 16 fibers per layer [4, 5]. Presently we investigate possible reasons for the staggering deviations to ensure that all detectors have similar quality close to the

demands of the design. The detector insert is completed by corresponding trigger substrates. The essential demand for these substrates is a good light yield to guarantee 100% trigger efficiency. The test beam campaign 2007 in a DESY 6 GeV electron beam has shown a sufficient light yield between 30 and 40 photo-electrons using clear fiber bundles as flexible light guides. The fibres are coupled by optical connectors through the vacuum flange to multi-anode PMTs (MAPMT) with 64 pixels. The MAPMTs are connected through a stack of PCBs to the MAROC read-out chip, which performs amplification, shaping, gain equalisation and discrimination of the signals. Signals from MAROC are further processed by a FPGA which samples the signals at 40 MHz, stores the data for the L1 latency and transmits the buffer serially to the motherboard in case of a positive trigger signal. All signals of a single ALFA detector with 23 MAPMTs are collected by the motherboard which transmits the signals via optical link to the ATLAS DAQ. The connection to the central ATLAS trigger processor is also done via optical link, while the control of the motherboard and connected components is achieved by an ELMB module. The scintillation signals from the individual fibers are amplified in the 64 channel MAPMTs H7546B. The gain and uniformity measurements to correct differences in the subsequent front-end electronics are performed for each device at DESY Hamburg. The front-end electronics consists of a so-called PMFs which are 3-layer-stacks of PCBs close to the MAPMTs. Each PMF contains a MAROC2 read-out chip, which performs amplification, shaping, gain equalisation and discrimination of the signals. Signals from MAROC2 are further processed by a FPGA which samples the signals at 40 MHz, stores the data for the L1 latency and transmits the buffer serially to the motherboard. For the test beam campaign with prototype-2 32 PMFs were produced in LAL Orsay. The S-curve measurements have shown are very good quality in terms of homogeneity, linearity and sensitivity to expected fiber light signal of 4 to 5 photo-electrons.

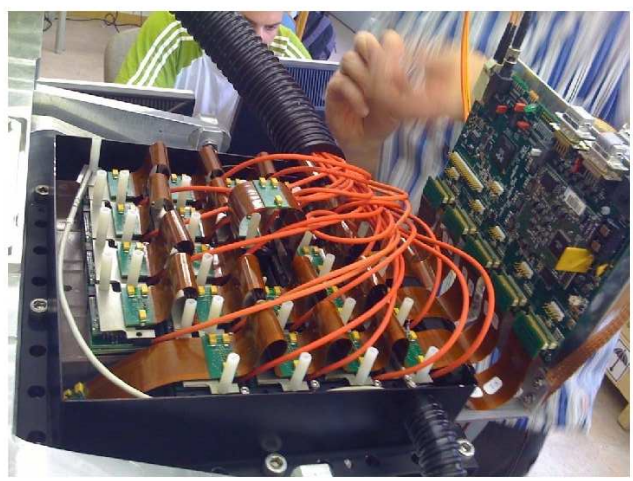

Fig. 5: Front-end electronics: Kapton cables each connected to 5 PMFs sitting on top of the MAPMTs.

The Roman Pot mechanics has to fulfill high demands on precision and positioning reproducibility. Mechanical and optical position measurements have been performed with a pre-

prototype. Some front-back and left-right distortions up to 200μm have been observed in extreme positions. However their contribution to the total luminosity error is uncritical below 0.2%. In addition the stiffness of the slides keeping the pots have been improved replacing the Aluminum by Steel slides. The mechanical components for all stations received from Prague and are now assembled at CERN.

In summer 2008 a full Roman Pot was tested in the CERN test beam H8. A telescope of silicon strip detectors has been used for tracking. The data analysis is underway and will be published as internal ATLAS note. The schedule of the ALFA installation depends on the LHC machine status. A possible scenario is the installation of the mechanics in spring 2009. The pots itself are machined at CERN and should be installed together with the station mechanics to avoid another break of the LHC vacuum. The production of fiber detectors could be finished 2009 and their installation completed in the shut down 2009/2010.

References

[1] ATLAS Coll., ATLAS Detector and Physics Performance Technical Design Report, ATLAS TDR 014, CERN/LHCC/1999-014, 1999.

[2] UA4 Coll., D.Bernard et al., Phys.Lett. 89 (2002) 1801.

[3] ATLAS Coll., ATLAS Forward Detectors for Measurement of Elastic Scattering and Luminosity, ATLAS TDR 018, CERN/LHCC/2008-004, 2008.

[4] S.Ask et al., Nucl.Instr. and Meth. A568 (2006) 588.

[5] F.Anghinolfi et al., JINST 2, 07004, 2007.

[6] H. Stenzel, Liminosity Calibration from Elastic Scattering, ATL-LUM-PUB-2007-001, 2007.

[7] T.Sjostrand et al., PHYTIA 6.4 Physics and Manual, JHE05 026, 2006.

[8] MADX homepage: http;//madx.web.cern.ch/madx.

Diffractive Physics in ALICE

R. Schicker
Physikalisches Inst., Philosophenweg 12, 69120 Heidelberg

Abstract
The ALICE detector at the Large Hadron Collider (LHC) consists of a central barrel, a muon spectrometer and neutron calorimeters at 0^o. Additional detectors for event classification and for trigger purposes are placed on both sides of the central barrel. Such a geometry allows the definition of a diffractive gap trigger by requiring no activity in the additional detectors. I discuss some physics topics which become accessible by this gap trigger.

1 The ALICE Experiment

The ALICE experiment is presently being commissioned at the Large Hadron Collider (LHC) [1, 2]. The ALICE experiment consists of a central barrel covering the pseudorapidity range $-0.9 < \eta < 0.9$ and a muon spectrometer in the range $-4.0 < \eta < -2.4$. Additional detectors for trigger purposes and for event classification exist in the range $-4.0 < \eta < 5.0$. The ALICE physics program foresees data taking in pp and PbPb collisions at luminosities up to $\mathcal{L}$ = $5 \times 10^{30} cm^{-2} s^{-1}$ and $\mathcal{L}$ = $10^{27} cm^{-2} s^{-1}$, respectively. An asymmetric system pPb will be measured at a luminosity of $\mathcal{L}$ = $10^{29} cm^{-2} s^{-1}$.

1.1 The ALICE Central Barrel

The detectors in the ALICE central barrel track and identify hadrons, electrons and photons in the pseudorapidity range $-0.9 < \eta < 0.9$. The magnetic field strength of 0.5 T allows the measurement of tracks from very low transverse momenta of about 100 MeV/c to fairly high values of about 100 GeV/c. The tracking detectors are designed to reconstruct secondary vertices resulting from decays of hyperons, D and B mesons. The granularity of the central barrel detectors is chosen such that particle tracking and identification can be achieved in a high multiplicity environment of up to 8000 particles per unit of rapidity. The main detector systems for these tasks are the Inner Tracking System, the Time Projection Chamber, the Transition Radiation Detector and the Time of Flight array. These systems cover the full azimuthal angle within the pseudorapidity range $-0.9 < \eta < 0.9$ and are described below. Additional detectors with partial coverage of the central barrel are a PHOton Spectrometer (PHOS), an electromagnetic calorimeter (EMCAL) and a High-Momentum Particle Identification Detector (HMPID).

1.1.1 The Inner Tracking System

The Inner Tracking System (ITS) consists of six cylindrical layers of silicon detectors at radii from 4 cm to 44 cm. The minimum radius is determined by the beam pipe dimensions whereas the maximum radius chosen is determined by the necessity of efficient track matching with the outer detectors in the central barrel. The innermost layer extends over the range $-2 < \eta < 2$

such that there is continous overlap with event classification detectors outside of the central barrel. Due to the high particle density of up to 80 particles/cm^2 and in order to achieve the required tracking resolution, pixel detectors have been chosen for the first two layers. Silicon drift detectors are located in the middle two layers whereas double sided silicon strip detectors are in the outer two layers.

1.1.2 The Time Projection Chamber

The Time Projection Chamber (TPC) is the main tracking detector in the central barrel. The inner and outer radii of the active volume are 84.5 cm and 246.6 cm, respectively. The full radial track length is measured in the pseudorapidity range $-0.9 < \eta < 0.9$ whereas tracks with at least one third of nominal radial length are covered in the pseudorapidity range $-1.5 < \eta < 1.5$. Particle identification is achieved by measuring the specific ionization loss. The chosen geometry results in a drift time of about 90 μs. This long drift time is the factor limiting the proton-proton luminosity to the value mentioned above.

1.1.3 The Transition Radiation Detector

The principal goal of the Transition Radiation Detector (TRD) is to provide electron identification in the momentum range larger than 1 GeV/c. In this range, the electron identification by energy loss in the TPC is no longer sufficient. Since the TRD is a fast tracker, the TRD information can be used for an efficient trigger on high transverse momentum electrons. In addition, the position information from the TRD system improves the tracking performance of the central barrel.

1.1.4 The Time of Flight Detector

The Time-Of-Flight (TOF) array is located at a radial distance from 3.7 m to 4.0 m. The TOF information is used for particle identification in the range 0.2 GeV/c $< p_T <$ 2.5 GeV/c. For this detector, the Multi-gap Resistive-Plate (MRPC) technology was chosen. A strip with an active area of 120x7.4 cm^2 consists of pads of 3.5 cm length and 2.5 cm width.

1.1.5 The Central Barrel Performance

The ITS, TPC and TRD detectors described above are the main tracking detectors in the central barrel. With the information from these detectors, particles with momenta as low as 100 MeV/c can be tracked.

Fig.1 shows the transverse momentum resolution as expected from simulations. The TPC alone achieves a resolution of approximately 3% at a transverse momentum of p_T = 10 GeV/c. Adding the information from ITS and TRD on the inner and outer side, respectively, improves the resolution considerably due to the increased leverage. The combined transverse momentum resolution from the ITS, TPC and TRD detector is expected to be about 3% at a transverse momentum of p_T = 100 GeV/c.

Particle identification is achieved in the central barrel by different methods. The specific energy loss is measured by the TPC, the TRD and the strip and drift detectors of the ITS. Fig.2 shows the combined particle identification capability by dE/dx measurement as a function of

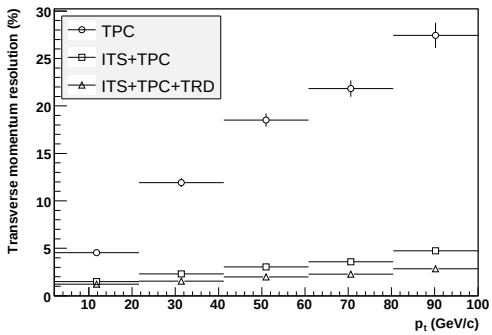

Fig. 1: Central barrel tracking resolution

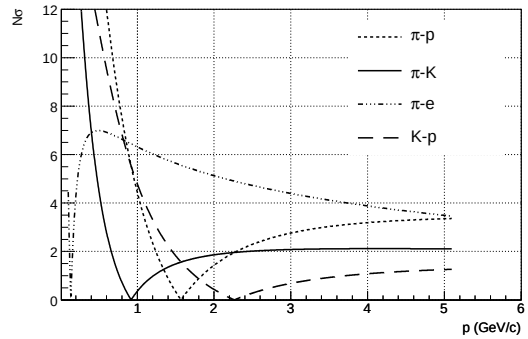

Fig. 2: Particle identification by dE/dx measurement

momentum. The separation of different particle species is shown in units of the resolution of the dE/dx measurement. The electron-pion separation at high momenta is significantly improved by the information of the TRD system.

1.2 The ALICE Zero Degree Neutron Calorimeter

The Zero Degree Neutron Calorimeters (ZDC) are placed on both sides of the interaction point at a distance of 116 m [3]. The ZDC information can be used to select different diffractive topologies. Events of the type $pp \rightarrow ppX$ do not deposit energy in these calorimeters, events $pp \rightarrow pN^*X$ will have energy in one of the calorimeters whereas events $pp \rightarrow N^*N^*X$ will have energy deposited in both calorimeters. Here, X denotes a centrally produced diffractive state from which the diffractive L0 trigger is derived as described below.

2 The ALICE diffractive gap trigger

Additional detectors for event classification and trigger purposes are located on both sides of the ALICE central barrel. First, an array of scintillator detectors (V0) is placed on both sides of the central barrel. These arrays are labeled V0A and V0C on the two sides, respectively. Each of these arrays covers a pseudorapidity interval of about two units with a fourfold segmentation of half a unit. The azimuthal coverage is divided into eight segments of 45^0 degrees hence each array is composed of 32 individual counters. Second, a Forward Multiplicity Detector (FMD) is located on both sides of the central barrel. The pseudorapidity coverage of this detector is $-3.4 < \eta < -1.7$ and $1.7 < \eta < 5.1$, respectively.

Fig.3 shows the pseudorapidity coverage of the detector systems described above. The geometry of the ALICE central barrel in conjunction with the additional detectors V0 and FMD is well suited for the definition of a rapidity gap trigger. The ALICE trigger system consists of a Central Trigger Processor (CTP) and is designed as a multi-level scheme with L0,L1 and L2 levels and a high-level trigger (HLT). A rapidity gap trigger can be defined by the requirement of signals coming from the central barrel detectors while V0 and FMD not showing any activity. Such a scheme requires a trigger signal from within the central barrel for L0 decision. The pixel detector of the ITS system is suited for delivering such a signal [4]. Alternatively, this L0 signal can be derived from the TOF detector.

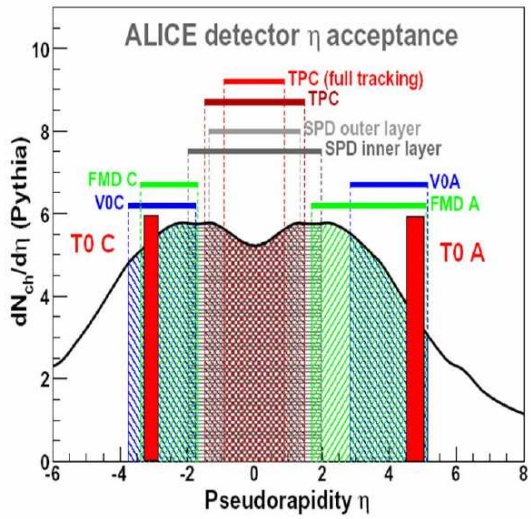

Fig. 3: Pseudorapidity coverage of trigger detectors and of detectors in central barrel

The high level trigger HLT has access to the information of all the detectors shown in Fig.3 and will hence be able to select events with rapidity gaps in the range $-4 < \eta < -1$ and $1 < \eta < 5$. These gaps extend over seven units of pseudorapidity and are hence expected to suppress minimum bias inelastic events by many orders of magnitude.

In addition to the scheme described above, the ALICE diffractive L0 trigger signal can be generated from the Neutron ZDC if no central state is present in the reaction. A L0 signal from ZDC does, however, not arrive at the CTP within the standard L0 time window. A L0 trigger from ZDC is therefore only possible during special data taking runs for which the standard L0 time limit is extended. The possibility of such data taking is currently under discussion.

3 ALICE diffractive physics

The tracking capabilities at very low transverse momenta in conjunction with the excellent particle identification make ALICE an unique facility at LHC to pursue a long term physics program of diffractive physics. The low luminosity of ALICE as compared to the other LHC experiments restricts the ALICE physics program to reactions with cross section at a level of a few nb per unit of rapidity.

Fig.4 shows the transverse momentum acceptance of the four main LHC experiments. Not shown in this figure is the acceptance of the TOTEM experiment which has a physics program of measurements of total cross section, elastic scattering and soft diffraction [5]. The acceptance of the TOTEM telescopes is in the range of $3.1 < |\eta| < 4.7$ and $5.3 < |\eta| < 6.5$. The CMS transverse momentum acceptance of about 1 GeV/c shown in Fig.4 represents a nominal value. The CMS analysis framework foresees the reconstruction of a few selected data samples to values as low as 0.2 GeV/c [6].

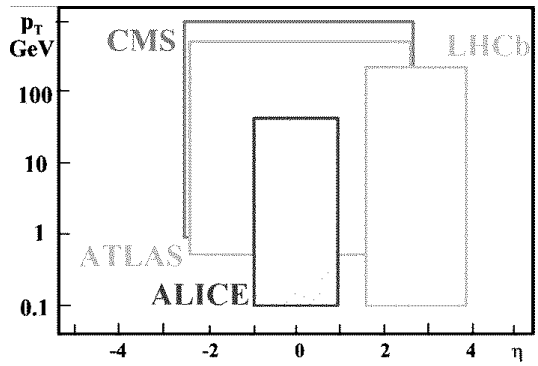

Fig. 4: Rapidity and transverse momentum acceptance of the LHC experiments

4 Signatures of the Pomeron

The geometry of the ALICE experiment is suited for measuring a centrally produced diffractive state with a rapidity gap on either side. Such a topology can result, among other, from double Pomeron exchange with subsequent hadronization of the central state. It is expected that the secondaries from Pomeron-Pomeron fusion events show markedly different characteristics as compared to secondaries from inelastic minimum bias events.

First, it is expected that the production cross section of glueball states in Pomeron fusion is larger as compared to inelastic minimum bias events. It will therefore be interesting to study the resonances produced in the central region when two rapidity gaps are required [7].

Second, the slope α' of the Pomeron trajectory is rather small: $\alpha' \sim 0.25$ GeV^{-2} in DL fit and $\alpha' \sim 0.1$ GeV^{-2} in vector meson production at HERA [8]. These values of α' in conjunction with the small t-slope (< 1 GeV^{-2}) of the triple Pomeron vertex indicate that the mean transverse momentum k_t in the Pomeron wave function is relatively large $\alpha' \sim 1/k_t^2$, most probably $k_t > 1$ GeV. The transverse momenta of secondaries produced in Pomeron-Pomeron interactions are of the order of this k_t. Thus the mean transverse momenta of secondaries produced in Pomeron-Pomeron fusion is expected to be larger as compared to inelastic minimum bias events.

Third, the large k_t described above corresponds to a large effective temperature. A suppression of strange quark production is not expected. Hence the K/π ratio is expected to be enhanced in Pomeron-Pomeron fusion as compared to inelastic minimum bias events [9]. Similarly, the η/π and η'/π ratios are expected to be enhanced due to the hidden strangeness content and due to the gluon components in the Fock states of η, η'.

5 Signatures of Odderon

The Odderon was first postulated in 1973 and is represented by color singlet exchange with negative C-parity [10]. Due to its negative C-parity, Odderon exchange can lead to differences between particle-particle and particle-antiparticle scattering. In QCD, the Odderon can be a three gluon object in a symmetric color state. Due to the third gluon involved in the exchange, a suppression by the coupling α_s is expected as compared to the two gluon Pomeron exchange.

However, finding experimental signatures of the Odderon exchange has so far turned out to be extremely difficult [11]. A continued non-observation of Odderon signatures would put considerable doubt on the formulation of high energy scattering by gluon exchange [12]. The best evidence so far for Odderon exchange was established as a difference between the differential cross sections for elastic pp and $p\bar{p}$ scattering at $\sqrt{s}$ = 53 GeV at the CERN ISR. The pp cross section displays a dip at t = -1.3 GeV^2 whereas the $p\bar{p}$ cross section levels off. Such a behaviour is typical for negative C-exchange and cannot be due to mesonic Reggeons only.

5.1 Signatures of Odderon Cross Sections

Signatures of Odderon exchanges can be looked for in exclusive reactions where the Odderon (besides the Photon) is the only possible exchange. Diffractively produced C-even states such as pseudoscalar or tensor mesons can result from Photon-Photon, Photon-Odderon and Odderon-Odderon exchange. Any excess measured beyond the well understood Photon-Photon contribution would indicate an Odderon contribution.

Diffractively produced C-odd states such as vector mesons $\phi, J/\psi, \Upsilon$ can result from Photon-Pomeron or Odderon-Pomeron exchange. Any excess beyond the Photon contribution would be indication of Odderon exchange.

Estimates of cross section for diffractively produced J/ψ in pp collisions at LHC energies were first given by Schäfer et al [13]. More refined calculations by Bzdak et al result in a t-integrated photon contribution of $\frac{d\sigma}{dy}\ |_{y=0} \sim 15$ nb and a t-integrated Odderon contribution of $\frac{d\sigma}{dy}\ |_{y=0} \sim 1$ nb [14]. These two numbers carry large uncertainties, the upper and lower limit of these numbers vary by about an order of magnitude. This cross section is, however, at a level where in 10^6 s of ALICE data taking the J/ψ can be measured in its e^+e^- decay channel at a level of 4% statistical uncertainty.

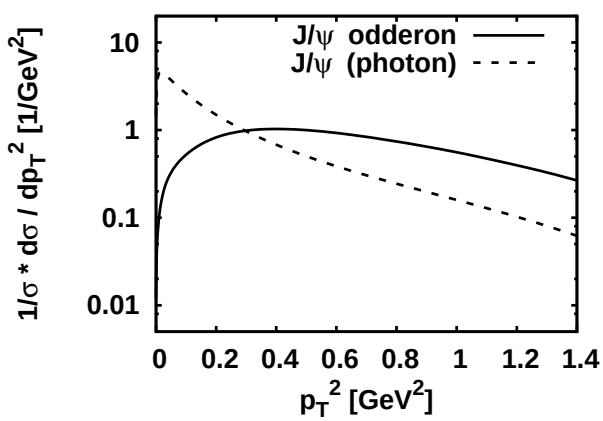

Fig. 5: The J/ψ transverse momentum distribution for the photon and Odderon contributions

Due to the different t-dependence, the Photon and Odderon contribution result in different transverse momentum distribution p_T of the J/ψ. The photon and Odderon contributions

are shown in Fig.5 by the dotted and solid lines, respectively. A careful transverse momentum analysis of the J/ψ might therefore allow to disentangle the Odderon contribution.

5.2 Signatures of Odderon Interference Effects

If the diffractively produced final state is not an eigenstate of C-parity, then interference effects between photon-Pomeron and photon-Odderon amplitudes can be analyzed.

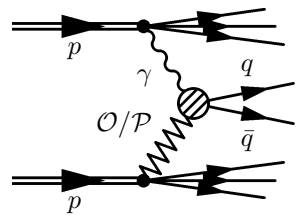

Fig. 6: photon-Pomeron and photon-Odderon amplitudes

Fig.6 shows the photon-Pomeron and the photon-Odderon amplitudes for $q\bar{q}$ production. A study of open charm diffractive photoproduction estimates the asymmetry in fractional energy to be on the order of 15% [15]. The forward-backward charge asymmetry in diffractive production of pion pairs is calculated to be on the order of 10% for pair masses in the range $1\,GeV/c^2 < m_{\pi+\pi-} < 1.3\,GeV/c^2$ [16, 17].

6 Photoproduction of heavy quarks

Diffractive reactions involve scattering on small-x gluons in the proton. The number density of gluons at given x increases with Q^2, as described by the DGLAP evolution. Here, Q^2 and x denote the kinematical parameters used in deep inelastice ep scattering. The transverse gluon density at a given Q^2 increases with decreasing x as described by the BFKL evolution equation. At some density, gluons will overlap and hence reinteract. In this regime, the gluon density saturates and the linear DGLAP and BFKL equation reach their range of applicability. A saturation scale $Q_s(x)$ is defined which represents the breakdown of the linear regime. Nonlinear effects become visible for $Q < Q_s(x)$.

Diffractive heavy quark photoproduction represents an interesting probe to look for gluon saturation effects at LHC. The inclusive cross section for $Q\bar{Q}$ photoproduction can be calculated within the dipole formalism. In this approach, the photon fluctuates into a $Q\bar{Q}$ excitation which interacts with the proton as a color dipole. The dipole cross section $\sigma(x,r)$ depends on x as well as on the transverse distance r of the $Q\bar{Q}$ pair. A study of inclusive heavy quark photoproduction in pp collisions at LHC energy has been carried out [18]. These studies arrive at differential cross sections for open charm photoproduction of $\frac{d\sigma}{dy}\mid_{y=0} \sim 1.3\ \mu$b within the collinear pQCD approach as compared to $\frac{d\sigma}{dy}\mid_{y=0} \sim 0.4\ \mu$b within the color glass condensate (CGC). The cross sections are such that open charm photoproduction seems measurable with good statistical

significance. The corresponding numbers for the cross section for bottom photoproduction are $\frac{d\sigma}{dy}\mid_{y=0} \sim 20$ nb and 10 nb, respectively.

Diffractive photoproduction is characterized by two rapidity gaps in the final state. In the dipole formalism described above, the two gluons of the color dipole interaction are in color singlet state. Diffractive heavy quark photoproduction cross sections in pp, pPb and PbPb collisions at LHC have been studied [19]. The cross sections for diffractive charm photoproduction are $\frac{d\sigma}{dy}\mid_{y=0} \sim 6$ nb in pp, $\frac{d\sigma}{dy}\mid_{y=0} \sim 9$ μb in pPb and $\frac{d\sigma}{dy}\mid_{y=0} \sim 11$ mb in PbPb collisions. The corresponding numbers for diffractive bottom photoproduction are $\frac{d\sigma}{dy}\mid_{y=0} \sim 0.014$ nb in pp, $\frac{d\sigma}{dy}\mid_{y=0} \sim 0.016$ μb in pPb and $\frac{d\sigma}{dy}\mid_{y=0} \sim 0.02$ mb in PbPb collisions.

Heavy quarks with two rapidity gaps in the final state can, however, also be produced by central exclusive production, i.e. two Pomeron fusion. The two production mechanisms have a different t-dependence. A careful analysis of the transverse momentum p_T of the $Q\bar{Q}$ pair might therefore allow to disentangle the two contributions.

Acknowledgments

I thank Otto Nachtmann and Carlo Ewerz for illuminating discussions and Leszek Motyka for preparing and communicating Figure 5.

References

[1] F. Carminati et al, ALICE Collaboration, 2004, J.Phys. G: Nucl. Part. Phys. **30** 1517

[2] B. Alessandro et al, ALICE Collaboration, 2006, J.Phys. G: Nucl. Part. Phys. **32** 1295

[3] R. Arnaldi et al, Nucl. Instr. and Meth. A **564** (2006) 235

[4] The ALICE collaboration, K. Aamodt et al., The ALICE experiment at the CERN LHC, 2008_JINST_3_S08002.

[5] K. Eggert, TOTEM a different LHC experiment, CERN colloquium, feb 21,2008

[6] D. d'Enterria et al, Addendum CMS technical design report, J. Phys. G34:2307-2455, 2007

[7] F. Close, A. Kirk, G. Schuler, Phys.Lett. B **477** (2000) 13

[8] A. Donnachie, P. Landshoff, Phys.Lett. B**595** (2004) 393

[9] T. Åkesson et al, Nucl. Phys. B **264** (1986) 154

[10] L. Lukaszuk, B. Nicolescu, Lett. Nuovo Cim. **8** (1973) 406

[11] C. Ewerz, Proceedings XII Rencontres de Blois (2005) 377

[12] S. Donnachie, G. Dosch, P.V. Landshoff, O. Nachtmann, Pomeron physics and QCD, Cambridge University Press (2002) 297

[13] A. Schäfer, L. Mankiewicz, O. Nachtmann, Phys.Lett. B **272** (1991) 419

[14] A. Bzdak, L. Motyka, L. Szymanowski, J.R. Cudell, Phys.Rev. D **75** (2007) 094023

[15] S.J. Brodsky, J. Rathsman, C. Merino, Phys.Lett. B **461** (1999) 114

[16] P. Hägler, B. Pire, L. Szymanowski, O.V. Teryaev, Phys.Lett. B **535** (2002) 117

[17] I.F. Ginzburg, I.P. Ivanov, N.N. Nikolaev, Eur.Phys.J. C**5** (2003) 02

[18] V.P. Goncalves, M.V. Machado, Phys.Rev.D **71** (2005) 014025

[19] V.P. Goncalves, M.V. Machado, Phys.Rev.D **75** (2007) 031502

Physics with forward FP420/FP220 tagging systems.

Peter Bussey[1]**and Pierre Van Mechelen*[2]
[1] Department of Physics and Astronomy, Faculty of Physical Sciences, University of Glasgow, U.K
[2] Department of Physics, Universiteit Antwerpen, Belgium

Abstract
We discuss selected physics topics in relation to proposals to upgrade the ATLAS and CMS detectors by the installation of forward silicon detector systems close to the beam line at distances of approximately 220 m and 420 m from the respective interaction points. The physics motivation and some of the aspects of the apparatus and its performance are briefly described.

1 Introduction

An important part of the physics programme at HERA has been the measurement of diffractive processes, in which the proton exchanges a colourless object, commonly referred to as the pomeron, with the incoming virtual photon. Two types of process here are of particular interest: the production of exclusive final states such as vector mesons, and hard processes in which the photon interacts with partonic components of the structure of the pomeron, which can be modelled in various ways. The hard processes can be induced by photons of varying virtuality, ranging from quasi-real photons to highly virtual photons that give deep inelastic scattering off the partons associated with the pomeron.

In a similar way, high energy photon-photon physics has been exploited at LEP, with processes that can be categorised in a similar manner. There is also an active program of diffractive physics at the Tevatron.

At the LHC, much higher energies are available than at HERA and LEP, enabling these physics programmes to be extended into areas where new physics can be discovered or studied. This is the subject of the present section. We outline first the physical setup that is envisaged, in which new detector systems will be installed close to the beam line at suitable locations downstream of the interaction points. We then present a summary of some of the new processes that should become open to investigation, and finally return to discuss the physical apparatus in further detail with an outline of its capabilities.

2 The basic proposal for forward detectors

Figure 1 illustrates the configuration of the LHC beamline on one side of an interaction point, showing the separate incoming and outgoing beams and the form of the particle trajectories on entering and leaving the interaction region. At distances greater than 260 m, the beam is dominated by the main bending magnets and is in the form of an irregular arc, which has been straightened

*Royal Society of Edinburgh / Scottish Executive Support Research Fellow 2008

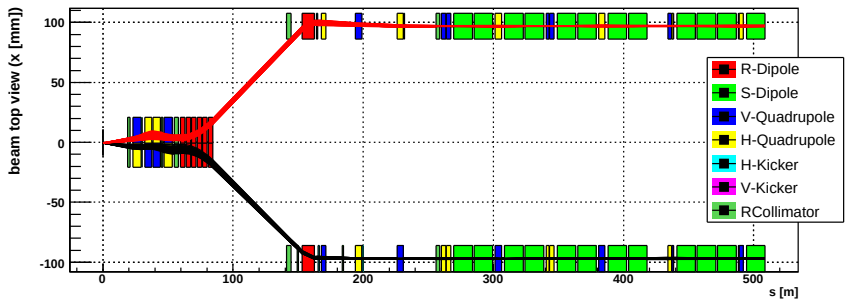

Fig. 1: Schematic representation of the LHC beamline on one side of an intersection point. The ATLAS or CMS detector is located at the origin of coordinates, and the incoming and outgoing beamlines are indicated, with the main bends straightened out for illustrative convenience.

out in the Figure. At two regions, namely around 220 m and 420 m from the interaction point, there are intervals in the beamline that are not occupied by magnets. Each of these regions provides approximately ten metres of clear space within which physics detectors can be stationed. It is proposed to install sets of silicon detectors in these regions, allowing them to be positioned as closely as possible to the outgoing beam. These detectors will detect diffractively scattered outgoing protons.

One or both protons in a pp collision may be scattered diffractively. In such a case, the fractional energy loss ξ suffered by the proton is typically small, as is the angle of scatter. These protons will continue to travel along the beam line, but in due course they will no longer be contained by the beam optics and will be bent either into a collimator or out of the beam line altogether. It is found that protons that have lost a few tens of GeV in the initial collision emerge out of the beam typically in the 420 m regions, and those that have lost a few hundreds of GeV emerge in the 220 m regions. By installing detector systems in these regions, we can identify the double diffractive production of exclusive centrally produced states whose mass is above a minimum value of the order of 100 GeV/c^2, provided that the state itself records a suitable signature in the central detector allowing its identification. Figure 2 illustrates the kind of process that we are interested in for the case of a Higgs particle denoted as H. A measurement of the energies of the outgoing protons makes possible a good determination of the mass of the centrally produced object, and in most cases this has better resolution than the measurement made in the central detector.

3 Central exclusive production

The central exclusive production of a Standard Model Higgs at the LHC has been the subject of a number of calculations. The cross section is strongly dependent on the gluon distributions that are assumed in the proton, and the detected cross section depends on the ability to trigger the process in the apparatus. Here we are faced with the difficulty that the present trigger electronics in ATLAS and CMS do not allow a first-level trigger to be based on the detection of a proton at 420 m, since the signal arrives too late. This forces the detection of a 120 GeV/c^2 central state to

be based on central detector triggers, which are not highly efficient in the case of a SM Higgs at this mass. In our favour is that the background of quark-antiquark jets is suppressed dynamically relative to the signal by the $J_z = 0$ selection rule [1]. An exclusive double-diffractively produced state is constrained to have $J^{PC} = 0^{++}$, so that if a Higgs or other particle is seen at all in this process, we have a good determination of its quantum numbers which may be hard to determine unambiguously by central detector measurements alone.

Recently the CDF Collaboration has observed for the first time the existence of central exclusive dijet production in hadronic collisions [2]. Exclusive production of the charmonium state χ_c has also been reported [3], with a cross section of the predicted magnitude. These are major milestones, since the central exclusive production of known final states can be used as "standard candles" to confirm mechanisms and extract cross sections with small model uncertainties. Establishing the potential experimental dijet background is an important item in the search for new particles such as the Higgs.

From Fig. 3 (left) it is clear that measurements of the proton structure at HERA and the Tevatron have a strong relevance to predicting the strength of a possible SM Higgs signal in double diffraction at LHC. With the set-up that is currently envisaged, the prospects seem rather marginal. However there are additional opportunities if the Higgs occurs within a supersymmetric framework. There are two particularly important parameters of the SUSY scenario, denoted as m_A and $\tan\beta$, within whose parameter space a number of the features of the theory can be illustrated. Figure 3 (right) illustrates the enhancements to the SM Higgs cross section that might be obtained for the lighter of the two neutral SUSY Higgs particles, denoted as h, and showing also some contours of different h masses, taken from Heinemeyer et al. [4].

On this basis, the quantity of LHC luminosity needed for 3-σ evidence and 5-σ discovery of neutral SUSY Higgs in the exclusive double-diffractive mode can be estimated, as illustrated for the heavier SUSY Higgs H in Fig. 4 [5]. Contour plots of this kind have been presented by these authors for the h and H in a variety of related situations. This gives improved hope of being able to make Higgs studies with forward detectors at the LHC, although there is no advance guarantee that the values of the SUSY parameters will be favourable and the integrated luminosity needed might be substantial.

More cleverly thought-out triggers and cuts may improve the situation. Figure 5 illustrates some studies carried out by Pilkington et al [6]. The mass of the central object has been reconstructed using modelled measurements of the forward proton trajectories at 420 m, with

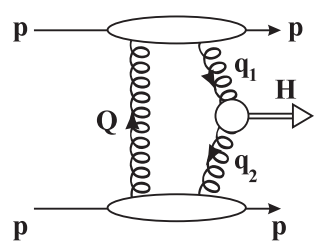

Fig. 2: Double diffractive production of a centrally produced object, denoted as H, by a colourless exchange modelled in terms of gluons.

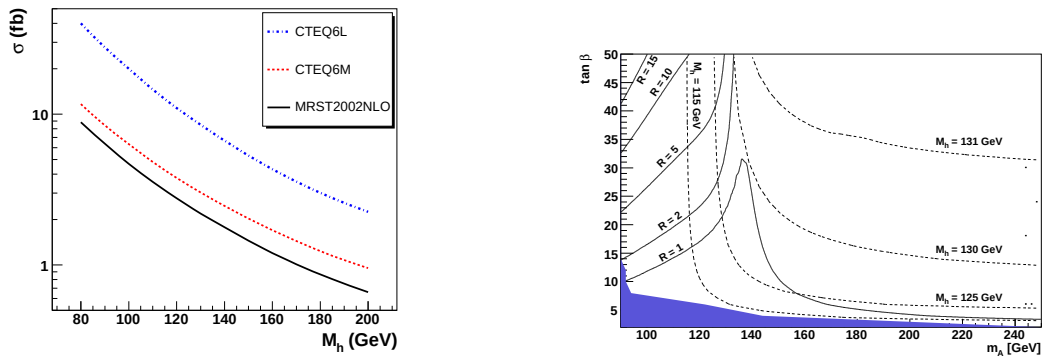

Fig. 3: Left: Variation of Higgs cross section with some parton models of the proton. Right: Contours for the ratio of signal events in the MSSM to those in the SM in the $h \to b\bar{b}$ channel in the m_A–$\tan\beta$ plane. The ratio is shown in the $M_h^{\max}$ benchmark scenario (with $\mu = +200$ GeV). The values of the mass of the light Higgs boson, M_h, are indicated by dashed contour lines. The CMS acceptance was approximately modelled.

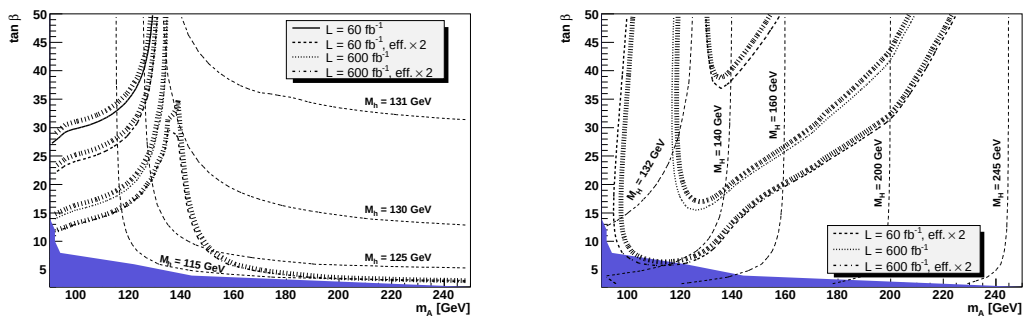

Fig. 4: Contours for 3-σ evidence (left) and 5-σ discovery (right) for the h and H SUSY Higgs in the scenario discussed in the text (S. Heinemeyer et al.)

estimated backgrounds from other processes included. During the first years of running, a measurement using 60 fb^{-1} seems a reasonable target and could produce evidence indicated by the first illustrated histogram. Higher luminosities will clearly assist, but will generate combinatorial backgrounds from overlapping events ("pile-up"). If these can be removed, as is envisaged, using precise timing measurements to isolate the event of interest, a signal might be seen giving a 5-σ discovery with 100 fb^{-1} of running.

Particular attention was given during the workshop to the study of event pile-up at the LHC (Taševský, Pilkington). By exploiting the difference between particle multiplicities in central exclusive and non-diffractive processes, a further reduction of the pile-up background may be possible. Here, only tracks from the primary vertex associated with the hard-scale event are relevant. Additional reduction factors of 10 to 100 may be possible; at present there are uncertainties here due to model dependence, soft underlying event tune dependence and track selection criteria.

4 Photoproduction processes.

TeV-energy protons are surprisingly efficient at radiating high energy photons. Single photoproduction off the second proton, and photon-photon processes are both of interest at LHC. Kinematically, photoproduction resembles diffractive scattering but with the tendency to a smaller transverse momentum transfer to the proton. The $\gamma\gamma$ cross sections are harder than the pomeron-pomeron processes, overtaking the latter in cross section at $W_{\gamma\gamma} \approx 1$ TeV. Since diffraction produces mainly gluon jets and photoproduction produces quark jets, there is little interference between the processes.

Single photoproduction will be of interest at the LHC in the production of electroweak particles. There are possibilities for the associated production of Higgs bosons and for the production of anomalous single top via FCNC. These processes are tagged by a single forward proton, but must be triggered and identified in the central detectors, and there will be potential difficulties at high luminosities since the use of timing to associate the forward protons with a central vertex requires two such forward protons. A number of generic cross sections are indicated in Fig. 6 (left), together with the forward detection system that will tag in different $W_{\gamma p}$ ranges.

The $\gamma\gamma$ process is capable of inducing the production of any type of charged particle-antiparticle pair. Of particular interest here is the possible production of charged SUSY particles, such as charginos and sleptons, whose signatures in the central detector will be high transverse energy leptons and missing energy carried by neutrinos or the lightest SUSY particle (LSP) if it is neutral. Figure 6 (right) shows cross sections for producing fermion and scalar charged particle pairs, compared to that for W^+W^- production, which is likely to be a very prolific background. ZZ production is possible only by anomalous couplings. The dimuon process is seen as good for the calibration of the forward detectors and even for LHC luminosity monitoring.

There are many possible SUSY mass scenarios. The possibilities that have been studied here are in terms of the so-called LM1 scenario, which involves a light LSP and light sleptons and charginos. This type of scenario will give the most favourable set of cross sections. The most natural variable to plot in order to separate SUSY signals from WW background would be the $W_{\gamma\gamma}$ value reconstructed from the forward protons (Fig. 7a)) However the background is

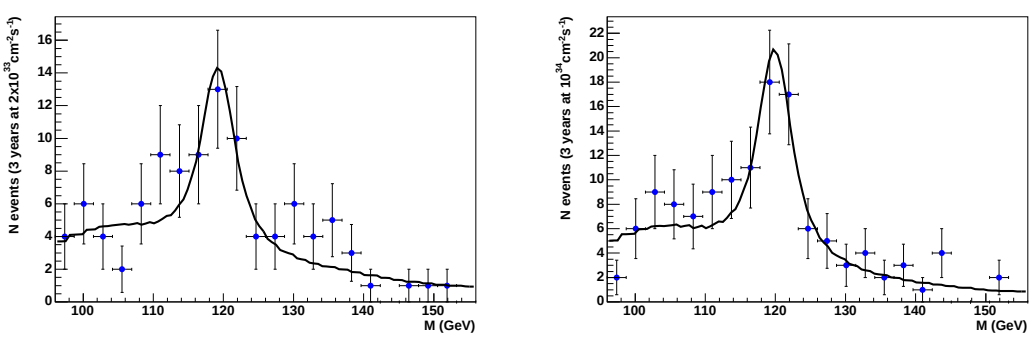

Fig. 5: Example analyses of an MSSM SUSY signal calculated with $\tan\beta = 40$ and $m_A = 120$ GeV (A. Pilkington).

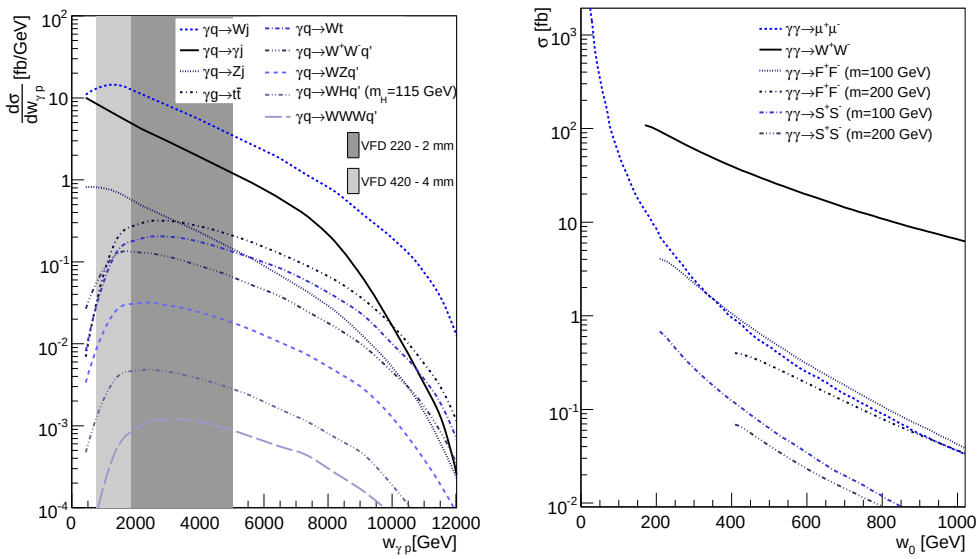

Fig. 6: Cross sections for various single photoproduction processes at LHC (left), as a function of photon-proton mass, and for various generic double photoproduction processes (right).

much more tractable when the variable $W_{miss} = \sqrt{E^2_{miss} - P^2_{miss}}$ is plotted (Fig. 7b), where the missing energy and momentum are calculated from the forward protons and the kinematics of the observed final state particles. Combinations of $W_{\gamma\gamma}$ and W_{miss} give even more power (Fig. 7c) and can generate a distribution (Fig. 7d) that might give a 5-σ discovery with only 25 fb^{-1} of integrated luminosity.

5 Other physics processes

An intriguing example of completely new physics has been proposed by A. White in which a new SU(5) gauge theory obviates the need for a Higgs particle and gives remarkable experimental signatures for which pomeron physics may be an essential diagnostic tool [8]. An extended range of SUSY processes may also be accessible. One study made during this workshop has been the detection of pairs of long-lived gluinos in central exclusive processes [9]. Such particles can occur in split-SUSY models, where the sfermions have masses far above the TeV scale. The gluinos are lighter and therefore long lived, and may form bound states with gluons or quarks called R-hadrons. These will mimic the behaviour of muons and may be detected in muon chambers. For $300 fb^{-1}$ approximately 10 events are expected for gluino masses up to 350 GeV. The advantage of using proton detectors lies again in the excellent accuracy for the reconstruction of the mass of the centrally produced object. The forward detectors at 220m and 420 m give access to the wide range of masses that such particle pairs may have.

Present space permits no more than a brief mention of other items in the range of physics processes that will be made observable by the use of forward tagging systems at LHC. The work initiated at HERA on hard pomeron scattering and structure can be continued by means of

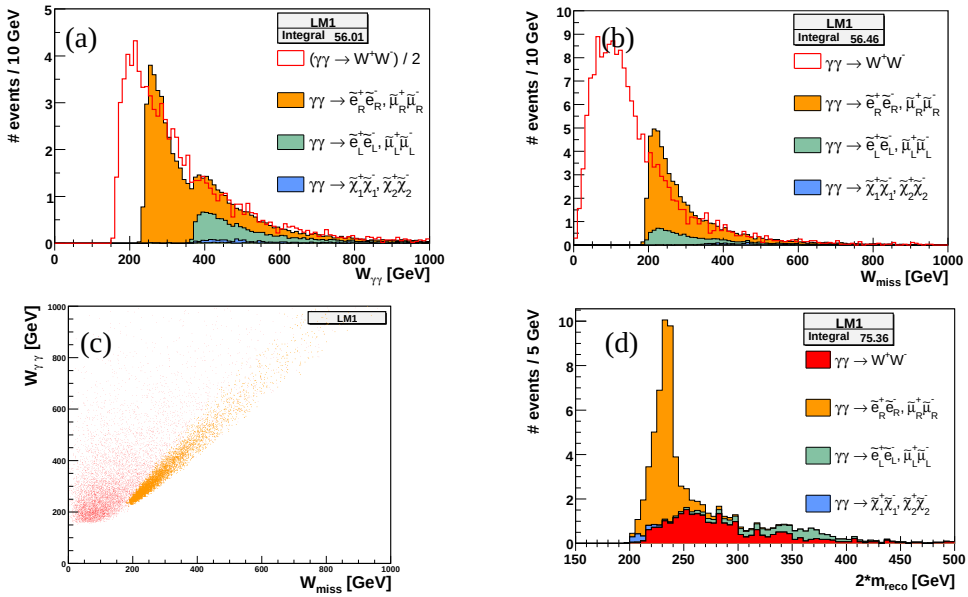

Fig. 7: Examples of the analysis of the double photoproduction of SUSY particles, as a function of the parameters $W_{\gamma\gamma}$ and W_{miss}, to illustrate a possible way to isolate a clean SUSY signal [7].

photon-pomeron and pomeron-pomeron processes. It should be noted that the $q\bar{q}$ final state is suppressed in the pomeron-pomeron process at low quark masses, assisting in the identification of potential new physics processes. There will be extended opportunities for further studies of the nature of the pomeron. In the early stages, at low LHC luminosities, the study of rapidity-gap survival will be interesting and important, generalised gluon distributions can be studied, and a variety of QCD effects can be investigated; a recent review by Khoze, Martin and Ryskin gives more details here [10].

6 The proposed apparatus

Traditionally, forward detection systems have consisted of relatively small installations mounted at suitable locations such that the detector systems can be moved towards the beam within localised structures known as Roman Pots. This idea has been expanded in the proposals for LHC so that there is planned to be an entire section of beam pipe that is movable, the so-called "Hamburg Pipe" scheme. It will be necessary to replace the cryostat connection between the portions of the beamline either side of the 420 m installations. Sets of silicon detectors will be mounted in the Hamburg Pipe. The best performance is envisaged if two sets of detectors are installed in each pipe, separated by approximately 10 m to make full use of the available space, so that the position and angle of the trajectory of an emerging proton can be measured. In the horizontal plane, precisions of approximately 10 μm in position and 1 μrad in angle should be obtainable. The vertical plane is less critical, and less good precisions in the vertical measurements will be accepted. The silicon detectors are of a recent "edgeless" technology to allow the sensitive area

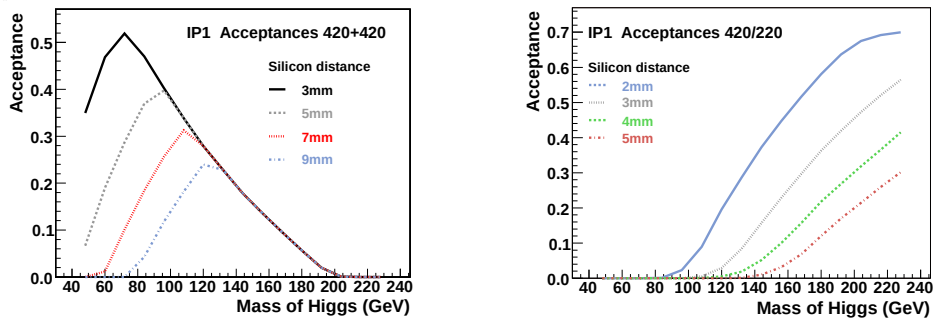

Fig. 8: Acceptance of the forward tagging systems as a function of the mass of the centrally produced system, taken here as a Higgs.

to be moved as close as possible to the main outgoing proton beam.

To perform the tracking of the protons into the relevant detector regions, two programs (FPtrack and Hector) have been written for ATLAS and CMS respectively [11]. They enable us to evaluate the acceptance of the apparatus under various conditions; this is illustrated in Fig. 8. The 420 m systems used on their own provide substantial acceptance for exclusively produced masses up to approximately 150 GeV/c^2, and even if the silicon can be moved only to 7 mm from the beam, the acceptance at the critical region of 120 GeV/c^2 is not affected. By using the 420 m systems in conjunction with those at 220 m, a greatly extended mass range is achieved with excellent acceptances.

Figure 9(a) illustrates the distribution of the outgoing protons at 420 m in position, horizontally and vertically. The vertical beam spread is small and The mass M_X of an exclusively produced final state can be evaluated if the momenta of the forward protons can be reconstructed; this is achievable by means of polynomial-based formulae in terms of the horizontal position and angle in the detector regions. The value of M_X is then $2\sqrt{p_0 - p_1)(p_0 - p_2)}$ for an incoming beam momentum p_0 and outgoing proton momenta p_1, p_2. Various uncertainties smear out this calculation, notably the intrinsic spread on p_0. Figure 9(b) shows the mass uncertainty that can be achieved under reasonable assumptions. In nearly all cases this is more precise than the direct measurement in the central detector. An exception to this is when the central state consists of two photoproduced muons. This promises to be a key process which can be used to calibrate the proton momentum measurements.

7 Summary

Forward tagging opens up a wide range of diffraction and photoproduction processes at LHC. Following from the HERA experiences, we hope to study these mechanisms at high energy, in which a number of new processes should be observable. There is discovery potential in some cases, while in others, known processes can be studied in more depth. This is a major new area of physics for the LHC.

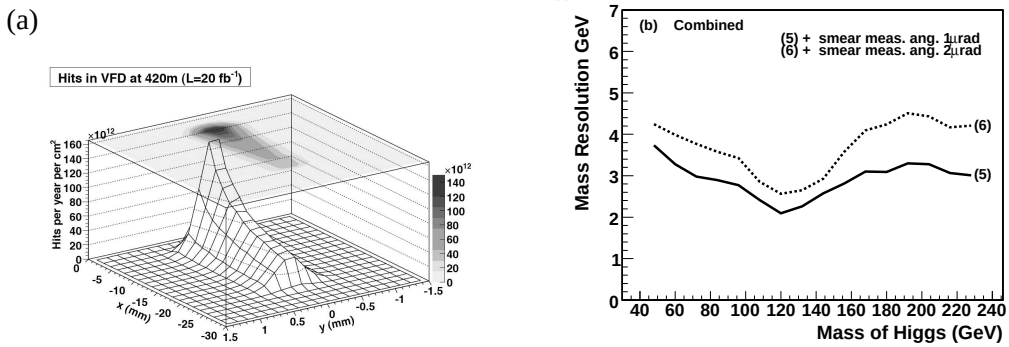

Fig. 9: (a) Typical distribution of a forward proton in a detector system at 420 m (X. Rouby). (b) Mass resolution using 420 m and/or 220 m detector systems if the resolution on the angular measurement is 1 μrad or 2 μrad. (PJB)

Acknowledgements

Many people have contributed to the work of this part of these Proceedings, through talks and discussion in this Workshop and elsewhere. We would especially mention T. Coughlin, B. Cox, M. Grothe, V. Khoze, A. Pilkington, X. Rouby, C. Royon, M. Taševský and S. Watts, whose presentations at the various meetings have helped to shape much of what is presented in this section.

References

[1] V. A. Khoze, A. D. Martin and M. G. Ryskin, Eur. Phys. J. **C 19**, 477 (2001), [Erratum-ibid. C **20**, 599 (2001)] .

[2] T. Aaltonen et al., Phys. Rev. **D 77**, 052004 (2008) .

[3] T. Aaltonen et al., arXiv: 0902.1271v1 (hep-ex) (2009) .

[4] S. Heinemeyer et al., Eur. Phys. J. **C 53**, 231 (2008) .

[5] S. Heinemeyer et al., arXiv: 0811.4571v1 (hep-ph) (2008) .

[6] B. E. Cox, F. K. Loebinger and A. D. Pilkington, JHEP 10 090 (2007) .

[7] N. Schul and K. Piotrzkowski, arXiv: 0806.1097v1 (hep-ph) (2008) .

[8] A. White, arXiv: 0708.1306v1 (2007), 0803.1151v1 (2008) (hep-ph) .

[9] P. J. Bussey, T. D. Coughlin, J. R. Forshaw, A. D. Pilkington, JHEP 0611 027 (2006) .

[10] V. A. Khoze, A. D. Martin and M. G. Ryskin, Eur. Phys. J. **C55**, 363 (2008) .

[11] P. J. Bussey, http://ppewww.physics.gla.ac.uk/ bussey/FPTRACK/
J. de Favereau, X. Rouby and K. Piotrzkowski, JINS **2** (2007) P09005 .

Chapter 5

Working Group
Cosmic Rays, HERA and the LHC

Convenors:

C. Diaconu (DESY and CPPM, Marseille),
Ch. Kiesling (MPI Munich)
T. Pierog (FZ Karlsruhe)

Introduction

A. Bunyatyan[1,2], *A. Cooper-Sarkar*[3], *C. Diaconu*[4,5], *R. Engel*[6], *C. Kiesling*[7], *K. Kutak*[4], *S. Ostapchenko*[8,9], *T. Pierog*[4], *T.C. Rogers*[10], *M.I. Strikman*[10], *T. Sako*[11].
[1] MPI, Heidelberg, Germany
[2] Yerevan Physics Institute, Armenia
[3] Oxford University, Dept of Physics, Oxford, UK
[4] DESY, Hamburg, Germany
[5] CPPM, Marseille, France
[6] Forschungszentrum Karlsruhe, Institut für Kernphysik, Karlsruhe, Germany
[7] Max-Planck-Institute for Physics, München, Germany
[8] Institutt for fysikk, NTNU Trondheim, Norway
[9] D. V. Skobeltsyn Institute of Nuclear Physics, Moscow State University, Russia
[10] Pennsylvania State University, United States
[11] Solar-Terrestrial Environment Laboratory, Nagoya University, Nagoya, Japan

Abstract
When particle physic started, cosmic ray were used as source of new particles. Nowadays particle physic is a fundamental key to understand the nature of the very high energy cosmic rays. Above 10^{14} eV, primary cosmic rays are detected via air showers whose development strongly rely on the physic of the forward region of hadronic interactions as tested in the HERA and LHC experiments. After an introduction on air shower phenomenology, we will review how HERA and LHC can constrain the physic used both in hadronic interaction model, or for photon or neutrino primaries.

1 Physics questions and problems

One of the central questions of astroparticle physics is that of the sources and propagation of cosmic rays. Even more than 90 years after the discovery of cosmic rays we still don't know their elemental composition at high energy and also the information on the energy spectrum is very limited [1–6]. Knowing the cosmic-ray composition is the key to understanding phenomena such as the *knee*, a change in the power-law index of the cosmic ray flux at about 3×10^{15} eV, the transition from galactic to extra-galactic cosmic rays, and the implications of the existence of ultra-high energy cosmic rays with $E > 10^{20}$ eV. In particular, composition information is essential for confirming or ruling out models proposed for the sources of ultra-high energy cosmic rays, many of which postulate new particle physics [7, 8].

The flux of cosmic rays is shown in Fig. 1 in the energy range from 10^{12} eV up to the highest energies. It has been scaled by $E^{2.5}$ to make the characteristic features of the spectrum clearly visible. In addition the equivalent energies of colliders, referring to proton-proton collisions, are indicated by arrows.

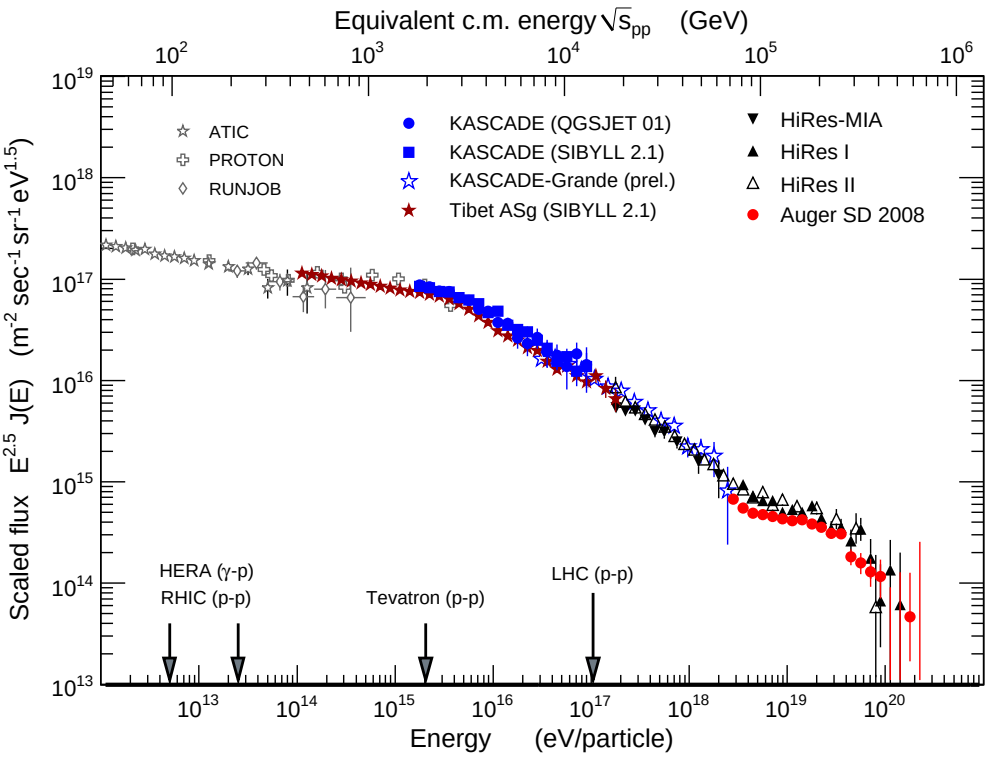

Fig. 1: All-particle flux of cosmic rays as obtained by direct measurements above the atmosphere by the ATIC [9], PROTON [10, 11], and RUNJOB [12] as well as results from air shower experiments. Shown are Tibet ASγ results obtained with SIBYLL 2.1 [13], KASCADE data (interpreted with two hadronic interaction models) [14], preliminary KASCADE-Grande results [15], and Akeno data [16,17]. The measurements at high energy are represented by HiRes-MIA [18, 19], HiRes I and II [20], and Auger [21].

The all-particle spectrum can be approximated by a broken power law $\propto E^{\gamma}$ with a spectral index $\gamma = -2.7$ below $E_k \approx 4 \times 10^{15}$ eV. At the *knee*, the spectral index changes to $\gamma \approx -3.1$. The power law index changes again at about $10^{18.5}$ eV, a feature that is called the *ankle*. At the very high end of the spectrum there seems to be a suppression of the flux. None of these features of the energy spectrum of cosmic rays is understood so far. In the following some of the related theoretical questions and models are presented for illustration.

- **Knee.** At the knee, the cosmic ray spectrum changes in a way that is very difficult to understand in models with a superposition of different sources, each producing a power-law flux. The knee could be feature of the acceleration process, it could be the result of propagation effects from the sources to Earth (leakage from the Galaxy), or it could be caused by new particle physics. Knowing the change of the elemental composition of cosmic rays through the knee energy region will help to distinguish some of the possible scenarios. Acceleration and propagation models of the knee predict that the spectra of individual elements should each exhibit a knee, however at an energy that is scaled by the

charge of the particle due to the coupling to astrophysical magnetic fields (for example, [22]). In contrast, models postulating new interaction physics (for example, [23]) and the *cannon ball* model [24] predict a scaling proportional to the number of nucleons of the nucleus (i.e. mass number). A review of the different scenarios and their predictions can be found in, for example, [25].

- **Ankle.** The ankle is often regarded as a signature of the transition from Galactic to extragalactic cosmic rays. Such a transition is expected in this energy range because of the strength of the Galactic magnetic fields being of the order of $3\ \mu$G [26]. Particles with energies above 10^{19} eV are not confined to the Galaxy. The exact energy of the transition is not known [27]. In the dip model the ankle is a result of the propagation of ultra-high energy cosmic rays through the microwave background radiation [28, 29]. Within this model, ultra-high energy cosmic rays have to be dominated by protons. Other models of the ankle explain the feature in the spectrum by the superposition of different power laws from Galactic and extragalactic sources [4, 30, 31]. In such a scenario the composition would most likely be mixed with contributions from both light and heavy elements, i.e. in the range from protons to iron nuclei.
- **Upper end of the spectrum.** A strong suppression of the particle flux above $E = 7 \times 10^{19}$ eV is expected from the interaction of cosmic rays with the cosmic microwave background radiation, the Greisen-Zatsepin-Kuzmin (GZK) effect [32, 33]. Both protons and nuclei suffer significant energy losses when propagating over distances larger than $\sim 100\,$Mpc. On the other hand, the sources could have reached their upper limit of acceleration or injection power and we would be mistaken by attributing the observations just to the GZK suppression. In any case the sources of such high energy particles have to be rather exotic [34]. One would have to build the LHC with a circumference of the length of the orbit of the planet Mercury to reach the same energy with the currently available technology. Particles of such energies also probe Lorentz invariance at extreme energies [35, 36] and hence allow to search for space-time fluctuations (for example, see [37, 38]).

To solve these questions, multi-messenger and multi-observable measurements are needed. First of all, the flux, composition and arrival direction distribution of cosmic rays will have to measured with high statistics and precision. Secondly, complementary information obtained from observing secondary particle fluxes (gamma-rays and neutrinos) will greatly help to disentangle different source and propagation scenarios [39, 40].

At energies above $10^5\,$GeV, the flux of cosmic rays is so low that it cannot be measured directly using particle detectors. Therefore all cosmic-ray measurements of higher energy are based on analyzing the secondary particle showers, called extensive air showers, which they produce in the atmosphere of the Earth. To interpret the characteristics of extensive air showers in terms of primary particle type and energy, detailed modeling of the various interaction and decay processes of the shower particles is needed (for example, see [41, 42]). In particular, the elemental composition of the cosmic-ray flux reconstructed form air shower data depends very much on the assumptions on hadronic multiparticle production.

2 Air shower phenomenology and hadronic interactions

A commonly employed technique to observe air showers is the measurement of secondary particles (electrons, photons and muons) reaching the ground [2]. Using an array of particle detectors (for example, sensitive to $e^{\pm}$ and $\mu^{\pm}$), the arrival direction and information on mass and energy of the primary cosmic ray can be reconstructed. The main observables are the number and the lateral and temporal distributions of the different secondary particles. At energies above $\sim 10^{17}$ eV, the longitudinal profile of a shower can be directly observed by measuring the fluorescence light induced by the charged particles traversing the atmosphere [43]. Two main observables can be extracted from the longitudinal shower profile: the energy deposit or the number of particles, $N_{\max}$, at the shower maximum and $\mathrm{X}_{\max}$, the atmospheric depth of the maximum. Again, these quantities can be used to estimate the energy and mass of the primary particles. Shower-to-shower fluctuations of all observables make it impossible to derive the mass of the primary particle on a shower-to-shower basis. On the other hand, these fluctuations provide very useful and complementary composition information.

To qualitatively understand the dependence of the air shower development on some basic parameters of particle interaction, decay, and production, a very simple toy model can be used. Although initially developed for electromagnetic (EM) showers [44] it can also be applied to hadronic showers [45].

First we consider a simplified electromagnetic shower of only one particle type. A particle of energy E produces in an interaction two new particles of the same type with energies $E/2$, after a fixed interaction length of λ_e. With n being the number of generations (consecutive interactions), the number of particles at a given depth $X = n \cdot \lambda_e$ follows from

$$N(X) = 2^n = 2^{X/\lambda_e}, \tag{1}$$

with the energy E per particle for a given primary energy E_0 being

$$E(X) = \frac{E_0}{2^{X/\lambda_e}}. \tag{2}$$

Defining the critical energy E_c (~ 85 MeV in air) as the energy below which continuous energy loss processes (i.e. ionization) dominate over particle production, one can make the assumption that the shower maximum is reached at a depth at which the energy of the secondary particles is degraded to E_c. Then two main shower observables are given by

$$N_{\max} = \frac{E_0}{E_c} \quad \text{and} \quad X^e_{\max}(E_0) \sim \lambda_e \cdot \ln\left(\frac{E_0}{E_c}\right). \tag{3}$$

Of course, this very simplified picture does not reproduce the detailed behavior of an EM shower, but two important features are well described: the number of particles at shower maximum is proportional to E_0 and the depth of shower maximum depends logarithmically on the primary energy E_0.

Generalizing this idea, a hadronic interaction of a particle with energy E is assumed to produce n_{tot} new particles with energy E/n_{tot}, two third of which being charged particles n_{ch} (charged pions) and one third being neutral particles n_{neut} (neutral pions). Neutral particles decay

immediately into em. particles particles ($\pi^0 \to 2\gamma$), feeding the em. shower component. After having traveled a distance corresponding to the mean interaction length $\lambda_{\rm ine}$, charged particles re-interact with air nuclei as long as their energy exceeds some typical decay energy $E_{\rm dec}$.

In the end, most of the energy of an air shower is carried by em. particles ($\sim 90\%$ for $n = 6$). The depth of shower maximum is given by that of the em. shower component, $X^e_{\rm max}$. As the first hadronic interaction produces em. particles of energy $\sim E_0/n_{\rm tot}$ one gets

$$X_{\rm max}(E_0) \sim \lambda_{\rm ine} + X^e_{\rm max}(E_0/n_{\rm tot}) \quad (4)$$

$$\sim \lambda_{\rm ine} + \lambda_e \cdot \ln\left(\frac{E_0}{n_{\rm tot} E_c}\right), \quad (5)$$

where $\lambda_{\rm ine}$ is the hadronic interaction length. This simplified expression for the shower depth of maximum neglects the em. sub-showers initiated by hadrons of later generations. The inclusion of higher hadronic generations does not change the structure of Eq. (5), see [46].

Following [45], we assume that all charged hadrons decay into muons when their energy reaches $E_{\rm dec}$. By construction, charged particles will reach the energy $E_{\rm dec}$ after n interactions

$$E_{\rm dec} = \frac{E_0}{(n_{\rm tot})^n}. \quad (6)$$

Since one muon is produced in the decay of each charged particle, we get for the number of muons in an hadronic shower

$$N_\mu = n^n_{\rm ch} = \left(\frac{E_0}{E_{\rm dec}}\right)^\alpha, \quad (7)$$

with $\alpha = \ln n_{\rm ch}/\ln n_{\rm tot} \approx 0.82 \ldots 0.95$ [46, 47]. The number of muons produced in an air shower depends not only on the primary energy and air density, but also on the charged and total particle multiplicities of hadronic interactions.

In case of showers initiated by nuclei, one can use the superposition model to deduce the expectation value for inclusive observables [48]. In this model, a nucleus with mass A and energy E_0 is considered as A independent nucleons with energy $E_{\rm h} = E_0/A$. This leads to

$$N^A_{\rm max} \approx A \cdot \frac{E_{\rm h}}{E_c} = \frac{E_0}{E_c} = N_{\rm max} \quad (8)$$

$$X^A_{\rm max} \approx X_{\rm max}(E_0/A) \quad (9)$$

$$N^A_\mu \approx A \cdot \left(\frac{E_0/A}{E_{\rm dec}}\right)^\alpha = A^{1-\alpha} \cdot N_\mu. \quad (10)$$

There is no mass dependence of the number of charged particles at shower maximum. The number of muons and the depth of maximum depend on the mass of the primary particle. The heavier the shower-initiating particle the more muons are expected for a given primary energy. For example, an iron-induced shower has about 1.4 times more muons than a proton shower of the same energy.

There are several code packages available for performing Monte Carlo simulations of extensive air showers. The more frequently used programs are AIRES [50], CORSIKA [51],

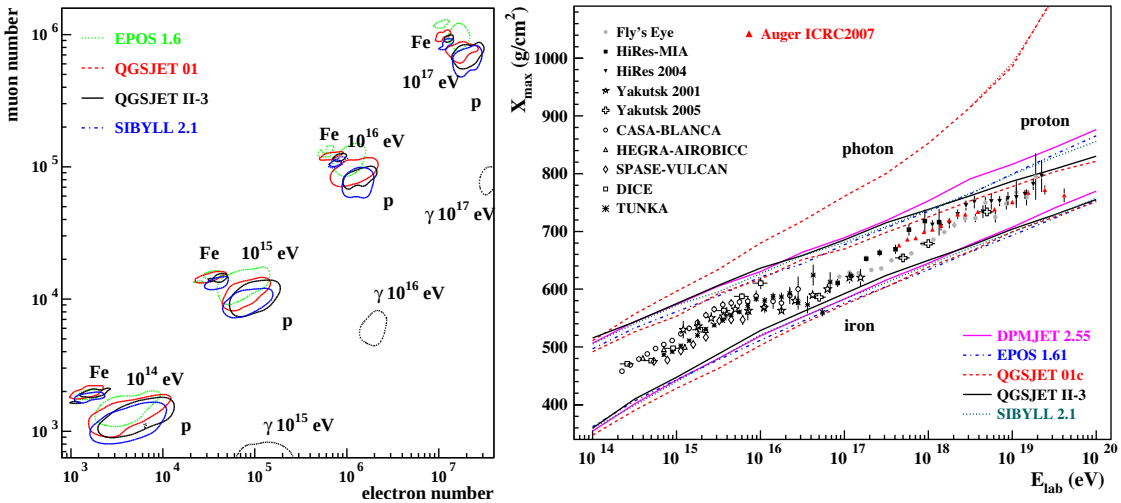

Fig. 2: Predictions for air shower observables for proton-, iron- and photon-induced showers. Left panel: Shown are the correlation between the number of electrons and muons at ground as expected with different hadronic interaction models (see text) [49]. Right panel: compilation of data of the mean depth of shower maximum and model predictions [49].

CONEX [52], SENECA [53], MOCCA [54], and COSMOS [55]. These packages provide either self-made hadronic interaction models that cover the full energy range from the particle production threshold to the highest energies or employ external models for the simulation of these interactions. Due to the different methods of modeling, external hadronic interaction models are typically optimized for low- or high-energy interactions.

Low-energy models describe hadronic interactions in terms of intermediate resonances (for example, the isobar model) and parametrizations of data. They are applicable in the energy range from the single particle production threshold up to several hundred GeV. Models that are often applied in simulations are FLUKA (which is a complete cascade simulation package that includes both low- and high-energy models) [56], GHEISHA [57], UrQMD [58], and the more specialized code SOPHIA [59]. Low-energy models are typically well-tuned to the large number of data sets from fixed target measurements. Still the differences between the model predictions are significant and can lead to very different muon densities in air shower simulations [60, 61].

High-energy interaction models are typically very complex models and based on Regge theory [62], Gribov's Reggeon calculus [63], and perturbative QCD. Central elements of these models are the production of QCD minijets and the formation of QCD color strings that fragment into hadrons. The most frequently used models are QGSJET 01 [64, 65] and II [66, 67], SIBYLL 2.1 [48, 68, 69], EPOS 1.6 [70, 71] and DPMJET II [72] and III [73, 74]. The extrapolation of these models to very high energy depends on the internal structure of the model and the values of the tuned model parameters and is, in general, rather uncertain. Different extrapolations obtained within one model by varying the parameters can be found in [75, 76] and represent only a lower limit to the uncertainty of the predictions.

Monte Carlo models typically applied in high energy physics are not used for air shower

simulations. Most of these models do not allow the simulation of particle production with air nuclei as target or are applicable in a rather limited energy range (however, see [77] for a study with HIJING [78]).

Detailed numerical simulations of extensive air showers confirm the overall functional relations between the shower energy, depth of shower maximum, and number of electrons and muons that have been derived within the simple Heitler-Matthews model. The expected correlation between the number of electrons and muons at a surface detector at sea level is shown in Fig. 2. The simulations were made for vertical showers with the air shower simulation package CORSIKA [51]. The predictions obtained for the interaction models QGSJET 01, QGSJET II.03, SIBYLL 2.1, and EPOS 1.6 are compared. While there is a reasonable discrimination power at low energy, the model-induced uncertainties do not allow us to discriminate between even the most extreme composition assumptions at ultra-high energy if only the number of muons and electrons is measured. The situation seems to be a somewhat better in case of the mean depth of shower maximum, but the model uncertainties are still very large.

It can be concluded from both simple cascade models of air showers and numerical studies [54,75,76,79] that the following characteristics of hadronic interactions are of central importance to air shower predictions

- Inelastic cross section for proton-air and pion/kaon-air interactions,
- Ratio between neutral and charged secondary particles (in other words, π^0 and all other particles),
- Energy distribution of the most energetic secondary particles,
- Multiplicity of high energy secondary particles,
- Scaling or scaling violation of secondary particle distributions,
- Cross section for diffractive dissociation (i.e. low-multiplicity events).

It is clear that hadronic interactions at both high and low energies are influencing the model predictions for air showers. Low-energy interactions do not influence the depth of shower maximum very much but are of direct relevance to the muon density at large lateral distance from the shower core, see [60, 61, 80].

3 Limitations of air shower simulations

Before discussing shortcomings of air shower simulations it has to be emphasized that modern simulation packages provide a very good overall description of air shower observables. The situation has very much improved in comparison to the early days of air shower simulation [81].

Modern cosmic-ray detectors like KASCADE [82] and the Pierre Auger Observatory [83] measure several observables for each shower. By choosing different observables, the model dependence of the reconstructed energy and primary particle mass can be estimated. Studies show that the uncertainty in interpreting the data from these experiments is dominated by the uncertainty in predicting hadronic multi-particle production in extensive air showers. In the following we will discuss some representative examples that illustrate the limitations of currently available hadronic interaction models and air shower simulation tools.

The KASCADE Collaboration analyzed the measured number of electrons and muons at detector level to derive the primary energy and composition of the showers in the knee energy

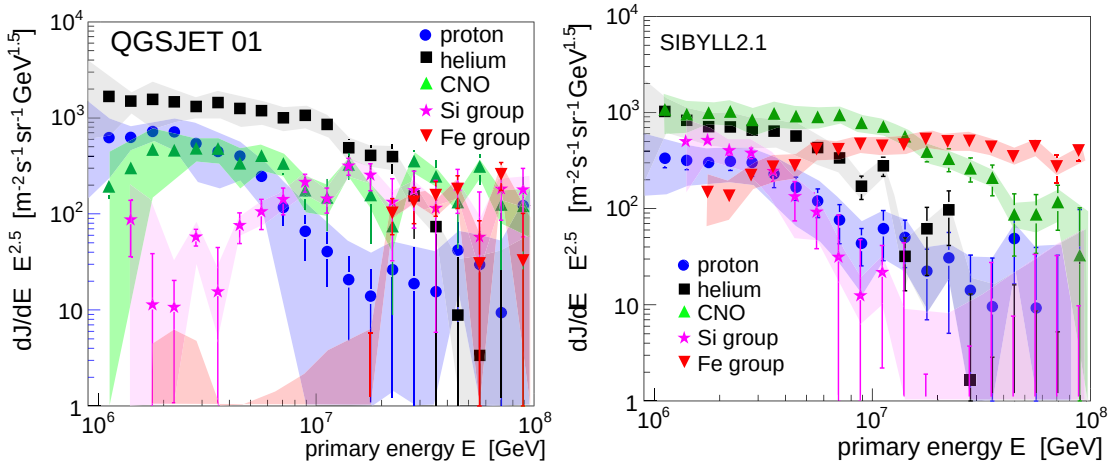

Fig. 3: Cosmic-ray flux for five elemental groups in the knee energy range as derived from KASCADE data using the hadronic interaction models QGSJET 01 (left panel) and SIBYLL 2.1 (right panel) [82].

region. Having collected more than 40 million showers it is still not possible to obtain a clear picture of the elemental composition [14]. Applying different hadronic interaction models leads to significantly different fluxes for the elemental groups considered in the analysis, see Fig. 3. In particular, the fundamental question of having a mass- or charge-dependent scaling of the knee positions of the individual flux components cannot be answered. Moreover, in an earlier study the KASCADE Collab. showed that selecting different observables gives inconsistent composition results even if the same hadronic interaction model is employed in the analysis [84].

A comparison of the world data set on electron-muon based and $X_{\max}$ based composition measurements, using the same hadronic interaction models, shows a systematic inconsistency between composition results based on surface detector data and that based on the measurement of the mean depth of shower maximum [85]. Analysis of the surface detector data indicate a heavier primary composition than one would expect from $\langle X_{\max} \rangle$ data. This is most clearly found in experiments that measure both $X_{\max}$ and an observable related to the number of muons. For example, the prototype experiment HiRes-MIA [86] studied showers in the energy range from 10^{17} to $10^{18.5}$ eV. The measured muon densities at 600 m from the core could only be interpreted as iron-dominated composition, but the mean $X_{\max}$ indicated a transition to a proton-dominated composition [19].

The analysis of Auger data with QGSJET II [87] leads to a similar discrepancy at an energy of about 10^{19} eV. Using universality features of very high energy showers $E > 10^{18}$ eV, one can relate the electromagnetic shower size at a lateral distance of 1000 m to the shower energy and the depth of shower maximum [88, 89]. The employed universality features are the same for showers simulated with the interaction models QGSJET II and SIBYLl 2.1. Considering showers at different angles and employing the independently measured depth of shower maximum, the observed muon signal can be set in relation to the predicted muon signal as shown in Fig. 4. Adopting the nominal energy scale of the Auger fluorescence detectors, the number of muons at 1000 m from the core is found to be twice as large as predicted by simulations with proton

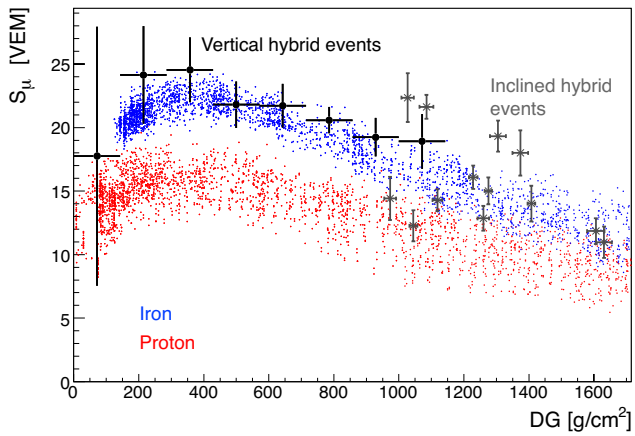

Fig. 4: Simulated and derived muon density as function of the detector depth relative to the depth of shower maximum, DG. The muon density is derived from Auger data at a distance of 1000 m from the shower core. The points show the prediction of simulations with QGSJET II and an energy increased by 30% relative to the reconstructed numinal shower energy, for details see [87].

showers. This number should be compared to that of iron-induced showers for which one expects a muon number increased by the factor 1.38 (QGSJET II) or 1.27 (SIBYLL 2.1). Increasing the energy scale by 30% as the constant intensity cut analysis of the data suggests and assuming a iron dominated composition seems to bring the surface detector data almost into agreement with the model predictions. On the other hand, the measured $\langle X_{\rm max} \rangle$ data is at variance with an iron-dominated composition hypothesis at 10^{19} eV.

4 Main sources of model uncertainties

In the foreseeable future soft multi-particle production will not be calculable within QCD. Therefore the modeling of cosmic-ray interactions will continue to strongly depend on the input from accelerator experiments. There are two principal types of input needed for model building. First of all, data on cross sections, secondary particle distributions and multiplicities, as well as parton densities form the basis for tuning the parameters of the models. Secondly, guidance from further development and experimental verification of theoretical and phenomenological concepts and ideas will be crucial for model development.

At the current stage even the most fundamental question of scaling of secondary particle distributions in the forward phase space region cannot be answered[1]. Within some models very strong scaling violation of the distribution of leading particles is expected [90]. So far there is no experimental proof of such a scenario. If realized in nature, the implications will be profound and most of the very high energy cosmic ray data will have to be interpreted in terms of a light composition. The lack of data on hadron production in forward direction, with the exception of HERA measurements, is one of the main source of model uncertainties. The HERA measure-

[1]Feynman scaling is, of course, violated for central particle production.

ments of leading proton and neutron distributions are the only high energy data available and indicate surprisingly small scaling violations [91]. It has to be expected that the leading particle distribution is correlated with the centrality of the interaction, as found in heavy ion collisions. LHC data from the big experiments [92] and LHCf [93] will be of decisive importance in this respect.

The energy fraction transferred in an interaction to particles of very short lifetime, that decay to photons and electrons, is of direct relevance to air shower simulations. Currently the particle distribution of neutral pions is derived indirectly from the distributions of charged secondaries. With the exception of the UA7 [94], no high energy data of secondary π^0 and photon distributions exist.

The extrapolation of the total and inelastic cross sections is currently hampered by the discrepant measurements from Tevatron experiments. Extrapolating the model cross section based on the CDF data [95] gives different air shower predictions than using the E710 [96] and E811 [97] data [76]. The measurement of the proton-proton cross section at LHC will reduce this uncertainty very much. Related to this cross section is, of course, the question of pion-proton and kaon-proton cross sections. The highest energy data available for the pion-nucleus cross section is that of SELEX [98]. There is no generally accepted theoretical model of how to extrapolate the ratio between proton-proton and meson-proton cross sections.

One further source of uncertainty stems from the fact that hadronic cross sections and secondary particle distributions are needed for the interaction with light nuclei in air shower simulations. At high energy, the calculation of such nuclear cross sections and particle distributions is not straightforward. At low energy, the Glauber approximation [99] is known to work remarkably well. Already the low-energy data indicates, however, the need for inelastic screening corrections for the calculation of which no reliable framework exists. For example, cross sections estimates based on air shower data indicate smaller particle production cross sections than current model extrapolations (see compilation in [100]).

One of the central theoretical questions that has to be addressed in all hadronic interaction models is that of the range of applicability of perturbative QCD. At high energy, most hadrons are produced in the fragmentation of minijets. It is of great importance to understand the correlations between individual parton-parton interactions, to which degree they can be considered independent from each other, their kinematic and color flow link to the remnants of the incoming hadrons, and the minimum momentum transfer for which such a picture can be applied. Closely related to this question is the modeling of non-linear effects in the low-x parton evolution and possible saturation or high-density shadowing effects. HERA data is of direct relevance in this respect as are RHIC measurements too. A high density of partons can also influence string fragmentation and modify particle yields relative to those measured at low energy. There are different model predictions that address this point (see, for example, [70, 101–103]) but the experimental data are not conclusive.

References

[1] S. P. Swordy *et al.*, Astropart. Phys. **18**, 129 (2002), astro-ph/0202159.

[2] A. Haungs, H. Rebel, and M. Roth, Rept. Prog. Phys. **66**, 1145 (2003).

[3] R. Engel and H. Klages, Comptes Rendus Physique **5**, 505 (2004).

[4] A. M. Hillas, J. Phys. **G31**, R95 (2005).

[5] K.-H. Kampert, Nucl. Phys. Proc. Suppl. **165**, 294 (2007), arXiv:astro-ph/0611884.

[6] K.-H. Kampert, J. Phys. Conf. Ser. **120**, 062002 (2008), arXiv:0801.1986 [astro-ph].

[7] P. Bhattacharjee and G. Sigl, Phys. Rev. **D51**, 4079 (1995), astro-ph/9412053.

[8] D. F. Torres and L. A. Anchordoqui, Rept. Prog. Phys. **67**, 1663 (2004), astro-ph/0402371.

[9] ATIC-2 Collaboration, H. S. Ahn *et al.* Prepared for 28th International Cosmic Ray Conference (ICRC 2003), Tsukuba, Japan, 31 Jul - 7 Aug 2003, 1853-1856.

[10] N. L. Grigorov *et al.*, Yad. Fiz. **11**, 1058 (1970).

[11] N. L. Grigorov *et al.* Proc. of 12th Int. Cosmic Ray Conf. (Hobart), vol. 2, p. 206, 1971.

[12] RUNJOB Collaboration, V. A. Derbina *et al.*, Astrophys. J. **628**, L41 (2005).

[13] Tibet ASγ Collaboration, M. Amenomori *et al.*, Astrophys. J. **678**, 1165 (2008), arXiv:0801.1803 [hep-ex].

[14] KASCADE Collaboration, T. Antoni *et al.*, Astropart. Phys. **24**, 1 (2005), astro-ph/0505413.

[15] A. Haungs *et al.* To appear in Proc. of XIV ISVHECRI 2006, Weihai, China, 2006.

[16] M. Nagano *et al.*, J. Phys. **G10**, 1295 (1984).

[17] M. Nagano *et al.*, J. Phys. **G18**, 423 (1992).

[18] HiRes-MIA Collaboration, T. Abu-Zayyad *et al.*, Astrophys. J. **557**, 686 (2001), astro-ph/0010652.

[19] HiRes-MIA Collaboration, T. Abu-Zayyad *et al.*, Phys. Rev. Lett. **84**, 4276 (2000), astro-ph/9911144.

[20] HiRes Collaboration, R. Abbasi *et al.*, Phys. Rev. Lett. **100**, 101101 (2008), arXiv:astro-ph/0703099.

[21] Pierre Auger Collaboration, J. Abraham *et al.*, Phys. Rev. Lett. **101**, 061101 (2008), arXiv:0806.4302 [astro-ph].

[22] E. G. Berezhko and H. J. Voelk (2007), arXiv:0704.1715 [astro-ph].

[23] A. A. Petrukhin, Nucl. Phys. Proc. Suppl. **151**, 57 (2006).

[24] A. Dar and A. De Rujula, Phys. Rep. **466**, 179 (2006), arXiv:hep-ph/0606199.

[25] J. R. Hoerandel, Astropart. Phys. **19**, 193 (2003), arXiv:astro-ph/0210453.

[26] J. L. Han, Nucl. Phys. Proc. Suppl. **175-176**, 62 (2008).

[27] C. De Donato and G. A. Medina-Tanco (2008), arXiv:0807.4510 [astro-ph].

[28] V. S. Berezinsky, S. I. Grigorieva, and B. I. Hnatyk, Astropart. Phys. **21**, 617 (2004), astro-ph/0403477.

[29] R. Aloisio *et al.*, Astropart. Phys. **27**, 76 (2007), astro-ph/0608219.

[30] T. Wibig and A. W. Wolfendale, J. Phys. **G31**, 255 (2005), astro-ph/0410624.

[31] D. Allard, E. Parizot, and A. V. Olinto, Astropart. Phys. **27**, 61 (2007), astro-ph/0512345.

[32] K. Greisen, Phys. Rev. Lett. **16**, 748 (1966).

[33] G. T. Zatsepin and V. A. Kuzmin, J. Exp. Theor. Phys. Lett. **4**, 78 (1966).

[34] A. M. Hillas, Ann. Rev. Astron. Astrophys. **22**, 425 (1984).

[35] S. R. Coleman and S. L. Glashow, Phys. Rev. **D59**, 116008 (1999), hep-ph/9812418.

[36] W. Bietenholz (2008), arXiv:0806.3713 [hep-ph].

[37] F. R. Klinkhamer (2007), arXiv:0710.3075 [hep-ph]. Invited talk at 3rd Mexican Meeeting on Mathematicsal and Experimental Physics, Mexico City, Mexico, 10-14 Sep 2007.

[38] S. T. Scully and F. W. Stecker (2008), arXiv:0811.2230 [astro-ph].

[39] W. Hofmann, J. Phys. Conf. Ser. **120**, 062005 (2008).

[40] J. K. Becker, Phys. Rept. **458**, 173 (2008), arXiv:0710.1557 [astro-ph].

[41] J. Knapp, D. Heck, S. J. Sciutto, M. T. Dova, and M. Risse, Astropart. Phys. **19**, 77 (2003), arXiv:astro-ph/0206414.

[42] L. Anchordoqui *et al.*, Ann. Phys. **314**, 145 (2004), hep-ph/0407020.

[43] Fly's Eye Collaboration, R. M. Baltrusaitis *et al.*, Nucl. Instrum. Meth. **A240**, 410 (1985).

[44] W. Heitler, *The Quantum Theory of Radiation*, third edition$^{\text{th}}$ edn. Oxford University Press, London, 1954.

[45] J. Matthews, Astropart. Phys. **22**, 387 (2005).

[46] J. Alvarez-Muniz, R. Engel, T. K. Gaisser, J. A. Ortiz, and T. Stanev, Phys. Rev. **D66**, 033011 (2002), astro-ph/0205302.

[47] T. Pierog, R. Engel, and D. Heck, Czech. J. Phys. **56**, A161 (2006), arXiv:astro-ph/0602190.

[48] J. Engel, T. K. Gaisser, T. Stanev, and P. Lipari, Phys. Rev. **D46**, 5013 (1992).

[49] D. Heck. Talk given at CORSIKA School 2008, see http://www-ik.fzk.de/corsika/corsika-school2008/ and private communication, 2008.

[50] S. J. Sciutto (1999), astro-ph/9911331.

[51] D. Heck, J. Knapp, J. Capdevielle, G. Schatz, and T. Thouw, *CORSIKA: a Monte Carlo code to simulate extensive air showers* (unpublished). Wissenschaftliche Berichte FZKA 6019, Forschungszentrum Karlsruhe, 1998.

[52] T. Bergmann *et al.*, Astropart. Phys. **26**, 420 (2007), astro-ph/0606564.

[53] H.-J. Drescher and G. R. Farrar, Phys. Rev. **D67**, 116001 (2003), astro-ph/0212018.

[54] A. M. Hillas, Nucl. Phys. Proc. Suppl. **52B**, 29 (1997).

[55] K. Kasahara *et al.*, *COSMOS* (unpublished). Http://cosmos.n.kanagawa-u.ac.jp/cosmosHome.

[56] F. Ballarini *et al.*, J. Phys. Conf. Ser. **41**, 151 (2006).

[57] H. Fesefeldt. Preprint PITHA-85/02, RWTH Aachen, 1985.

[58] M. Bleicher *et al.*, J. Phys. G: Nucl. Part. Phys. **25**, 1859 (1999).

[59] A. Mücke, R. Engel, J. P. Rachen, R. J. Protheroe, and T. Stanev, Comput. Phys. Commun. **124**, 290 (2000), astro-ph/9903478.

[60] H.-J. Drescher, M. Bleicher, S. Soff, and H. Stoecker, Astropart. Phys. **21**, 87 (2004), astro-ph/0307453.

[61] C. Meurer, J. Bluemer, R. Engel, A. Haungs, and M. Roth, Czech. J. Phys. **56**, A211 (2006), arXiv:astro-ph/0512536.

[62] P. D. B. Collins, *An Introduction to Regge Theorie & High Energy Physics*,. Cambridge University Press,, Cambridge, 1977.

[63] V. N. Gribov, Sov. Phys. JETP **26**, 414 (1968).

[64] N. N. Kalmykov and S. S. Ostapchenko, Phys. Atom. Nucl. **56**, 346 (1993).

[65] N. N. Kalmykov, S. S. Ostapchenko, and A. I. Pavlov, Nucl. Phys. Proc. Suppl. **52B**, 17 (1997).

[66] S. Ostapchenko, Phys. Rev. **D74**, 014026 (2006), arXiv:hep-ph/0505259.

[67] S. Ostapchenko, Phys. Lett. **B636**, 40 (2006), arXiv:hep-ph/0602139.

[68] R. S. Fletcher, T. K. Gaisser, P. Lipari, and T. Stanev, Phys. Rev. **D50**, 5710 (1994).

[69] R. Engel, T. K. Gaisser, T. Stanev, and P. Lipari. Prepared for 26th International Cosmic Ray Conference (ICRC 99), Salt Lake City, Utah, 17-25 Aug 1999.

[70] K. Werner, F.-M. Liu, and T. Pierog, Phys. Rev. **C74**, 044902 (2006), arXiv:hep-ph/0506232.

[71] T. Pierog and K. Werner, Phys. Rev. Lett. **101**, 171101 (2008), arXiv:astro-ph/0611311.

[72] J. Ranft, Phys. Rev. **D51**, 64 (1995).

[73] S. Roesler, R. Engel, and J. Ranft, *The Monte Carlo event generator DPMJET-III at cosmic ray energies* (unpublished). Prepared for 27th International Cosmic Ray Conference (ICRC 2001), Hamburg, Germany, 7-15 Aug 2001, p. 439.

[74] F. W. Bopp, J. Ranft, R. Engel, and S. Roesler, Phys. Rev. **C77**, 014904 (2008), hep-ph/0505035.

[75] M. Zha, J. Knapp, and S. Ostapchenko (2003). Prepared for 28th International Cosmic Ray Conference (ICRC 2003), Tsukuba, Japan, 31 Jul - 7 Aug 2003, p. 515-518.

[76] R. Engel, Nucl. Phys. Proc. Suppl. **122**, 40 (2003).

[77] V. Topor Pop, M. Gyulassy, and H. Rebel, Astropart. Phys. **10**, 211 (1999), nucl-th/9809014.

[78] M. Gyulassy and X.-N. Wang, Comput. Phys. Commun. **83**, 307 (1994), arXiv:nucl-th/9502021.

[79] R. Luna, A. Zepeda, C. A. Garcia Canal, and S. J. Sciutto, Phys. Rev. **D70**, 114034 (2004), hep-ph/0408303.

[80] H.-J. Drescher and G. R. Farrar, Astropart. Phys. **19**, 235 (2003), hep-ph/0206112.

[81] T. K. Gaisser, R. J. Protheroe, K. E. Turver, and T. J. L. Mccomb, Rev. Mod. Phys. **50**, 859 (1978).

[82] KASCADE Collaboration, T. Antoni *et al.*, Nucl. Instrum. Meth. **A513**, 490 (2003).

[83] Pierre Auger Collaboration, J. Abraham *et al.*, Nucl. Instrum. Meth. **A523**, 50 (2004).

[84] KASCADE Collaboration, T. Antoni *et al.*, Astropart. Phys. **16**, 245 (2002), astro-ph/0102443.

[85] J. R. Hörandel, J. Phys. **G29**, 2439 (2003), astro-ph/0309010.

[86] HiRes Collaboration, T. Abu-Zayyad *et al.*, Nucl. Instrum. Meth. **A450**, 253 (2000).

[87] Pierre Auger Collaboration, R. Engel (2007), arXiv:0706.1921 [astro-ph].

[88] Pierre Auger Collaboration, A. S. Chou *et al.* Proc. of 29th Int. Cosmic Ray Conference (ICRC 2005), Pune, India, 3-11 Aug 2005, p. 319.

[89] F. Schmidt, M. Ave, L. Cazon, and A. S. Chou, Astropart. Phys. **29**, 355 (2008), arXiv:0712.3750 [astro-ph].

[90] H. J. Drescher, A. Dumitru, and M. Strikman, Phys. Rev. Lett. **94**, 231801 (2005), arXiv:hep-ph/0408073.

[91] R. Engel, Nucl. Phys. B (Proc. Suppl.) **75A**, 62 (1999), astro-ph/9811225.

[92] M. Albrow *et al.*, *Prospects for diffractive and forward physics at the LHC* (unpublished). CERN-LHCC-2006-039, CMS Note-2007/002, TOTEM Note 06-5.

[93] T. Sako *et al.*, Nucl. Instrum. Meth. **A578**, 146 (2007).

[94] UA7 Collaboration, E. Pare *et al.*, Phys. Lett. **B242**, 531 (1990).

[95] CDF Collaboration, F. Abe *et al.*, Phys. Rev. **D50**, 5550 (1994).

[96] E710 Collaboration, N. A. Amos *et al.*, Phys. Rev. Lett. **63**, 2784 (1989).

[97] E811 Collaboration, C. Avila *et al.*, Phys. Lett. **B445**, 419 (1999).

[98] SELEX Collaboration, U. Dersch *et al.*, Nucl. Phys. **B579**, 277 (2000), arXiv:hep-ex/9910052.

[99] R. J. Glauber and G. Matthiae, Nucl. Phys. **B21**, 135 (1970).

[100] R. Ulrich, J. Blümer, R. Engel, F. Schüssler, and M. Unger (2007), arXiv:0709.1392 [astro-ph]. In Proc. of 12th Int. Conf. on Elastic and Diffractive Scattering, Hamburg, May 21 - 25, 2007.

[101] C. Pajares, D. Sousa, and R. A. Vazquez, Phys. Rev. Lett. **86**, 1674 (2001), arXiv:astro-ph/0005588.

[102] J. Dias de Deus, M. C. Espirito Santo, M. Pimenta, and C. Pajares, Phys. Rev. Lett. **96**, 162001 (2006), arXiv:hep-ph/0507227.

[103] J. Alvarez-Muniz *et al.*, Astropart. Phys. **27**, 271 (2007), hep-ph/0608050.

Experimental Results

A. Bunyatyan, A. Cooper-Sarkar, C. Diaconu, R. Engel, C. Kiesling, K. Kutak, S. Ostapchenko, T. Pierog, T.C. Rogers, M.I. Strikman, T. Sako

1 From HERA to LHC and Cosmic Rays

There seem to be two prime motivations for discussing HERA data in connection with the future running at the LHC and the physics of cosmic rays. First of all, HERA provides a precise picture of the structure of the proton, which are the scattering partners at the LHC. Concerning cosmic ray physics, the electron-proton (ep) reactions at HERA can be viewed as collisions of ultra-high-energy photons - emitted by the electron - with nuclear matter. Comparing to the cosmic ray energy spectrum impinging on the earth's atmosphere, the HERA collider provides a photon beam equivalent to 50 TeV on a stationary proton target, lying about half way on a logarithmic scale, at about almost 10^{14} eV, between the intensity maximum at 1 GeV and the "ankle" of the cosmic ray energy spectrum. Such high energy photon-proton collisions are of utmost importance for observational astrophysics, in particular for the understanding of the interactions of ultra-high-energy cosmic photons with our atmosphere which usually serves as the target in the cosmic ray experiments.

High energy photon interactions with hadronic matter are governed mainly by the strong interaction, which can be successfully described by quantum chromodynamics (QCD) as long as some "hard scale" of order several GeV is present in the reactions under study. Owing to the photon in the initial state, the overall size of the cross sections, however, is small, being proportional to the square of the fine-structure constant α. In view of the LHC, the HERA data give direct information on quantities related to QCD, most importantly the parton distribution functions (pdfs) within the nucleon, and the running strong coupling α_S, determining the overall strength of the partonic branching processes. These quantities, among others, are important ingredients to the Monte Carlo programs simulating cosmic ray showers in the atmosphere. There is, however, another interesting area in cosmic ray research, where HERA can provide important information, namely ultra-high energy neutrino scattering, which can be inferred from $ep \to \nu X$ reactions at HERA. Also here, the neutrino energy accessible at HERA is equivalent to about 50 TeV on a stationary proton target.

In the following we will briefly summarize the data on the total photoproduction cross section from HERA and present some recent results on inclusive scattering, discussing the extraction of the parton distribution functions from a combined data set of the two collider experiments H1 and ZEUS. We will then discuss jet final states with emphasis on the phase space near the forward (proton) direction. These data shed light on the parton evolution models and also enable a unique measurement of the running strong coupling, providing new insight into QCD dynamics at very low values of the Bjorken variable x. We finally mention the relevance of the HERA charged current cross sections for the expectation of ultra-high energy neutrino nucleon cross sections, which will be elaborated in more detail in section 3.

The HERA Physics Mission One of the most successful tools for unraveling the structure of hadrons, most importantly of the nucleons, is deep-inelastic scattering (DIS) using charged leptons as probes. The HERA collider at the Deutsches Elektronen-Synchrotron DESY in Hamburg has provided the highest available center-of-mass energies for the collision of electrons and positrons with protons. HERA has been running from 1992 until mid 2007, accumulating a total of about 500 pb^{-1} for each of the two colliding beam experiments H1 [1] and ZEUS [2]. The data taking was divided into two phases, separated by a massive luminosity upgrade program in the years 2001-2002. As a further benefit of the upgrade, HERA also provided longitudinally polarized electron and positron beams, giving access to sensitive tests of the electroweak theory and allowing to carry out unique searches for the production of new heavy particles. While the electroweak sector was tested in electron-quark scattering at an unprecedented level, the hope for discovering "New Physics" at HERA did not materialize.

Photoproduction at HERA Measuring the total hadronic photoproduction cross section at high center-of-mass energies gives access to the asymptotic behavior of cross sections in general. The energy dependences of the total cross sections for pp, $\bar{p}p$, Kp and πp are well described by Regge theory [3]. Phenomenological fits based on this (non-perturbative) theory are successfully parameterizing all the hadronic cross sections in the full energy range (above the s-channel resonance region) using the common form

$$\sigma_{\text{tot}} = A \cdot s^{\epsilon} + B \cdot s^{-\eta},$$

where s is the square of the center-of-mass energy and A and B are constants. The parameter ϵ describes the weak energy dependence at high energies ($1 + \epsilon$ is the "Pomeron intercept", which is about 1.09).

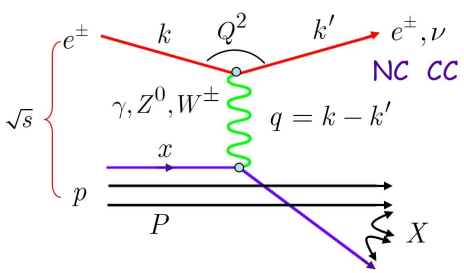

Fig. 1: Lowest order Feynman diagram for deep-inelastic electron-proton scattering in the parton picture, showing the relevant kinematic quantities characterizing inclusive DIS reactions and photoproduction (see text). The hadronic final state "fragmented" from the scattered and spectator partons is indicated by X.

The photon-proton total cross section is measured in the process $ep \to e\gamma p \to eX$, where the initial state electron has radiated a photon, which is then absorbed by the proton, producing a hadronic final state X. The event kinematics (see fig. 1 for a general lowest order Feynman diagram) is best described in terms of the Lorentz-invariant photon virtuality Q^2, and the event inelasticity y, both defined as

$$Q^2 = -q^2 = -(k - k')^2$$

and

$$y = \frac{p \cdot q}{p \cdot k}.$$

The square of the photon-proton center-of-mass energy W, i.e. the mass squared of the hadronic system X, is given by

$$W^2 = (q+p)^2 = 4E_e E_p y.$$

The photon virtuality has a kinematic minimum due to the finite electron mass m_e, and is given by

$$Q^2_{\min} = \frac{m_e^2 y^2}{1-y}.$$

The photoproduction cross section is related to the double differential electroproduction cross section (which is actually observed experimentally) by the equivalent photon approximation [4], which can be written as

$$\frac{d^2\sigma^{ep}}{dydQ^2} = \frac{\alpha}{2\pi Q^2}\left[\left(\frac{1+(1-y)^2}{y} - \frac{2(1-y)}{y}\frac{Q^2_{\min}}{Q^2}\right)\cdot\sigma_T^{\gamma p}(y,Q^2) + \frac{2(1-y)}{y}\cdot\sigma_L^{\gamma p}(y,Q^2)\right],$$

where $\sigma_T^{\gamma p}$ ($\sigma_L^{\gamma p}$) is the cross section for transversely (longitudinally) polarized photon on protons. Since the virtuality of the photon is small by excluding deep inelastic scattering events ($Q^2_{\max} \sim 0.02$ GeV^2), the longitudinal cross section is expected to be small. Integrating over Q^2 gives the total γp cross section in terms of the single ep differential cross section:

$$\sigma^{\gamma p}_{\rm tot}(y) = \frac{2\pi}{\alpha}\left[\frac{1+(1-y)^2}{y}\ln\frac{Q^2_{\max}}{Q^2_{\min}} - \frac{2(1-y)}{y}\left(1-\frac{Q^2_{\min}}{Q^2_{\max}}\right)\right]^{-1}\cdot\frac{d\sigma^{ep}(y)}{dy}$$

The event inelasticity y is given by the acceptance of the electron tagging systems and can be integrated over, so that $\sigma^{\gamma p}_{\rm tot}(W)$ can be determined. The results of the measurements from HERA [5, 6] are shown in fig 2, together with the low energy data [7] and a phenomenological Regge fit [8] using hadron data, marked as "DL98". The compatibility of the photoproduction cross section with the hadronic data supports the universal energy dependence of all total cross sections at asymptotic energies.

Quantum Chromodynamics in the HERA Regime Quantum Chromodynamics (QCD) is expected to describe the strong interactions between quarks and gluons. At distances small compared to the nucleon radius, or equivalently large momentum transfer Q^2 where the strong coupling $\alpha_{\rm S}$ is small, perturbative QCD (pQCD) gives an adequate quantitative account of hadronic processes. The total cross sections, however, are dominated by long range forces ("soft interactions"), where a satisfactory understanding of QCD still remains a challenge. This is most importantly so also for all transitions of partons to hadrons in the final state ("fragmentation process"). In addition, non-perturbative effects govern the DIS kinematics through the momentum distribution ("parton distribution functions", or "pdfs") of the initial partons, interacting with the electrons via photon or Z^0 exchange (see fig.1). The latter is important only at very large Q^2, i.e. around or beyond the mass of the Z^0. The division between the non-perturbative and the perturbative regimes is defined by the factorization scale, which should be sufficiently large ($\mathcal{O}$(few GeV^2) to hope for a convergent perturbative expansion in the strong coupling constant $\alpha_{\rm S}$.

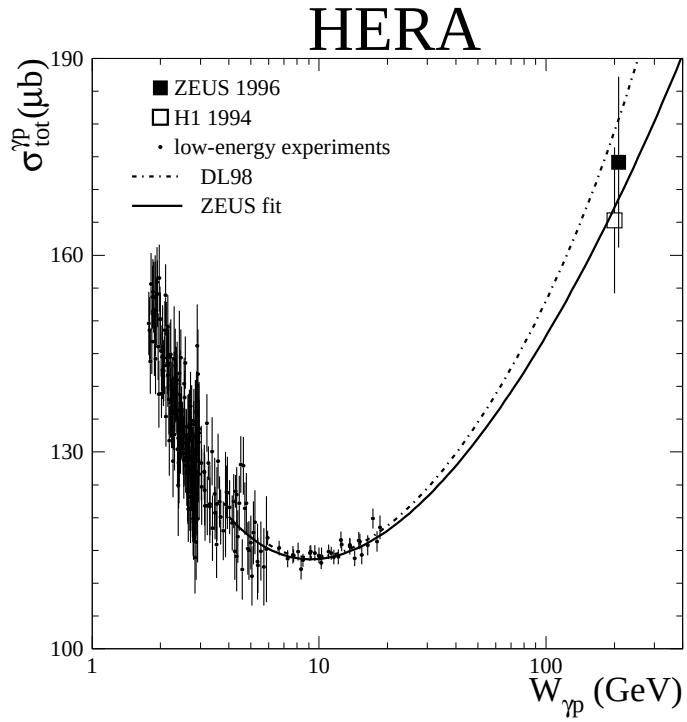

Fig. 2: Measurements of the total photoproduction cross section $\sigma_{\gamma p}$ for positron-proton scattering from early measurements of H1 [5] and ZEUS [6].

Within the framework of perturbative QCD, the DIS cross section at the parton level is generically given by

$$\sigma = \sum_i \sigma_{\gamma^* i}(Q^2) \otimes x f_i(x, Q^2), \tag{1}$$

where Q^2 is the virtuality of the exchanged boson (here: the virtual photon γ^*), x is the momentum fraction (Bjorken x) of the incoming parton, and $\sigma_{\gamma^* i}$ is the total virtual photon-parton cross section. In this expression the factorization theorem of QCD [9] has been used, separating the cross section into a hard scattering part between the exchanged virtual photon and the incoming parton i, convoluted with a part (including a non-perturbative contribution) describing the momentum distribution $x f_i(x, Q^2)$ of parton i within the proton. In eq.(1) one recognizes the incoherent summing of quark contributions, which is justified by the property of asymptotic freedom. Asymptotic freedom states that the interaction between the partons within the proton, characterized by the strong coupling constant α_S become weak at large Q^2 ($\alpha_S \to 0$ as $Q^2 \to \infty$). In this way the scattering process of the electron with the partons of the proton can be treated incoherently.

Figure 1 also indicates the kinematics in the HERA regime. Here, s is the square of the total ep center of mass energy. The four-momentum transfer squared Q^2 is given by the scattered electron alone, the Bjorken variable x and the inelasticity y (equal to the energy fraction transferred from the electron to the virtual photon in the proton rest frame, see above), with x

given by

$$x = \frac{Q^2}{2\,P \cdot q}. \tag{2}$$

Only two of the three quantities in eq. (2) are independent, they are related via $Q^2 = sxy$. Another interesting quantity is the total mass M_X of the hadronic final state, given by

$$M_X^2 \equiv W^2 = (q+P)^2 = \frac{Q^2(1-x)}{x} \tag{3}$$

This relation shows that low x reactions correspond, at fixed Q^2, to large values of W^2, i.e. large invariant masses of the hadronic final state. Due to the high colliding beam energies (protons at 920 GeV, electrons at 27.6 GeV), HERA provided a large range of exploration for x and Q^2, extending the reach of previous fixed target experiments by more than 2 orders of magnitude in x and Q^2.

The double differential cross section for ep scattering is written in terms of structure functions as (see, e.g. [10])

$$\frac{d^2\sigma\,(e^{\pm}p)}{dx\,dQ^2} = \frac{2\pi\alpha^2}{xQ^4} Y_+ \left[F_2 - \frac{y^2}{Y_+} F_L \mp \frac{Y_-}{Y_+} xF_3 \right], \tag{4}$$

where the functions $Y_\pm$ are given by $Y_\pm = 1 \pm (1-y)^2$, and the structure functions, apart from coupling constants, are combinations of the parton distribution functions. For the case of pure photon exchange, valid at low Q^2, one obtains

$$F_2(x,Q^2) = \sum_{i=u,d,\ldots} e_i^2 x f_i(x,Q^2). \tag{5}$$

where the sum extends over all partons within the proton of charge e_i. As indicated in fig. 1, all reactions with neutral boson exchange are called "neutral current (NC)" reactions, those with $W^\pm$ exchange (here the final state lepton is a neutrino) are called "charged current (CC)" reactions.

The non-perturbative parton distribution functions $f_i(x)$ cannot be calculated from first principles and have therefore to be parameterized at some starting scale Q_0^2. Perturbative QCD predicts the variation of f_i with Q^2, i.e. $f_i = f_i(x,Q^2)$ via a set of integro-differential evolution equations, as formulated by Altarelli and Parisi ("DGLAP" equations, see [11]). The predicted Q^2 dependence ("scaling violations") of the structure function F_2, see eq. (5), are nicely supported by the data from HERA [12].

Low x Physics and the Parton Distribution Functions At distances small compared to the nucleon radius, or equivalently large momentum transfer Q^2 between the incoming and outgoing leptons, perturbative QCD (pQCD) gives an adequate quantitative account of hadronic processes in DIS. The most "elementary"observable in electron-proton scattering is the inclusive DIS cross section, where basically only the 4-vectors of the scattered lepton or the produced hadronic final state are measured.

Inclusive ep scattering can be divided into two distinct classes: Neutral current (NC) reactions ($ep \to eX$), and Charged Current (CC) reactions ($ep \to \nu X$). In NC reactions, a photon or

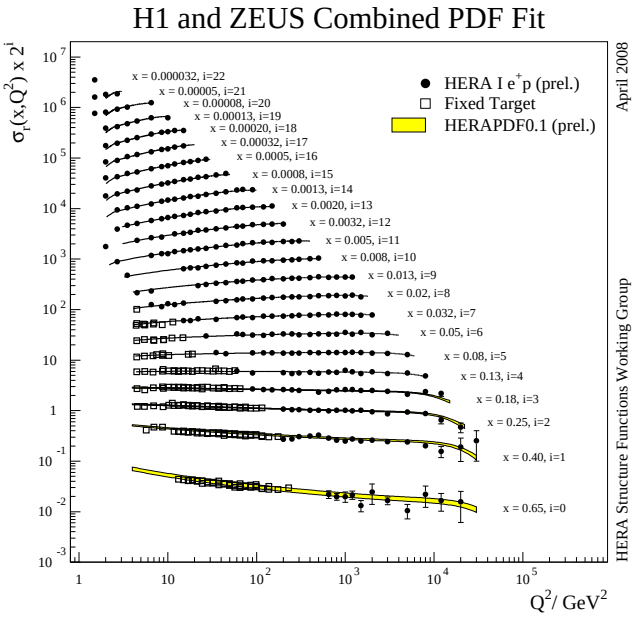

Fig. 3: Measurements of the reduced cross section $\sigma_r(x, Q^2)$ for positron-proton scattering, based on the combined data of H1 and ZEUS [12]. The data show clear evidence for scaling violations, as expected from gluon emission of the initial quarks participating in the hard scattering process. The scaling violations are very well described by pQCD NLO fit HERAPDF 0.1 [13]. At low Q^2, the data from some fixed target experiments are also shown.

a Z^0 is exchanged between the electron and a quark emitted from the proton. The corresponding double-differential cross section $d^2\sigma/dxdQ^2$, or the so-called "reduced" cross section σ_r factorizing out known kinematic terms, can be written in the following way (similar expressions also hold for the CC reactions):

$$\sigma_r(x, Q^2) \equiv \left(\frac{xQ^4}{2\pi\alpha^2 Y_+}\right) \frac{d^2\sigma\,(e^{\pm}p)}{dx\,dQ^2} = F_2 - \frac{y^2}{Y_+} F_L \mp \frac{Y_-}{Y_+} xF_3 \tag{6}$$

Here, the three (positive definite) structure functions F_2, F_L and xF_3 depend both on x and Q^2, and contain the (non-perturbative) parton distribution functions (pdfs). The structure function F_2 contains contributions from quarks and antiquarks ($\sim x(q + \bar{q})$), F_L is dominated by the gluon distribution ($\sim xg$), and xF_3 is sensitive to the valence quarks ($\sim x(q - \bar{q})$).

At low Q^2 and low y the structure functions xF_3 (from Z^0 exchange) and F_L (suppressed by the factor y^2) can be safely neglected. Residual (small) contributions from F_L can also be modeled using pQCD. In this case the structure function F_2 can be extracted at each point of x and Q^2 from the "reduced" cross section σ_r (see eq. (6)). Measurements of σ_r from the combined H1 and ZEUS data [12] are shown in fig. 3. The data, most importantly their Q^2 dependence, are very well described by NLO pQCD.

Figure 4 shows the pdfs resulting from the NLO pQCD fit HERAPPDF 0.1 to the combined NC and CC double-differential cross sections from both HERA experiments [13]. The

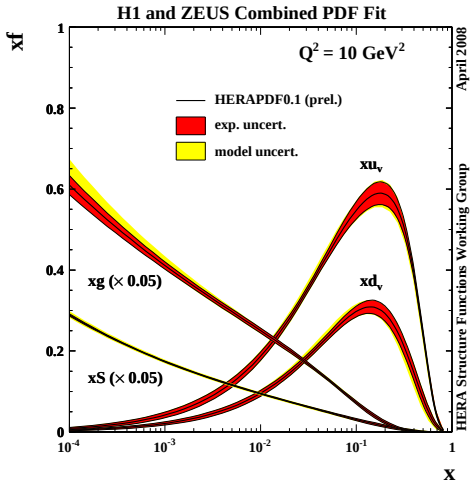

Fig. 4: The parton distribution functions from QCD fits to the HERA data on NC and CC inclusive reactions, using the combined data from H1 and ZEUS (HERAPDF 0.1) [13].

resulting uncertainties of the pdfs have drastically shrunk due to the combination of the HERA data. It should also be noted that the pdfs for the gluon and the sea quarks, even at the lowest values of Bjorken x, and for all values of Q^2, keep rising with decreasing x. This means that parton saturation has not been observed within the kinematic range of HERA - assuming that the parameterisation used in the fits would be flexible enough to allow the observation of such behaviour.

From fig. 4 one clearly sees that the gluon distribution is dominating the low x behavior of the DIS cross sections. At low x, the structure function F_2 can be satisfactorily parameterized as being proportional to $x^{-\lambda}$. Figure 5 shows the values of λ as function of Q^2. One can observe a clear decrease of λ with decreasing Q^2, touching the hadron-hadron limit (and also photoproduction, see the left-most data point) at a photon virtuality around 1 GeV^2.

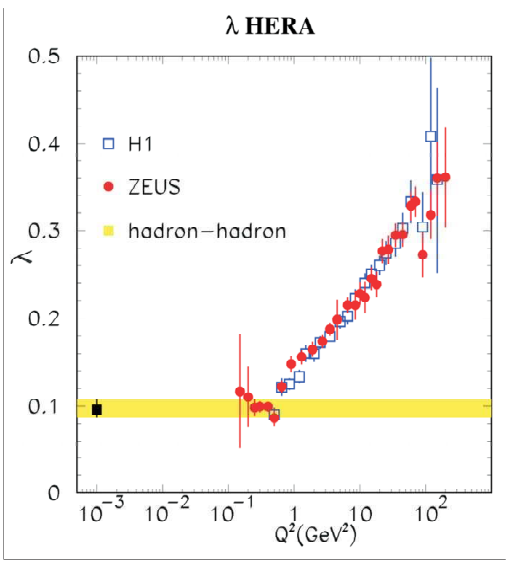

Fig. 5: Measurements of the slope of F_2 for deep inelastic scattering as function of Q^2. To the far left, the photoproduction point $\epsilon \equiv \lambda$ is also drawn. .

Jet Production Collimated bundles of particles ("jets") are carrying the kinematic information of the partons emerging from DIS reactions at HERA and other high p_t colliding beam experiments. The study of jet production is therefore a sensitive tool to test the predictions of perturbative QCD and to determine the strong coupling constant α_s over a wide range of Q^2.

Several algorithms exist to cluster individual final state hadrons into jets, but most commonly used at HERA is the so-called k_T clustering algorithm [14]. The jet finding is usually executed in the hadronic center of mass system. which is, up to a Lorentz boost, equivalent to the Breit frame. At the end of the algorithm, the hadrons are collected into a number of jets.

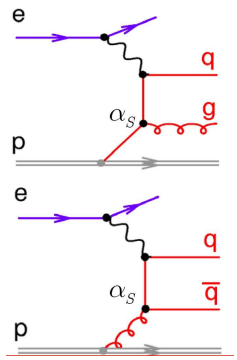

Fig. 6: Feynman diagrams for LO jet production. The upper subgraph is called "QCD Compton", the lower subgraph is called "boson-gluon fusion". Both graphs contribute to two-jet final states. Events with three jets can be interpreted as a di-jet process with additional gluon radiation from one of the involved quark lines, or as a gluon splitting into a quark-antiquark pair. These processes are of order $\mathcal{O}(\alpha_s^2)$ (NLO).

At leading order (LO) in α_s, di-jet production (see fig. 6) proceeds via the QCD Compton process ($\gamma^* q \rightarrow qg$) and boson-gluon fusion ($\gamma^* g \rightarrow q\bar{q}$). The cross section for events with three jets is of $\mathcal{O}(\alpha_s^2)$. These events can be interpreted as coming from a di-jet process with additional gluon radiation or gluon splitting (see caption of fig. 6), bringing the QCD calculation to next-to-leading order (NLO).

In jet physics, two different "hard" scales can be used to enable NLO (and higher) calculations: the variable Q, and the transverse energy E_T of the jets. Figure 7 shows the differential cross sections for inclusive jet production at high Q^2 as measured by the ZEUS Collaboration [15], both with respect to Q^2 and E_T. The data are compared to NLO calculations, using the renormalization and factorization scales as indicated in the figure. Both schemes are able to describe the data very well, indicating the validity of the choice of any of the two hard scales. Given the experimental and theoretical uncertainties at these large scales, no higher order (beyond NLO) corrections seem necessary.

Forward Jets All of the analyses regarding the observables mentioned in the previous chapters rest on the DGLAP Q^2 evolution scheme for the pdfs involved. Potential deviations observed a certain regions of phase space (low x, low Q^2) are usually attributed to the limited order of the presently computed QCD matrix elements (LO, NLO, sometimes NNLO). Especially for low x ($\approx 10^{-4}$), but sufficiently large Q^2 ($>$ a few GeV^2), there has been a vivid debate about the validity of the DGLAP approach. In this kinematic regime the initial parton in the proton can induce a QCD cascade, consisting of several subsequent parton emissions, before eventually an interaction with the virtual photon takes place (see fig. 8). QCD calculations based on the "direct" interaction between a point-like photon and a parton from the evolution chain, as given

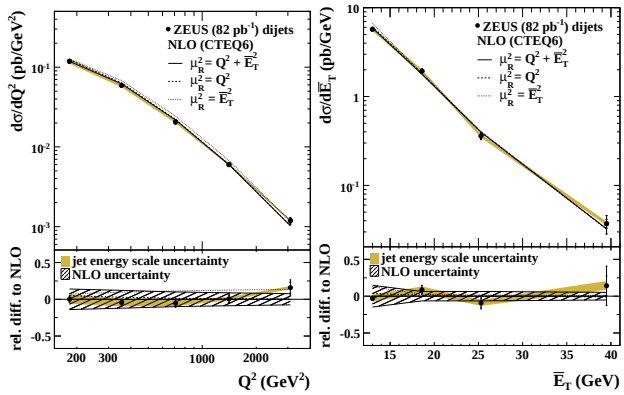

Fig. 7: Differential cross sections for inclusive jet production from the ZEUS experiment [15]. Also shown are the predictions from next-to-leading order QCD calculations, which give a good description of the data.

by the DGLAP approach, are very successful in describing, e.g. the unexpected rise of F_2 with decreasing x over a large range in Q^2 [16].

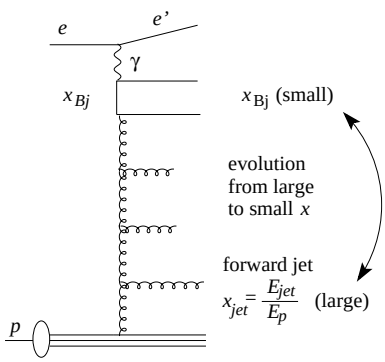

Fig. 8: Schematic diagram of ep scattering producing a forward jet. The evolution in the longitudinal momentum fraction x, from large $x_{\rm jet}$ to small $x_{\rm Bj}$, is indicated.

For low values of x, there is, however, a technical reason to question the validity of the DGLAP evolution approach: Since it resums only leading $\log(Q^2)$ terms, the approximation may become inadequate for very small x, where $\log(1/x)$ terms become important in the evolution equations. In this region the BFKL scheme [17] is expected to describe the data better, since in this scheme terms in $\log(1/x)$ are resummed.

The large phase space available at low x (see eq.(3)) makes the production of forward jets (in the angular region close to the proton direction) a particularly interesting topic for the study of parton dynamics, since jets emitted in this region lie well away in rapidity from the photon end of the evolution ladder (see fig. 8). Concerning the forward jets there is a clear dynamic distinction between the DGLAP and BFKL schemes: In the DGLAP scheme, the parton cascade resulting from hard scattering of the virtual photon with a parton from the proton is ordered in parton virtuality. This ordering along the parton ladder implies an ordering in transverse energy E_T of the partons, so that the parton participating in the hard scatter has the highest E_T. In the BFKL scheme there is no strict ordering in virtuality or transverse energy. The BFKL evolution therefore predicts that a larger fraction of low x events will contain high-E_T forward jets than is predicted by the DGLAP evolution.

Both ZEUS [18] and H1 [19] have studied forward jet production, where "forward" typically means polar emission angles less than about 20 degrees relative to the proton direction. As

a first example, the single differential cross sections $d\sigma/dx$ from H1 are shown in fig. 9. The data are compared to LO and NLO QCD calculations [20] (a), and several Monte Carlo models (b and c). The NLO calculation in (a) is significantly larger than the LO calculation. This reflects the fact that the contribution from forward jets in the LO scenario is kinematically suppressed. Although the NLO contribution opens up the phase space for forward jets and considerably improves the description of the data, it still fails by a factor of 2 at low x. In fig. 9b the predictions from the CASCADE Monte Carlo program [21] is shown, which is based on the CCFM formalism [22]. The CCFM equations provide a bridge between the DGLAP and BFKL descriptions by resumming both $\log(Q^2)$ and $\log(1/x)$ terms, and are expected to be valid over a wider x range. The model predicts a somewhat harder x spectrum, and fails to describe the data at very low x. In part (c) of the figure, the predictions ("RG-DIR") from the LO Monte Carlo program RAPGAP [23] is shown, which is supplemented with initial and final state parton showers generated according to the DGLAP evolution scheme. This model, which implements only direct photon interactions, gives results similar to the NLO calculations from part (a), and falls below the data, particularly at low x. The description is significantly improved, if contributions from resolved virtual photon interactions are included ("RG-DIR+RES"). However, there is still a discrepancy in the lowest x bin, where a possible BFKL signal would be expected to show up most prominently. The Color Dipole Model (CDM) [24], which allows for emissions non-ordered in transverse momentum, shows a behavior similar to RG-DIR+RES.

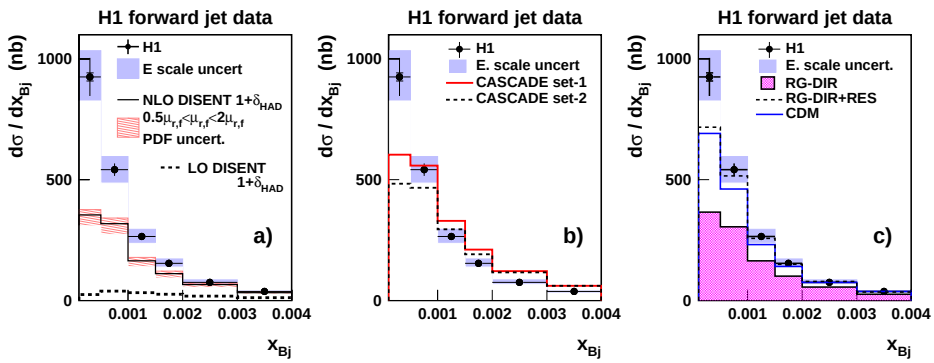

Fig. 9: Single differential cross sections for forward jets as functions of x from the H1 experiment [19], compared to NLO predictions [20] in (a), and QCD Monte Carlo models [23, 24] in (b) and (c). The dashed line in (a) shows the LO contribution.

For a more detailed study the forward jet sample was divided into bins of $p^2_{t,\mathrm{jet}}$ and Q^2. The triple differential cross section $d^3\sigma/dxdQ^2dp^2_{t,\mathrm{jet}}$ versus x is shown in fig. 10 for several regions in Q^2 and $p^2_{t,\mathrm{jet}}$. In addition, the expectations from the above mentioned QCD models are presented. Using the ratio $r = p^2_{t,\mathrm{jet}}/Q^2$, various regimes can be distinguished: For $p^2_{t,\mathrm{jet}} < Q^2$ $(r < 1)$ one expects a DGLAP-like behavior, dominated by direct photon interactions (see fig. 10 c). Due to the large bin sizes, however, the ranges of r can be quite large, so that r in this bin can assume values up to 1.8 due to admixtures from events with $p^2_{t,\mathrm{jet}} > Q^2$. This may explain why the DGLAP direct model (RG-DIR), although closer to the data in this bin than in any other, does not quite give agreement with the data except at the highest x-bin. In the region

$p^2_{t,\mathrm{jet}} \approx Q^2$ ($r \approx 1$, see fig. 10 b and f), DGLAP suppresses parton emission, so that BFKL dynamics may show up. However, the DGLAP resolved model (RG-DIR+RES) describes the data reasonably well.

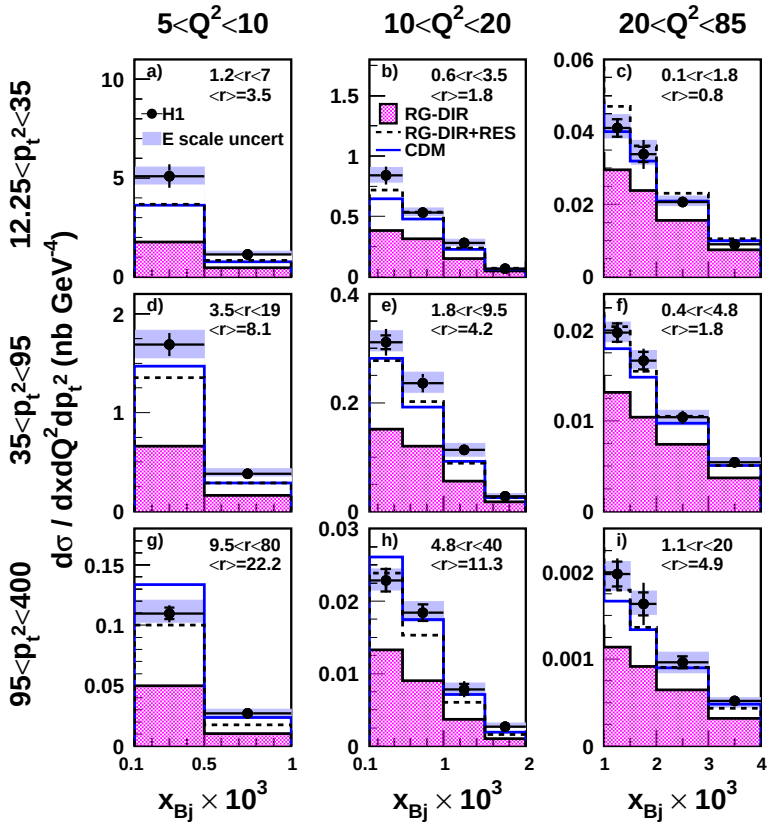

Fig. 10: Triple differential cross sections for forward jet production as function of x in bins of Q^2 and $p^2_{t,\mathrm{jet}}$, compared to various Monte Carlo calculations (see text).

The regime of $p^2_{t,\mathrm{jet}} > Q^2$ ($r > 1$, see fig. 10 d, g and h), is typical for processes where the virtual photon is resolved, i.e. the incoming parton from the proton vertex interacts with a parton from the photon. As expected, the DGLAP resolved model (RG-DIR+RES) provides a good overall description of the data, again similar to the CDM model. However, it can be noted that in regions where r is largest and x is small, CDM shows a tendency to overshoot the data. DGLAP direct (RG-DIR), on the other hand, gives cross sections which are too low. Although the above analysis tries to isolate "BFKL regions" from "DGLAP regions", the conclusion on underlying dynamics cannot be reached, most importantly since the "BFKL region" ($r \approx 1$) is apparently heavily contaminated by "DGLAP-type" events. In addition, the two "different" evolution approaches, RG-DIR+RES ("DGLAP") and CDM ("BFKL"), give similar predictions.

In a further step, the parton radiation ladder (see fig. 8) is examined in more detail by looking also at jets in the region of pseudorapidity, $\eta = -\ln\tan(\theta/2)$, between the scattered electron (η_e) and the forward jet (η_{forw}). In this region a "2-jet + forward" sample was selected,

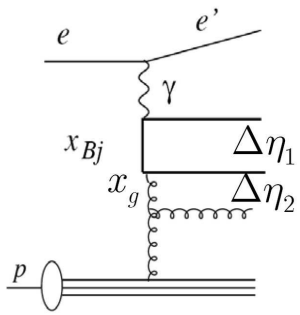

Fig. 11: Kinematic regions for the event sample "2jets + forward" (see text). The quarks in the photon-gluon fusion process are q_1 (upper solid line) and q_2 (lower solid line). The rapidity gap between q_1 and q_2 is denoted by $\Delta\eta_1$, the gap between q_2 and the forward jet is denoted by $\Delta\eta_2$.

requiring at least 2 additional jets, with $p_{t,\mathrm{jet}} > 6$ GeV for all three jets, including the forward jet. In this scenario, evolution with strong k_t ordering is obviously disfavored. The jets are ordered in rapidity according to $\eta_{\mathrm{forw}} > \eta_{\mathrm{jet2}} > \eta_{\mathrm{jet1}} > \eta_e$. Two rapidity intervals are defined between the two additional jets and the forward jet (see fig. 12): $\Delta\eta_1 = \eta_{\mathrm{jet2}} - \eta_{\mathrm{jet1}}$ is the rapidity interval between the two additional jets, and $\Delta\eta_2 = \eta_{\mathrm{forw}} - \eta_{\mathrm{jet2}}$ is the interval between jet 2 and the forward jet. If the di-jet system originates from the quark line coupling to the photon (see fig. 12), the phase space for evolution in x between the di-jet system and the forward jet is increased by requiring that $\Delta\eta_1$ is small and that $\Delta\eta_2$ is large: Requiring $\Delta\eta_1 < 1$ will favor small invariant masses of the di-jet system. As a consequence, x_g will be small, leaving the rest for additional radiation. When, on the other hand, $\Delta\eta_1$ is required to be large ($\Delta\eta_1 > 1$) BFKL-like evolution may then occur between the two jets from the di-jet system or, when both $\Delta\eta_1$ and $\Delta\eta_2$ are small, between the di-jet system and the hard scattering vertex. Note that the rapidity phase space is restricted only for the forward jet.

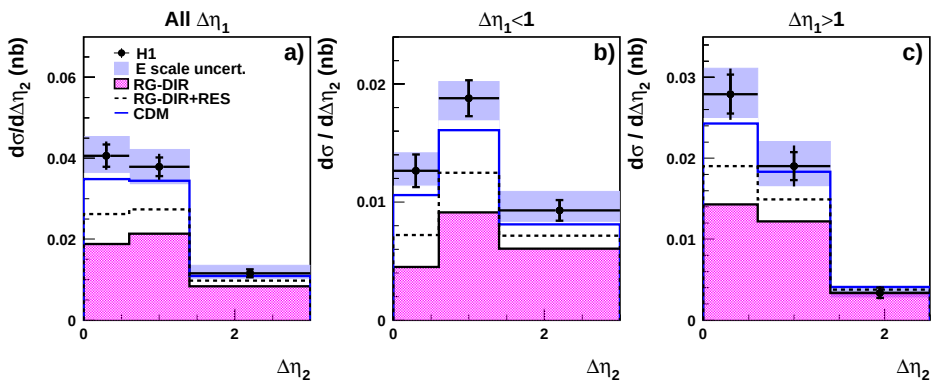

Fig. 12: Cross section for events with a reconstructed high transverse momentum di-jet system and a forward jet from the H1 experiment [19], as function of $\Delta\eta_2$ for two regions of $\Delta\eta_1$. The data are compared to predictions of "DGLAP-like (RG-DIR+RES) and "BFKL-like" (CDM) Monte Carlo models (see text).

As argued above, this study disfavors evolution with strong ordering in k_t due to the common requirement of large $p_{t,\mathrm{jet}}$ for the three jets. Radiation which is not ordered in k_t may occur at any location along the evolution chain, depending on the values of $\Delta\eta_1$ and $\Delta\eta_2$. Figure 12 show the measured cross sections as function of $\Delta\eta_2$ for all data, and separated into the two regions of $\Delta\eta_1$ discussed above. One can see that here the CDM model is in good agreement with

the data in all cases, while the DGLAP models predict cross sections which are too low, except when both $\Delta\eta_1$ and $\Delta\eta_2$ are large. For this topology all models (and the NLO calculation, not shown) agree with the data, indicating that the available phase space for evolution is exhausted.

It is important to realize that the "2+forward jet" sample indeed seems to differentiate between the CDM and DGLAP resolved models, in contrast to the more inclusive samples (see fig. 10). The conclusion is that additional breaking of the k_t ordering, beyond what is included in the resolved photon model, is required by the data, pointing towards some evidence for BFKL dynamics. It is, however, not excluded that such effects may also be described by higher order DGLAP calculations, which may become available in the future. Further investigations using forward particle emission will be discussed below (see section 2).

The Strong Coupling Constant One of the most important measurements using multi-jet final states is the determination of the strong coupling constant $\alpha_{\rm S}$. At HERA, this measurement is particularly interesting, since $\alpha_{\rm S}$ can be determined in a single experiment over a large range of Q or E_T. Observables which are sensitive to $\alpha_{\rm S}$ come from various sources, such as inclusive jets, jet ratios (number of three jets relative to the number of two jets), and event shape variables (thrust, jet masses, angles between jets etc.). A recent compilation of $\alpha_{\rm S}$ determinations [25] from the two HERA experiments H1 and ZEUS, using various jet observables and the HERA I data set, is shown in fig. 13. An NLO fit to these data yields a combined value of $\alpha_{\rm S}(M_Z) = 0.1198 \pm 0.0019(\exp.) \pm 0.0026(\rm th.)$. The dominating theoretical error arises from the uncertainty due to terms beyond NLO, which is estimated by varying the renormalization scale by the "canonical" factors 0.5 and 2. A recent preliminary result obtained by the H1 Collaboration using the full HERA data set and based on multiple observables in inclusive and multi-jet events displays an experimental error below 1% [26]: $\alpha_s = 0.1182 \pm 0.0008(exp)^{+0.0041}_{-0.0031}(th.) \pm 0.0018$. This illustrates the potential for a very precise measurement of the strong coupling using the full HERA data set.

Ultra-High Energy Neutrino Reactions With the era of high energy neutrino astrophysics approaching, it is interesting to review our knowledge about the neutrino-nucleon cross section at ultra-high energies beyond $\mathcal{O}(10$ TeV). Such energies can indeed be reached with the HERA collider, as was discussed in the introduction. Looking at the charged current reaction $ep \to \nu X$ measured at HERA, a cut in the transverse neutrino momentum of $p_\perp > 25$ GeV is necessary for a clean separation of CC events from the background. The extrapolation to $p_\perp = 0$ can be done within the Standard model, yielding a cross section for νN on a stationary target of about 200 pb at 50 TeV neutrino energy. Figure 14 shows the measurements from fixed target experiments and the HERA point. Also given are the linear extrapolation (corresponding to $M_W = \infty$) and the prediction of the Standard Model ($M_W = 80$ GeV). As one can see, the neutrino nucleon cross section shows no anomaly, as could, for example, be expected by electroweak instanton effects proposed [27] as a source of possible cosmic ray events beyond the GZK cutoff. While the evidence for such events has become weaker recently [28,29], the search for instanton effects at HERA [30] has also been inconclusive so far. More details on the expectations of neutrino cross sections at asymptotic energies are presented further below (see section 3).

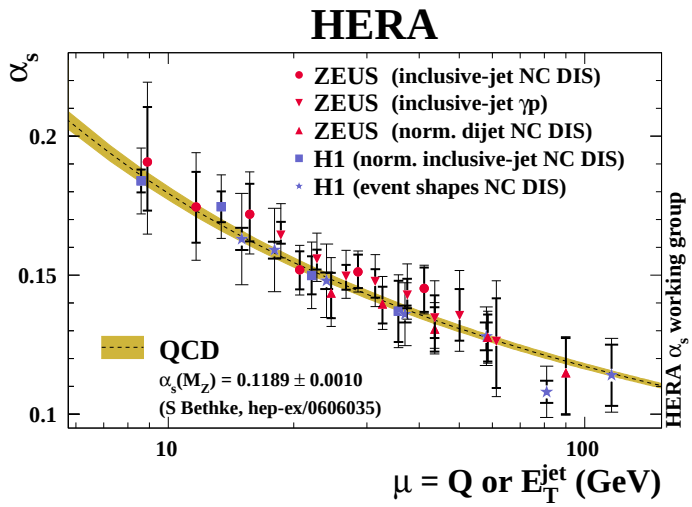

Fig. 13: Compilation of $\alpha_S(\mu)$ measurements from H1 and ZEUS [25], based on jet variables as indicated. The dashed line shows the two loop solution of the renormalization group equation, evolving the 2006 world average for $\alpha_S(M_Z)$. The band denotes the total uncertainty of the prediction.

2 Forward particles from HERA to LHC

Forward Particles at HERA In ep scattering at HERA, a significant fraction of events contains a low-transverse momentum baryon carrying a large fraction of the incoming proton energy. Although the production mechanism of these leading baryons is not completely understood, exchange models [31] give a reasonable description of the data (Fig. 15). In this picture, the incoming proton emits a virtual particle which undergoes the deep inelastic scattering process with the incoming beam electron.

To measure the very forward particles, both the H1 and the ZEUS experiments have been equipped with the Forward Proton Spectrometers (LPS, FPS and VFPS) and the Forward Neutron Calorimeters (FNC). The Forward Proton Spectrometers are several Roman Pot detectors placed at different positions along the beamline in the direction of proton beam, between 24 and 220 m from the interaction point. They measure the energy and momentum of the protons which are scattered through the very small angles and keep a momentum fraction of the initial proton between 0.4 and 1.

The Forward Neutron Calorimeters were installed at $\theta = 0°$ and at 106 m from the interaction point in the proton beam direction. These are lead-scintillator sandwich calorimeters with energy resolution $\sigma(E)/E = 70\%/\sqrt{E}$ for the ZEUS-FNC and $\sigma(E)/E = 63.4\%/\sqrt{E} \oplus 3\%$ for the H1-FNC. The size and weight of the FNC are defined by the space available in the HERA tunnel. The detectors are about 2m long with $\sim 70 \times 70\ cm^2$ transverse size. Below the H1 and ZEUS-FNC calorimeters are briefly described.

The general view of the H1-FNC is shown in Fig. 16(left). It consists of the Main Calorimeter and the Preshower. In addition, two layers of veto counters situated at the distance of 2m in front of Preshower are used to veto charged particles. The Preshower is $\sim$ 40cm ($\sim 1.5\lambda$)

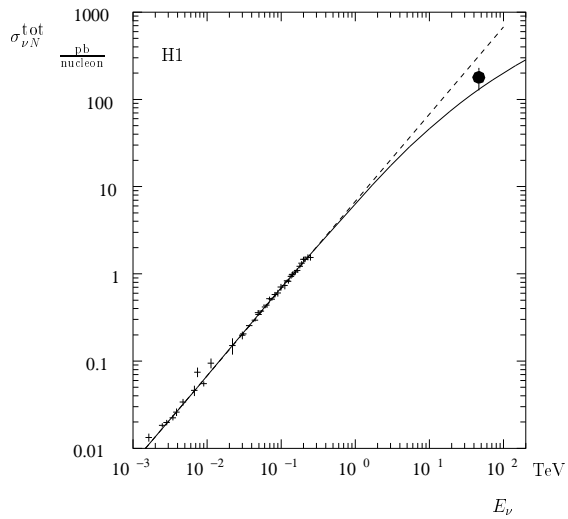

Fig. 14: Measurement of the neutrino nucleon total cross section inferred from the HERA charged current data (full circle), and various fixed target neutrino experiments (crosses).

long lead–scintillator sandwich calorimeter, it is placed in front of the Main Calorimeter. The electromagnetic showers completely develop in Preshower, while the hadronic showers leave in Preshower ∼40% of their energy (electromagnetic component). So the position resolution for the showers started in Preshower are defined by the electromagnetic component of the shower. Constructively the Preshower consists of two sections: the electromagnetic and the hadronic ones, each of them is composed of 12 planes. The transverse size of the scintillating plates is $26\times26\ \mathrm{cm}^2$. Each scintillating plate has 45 grooves where 1.2mm wavelength shifters are glued in. In order to obtain a good spatial resolution, the orientation of fibres is changed in turn from horizontal to vertical for alternating planes. On each plate the fibres are combined by five into nine strips. Longitudinally the strips are combined in 9 vertical and 9 horizontal towers. The energy resolution for electromagnetic showers is $\sim 20\%/\sqrt{E\ [\mathrm{GeV}]}$ and the spatial resolution

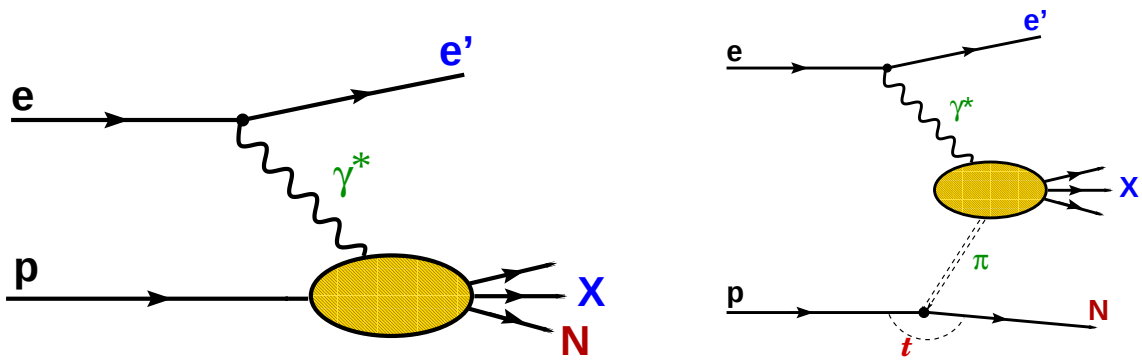

Fig. 15: (left) HERA *ep* scattering event with the final state baryon in the proton fragmentation system, (right) Leading baryon production via an exchange process.

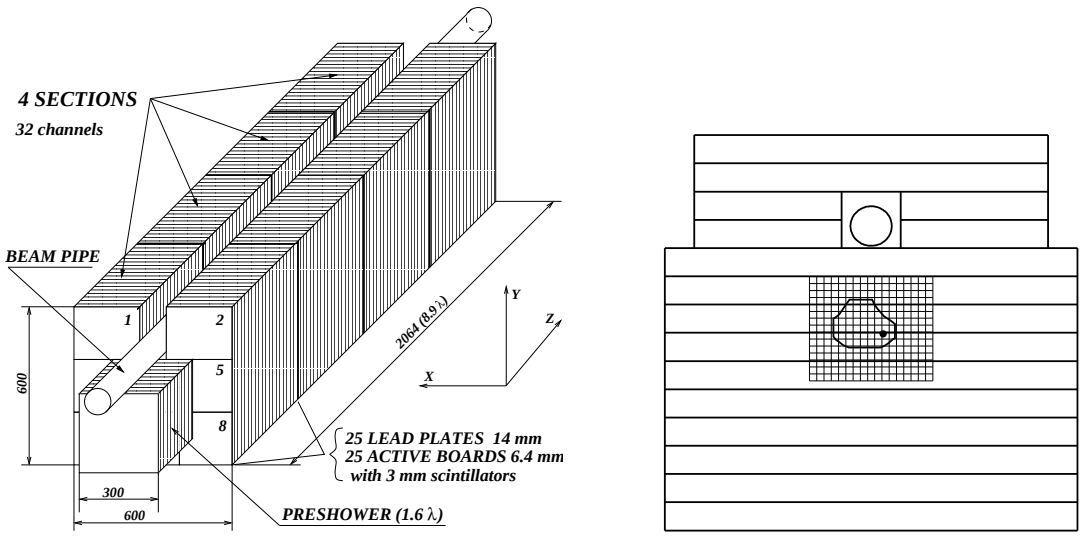

Fig. 16: General view of the H1-FNC calorimeter (left) and ZEUS-FNC calorimeter (right).

is $\sim$2mm. Apart from improvement of the energy and position resolution the Preshower provides efficient separation of electromagnetic and hadronic showers. The Main Calorimeter of H1-FNC is a sandwich-type calorimeter consisting of four identical sections with transverse dimensions 60×60 cm^2 and length of 51.5 cm. Each section consists of 25 lead absorber plates 14 mm-thick, and 25 active boards with 3 mm scintillators. Each active board is made of 8 scintillating tiles with the transverse size of 20 $\times$20 cm or 20 $\times$26 cm. The 25 tiles of one section with the same transverse position form a "tower". All together there are 32 towers in all four sections. In the top part of the calorimeter there is a opening for the proton beam vacuum pipe which is going through the calorimeter as seen from Fig. 16. The total length of the Main FNC calorimeter is 206.5 cm.

The structure of the ZEUS-FNC calorimeter is shown in Fig. 16(right). It is a finely segmented, compensating, sampling calorimeter with 134 layers of 1.25cm-thick lead plates as absorber and 2.6mm-thick scintillator plates as the active material. The scintillator is read out on each side with wavelength-shifting light guides coupled to photomultiplier tubes. It is segmented longitudinally into a front section, seven interaction-lengths deep, and a rear section, three interaction-lengths deep. The front section is divided vertically into 14 towers, each 5cm high. Inside the calorimeter at a depth of one interaction length a forward neutron tracker (FNT) is installed. It is a scintillator hodoscope designed to measure the position of neutron showers. Each scintillator finger is 16.8cm long, 1.2cm wide and 0.5cm deep; 17 are used for X position reconstruction and 15 for Y. The position of the FNT hodoscope in the FNC is indicated in Fig. 16.

The acceptance of the FNC calorimeters is defined by the aperture of the HERA beam line magnets and is limited to neutron scattering angles of $\theta_n < 0.8$ mrad with approximately 30% azimuthal coverage (see Fig. 17). Thus the transverse momenta of neutrons are limited to $p_{T,n}^{max} = 0.656 \cdot x_L$ for proton beam energy of 920 GeV. The overall acceptance of the FNC,

taking account of beam-line geometry, inactive material, beam tilt and angular spread, as well as the angular distribution of the neutrons, is ∼20% at low x_l, where the $p_{T,n}$ range covered is small, but increases monotonically, exceeding 30% at high x_L.

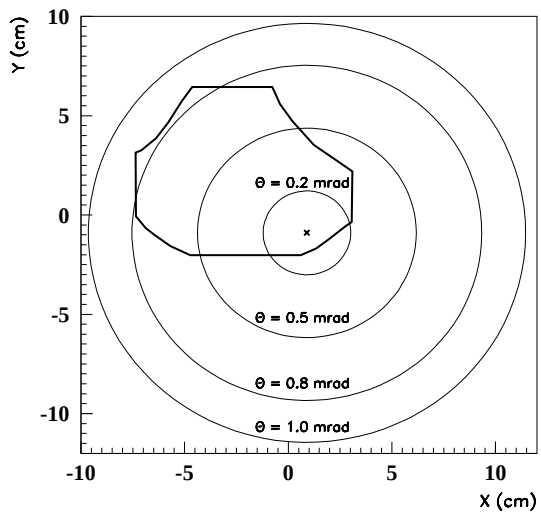

Fig. 17: The geometrical acceptance of FNC calorimeter defined by the aperture of the HERA beam-line elements.

Physics with Leading Neutrons The main goal of the FNC calorimeters is to measure the energy and angles of fast neutrons from the reaction $ep \to e' + X + n$ (see Fig. 15). The H1 and ZEUS Collaborations provided many results on leading neutron production in DIS, photoproduction, in events containing jets or charm in the final state [32]. The results are successfully interpreted within the approach that at high $x_L = E_n/E_p$ and low $p_{T,n}$ the dominant mechanism of forward neutron production is the π^+-exchange.

An example of the observed neutron energy and the transverse momentum distributions for the deep-inelastic scattering (DIS) events is shown in Fig. 18 and compared with the Monte Carlo simulation [33]. The distribution is well described by the pion exchange Monte Carlo simulation (RAPGAP) with some admixture of the standard DIS Monte Carlo simulation (DJANGO).

Based on the assumption that at high x_L the leading neutron production is dominated by the pion exchange mechanism, the measurement of DIS cross sections in events with leading neutrons can provide an important information about the pion structure. The quark and gluon distributions of the pion have previously been constrained using Drell–Yan data and direct photon production data obtained by πp scattering experiments and are limited to high x ($x > 0.1$) values. Figure 19 shows $F_2^{LN(3)}/\Gamma_\pi$ as a function of β for fixed values of Q^2. Here, $F_2^{LN(3)}$ is the measured semi-inclusive structure function for leading neutron production, Γ_π is the integrated pion flux, and $\beta = x/(1-x_L)$ is a Bjorken scaling variable for the virtual pion. Thus, $F_2^{LN(3)}/\Gamma_\pi$ can be interpreted as a pion structure function F_2^π and can distinguish between the different parameterisations of the pion structure function (Fig. 19). Moreover, using the measured rate

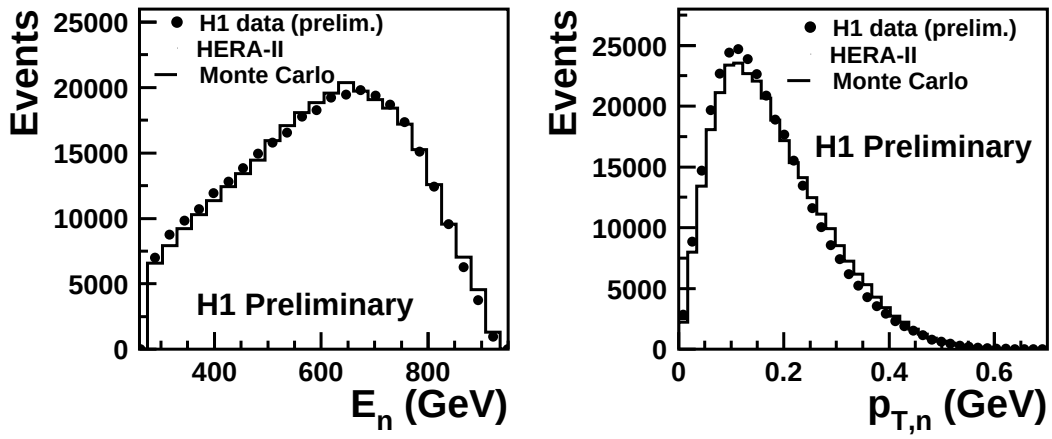

Fig. 18: The observed neutron energy spectrum and the transverse momentum p_T distribution from the DIS interactions. The data distribution is compared with the Monte Carlo simulation, which is the mixture of RAPGAP with pion exchange and the DJANGO models.

of leading neutron production in DIS, the total probability of $p \to n\pi^+$ fluctuation in DIS of 16–25% was estimated [34].

In exchange models, neutron absorption can occur through rescattering. Absorption is a key ingredient in calculations of gap-survival probability in pp interactions at the LHC, critical in interpreting hard diffractive processes, including central exclusive Higgs production. In the processes with leading neutron production, due to the rescattering the neutron may migrate to lower x_L and higher p_T such that it is outside of the detector acceptance. The rescattering can also transform the neutron into a charged baryon which may also escape detection. Since the size of the virtual photon is inversely related to Q^2, more neutron rescattering would be expected for photoproduction ($Q^2 \approx 0$) than for deep inelastic scattering. The size of the n-π system is inversely proportional to the neutron p_T, so rescattering removes neutrons with large p_T. Thus rescattering results in a depletion of high p_T neutrons in photoproduction relative to DIS: a violation of vertex factorization. Figure 20 shows the ratio of the x_L distributions for photoproduction and DIS. In the range $0.2 < x_L < 0.4$, the ratio drops slightly but rises for higher x_L values, exceeding unity for $x_L > 0.9$. The deviation of the ratio from unity is a clear violation of vertex factorization. The dashed and solid curves in Fig. 20 are the expectation for the suppression of leading neutrons in photoproduction relative to DIS from a model of pion exchange with neutron absorption [35], Within the normalization uncertainty the data are well described by the absorption model. Also shown in Fig. 20 is another model [36] which employs the optical theorem together with multi-Pomeron exchanges to describe all possible rescattering processes of the leading hadron, resulting in absorptive effects. With the correction for different W dependences, the prediction is close in magnitude to the data.

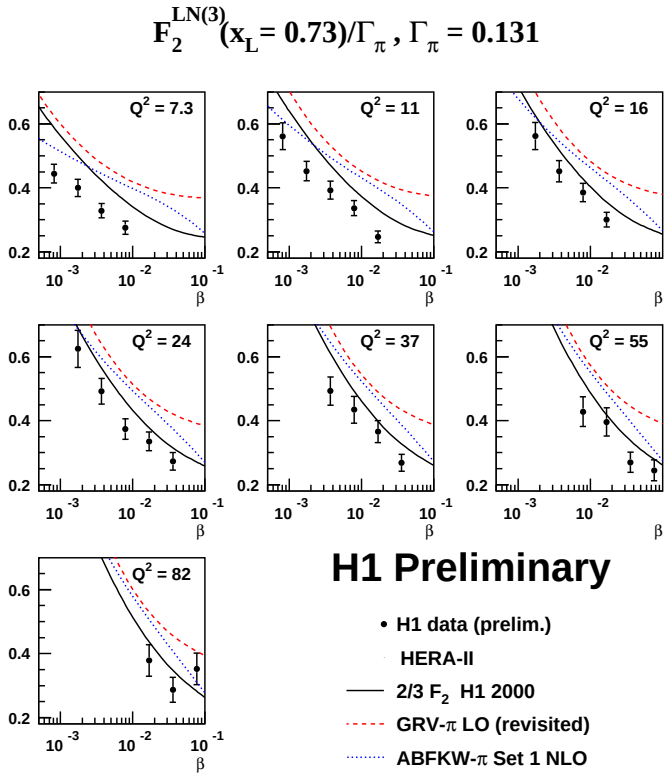

Fig. 19: $F_2^{LN(3)}/\Gamma_\pi$ at $x_L = 0.73$ plotted as a function of β for fixed values of Q^2. The quantity Γ_π is the p_T integrated pion flux factor.

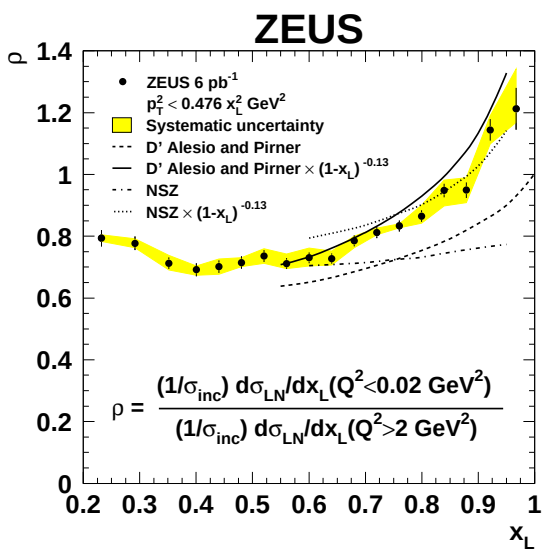

Fig. 20: Ratio of photoproduction and DIS x_L distributions, compared to the different rescattering models (see text)

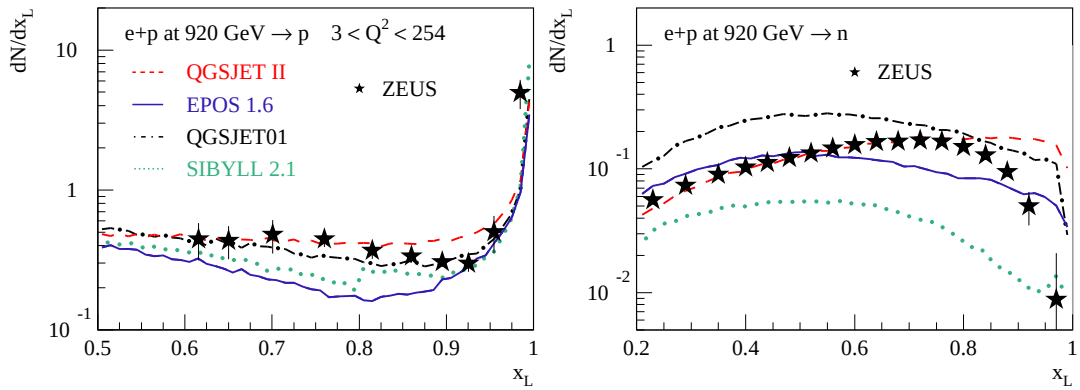

Fig. 21: Comparison of the leading proton and the leading neutron spectra measured at HERA (ZEUS [37]) with the predictions of the models used for cosmic ray analyses.

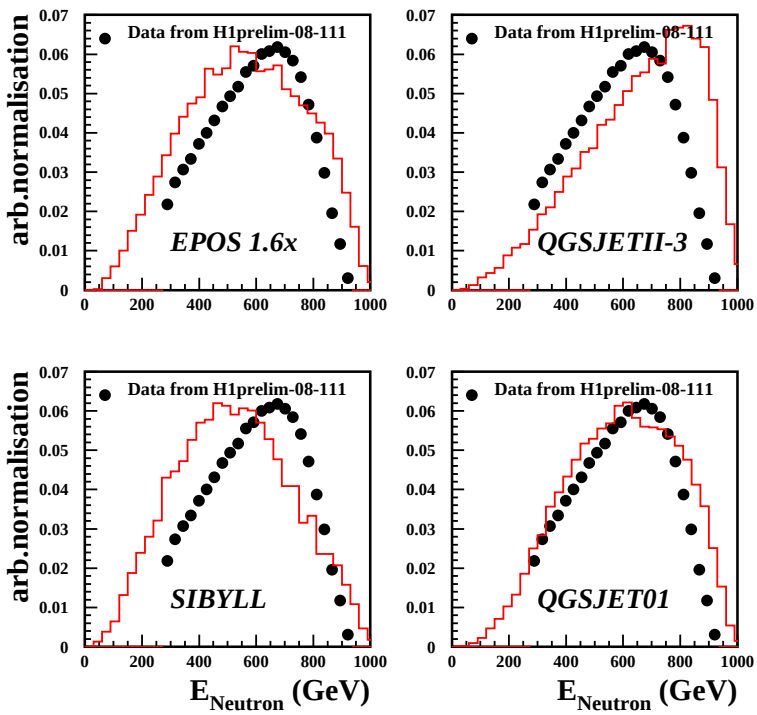

Fig. 22: Comparison of the leading neutron energy spectra measured at HERA (H1 [33]) with the predictions of the models used for cosmic ray analyses. The distributions are normalised to compare the shapes.

Forward Particles at HERA and Cosmic Rays The measurements of forward particles at HERA may provide valuable information for the physics of ultra-high energy cosmic rays. Despite the huge difference between the energy ranges accessible in the cosmic rays and the colliders, we may assume that the hadron production in the proton fragmentation region doesn't depend much on the energy and the type of interacting particle. The longitudinal segmentation of the FNC calorimeters at HERA allows to separate signals from the neutrons from that of photons, thus the experiments can measure the differential distributions of x_L and p_T for the neutrons and the photons. Moreover, the measurements can be made also for the different proton beam energies (we recall that the last three months the HERA collider was running at lower proton beam energies). The cosmic ray models can make predictions for these measurements and be tuned accordingly.

Comparison of the leading proton and the leading neutron spectra measured at HERA with the predictions of the models used for cosmic ray analyses are shown in Figs. 21 and 22. Here, the comparison is made before the detailed tunings of the models. It demonstrates that the HERA measurements are indeed sensitive to the differences between the models and can be used for the tuning of model parameters.

To summarise, the HERA experiments provide a wealth of measurements of leading baryon production. These measurements give an important input for an improved theoretical understanding of the proton fragmentation mechanism. The HERA data on forward particle production can help to reduce the uncertainty in the model predictions for very high energy cosmic ray air showers.

Forward Particles at LHC At the LHC, the collision energy of protons, $\sqrt{s}$=14 TeV, corresponds to 10^{17} eV in the laboratory system. So the measurements at the LHC are important to constrain the interaction models used in the cosmic-ray studies. The LHC is also capable of colliding different kind of ions. Measurements of ion collisions especially to simulate the interactions between cosmic-rays and atmosphere are also valuable. In the collider experiments, most of the collision energy flows into the very forward direction that is not covered by the general purpose detectors like ATLAS and CMS in case of the LHC. Dedicated experiments to cover these high rapidity region are necessary for the cosmic-ray studies. Fig. 23 shows the energy flux in 14 TeV collisions as a function of pseudo-rapidity η. Two independent experiments LHCf, TOTEM, and sub-detectors of the big experiments ZDCs are capable of measuring very forward particles. Coverage of each experiment in pseudo-rapidity is also indicated in Fig. 23 by arrows. Because each experiment has different capability (charged or neutral particle measurement, hadron or electromagnetic calorimeter, calorimeter or tracker, infinite or finite pseudo-rapidity coverage, aperture, position/energy resolutions), they provide complementary data for total understanding of the very forward particles.

LHCf (LHC forward) is an experiment dedicated to solve the cosmic-ray problems [38]. The experiment is a kind of ZDC (Zero Degree Calorimeter) but optimized to discriminate the interaction models used in the cosmic-ray studies. In LHC, at 140 m away from IP1 the beam pipe makes a transition from a common beam pipe facing the IP to two separate beam pipes joining to the arcs of LHC (the Y vacuum chamber). LHCf has installed two detectors in this 96 mm gap between two pipes at either side of IP1 and will measure the neutral particles of

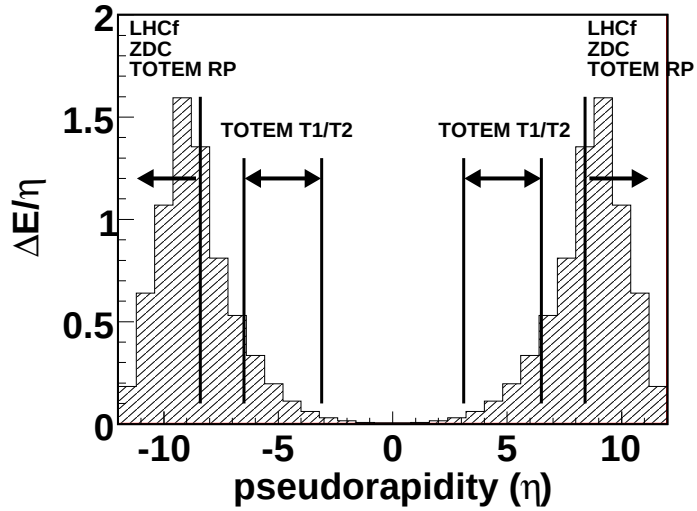

Fig. 23: pseudo-rapidity distribution at LHC

η>8.4. Each detector has two sampling calorimeter towers with 44 X_0 made of plastic scintillators and tungsten. The transverse cross-section of the calorimeters ranges from 20 mm$\times$20 mm to 40 mm$\times$40 mm. One detector has Scifi and MAPMT, and the other has silicon strip tracker for position measurements. The detectors can measure the energy and P_T distributions of gamma-rays and neutrons. Small double-tower configuration enables analysis of π^0 mass reconstruction by measuring the energies and positions of decayed gamma-ray pairs, consequently the determination of the π^0 energy spectrum. With the energy resolution better than 5% for gamma-rays and 30% for hadrons, and position resolution better than 0.2 mm, major models used in the CR studies can be discriminated as shown in Fig. 24. A comparison study considering some recent models has also predicted large variation from model to model that can be confirmed by the LHCf measurements [39]. LHCf can also study the Landau-Pomeranchuk-Migdal (LPM) effect in detail. In the tungsten calorimeter, electromagnetic showers of >TeV energy show >10% deviation from the non-LPM expectation. LHCf is planning to take data in the early stage of the LHC commissioning.

TOTEM is an experiment to measure the total cross section in the proton collisions at IP5 in the LHC [38]. TOTEM measures the numbers of the proton elastic scattering using the Roman Pot detectors and inelastic scattering using the so-called telescopes surrounding the beam pipe. The RP detectors also measure the position of the elastically scattered protons to determine dN_{el}/dt at t=0 extrapolation. Combining these measurements and the optical theorem, TOTEM will determine the total cross section with $\pm$1 mb error.

ZDCs are the sub detectors of the ATLAS, CMS and ALICE experiments. Except a part of the ALICE ZDC (ZP), all ZDCs are installed in the place where the beam pipe is separated into two as was the case of LHCf. The prime motivation of the ZDCs is to determine the energy

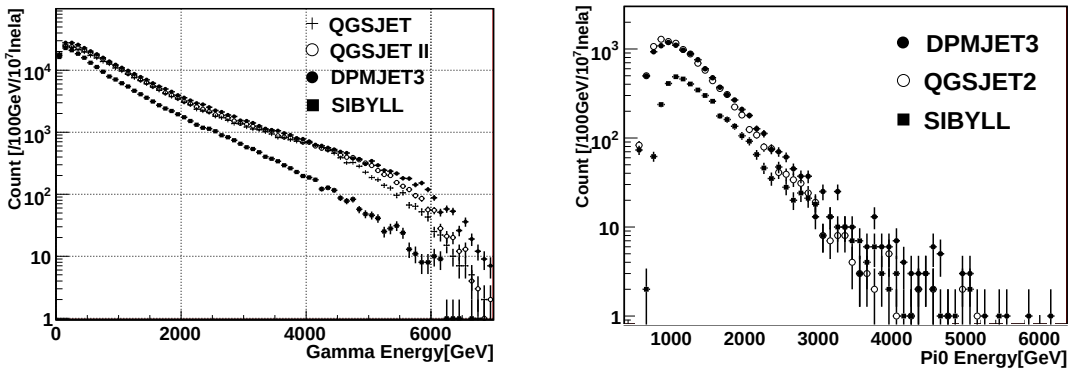

Fig. 24: Energy spectra of single γ-rays and π^0's expected in the LHCf measurement using different interaction models.

carried by the spectator nucleons in ion collisions. For this purpose, ZDCs have as wide aperture as possible in the limited volume and as thick material as possible to measure the energy flow of the nucleons.

In summary, the LHC gives an unprecedented opportunity to constrain the interaction models used in the cosmic-ray studies. The integration of the data from not only the experiment dedicated for the cosmic-ray science (LHCf) but also the others, especially the forward experiments introduced above is important to constrain the interaction models used in the cosmic-ray studies.

3 Neutrino cross section and uncertainties

Predictions of neutrino cross-sections at high energies have sizeable uncertainties which derive largely from the measurement uncertainties on the parton distribution functions (PDFs) of the nucleon. In the framework of the quark-parton model, high energy scattering accesses very large values of Q^2, the invariant mass of the exchanged vector boson, and very small values of Bjorken x, the fraction of the momentum of the incoming nucleon taken by the struck quark. Thus when evaluating uncertainties on high energy neutrino cross-sections it is important to use the most up to date information from the experiments at HERA, which have accessed the lowest-x and highest Q^2 scales to date. The present paper outlines the use of the ZEUS-S global PDF fit formalism [40], updated to include *all* the HERA-I data. Full details are given in [41].

Conventional PDF fits use the Next-to-leading-order (NLO) Dokshitzer-Gribov-Lipatov-Altarelli-Parisi (DGLAP) formalism of QCD to make predictions for deep inelastic scattering (DIS) cross-sections of leptons on hadrons. At low-x where the gluon density is rising rapidly it is probably necessary to go beyond the DGLAP formalism in order to resum $\ln(1/x)$ diagrams, or even to consider non-linear terms which describe gluon recombination. Such approaches are beyond the scope of the present discussion, which is concerned with the more modest goal of estimating the uncertainties on high energy neutrino cross-sections which are compatible with

the conventional NLO DGLAP formalism. As a corollary, if cross-sections much outside the uncertainty bands presented here are observed, it would be a clear signal of the need for extensions to conventional formalism.

This work provide an update on the neutrino cross-sections in the literature [42] which used PDF sets which no longer fit modern data from HERA and an *ad hoc* procedure for estimating PDF uncertainties. There are several improvements on previous work. Firstly, a recent PDF analysis which includes data from all HERA-I running [40] is used. Secondly, a consistent approach to PDF uncertainties – both model uncertainties and, more importantly, the uncertainties which derive from the correlated systematic errors of the input data sets is used. Thirdly, NLO rather than LO calculations are used throughout. Fourthly, a general-mass variable flavour number scheme [43] is used to treat heavy quark thresholds.

The PDF fit formalism of the published ZEUS-S global PDF analysis [40] is used, but this fit is updated as follows. First, the range of the calculation has been extended up to $Q^2 = 10^{12}$ GeV^2 and down to $x = 10^{-12}$. Second, *all* inclusive cross-section data for neutral and charged current reactions from ZEUS HERA-I running (1994–2000) are included in the fit. Third, the parametrization is extended from 11 to 13 free parameters, input at $Q_0^2 = 7$ GeV^2.

The most significant source of uncertainties on the PDFs comes from the experimental uncertainties on the input data. The PDFs are presented with full accounting for uncertainties from correlated systematic errors (as well as from statistical and uncorrelated sources) using the conservative OFFSET method. The uncertainty bands should be regarded as 68% confidence limits. The PDF central values and uncertainties from this updated ZEUS-S-13 fit are comparable to those on the published ZEUS-S fit [40], as well as the most recent fits of the CTEQ [44] and MRST [45] groups.

Previous work [42] treated heavy quark production by using a zero-mass variable flavour number scheme, with slow-rescaling at the b to t threshold. The exact treatment of the $b \to t$ threshold is not very important for the estimation of high energy neutrino cross-sections since the contribution of the b is supressed, but the correct treatment of heavy quark thresholds is important in determining the PDFs for lower Q^2 ($\lesssim 5000$ GeV^2) and middling x ($5\times10^{-5} \lesssim x \lesssim 5\times10^{-2}$) and this is a kinematic region of relevance to the present study.

The results of this study show that the PDF uncertainty on the neutrino (and antieutrino) charged current (CC) cross-sections remains modest ($< 15\%$) even at the highest energies considered here: $s = 10^{12}$ GeV^2. The reason for this is that the high energy ($E_\nu > 10^7$ GeV) νN and $\bar{\nu} N$ cross-sections are dominated by sea quarks produced by gluon splitting $g \to q\bar{q}$ and, although the PDF uncertainty on the sea quarks is large at low-x and low Q^2, the dominant contributions to the cross-sections do *not* come from very low Q^2 values. The dominant contributions come from the kinematic region $50 \lesssim Q^2 \lesssim 10^4$ GeV^2 (where the exact region moves up gradually with s). The contribution of higher Q^2 ($Q^2 > M_W^2$) is suppressed by the W-propagator. Furthermore, there is a restriction on the lowest value of x probed for each Q^2 value due to the kinematic cut-off ($y < 1$ and since $x = Q^2/sy$, we must have, $x > Q^2/s$). This kinematic cut-off ensures that higher Q^2 values do not probe very low-x until the neutrino energies are very high indeed. For example, at $E_\nu = 1.9 \times 10^7$ GeV, the important range is $10^{-6} \lesssim x \lesssim 10^{-3}$, while for $E_\nu = 5.3 \times 10^9$ GeV, this moves down to $10^{-8} \lesssim x \lesssim 10^{-4}$. Full details on the PDF uncertainties and the predictions for the neutrino and antineutrino double

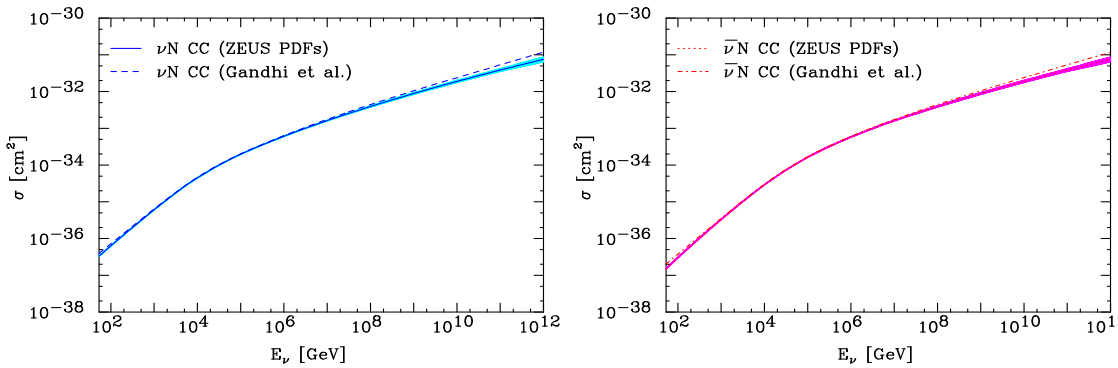

Fig. 25: The total CC cross-section at ultra high energies for neutrinos (left) and antineutrinos (right) along with the $\pm 1\sigma$ uncertainties (shaded band), compared with the previous calculation by Gandhi *et al*.

differential cross-sections are given in reference [41].

The total CC cross-sections are obtained by integrating the predicted double differential cross-sections $\mathrm{d}^2\sigma/\mathrm{d}x\mathrm{d}y$. These cross-sections are illustrated in Fig. 25 together with their uncertainties due to the PDFs, including both model uncertainties and the experimental uncertainties of the input data sets. The trend of the PDF uncertainties at high neutrino energy can be understood by noting that as one moves to higher and higher neutrino energies one also moves to lower and lower x where the PDF uncertainties are increasing. At lower neutrino energies ($10^2 < E_\nu < 10^7$ GeV) the high-x region becomes important and the neutrino and antineutrino cross-sections are *different* due to the valence PDF contribution. The onset of the linear dependence of the cross-section on s for $s < M_W^2$ can be seen. The trend of the PDF uncertainties in the low energy region can be understood as follows: as one moves to lower neutrino energies one moves out of the very low-x region such that PDF uncertainties decrease. These uncertainties are smallest at $10^{-2} \lesssim x \lesssim 10^{-1}$, corresponding to $s \sim 10^5$. Moving to yet lower neutrino energies brings us into the high-x region where PDF uncertainties are larger again.

Figure 25 also compares our CC cross-section to the widely used leading-order calculation of Gandhi *et al* [42]. The present results show a less steep rise of the cross-section at high energies, reflecting the fact that more recent HERA cross-section data display a less dramatic rise at low-x than the early data.

In conclusion, the charged current neutrino cross-section at NLO have been calculated in the Standard Model using the best available DIS data along with a careful estimate of the associated uncertainties. if cross-sections much outside the uncertainty bands presented here are observed at UHE cosmic neutrino detectors, it would be a clear signal of the need for extensions to conventional QCD DGLAP formalism.

References

[1] H1 Collaboration, I. Abt *et al.*, Nucl. Instrum. Meth. **A386**, 310 (1997).

[2] ZEUS Collaboration, U. e. ZEUS-Collab., Holm, Status Report (unpublished), http://www-zeus.desy.de/bluebook/bluebook.html (1993).

[3] P. D. B. Collins. Cambridge 1977, 445p.

[4] V. N. Gribov, V. M. Shekhter, V. A. Kolkunov, and L. B. Okun, Sov. Phys. JETP **14**, 1308 (1962).

[5] H1 Collaboration, S. Aid *et al.*, Z. Phys. **C69**, 27 (1995), arXiv:hep-ex/9509001.

[6] ZEUS Collaboration, S. Chekanov *et al.*, Nucl. Phys. **B627**, 3 (2002), arXiv:hep-ex/0202034.

[7] D. O. Caldwell *et al.*, Phys. Rev. Lett. **40**, 1222 (1978); HERA and COMPAS Groups Collaboration, S. I. Alekhin *et al.* CERN-HERA-87-01.

[8] A. Donnachie and P. V. Landshoff, Phys. Lett. **B437**, 408 (1998), arXiv:hep-ph/9806344.

[9] J. C. Collins and D. E. Soper, Ann. Rev. Nucl. Part. Sci. **37**, 383 (1987).

[10] F. Halzen and A. D. Martin. New York, Usa: Wiley (1984) 396p.

[11] V. N. Gribov and L. N. Lipatov, Sov. J. Nucl. Phys. **15**, 438 (1972); G. Altarelli and G. Parisi, Nucl. Phys. **B126**, 298 (1977); Y. L. Dokshitzer, Sov. Phys. JETP **46**, 641 (1977).

[12] H. Collaboration, Preliminary Result H1prelim 07-007 (2007); Z. Collaboration, Preliminary Result ZEUS-prel 07-026 (2007).

[13] H. Collaboration, Preliminary Result H1prelim 08-045 (2008); Z. Collaboration, Preliminary Result ZEUS-prel 08-003 (2008).

[14] S. D. Ellis and D. E. Soper, Phys. Rev. **D48**, 3160 (1993), arXiv:hep-ph/9305266.

[15] ZEUS Collaboration, S. Chekanov *et al.*, Nucl. Phys. **B765**, 1 (2007), arXiv:hep-ex/0608048.

[16] H1 Collaboration, C. Adloff *et al.*, Eur. Phys. J. **C13**, 609 (2000), arXiv:hep-ex/9908059; ZEUS Collaboration, S. Chekanov *et al.*, Eur. Phys. J. **C21**, 443 (2001), arXiv:hep-ex/0105090.

[17] E. A. Kuraev, L. N. Lipatov, and V. S. Fadin, Sov. Phys. JETP **44**, 443 (1976); I. I. Balitsky and L. N. Lipatov, Sov. J. Nucl. Phys. **28**, 822 (1978).

[18] ZEUS Collaboration, S. Chekanov *et al.*, Eur. Phys. J. **C52**, 515 (2007), arXiv:0707.3093 [hep-ex].

[19] H1 Collaboration, A. Aktas *et al.*, Eur. Phys. J. **C46**, 27 (2006), arXiv:hep-ex/0508055.

[20] S. Catani and M. H. Seymour, Nucl. Phys. **B485**, 291 (1997), arXiv:hep-ph/9605323.

[21] H. Jung and G. P. Salam, Eur. Phys. J. **C19**, 351 (2001), arXiv:hep-ph/0012143; H. Jung, Comput. Phys. Commun. **143**, 100 (2002), arXiv:hep-ph/0109102.

[22] M. Ciafaloni, Nucl. Phys. **B296**, 49 (1988); S. Catani, F. Fiorani, and G. Marchesini, Nucl. Phys. **B336**, 18 (1990).

[23] H. Jung, Comp. Phys. Commun. **86**, 147 (1995).

[24] L. Lonnblad, Comput. Phys. Commun. **71**, 15 (1992).

[25] H. Collaboration, Preliminary Result H1prelim 07-132 (2007); Z. Collaboration, Preliminary Result ZEUS-prel 07-025 (2007).

[26] H. Collaboration, Preliminary Result H1prelim 08-031 (2008).

[27] Z. Fodor, S. D. Katz, A. Ringwald, and H. Tu, Phys. Lett. **B561**, 191 (2003), arXiv:hep-ph/0303080.

[28] HiRes Collaboration, R. Abbasi *et al.*, Phys. Rev. Lett. **100**, 101101 (2008), arXiv:astro-ph/0703099.

[29] K.-H. Kampert, J. Phys. Conf. Ser. **120**, 062002 (2008), arXiv:0801.1986 [astro-ph].

[30] H1 Collaboration, C. Adloff *et al.*, Eur. Phys. J. **C25**, 495 (2002), arXiv:hep-ex/0205078; ZEUS Collaboration, S. Chekanov *et al.*, Eur. Phys. J. **C34**, 255 (2004), arXiv:hep-ex/0312048.

[31] J. D. Sullivan, Phys. Rev. **D5**, 1732 (1972); H. Holtmann, G. Levman, N. N. Nikolaev, A. Szczurek, and J. Speth, Phys. Lett. **B338**, 363 (1994); B. Kopeliovich, B. Povh, and I. Potashnikova, Z. Phys. **C73**, 125 (1996), arXiv:hep-ph/9601291; M. Przybycien, A. Szczurek, and G. Ingelman, Z. Phys. **C74**, 509 (1997), arXiv:hep-ph/9606294; A. Szczurek, N. Nikolaev, and J. Speth, Phys. Lett. **B428**, 383 (1998), arXiv:hep-ph/9712261.

[32] H1 Collaboration, C. A. e. a. H1 Coll., Eur. Phys. J. **C6**, 587 (1999), arXiv:hep-ex/9811013; ZEUS Collaboration, J. B. e. a. ZEUS Coll., Nucl. Phys. **B596**, 3 (2001),

arXiv:hep-ex/0010019;
ZEUS Collaboration, S. C. e. a. ZEUS Coll., Nucl. Phys. **B637**, 3 (2002), arXiv:hep-ex/0205076;
ZEUS Collaboration, S. C. e. a. ZEUS Coll., Phys. Lett. **B590**, 143 (2004), arXiv:hep-ex/0401017;
ZEUS Collaboration, S. C. e. a. ZEUS Coll., Phys. Lett. **B610**, 199 (2005), arXiv:hep-ex/0404002;
H1 Collaboration, A. A. e. a. H1 Coll., Eur. Phys. J. **C41**, 273 (2005), arXiv:hep-ex/0501074;
ZEUS Collaboration, S. C. e. a. ZEUS Coll., Nucl. Phys. **B776**, 1 (2007), arXiv:hep-ex/0702028;
F. A. e. a. H1 Coll., *Leading Neutron Production in DIS at HERA* . H1prelim-08-111, presented at ICHEP-08, Philadelphia, 2008.

[33] H1 Collaboration, *Leading Neutron production in DIS at HERA* . H1-Preliminary-08-111, presented at ICHEP-2008, Philadelphia, 2008.

[34] A.Bunyatyan and B.Povh, Eur. Phys. J. **A27**, 359 (2006), arXiv:hep-ph/0603235.

[35] U. D'Alesio and H. J. Pirner, Eur. Phys. J. **A7**, 109 (2000), arXiv:hep-ph/9806321.

[36] N. Nikolaev, J. Speth, and B. G. Zakharov, *Absorptive corrections to the one pion exchange and measurability of the small-x pion structure function at HERA*. Preprint KFA-IKP(TH)-1997-17, 1997. arXiv:hep-ph/9708290.

[37] ZEUS Collaboration, S. C. e. a. ZEUS Coll., Nucl. Phys. **B658**, 3 (2003), arXiv:hep-ex/0210029.

[38] LHCf Collaboration, O. Adriani *et al.*, JINST **3**, S08006 (2008).

[39] H.-J. Drescher, Phys. Rev. **D77**, 056003 (2008), arXiv:0712.1517 [hep-ph].

[40] ZEUS Collaboration, S. Chekanov *et al.*, Phys. Rev. **D67**, 012007 (2003), arXiv:hep-ex/0208023.

[41] A. Cooper-Sarkar and S. Sarkar, JHEP **01**, 075 (2008), arXiv:0710.5303 [hep-ph].

[42] R. Gandhi, C. Quigg, M. H. Reno, and I. Sarcevic, Phys. Rev. **D58**, 093009 (1998), arXiv:hep-ph/9807264.

[43] R. S. Thorne and R. G. Roberts, Phys. Rev. **D57**, 6871 (1998), arXiv:hep-ph/9709442;
R. S. Thorne, Phys. Rev. **D73**, 054019 (2006), arXiv:hep-ph/0601245.

[44] J. Pumplin *et al.*, JHEP **07**, 012 (2002), arXiv:hep-ph/0201195;
W. K. Tung *et al.*, JHEP **02**, 053 (2007), arXiv:hep-ph/0611254.

[45] A. D. Martin, R. G. Roberts, W. J. Stirling, and R. S. Thorne, Eur. Phys. J. **C23**, 73 (2002), arXiv:hep-ph/0110215;
A. D. Martin, W. J. Stirling, R. S. Thorne, and G. Watt, Phys. Lett. **B652**, 292 (2007), arXiv:0706.0459 [hep-ph].

Model predictions for HERA, LHC and cosmic rays

A. Bunyatyan, A. Cooper-Sarkar, C. Diaconu, R. Engel, C. Kiesling, K. Kutak, S. Ostapchenko, T. Pierog, T.C. Rogers, M.I. Strikman, T. Sako

1 Hadron production

Min-bias model comparison The simple approach of section [1] allows us to extract the main observables which lead the air shower development, namely:

- cross section
- multiplicity
- forward spectra (inelasticity)
- (anti)baryon production

We will compare the commonly used hadronic interaction models for air shower simulations at HERA and LHC energies for these observables.

Hadronic interaction models There are several hadronic interaction models commonly used to simulate air showers. For high energy interactions ($E_{\rm lab} \gtrsim 100$ GeV), the models studied here are EPOS 1.6 [2,3], QGSJET 01 [4], QGSJET II [5,6], and SIBYLL 2.1 [7–9]. The physics models and assumptions are discussed in, for example, [10]. All the high-energy interaction models reproduce accelerator data reasonably well but predict different extrapolations above $E_{\rm cms} \sim$1.8 TeV ($E_{\rm lab} \sim 10^{15}$ eV) that lead to very different results at high energy [11, 12]. The situation is different at low energy where several measurements from fixed target experiments are available [13]. There one of the main problems is the extrapolation of measurements to the very forward phase space region close to the beam direction and the lack of measurements of pion-induced interactions. Both HERA and LHC can help to constrain these models.

Cross section As seen a previous section, the cross section is very important for the development of air showers and in particular for the depth of shower maximum. As a consequence, the number of electromagnetic particles at ground is strongly correlated to this observable (if the shower maximum is closer to ground, the number of particle is higher).

The proton-proton scattering total cross section is usually used as an input to fix basic parameters in all hadronic interaction models (see paragraph on total cross section below). Therefore, as shown Fig. 1 lefthand-side, the p-p total cross section is very well described by all the models at low energy, where data exists. And then it diverges above 2 TeV center-of-mass (cms) energy because of different model assumption. Thanks to the TOTEM experiment, the cross section will be measured accurately at LHC energy allowing a strong reduction of the model uncertainty ($\sim$20%). In all the figures of this subsection EPOS 1.6 is represented by a full (blue) line, QGSJET II by a dashed (red) line, QGSJET 01 by a dash-dotted (black) line and SIBYLL 2.1 by a dotted (green) line.

From p-p to proton-air interactions, the Glauber model is used in all models but with different input parameters depending on nuclear effects (none in SIBYLL 2.1, strong in QGSJET II).

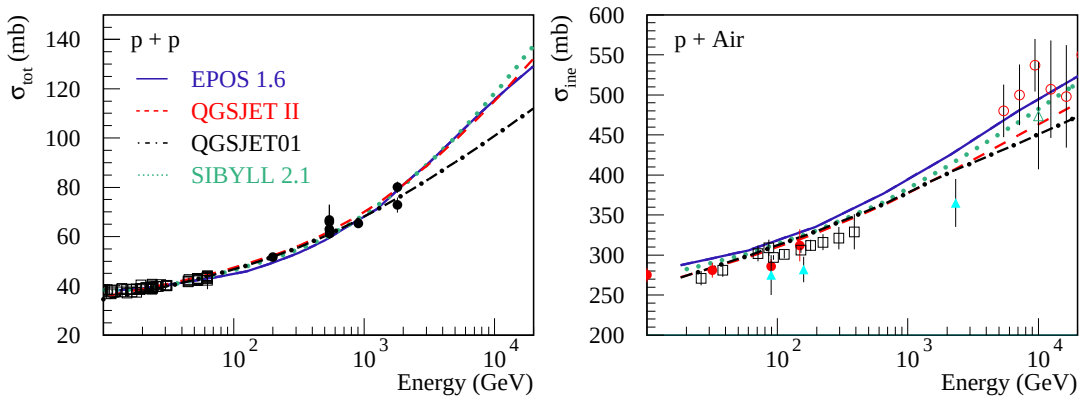

Fig. 1: Total cross section of p-p collision (lefthand-side) and inelastic proton-air cross section (righthand-side) as calculated with EPOS 1.6 (full line), QGSJET II (dashed line), QGSJET 01 (dash-dotted line) and SIBYLL 2.1 (dotted line). Points are data from accelerator [14] and cosmic ray experiment [15].

So comparing the models to each other (Fig. 1 righthand-side), differences appear even at low energy where the p-p cross section are similar. And at high energy the spread is again larger. Furthermore, the simulated cross sections seem all to increase faster than the measured one, even at low energy (< 1 Tev) where direct measurement of single hadrons from cosmic rays can be done at ground [15] (almost accelerator like measurement since proton flux is known). Proton-Carbon interactions at LHC would be very helpful to solve this problem.

Multiplicity According to Sec. [1], the multiplicity plays a similar kind of role as the cross section, but with a weaker dependence (log). On the other hand, the predictions from the models have much larger differences. As shown Fig. 2, going from the multiplicity of charged particles with $|\eta| < 3$ for nondiffractive collisions at 900 GeV cms energy (lefthand-side), where models agree with the UA5 data [16], to the multiplicity of charged particles (minimum bias) at 14 TeV (LHC) (righthand-side), the discrepancy can be larger than a factor of 2 in the tail of the distribution (and the shape is different). The EPOS model predicts much smaller multiplicity than QGSJET II.

The multiplicity distribution of charged particles is a very good test of the fundamental property of the hadronic interaction models and it should be one of the first result of the LHC experiments.

Forward spectra Forward particle distributions are crucial for air shower development because most of the energy is carried by these particles (and not the ones in the central region). The forward spectra have been measured in fixed target experiment at energies of few hundreds of GeV (few tens of GeV in cms energy) and the models reproduce this data correctly since they are used to fix some model parameters.

At higher energy, hadron collider experiments could not measure particles in the very

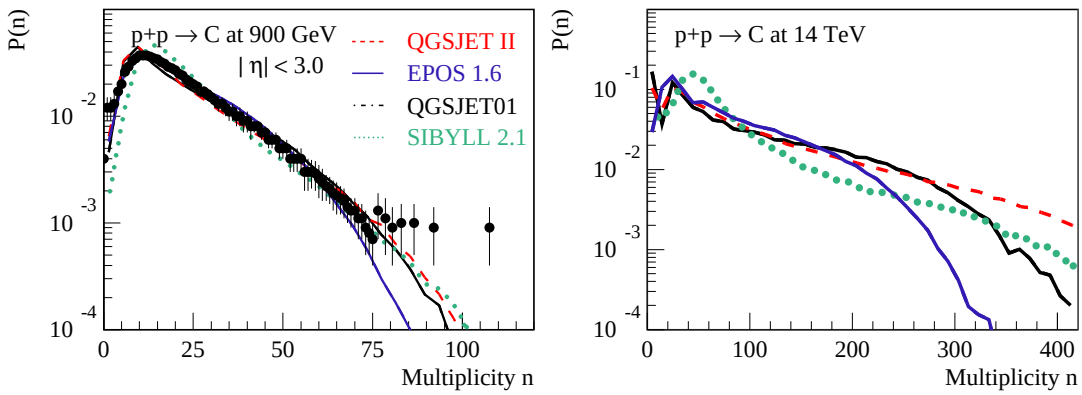

Fig. 2: Multiplicity distribution of $\overline{p}$-p collision at 900 GeV cms energy (lefthand-side) and 14 TeV (righthand-side) as calculated with EPOS 1.6 (full line), QGSJET II (dashed line), QGSJET 01 (dash-dotted line) and SIBYLL 2.1 (dotted line). Points are data [16].

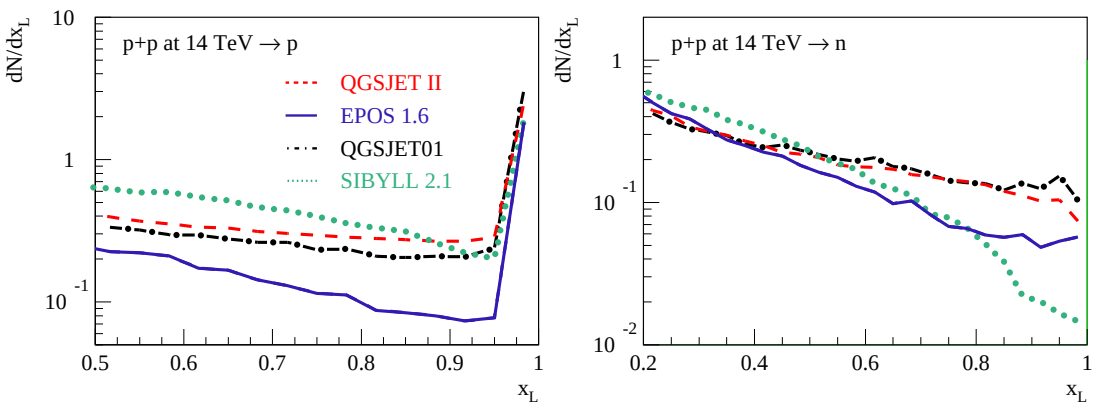

Fig. 3: Longitudinal $x_L = p_L/P_{Beam}$ distribution from p-p collision at 14 TeV cms energy for proton (lefthand-side) and neutron (righthand-side) as calculated with EPOS 1.6 (full line), QGSJET II (dashed line), QGSJET 01 (dash-dotted line) and SIBYLL 2.1 (dotted line).

forward region. But we can test the models thanks to the electron-proton HERA collider where proton or neutron production on the proton side can be measured up to very high longitudinal momentum. Results are shown Fig. [17]. While the models agree on x_L distributions at low energy, we can observe differences between them at HERA energy and in particular for EPOS 1.6 which seems to have a too strong proton dissociation in the forward region compared to the ZEUS experiment [18].

Various experiments at LHC (cf sec. [19]) should provide very usefull new data in this kinematic region, where we can see on Fig. 3, that the discrepency between the models is very large.

(Anti)Baryon production In the forward region, the number of (anti)baryons is very important for the number of muons produced in air shower. The process is well described in [20], where it is also shown that the number of antiprotons on the projectile side of π-carbon collision can only be reproduced correcly by the EPOS model. This is due to a more sophisticated remnant treatment in this model which allows baryon number transfer from the inner part of the collision to the forward (or backward) region.

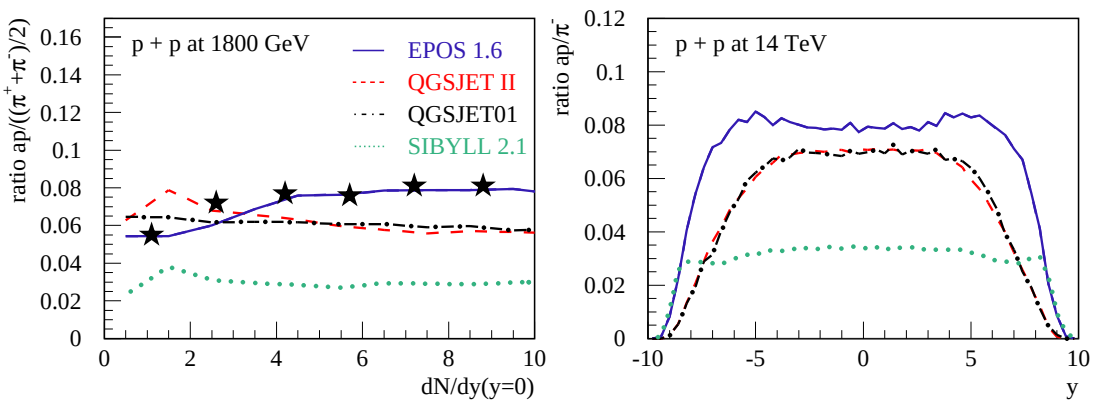

Fig. 4: Ratio of anti-proton over pion in $\overline{p}$-p scattering at 1.8 TeV cms energy as a function of the plateau height (lefthand-side) and rapidity distribution of this ratio for p-p interactions at LHC as calculated with EPOS 1.6 (full line), QGSJET II (dashed line), QGSJET 01 (dash-dotted line) and SIBYLL 2.1 (dotted line). Points are data [21, 22].

Another particularity of the (anti)baryons is that their production increase faster with the energy that the pion production. In other words, the ratio $\overline{p}/\pi$ increase with energy. At the highest measured energy (TEVATRON [22]), we can see on the lefthand-side of Fig. 4, that only EPOS describes correctly this ratio as a function of the event multiplicity. Other models are too low.

Extrapolating to LHC, the difference between the models appears clearly on the rapidity distribution of the $\overline{p}/\pi^-$ as shown Fig. 4 on the righthand-side. This ratio at midrapidity seems to saturate since the values at LHC are similar to the ones at TEVATRON, but the shape is really different comparing the models. Because of its remnant structure, EPOS predicts much more antiproton in the forward region of non-diffractive events ($|y| \sim 7$).

This explain why air showers simulated with EPOS contain more muons. Measurement of (anti)-baryon distributions at LHC will be very important to constrain muon number in air showers.

Total cross section Among the most important quantities relevant for hadronic model applications to cosmic ray (CR) physics is the total hadron-hadron cross section $\sigma^{\rm tot}$. The reason for that is twofold. First of all, the knowledge of the total cross section implies the knowledge of the corresponding elastic scattering amplitude, taken the optical theorem relation between the two quantities. Hence, one is able to calculate the corresponding inelastic cross section and, using the Glauber formalism, to generalize these results to hadron-nucleus collisions. In turn, inelastic hadron-air cross sections are crucial quantities for the description of CR-induced nuclear-electromagnetic cascades in the atmosphere, so-called extensive air showers (EAS).

Secondly, with the total cross section being the sum of partial contributions of all possible final states for a given reaction, optical theorem allows one, within a particular model approach, to establish a correspondence between various contributions to the elastic scattering amplitude and partial probabilities of particular configurations of the interaction. Thus, available experimental information on the energy dependence of $\sigma^{\rm tot}_{pp}$ may significantly constrain model predictions for basic characteristics of hadron production in the high energy asymptotics.

In particular, such a mapping is provided by the Gribov's Reggeon Field Theory (RFT) [23], where elastic hadron-hadron scattering is described by multiple exchanges of composite objects – Pomerons. Correspondingly, inelastic cross section may be obtained as a sum of contributions of certain unitarity cuts of elastic scattering diagrams, applying the Abramovskii-Gribov-Kancheli (AGK) cutting rules [24]. There, partial contributions to $\sigma^{\rm inel}_{ad}$ correspond to configurations of the interaction with a given number of 'elementary' production processes, the latter being described as 'cut Pomerons'. In fact, the essence of the AGK rules is that there is no interference between final states with different numbers of 'cut Pomerons', thanks to the fact that they occupy different regions of the phase space.

The described scheme takes an especially simple form if one assumes eikonal vertices for Pomeron-hadron coupling. However, one has to take into consideration contributions of multiparticle intermediate states for the projectile and target hadrons, 'between' Pomeron exchanges. The latter give rise to the diffraction dissociation and inelastic screening, the two phenomena being closely related to each other. Restricting oneself with low mass intermediate states only, one can develop a scheme of Good-Walker type, considering Pomeron-hadron coupling to be a matrix, whose elements correspond to transitions between hadronic elastic scattering eigenstates, and to obtain for total and absorptive (non-diffractive) hadron a - hadron d cross sections [25]

$$\sigma^{\rm tot}_{ad}(s) = 2\sum_{i,j} C_{i/a}\, C_{j/d} \int d^2b \, \left(1 - e^{-\lambda_{i/a}\,\lambda_{j/d}\,\chi^{\rm P}_{ad}(s,b)}\right) \tag{1}$$

$$\sigma^{\rm abs}_{ad}(s) = \sum_{i,j} C_{i/a}\, C_{j/d} \int d^2b \, \left(1 - e^{-2\,\lambda_{i/a}\,\lambda_{j/d}\,\chi^{\rm P}_{ad}(s,b)}\right) \quad , \tag{2}$$

where the Pomeron exchange eikonal $\chi^{\rm P}_{ad}(s,b)$ is the imaginary part of the corresponding amplitude in the impact parameter representation (the small real part can be neglected in high energy

asymptotics) and $C_{i/a}$, $\lambda_{i/a}$ are relative weights and relative strengths of elastic scattering eigenstates for hadron a.

Apart from the very possibility of introducing diffraction dissociation, the above-described treatment has two important differences from the purely eikonal scheme. First, both total and inelastic cross sections are reduced, the effect being enhanced for a scattering on a nuclear target. Predictions of cosmic ray interaction models for $\sigma^{\rm inel}_{h-{\rm air}}$ sizably differ, depending on whether or not the inelastic screening corrections are taken into account and being in contradiction with available data in the latter case, see Fig. 1. Secondly and even more importantly, one obtains significantly bigger fluctuations of multiplicity of produced particles and of numbers of 'wounded' nucleons in hadron-nucleus and nucleus-nucleus interactions, which has a strong impact on specifing the 'centrality' of nuclear collisions in collider applications. It is worth stressing, however, that the described quasi-eikonal scheme can not treat high mass multi-particle intermediate states which give rise to high mass diffraction processes and result in additional screening contributions. The solution of the problem is provided by taking into consideration so-called enhanced diagrams corresponding to Pomeron-Pomeron interactions [5, 26, 27].

In hadronic interaction models, the Pomeron eikonal $\chi^{\rm P}_{ad}$ is usually split into two parts, corresponding to partial contributions of 'soft' and 'semi-hard' parton cascades to elementary scattering process [4, 28]:

$$\chi^{\rm P}_{ad}(s,b) = \chi^{\rm P_{soft}}_{ad}(s,b) + \chi^{\rm P_{sh}}_{ad}(s,b) \tag{3}$$

In particular, in the 'mini-jet' approach [28] the 'semi-hard' eikonal is expressed as the product of the corresponding inclusive cross section $\sigma^{\rm jet}_{ad}(s,p_{t,\rm cut})$ for the production of parton jets with transverse momentum exceeding some cutoff $p_{t,\rm cut}$ and the hadron overlap function $A(b)$ (convolution of hadronic form factors):

$$\chi^{\rm mini-jet}_{ad}(s,b) = \sigma^{\rm jet}_{ad}(s,p_{t,\rm cut})\; A(b)\,, \tag{4}$$

where the inclusive jet cross section is given by a convolution of parton distribution functions (PDFs) $f_{i/a}(x,Q^2)$ with the parton scatter cross section $d\sigma^{2\to 2}_{ij}/dp_t^2$:

$$\sigma^{\rm jet}_{ad}(s,p_{t,\rm cut}) = \sum_{i,j}\int dx^+dx^-dp_t^2\; f_{i/a}(x^+,p_t^2)\; f_{j/d}(x^-,p_t^2)\; \frac{d\sigma^{2\to 2}_{ij}}{dp_t^2}\;\Theta(p_t^2-p_{t,\rm cut}^2) \tag{5}$$

However, when realistic PDFs are employed, the steep energy rise of $\sigma^{\rm jet}_{pp}$ leads to a contradiction between the predicted and measured $\sigma^{\rm tot}_{pp}$. To overcome the problem, one usually assumes that the low-x rise of hadronic PDFs is strongly damped by parton saturation effects which are often mimicked via using an energy-dependent p_t-cutoff: $p_{t,\rm cut} = p_{t,\rm cut}(s)$ [29]. Recently, one attempted to derive constraints on the required $p_{t,\rm cut}(s)$ dependence, based on the ansatz (4) [30]. Nevertheless, the situation remains puzzling: on one hand, one needs significant saturation effects in order to damp the quick energy rise of $\sigma^{\rm tot}_{pp}$, on the other – no such a strong saturation has been observed in DIS experiments at HERA. A possible solution is that the factorization ansatz (4) for the semi-hard eikonal becomes invalid when non-linear corrections to parton dynamics are taken into account [6]. The latter is easy to understand when bearing in mind that the QCD

factorization applies to fully inclusive quantities only, an example being the inclusive jet cross section (5), while being inapplicable for calculations of hadronic cross sections and of partial probabilities of particular final states. As was shown in [6], the semi-hard eikonal still can be cast in the form similar to (4-5), however, with the usual PDFs $f_{i/a}(x, Q^2)$ being replaced by reaction-dependent ones. Unlike the usual PDFs measured in DIS, those descibe parton evolution *during the interaction process*, which is thus influenced by parton re-scattering on the partner hadron, as depicted in Fig. 5.

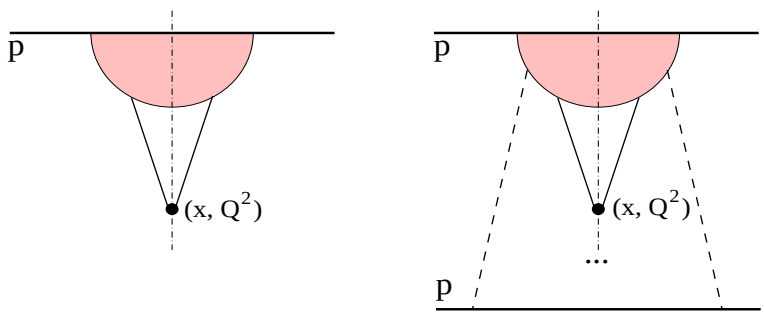

Fig. 5: Schematic view of parton distributions as "seen" in DIS (left) and in proton-proton collision (right). Low x parton (sea quark or gluon) originates from the initial state "blob" and interacts with a highly virtual "probe". In proton-proton interaction the initial "blob" itself is affected by the collision process – due to additional soft re-scatterings on the target, indicated by dashed lines.

Screening and saturation effects in MC models Crucial differences between present hadronic MC generators are related to how they treat nonlinear interaction effects emerging in the high parton density regime. The latter appear naturally when considering hadron-hadron and, especially, nucleus-nucleus scattering in the limit of high energies and small impact parameters, where a large number of parton cascades develops in parallel, being closely packed in the interaction volume. In the QCD framework, the corresponding dynamics is described as merging of parton ladders, leading to the saturation picture: at a given virtuality scale the parton density can not exceed a certain value; going to smaller momentum fractions x, further parton branching is compensated by merging of parton cascades [31]. Importantly, at smaller x, the saturation is reached at higher and higher virtuality scale $Q^2_{\rm sat}(x)$. The approach has been further developed in the large N_c-based color glass condensate (CGC) framework, where detailed predictions for the $Q^2_{\rm sat}(x)$ behavior have been derived [32].

In MC generators, one usually attempts to mimic the saturation picture in a phenomenological way. Standard method, employed, e.g., in the SIBYLL model [7–9], is to treat the virtuality cutoff Q^2_0 between soft and semihard parton processes as an effective energy-dependent saturation scale: $Q^2_0 = Q^2_{\rm sat}(s)$ and to neglect parton (and hadron) production at $|q^2| < Q^2_0(s)$. The parameters of the corresponding $Q^2_0(s)$ parametrization are usually tuned together with the other model parameters by fitting the measured proton-proton cross section.

A more sophisticated procedure has been applied in the EPOS model [3], where effective

saturation effects, being described by a set of parameters, depend on energy, impact parameter, types of interacting hadrons (nuclei). The corresponding mechanism influences not only the configuration of the interaction (how many processes of what type occur) but also the energy partition between multiple scattering processes and the hadronization procedure, the relevant parameters being fitted both with cross section and with particle production data.

An alternative approach has been employed in the QGSJET II model [5, 6], providing a microscopic treatment of nonlinear effects in the RFT framework: describing the latter by means of enhanced diagrams [26], corresponding to Pomeron-Pomeron interactions. In particular, the procedure proposed in [5] allowed one to resum contributions of dominant enhanced graphs to the scattering amplitude to all orders in the triple-Pomeron coupling. Furthermore, to treat secondary particle production, the unitarity cuts of the corresponding diagrams have been analyzed and a procedure has been worked out to resum the corresponding contributions for any particular final state of interest [27], which allowed one to implement the algorithm in the MC generator and to sample various configurations of the interaction in an iterative fashion. The main drawback of the approach is the underlying assumption that Pomeron-Pomeron coupling is dominated by soft ($|q^2| < Q_0^2$) parton processes. Thus, in contrast to the perturbative CGC treatment, the model has no dynamical evolution of the saturation scale: the saturation may only be reached at the Q_0^2 scale; at $|q^2| > Q_0^2$ parton evolution is described by purely linear DGLAP formalism.

Fragmentation of hadrons at ultra high energies Currently practically no experimental information is available on production of leading hadrons ($x_F \geq 0.1$) in the hadron - hadron collisions at the collider energies. At fixed target energies production of leading hadrons involves several partons of the projectile. For example, production of baryons in $x_F \geq 0.4$ predominantly involves at least two valence quarks of the proton, which did not experience a significant inelastic interaction, leading to a rather flat distribution in x_F. Similarly, the spectrum of the leading pions is much harder than the one corresponding to the fragmentation of one quark of the proton.

At high energies a novel situation emerges since a parton of the projectile with a given x_{pr} can resolve partons in the target with smaller and smaller $x_T \geq 4k_t^2/(x_{pr}s_{NN})$. Here k_t is typical parton transverse momentum in the interaction. The cross section of inelastic interaction is proportional to the gluon density at $x = x_T, Q^2 \sim 4k_t^2$. For $x_{pr} = 0.3, k_t = 1$ GeV/c at LHC (GZK) energies x down to $\sim 10^{-7}(10^{-10})$ are resolved. As a result, probability of inelastic interaction for a parton passing at a fixed distance ρ from the center of the other nucleon grows with energy roughly as $s^n, n \geq 0.25$ until it reaches values close to one - the black disk regime (BDR). For example, at LHC energies, at $\rho =$ 1 fm the interaction is black for the leading quarks with $p_t^2 \leq 1$ (GeV/c)^2 and for leading gluons with $p_t^2 \leq 2(GeV/c)^2$, see [33] for the review. Between LHC and GZK energies the strength of interaction for fixed ρ, and given virtuality is expected to increase by at least a factor of five extending further the region of ρ where interaction remains black up to large virtualities. The range of ρ where interaction is black grows as a power of energy, while soft diffusion changes the radius of strong interaction logarithmically. Hence the fraction of peripheral inelastic collisions in which leading partons of the nucleon remain spectators should decrease with energy. (Obviously the effect is even stronger for the cosmic ray interactions with air ($\langle A \rangle \sim 14$).)

In the BDR two effects modify fragmentation. One is that interaction selects configura-

tions in the colliding hadrons with large transverse momenta comparable to the scale of the BDR for given x_{pr}, ρ. This effectively results in the fractional energy losses [34,35]. The second effect is the loss of coherence between the leading partons as they receive large transverse momenta and cannot fragment jointly to the same leading hadron. As a result, the projectile becomes "shattered": The leading partons with $x \sim 0.2$ fragment independently into minijets with transverse momenta of few GeV and rapidities

$$y_{\text{minijet}} = y_{max} + \ln x - \ln(p_{\text{t BDR}}/m_N), \tag{6}$$

where $y_{max} = \ln(p_N/m_N)$. Production of hadrons from these minijets proceeds independently over a range of rapidities determined by condition that transverse momentum of hadrons in the jets due to primordial transverse momentum of a parton is larger than the soft transverse momentum scale $p_{\text{t soft}} \sim 0.4$ GeV/c. In the fragmentation process the transverse momentum of the primary parton is shared by produced partons in proportion of their light cone fractions. Hence, one can estimate the range of fractions, z, of the jet momentum where fragmentation of partons can be treated as independent:

$$z = p_{\text{t soft}}/p_{\text{t BDR}}. \tag{7}$$

For $p_{\text{t BDR}} \sim 1$ GeV/c and $x \sim 0.2 \div 0.25$ this corresponds to $x_F \geq 0.1$. With increase of energy the range where independent fragmentation is valid should expand.

In the central $p(\pi)A$ collisions where nucleus edge effects can be neglected the differential multiplicity of leading hadrons, integrated over $p_\perp$, is approximately given by the convolution of the nucleon parton density, f_a, with the corresponding parton fragmentation function, $D_{h/a}$, at the scale $Q^2_{eff} = 4p^2_{t,\text{BDR}}$ [34, 36–38]:

$$\frac{1}{N}\left(\frac{dN}{dx_F}\right)^{p+A\to h+X} = \sum_{a=q,g}\int_{x_F}^1 dx\, x f_a(x, Q^2_{eff}) D_{h/a}(x_F/x, Q^2_{eff}), \tag{8}$$

where N is total number of inelastic events. Eq.8 leads to a much steeper decrease of the forward spectrum with x_F than the one observed in soft collisions, and, in particular, to the π/N ratio $\gg 1$ for $x_F \geq 0.2$. Hence the large x_F inclusive spectrum is likely to be dominated by very peripheral collisions which constitute progressively smaller fraction of the collisions with increase of energy. Hence one expects that the forward multiplicity will decrease with energy. Another manifestation of this mechanism is broadening of the transverse distribution of the forward hadrons which essentially reflects transverse momenta of the forward jets [36].

First studies of these effects for GZK energies were performed in [36]. It was found that a strong increase of the gluon densities at small x leads to a steeper x_F-distribution of leading hadrons as compared to low energy collisions and results in a significant reduction of the position of the shower maximum, X_{max}. Account of this effect in the models currently used for the interpretation of the data may shift fits of the composition of the cosmic ray spectrum near the GZK cutoff towards lighter elements.

In the near future it will be possible to test experimentally these prediction in the central deuteron - gold collisions at RHIC. Another possibility is to study pp collisions at the LHC with special centrality triggers [39]. At the same time such measurements would not test dynamics

of fragmentation in ultra high-energy pion - nucleus collisions which constitute the bulk of the air showers. The interaction which is most similar to πA interactions (especially for low p_t) and could be studied at the collider energies in ultraperipheral heavy ion collisions is γA collisions. In such collisions nuclei collide at large impact parameters where one nucleus effectively serves as a a source of the Weizsacker-Williams photons. At the LHC one can probe a wide range of energies $W_{\gamma N} \leq 1$ TeV [40]. For $W_{\gamma N} \leq 200$ GeV it will be possible to compare forward spectra to the HERA data on the γp collisions. It will be also possible to study forward spectrum as a function of $W_{\gamma N}$.

2 Ultra-high energy photons and s-channel unitarity

Photon cross sections at ultra-high energies Extrapolations of γp and γA cross sections to extremely high energies are frequently used in studies of ultra-high energy (UHE) cosmic rays. In particular, the UHE photon cross section is related to the cosmic ray air shower maximum, X_{max} (see [41] and references therein for a recent review). Furthermore, the identity of the primary particle affects the shape of the resulting air-shower.

At UHE energies, the incident photon interacts with the hadron target by first fluctuating into a virtual hadronic state a large distance ahead of the target. Probability of such interaction may become comparable to the probability of the electromagnetic interactions in the media, see review in [42]. Each of the virtual hadronic states interacts with the target with a strength characterized by its transverse size (which is inversely related to the state's virtuality). As the center-of-mass energy increases, there is an increasingly large contribution to the photon wavefunction from very small size quark-antiquark pairs.

It can be argued on the basis of general assumptions that the asymptotic energy dependence of photon cross sections is a power of $\ln s$ somewhere between 2 and 3 [43, 44]. An important point is that one cannot directly apply the Froissart bound, $\sigma_{tot} \sim \sigma_{\pi N} \propto \ln^2 s$, to photon-hadron interactions because the incident photon wavefunction is non-normalizable – there is an ultra-violet divergent contribution coming from small size configurations. Furthermore, a model based on the combined contributions of a hard Pomeron and a soft Pomeron [45] badly violates unitarity in the asymptotic limit because of the power-law behavior of the cross section. (This is true even if eikonalization is used to enforce s-channel unitarity, because the power-law growth of the basic cross section leads to a power-law growth of the radius of the interaction in impact parameter space.) See [46] and references therein for a review of the different types of energy dependence for the γp cross section predicted from various models.

Constraints on the growth of the photon cross section can be obtained by enforcing s-channel unitarity in impact parameter space for each individual hadronic state in the photon wavefunction. The method that we focus on here is the one used in [47] to address the unitarity limit in HERA data, and extended to the UHE real photon case in [43]. In this approach, the large size configurations have cross sections that grow at a rate typical of hadron-hadron interactions, while small size configurations have cross sections that grow according to leading twist (LT) pQCD. Intermediate sizes are obtained by extrapolating between these two regions. Configurations that grow according to LT pQCD quickly become too large to be realistic and violate s-channel unitarity. The approach in [43] is simply to allow this rapid growth, but to cut off

impact parameter dependent cross sections at their maximum possible values when they start to violate unitarity. The advantage of this approach is that it provides a conservative upper bound on the γp cross section. The main disadvantage is that it does not address the details of the higher-twist dynamical effects and/or non-perturbative effects that tame the cross section and are ultimately responsible for enforcing unitarity.

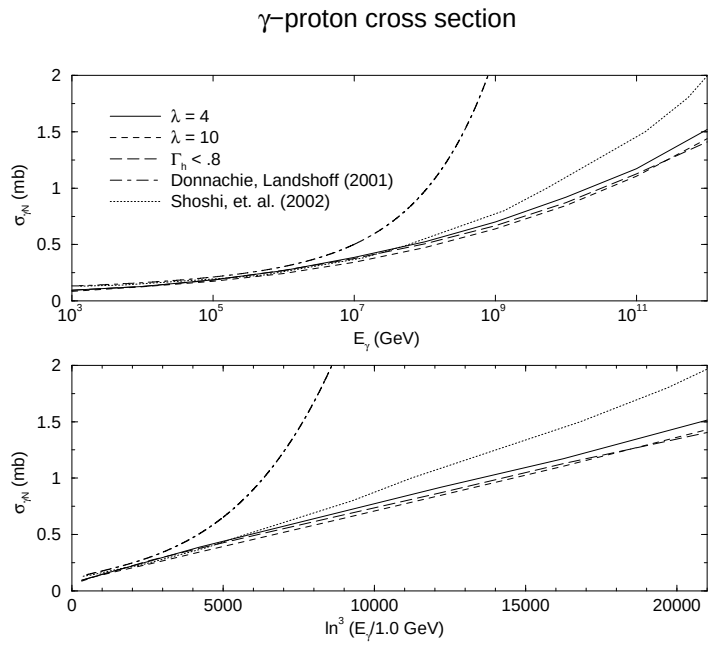

Fig. 6: The solid line is the dependence obtained the lower dashed lines show the sensitivity to variations in model parameters.

Figure 6 is taken from [43] and compares the unitarity-corrected model with models that allow a violation of s-channel unitarity. It should also be noted that the model of [43] is consistent with other extrapolations (see, e.g., [48]) based on logarithmic energy growth. Note that, although the unitarity corrections in [43] provide a conservative amount of taming, it still leads to a cross section that is less than what is predicted from parameterizations that use a power-law behavior for the basic cross section.

Charm contribution The framework in the previous section also allows for an estimate of the contribution to the photon cross section from charmed mesons.

The contribution of charm in the photon wavefunction is generally suppressed by the mass of the charm quark. However, at extremely high energies, there are large contributions from highly virtual quark-antiquark fluctuations, and for these fluctuations the suppression from the charm mass becomes negligible. If the energy is high enough that the γp cross section is entirely dominated by these very small quark-antiquark pairs, then we expect a full recovery of flavor SU(4) symmetry. In other words, we could expect up to 40% of the cross section to be due to charm quarks. An analysis of this type was performed in [43] and shows that a significant contribution, around 25% of the cross section, is due to charm quarks. See also recent work in [49].

The enhancement of the charm production in the fragmentation region in the high gluon density regime should occur also for the hadron induced cascades. It should lead to an enhancement of the production of ultra-high energy muons in the cores of air showers with energies comparable with the GZK cutoff.

Nuclear targets For γA interactions, a natural expectation is that one can directly extend the analysis for the proton target discussed in the previous section to the nuclear case by replacing the impact parameter dependent parton distribution function of the proton with the corresponding distribution function for a nucleus. However, allowing the full disk of the nuclear target to grow black yields cross sections that are even larger than what one expects from a naive extension of a Glauber type model of photon-nucleus cross sections. In a more realistic treatment, therefore, we can simply use the γp cross section from section 2 in a Glauber-Gribov treatment of the interaction with a nuclear target. A large value of the $\sigma^{\gamma N}_{diffr}/\sigma^{\gamma N}_{tot} \sim 1/2$ results in a large nuclear shadowing and hence slower increase of the $\gamma - A$ cross section with energy than in the γp case. The resulting cross section from [43] is shown in Fig. 7.

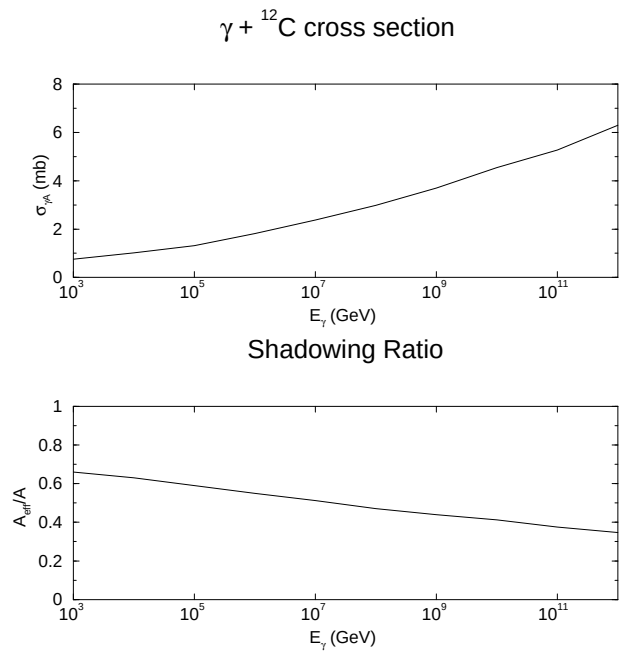

Fig. 7: The upper plot shows the cross section for a photon to scatter off Carbon using the basic cross section from section (2). The lower plot shows the corresponding shadowing ratio.

3 Extrapolation of neutrino cross section

Extrapolation of neutrino cross-section towards very high energy is needed if we want to estimate flux of ultrahigh energy neutrinos of extragalactic sources like Active Galactic Nuclei. Such estimation might be useful for Ice Cube experiment which can detect neutrinos of energy 10^{12} GeV and higher. The dominant interaction with matter at such energies is Deep Inelastic Scattering on

nucleons and in particular with the gluonic component. This gluonic system is probed roughly at $x = 10^{-8}$. In order to be consistent with unitarity bound which states that total cross-section should grow not faster than $\log^2 1/x$ one has to allow for gluon recombination effects which reduce the rate of growth of gluon density. The most suitable approach to calculate the UHE neutrino nucleon cross-section is the k_t factorisation approach (high energy factorisation). Within this scheme in order to calculate the neutrino cross-section one performs convolution of transverse momentum dependent hard matrix element (which in this case is weak boson-gluon fusion) with unintegrated gluon distribution which takes into account high energy effects. The evolution equation which introduces a large part of recombination effects in lepton-nucleon scattering is the Balitsky-Kovchegov [50] equation. This equation generalizes the BFKL [51] equation. It consists of a linear term which accounts for fast grow of gluon density at moderate values of x and nonlinear term which comes with negative sign which tames the growth of gluon density at low x. In reference [52] the calculation of $F_2(x, Q^2)^{CC,NC}$ using the BK equation (with subleading corrections) was performed and the UHE neutrino-nucleon cross-section was calculated. This calculation shows (see Fig. 8 (right)) that nonlinear effects reduce cross-section roughly by a factor of two as compared to approach based on linear evolution equation (BFKL with subleading corrections). In the calculation it was assumed that gluons are uniformly distributed in the nucleon. A more realistic initial distribution would increase slightly the cross section as compared to obtained from uniformly distributed gluons.

References

[1] A. Bunyatyan et al, *Introduction*. These proceedings.

[2] H. J. Drescher, M. Hladik, S. Ostapchenko, T. Pierog, and K. Werner, Phys. Rept. **350**, 93 (2001), arXiv:hep-ph/0007198.

[3] K. Werner, F.-M. Liu, and T. Pierog, Phys. Rev. **C74**, 044902 (2006), arXiv:hep-ph/0506232.

[4] N. N. Kalmykov, S. S. Ostapchenko, and A. I. Pavlov, Nucl. Phys. Proc. Suppl. **52B**, 17 (1997).

[5] S. Ostapchenko, Phys. Lett. **B636**, 40 (2006), arXiv:hep-ph/0602139.

[6] S. Ostapchenko, Phys. Rev. **D74**, 014026 (2006), arXiv:hep-ph/0505259.

[7] R. S. Fletcher, T. K. Gaisser, P. Lipari, and T. Stanev, Phys. Rev. **D50**, 5710 (1994).

[8] J. Engel, T. K. Gaisser, T. Stanev, and P. Lipari, Phys. Rev. **D46**, 5013 (1992).

[9] R. Engel, T. K. Gaisser, T. Stanev, and P. Lipari. Prepared for 26th International Cosmic Ray Conference (ICRC 99), Salt Lake City, Utah, 17-25 Aug 1999.

[10] S. Ostapchenko, Czech. J. Phys. **56**, A149 (2006), arXiv:hep-ph/0601230.

[11] J. Knapp, D. Heck, S. J. Sciutto, M. T. Dova, and M. Risse, Astropart. Phys. **19**, 77 (2003), arXiv:astro-ph/0206414.

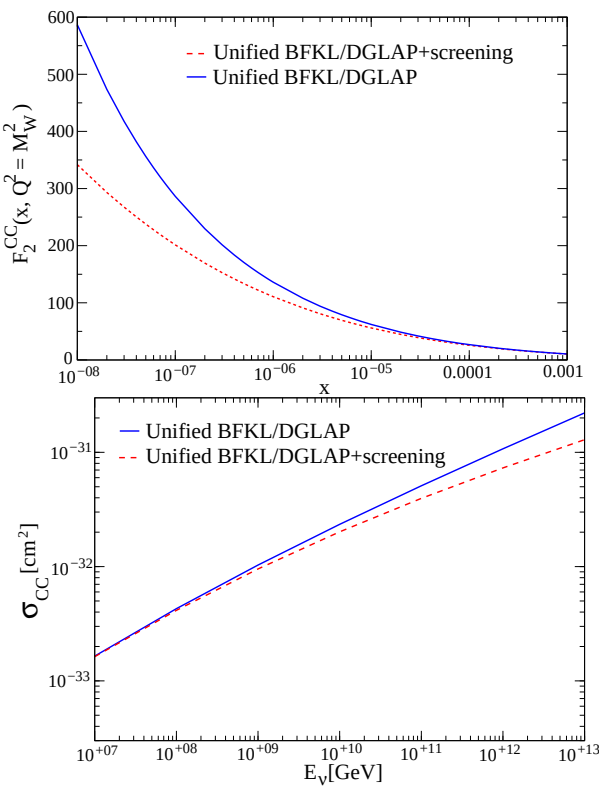

Fig. 8: (left) Charged current $F_2^{CC}(x, Q^2)$ structure function , (right) neutrino cross-section obtained from BK (with subleading corrections) and from BFKL (with subleading corrections)

[12] R. Engel and H. Rebel, Acta Phys. Polon. **B35**, 321 (2004).

[13] C. Meurer, J. Bluemer, R. Engel, A. Haungs, and M. Roth, Czech. J. Phys. **56**, A211 (2006), arXiv:astro-ph/0512536.

[14] Particle Data Group Collaboration, C. Caso *et al.*, Eur. Phys. J. **C3**, 1 (1998).

[15] H. H. Mielke, M. Foeller, J. Engler, and J. Knapp, J. Phys. **G20**, 637 (1994); G. b. Yodh, S. c. Tonwar, T. k. Gaisser, and R. w. Ellsworth, Phys. Rev. **D27**, 1183 (1983); M. Honda *et al.*, Phys. Rev. Lett. **70**, 525 (1993); R. M. Baltrusaitis *et al.*, Phys. Rev. Lett. **52**, 1380 (1984).

[16] UA5 Collaboration, R. E. Ansorge *et al.*, Z. Phys. **C43**, 357 (1989).

[17] A. Bunyatyan et al, *Experimental results (see fig 6)*. These proceedings.

[18] ZEUS Collaboration, S. C. e. a. ZEUS Coll., Nucl. Phys. **B658**, 3 (2003), arXiv:hep-ex/0210029.

[19] A. Bunyatyan et al, *Experimental results*. These proceedings.

[20] T. Pierog and K. Werner, Phys. Rev. Lett. **101**, 171101 (2008), arXiv:astro-ph/0611311.

[21] NA49 Collaboration, T. Susa, Nucl. Phys. **A698**, 491 (2002).

[22] E735 Collaboration, T. Alexopoulos *et al.*, Phys. Rev. **D48**, 984 (1993).

[23] V. N. Gribov, Sov. Phys. JETP **26**, 414 (1968); V. N. Gribov, Sov. Phys. JETP **29**, 483 (1969).

[24] V. A. Abramovsky, V. N. Gribov, and O. V. Kancheli, Yad. Fiz. **18**, 595 (1973).

[25] A. B. Kaidalov, Phys. Rept. **50**, 157 (1979).

[26] J. L. Cardy, Nucl. Phys. **B75**, 413 (1974); A. B. Kaidalov, L. A. Ponomarev, and K. A. Ter-Martirosian, Yad. Fiz. **44**, 722 (1986).

[27] S. Ostapchenko, Phys. Rev. **D77**, 034009 (2008), arXiv:hep-ph/0612175.

[28] L. Durand and P. Hong, Phys. Rev. Lett. **58**, 303 (1987); X.-N. Wang, Phys. Rept. **280**, 287 (1997), arXiv:hep-ph/9605214; F. M. Liu, H. J. Drescher, S. Ostapchenko, T. Pierog, and K. Werner, J. Phys. **G28**, 2597 (2002), arXiv:hep-ph/0109104.

[29] F. W. Bopp, R. Engel, D. Pertermann, and J. Ranft, Phys. Rev. **D49**, 3236 (1994).

[30] T. C. Rogers, A. M. Stasto, and M. I. Strikman, Phys. Rev. **D77**, 114009 (2008), arXiv:0801.0303 [hep-ph].

[31] L. V. Gribov, E. M. Levin, and M. G. Ryskin, Phys. Rept. **100**, 1 (1983).

[32] J. Jalilian-Marian, A. Kovner, A. Leonidov, and H. Weigert, Nucl. Phys. **B504**, 415 (1997), arXiv:hep-ph/9701284;
E. Iancu, A. Leonidov, and L. D. McLerran, Nucl. Phys. **A692**, 583 (2001), arXiv:hep-ph/0011241.

[33] L. Frankfurt, M. Strikman, and C. Weiss, Ann. Rev. Nucl. Part. Sci. **55**, 403 (2005), arXiv:hep-ph/0507286.

[34] L. Frankfurt, V. Guzey, M. McDermott, and M. Strikman, Phys. Rev. Lett. **87**, 192301 (2001), arXiv:hep-ph/0104154.

[35] L. Frankfurt and M. Strikman, Phys. Lett. **B645**, 412 (2007).

[36] A. Dumitru, L. Gerland, and M. Strikman, Phys. Rev. Lett. **90**, 092301 (2003), arXiv:hep-ph/0211324.

[37] A. Berera, M. Strikman, W. S. Toothacker, W. D. Walker, and J. J. Whitmore, Phys. Lett. **B403**, 1 (1997), arXiv:hep-ph/9604299.

[38] F. Gelis, A. M. Stasto, and R. Venugopalan, Eur. Phys. J. **C48**, 489 (2006), arXiv:hep-ph/0605087.

[39] H. J. Drescher and M. Strikman, Phys. Rev. Lett. **100**, 152002 (2008).

[40] K. Hencken *et al.*, Phys. Rept. **458**, 1 (2008), arXiv:0706.3356 [nucl-ex].

[41] R. A. Vazquez, Nucl. Phys. Proc. Suppl. **175-176**, 487 (2008).

[42] S. Klein, Rev. Mod. Phys. **71**, 1501 (1999), arXiv:hep-ph/9802442.

[43] T. C. Rogers and M. I. Strikman, J. Phys. **G32**, 2041 (2006), arXiv:hep-ph/0512311.

[44] V. N. Gribov, Zh. Eksp. Teor. Fiz. **57**, 1306 (1969). SLAC-TRANS-0102;
L. B. Bezrukov and E. V. Bugaev, Yad. Fiz. **33**, 1195 (1981);
E. Gotsman, E. M. Levin, and U. Maor, Eur. Phys. J. **C5**, 303 (1998), arXiv:hep-ph/9708275.

[45] A. Donnachie and P. V. Landshoff, Phys. Lett. **B518**, 63 (2001), arXiv:hep-ph/0105088.

[46] E. V. Bugaev, Nucl. Phys. Proc. Suppl. **175-176**, 117 (2008).

[47] M. McDermott, L. Frankfurt, V. Guzey, and M. Strikman, Eur. Phys. J. **C16**, 641 (2000), arXiv:hep-ph/9912547.

[48] M. M. Block and F. Halzen, Phys. Rev. **D70**, 091901 (2004), arXiv:hep-ph/0405174.

[49] V. P. Goncalves and M. V. T. Machado, JHEP **04**, 028 (2007), arXiv:hep-ph/0607125.

[50] I. Balitsky, Nucl. Phys. **B463**, 99 (1996), arXiv:hep-ph/9509348; Y. V. Kovchegov, Phys. Rev. **D60**, 034008 (1999), arXiv:hep-ph/9901281.

[51] E. A. Kuraev, L. N. Lipatov, and V. S. Fadin, Sov. Phys. JETP **45**, 199 (1977).

[52] K. Kutak and J. Kwiecinski, Eur. Phys. J. **C29**, 521 (2003), arXiv:hep-ph/0303209.

Summary

A. Bunyatyan, A. Cooper-Sarkar, C. Diaconu, R. Engel, C. Kiesling, K. Kutak, S. Ostapchenko, T. Pierog, T.C. Rogers, M.I. Strikman, T. Sako

Since their beginning the studies of cosmic ray and elementary particle physics have always be closely related and it has been demonstrated that the very high energy cosmic ray puzzle can not be solved without the results of the HERA or LHC experiments.

Using a simple cascade model, it is possible to find the main parameters of hadronic interactions that influence air shower predictions. These parameters, namely the inelastic cross sections, the secondary particle multiplicity, the inelasticity, and the ratio of charged to neutral hadrons, depend of the hadronic interaction model. As a consequence, realistic simulations of hadron induced air-showers are model-dependent, leading to theoretical uncertainties in the analysis of experimental data. For a ground based detector, the model-related systematic error on energy estimation can be as large as about 20% at 10^{19} eV if the mass of the primary particle is unknown. The theoretical uncertainties of the energy reconstruction are much smaller for fluorescence light detectors (less than 5% even for unknown primary particle mass). The model dependence of the primary mass estimation is crucial and currently the mass composition can only be derived for a given hadronic model. As a consequence, the models have to be carefully tested at the highest energy reached in experiments and especially in the forward region where HERA and LHC can provide crucial informations.

The data on the total photoproduction cross section and jet final states with emphasis on the phase space near the forward (proton) direction from HERA have been summarized, discussing the extraction of the parton distribution functions from a combined data set of the two collider experiments H1 and ZEUS. These data shed light on the parton evolution models and also enable a unique measurement of the running strong coupling, providing new insight into QCD dynamics at very low values of the Bjorken variable x.

In addition, the HERA experiments provide a wealth of measurements of leading baryon production. These measurements give an important input for an improved theoretical understanding of the proton fragmentation mechanism. As shown, the HERA data on forward particle production can help to reduce the uncertainty in the model predictions for very high energy cosmic ray air showers.

In the near future, the integration of the data from not only the LHC experiment dedicated for the cosmic ray science (LHCf) but also the others, especially the forward experiments introduced in [1] will be important to constrain the interaction models used in the cosmic-ray studies.

The charged current neutrino cross-section at NLO have been calculated in the Standard Model using the best available DIS data along with a careful estimate of the associated uncertainties. If cross-sections much outside the uncertainty bands presented here are observed at UHE cosmic neutrino detectors, it would be a clear signal of the need for extensions to conventional QCD DGLAP formalism.

Finally the extrapolation of photoproduction and neutrino cross-section towards very high energy is needed if we want to estimate flux of ultrahigh energy photons and neutrinos of ex-

tragalactic sources like Active Galactic Nuclei. Such estimation might be useful for the Pierre Auger Observatory to set a proper limit on the photon flux and Ice Cube experiment which can detect neutrinos of energy 10^{12} GeV and higher. Here again, the best constrains are given by both HERA and LHC experiments.

Acknowledgments The research of M.S. was supported by the United States Department of Energy. S.O. would like to acknowledge the support of the European Commission under the Marie Curie IEF Programme (grant 220251).

References

[1] A. Bunyatyan et al, *Experimental results*. These proceedings.

Chapter 6

Working Group Monte Carlo and Tools

Convenors:

P. Bartalini (Taiwan, CMS),
S.Chekanov (Argonne, ZEUS),
F. Krauss (IPP Durham),
S. Gieseke (U. Karlsruhe),

Introduction

P. Bartalini[a], *S. Chekanov* [b], *S. Gieseke*[c] *and F. Krauss* [d]
[a] National Taiwan University, Taiwan
[b] HEP Division, Argonne National Laboratory, USA
[c] Institut für Theoretische Physik, Universität Karlsruhe, Germany
[d] Department of Physics, Durham University, UK

As for the previous HERA-LHC workshop, the main goals of the WG5 working group during 2006–2008 were: 1) To examine and improve Monte Carlo models for the LHC data using the experience and ideas from the HERA experiments; 2) To develop analysis frameworks to be used to tune and validate Monte Carlo models; 3) To review and further develop data analysis tools, common interfaces and libraries, which have their origin at HERA and can be useful for studies at the LHC.

Over the past few years, the working group has covered various aspects of data analysis tools and Monte Carlo models, from the conceptually simple ideas through technically detailed projects. Below we will briefly discuss several topics covered by the participants of the WG5 working group.

1 Monte Carlo event generators

There has been considerable progress in the development of Monte Carlo event generators during this workshop. In the working group, we had a very broad coverage of almost all existing Monte Carlo event generators which are expected to be used at the LHC. We have particularly discussed the developments of ALPGEN, PYTHIA8 , HERWIG++, CASCADE, MC@NLO, THEPEG and Forward Physics Monte Carlo (FPMC) [1, 2]. A lot of progress has been made in different areas of simulation.

On the perturbative level, the matching of parton showers with high order matrix elements was discussed and developed extensively. The matching of high jet multiplicity matrix elements with multiple parton shower emissions was discussed as well as matching parton showers with complete next–to–leading order calculations.

The most important question for this workshop was whether we had the necessary tools for the LHC era and whether there was something that HERA could still contribute. Several new Monte Carlo event generators, such as PYTHIA 8, HERWIG++ and SHERPA, are completely new programs, all written in C++, that partly aim to be the successors of the FORTRAN event generators that had already been widely used at HERA. These Monte Carlo models are not just simple rewrites of the existing codes: as was discussed, in many respects, the simulation of the underlying physics in such Monte Carlo models is more sophisticated than in the previous FORTRAN-based versions. New parton shower models, new models for the underlying event and a more sophisticated simulation of the non–perturbative hadronization was discussed. A lot of emphasis has been put on the discussion of underlying event physics as some progress in understanding was expected from the latest HERA results. Details will be discussed in the following section.

In addition to a pure technical description of the progress made in the development of such models, we had several studies showing the relevance and importance of these models to the LHC physics, especially for the direct photons (γ+jet), top-pair production, Wt and the forward-jet physics [2, 3]. We have learned that the current event generators work satisfactorily for the description of HERA data, but the LHC experiments will substantially increase the demands on the physics models implemented in such models.

2 Multiple Parton Interactions in Monte Carlo generators

In the years '80, the evidence for Double Scattering (DS) phenomena in the high-p_T phenomenology of hadron colliders [4] suggested the extension of the same perturbative picture to the soft regime, giving rise to the first implementation of the Multiple Parton Interaction (MPI) processes in a QCD Monte Carlo model [5] which was very successful in reproducing the UA5 charged multiplicity distributions [6].

On top of the general Minimum Bias (MB) observables these MPI models turn out to be particularly adequate to describe the Underlying Event (UE) physics at Tevatron [7], in particular they partly account for the pedestal effect (i.e. the enhancement of the Underlying Event activity with the energy scale of the interaction) as the effect of an increased probability of multiple partonic interactions in case a hard collision has taken place. A second important effect that can contribute to the pedestal effect is the increase in initial state radiation associated to the presence of a hard scattering.

Examples of MPI models are implemented in the general purpose simulation programs PYTHIA [8], HERWIG/JIMMY [9, 10] and SHERPA [11]. Other successful descriptions of UE and MB at hadron colliders are achieved by alternative approaches like PHOJET [12], which was designed to describe rapidity gaps and diffractive physics (relying on both perturbative QCD and Dual Parton Models). The most recent PYTHIA versions [13] adopt an optional alternative description of the colliding partons in terms of correlated multi-parton distribution functions of flavours, colors and longitudinal momenta.

From the contributions to the MC and multi-jet working groups of this HERA/LHC workshop, it is clear that the MPI are currently experiencing a growing popularity and are presently widely invoked to account for observations that would not be explained otherwise.

While preparing the ground for the traditional DS, MB and UE measurements at the LHC along the Tevatron experience (also complemented with the recent UE HERA results), new feasibility studies are proposed which in perspective will constitute a challenge to the performances of the MPI models: the usage of jet clustering algorithms providing an automated estimation of the UE activity, the investigation of the mini-jet structure of the MB events, the estimation of large pseudo-rapidity activity correlations, the connection between the partonic cross sections and the rapidity gap suppression in the hard diffractive events.

At the same time, the implementation of the MPI effects in the Monte Carlo models is quickly proceeding through an increasing level of sophistication and complexity that has already a deep impact on the analysis strategies at the LHC. For example new MC tools like PYTHIA8 and HERWIG++ can now be used in order to estimate complementary Standard Model backgrounds to searches coming from DS.

Further progress in the description of the MPI might be achieved with the introduction of a dynamical quantum description of the interacting hadrons, providing also a modeling of the diffractive interactions in the same context.

3 Introduction to Monte Carlo validation and analysis tools

The RIVET library, a successor to the successful HERA-oriented generator-analysis library, HZTOOL, is getting to be popular at the LHC for validating the performance of event generator and tuning [14]. Unlike FORTRAN-based HZTOOL, RIVET is written in object-oriented C++, and it is primarily a library which can be used from within any analysis framework.

For Monte Carlo tuning, the so-called PROFESSOR system [14] was recently successfully used for PYTHIA6 tuning. This led to a substantial improvement on the existing default tune, thus it can greatly aid the setup of new generators for LHC studies.

In this working group, we have moved beyond Monte Carlo specific validation tools. As an example, jHepWork analysis framework [15] presented at this working group can be considered as a multi-platform alternative to ROOT since it was written in Java. The framework can be useful for both experimentalists and theorists.

4 Conclusions

The presented proceedings describe the results of the work performed in the WG5 working group over several years between 2006–2008. Hopefully, we have provided a correct balance between experimental and theoretical results. As conveners of this working group, we were impressed by the quality and diversity of the presented results. The high quality of the presentations stimulated lively discussions often leading to new ideas and insights into the working group topics.

We would like to thank all participants for their work. We also thank all the organizers for the excellent organization of this workshop.

References

[1] L. Lenzi, *Alpgen and* SHERPA *in* $z/\gamma^* + jets$ *at the* LHC *(these proceedings)*;
M. Bähr *et al., Herwig++ status report (these proceedings)*;
T. Sjöstrand, PYTHIA 8 *status report (these proceedings)*;
M. Deak, H. Jung, and K. Kutak, *Cascade (these proceedings)*.

[2] C. White, *Single top production in the* wt *mode with* MC@NLO *(these proceedings)*;
L. Lonnblad, *Toolkit for high energy physics event generation (these proceedings)*;
M. Boonekamp, V. Juránek, O. Kepka, and C. Royon, FORWARD PHYSICS MONTE CARLO *(these proceedings)*.

[3] S. Albino, *Perturbative description of inclusive single hadron production at hera (these proceedings)*;
R. Blair, S. Chekanov, G. Heinrich, A. Lipatov, and N. Zotov, *Direct photon production at* HERA, *the* TEVATRON *and the* LHC *(these proceedings)*;
R. Chierici, *Generator comparison for top-pair production (these proceedings)*;
P. Stephens and A. van Hameren, *Propagation of uncertainty in a parton shower (these proceedings)*.

[4] Axial Field Spectrometer Collaboration, T. Akesson *et al.,* Z. Phys. **C34**, 163 (1987);
UA2 Collaboration, J. Alitti *et al.,* Phys. Lett. **B268**, 145 (1991);
CDF Collaboration, F. Abe *et al.,* Phys. Rev. **D47**, 4857 (1993).

[5] T. Sjostrand and M. van Zijl, Phys. Lett. **B188**, 149 (1987).

[6] UA5 Collaboration, G. J. Alner *et al.,* Z. Phys. **C33**, 1 (1986).

[7] CDF Collaboration, A. Affolder *et al.,* Phys. Rev. **D65**, 092002 (2002);
CDF Collaboration, D. Acosta *et al.,* Phys. Rev. **D70**, 072002 (2004).

[8] T. Sjostrand *et al.,* Comput. Phys. Commun. **135**, 238 (2001). `hep-ph/0010017`.

[9] G. Corcella *et al.,* JHEP **101**, 010 (2001). `hep-ph/0011363`.

[10] J. M. Butterworth, J. R. Forshaw, and M. H. Seymour, Z. Phys. **C72**, 637 (1996). `hep-ph/9601371`.

[11] T. Gleisberg *et al.,* JHEP **02**, 056 (2004). `hep-ph/0311263`.

[12] F. W. Bopp, R. Engel, and J. Ranft (1998). `hep-ph/9803437`.

[13] T. Sjostrand *et al.,* JHEP **05**, 026 (2006). `hep-ph/0603175`.

[14] A. Buckley, *Tools for event generator tuning and validation (these proceedings)*.

[15] S. Chekanov, JHEPWORK - JAVA *object-oriented data analysis framework (these proceedings)*.

A multi-channel Poissonian model for multi-parton scatterings

Daniele Treleani
Dipartimento di Fisica Teorica dell'Università di Trieste,
INFN and ICTP, Trieste, I 34014 Italy

Abstract
Multiple parton interactions are typically implemented in Montecarlo codes by assuming a Poissonian distribution of collisions with average number depending on the impact parameter. A possible generalization, which links the process to hadronic diffraction, is shortly discussed.

1 The simplest Poissonian model

A standard way to introduce multiple parton interactions in Montecarlo codes is to assume a Poissonian distribution of multiple parton collisions, with average number depending on the value of the impact parameter. The motivations were discussed long ago in several articles [1] [2] [3]: One introduces the three dimensional parton density $D(x,b)$, namely the average number of partons with a given momentum fraction x and with transverse coordinate b (the dependence on flavor and on the resolution of the process is understood) and one makes the simplifying assumption $D(x,b) = G(x)f(b)$, with $G(x)$ the usual parton distribution function and $f(b)$ normalized to one. The inclusive cross section for large p_t parton production σ_S may hence be expressed as

$$\sigma_S = \int_{p_t^c} G(x)\hat{\sigma}(x,x')G(x')dxdx' = \int_{p_t^c} G(x)f(b)\hat{\sigma}(x,x')G(x')f(b-\beta)d^2bd^2\beta dxdx' \quad (1)$$

where p_t^c is a cutoff introduced to distinguish hard and soft parton collisions and β the hadronic impact parameter. The expression allows a simple geometrical interpretation, given the large momentum exchange which localizes the partonic interaction inside the overlap volume of the two hadrons.

Neglecting all correlations in the multi-parton distributions, the inclusive cross section for a double parton scattering σ_D is analogously given by

$$\begin{aligned}\sigma_D &= \frac{1}{2!}\int_{p_t^c} G(x_1)f(b_1)\hat{\sigma}(x_1,x_1')G(x_1')f(b_1-\beta)d^2b_1dx_1dx_1' \times \\ &\qquad \times G(x_2)f(b_2)\hat{\sigma}(x_2,x_2')G(x_2')f(b_2-\beta)d^2b_2dx_2dx_2'd^2\beta \\ &= \int \frac{1}{2!}\Big(\int_{p_t^c} G(x)f(b)\hat{\sigma}(x,x')G(x')f(b-\beta)d^2bdxdx'\Big)^2 d^2\beta \end{aligned} \quad (2)$$

which may be readily generalized to the case of the inclusive cross section for N-parton scatterings σ_N:

$$\sigma_N = \int \frac{1}{N!}\Big(\int_{p_t^c} G(x)f(b)\hat{\sigma}(x,x')G(x')f(b-\beta)d^2b dx dx' \Big)^N d^2\beta \tag{3}$$

The cross sections are divergent for $p_t^c \to 0$. The unitarity problem is solved by normalizing the integrand which, being dimensionless, may be understood as the probability to have a Nth parton collision process in a inelastic event:

$$\int_{p_t^c} G(x)f(b)\hat{\sigma}(x,x')G(x')f(b-\beta)d^2b dx dx' \equiv \sigma_S F(\beta), \qquad \frac{(\sigma_S F(\beta))^N}{N!} e^{-\sigma_S F(\beta)} \equiv P_N(\beta) \tag{4}$$

here $P_N(\beta)$ the probability of having N parton collisions in a hadronic interaction at impact parameter β. By summing all probabilities one obtains the hard cross section σ_{hard}, namely the contribution to the inelastic cross section due to all events with *at least* one parton collision with momentum transfer greater than the cutoff p_t^c:

$$\sigma_{hard} = \sum_{N=1}^{\infty} \int P_N(\beta) d^2\beta = \sum_{N=1}^{\infty} \int d^2\beta \frac{(\sigma_S F(\beta))^N}{N!} e^{-\sigma_S F(\beta)} = \int d^2\beta \Big[1 - e^{-\sigma_S F(\beta)}\Big] \tag{5}$$

Notice that σ_{hard} is finite in the infrared limit, which allows to express the inelastic cross section as $\sigma_{inel} = \sigma_{soft} + \sigma_{hard}$ with σ_{soft} the soft contribution, the two terms σ_{soft} and σ_{hard} being defined through the cutoff in the momentum exchanged at parton level, p_t^c.

An important property is that the single parton scattering inclusive cross section is related to the average number of parton collisions. One has:

$$\langle N \rangle \sigma_{hard} = \int d^2\beta \sum_{N=1}^{\infty} N P_N(\beta) = \int d^2\beta \sum_{N=1}^{\infty} \frac{N[\sigma_S F(\beta)]^N}{N!} e^{-\sigma_S F(\beta)} = \int d^2\beta \sigma_S F(\beta) = \sigma_S \tag{6}$$

and more in general one may write:

$$\begin{aligned} \frac{\langle N(N-1)\dots(N-K+1)\rangle}{K!}\sigma_{hard} &= \int d^2\beta \sum_{N=1}^{\infty} \frac{N(N-1)\dots(N-K+1)}{K!} P_N(\beta) \\ &= \int d^2\beta \frac{1}{K!}[\sigma_S F(\beta)]^K = \sigma_K \end{aligned} \tag{7}$$

One should stress that the relations between σ_S and $\langle N \rangle$ and between σ_K and $\langle N(N-1)\dots(N-K+1)\rangle$ do not hold only in the case of the simplest Poissonian model. It can be shown that the validity is indeed much more general [4] [5].

2 The multi-channel Poissonian model

An implicit assumption in the Poissonian model is that the hadron density is the same in each interaction. On the other hand the hadron is a dynamical system, which fluctuates in different configurations in a time of the order of the hadron scale, much longer as compared with the time of a hard interaction. Interactions may hence take place while hadrons occupy various configurations, even significantly different as compared with the average hadronic configuration. A measure of the size of the phenomenon is given by hadronic diffraction.

The multichannel eikonal model [6] allows a simple description of hadronic diffraction. In the multichannel model the hadron state ψ_h is represented as a superposition of eigenstates ϕ_i of the T-matrix, while the interaction is described by eikonalized multi-Pomeron exchanges.

$$\psi_h = \sum_i \alpha_i \phi_i \tag{8}$$

The eigenstates of the T-matrix can only be absorbed or scatter elastically and the cross sections of the physically observed states ψ_h can be expressed by the combinations of the cross sections between the eigenstates ϕ_i and ϕ_j as shown below:

$$\begin{aligned} \sigma_{tot} &= \sum_{i,j} |\alpha_i|^2 |\alpha_j|^2 \sigma_{tot}^{ij} \\ \sigma_{el} + \sigma_{sd} + \sigma_{dd} &= \sum_{i,j} |\alpha_i|^2 |\alpha_j|^2 \sigma_{el}^{ij} \\ \sigma_{in} &= \sum_{i,j} |\alpha_i|^2 |\alpha_j|^2 \sigma_{in}^{ij} \end{aligned}$$

In a single Pomeron exchange, one may distinguish between hard and soft inelastic interactions, according with the presence or absence of large p_t partons in the final state. One may thus write:

$$\sigma^{ij} = \sigma_J^{ij} + \sigma_S^{ij} \tag{9}$$

where the labels J or S correspond to the presence or absence of large p_t partons in the final state. One hence obtains the following expression of the hard cross section [7]:

$$\begin{aligned} \sigma_{hard} &= \sum_{i,j} |\alpha_i|^2 |\alpha_j|^2 \sigma_{hard}^{ij} = \sum_{i,j} |\alpha_i|^2 |\alpha_j|^2 \int d^2\beta \Big[1 - e^{-\sigma_J^{ij}(\beta)}\Big] \\ &= \sum_{i,j,N} |\alpha_i|^2 |\alpha_j|^2 \int d^2\beta \frac{(\sigma_J^{ij}(\beta))^N}{N!} e^{-\sigma_J^{ij}(\beta)} \end{aligned} \tag{10}$$

which, being a superposition of Poissonians, represents the natural generalization of the result of the simplest Poissonian model.

The easiest implementation of the multi-channel eikonal model is in the case of two eigenstates:

$$\psi_h = \frac{1}{\sqrt{2}}\phi_1 + \frac{1}{\sqrt{2}}\phi_2 \tag{11}$$

One obtains:

$$\sigma_{hard} = \frac{1}{4}\sigma^{11}_{hard} + \frac{1}{2}\sigma^{12}_{hard} + \frac{1}{4}\sigma^{22}_{hard} \tag{12}$$

while the N-parton scattering inclusive cross section σ_N is given by:

$$\sigma_N = \frac{\sigma_S^N}{N!}\left\{\frac{1}{4}\int [F_{11}(\beta)]^N d^2\beta + \frac{1}{2}\int [F_{12}(\beta)]^N d^2\beta + \frac{1}{4}\int [F_{22}(\beta)]^N d^2\beta\right\} \tag{13}$$

where F_{ij} are the superpositions of the parton densities of the different eigenstates ϕ_i and ϕ_j. The case of gaussian parton densities is particularly simple. One has

$$F_{ij}(\beta) = \frac{1}{\pi(R_i^2 + R_j^2)} \times \exp\Big(\frac{-\beta^2}{R_i^2 + R_j^2}\Big) \tag{14}$$

One may take for the radii of the two parton densities $R_1^2 = R^2/2$ and $R_2^2 = 3R^2/2$, in such a way that R^2 is the average hadron size. With this choice the variance of the distribution is $\omega_\sigma = 1/4$, in agreement with the analysis of [8]. The explicit expression of the inclusive cross section σ_N is:

$$\sigma_N = \frac{\sigma_S^N}{NN!(\pi R^2)^{N-1}}\left\{\frac{1}{4}\left(\frac{1}{\frac{1}{2}+\frac{1}{2}}\right)^{N-1} + \frac{1}{2}\left(\frac{1}{\frac{1}{2}+\frac{3}{2}}\right)^{N-1} + \frac{1}{4}\left(\frac{1}{\frac{3}{2}+\frac{3}{2}}\right)^{N-1}\right\} \tag{15}$$

In the figure the relative weights of the overlaps between the various configurations are shown for different inclusive cross sections σ_N. In the case of a single collision all four different configurations contribute with the same weight. When N grows the contribution of the overlap between the most compact and dense configurations becomes increasingly important and, for N=5, it acconts for almost 90% of the cross section.

Notice that the result obtained in the multi-channel eikonal model *is very different* with respect to the result obtained when terms with various transverse sizes are introduced directlly in the hadronic parton density of the simplest Poissonian model. In PYTHIA [2] [9] the hadron density is represented by the sum of two gaussians with same weight and different size. The overlap function is hence given by

$$\frac{1}{4}F_{11}(\beta) + \frac{1}{2}F_{12}(\beta) + \frac{1}{4}F_{22}(\beta) \tag{16}$$

where F_{ij} are given by Eq.14, with R_1 and R_2 the radii of the two gaussians used to construct the actual hadronic parton density. The resulting expression of the inclusive cross sections is

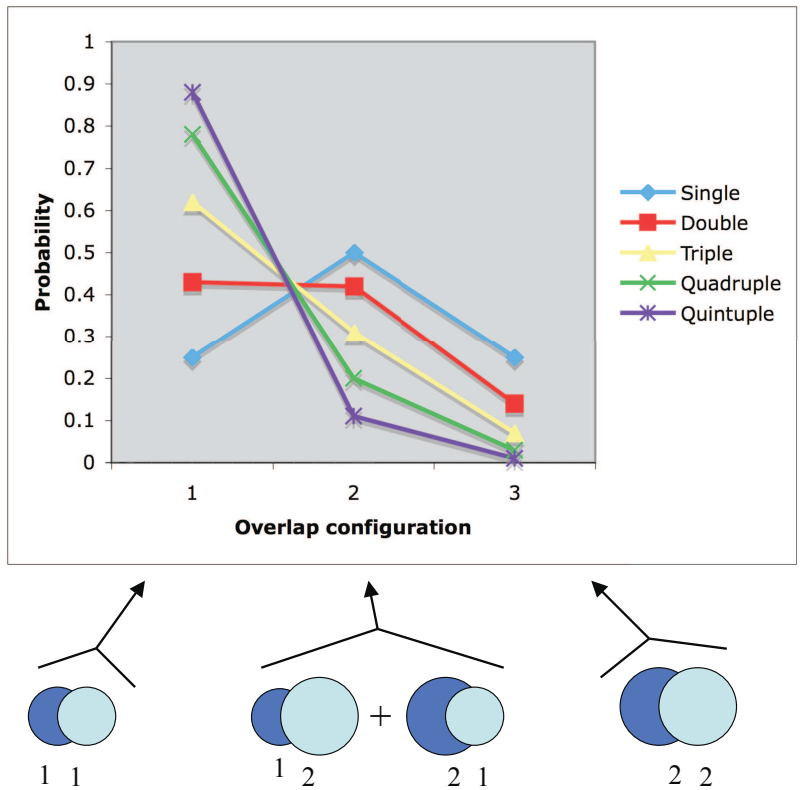

Fig. 1: Relative contributions to the inclusive cross section σ_N of the overlaps between the different hadronic configurations for $1 \leq N \leq 5$

$$\sigma_N = \frac{\sigma_S^N}{N!} \int \left[\frac{1}{4}F_{11}(\beta) + \frac{1}{2}F_{12}(\beta) + \frac{1}{4}F_{22}(\beta)\right]^N d^2\beta \tag{17}$$

which should be compared with the inclusive cross section derived in the two-states eikonal model (expression in Eq.13).

3 Concluding remarks

In the present note it has been shown how the importance of small size hadronic configurations is emphasized by geometry in the multi-parton inclusive cross sections σ_N at large N. Here one has assumed that the transverse fluctuations of the hadron do not affect its parton content. In the two-states-model of hadronic diffraction one needs however to enhance the strength of the

Pomeron coupling between diffractive eigenstates with small radii, in order to fit the available data on elastic, inelastic, single and double diffractive cross sections [10], which corresponds to an increase of the parton content when the hadron occupies a configuration with small transverse size. In the analysis [8] hadronic diffraction is on the contrary fitted in a model where the number of partons decreases when the hadron occupies small size configurations. While in the former case the enhanced role of small transverse size configurations in multiparton collisions is amplified [7], in the latter it is on the contrary reduced [11].

The study of hadronic diffraction and of multiparton scatterings at the LHC may hence provide non trivial informations on the correlation between the parton content of the hadron and its transverse size. In addition to the measurements of hadronic diffraction and of multi-jets cross sections in hadron-hadron collisions, an important handle, to gain a better insight into this aspect of the hadron structure, may be represented by the measurement of multi-jets cross sections in hadron-nucleus collisions, where a model independent separation of the longitudinal and transverse parton correlations is, in principle, possible [12].

References

[1] Capella, A. and Tran Thanh Van, J. and Kwiecinski, J., Phys. Rev. Lett. **58**, 2015 (1987).

[2] Sjostrand, T. and van Zijl, M., Phys. Rev. **D36**, 2019 (1987).

[3] Ametller, L. and Treleani, D., Int. J. Mod. Phys. **A3**, 521 (1988).

[4] Calucci, G. and Treleani, D., Int. J. Mod. Phys. **A6**, 4375 (1991).

[5] Calucci, G. and Treleani, D., Phys. Rev. **D57**, 503 (1998).

[6] Gotsman, E. and Levin, E. and Maor, U., Phys. Lett. **B452**, 387 (1999).

[7] Treleani, Daniele, Phys. Rev. **D76**, 076006 (2007).

[8] Blaettel, B. and Baym, G. and Frankfurt, L. L. and Heiselberg, H. and Strikman, M., Phys. Rev. **D47**, 2761 (1993).

[9] Sjostrand, T. and Mrenna, S. and Skands, P., JHEP **05**, 026 (2006).

[10] Gotsman, E. and Levin, E. and Maor, U. (2007).

[11] Frankfurt, L. and Strikman, M. and Treleani, D. and Weiss, C. (2008).

[12] Strikman, M. and Treleani, D., Phys. Rev. Lett. **88**, 031801 (2002).

CERN-PH-TH-2008-195
KA-TP-22-2008
MCnet/08/11

Underlying events in Herwig++*

Manuel Bähr[1]*, Stefan Gieseke*[1] *and Michael H. Seymour*[2]
[1] Institut für Theoretische Physik, Universität Karlsruhe,
[2] Physics Department, CERN, and
School of Physics and Astronomy, University of Manchester.

Abstract
In this contribution we describe the new model of multiple partonic interactions (MPI) that has been implemented in Herwig++. Tuning its two free parameters is enough to find a good description of CDF underlying event data. We show extrapolations to the LHC and compare them to results from other models.

1 Introduction

With the advent of the Large Hadron Collider (LHC) in the near future it will become increasingly important to gain a detailed understanding of all sources of hadronic activity in a high energy scattering event. An important source of additional soft jets will be the presence of the underlying event. From the experimental point of view, the underlying event contains all activity in a hadronic collision that is not related to the signal particles from the hard process, e.g. leptons or missing transverse energy. The additional particles may result from the initial state radiation of additional gluons or from additional hard (or soft) scatters that occur during the same hadron–hadron collision. Jet measurements are particularly sensitive to the underlying event because, although a jet's energy is dominated by the primary hard parton that initiated it, jet algorithms inevitably gather together all other energy deposits in its vicinity, giving an important correction to its energy and internal structure.

In this note, based on Ref. [1], we want to focus on the description of the hard component of the underlying event, which stems from additional hard scatters within the same proton. Not only does this model give us a simple unitarization of the hard cross section, it also allows to give a good description of the additional substructure of the underlying events. It turns out that most activity in the underlying event can be understood in terms of hard minijets. We therefore adopt this model, based on the model JIMMY [2], for our new event generator Herwig++ [3].

An extension to this model along the lines of [4], which also includes soft scatters is underway and will most probably be available for the next release of Herwig++. Covering the entire p_t range will also allow us to describe minimum bias interactions. We have examined the parameter space of such models at Tevatron and LHC energies in Ref. [5]. Existing measurements and the possible range of LHC measurements are used there to identify the maximally allowed parameter space.

*to appear in the proceedings of the HERA and the LHC workshop.

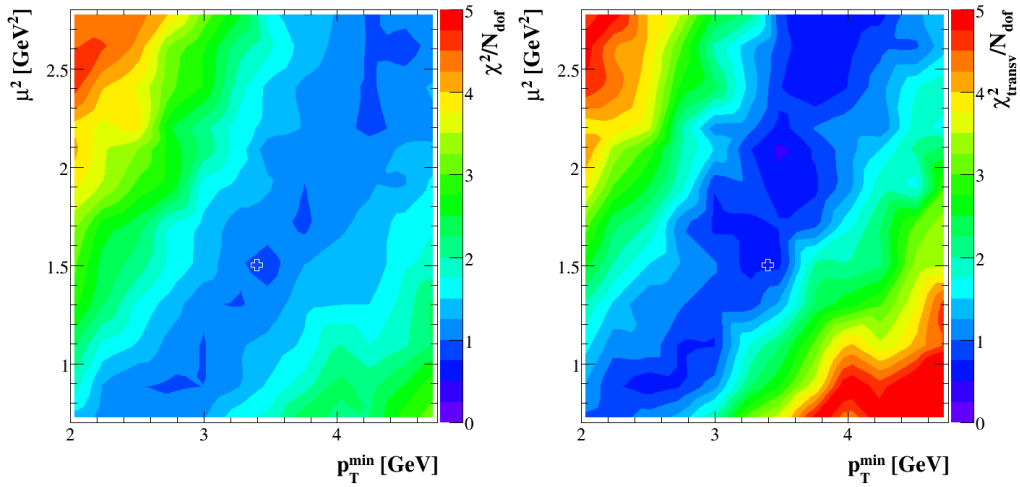

Fig. 1: Contour plots for the χ^2 per degree of freedom of all discussed observables (left) and only the ones from the transverse region (right). The cross indicates the location of our preferred tune.

2 Tevatron results

We have performed a tune of the model by calculating the total χ^2 against the jet data ($p_t^{\text{ljet}} > 20\,\text{GeV}$) from Ref. [6]. For this analysis each event is partitioned into three parts, the **towards, away** and **transverse** regions. These regions are equal in size in $\eta - \phi$ space and classify where particles are located in this space with respect to the hardest jet in the event. We compare our predictions to data for the average number of charged particles and for the scalar p_t sum in each of these regions.

The parameter space for this tune is two dimensional and consists of the p_t cutoff $p_t^{\min}$ and the inverse hadron radius squared, μ^2. In Fig. 2 we show the χ^2 contour for describing all six observables and especially those from the transverse region, which is particularly sensitive to the underlying event. For these, and all subsequent plots, we have used Herwig++ version 2.2.1 and the built-in MRST 2001 LO [7] PDFs. All parameters, apart from the ones we were tuning, were left at their default values.

The description of the Tevatron data is truly satisfactory for the entire range of considered values of $p_t^{\min}$. For each point on the x-axis we can find a point on the y-axis to give a reasonable fit. Nevertheless an optimum can be found between $3 \ldots 4$ GeV. The strong and constant correlation between $p_t^{\min}$ and μ^2 is due to the fact that a smaller hadron radius will always balance against a larger p_t cutoff as far as the underlying event activity is concerned. As a default tune we use $p_t^{\min} = 3.4\,\text{GeV}$ and $\mu^2 = 1.5\,\text{GeV}^2$, which results in an overall χ^2/N_{dof} of 1.3.

3 LHC extrapolation

We start the discussion of our predictions for the LHC with the plot in Fig. 2. The plot shows the mean charged multiplicity as a function of pseudorapidity, η. We show Herwig++ with and without MPI. We used QCD jet production with a minimal p_T of 20 GeV as signal process. The

MPI parameters were left at their default values, i.e. the fit to Tevatron CDF data. The effect of MPI is clearly visible, growing significantly from the Tevatron to the LHC.

For calculating the LHC extrapolations we left the MPI parameters at their default values, i.e. the fit to Tevatron CDF data. In Ref. [8] a comparison of different predictions for an analysis modelled on the CDF one discussed earlier was presented. As a benchmark observable the charged particle multiplicity in the transverse region was used. We show this comparison in Fig. 3 together with our simulation. All expectations reached a plateau in this observable for $p_t^{\mathrm{ljet}} > 10$ GeV. Our prediction for this observable also reached a roughly constant plateau within this region. The height of this plateau can be used for comparison. In Ref. [8] PYTHIA 6.214 [9] ATLAS tune reached a height of ~ 6.5, PYTHIA 6.214 CDF Tune A of ~ 5 and PHOJET 1.12 [10] of ~ 3. Our model reaches a height of ~ 5 and seems to be close to the PYTHIA 6.214 CDF tune, although our model parameters were kept constant at their values extracted from the fit to Tevatron data.

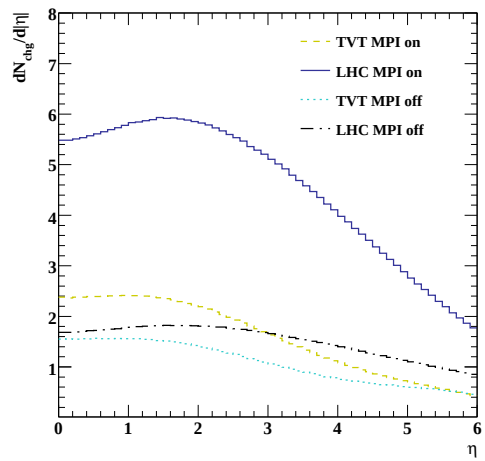

Fig. 2: Differential multiplicity distribution with respect to $|\eta|$. The different data sets are: Tevatron with MPI off, LHC with MPI off, Tevatron with MPI on and LHC with MPI on.

We have seen already in the previous section that our fit results in a flat valley of parameter points, which all give a very good description of the data. We will briefly estimate the spread of our LHC expectations, using only parameter sets from this valley. The range of predictions that we deduce will be the range that can be expected assuming no energy dependence on our main parameters. Therefore, early measurements could shed light on the potential energy dependence of the input parameters by simply comparing first data to these predictions. We extracted the average value of the two transverse observables for a given parameter set in the region $20\,\mathrm{GeV} < p_t^{\mathrm{ljet}} < 30\,\mathrm{GeV}$. We did that for the best fit points at three different values for p_t^{min}, namely 2 GeV, 3.4 GeV and 4.5 GeV, and found an uncertainty of about 7 % for the multiplicity and 10 % for the sum of the transverse momentum.

LHC predictions	$\langle N_{\mathrm{chg}}\rangle^{\mathrm{transv}}$	$\langle p_t^{\mathrm{sum}}\rangle^{\mathrm{transv}}[\,\mathrm{GeV}]$
TVT best fit	5.1 ± 0.3	5.0 ± 0.5

Table 1: LHC expectations for $\langle N_{\mathrm{chg}}\rangle$ and $\langle p_t^{\mathrm{sum}}\rangle$ in the transverse region. The uncertainties are obtained from varying p_t^{min} within the range we considered. For μ^2 we have taken the corresponding best fit (Tevatron) values.

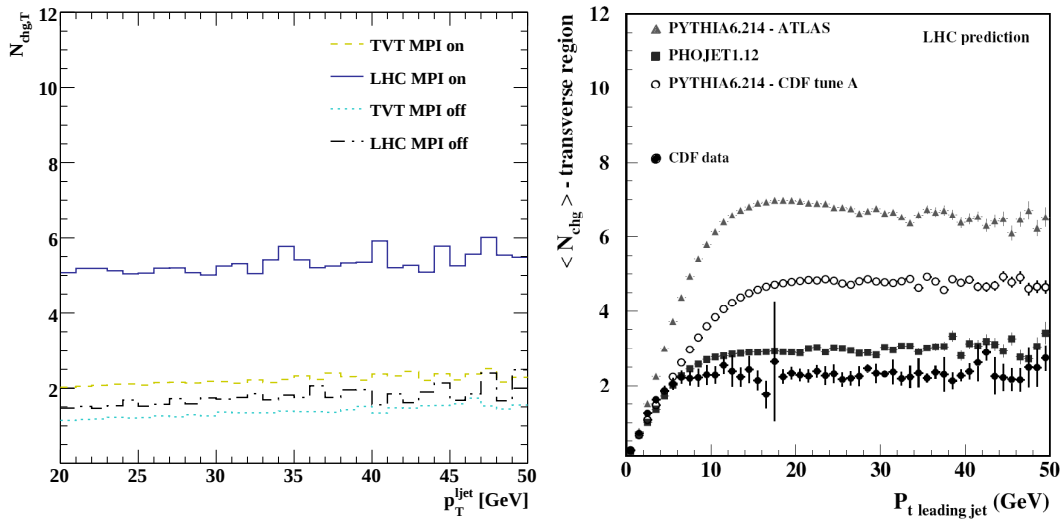

Fig. 3: Multiplicity in the transverse region for LHC runs with Herwig++ (left) and the same observable for several other generators (right), taken from Ref. [8]. The different data sets for the left plot are (from bottom to top): Tevatron with MPI off, LHC with MPI off, Tevatron with MPI on and LHC with MPI on.

Acknowledgements

We would like to thank our collaborators on the Herwig++ project for many useful discussions. We wish to thank the organisers of the workshop for a very pleasant atmosphere. This work was supported in part by the European Union Marie Curie Research Training Network MCnet under contract MRTN-CT-2006-035606 and the Helmholtz–Alliance “Physics at the Terascale”. MB was supported by the Landesgraduiertenförderung Baden-Württemberg.

References

[1] M. Bähr, S. Gieseke, and M. H. Seymour, *Simulation of multiple partonic interactions in Herwig++*, *JHEP* **07** (2008) 076, [arXiv:0803.3633].

[2] J. M. Butterworth, J. R. Forshaw, and M. H. Seymour, *Multi-Parton Interactions in Photoproduction at HERA*, *Z. Phys.* **C72** (1996) 637–646, [hep-ph/9601371].

[3] M. Bähr *et. al.*, *Herwig++ Physics and Manual*, arXiv:0803.0883.

[4] I. Borozan and M. H. Seymour, *An eikonal model for multiparticle production in hadron hadron interactions*, *JHEP* **09** (2002) 015, [hep-ph/0207283].

[5] M. Bähr, J. M. Butterworth, and M. H. Seymour, *The Underlying Event and the Total Cross Section from Tevatron to the LHC*, arXiv:0806.2949.

[6] **CDF** Collaboration, A. A. Affolder *et. al.*, *Charged jet evolution and the underlying event in $p\bar{p}$ collisions at 1.8 TeV*, *Phys. Rev.* **D65** (2002) 092002.

[7] A. D. Martin, R. G. Roberts, W. J. Stirling, and R. S. Thorne, *MRST2001: Partons and alpha(s) from precise deep inelastic scattering and Tevatron jet data*, *Eur. Phys. J.* **C23** (2002) 73–87, [hep-ph/0110215].

[8] S. Alekhin *et. al.*, *HERA and the LHC - A workshop on the implications of HERA for LHC physics: Proceedings Part A*, hep-ph/0601012.

[9] T. Sjöstrand, L. Lönnblad, and S. Mrenna, *PYTHIA 6.2: Physics and manual*, hep-ph/0108264.

[10] R. Engel, *Photoproduction within the two component dual parton model. 1. Amplitudes and cross-sections*, *Z. Phys.* **C66** (1995) 203–214.

Multiple Interactions at HERA

H. Jung[a], *Ll. Marti*[a], *T. Namsoo*[a], *S. Osman*[b]

[a] DESY, Hamburg, Germany
[b] Physics Department, University of Lund, Lund, Sweden

Abstract

The study of Multiple Parton Interactions (MPI) has been an important subject at hadron colliders. In lepton-hadron collisions at HERA, the photon can interact as a point-like particle or as a composite hadron-like system. Event samples with an enriched direct- or resolved-photon component can be selected by choosing events with high or low x_γ or Q^2 values. This was done in the three measurements presented here, which were conducted at HERA by the H1 and ZEUS collaborations. Two measurements in photoproduction are presented. The first looks at three- and four-jet events and the second, at the charged particle multiplicity in dijet events. Also presented is a measurement of the multiplicity of low p_T jets in inclusive one-jet deep inelastic scattering events. In all three analyses possible effects of MPI were found.

1 Introduction

In ep collisions at HERA the mediator boson was a virtual photon[1] which can be characterized by two variables namely, the photon virtuality, Q^2, and the inelasticity, y. The life-time of an $e\gamma$-state is of the order $\sim 1/Q^2$. Within this life-time the photon can develop $q\bar{q}$-fluctuations. The life-time of these fluctuations are constant as a function of the characteristic p_T of the interacting partons and are of the order $\sim 1/p_T^2$. Therefore, these fluctuations are important only if $Q^2 \ll p_T^2$. In this case, the photon can fluctuate into a $q\bar{q}$ pair or even more complicated states and these events have similar characteristics to hadron-hadron collisions.

QCD Monte Carlo programs (MC) simulate ep collisions at leading order in α_s, $\mathcal{O}(\alpha\alpha_s)$, with a 2-to-2 parton scattering. The events are simulated with initial as well as final parton state radiation and the contributions from the break up of the proton. Finally, hadronisation models are applied so that colourless particles are produced. In this picture, the primary two hard partons lead to two jets. The underlying event is defined as everything except the lowest order process. Ideally, the lowest order process is not affected by the underlying event but experimentally contributions from the underlying event are present in these jets and cannot be disentangled. The underlying event is therefore the initial and final state radiation and the remnant-remnant interactions as well as re-scatters off the remnants. These two last contributions are referred to as multiple parton interactions (MPI). In perturvative Quantum Chromodynamics (pQCD), the AGK cutting rules [1–3] can be used to relate the different contributions to ep scattering, diffraction and single or multiple scattering, via multiple exchange of BFKL Pomerons.

[1] For the photon virtuality range considered in these analyses.

Remnant-remnant interactions can only be present if the interacting particles have a composite structure via multi-parton exchange. In lepton-proton collisions this is only possible if the photon is resolved. The fraction of the photon energy entering in the hard scattering x_γ may be used to select enriched samples by resolved or point-like (direct) photons. Thus, at LO parton level, $x_\gamma = 1$ for direct processes whereas in the resolved case, $x_\gamma < 1$. Experimentally, the variable x_γ^{obs} is used. It is defined in terms of the two hardest jets, Jet_1 and Jet_2, and the hadronic final state (HFS) as:

$$x_\gamma^{obs} = \frac{\sum_{h \in Jet_1}(E - P_z) + \sum_{h \in Jet_2}(E - P_z)}{\sum_h (E - P_z)}, \tag{1}$$

where the sums in the nominator run over the hadrons in Jet_1 and Jet_2, while the sum in the denominator runs over all hadrons in the entire HFS.

In the past, the underlying event was studied at HERA in the photoproduction regime [4,5] but not in deep inelastic scattering (DIS). The next sections are organized as follows. Firstly, a three- and four-jet cross section measurement in photoproduction is presented. Then two different analyses with similar strategies are shown, in which four regions in the azimuthal angle ϕ are defined with respect to the leading jet, i.e. that with the highest E_T in the event. The first of these analyses is a charged particle multiplicity measurement in dijet photoproduction. The second is a mini-jet multiplicity measurement in DIS, where a mini-jet refers to a jet with low transverse momentum.

2 Three- and four-jet events in photoproduction

The leading order for an n-jet event, via a single chain exchange, is $\mathcal{O}(\alpha\alpha_s^{n-1})$. However, n-jet events can also be generated via MPI, where several chains are present. Moreover, even soft MPI may affect the distribution of multi-jet events by adding or redistributing the energy flow generated by a primary process.

The ZEUS collaboration studied the multi-jet production in the photoproduction regime [6], where $Q^2 < 1$ GeV^2 and $0.2 < y < 0.85$. Three- and four-jet events, where the jets were defined with the k_T clustering algorithm [7] and require to have transverse energies $E_T^{jets} > 6$ GeV, were studied in the pseudorapidity range $|\eta^{jets}| < 2.4$. Furthermore, these events were studied in two different n-jet invariant mass regions, namely, $25 < M_{n-jets} < 50$ GeV and $M_{n-jets} > 50$ GeV, referred to as the low- and high-mass regions, respectively. The cross sections of the three- and four-jet low- and high-mass samples were measured differentially.

The data were compared to predictions from two $\mathcal{O}(\alpha\alpha_s)$ matrix element MC programs supplemented with parton showers, HERWIG 6.505 [8–10] and PYTHIA 6.206 [11], both with and without MPI. In the case of HERWIG , MPI events were simulated via an interface to JIMMY 4.0 [12], which is an impact parameter dependent model. For PYTHIA , MPI were generated using the so-called "simple model" [13].

In addition, the three-jet sample was compared to the fixed order ($\mathcal{O}(\alpha\alpha_s^2)$) calculation by Klasen, Kleinwort und Kramer [14]. This calculation corresponds to the three-jet LO and, at the time, was the highest order prediction available in photoproduction. Thus, no calculation was available for the four-jet sample.

The three- and four-jet cross sections are shown as a function of M_{n-jets} in figure 1. In general, both cross sections decrease exponentially with increasing M_{n-jets}. The HERWIG and PYTHIA predictions with and without MPI are also shown. They are normalized to the high invariant n-jets mass region ($M_{n-jets} > 50$ GeV), i.e. they are scaled to describe the high M_{n-jets} cross section. Both HERWIG and PYTHIA without MPI fail to describe the cross section dependence. When MPI are included, however, they are in quite good agreement with data. The discrepancy is larger in the four-jet case. The PYTHIA model was run using its default setting whereas the JIMMY model was tuned to the presented data [6].

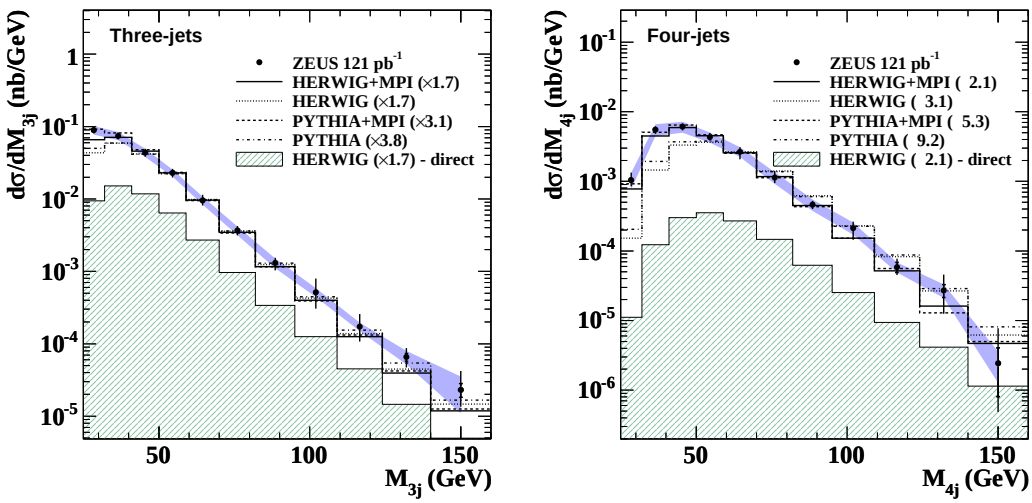

Fig. 1: Measured cross section as a function of (a) M_{3-jets} and (b) M_{4-jets} (solid circles). The inner and outer error bars and the shaded band represent the statistical, the statistical and the systematic added in quadrature and the calorimeter energy scale uncertainties, respectively.

Shown in Fig. 2a) is the measured three-jet cross section as a function of M_{3-jets}, compared to the fixed LO calculation for this process, $\mathcal{O}(\alpha\alpha_s^2)$. This calculation was corrected for hadronisation effects and MPI. The hadronisation and MPI corrections and their estimated uncertainties are shown in 2b). The hadronisation corrections are constant in M_{3-jets}, while MPI corrections increase towards low M_{3-jets}. The theoretical uncertainties on both the MPI corrections and the pQCD predictions are large. The magnitude and the shape of the calculation is consistent with the data within the large theoretical uncertainties. This is best seen in Fig. 2c) where the ratio data over theory is shown. Without the large MPI corrections the theoretical description would be far much worse at low M_{3-jets}.

3 Charged particle multiplicity in photoproduction

As described above, in quasi-real photoproduction ($Q^2 \sim 0$) the photon can develop a hadronic structure, where remnant-remnant interactions may be present and therefore the particle production can be enhanced. However, the actual particle multiplicity depends not only on the number of multiple parton scatterings but also on the hadronisation and on the colour connections between

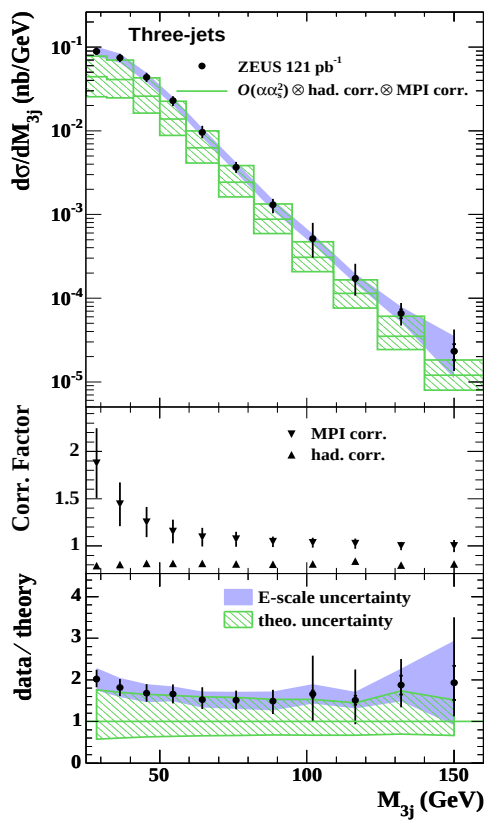

Fig. 2: (a) Measured three-jets cross section as a function of M_{3-jets} compared with an $\mathcal{O}(\alpha\alpha_s^2)$ prediction, corrected for hadronisation and MPI effects. (b) The hadronisation and MPI correction factors as a function of M_{3-jets}. (c) The ratio of the M_{3-jets} cross section divided by the theoretical prediction. The theoretical uncertainty is represented by shaded bands.

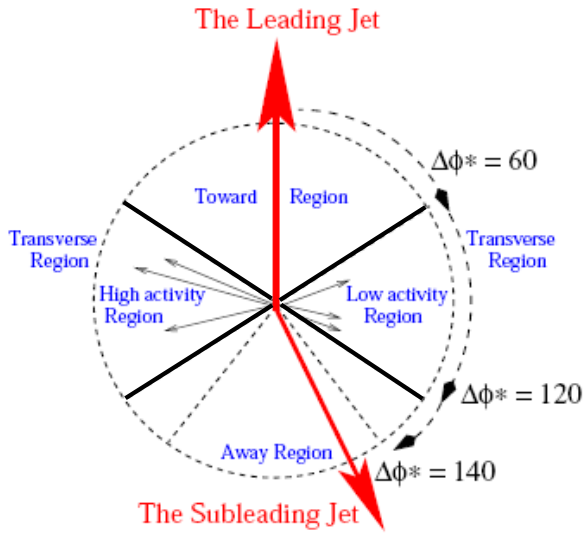

Fig. 3: Definition of the four azimuthal regions. The toward region is defined by the leading jet and by this means defines the away and transverse regions. The scalar sum of the transverse momenta $P_t^{sum} = \sum_i^{tracks/HFS} P_T^i$ calculated in each transverse region defines the high and low activity region eventwise in the charged particle multiplicity and mini-jet analyses, respectively.

the multiple parton scatterings and the remnants. Within the model used [15], different colour connection scenarios are possible. Two scenarios are studied. In the first scenario, each hard scattering is independent of the other and therefore is connected only to the remnants, which gives long colour strings. In the second scenario, the colour strings are rearranged in order to provide shorter strings, i.e. the hard scatterings are colour connected with each other, which compared with the first scenario produces fewer particles.

This was studied in the H1 collaboration by using a dijet photoproduction sample, where $Q^2 < 0.01$ GeV^2 and $0.3 < y < 0.65$, looking at charged particles with transverse energies $P_T^{track} > 150$ MeV in the pseudorapidity range $|\eta^{track}| < 1.5$. The jets were defined using the k_T clustering algorithm [7] and were required to have transverse momentum $P_T^{jets} > 5$ GeV and $|\eta^{jets}| < 1.5$.

Four regions in the azimuthal angle, ϕ, were then defined with respect to the leading jet as indicated in Fig. 3 in analogy to the CDF collaboration [16]. The leading jet (Jet_1) defines the toward region, whereas the subleading jet, the jet with the next highest P_T^{jet}, is usually in the away region, although not necessarily. The transverse regions are less effected by the hard interaction and thus, expected to be more sensitive to the MPI. For each event, the hemisphere which has the highest scalar sum of the transverse momenta, $P_t^{sum} = \sum_i^{tracks} P_T^i$, is refered to as the high-transverse-activity hemisphere. The other is referred to as the low-transverse-activity hemisphere.

The average track multiplicity, $\langle N_{charged} \rangle$, is shown in figures 4 and 5 as a function of $P_T^{Jet_1}$ for resolved photon enriched events, $x_\gamma^{obs} < 0.7$ (left) and direct photon enriched events, $x_\gamma^{obs} > 0.7$ (right). In the toward and away regions, the average track multiplicity increases with

$P_T^{Jet_1}$ as shown in figure 4. In the $x_\gamma^{obs} > 0.7$ region (right) the measurements are reasonably well described by the simulation containing only one hard interaction with parton showers and hadronisation, whereas in the region $x_\gamma^{obs} < 0.7$ (left) this is clearly not enough, especially at the lower values of $P_T^{Jet_1}$. MPI contributes as a pedestal and brings the prediction to a good agreement with the measurement.

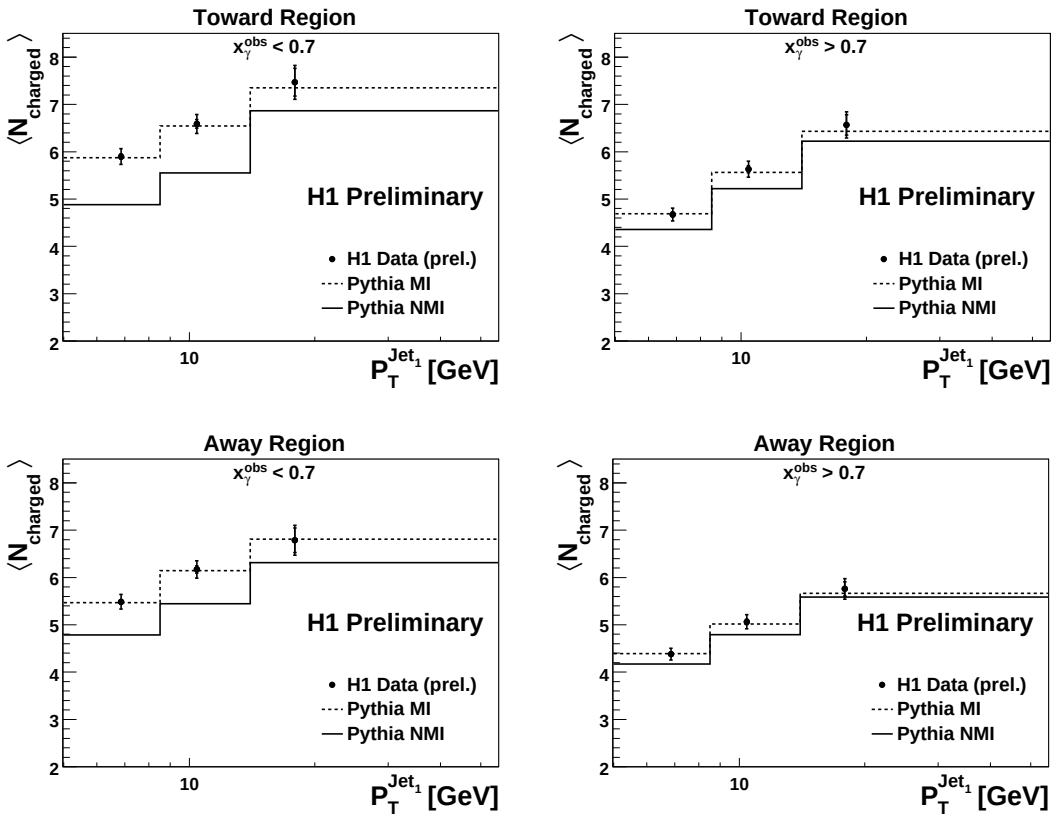

Fig. 4: Charged particle multiplicity for $x_\gamma^{obs} < 0.7$ (left) and for $x_\gamma^{obs} > 0.7$ (right). The leading jet (Jet_1) is contained in the toward region, whereas the subleading jet, the second jet with highest P_T^{jet}, is usually in the away region, although not necessarily. Data is compared to PYTHIA with and without MPI.

In the transverse regions, shown in figure 5, the measured average track multiplicity decreases with $P_T^{Jet_1}$. At high x_γ^{obs} (right) the predicted average charged particle multiplicity with and without MPI also decreases with $P_T^{Jet_1}$, although only PYTHIA with MPI describes data. At low x_γ^{obs} (left) the PYTHIA prediction without MPI tends to increase with $P_T^{Jet_1}$ while PYTHIA with MPI decreases with $P_T^{Jet_1}$ giving the best description of the data.

We studied[2] also the different colour string scenarios in Fig. 6 where the transverse regions are shown. In the present simulation the long string configuration is preferred.

[2]This is done in PYTHIA by the parameters PARP(86) = 0.66 and PARP(85) = 0.33, giving the probability that an additional interaction gives two gluons and the probability that an additional interaction gives two gluons with colour

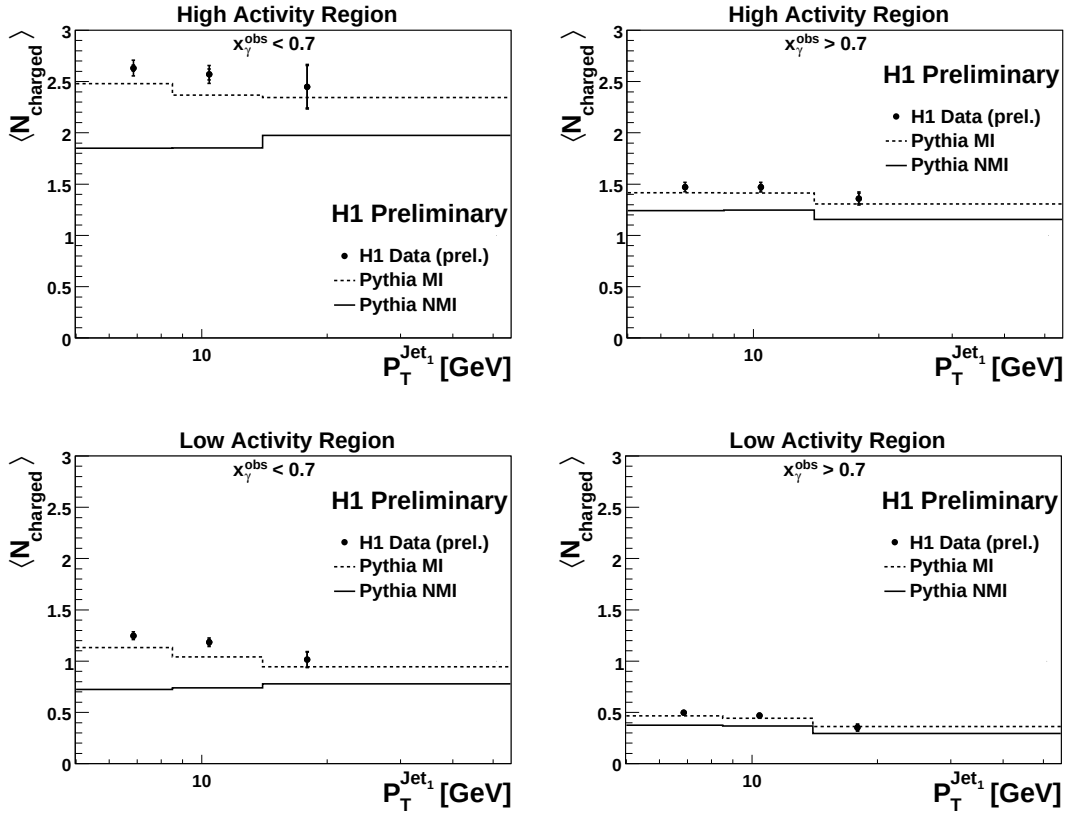

Fig. 5: Charged particle multiplicity for $x_\gamma^{obs} < 0.7$ (left) and for $x_\gamma^{obs} > 0.7$ (right). The transverse high activity regions, upper plots, are defined as the transverse region with a higher P_t^{sum} compared to the low activity regions, down. Data is compared to PYTHIA with and without MPI.

4 Mini-jet multiplicity in DIS

The photon is more likely to develop a hadronic structure before interacting with the proton in photoproduction than in DIS. In DIS, the characteristic interaction time scales like $\sim 1/Q^2$ and at high Q^2, it is too short for the fluctuations to occur. At HERA diffraction plays an important role at low x_{Bj}, and also at high Q^2. These events can be explained by the exchange of Pomerons. The AGK cutting rules relates the different contributions from diffraction and single or multiple parton scattering. Thus, it is interesting to study if evidence for multiple parton scattering can be seen within the data.

The H1 collaboration studied events in the kinematic region $5 < Q^2 < 100$ GeV^2 and $0.1 < y < 0.7$. Events with at least one jet with $E_T^{jet} > 5$ GeV and in the laboratory pseudorapidity range $-1.7 < \eta^{jet} < 2.79$ were selected[3] using the k_T clustering algorithm [7]. The HFS was required to have an invariant mass $W > 200$ GeV.

connections to nearest neighbours, respectively.

[3]Applied both in the hadronic centre-of-mass frame (HCM) and in the laboratory frames.

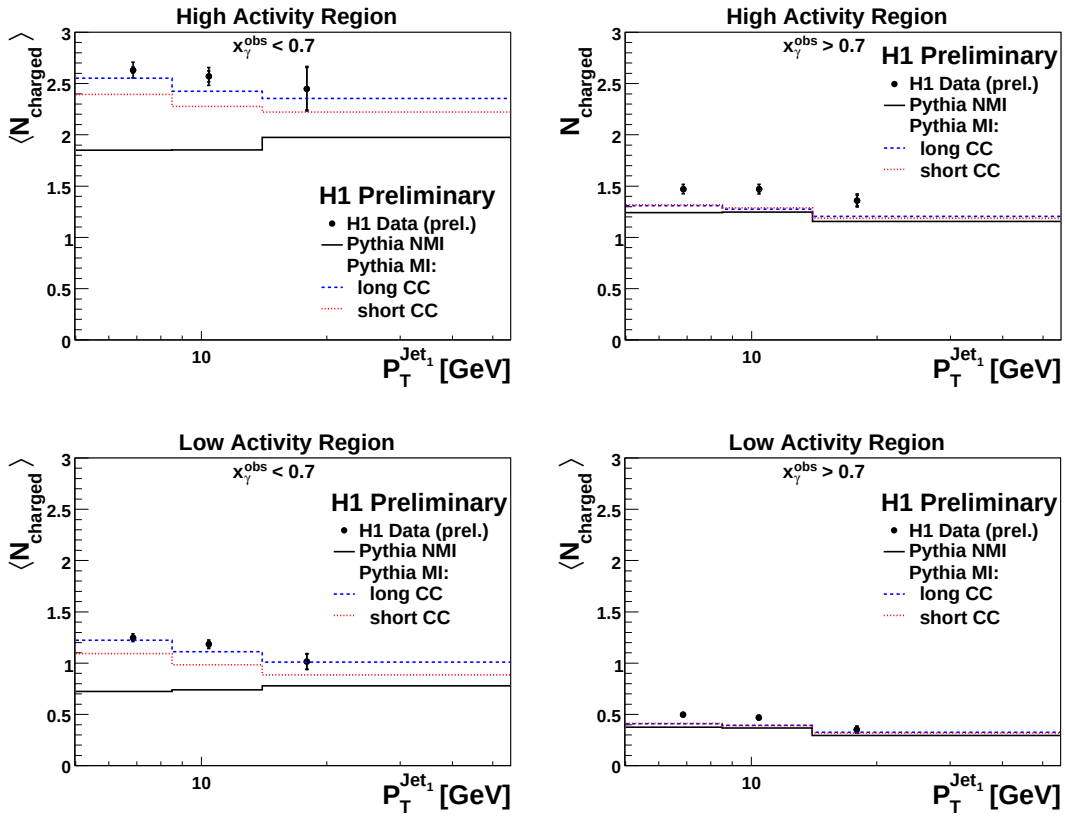

Fig. 6: Charged particle multiplicity for $x_\gamma^{obs} < 0.7$ (left), and for $x_\gamma^{obs} > 0.7$ (right). The transverse high activity regions, upper plots, are defined as the transverse region with a higher P_t^{sum} compared to the low activity regions, down. Here data is compared to PYTHIA without MPI and PYTHIA with MPI and high probability for long colour string connections, long CC, and short colour string connections, short CC.

The leading jet defines a toward, an away and two transverse regions (Fig. 3). The average multiplicity of jets with $E_T^{mini} > 3$ GeV, the so-called mini-jets, was measured, $\langle N_{minijet} \rangle$ in the range $-1.7 < \eta < 2.79$ for the four $\Delta\phi^*$ regions. A possible signature of MPI would be an increased value of $\langle N_{minijet} \rangle$, especially in the less populated high- and low-activity transverse regions and for the lower Q^2 values.

In Figure 7 the measured average mini-jet multiplicity is shown as a function of the transverse momentum of the leading jet in the hadronic centre-of-mass (HCM) frame, $P^*_{T,1j}$. The data are compared to the predictions of RAPGAP [17], ARIADNE [18] and PYTHIA . The former two do not include MPI whereas PYTHIA was run both with and without MPI.

The toward region data are reasonably well described by all four MC. While RAPGAP and PYTHIA
marginally underestimate $\langle N_{minijet} \rangle$ at low $P^*_{T,1j}$ in the lowest Q^2 bin ARIADNE slightly overestimates the data. The PYTHIA description is improved by the introduction of MPI at low Q^2.

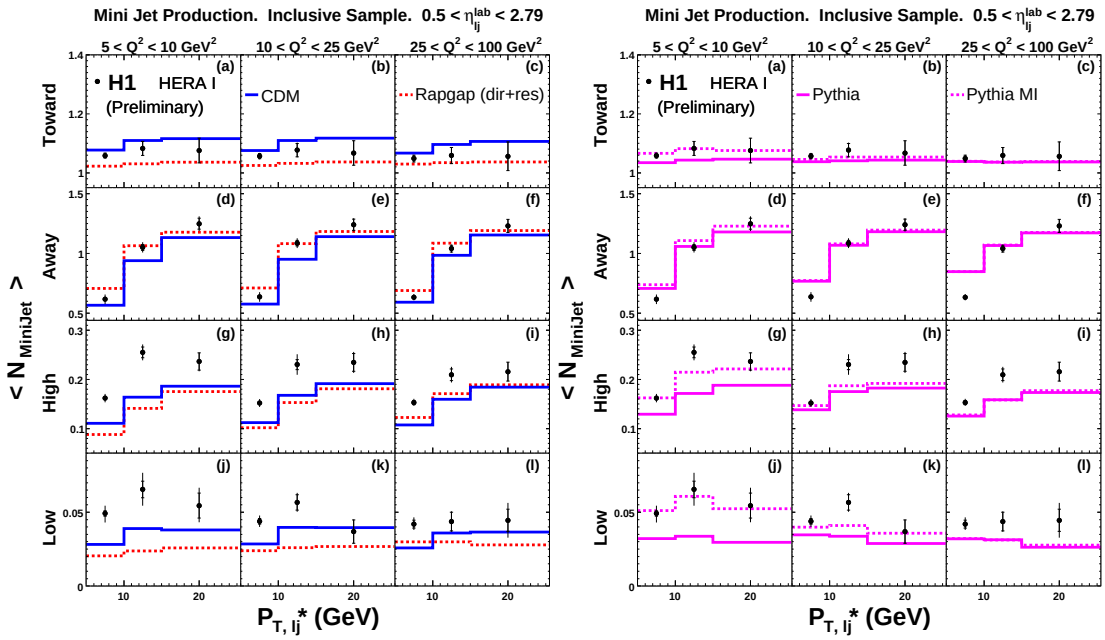

Fig. 7: The $\langle N_{minijet} \rangle$data, in all four azimuthal regions, as a function of $P^*_{T,1j}$ in three Q^2 bins. Also shown are the predictions from four MC models.

The overall description in the away region is good. The PYTHIA model predicts the away region to be the least sensitive to MPI. In the low and high activity transverse regions all the MC that do not include MPI underestimate the data in all $P^*_{T,1j}$ and Q^2 bins. This is more pronounced at low $P^*_{T,1j}$ and Q^2 values. The introduction of MPI in PYTHIA certainly aids in the description of the low Q^2 data. However, at large Q^2 the effect of MPI is very small according to the simulation and so PYTHIA underestimates the Q^2 data.

5 Conclusions

In all three analyses, both in photoproduction and in DIS, contributions from MPI are suggested. The three- and four-jet photoproduction cross sections shapes cannot be described by the $\mathcal{O}(\alpha\alpha_s)$ plus parton shower calculations. In the three-jet case the LO pQCD calculation needs to include the estimated hadronisation and MPI effects to describe data, where the latter has a large contribution towards low M_{3-jets}.

Both the charged particle and the mini-jet multiplicities are larger than predicted by MCs not including MPI. More specifically, the charged particle multiplicity as a function of $P_T^{Jet_1}$ predictions have a different shape depending on whether MPI is included or not in the transverse regions for low x_γ^{obs} values as seen by PYTHIA . The multiplicity can be only described in all regions properly when MPI are included. In the mini-jet analysis, the measured multiplicity is larger than the predictions by the parton shower and colour dipole model MCs. MPI, as predicted by PYTHIA , helps to describe the distributions at low Q^2 values but does not contribute at higher virtualities.

Higher partonic activity than predicted by standard MC is seen by all three analyses. These effects are also seen in DIS and at low and moderate Q^2 can be reasonably well described by including MPI.

References

[1] Abramovsky, V. A. and Gribov, V. N. and Kancheli, O. V., Yad. Fiz. **18**, 595 (1973).

[2] Bartels, J. and Salvadore, M. and Vacca, G. P., Eur. Phys. J. **C42**, 53 (2005).

[3] Bartels, J. Prepared for Gribov-75: Memorial Workshop on Quarks, Hadrons, and Strong Interactions, Budapest, Hungary, 22-24 May 2005.

[4] Derrick, M. and others, Phys. Lett. **B348**, 665 (1995).

[5] Aid, S. and others, Z. Phys. **C70**, 17 (1996).

[6] Namsoo, T., *Three- and Four-Jet States in Photoproduction at HERA.* Ph.D. Dissertation, Bristol University, September 2005.

[7] Catani, S. and Dokshitzer, Yuri L. and Seymour, M. H. and Webber, B. R., Nucl. Phys. **B406**, 187 (1993).

[8] Corcella, G. and others, JHEP **01**, 010 (2001).

[9] Corcella, G. and others (2002).

[10] Marchesini, G. and others, Comput. Phys. Commun. **67**, 465 (1992).

[11] Sjostrand, Torbjorn and Lonnblad, Leif and Mrenna, Stephen (2001).

[12] Butterworth, J. M. and Forshaw, Jeffrey R. and Seymour, M. H., Z. Phys. **C72**, 637 (1996).

[13] Sjostrand, Torbjorn and Mrenna, Stephen and Skands, Peter, JHEP **05**, 026 (2006).

[14] Klasen, Michael, Eur. Phys. J. **C7**, 225 (1999).

[15] Sjostrand, Torbjorn and van Zijl, Maria, Phys. Rev. **D36**, 2019 (1987).

[16] Acosta, Darin E. and others, Phys. Rev. **D65**, 072005 (2002).

[17] Jung, Hannes, Comp. Phys. Commun. **86**, 147 (1995).

[18] Lonnblad, Leif, Comput. Phys. Commun. **71**, 15 (1992).

Modeling the underlying event: generating predictions for the LHC

Arthur Moraes
University of Glasgow, UK

Abstract
This report presents tunings for PYTHIA 6.416 and JIMMY 4.3 to the underlying event. The MC generators are tuned to describe underlying event measurements made by CDF for $p\overline{p}$ collisions at $\sqrt{s}$ = 1.8 TeV. LHC predictions for the underlying event generated by the tuned models are also compared in this report.

1 Introduction

Over the last few years, the Tevatron experiments CDF and D0 have managed to reduce uncertainties in various measurements to a level in which the corrections due to the underlying event (UE) have become yet more relevant than they were in Run I analyses. Studies in preparation for LHC collisions have also shown that an accurate description of the underlying event will be of great importance for reducing the uncertainties in virtually all measurements dependent on strong interaction processes. It is therefore very important to produce models for the underlying event in hadron collisions which can accurately describe Tevatron data and are also reliable to generate predictions for the LHC.

The Mote Carlo (MC) event generators PYTHIA [1] and HERWIG [2] are largely used for the simulation of hadron interactions by both Tevatron and LHC experiments. Both generators are designed to simulate the event activity produced as part of the underlying event in proton-antiproton ($p\overline{p}$) and proton-proton (pp) events. HERWIG, however, needs to be linked to dedicated package, named "JIMMY" [3, 4], to produce the underlying event activity.

PYTHIA 6.2 has been shown to describe both minimum bias and underlying event data reasonably well when appropriately tuned [5–7]. Major changes related to the description of minimum bias interactions and the underlying event have been introduced in PYTHIA 6.4 [1]. There is a new, more sophisticated scenario for multiple interactions, new p_T-ordered initial- and final-state showers (ISR and FSR) and a new treatment of beam remnants [1].

JIMMY [4] is a library of routines which should be linked to the HERWIG MC event generator [2] and is designed to generate multiple parton scattering events in hadron-hadron events. JIMMY implements ideas of the eikonal model which are discussed in more detail in Ref. [3, 4].

In this report we present a tuning for PYTHIA 6.416 which has been obtained by comparing this model to the underlying event measurements done by CDF for $p\overline{p}$ collisions at 1.8 TeV [8, 9]. We also compare the ATLAS tune for HERWIG 6.510 with JIMMY 4.3 to these data distributions [10].

2 MC predictions vs. UE data

Based on the CDF analysis [9], the underlying event is defined as the angular region in ϕ which is transverse to the leading charged particle jet.

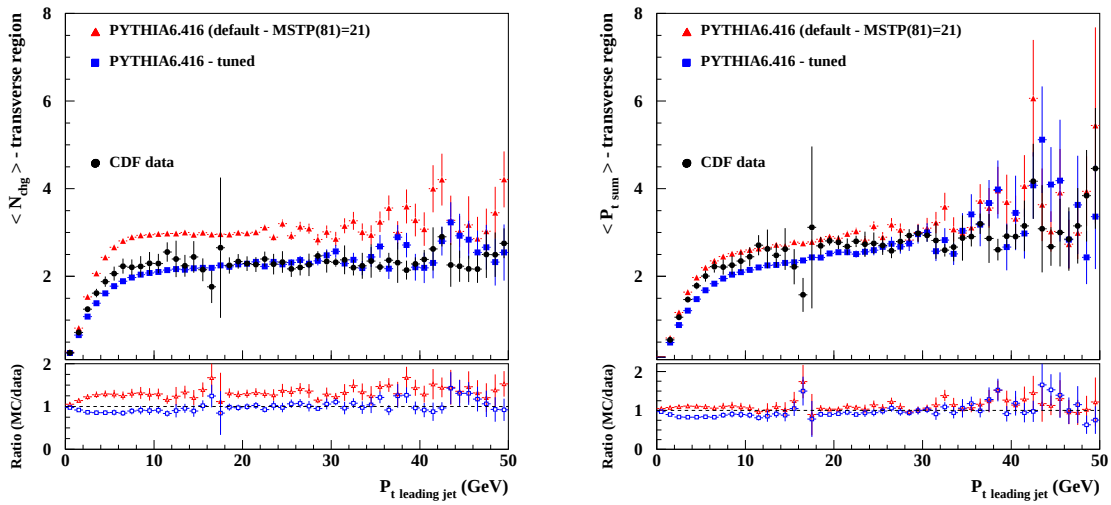

(a) (b)

Fig. 1: PYTHIA 6.416 predictions for the underlying event compared to the $< \mathrm{N}_{chg} >$ (a) and $< \mathrm{p}_T^{SUM} >$ (b).

Figure 1 shows the PYTHIA 6.416 predictions for the underlying event compared to the CDF data for the average charged particle multiplicity, $< \mathrm{N}_{chg} >$ (charged particles with $\mathrm{p}_T > 0.5$ GeV and $|\eta| < 1$) and average sum of charged particle's transverse momentum, $< \mathrm{p}_T^{sum} >$ in the underlying event [9]. Two MC generated distributions are compared to the data in these plots: one generated with all default settings in PYTHIA 6.416 except for the explicit selection of the new multiple parton interaction and new parton shower model, which is switched on by setting MSTP(81)=21 [1], and a second distribution with a tuned set of parameters. This particular PYTHIA 6.416 - tune was prepared for use in the 2008 production of simulated events for the ATLAS Collaboration. The list of tuned parameters is shown in table 1.

The guiding principles to obtain the parameters listed in Table 1 were two: firstly the new multiple parton interaction model with interleaved showering and colour reconnection scheme was to be used and, secondly, changes to ISR and FSR parameters should be avoided if at all possible.

In order to obtain a tuning which could successfully reproduce the underlying event data, we have selected a combination of parameters that induce PYTHIA to preferably chose shorter strings to be drawn between the hard and the soft systems in the hadronic interaction. We have also increased the hadronic core radius compared to the tunings used in previous PYTHIA versions, such as the ones mentioned in Ref. [6, 7]. As can be seen in fig. 1 PYTHIA 6.416 - tuned describes the data.

Default [1]	**PYTHIA 6.416 - tuned**	**Comments**
MSTP(51)=7 CTEQ5L	MSTP(51)=10042 MSTP(52)=2 CTEQ6L (from LHAPDF)	PDF set
MSTP(81)=1 (old MPI model)	MSTP(81)=21 (new MPI model)	multiple interaction model
MSTP(95)=1	MSTP(95)=2	method for colour reconnection
PARP(78)=0.025	PARP(78)=0.3	regulates the number of attempted colour reconnections
PARP(82)=2.0	PARP(82)=2.1	$p_{T_{\min}}$ parameter
PARP(83)=0.5	PARP(83)=0.8	fraction of matter in hadronic core
PARP(84)=0.4	PARP(84)=0.7	hadronic core radius

Table 1: PYTHIA 6.416 - tuned parameter list for the underlying event.

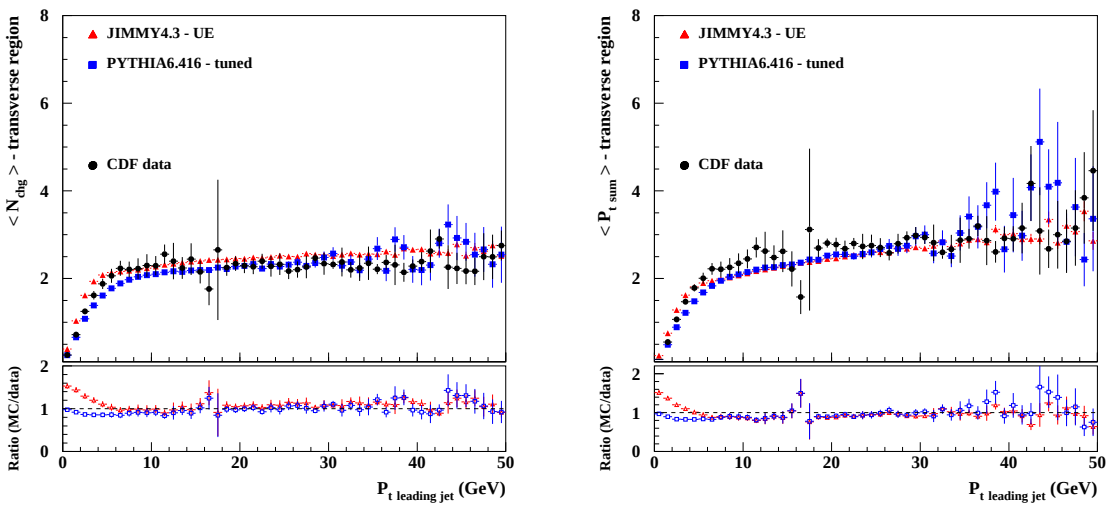

(a) (b)

Fig. 2: PYTHIA 6.416 - tuned and JIMMY 4.3 - UE predictions for the underlying event compared to the $< N_{chg} >$ (a) and $< p_T^{SUM} >$ (b).

Figure 2 shows PYTHIA 6.416 - tuned and JIMMY4.3 - UE [10] predictions for the underlying event compared to the CDF data for $< N_{chg} >$ and $< p_T^{sum} >$. Both models describe the data reasonably well. However, as shown in fig. 3, the ratio $< p_T^{sum} > / < N_{chg} >$ is better de-

scribed by PYTHIA 6.416 - tuned. This indicates that charged particles generated by JIMMY4.3 - UE are generally softer than the data and also softer than those generated by PYTHIA 6.416 - tuned.

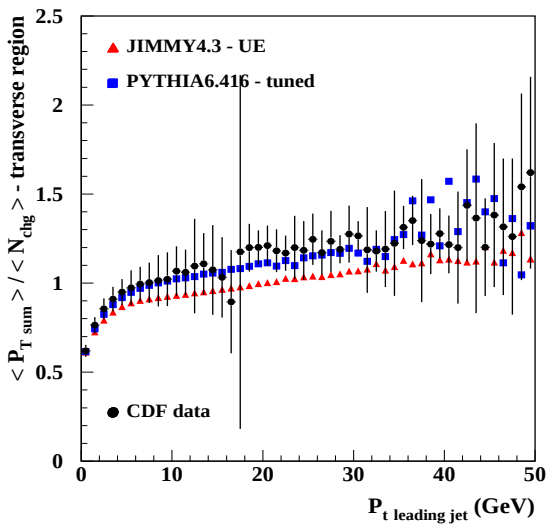

Fig. 3: PYTHIA 6.416 - tuned and JIMMY 4.3 - UE predictions for the underlying event compared to the ratio $< \mathrm{p}_T^{SUM} > / < \mathrm{N}_{chg} >$.

Another CDF measurement of the underlying event event was made by defining two cones in $\eta - \phi$ space, at the same pseudorapidity η as the leading E_T jet (calorimeter jet) and $\pm\pi/2$ in the azimuthal direction, ϕ [8]. The total charged track transverse momentum inside each of the two cones was then measured and the higher of the two values used to define the "MAX" cone, with the remaining cone being labelled "MIN" cone.

Figure 4 shows PYTHIA 6.416 - tuned predictions for the underlying event in $\mathrm{p\overline{p}}$ collisions at $\sqrt{\mathrm{s}}$ = 1.8 TeV compared to CDF data [8] for $< \mathrm{N}_{chg} >$ and $< \mathrm{P}_T >$ of charged particles in the MAX and MIN cones. PYTHIA 6.416 - tuned describes the data reasonably well. However, we notice that the $< \mathrm{P}_T >$ in the MAX cone is slightly harder than the data.

3 LHC predictions for the UE

Predictions for the underlying event in LHC collisions (pp collisions at $\sqrt{\mathrm{s}}$ = 14 TeV) have been generated with PYTHIA 6.416 - tuned and JIMMY 4.3 - UE. Figure 5 shows $< \mathrm{N}_{chg} >$ and $< \mathrm{p}_T^{SUM} >$ distributions for the region transverse to the leading jet (charged particles with $\mathrm{p}_T > 0.5$ GeV and $|\eta| < 1$), as generated by PYTHIA 6.416 - tuned (table 1) and JIMMY 4.3 - UE [10]. The CDF data ($\mathrm{p\overline{p}}$ collisions at $\sqrt{\mathrm{s}}$ = 1.8 TeV) for the underlying event is also included in Fig. 5 for comparison.

A close inspection of predictions for the $< \mathrm{N}_{chg} >$ in the underlying event given in fig.

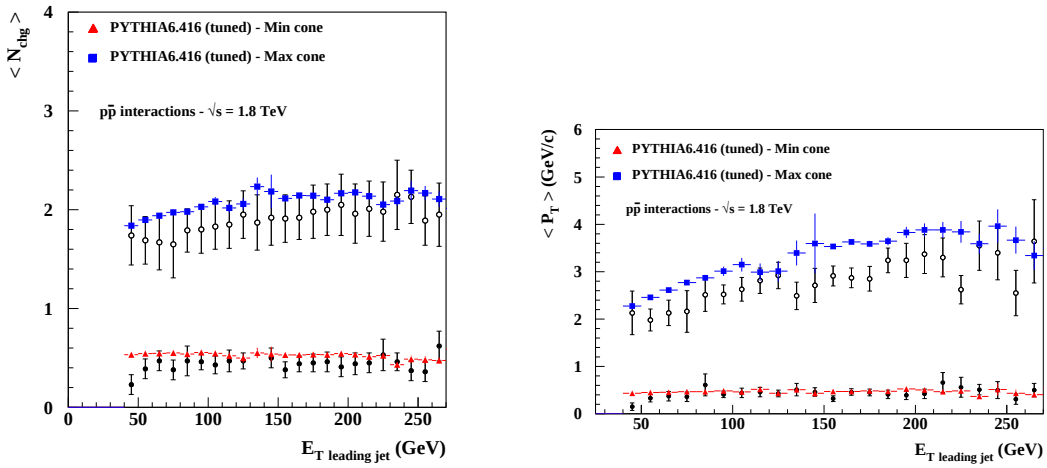

Fig. 4: (a) Average charged particle multiplicity, $< \mathrm{N}_{chg} >$, in MAX (top distributions) and MIN (bottom distributions) cones; (b) average total P_T of charged particles in MAX and MIN cones.

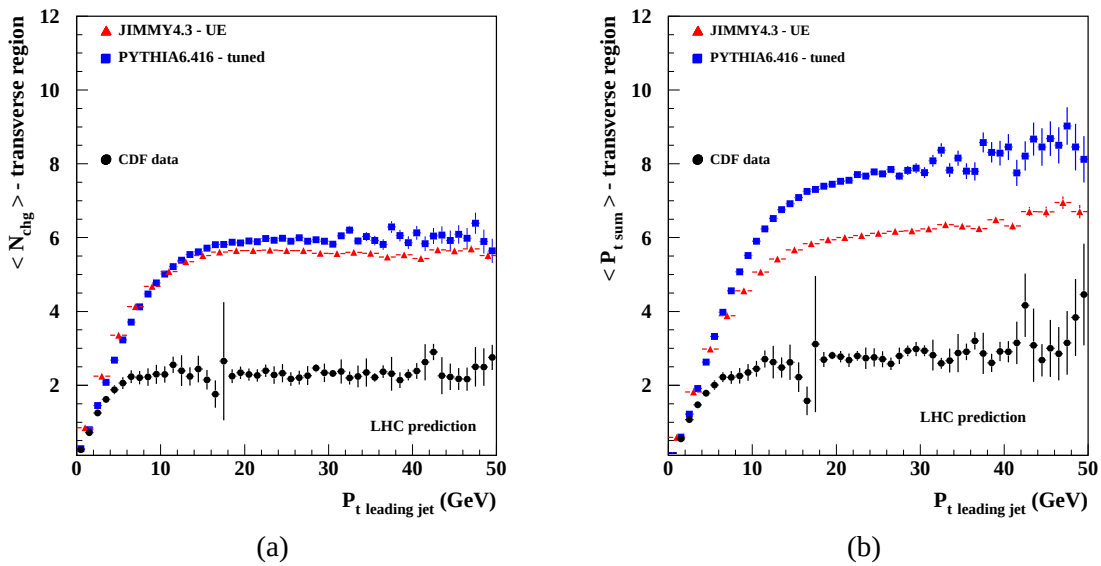

Fig. 5: PYTHIA 6.416 - tuned and JIMMY4.3 - UE predictions for the underlying event in pp collisions at $\sqrt{\mathrm{s}}$ = 14 TeV for (a) $< \mathrm{N}_{chg} >$ and (b) $< \mathrm{p}_T^{SUM} >$ (b).

5(a), shows that the average charged particle multiplicity for events with leading jets with $\mathrm{P}_{t_{\mathrm{ljet}}} > 15$ GeV reaches a plateau at ~ 5.5 charged particles according to both PYTHIA 6.416 - tuned and JIMMY4.3-UE. This corresponds to a rise of a factor of ~ 2 in the plateau of $< \mathrm{N}_{chg} >$ as

the colliding energy is increased from $\sqrt{s}$ = 1.8 TeV to $\sqrt{s}$ = 14 TeV.

The $< p_T^{SUM} >$ distributions in Fig. 5(b) show that PYTHIA 6.416 - tuned generates harder particles in the underlying event compared to JIMMY 4.3-UE. This is in agreement with the results shown in fig. 3, although for the LHC prediction the discrepancy between the two models is considerably larger than the observed at the Tevatron energy.

The difference between the predictions for the charged particle's p_T in the underlying event is a direct result of the tuning of the colour reconnection parameters in the new PYTHIA 6.4 model. This component of the PYTHIA model has been specifically tuned to produce harder particles, whereas in JIMMY4.3 - UE this mechanism (or an alternative option) is not yet available.

4 Conclusions

In this report we have compared tunings for PYTHIA 6.416 1 and JIMMY4.3 [10] to the underlying event. Both models have shown that, when appropriately tuned, they can describe the data.

In order to obtain the parameters for PYTHIA 6.416 - tuned, we have deliberately selected a combination of parameters that generate shorter strings between the hard and the soft systems in the hadronic interaction. We have also increased the hadronic core radius compared to the tunings used in previous PYTHIA versions (see Refs. [6, 7] for example).

We have noticed that PYTHIA 6.416 - tuned and JIMMY 4.3 - UE generate approximately the same densities of charged particles in the underlying event. This is observed for the underlying event predictions at the Tevatron and LHC energies alike.

However, there is a considerable disagreement between these tuned models in their predictions for the pT spectrum in the underlying event, as can be seen in figs. 3 and 5(b). PYTHIA 6.416 - tuned has been calibrated to describe the ratio $< p_T^{sum} >/< N_{chg} >$, which has been possible through the tuning of the colour reconnection parameters in PYTHIA. JIMMY4.3 - UE has not been tuned to this ratio.

As a final point, we would like to mention that this is an "*ongoing*" study. At the moment these are the best parameters we have found to describe the data, but as the models are better understood, the tunings could be improved in the near future.

References

[1] T. Sjostrand, S. Mrenna and P. Skands, JHEP **05**, 026 (2006).

[2] Corcella, G. et al, JHEP **01**, 010 (2001).

[3] Butterworth, J. M. and Forshaw, J. R. and Seymour, M. H., Z. Phys. C **72**, 637 (1996).

[4] J. M. Butterworth and M. H. Seymour, *JIMMY4: Multiparton Interactions in Herwig for the LHC*, October 2004.

[5] Sjostrand, T. and Zijl, M. van, Phys. Rev. D **36**, 2019 (1987).

[6] A. Moraes, C. Buttar and I. Dawson, Eur. Phys. J. C **50**, 435 (2007).

[7] R. Field, *Min-Bias and the Underlying Event at the Tevatron and the LHC*, October 2002. (talk presented at the Fermilab ME/MC Tuning Workshop, Fermilab).

[8] D. Acosta, et al, Phys. Rev. **D70**, 072002 (2004).

[9] T. Affolder, et al, Phys. Rev. **D65**, 092002 (2002).

[10] C. Buttar, et al, *Physics at Tev Colliders 2005 - QCD, EW and Higgs Working Group: Summary Report*, April 2006.

Measurement of the Underlying Event in Jet Topologies using Charged Particle and Momentum Densities

F. Ambroglini[a], *P. Bartalini*[b], *F. Bechtel*[c], *L. Fanò*[d], *R. Field*[e]
a) University of Trieste, Italy. b) National Taiwan University, Taiwan. c) Hamburg University, Germany. d) University of Perugia, Italy. e) University of Florida, USA.

Abstract

A study of Underlying Events with the CMS detector under nominal and start-up conditions is discussed. Using charged particle densities in charged particle jets, it will be possible to discriminate between QCD models with different multiple parton interaction schemes, which correctly reproduce Tevatron data but give different predictions when extrapolated to the LHC energy. This will permit improving and tuning Monte Carlo models at LHC start-up, and opens prospects for exploring QCD dynamics in proton-proton collisions at 14 TeV.

1 Introduction

From a theoretical point of view, the underlying event (UE) in a hadron-hadron interaction is defined as all particle production accompanying the hard scattering component of the collision. From an experimental point of view, it is impossible to separate these two components. However, the topological structure of hadron-hadron collisions can be used to define physics observables which are sensitive to the UE.

The ability to properly identify and calculate the UE activity, and in particular the contribution from Multiple Parton Interactions – MPI [1], has direct implications for other measurements at the LHC.

This work is devoted to the analysis of the sensitivity of UE observables, as measured by CMS, to different QCD models which describe well the Tevatron UE data but largely differ when extrapolated to the LHC energy. MPI are implemented in the PYTHIA simulations [2], for which the following tunes are considered: tune DW (reproducing the CDF Run-1 Z boson transverse momentum distribution [3]), tune DWT (with a different MPI energy dependence parametrization [4]) and tune S0 (which uses the new multiple interaction model implemented in PYTHIA [5]). In addition, an Herwig [6] simulation has also been performed, providing a useful reference to a model without multiple interactions.

2 Analysis strategy

Significant progress in the phenomenological study of the UE in jet events has been achieved by the CDF experiment at the Tevatron [7, 8]. In the present work, plans are discussed to study the topological structure of hadron-hadron collisions and the UE at the LHC, using only charged particle multiplicity and momentum densities in charged particle jets. A charged particle jet

(referred to as a *charged jet* from now on) is defined using charged particles only, with no recourse to calorimeter information. Different integrated luminosity scenarios are considered: 1, 10 and 100 pb^{-1}. The foreseen start-up CMS tracker alignment precision is applied in the case of 1 pb^{-1}.

The direction of the leading charged jet, which in most cases results from the hard scattering, is used to isolate different hadronic activity regions in the $\eta - \phi$ space and to study correlations in the azimuthal angle ϕ. The plane transverse to the jet direction is where the 2-to-2 hard scattering has the smallest influence and, therefore, where the UE contributions are easier to observe.

In order to combine measurements with different leading charged jet energies, events are selected with a Minimum Bias (MB) trigger [9] and with three triggers based on the transverse momentum of the leading calorimetric jet ($P_T^{calo} > 20, 60$ and 120 GeV/c).

Charged jets are reconstructed with an iterative cone algorithm with radius $R = 0.5$, using charged particles emitted in the central detector region $|\eta| < 2$. Two variables allow evaluating charged jet performances: the distance $\Delta R = \sqrt{\Delta\phi^2 + \Delta\eta^2}$ between the leading charged jet and the leading calorimetric jet, and the ratio of their transverse momenta P_T (transverse momenta are defined with respect to the beam axis). The transverse momentum of the leading charged jet is used to define the hard scale of the event.

Figure 1 presents, for the four trigger streams, the density $\mathrm{d}N/\mathrm{d}\eta\mathrm{d}\phi$ of the charged particle multiplicity and the density $\mathrm{d}p_T^{sum}/\mathrm{d}\eta\mathrm{d}\phi$ of the total charged particle transverse momentum p_T^{sum}, as a function of the azimuthal distance to the leading charged jet. Enhanced activity is observed around the jet direction, in the "toward" region ($\simeq 0$ degrees from the jet direction), together with a corresponding rise in the "away" region ($\simeq 180$ degrees), due to the recoiling jet. The "transverse" region ($\simeq \pm 90$ degrees) is characterized by a lower activity and almost flat density distributions, as expected.

3 UE observable measurement

3.1 Data samples

The data samples used for the present analysis are based on the DWT PYTHIA tune. MB and QCD dijet event samples, generated in bins of the transverse momentum $\hat{p}_T$ of the hard process, were reweighted according to their cross sections, the dijet events being merged into a single stream called hereafter JET. On that sample the calorimetric thresholds are applied in order to obtain the different trigger streams considered in the presented analysis The samples were reweighted according to the integrated luminosities corresponding to the different scenarios studied below, with consistent statistical precision in the relevant figures.

3.2 Tracking

Tracks of charged particles with $P_T > 0.9$ GeV/c are reconstructed in CMS following the procedure described in [10]. The possibility to build the UE observables using tracks with $p_T > 0.5$ GeV/c enhances sensitivity to the differences between the models. The standard CMS tracking algorithm was, thus, adapted to a 0.5 GeV/c threshold, by decreasing the p_T cut of the seeds and of the trajectory builder, and adapting other parameters of the trajectory reconstruction to optimize performance.

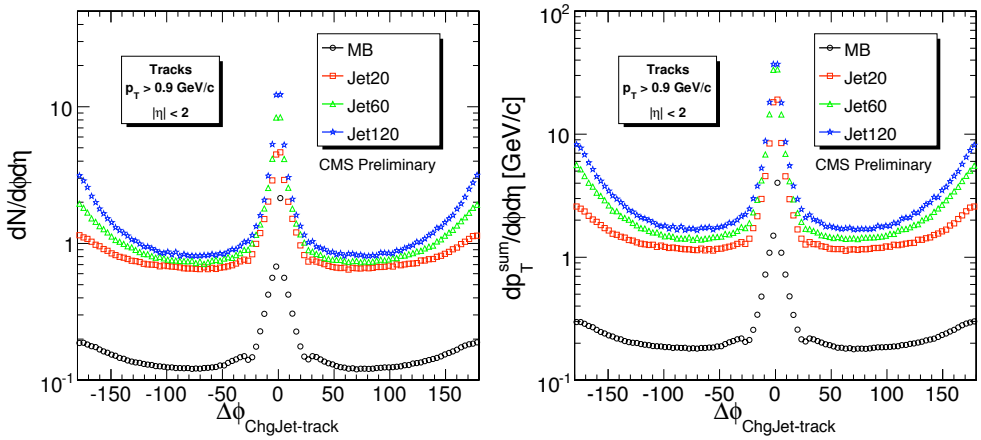

Fig. 1: Densities $\mathrm{d}N/\mathrm{d}\eta\mathrm{d}\phi$ of charged particle multiplicity (*left*) and $\mathrm{d}p_T^{sum}/\mathrm{d}\eta\mathrm{d}\phi$ of total charged transverse momentum (*right*), as a function of the azimuthal distance to the leading charged jet direction.

3.3 Results on density measurements

The corrected densities $\mathrm{d}N/\mathrm{d}\eta\mathrm{d}\phi$ of charged particle multiplicity and $\mathrm{d}p_T^{sum}/\mathrm{d}\eta\mathrm{d}\phi$ of charged tranverse momentum are presented in Figure 2 for the transverse region. The data, corresponding to an integrated luminosity of 10 pb^{-1}, are reported at the reconstruction level, using the DWT tune. The average corrections for both the P_T scale and the UE observables are found to be independent from the particular model used for the simulations.

Two contributions to the hadronic activity can be identified: a fast saturation of the UE densities for charged jets with $P_T < 20$ GeV/c, and a smooth rise for $P_T > 40$ GeV/c. The former is due to the MPI contribution while the latter is due to initial and final state radiation, which keeps increasing with the hard scale of the event.

The statistical precision and the alignment conditions correspond to those achieved with an integrated luminosity of 100 pb^{-1}. The curves represent the predictions of the different PYTHIA (DW, DWT and S0 tunes) and HERWIG simulations.

With respect to the standard 0.9 GeV/c scenario, lowering the P_T threshold for track reconstruction to 0.5 GeV/c turns out to lead to an increase of about 50% of the charged particle multiplicity and of about 30% of the charged transverse momentum density, slightly enhancing the discrimination power between the different models in the charged jet P_T region below 40 GeV/c.

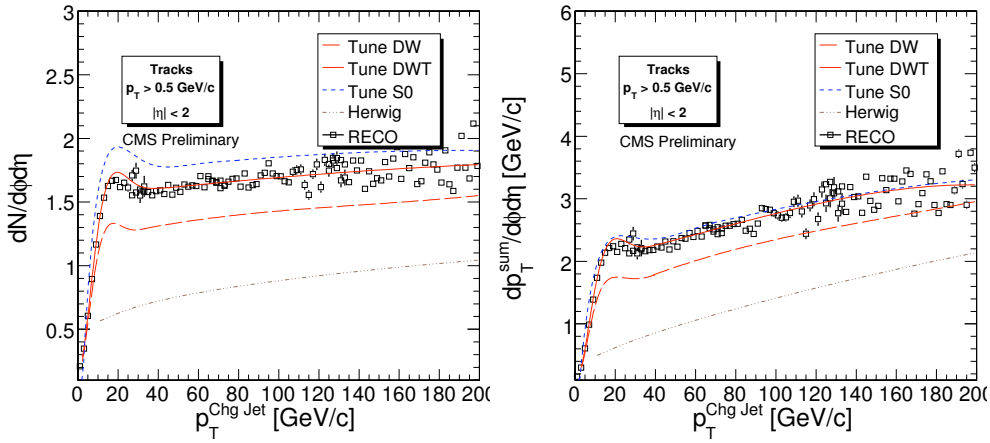

Fig. 2: Densities $\mathrm{d}N/\mathrm{d}\eta\mathrm{d}\phi$ (*left*) and $\mathrm{d}p_T^{sum}/\mathrm{d}\eta\mathrm{d}\phi$ (*right*) for tracks with $p_t > 0.5$ GeV/c, as a function of the leading charged jet P_T, in the transverse region, for an integrated luminosity of 100 pb^{-1} (corrected distributions).

3.4 Results using observable ratios

The ratios between (uncorrected) UE density observables in the transverse region, for charged particles with $p_T > 0.9$ GeV/c and with $p_T > 1.5$ GeV/c, are presented in Figure 3, for an integrated luminosity of 100 pb^{-1}. Ratios are shown here as obtained after track reconstruction, without applying additional reconstruction corrections; given the uniform performance of track reconstruction, the ratios presented here at detector level are similar to those at generator level. These ratios show a significant sensitivity to differences between different MPI models, thus providing a feasible (and original) investigation method.

4 Start-up conditions

The CMS tracking performance at the LHC start-up, with an integrated luminosity of the order of 1 pb^{-1}, will be affected by imperfect knowledge of detector element alignment. This additional error to the reconstructed positions of charged particle hits in the tracker system is taken into account by the *alignment position error* (APE) tool [11] [12] [13].

Figure 4 compares the tracker performance between the case of an ideally aligned detector and the case of a misaligned detector, before and after using the APE tool. The track reconstruction efficiency is seriously degraded by the mis-alignment, but it can be completely recovered using the APE tool, thanks to an increase in the spatial window used to find compatible hits during the trajectory building. The larger search window recovers many good hits which would otherwise be lost, at the expense of significantly increasing the rate of fake tracks. The relative

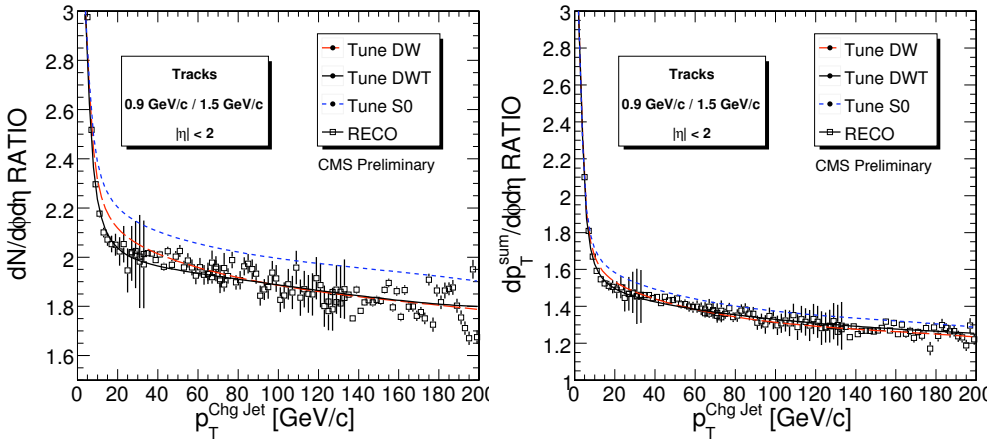

Fig. 3: Ratio of the UE event observables, computed with track transverse momenta $p_T > 1.5$ GeV/c and $p_T > 0.9$ GeV/c: densities $\mathrm{d}N/\mathrm{d}\eta\mathrm{d}\phi$ (*left*) and $\mathrm{d}p_T^{sum}/\mathrm{d}\eta\mathrm{d}\phi$ (*right*), as a function of the leading charged jet P_T, in the transverse region, for an integrated luminosity of 100 pb^{-1} (uncorrected distributions).

p_T resolution, also shown in Figure 4, is seen to be almost fully recovered after correcting the misalignment.

5 Conclusions

The predictions on the amount of hadronic activity in the region transverse to the jets produced in proton-proton interactions at the LHC energies are based on extrapolations from lower energy data (mostly from the Tevatron). These extrapolations are uncertain and predictions differ significantly among model parameterisations. It is thus important to measure the UE activity at the LHC as soon as possible, and to compare those measurements with Tevatron data. This will lead to a better understanding of the QCD dynamics and to improvements of QCD based Monte Carlo models aimed at describing "ordinary" events at the LHC, an extremely important ingredient for "new" physics searches.

Variables well suited for studying the UE structure and to discriminate between models are the densities $\mathrm{d}N/\mathrm{d}\eta\mathrm{d}\phi$ of charged particle multiplicity and $\mathrm{d}p_T^{sum}/\mathrm{d}\eta\mathrm{d}\phi$ of total charged particle transverse momentum p_T^{sum}, in charged particle jets. An original approach is proposed, by taking the ratio of these variables for different charged particle p_T thresholds.

At LHC start-up, the first pb^{-1} of collected data will be mainly intended to calibrate the analysis tools. Even with such a low integrated luminosity, it will be possible to perform a first measurement of the UE activity in charged jet events. With 10 pb^{-1} and a partially calibrated de-

tector, it will be possible to control systematic uncertainties on the UE observables, to keep them at the level of the statistical errors and to perform a first discrimination between UE models. Extending the statistics to 100 pb^{-1} and exploiting the uniform performance of track reconstruction for $p_T > 1.5$ GeV/c and $p_T > 0.9$ GeV/c, the ratio of observables will probe more subtle differences between models.

References

[1] T. Sjostrand and M. van Zijl, Phys. Lett. **B188**, 149 (1987).

[2] T. Sjostrand *et al.*, JHEP **05**, 026 (2006). hep-ph/0603175.

[3] CDF Collaboration, F. Abe *et al.*, Phys. Rev. Lett. **67**, 2937 (1991).

[4] CMS Collaboration, D. Acosta *et al.*, CERN CMS-NOTE-2006-067 (2006).

[5] P. Skands and D. Wicke, Eur. Phys. J. **C52**, 133 (2007). hep-ph/0703081.

[6] G. Corcella *et al.*, JHEP **101**, 010 (2001). hep-ph/0011363.

[7] CDF Collaboration, A. Affolder *et al.*, Phys. Rev. **D65**, 092002 (2002).

[8] CDF Collaboration, D. Acosta *et al.*, Phys. Rev. **D70**, 072002 (2004).

[9] CMS Collaboration, R. Hollis *et al.*, Physics Analysis Summary **PAS**, QCD (2007).

[10] CMS Collaboration, W. Adam *et al.*, CERN CMS-NOTE-2006-041 (2006).

[11] CMS Collaboration, P. Vanlaer *et al.*, CERN CMS-NOTE-2006-029 (2006).

[12] CMS Tracker Collaboration, CERN CMS-NOTE- in preparation.

[13] CMS Collaboration, G. Bayatian *et al.*, J. Phys. **G34**, 995 (2007).

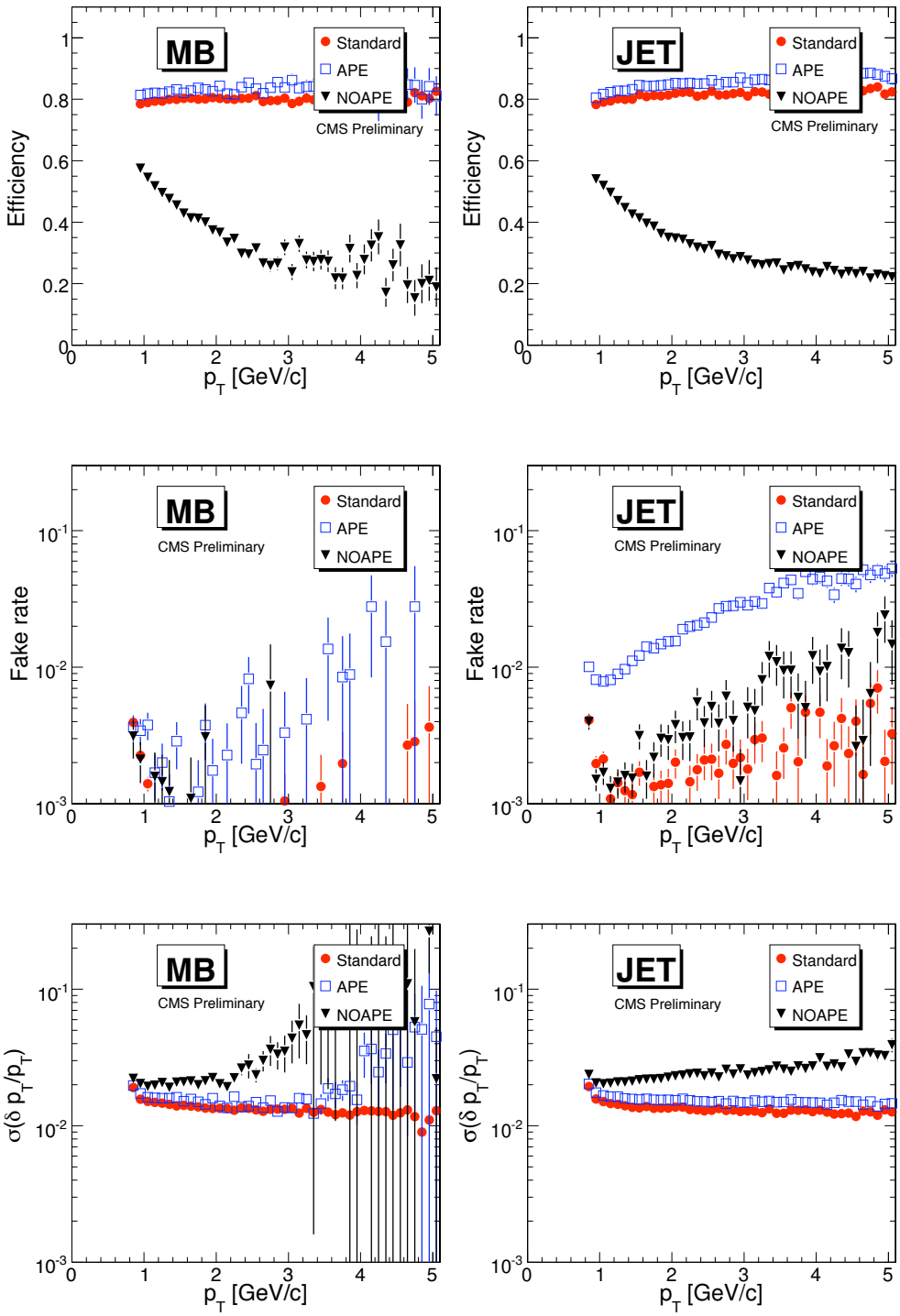

Fig. 4: Tracking performance for an ideal tracker (*circles*), for a misaligned tracker as expected at start-up (*triangles*) and for a misaligned tracker with use of the APE tool (*squares*), for charged particles with $p_T > 0.9$ GeV/c from the MB (*left*) and JET (*right*) samples: track reconstruction efficiency, fake track rate and relative p_T resolution, as a function of the leading charged jet P_T.

Double-Parton-Scattering in Photon-Three-Jet Final States at the LHC

Florian Bechtel
Hamburg University

Abstract
The possible detection of double-parton-scattering in final states with one photon and three jets at the LHC is discussed. We study suitable variables to discriminate double-parton-scattering from shower contributions. Predictions of two event generators with different multiple interaction models are compared.

1 Direct Observation of Multiple Parton Interactions

There are good reasons to expect that multiple parton-parton scatterings will occur in most pp collisions at the LHC. For one, including multiple interactions in event generators greatly improves the description of the *underlying event* at the Tevatron. But hadronic event generators have many ingredients, making it difficult to conclude unambiguously the observation of multiple scattering.

Instead, a direct observation of multiple interactions involving final states accessible to a perturbative treatment would rule out other interpretations of the underlying event data. Four high-p_T jets from two independent scatters in the same pp or $p\bar{p}$ collision (*double-parton-scattering, DPS*) is the most prominent process. A four-jet-signature with two pairs of jets where the members of each pair have equal and opposite transverse momentum has been searched for by the AFS experiment [1] at CERN ISR, by the UA2 experiment [2] at CERN SppS and most recently by the CDF experiment [3] at the Tevatron.

Despite the large jet cross sections, the above searches had to face significant backgrounds as there are three possible ways to group four jets into two pairs. On top, the jet energy measurement is best at large energies where the cross section for double-parton scattering is small. Lowering the jet E_T threshold complicates the identification of an E_T-balanced pair as the measured jet E_T's deviate from their true value.

In a new approach to detect DPS, the CDF experiment studied final states with one photon and three jets [4] looking for pairwise balanced photon-jet and dijet combinations. The data sample was selected with CDF's inclusive photon trigger, hence allowing to search for jets down to low energies. Measuring the photon's transverse energy more precise than the jet's transverse energy helps to identify an E_T-balanced pair.

2 Simulation of Double-Parton-Scattering

We present generator-level studies with version 8.108 of the PYTHIA [5] event generator program and with version $2.2.0$ of the HERWIG++ [6] program. Both event generators model the underlying event including additional interactions, which are described in the context of perturbative QCD [7, 8].

Photon	$E_T(\gamma) \geq 20$ GeV
	$\lvert\eta(\gamma)\rvert \leq 2.5$
Jets	$E_T(\text{jet}) \geq 20$ GeV
	$E_T(\text{jet 2})/E_T(\text{jet 1}) < 0.8$
	$\lvert\eta(\text{jet})\rvert \leq 5$
	$\Delta R(\gamma,\text{jet}) \geq 0.2$
Missing normalized p_T	$\lvert\sum_i \vec{p}_{Ti}\rvert / \sum_i \lvert\vec{p}_{Ti}\rvert \leq 0.1\ ,\ i \in \{\gamma, 1, 2, 3\}$

Table 1: Kinematic selection of photon-three-jet combinations.

We compare PYTHIA default, shower-only, multiple-interactions-only and HERWIG++ default. Prompt-photon events were simulated in 5 GeV-bins of $\hat{p}_T$ for PYTHIA, $E_T(\gamma)$ for HERWIG++, of 100000 events each starting at $\hat{p}_T = 10$ GeV/c and going up to 100 GeV/c. Additional jets come from multiple interactions or from parton showers. The respective samples were normalized to the total prompt photon production cross section. Note that this will give unphysical normalizations for the PYTHIA settings with one or several options switched off, but helps to identify phase space regions with enhanced contributions from multiple interactions.

3 Event Selection and Background Discrimination

A longitudinally invariant k_T-jet algorithm [9] with $R = 0.4$ was run after the hadronization step on all stable particles, except neutrinos. Kinematic selections on photon and jets are summarized in Table 1.

The polar acceptances of the CMS electromagnetic and hadronic calorimeter are reflected in pseudorapidity cuts of $|\eta(\gamma)| \leq 2.5$ and $|\eta(\text{jet})| \leq 5$, respectively. Photons and jets are required to have transverse energies above 20 GeV, corresponding to the reconstruction threshold [10]. Fig. 1 illustrates the three-jet thresholds for the various generator settings: The minimal jet transverse momentum is shown for the softest jet in the photon-three-jet-system. Jets from multiple interactions are softer in p_T than jets from initial state radiation: A balance has to be found between selecting a jet p_T threshold where jet reconstruction is of sufficient quality and a p_T threshold that still allows multiple interactions to contribute significantly to the final state. PYTHIA predicts more photon-three-jet combinations with one jet having a transverse momentum smaller than 25 GeV/c while at large transverse momenta, HERWIG++ and PYTHIA agree (Fig. 1 right).

In double-parton-scattering events, both scatterings are supposed to be uncorrelated in scale and direction. To test this assumption, AFS and CDF investigated azimuthal correlations between pairs (Fig. 2). Both chose to study the azimuthal difference between p_T-vectors representing each of the pairs. AFS constructed said p_T-vector from the vector difference between the two objects (upper), while CDF constructed the pair's p_T from the vector sum (lower). As the pair p_T must not be zero in order to compare its direction to the other pair's p_T, both methods fail for specific configurations: The AFS method fails for objects going in the same direction, while the CDF method fails for perfectly balanced objects. Both event generators predict similar shapes for the selected phase space, but PYTHIA's total cross section prediction is larger than HERWIG++'s, corresponding to a prediction of more photon-three-jet topologies in the detector

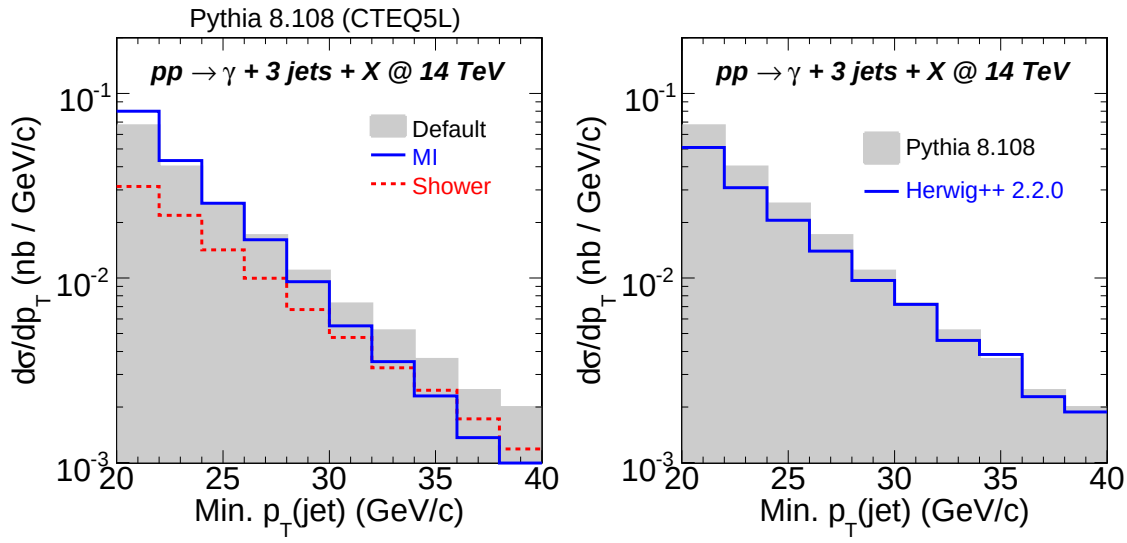

Fig. 1: Minimal jet p_T in photon-three-jet combinations. Comparison between three PYTHIA and default HERWIG prediction.

acceptance.

4 Conclusions

We studied predictions of two event generators for the production of prompt photons accompanied by three jets at the LHC. This final state is sensitive to detecting multiple interactions in double-parton-scattering events.

Detecting double-parton-scattering in photon-three-jet final states requires jet reconstruction in a region of phase space where multiple interactions contribute significantly to the photon-three-jet cross section, i. e. at small transverse energies. A promising approach might be the reconstruction of jets from tracks which have been demonstrated to give a reasonable response down to small transverse energies [11]. It will also be beneficial to reconsider double-parton-scattering processes in clean final states, such as double-Drell-Yan production of four muons.

Acknowledgements

The author acknowledges financial support by the Marie Curie Fellowship program for Early Stage Research Training, by MCnet (contract number MRTN-CT-2006-035606) and by the German Federal Ministry of Education and Research (BMBF).

References

[1] Akesson, T. and others, Z. Phys. **C34**, 163 (1987).

[2] Alitti, J. and others, Phys. Lett. **B268**, 145 (1991).

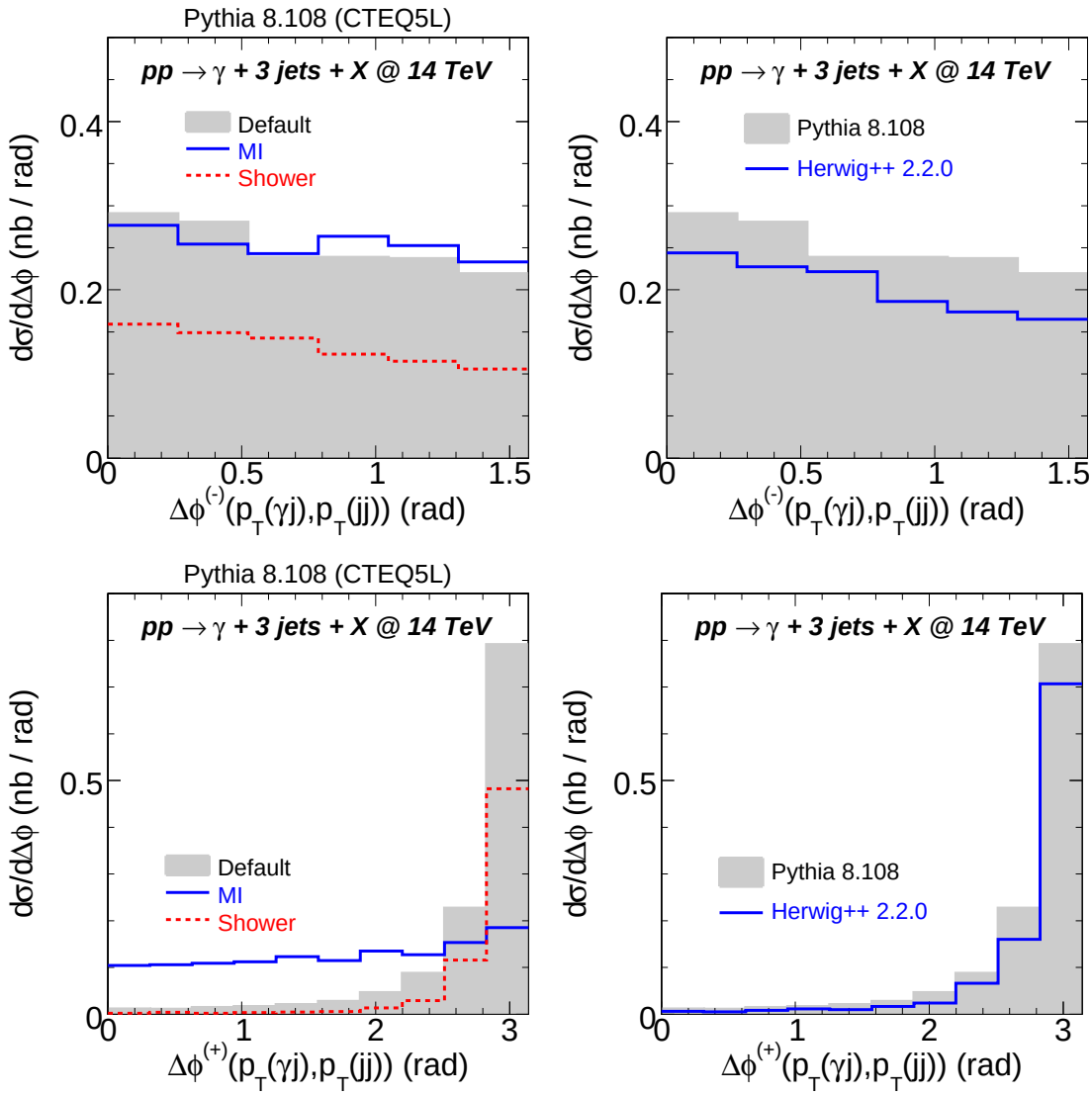

Fig. 2: Event shape variables for the photon-three-jet system.

[3] Abe, F. and others, Phys. Rev. **D47**, 4857 (1993).

[4] Abe, F. and others, Phys. Rev. **D56**, 3811 (1997).

[5] Sjostrand, Torbjorn and Mrenna, Stephen and Skands, Peter, JHEP **05**, 026 (2006); Sjostrand, Torbjorn and Mrenna, Stephen and Skands, Peter, Comput. Phys. Commun. **178**, 852 (2008).

[6] Bahr, M. and others (2008).

[7] Sjostrand, Torbjorn and van Zijl, Maria, Phys. Lett. **B188**, 149 (1987); Sjostrand, T. and Skands, P. Z., JHEP **03**, 053 (2004); Sjostrand, T. and Skands, P. Z., Eur. Phys. J. **C39**, 129 (2005).

[8] Bahr, Manuel and Gieseke, Stefan and Seymour, Michael H., JHEP **07**, 076 (2008).

[9] Catani, S. and Dokshitzer, Yuri L. and Seymour, M. H. and Webber, B. R., Nucl. Phys. **B406**, 187 (1993); Ellis, Stephen D. and Soper, Davison E., Phys. Rev. **D48**, 3160 (1993).

[10] Bayatian, G. L. and others. CERN-LHCC-2006-001.

[11] Bayatian, G. L. and others, J. Phys. **G34**, 995 (2007).

Underlying Event Studies with CASTOR in the CMS Experiment

Zuzana Rúriková[a], *Armen Bunyatyan*[b]
[a] DESY, Hamburg
[b] MPI-K, Heidelberg and YerPhI, Yerevan

Multi-parton interactions (MI) play a significant role in soft and high p_T processes. Especially in case of LHC where the proton beams collide at very large energies, the understanding of MI is becoming crucial for the high precision measurements. Up to now various Monte Carlo (MC) models have been tuned to describe the Tevatron data [1], exploiting mainly the charged particle multiplicities and particle energy flows in the central η region. In the near future the full angular coverage of the CMS detector from the central to the most forward region ($0 < \eta < 6.6$) will allow to study MI over a large rapidity range, which was not possible before.

Since the multi-parton interactions occur between the remnant partons of the colliding particles, the energy flow in the very forward region covered by the CASTOR calorimeter [2] ($5.2 < \eta < 6.6$) is expected to be strongly affected and hence ideal for the MI model tuning. In addition one can study the long range correlations (correlation between activity in central and forward region) which where observed already at HERA and UA5 [3].

Results shown here are based on a generator level analysis of inclusive QCD processes [1] with PYTHIA MC 6.4.14, using several widely used MI tunes, such as Rick Field's tune A, Sandhoff-Skands tune S0 and also extreme scenario with MI being switched off.

In order to study the long range correlations the triggering on energy deposit in CASTOR η region is performed. Four energy ranges in the CASTOR (E_{CAST}) are investigated. For each E_{CAST} bin the charged particle multiplicities as well as particle energy flow in central rapidity region are investigated (see figure 1). In order to mimic the detection threshold effects a minimum energy cut of 1 GeV is applied to all stable generated particles.

One can see that in case without MI no long range correlations are observed, i.e. charge particle multiplicities look the same for all E_{CAST} energy bins, as one would expect. On the other hand, when MI are included there is a clear correlation, larger energies in CASTOR region imply higher charged particle multiplicities and particle energy flow in the central region. Furthermore triggering on CASTOR enhances the differences between various MI tunes, and thus may contribute to better understanding of multi-parton interaction picture.

Study of multi-parton interactions within the hard processes, such as top production, is becoming extremely interesting since they are one of the major items of the LHC physics program. Therefore charged particle multiplicities (Fig.2 - upper plots) and particle energy flow observables were studied for the top processes [2] and were compared with the distributions for inclusive QCD processes (Fig.1). No selection cuts for top-quark reconstruction were applied. Besides much higher charged particle multiplicities and energy flow in central rapidity region in case of top production, which is due to the presence of hard scale, there is clearly more underlying event activity than in QCD processes. This can be easily seen for example by comparing the MC pre-

[1] PYTHIA parameters: MSEL= 1 (hard QCD processes), CKIN$(3) = 5$GeV (min. $\hat{p}_\perp$ for hard process).
[2] PYTHIA parameters: MSEL= 6 ($t\bar{t}$ production).

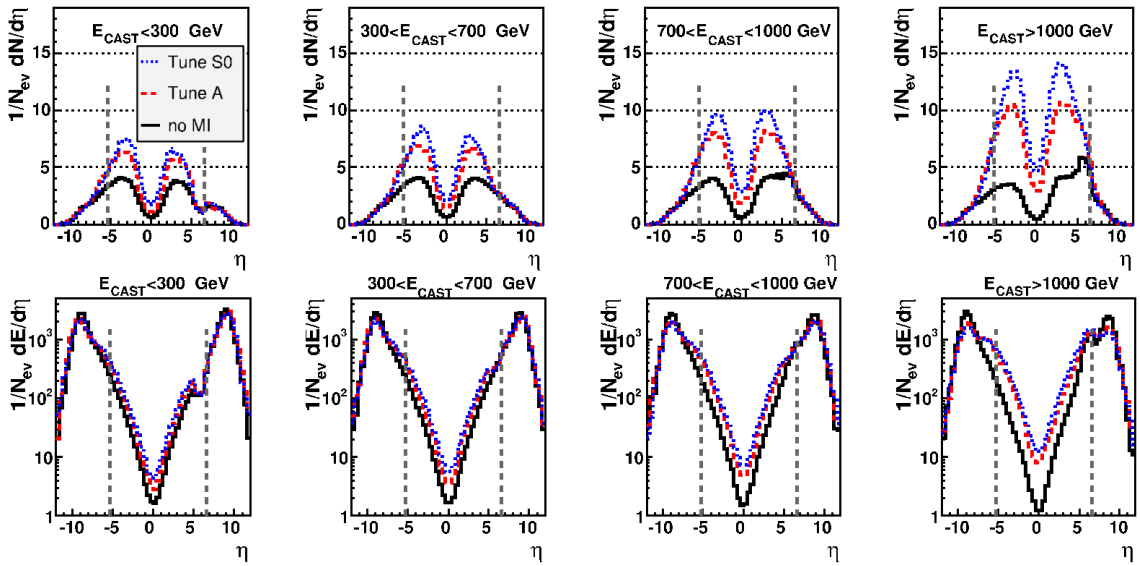

Fig. 1: Charged particle multiplicities (upper plots) and particle energy flow (lower plots) as function of η for four different CASTOR energy bins. Shown is PYTHIA MC prediction for inclusive QCD processes. The dashed vertical lines indicate the acceptance of the CMS detector.

diction with and without MI for inclusive QCD processes and for top processes separately. The differences amount to 2-5 particles per rapidity bin (Fig.2 - middle plots).

This suggests that a naive approach of subtracting underlying event contribution as determined for inclusive QCD processes from the top events would not work. As already seen from CDF measurements [1] the underlying event depends strongly on the collision centrality. The harder the collision is, the more underlying event activity one expects to see. This feature is also implemented into PYTHIA MC which is used in this analysis. After demanding a hard scale for inclusive QCD events in form of $E_{\mathrm{T}}^{\mathrm{jet}} > 40$ GeV the differences between underlying event in QCD and in top events do almost disappear (Fig.2 - bottom plots).

Understanding of underlying event is essential also for all kind of measurements which involve high E_{T} jets in the final state. As the hadronic jets are the direct products of the parton hadronisation, the jet measurements give a look inside the dynamics of hard interaction. However, the underlying event produces additional energy in the available phase space which is largely uncorrelated with the partons originating from the hard interaction. This additional 'pedestal' energy is added by the jet reconstruction algorithms to the 'true' jet energy, thus spoiling the relation of the 'jets to the partons. However, as shown below, it is possible to estimate the 'pedestal' energy from the measurements in the forward calorimeters and subtract it from the reconstructed jet energy.

The analysis is done using the PYTHIA simulation using the different options for multi-parton interactions as well as without multi-parton interactions. Events are selected in which the jets are reconstructed by the inclusive $k_{\perp}$ algorithm with transverse energies above 10 GeV and the jet axis at the central pseudorapidities ($-3 < \eta^{\mathrm{jet}} < 3$). Figure 3 shows the transverse energy

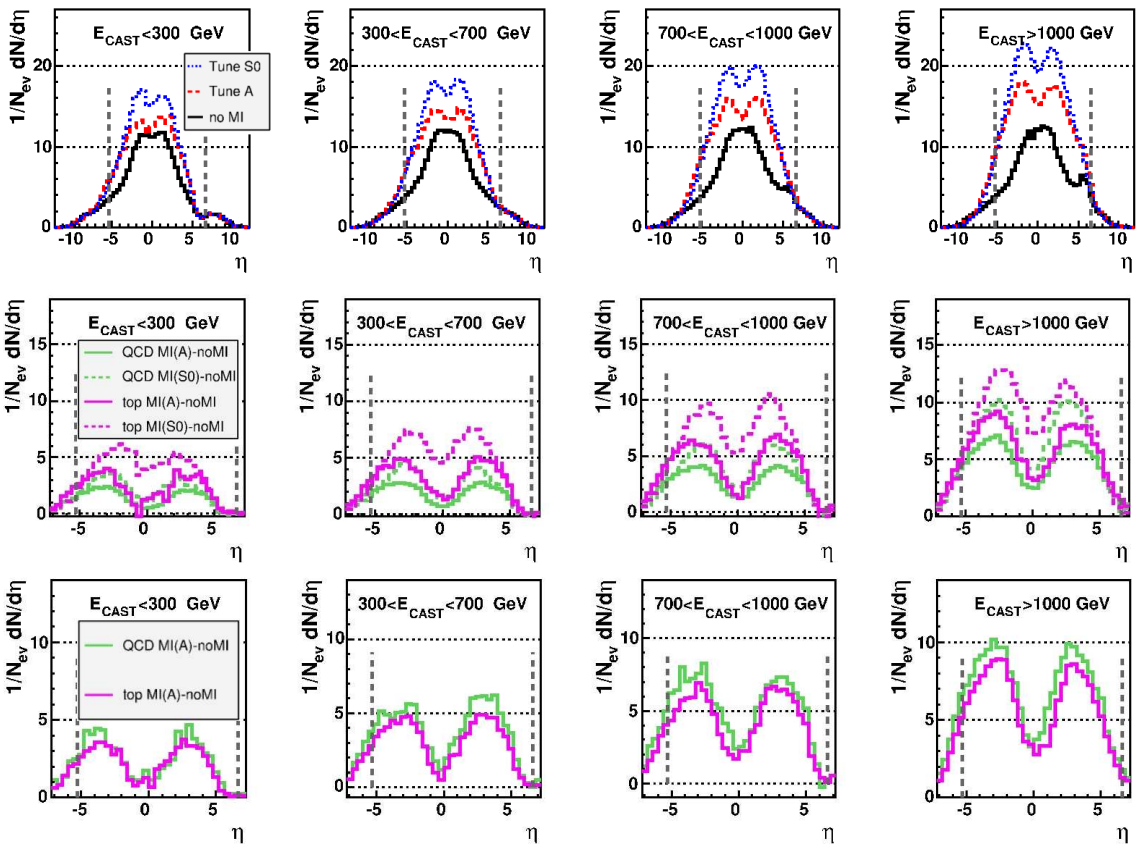

Fig. 2: Upper plots: charged particle multiplicities as a function of η for four different CASTOR energy bins. Shown is PYTHIA MC prediction for top processes. Middle plots: the charged particle multiplicities due to underlying event activity (MC with MI - MC without MI) as a function of η in top as well as inclusive QCD processes. Bottom plots: the charged particle multiplicities due to underlying event activity as a function of η in top and in inclusive QCD processes after demanding a presence of a hard jet $E_{\mathrm{T}}^{\mathrm{jet}} > 40$ GeV in the central rapidity region $|\eta| < 2.5$. The dashed vertical lines indicate the acceptance of the CMS detector.

flow around the jet as a function of pseudorapidity. The different lines correspond to the different ranges of jet pseudorapidities ([-3,-2.5], [-1.5,-1], [0,0.5], [1,1.5], [2,2.5]), and two different jet transverse energy ranges ([10-20 GeV], [20-30 GeV]). Only transverse energies within one radian in azimuth of the jet are included. The left plot corresponds to the simulation without multi-parton interaction and the right plot for simulation with multi-parton interaction. The plots clearly show the effect of the underlying event pedestal when the multi-parton interactions are simulated. It is also observed that the level of pedestal doesn't depend on the jet pseudorapidity, but it gets higher for higher jet energies, i.e. it depends on the hardness of the interaction.

The idea of the method to determine and subtract the pedestal energy within the jet is demonstrated in the Fig.4. In the left upper figure the jet profile as a function of pseudorapidity is shown for the PYTHIA simulation which includes multi-parton interaction. For this figure the events are used which contain a jet with transverse energy above 10 GeV in the pseudorapidity

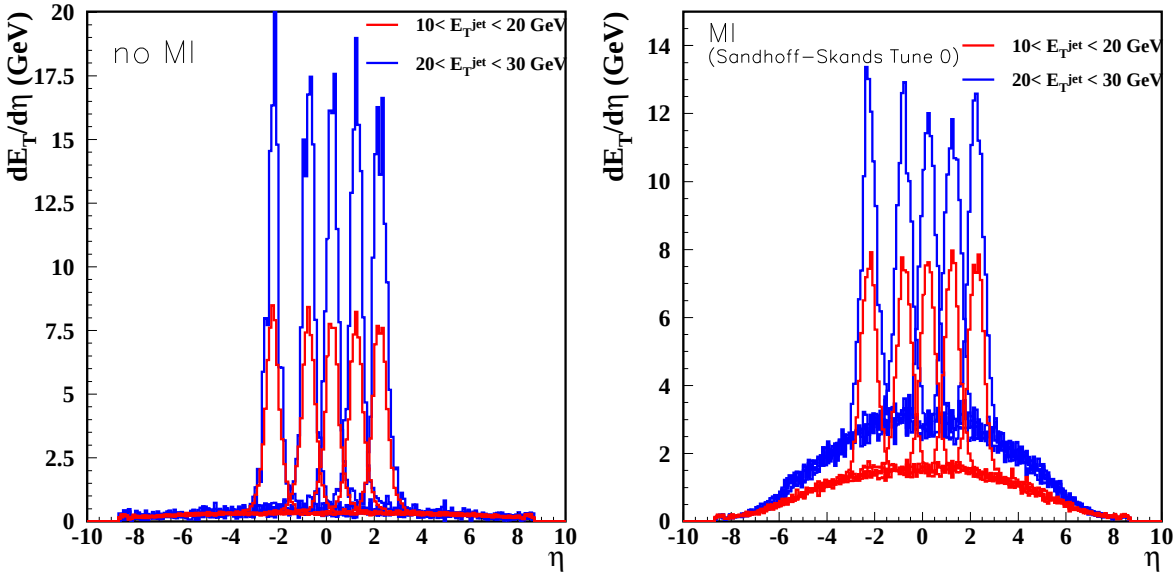

Fig. 3: The transverse energy distributions around the jets (jet profile) as a function of pseudorapidity. The left plot is obtained from the PYTHIA simulation without multi-parton interactions, while the right plot is for PYTHIA with multi-parton interactions. The different lines represent the different pseudorapidity ranges of the jets ([-3,-2.5], [-1.5,-1], [0,0.5], [1,1.5], [2,2.5]) and the different transverse energy ranges of the jets ([10-20 GeV], [20-30 GeV]).

range $0 < \eta^{\rm jet} < 0.5$. The transverse energy measured in the acceptance range of the CASTOR calorimeter ($5.2 < \eta < 6.6$) is also shown by the red hatched area. The blue hatched area below the jet cone is the contribution of pedestal to the jet energy measurement determined with the method described here.

As the underlying event pedestal seem to be independent on the position of the jet in the central detector, we may attempt to describe the pedestal by a simple function. The possible function can be

$$f(\eta) = \frac{A}{1 + B \cdot e^{|\eta|-4}} \tag{1}$$

This function depends on two free parameters A and B and seems to describe the pedestals for the different models of multi-parton interactions and for the different cuts on jet transverse energies and pseudorapidities. The two free parameters could be the measured energies in the forward calorimeters, like CASTOR, which are away from the central region and don't get contribution from the energy of hard interaction. The function doesn't contain direct dependence on the $E_{\rm T}$ of the jet, because there are strong correlations of $E_{\rm T}^{\rm jet}$ with the energy of pedestal and, correspondingly, with the energy in the forward calorimeters (see Fig.3). Therefore the $E_{\rm T}^{\rm jet}$ dependence can be absorbed in the A and B parameters. In principle, the parameters A and B in eq.1 are strongly correlated, thus even the single energy measurement in the CASTOR can already provide the estimate of the pedestal under the jet. An example of the the fit of pedestal by this function is shown in Fig.4 (right) and the level of pedestal under the jet determined by

this method is shown in the Fig.4 (left) as a blue hatched histogram. As is seen, this approach gives reasonable result and can be developed further and used in analyses.

It should be noted, that presented studies have been done using the Lund fragmentation mechanism in PYTHIA. In principle, using another Monte Carlo or fragmentation models (CASCADE, ARIADNE, etc.) may lead to the different energy distribution of the underlying event. This may require the optimisation of the function of eq.1. The reliability of this method can be also improved by using an additional measurements of forward energy (in addition to the CASTOR), for example from the HF calorimeter.

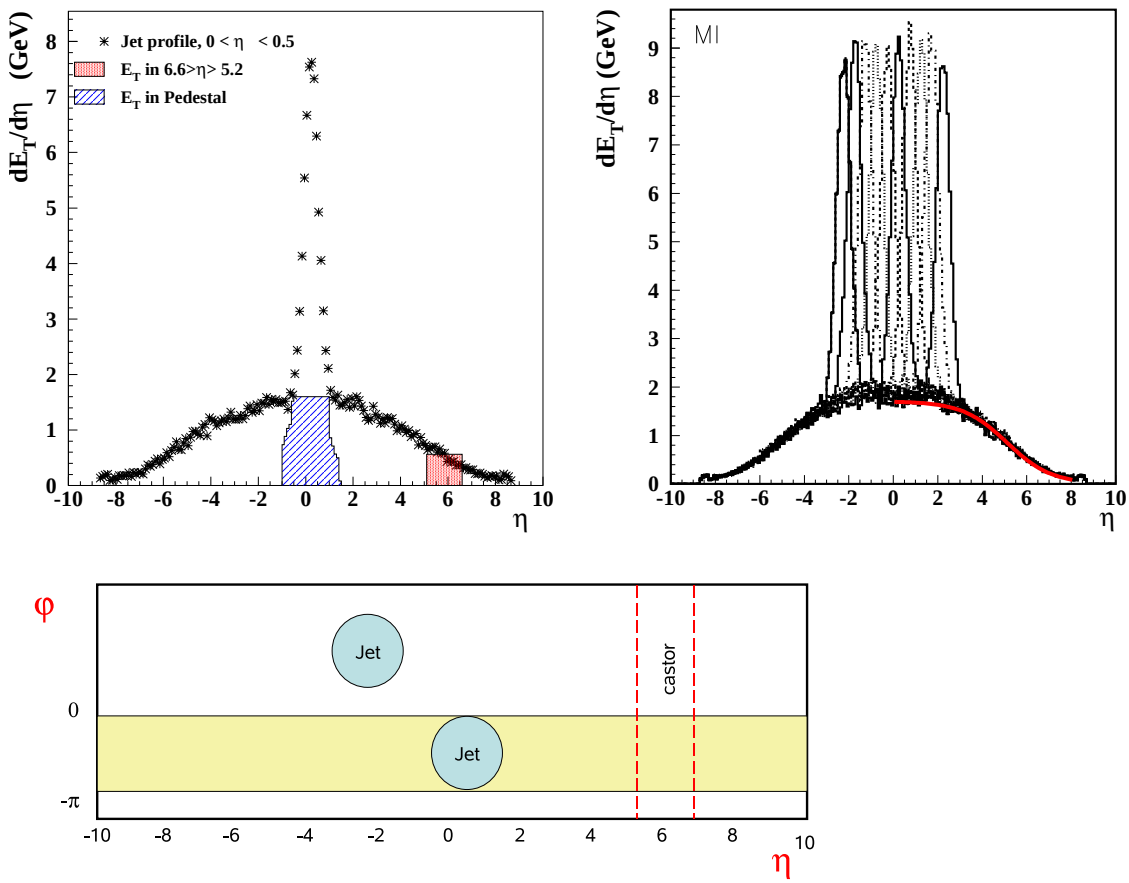

Fig. 4: *(left)* The transverse energy distributions around the jets (jet profile) as a function of pseudorapidity for the jets with $0 < \eta^{\rm jet} < 0.5$ and $10 < E_{\rm T}^{\rm jet} < 20\ GeV$. The red hatched histogram is the level of transverse energy in the pseudorapidity range of the CASTOR ($5.2 < \eta < 6.6$). The blue hatched histogram below the jet area is the pedestal level determined from the method described in this report. *(right)* The jet profile as a function of pseudorapidity for jets with $10 < E_{\rm T}^{\rm jet} < 20\ GeV$. The different lines correspond to the different ranges of the jet pseudorapidity. The solid line on the right tail of distribution shows the result of the fit of pedestal by a function of eq.1.

In conclusion, the studies presented here show that the forward region is very sensitive to the multi-parton interactions. The measurements in the forward calorimeters, such as CASTOR,

can be used to discriminate between the various MI models and to improve the jet reconstruction in the central region. Nevertheless further studies with detailed simulation of detector response are essential. Simple smearing of particle energies in η CASTOR region according to the resolution as measured in test beam 2007 has already been tried, and leads to similar results.

References

[1] [CDF Collaboration], Phys. Rev. D **70** (2004) 072002.

[2] CASTOR web page, $http://cmsdoc.cern.ch/castor$.

[3] T. Sjostrand and M. van Zijl, *A multiple-interaction model for the event structure in hadron collisions*, Phys. Rev. D **36** (1987) 2019-2041.

Direct photon production at HERA, the Tevatron and the LHC

R. E. Blair [a], *S. Chekanov* [a], *G. Heinrich* [b], *A.Lipatov* [c] *and N.Zotov* [c]

[a] HEP Division, Argonne National Laboratory, 9700 S.Cass Avenue, Argonne, IL 60439, USA
[b] Institute for Particle Physics Phenomenology, Department of Physics, University of Durham, Durham, DH1 3LE, UK
[c] SINP, Moscow State University, 119991 Moscow, Russia

Abstract

We review several most recent prompt-photon measurements at HERA and the Tevatron and discuss their implication for future measurements at the LHC. A comparison to Monte Carlo models, as well as to NLO QCD predictions based on the standard DGLAP and the k_T-factorization approaches is discussed. Effects from renormalization and factorization scale uncertainties, as well as uncertainties on the gluon density distribution inside a proton are discussed.

1 Introduction

Events with an isolated photon are an important tool to study hard interaction processes since such photons emerge without the hadronization phase. In particular, final states of ep and pp collisions with a prompt photon together with a jet are more directly sensitive to the underlying QCD process than inclusive prompt photon measurements.

The results on prompt-photon production provided by HERA are important for the interpretation of the LHC data. Unlike pp collisions, ep collisions involve a point-like incoming lepton, which leads to some simplification in the description of the prompt-photon production in ep compared to pp. At HERA, the quark content of the proton is probed through the elastic scattering of a photon by a quark, $\gamma q \to \gamma q$ (see Fig. 1). Such QED events are significantly simpler than lowest-order compton-like $qg \to q\gamma$ events which are dominant in pp collisions (see Fig. 2, left figure). The latter process has direct sensitivity to the strong coupling constant and requires much better understanding of the gluon structure function inside both incoming protons than for the lowest-order diagram in ep collisions.

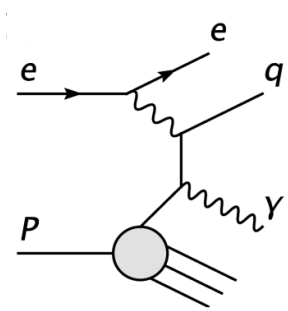

Fig. 1: Lowest-order diagram (Compton scattering) for γ+jet events in ep collisions.

Despite the difference between ep and pp collisions concerning certain lowest-order diagrams, a large class of partonic contributions are similar between ep and pp collisions, due to the hadronic nature of the resolved photon. In particular, a contribution to prompt-photon events from the $gq \to q\gamma$ process in photoproduction, in which the photon displays its hadronic structure [1–4], leads to significant sensitivity to the gluon structure

function as is the case in pp collisions (see Fig. 2, the two figures on the right). Therefore, analysis of HERA data can make a bridge between a better understood ep case and the less understood pp case, since apart from the convolution with different structure functions, photoproduction diagrams ep collisions involving a resolved photon are essentially the same as diagrams in pp collisions.

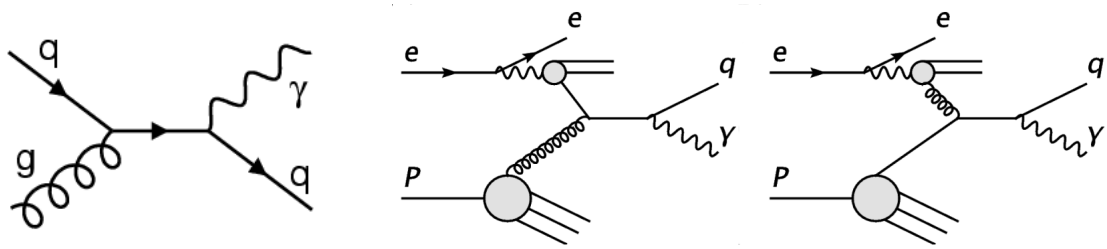

Fig. 2: The dominant diagram for prompt-photon events in pp collisions (left figure) compared to two resolved photon diagrams in ep photoproduction (see Section 2 for more details).

Prompt-photon events in ep collisions can constrain both quark and gluon parton densities (PDFs). In addition, differences between collinear factorization and k_T factorization in the description of the underlying hard subprocesses can be studied in detail. This is important not only for a better understanding of QCD dynamics, but also has direct implications for searches of exotic physics at the LHC, in which prompt-photon production is the main background. A number of QCD predictions [2–6] can be confronted with the data and some of them will be described in more detail below.

2 Photoproduction of prompt photons at NLO

In the photoproduction ep scattering processes, the electron is scattered at small angles, emitting a quasi-real photon which scatters with the proton. The spectrum of these photons can be described by the Weizsäcker-Williams approximation [7]. The photons will take part in the hard interaction either directly, or through their "partonic" content, in which case a parton stemming from the *resolved* photon participates in the hard subprocess. Similarly, a photon in the final state can either originate directly from the hard interaction or from the fragmentation of a parton. Therefore, one can distinguish four categories of subprocesses: 1) direct direct, 2) direct fragmentation, 3) resolved direct and 4) resolved fragmentation. Examples of leading order diagrams of each class are shown in Fig. 3. Beyond leading order, this distinction becomes ambiguous. For example, the NLO corrections to the direct part involve final state collinear quark-photon pairs which lead to divergences which are absorbed into the fragmentation function, such that only the sum of these contributions has a physical meaning. The complete NLO corrections to all four parts have been calculated in [4] for inclusive prompt photons and in [8] for photon plus jet final states. A public program EPHOX, written as a partonic event generator, is available from [9]. The NLO corrections to the direct-direct part also have been calculated in [3, 10] for the inclusive and photon plus jet final state.

The γ-p scattering processes are of special interest since they are sensitive to both the partonic structure of the photon as well as of the proton. They offer the possibility to constrain

the (presently poorly known) gluon distributions in the photon, since in a certain kinematic region the subprocess $qg \to \gamma q$, where the gluon is stemming from a resolved photon, dominates [5].

Working within the framework of collinear factorization, i.e. assuming that the transverse momenta of the partons within the proton can be neglected and other non-perturbative effects can be factorized from the hard interaction at high momentum transfers, the cross section for $ep \to \gamma X$ can symbolically be written as a convolution of the parton densities for the incident particles (respectively fragmentation function for an outgoing parton fragmenting into a photon) with the partonic cross section $\hat{\sigma}$:

$$d\sigma^{ep\to\gamma X}(P_p, P_e, P_\gamma) = \sum_{a,b,c} \int dx_e \int dx_p \int dz\, F_{a/e}(x_e, M) F_{b/p}(x_p, M_p) D_{\gamma/c}(z, M_F) \\ d\hat{\sigma}^{ab\to cX}(x_p P_p, x_e P_e, P_\gamma/z, \mu, M, M_p, M_F)\ , \quad (1)$$

where M, M_p are the initial state factorization scales, M_F the final state factorization scale, μ the renormalization scale and a, b, c run over parton types. In the NLO calculations shown in Fig. 4, all these scales are set equal to p_T^γ and varied simultaneously. The functions $F_{b/p}(x_p, M_p)$ are the parton distribution functions in the proton, obeying DGLAP evolution. Note that including initial state radiation at NLO in the partonic calculation means that the partons taking part in the hard interaction can pick up a nonzero transverse momentum. In certain cases, this additional "k_T-kick" seems to be sufficient to describe the data well. For example, a study of the effective transverse momentum $\langle k_T \rangle$ of partons in the proton has been made by ZEUS [11]. Comparing the shapes of normalized distributions for $\langle k_T \rangle$-sensitive observables to an NLO calculation, it was found that the data agree well with NLO QCD without extra intrinsic $\langle k_T \rangle$ [8].

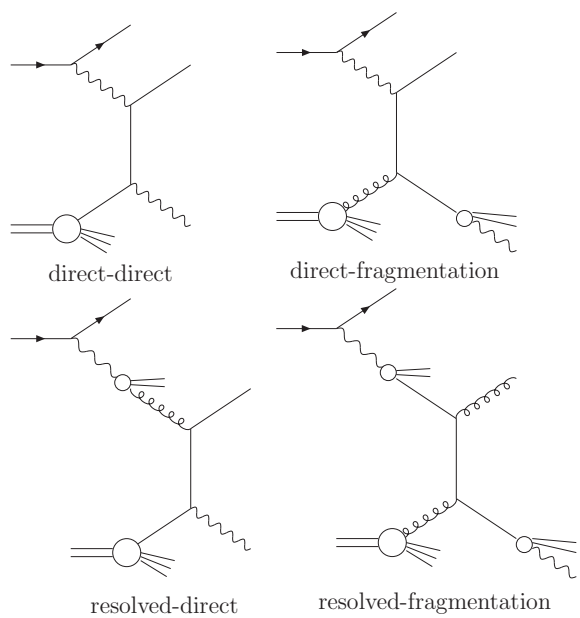

Fig. 3: Examples of contributing subprocesses at leading order to each of the four categories in ep collisions.

The "resolved" contributions are characterized by a resolved photon in the initial state where a parton stemming from the photon instead of the photon itself participates in the hard subprocess. In these cases, $F_{a/e}(x_e, M)$ is given by a convolution of the Weizsäcker-Williams spectrum $f^e_\gamma(y)$ with the parton distributions in the photon:

$$F_{a/e}(x_e, M) = \int_0^1 dy\, dx_\gamma\, f^e_\gamma(y)\, F_{a/\gamma}(x_\gamma, M)\, \delta(x_\gamma y - x_e)\ . \tag{2}$$

The cases with "direct" attributed to the initial state photon correspond to $a = \gamma$, so $F_{a/\gamma} = \delta(1 - x_\gamma)$ and $F_{a/e}$ in eq. (2) collapses to the Weizsäcker-Williams spectrum. The cases "direct-direct" and "resolved-direct" correspond to $c = \gamma$, so $D_{\gamma/c}(z, M_F) = \delta_{c\gamma}\delta(1 - z)$ in (1), i.e. the prompt photon is produced directly in the hard subprocess and not from the fragmentation of a hard parton.

If additional jets are measured, eq. (1) also contains a jet function, which defines the clustering of the final state partons other than the photon into jets. Prompt photon production in association with a jet offers more possibilities to probe the underlying parton dynamics. It allows for the definition of observables that provide information about the longitudinal momentum fractions x^γ, x^p carried by the particles taking part in the hard interaction. The partonic x^γ, x^p are not observable, but one can define the observables

$$\begin{aligned} x^\gamma_{obs} &= \frac{p^\gamma_T\, \mathrm{e}^{-\eta^\gamma} + p^{\mathrm{jet}}_T\, \mathrm{e}^{-\eta^{\mathrm{jet}}}}{2E^\gamma}\ , \\ x^p_{obs} &= \frac{p^\gamma_T\, \mathrm{e}^{\eta^\gamma} + p^{\mathrm{jet}}_T\, \mathrm{e}^{\eta^{\mathrm{jet}}}}{2E^p}\ , \end{aligned} \tag{3}$$

which, for direct photons in the final state, coincide with the partonic x^γ, x^p at leading order. Unique to photoproduction processes is the possibility to "switch on/off" the resolved photon by suppressing/enhancing large x^γ. As $x^\gamma = 1$ corresponds to direct photons in the initial state, one can obtain resolved photon enriched data samples by placing a cut $x^\gamma_{obs} \leq 0.9$. Another possibility to enhance or suppress the resolved photon component is to place cuts on p_T and rapidity. From eq. (3) one can easily see that x^γ_{obs} is small at low $p^{\gamma,\mathrm{jet}}_T$ values and large rapidities. Small x^γ-enriched data samples could be used to further constrain the parton distributions in the real photon, in particular the gluon distribution, as investigated e.g. in [5]. Similarly, one can suppress the contribution from the resolved photon to probe the proton at small x^p by direct γ-p interactions [5].

In order to single out the prompt photon events from the background of secondary photons produced by the decays of light mesons, isolation cuts have to be imposed on the photon signals in the experiment. A widely used isolation criterion is the following: A photon is isolated if, inside a cone centered around the photon direction in the rapidity and azimuthal angle plane, the amount of hadronic transverse energy E^{had}_T deposited is smaller than some value $E_{T,\max}$:

$$\begin{array}{rcl} \text{for}\ \ (\eta - \eta_\gamma)^2 & + & (\phi - \phi_\gamma)^2 \leq R, \\ E^{\mathrm{had}}_T & \leq & E_{T,\max}\,. \end{array} \tag{4}$$

HERA experiments mostly used $E_{T,\max} = \epsilon\, p^\gamma_T$ with $\epsilon = 0.1$ and R = 1. Isolation not only reduces the background from secondary photons, but also substantially reduces the contribution

from the fragmentation of hard partons into high-p_T photons. When comparing the result of partonic calculation to data, photon isolation is a delicate issue. For example, a part of the hadronic energy measured in the cone may come from the underlying event; therefore even the direct contribution can be cut by the isolation condition if the latter is too stringent.

3 k_T-factorization approach

A complementary description is offered by the k_T-factorization approach [12], which relies on parton distribution functions where the k_T-dependence has not been integrated out.

In the framework of k_T-factorization approach the treatment of k_T-enhancement in the inclusive prompt photon suggests a possible modification of the above simple k_T smearing picture. In this approach the transverse momentum of incoming partons is generated in the course of non-collinear parton evolution under control of relevant evolution equations. In the papers [6, 13] the Kimber-Martin-Ryskin (KMR) formalism [14] was applied to study the role of the perturbative components of partonic k_T in describing of the observed E_T spectrum at HERA and Tevatron. The proper off-shell expressions for the matrix elements of the partonic subprocesses and the KMR-constructed unintegrated parton densities obtained independently were used in [13] to analyze the Tevatron data.

4 Comparison with HERA results

Recently published [15] ZEUS differential cross sections as functions of E_T and η for the prompt-photon candidates and for the accompanying jets have revealed some difference with both Monte Carlo predictions and the next-to-leading order (NLO) calculations based on the collinear factorization and the DGLAP formalism [3, 4], as shown in Fig. 4. The data are compared to QCD calculations performed by Krawczyk and Zembrzuski (KZ) [3], by Fontannaz, Guillet and Heinrich (FGH) [4], by A. Lipatov and N. Zotov (LZ) [6] and and PYTHIA 6.4 [16] and HERWIG 6.5 [17] Monte Carlo models. The MC differential cross sections do not rise as steeply at low E_T^γ as do the data. It should be pointed out that no intrinsic transverse momentum of the initial-state partons in the proton was assumed for these calculations. The QCD calculation [6] based on the k_T-factorization [12] and the Kimber-Martin-Ryskin (KMR) prescription [14] for unintegrated quark and gluon densities, gives the best description of the E_T and η cross sections.

In the photon-rapidity distribution of Fig. 4, the data lying above the NLO theory prediction at low values of η^γ could be explained by the fact that in this region, x^p_{obs} is small, as can be seen from Eq. (3), and therefore k_T-effects may be important. On the other hand, this is not corroborated by the jet rapidity distribution, which has a problem at high $\eta^{\rm jet}$, corresponding to small x^γ_{obs}. Indeed, a direct measurement [15] of x^γ_{obs} shows that the differences with NLO are mainly at low values of the x^γ_{obs} distribution. In this region, resolved photon events dominate, which may indicate that resolved photon remnants could have lead to an increase in the number of jets which have passed the experimental cuts, while these events are not accounted for in the partonic calculation.

The inclusive prompt photon data [18, 19] lie above the NLO theory prediction in the whole rapidity range, except for the bin of largest rapidity, where the agreement is good after hadronization corrections, see Fig. 5.

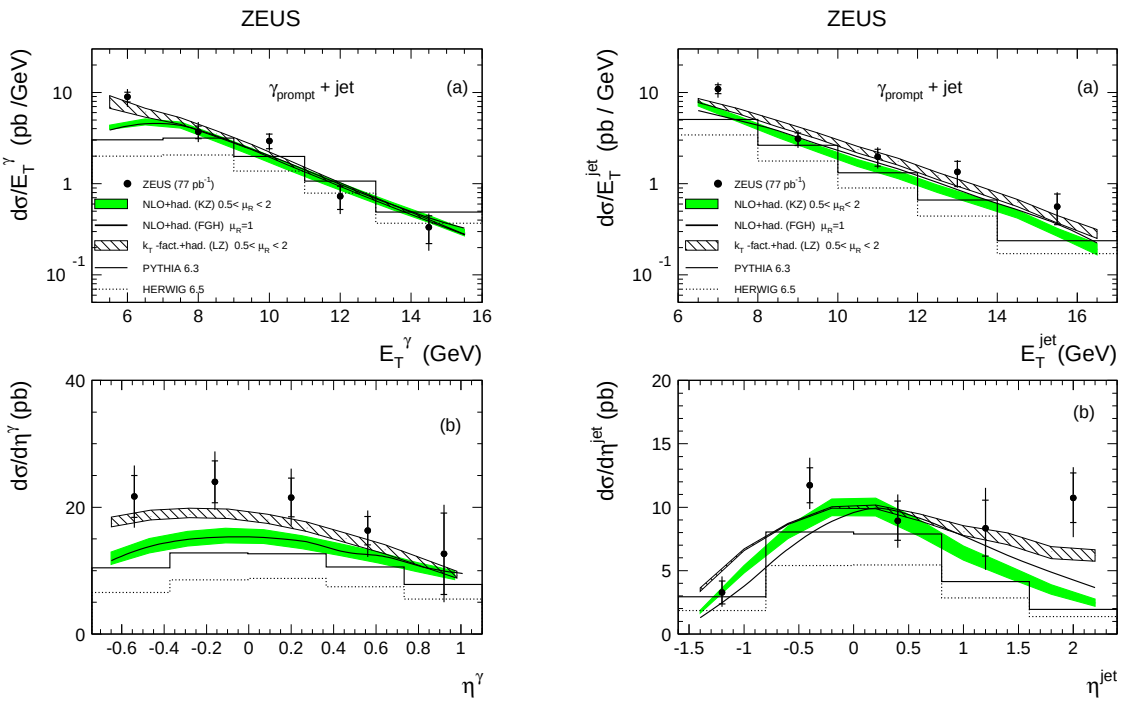

Fig. 4: The differential γ+jet cross sections as functions of E_T and η of the prompt photon and the jet. The data are compared to QCD calculations and Monte Carlo models as described in the text. The shaded bands correspond to a typical scale uncertainty which was obtained by changing the renormalization and factorization scales simultaneously by a factor of 0.5 and 2 respectively.

Interestingly, ZEUS investigated what happens if the minimum transverse energy of the prompt photon is increased to 7 GeV, and found that in this case, the NLO calculations are in good agreement [15] , which suggests that non-perturbative effects may produce the discrepancy. See [20] and references therein for more details.

The H1 experimental data in photoproduction [18] are shown in Figs. 5 and 6. Both inclusive and γ+jet cross sections were compared to the FGH NLO calculations after hadronization corrections. The H1 data [18] referred to the kinematic region defined by $5 < E_T^\gamma < 10$ GeV, $-1 < \eta^\gamma < 0.9$ and $0.2 < y < 0.7$, which is rather similar to the ZEUS measurement shown in Fig. 4. Similar to the ZEUS case, MC predictions were found to underestimate the H1 cross sections, while NLO QCD gives a much better description. After taking into account hadronization and multiple interaction effects, NLO calculations predict somewhat smaller cross sections compared the measurements [18].

The H1 experimental data in photoproduction [18] were also compared to the k_T-factorization approach [6]. Comparison with the k_T factorization approach indicates somewhat better agreement, as shown in Fig. 7 (see [6] for details). One can see that the measured distributions are reasonably well described except the moderate E_T^γ region and in the pseudorapidity region

$-0.4 \leq \eta^\gamma \leq 0.9$ only. For $-1 \leq \eta^\gamma \leq -0.4$ the k_T-factorization predictions are mostly below the experimental points. The discrepancy between data and theory at negative η^γ is found to be relatively strong at low values of the initial photon fractional momentum y. The effect of scale variations in transverse energy distributions is rather large: the relative difference between results for $\mu = E_T^\gamma$ and results for $\mu = E_T^\gamma/2$ or $\mu = 2E_T^\gamma$ is about 15% within the k_T-factorization approach, which is due to missing higher order corrections. The scale dependence of the NLO QCD calculations in the collinear factorization approach is below the 10% level.

The individual contributions from the direct and resolved production mechanisms to the total cross section in the k_T-factorization approach is about 47% and 53%, respectively. The contributions of single resolved processes

$$q(k_1) + g(k_2) \to \gamma(p_\gamma) + q(p'),$$

$$g(k_1) + q(k_2) \to \gamma(p_\gamma) + q(p'),$$

$$q(k_1) + q(k_2) \to \gamma(p_\gamma) + g(p').$$

account for 80%, 14% and 6% respectively.

The transverse energy E_T^γ and pseudorapidity η^γ distributions for γ+jet events measured by H1 are compared to the k_T-factorization predictions in Fig. 8 (see also Ref. [6]). In contrast to the inclusive case, one can see that the k_T-factorization predictions are consistent with the data in most bins, although some discrepancies are present. The theoretical results are lower than the experimental data at negative η^γ and higher at positive η^γ. The scale variation as it was described above changes the estimated cross sections by about 10%. Note that such disagreement between predicted and measured cross sections has also been observed for the NLO QCD calculations in the collinear factorization approach, see Fig. 6.

Figure 9 shows the x_{obs}^γ and x_{obs}^p distributions (see Eq. 3) measured by H1. One can see that k_T factorization predictions reasonably well agree with the experimental data. The NLO calculations [3, 4] without corrections for hadronization and multiple interactions give similar results.

The H1 Collaboration [21] also has performed γ+jet measurements in DIS for $Q^2 > 4$ GeV^2. The NLO calculations [22], which are only available for γ+jet final state, failed to describe normalization of the cross sections, although the agreement in shape was found to be reasonable (Fig. 10). No k_T factorization prediction available for DIS.

In summary, some differences with NLO QCD were observed in both photoproduction and DIS. Differences at low P_T^γ can be due to the treatment of the fragmentation contribution in NLO calculations. Further, it would be interesting to see the effect of calculations beyond NLO QCD. The approach based on the k_T factorization has better agreement with the data, but such calculations have larger theoretical uncertainties.

5 Comparison with Tevatron results

Isolated photons in $p\bar{p}$ collisions at Tevatron have been measured recently by the CDF [23, 24] and D0 [25–28] Collaborations.

Measurements of $p\bar{p} \to \gamma + \text{jet} + X$ for 30 GeV $\leq p_T^\gamma \leq 300$ GeV have very recently been published by D0 [28]. The comparison to theory is done separately for different regions in rapidity of the photon and the jet. The NLO partonic Monte Carlo program JETPHOX [9, 29] was used to compare the data to theory at next-to-leading order. It was shown that the NLO calculations are not sufficient to describe the shape of P_T^γ distributions in different rapidity regions, as can be seen in Figure 11. At present, the comparison with the k_T-factorization prediction is in progress.

Differences with the collinear factorization approach have been seen previously as well. Both CDF [23] and D0 [26] cross sections were found to be above[1] NLO predictions at low P_T^γ. However, RHIC has also measured prompt photon production in pp collisions at $\sqrt{s} = 200$ GeV and found good agreement with NLO theory in the collinear factorization approach [20, 30].

The same data were compared to the k_T factorization approach in [13]. Figures 12 and 13 show the CDF [23] and D0 [26] measurements for the $d\sigma/dE_T^\gamma d\eta^\gamma$ cross sections calculated at $\sqrt{s} = 630$ and 1800 GeV in central and forward kinematic regions together with the k_T factorization predictions. One can see that theoretical predictions agree with the experimental data within the scale uncertainties. However, the results of the calculation with the default scale tend to underestimate the data in the central kinematic region and agree with the D0 data in the forward η^γ region. The collinear NLO QCD calculations give a similar description of the data: generally there is a residual negative slope in the ratio of the data over the prediction as a function of E_T^γ. The scale dependence of the k_T factorization results is rather large ($20 - 30\%$), due to the fact that these are leading order calculations.

The double differential cross sections $d\sigma/dE_T^\gamma d\eta^\gamma$ are usually the most difficult observables to describe using QCD predictions. Yet, as it can be seen from Fig. 13, the k_T-factorization predictions agree well with D0 [25] and CDF [23] data both in shape and normalization. There are only rather small overestimations of the data at low E_T^γ values in Figs. 13 in the forward region. Again, the scale dependence of our calculations is about 20–30%. The theoretical uncertainties of the collinear NLO predictions are smaller (about 6% [25]), which is to be expected as inclusion of higher order terms reduces the scale uncertainty.

One can conclude that the results of calculations in the k_T-factorization approach in general agree well with Tevatron experimental data, within a large scale uncertainty.

6 Prompt photons at LHC

The direct photon production at LHC has significantly higher cross sections compared to the ones measured at Tevatron and HERA. The prompt-photon cross section at LHC is more than a factor of hundred higher than that at Tevatron and a factor of 10^5 larger than that for photoproduction at HERA, assuming a similar kinematic range ($\mid \eta^\gamma \mid < 2$), as shown in Fig. 14. This will allow to explore the TeV energy scale already in a few years of data taking.

Figure 15 shows the comparison between PYTHIA and HERWIG Monte Carlo models and JETPHOX LO and NLO calculations. The cross sections for $\gamma + jet$ events were calculated for $\mid \eta^\gamma \mid < 2$, $P_T^\gamma > 100$ GeV and $P_T^{jet} > 105$ GeV. The cuts on the transverse momenta are asymmetric to avoid instabilities in the NLO calculations. An isolation requirement $E_T^\gamma >$

[1] For D0, the difference was mainly concentrated in the central rapidity region.

$0.9\,E_T^{tot}$ was imposed, where E_T^{tot} is the total energy of the jet which contains prompt photon. Jets were reconstructed with the longitudinally-invariant k_T algorithm in inclusive mode [31].

The NLO QCD calculation is 30–40% higher than that predicted by PYTHIA. On the other hand, PYTHIA is 20% above HERWIG. It is interesting to observe that the level of discrepancy between PYTHIA and HERWIG is about the same as that observed at HERA at much lower transverse momenta (for example see Fig. 4). However, there is no significant difference between NLO and PYTHIA at $P_T^\gamma > 10$ GeV for ep, while at the LHC energy range the difference between NLO and PYTHIA is rather significant. Certainly, the overall normalization of Monte Carlo programs like PYTHIA or HERWIG has to be adjusted, as these programs cannot account for contributions from loop corrections at higher orders.

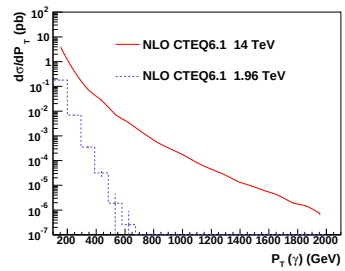

Fig. 14: The P_T^γ cross section for γ+jet events predicted by NLO QCD for the Tevatron and the LHC kinematic range.

Scale uncertainties were estimated by changing the renormalization and factorization scales in the range $0.5 < \mu_f, \mu_R < 2$. The relative difference between predicted cross sections is shown in Fig. 16. To make quantitative statements on scale uncertainties with the present level of statistical errors in calculations using JETPHOX, a linear fit was performed to determine the trend of the relative differences with increase of P_T^γ. As it can be seen, the scale uncertainty is about 10% and slowly increases with P_T^γ .

To estimate the uncertainty associated with the gluon density, the calculations have been performed using two CTEQ6.1M sets (15 and 30) which correspond to two extremes in the gluon density at large x [32]. Fig. 17 shows the relative difference between those two sets as a function of P_T^γ. It is seen that the gluon uncertainty is almost a factor of two larger compared to the scale uncertainty estimated above. No statistically significant difference has been observed between the cross sections calculated using CTEQ6.1M and MRST04. This is not totally surprising as both sets have similar input data for the global fit analysis.

The predictions for the k_T factorization approach were obtained for a wider pseudorapidity range, for both central and forward pseudo-rapidities η^γ. As a representative example, we will define the central and forward kinematic regions by the requirements $|\eta^\gamma| < 2.5$ and $2.5 < |\eta^\gamma| < 4$, respectively. The transverse energy E_T^γ distributions of the inclusive prompt photon production in different η^γ ranges at $\sqrt{s} = 14$ TeV are shown in Figs. 18. One can see that variation in scale μ changes the estimated cross sections by about 20–30%. However, as it was already discussed above, there are additional theoretical uncertainties due to the non-collinear parton evolution, and these uncertainties are not well studied up to this time. Also the extrapolation of the available parton distribution to the region of lower x is a special problem at the LHC energies. In particular, one of the problem is connected with the correct treatment of saturation effects in small x region. Therefore, more work needs to be done until these uncertainties will be reduced.

Thus, the calculation based on the k_T factorization approach shows a larger scale uncertainty compared to the collinear factorization approach: for $P_T^\gamma \sim 100$ GeV, the overall uncertainty for the NLO calculations is expected to be around 10%, while it reaches 20–30% for the

k_T-factorization calculations for the same P_T^γ range, due to the fact that the latter are at leading order in α_s. As the residual scale dependence of missing higher order terms resides in logarithms involving ratios of P_T^2 and scales μ^2, the effect becomes more dramatic at the LHC energy.

7 Summary

In this review, we have attempted to summarize recent progress in the description of prompt photon production at HERA, the Tevatron and the LHC. At HERA, some differences with NLO were observed in both photoproduction and DIS. The deficiencies at low P_T^γ values may indicate that non-perturbative effects at small P_T^γ play a non-negligible role. Also, one should expect that adding high-order corrections to the collinear-factorization approach should improve the description. Similar conclusions can be drawn for the Tevatron data which, as in the HERA case, has differences with NLO in the lowest P_T^γ region. Recently, significant differences with NLO were observed by the Tevatron for the shapes of P_T^γ distributions differential in η^γ. On the other hand, RHIC observes good agreement with NLO QCD. Considering the fact that RHIC uses a photon isolation method which is different from the usual cone isolation, the differences mentioned above may also have to do with isolation criteria acting differently in a partonic calculation than in the full hadronic environment of the experiment.

An alternative approach based on the k_T factorization generally improves the description of the HERA and the Tevatron data, but it has larger theoretical uncertainties. As for NLO, high-order corrections to the k_T-factorization approach should improve the description of the data. The applicability of the k_T factorization to the LHC data will be tested with the arrival of the first LHC data, but it is already evident that significant theoretical uncertainties are expected for the description of prompt-photon cross sections at LHC. Using the the collinear factorization approach, uncertainties of NLO calculations are expected to be 10–20% at about 1 TeV photon transverse momenta, and significantly larger for the k_T-factorization calculations. These uncertainties have to be reduced in the future for detailed comparison of the LHC data with the QCD predictions.

In all cases, PYTHIA and HERWIG predictions fail to describe prompt-photon cross sections, both in shape and normalization. Generally, HERWIG is significantly below PYTHIA. This could have a direct impact on the future LHC measurements, in particular for exotic searches which often rely on Monte Carlo predictions for estimations of rates for background events.

Acknowledgments. This work supported in part by the U.S. Department of Energy, Division of High Energy Physics, under Contract DE-AC02-06CH11357.

References

[1] J. F. Owens, Rev. Mod. Phys. **59**, 465 (1987).

[2] L. Gordon and W. Vogelsang, Phys. Rep. **D52**, 58 (1995).

[3] M. Krawczyk and A. Zembrzuski, Phys. Rev. **D64**, 14017 (2001).

[4] M. Fontannaz, J. P. Guillet, and G. Heinrich, Eur. Phys. J. **C21**, 303 (2001).

[5] M. Fontannaz and G. Heinrich, Eur. Phys. J. **C 34**, 191 (2004).

[6] A. Lipatov and N. Zotov, Phys. Rev. **D72**, 054002 (2005).

[7] C. F. von Weizsacker, Z. Phys. **88**, 612 (1934).
E. J. Williams, Phys. Rev. **45**, 729 (1934).

[8] M. Fontannaz, J. P. Guillet, and G. Heinrich, Eur. Phys. J. **C 22**, 303 (2001).

[9] PHOX programs. Available at http://lappweb.in2p3.fr/lapth/phox_family/main.html.

[10] A. Zembrzuski and M. Krawczyk, Photoproduction of isolated photon and jet at the DESY HERA, 2003, hep-ph/0309308.

[11] ZEUS Collaboration, S. Chekanov *et al.*, Phys. Lett. **B511**, 19 (2001).

[12] E. M. Levin *et al.*, Sov. J. Nucl. Phys. **53**, 657 (1991).
S. Catani, M. Ciafaloni, and F. Hautmann, Nucl. Phys. **B366**, 135 (1991).
J. Collins and R. Ellis, Nucl. Phys. **B360**, 3 (1991).

[13] A. V. Lipatov and N. P. Zotov, J. Phys. **G34**, 219 (2007).

[14] M. A. Kimber, A. D. Martin, and M. G. Ryskin, Phys. Rev. **D63**, 114027 (2001).
G. Watt, A. D. Martin, and M. G. Ryskin, Eur. Phys. J. **C31**, 73 (2003).

[15] ZEUS Collaboration, S. Chekanov *et al.*, Eur. Phys. J. **C49**, 511 (2007).

[16] T. Sjostrand, S. Mrenna, and P. Skands, JHEP **05**, 026 (2006).

[17] G. Corcella *et al.*, JHEP **01**, 010 (2001).
G. Corcella *et al.*, (2002), hep-ph/0210213.

[18] H1 Collaboration, A. Aktas *et al.*, Eur. Phys. J. **C38**, 437 (2005).

[19] ZEUS Collaboration, J. Breitweg *et al.*, Phys. Lett. **B472**, 175 (2000).

[20] G. Heinrich, Proceedings of the International Conference Photon2007, Paris, France (2007).

[21] H1 Collaboration, F. D. Aaron *et al.*, Eur. Phys. J. **C54**, 371 (2008).

[22] A. Gehrmann-De Ridder, G. Kramer, and H. Spiesberger, Nucl. Phys. **B578**, 326 (2000).

[23] CDF Collaboration, D. E. Acosta *et al.*, Phys. Rev. **D65**, 112003 (2002).

[24] CDF Collaboration, D. E. Acosta *et al.*, Phys. Rev. **D70**, 074008 (2004).

[25] D0 Collaboration, B. Abbott *et al.*, Phys. Rev. Lett. **84**, 2786 (2000).

[26] D0 Collaboration, V. M. Abazov *et al.*, Phys. Rev. Lett. **87**, 251805 (2001).

[27] D0 Collaboration, V. M. Abazov *et al.*, Phys. Lett. **B639**, 151 (2006).

[28] D0 Collaboration, V. M. Abazov *et al.*, (2008), hep-ex/0804.1107.

[29] P. Aurenche, M. Fontannaz, J.-P. Guillet, E. Pilon, and M. Werlen, Phys. Rev. **D73**, 094007 (2006).

[30] PHENIX Collaboration, S. S. Adler *et al.*, Phys. Rev. Lett. **98**, 012002 (2007).

[31] S. Ellis and D. Soper, Phys. Rev. **D48**, 3160 (1993).
S. Catani *et al.*, Nucl. Phys. **B406**, 187 (1993).

[32] D. Stump *et al.*, JHEP **310**, 46 (2003).

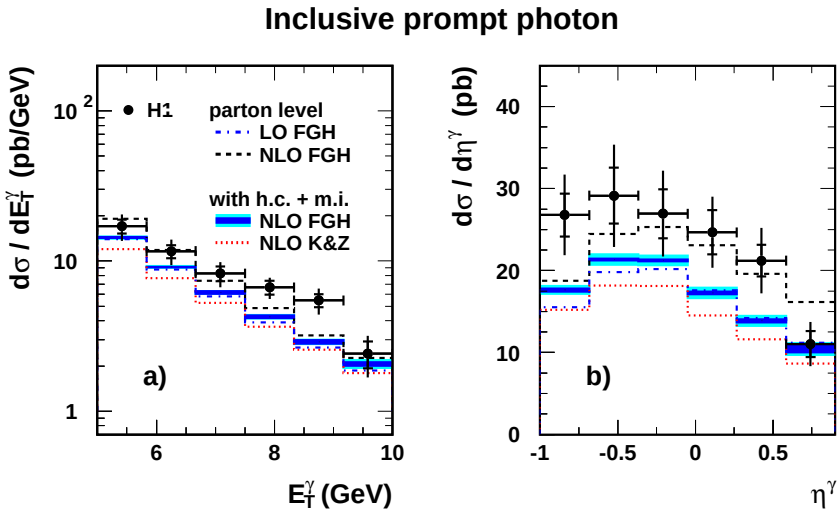

Fig. 5: The differential cross section $d\sigma/dE_T$ and $d\sigma/d\eta^\gamma$ as functions of E_T^γ and η^γ of the inclusive prompt photon photoproduction calculated at $-0.7 < \eta^\gamma < 0.9$ and $0.2 < y < 0.9$. The data are compared to two different NLO calculations.

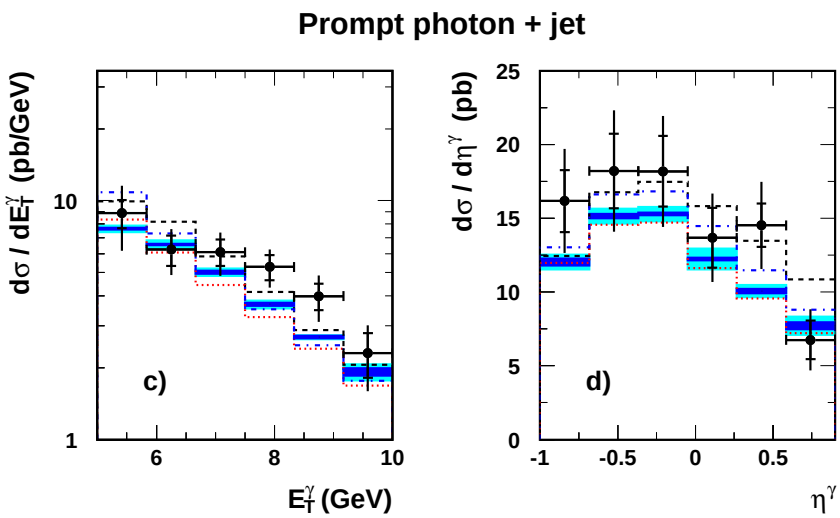

Fig. 6: Same as in Fig. 5, but for γ+jet events with the additional jet cuts: $-1 < \eta^{\rm jet} < 2.3$ and $E_T^{\rm jet} > 4.5$ GeV.

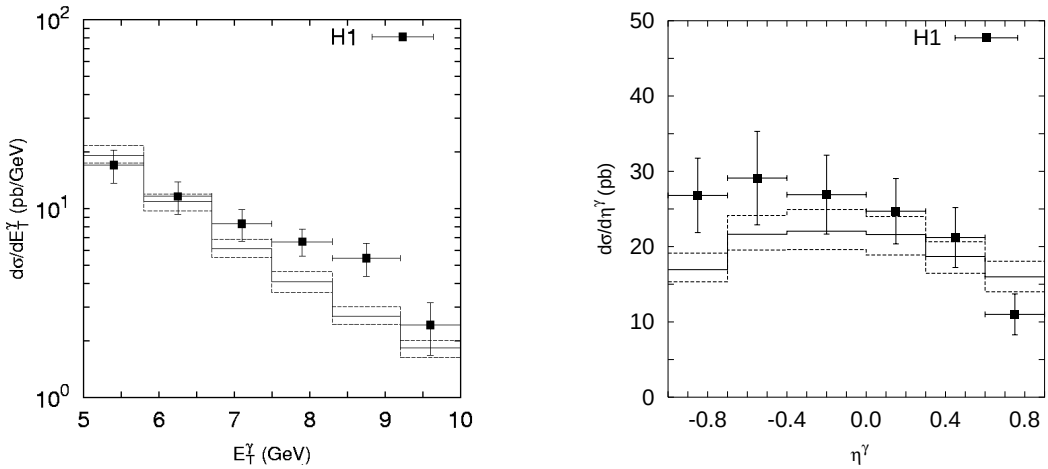

Fig. 7: The differential cross section $d\sigma/dE_T$ and $d\sigma/d\eta^\gamma$ as functions of E_T^γ and η^γ of the inclusive prompt photon photoproduction calculated at $-0.7 < \eta^\gamma < 0.9$ and $0.2 < y < 0.9$. The data are compared to the k_T- factorization calculations. The bands correspond to a typical renormalization scale uncertainty which was obtained by changing μ_R by a factor of 0.5 and 2.

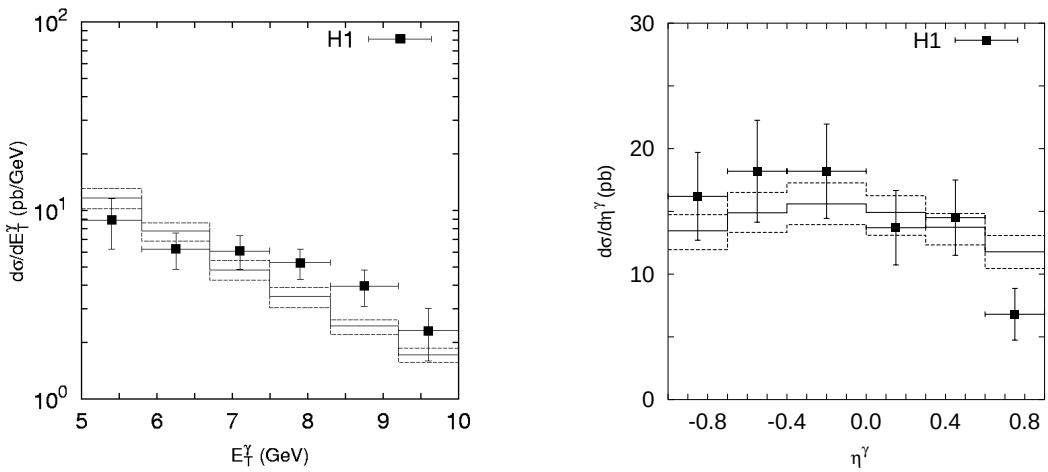

Fig. 8: Same as Fig. 7, but for γ+jet events with the additional jet cuts: $-1 < \eta^{\rm jet} < 2.3$ and $E_T^{\rm jet} > 4.5$ GeV.

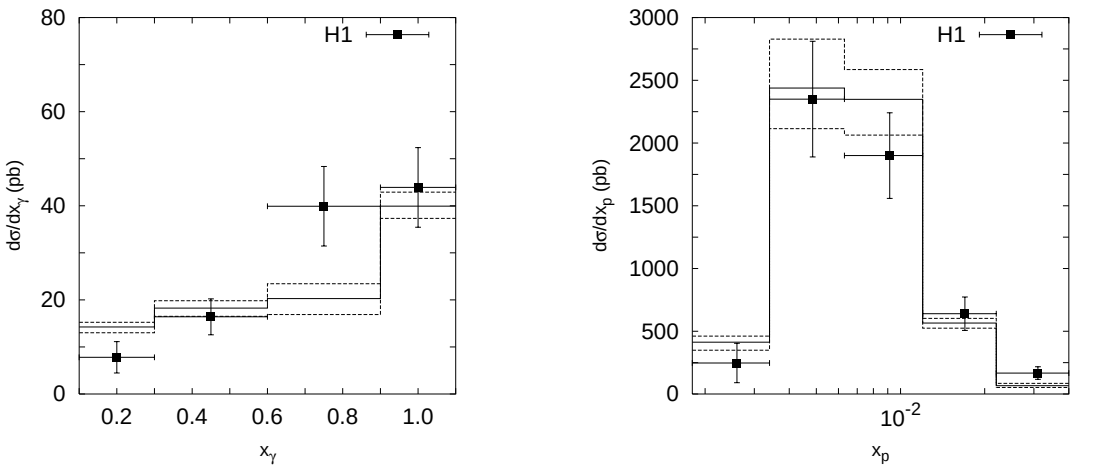

Fig. 9: The differential cross section $d\sigma/dx_\gamma$ and $d\sigma/dx_p$ of prompt photon + jet production calculated at $5 < E_T^\gamma < 10$ GeV and $0.2 < y < 0.7$ with an additional jet requirement $-1 < \eta^{\rm jet} < 2.3$ and $E_T^{\rm jet} > 4.5$ GeV.

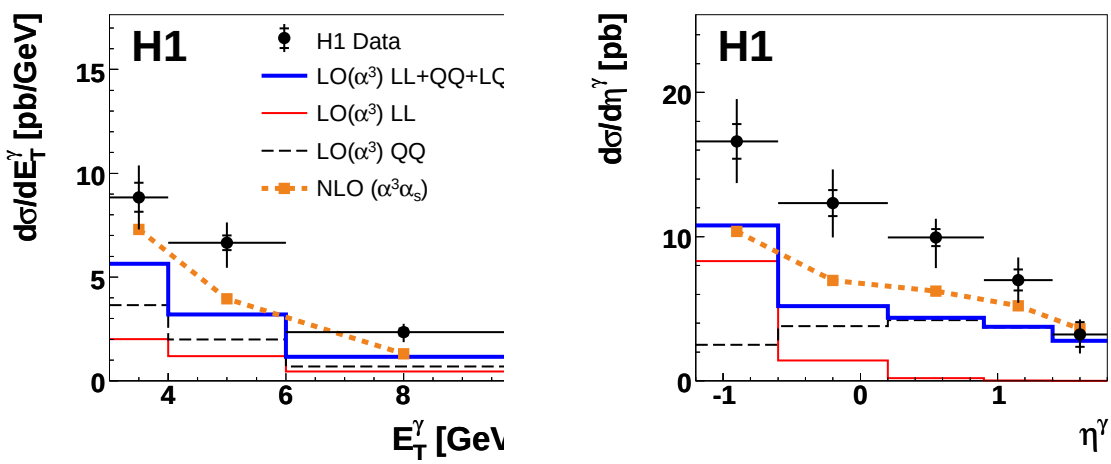

Fig. 10: The differential γ+jet cross sections as functions of E_T and η of the prompt photon in DIS. The data are compared to LO and NLO calculations.

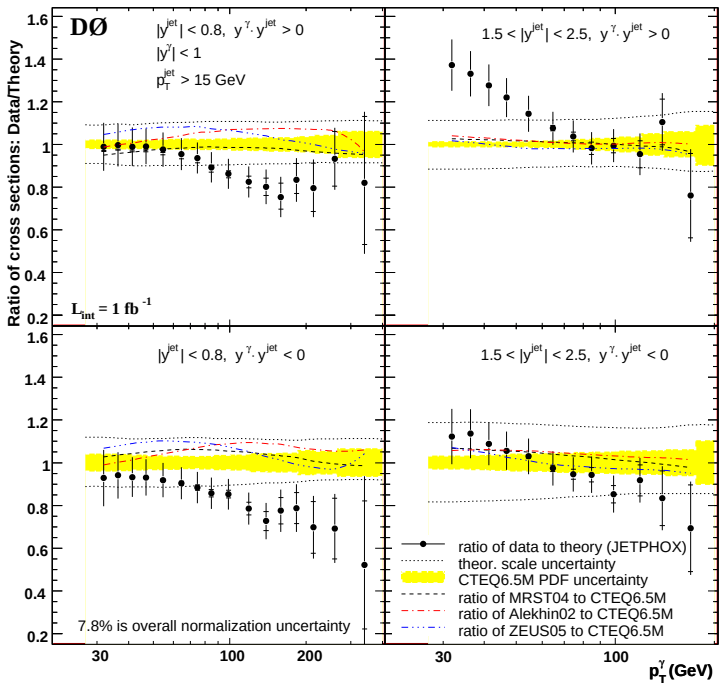

Fig. 11: The ratios of the triple-differential cross section measured by D0 compared to to the NLO QCD prediction using JETPHOX. See details in Ref. [28].

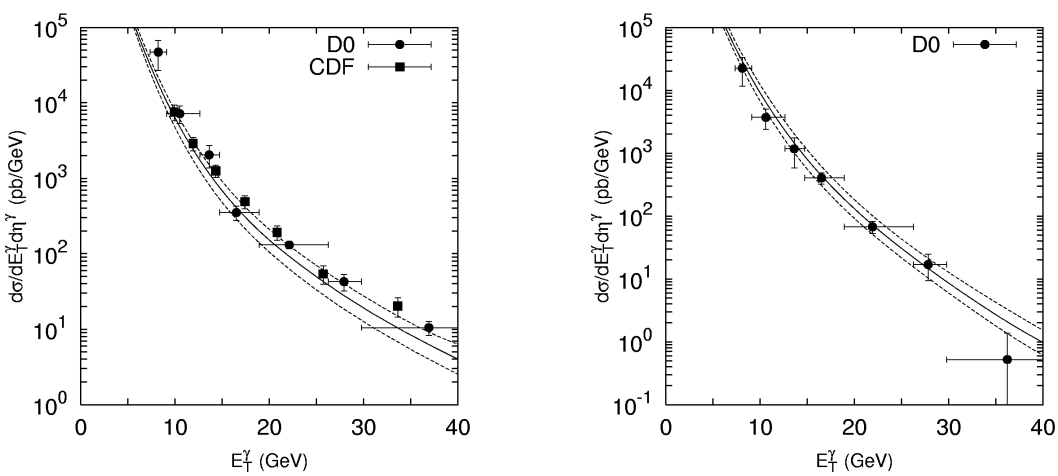

Fig. 12: The double differential cross section $d\sigma/dE_T^{\gamma}d\eta^{\gamma}$ of inclusive prompt photon production at $\sqrt{s} = 630$ GeV and $|\eta^{\gamma}| < 0.9$ (left plot) and $1.6 < |\eta^{\gamma}| < 2.5$ (right panel). The solid line corresponds to the default scale $\mu = E_T^{\gamma}$ of the k_T factorization predictions, whereas upper and lower dashed lines correspond to the $\mu = E_T^{\gamma}/2$ and $\mu = 2E_T^{\gamma}$.

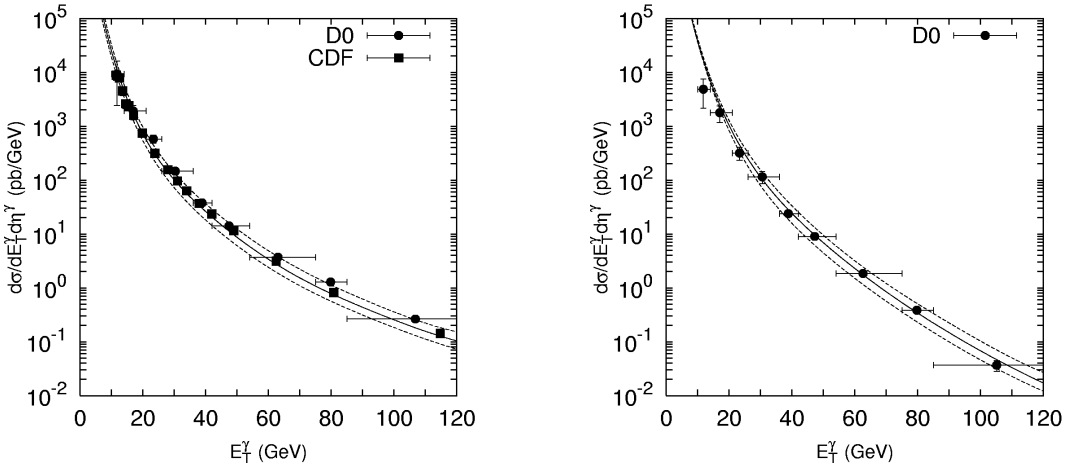

Fig. 13: The double differential cross section $d\sigma/dE_T^\gamma d\eta^\gamma$ of inclusive prompt photon production at $\sqrt{s} = 1800$ GeV and $|\eta^\gamma| < 0.9$ (left plot) and $1.6 < |\eta^\gamma| < 2.5$ (right plot). The solid line corresponds to the default scale $\mu = E_T^\gamma$, whereas upper and lower dashed lines correspond to the $\mu = E_T^\gamma/2$ and $\mu = 2E_T^\gamma$ for the k_T factorization calculations.

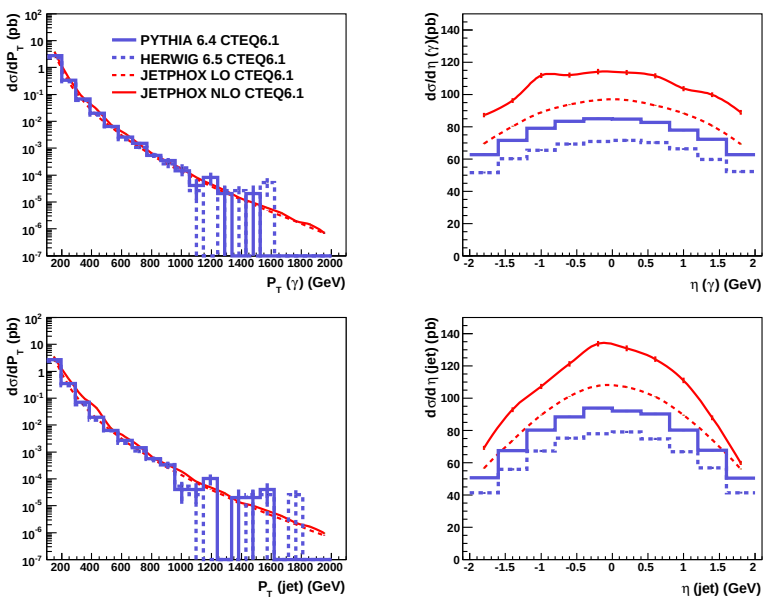

Fig. 15: Comparisons of Monte Carlo models with LO and NLO calculations as implemented in JETPHOX.

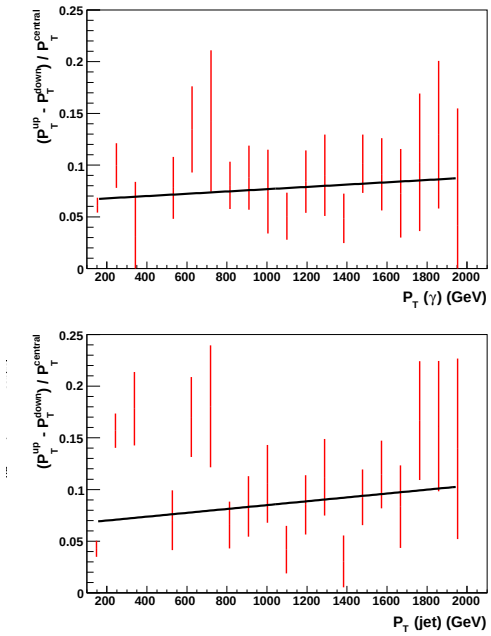

Fig. 16: Relative difference between the cross section estimated with $\mu = 0.5$ (P_T^{up}) and $\mu = 2$ (P_T^{down}) as a function of P_T for gamma and jet. The line represents a linear fit.

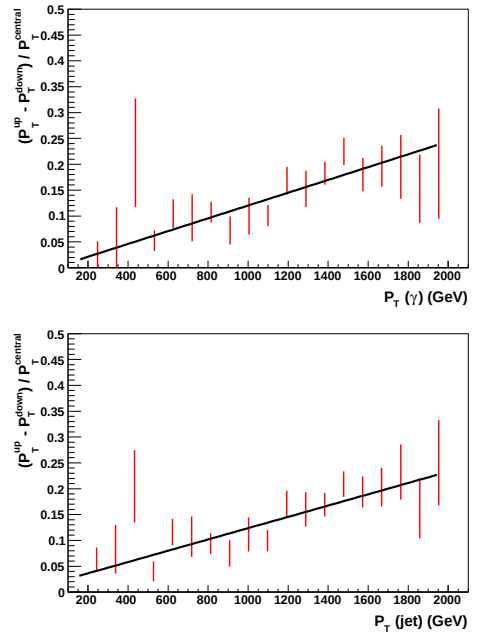

Fig. 17: Relative difference between the cross section estimated with CTEQ6.1M set=-15 (P_T^{up}) and set =15 (P_T^{down}) as a function of P_T for gamma and jet. The line represents a linear fit.

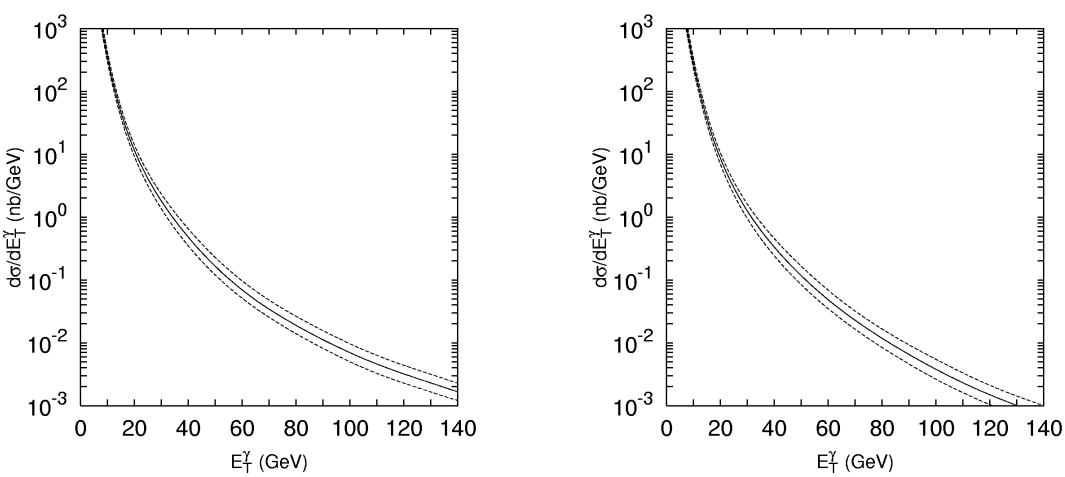

Fig. 18: Left plot: The k_T factorization predictions for differential cross sections $d\sigma/dE_T^\gamma d\eta^\gamma$ at $\sqrt{s} = 14$ TeV GeV and $|\eta^\gamma| < 2.5$ (left plot); at $2.5 < \eta^\gamma < 4.0$ (right plot). The solid line corresponds to the default scale $\mu = E_T^\gamma$, whereas upper and lower dashed lines correspond to the $\mu = E_T^\gamma/2$ and $\mu = 2E_T^\gamma$.

Propagation of Uncertainty in a Parton Shower*

Philip Stephens† *and André van Hameren*‡
†Kennesaw State University, Department of Physics, 1000 Chastain Road, Kennesaw, GA 30144, USA
‡The H. Niewodniczański Institute of Nuclear Physics, Polish Academy of Sciences, Radzikowskiego 152, 31-342 Kraków, Poland

Abstract
Presented here is a technique of propagating uncertainties through the parton shower by means of an alternate event weight. This technique provides a mechanism to systematically quantify the effect of variations of certain components of the parton shower leading to a novel approach to probing the physics implemented in a parton shower code and understanding its limitations. Further, this approach can be applied to a large class of parton shower algorithms and requires no changes to the underlying implementation.

1 Introduction

As we enter a new era of particle physics, precise knowledge of quantum chromodynamics (QCD) will become increasingly important in order to understand the physics beyond the standard model. Currently, one of the most useful tools for studying QCD is the parton shower approximation. This tool provides a mechanism to connect few-parton states to the real world of high-multiplicity hadronic final states while retaining the enhanced collinear and soft contributions to all orders.

Use of parton shower Monte Carlos (MC) has become common-place. Often, when one needs an estimate of the uncertainty of a MC prediction several different MC programs are used and the differences between them is considered the error [1]. Though this technique of estimating the error of the MC is generally acceptable, it does little to provide insight into the physics. It has been shown [2] that the uncertainties in both the perturbative expansion and the parton distribution functions indeed can lead to effects of the order of ten percent. We propose here a technique in which the known uncertainties of the physics can be propagated through the parton shower framework. This technique provides alternate weights to an event generated by a MC without having to change the basic structure of the MC program. We feel this technique could be valuable when determining how various improvements in the parton shower will impact the MC predictions. Furthermore, this gives a more satisfactory description of the errors in a MC prediction.

*This work is partly supported by the EU grant mTkd-CT-2004-510126 in partnership with the CERN Physics Department and by the Polish Ministry of Scientific Research and Information Technology grant No 620/E-77/6.PRUE/DIE 188/2005-2008.

2 Variation of Parton Shower

In many parton showers [3–6] one starts with the fundamental probability density (for one emission) defined as

$$\mathcal{P} = f_R(\vec{y}) \exp\left(- \int^{\xi(\vec{y})} d^n \vec{y'} f_V(\vec{y'}) \right). \tag{1}$$

Here the function $f_R(\vec{y})$ is the distribution of the real emission while $f_V(\vec{y})$ is the virtual contribution. In both cases the precise definition of $\vec{y}$ is specific to the implementation. Furthermore, the limits of integration in the virtual component are also specific to the implementation: how the infra-red limit is treated, the definition of resolvable versus unresolvable emissions and the ordering of variables. For a time-like shower $f_R = f_V$ and is given by

$$f_R(\vec{y}) = \frac{\alpha_S(g(\vec{y}))}{2\pi} P(\vec{y}), \tag{2}$$

where $g(\vec{y})$ is some abstract function used to determine the scale of the running coupling. We find a similar result for the constrained MC [5]; for a space-like shower using the backward evolution algorithm we find $f_R = f_V f(x, \vec{y})$ and

$$f_V(\vec{y}; x) = \frac{\alpha_S(g(\vec{y}))}{2\pi} \frac{f(x/z, \vec{y})}{f(x, \vec{y})} P(\vec{y}), \tag{3}$$

where $f(x, \vec{y})$ is the PDF at energy fraction x and scale given by some combination of the components of $\vec{y}$. We can explicitly see that one of the components of $\vec{y}$ is z, a momentum fraction.

In the forward (time-like) evolution algorithm, as well as the non-Markovian algorithm, $P(\vec{y})$ is just the Alteralli-Parisi [7] splitting function divided by the scale. In the numerical results here we consider only the forward evolution algorithm; in the last section we propose a use for this technique in a backward evolution algorithm for CCFM.

We now define a functional to represent our functions $f_R(\vec{y})$ and $f_V(\vec{y})$

$$F_R[\boldsymbol{\varphi}(\vec{y})] = f_R(\vec{y})\,;\; F_V[\boldsymbol{\varphi}(\vec{y})] = f_V(\vec{y}). \tag{4}$$

Here $\boldsymbol{\varphi}(\vec{y})$ are the functional components of $F_{R/V}$ which we want to vary (e.g. the running coupling or the kernel). This defines the distribution of one branching as

$$\mathcal{P}[\boldsymbol{\varphi}(\vec{y})] = F_R[\boldsymbol{\varphi}(\vec{y})] \exp\left(- \int^{\xi(\vec{y})} d^n \vec{y'} F_V[\boldsymbol{\varphi}(\vec{y'})] \right). \tag{5}$$

We can find the variation of this by

$$\delta\mathcal{P} = \mathcal{P}[(\boldsymbol{\varphi} + \delta\boldsymbol{\varphi})(\vec{y})] - \mathcal{P}[\boldsymbol{\varphi}(\vec{y})]. \tag{6}$$

If we define

$$\delta F_{R/V} = F_{R/V}[(\boldsymbol{\varphi} + \delta\boldsymbol{\varphi})(\vec{y})] - F_{R/V}[\boldsymbol{\varphi}(\vec{y})], \tag{7}$$

then

$$\delta\mathcal{P} = \mathcal{P}\left(1 + \frac{\delta F_R}{F_R}\right) \exp\left(- \int^{\xi(\vec{y})} d^n \vec{y'} \delta F_V \right) - \mathcal{P}, \tag{8}$$

from which we have a weight

$$w \equiv \frac{\mathcal{P}+\delta\mathcal{P}}{\mathcal{P}} = \left(1+\frac{\delta F_R}{F_R}\right)\exp\left(-\int^{\xi(\vec{y})} d^n\vec{y}'\delta F_V\right). \tag{9}$$

The weights defined in eqn. (9) are relative to the original probability density for one emission. To get the total weight for the full event, we must consider

$$\mathcal{P}_E[\boldsymbol{\varphi},\{\vec{y}_i\}] = \prod_i \mathcal{P}[\boldsymbol{\varphi}(\vec{y}_i)], \tag{10}$$

and thus

$$\delta\mathcal{P}_E = \mathcal{P}_E[\boldsymbol{\varphi}+\delta\boldsymbol{\varphi},\{\vec{y}_i\}] - \mathcal{P}_E[\boldsymbol{\varphi},\{\vec{y}_i\}]. \tag{11}$$

This leads to a total event weight given by

$$w_E \equiv \frac{\mathcal{P}_E+\delta\mathcal{P}_E}{\mathcal{P}_E} = \prod_i w_i. \tag{12}$$

3 Example Parton Shower Kinematics

For the examples given here we will use as a model bremstrahlung emissions from one quark line. For the numerical results presented in the following sections we use a concrete implementation of the kinematics of the Herwig++ parton shower [3, 8]. In terms of those, we have

$$F_R[\boldsymbol{\varphi}(\vec{y})] = F[(\alpha_S, P_{qq})(z,\tilde{q}^2)] = \frac{1}{2\pi\tilde{q}^2}\alpha_S(z,\tilde{q}^2)P_{qq}(z,\tilde{q}^2)\,, \tag{13}$$

where P_{qq} is the splitting kernel, z is the splitting variable, and $\tilde{q}^2$ is the evolution variable.

4 Kernel Variations

Varying the structure of the splitting kernel may be an interesting example. For example, one could start with the collinear splitting kernels and vary them by the mass dependent quasi-collinear kernels to see whether such changes introduce dramatic effects on a set of observables. The benefit to the procedure presented here is that there is no need to change the fundamental structure of a given MC. In fact one could add an option to their code to keep track of the alternate weights, without changing at all their basic MC program logics and structures. One caveat is that though this method will give an accurate estimate of the variations given, this is only true for regions of phase space in which the original MC fills. If some regions of phase space are empty, or rarely entered, the changes in that region due to the variation will still lack significant statistics.

The collinear kernel is simply

$$P_{qq}(z) = \frac{1+z^2}{1-z}. \tag{14}$$

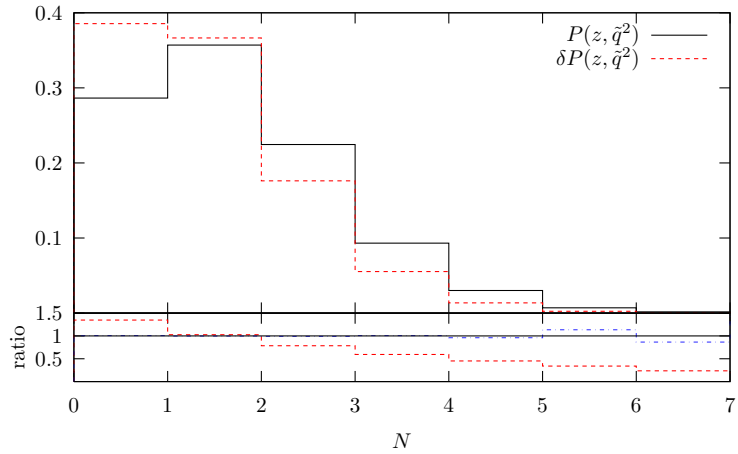

Fig. 1: The distribution of the number of emissions for the collinear kernel and the quasi-collinear kernel for $m^2 = (175\ \mathrm{GeV})^2$ and $\tilde{q}^2 = (1\mathrm{TeV})^2$. The solid line shows the result when the quasi-collinear kernel is used, the dashed line shows the result when the variation in eqn. (15) is applied and the events are weighted. Again, the second panel shows the ratio of the varied to the unvaried MC.

To obtain the quasi-collinear kernel, we must define a variance of

$$\delta P_{qq}(z,\tilde{q}^2) = -\frac{2m^2}{z(1-z)\tilde{q}^2}. \tag{15}$$

With this variance we find the alternate weight, for the ith emission, is given by

$$w_{P_i} = \left(1 + \frac{\delta P_{qq}(z_i,\tilde{q_i}^2)}{P_{qq}(z_i,\tilde{q_i}^2)}\right) \exp\left(-\int_{\tilde{q}_i^2}^{\tilde{q}_{i-1}^2} \frac{d\tilde{q}^2}{\tilde{q}^2} \int_{z_i^-}^{z_i^+} dz\, \alpha_S \left[z^2(1-z)^2\tilde{q}^2\right] \delta P_{qq}(z,\tilde{q}^2)\right), \tag{16}$$

and the total weight due to the kernel variation is the product of the weight for each emission. This weight is normalized to a weight 1 event with no variations.

We now show the result of this variation when showering a top quark with mass $175\ \mathrm{GeV}$ from an initial scale of $1\ \mathrm{Tev}$. In figure 1 we show the effect that the quasi-collinear variation has on the distribution of the number of emissions. As would be expected, for larger masses we have fewer emissions. Figure 2 shows the $p_\perp^2$ spectrum of the outgoing quark. The figures are divided into two panels. The top panel shows the results while the bottom panel shows the ratio of the reweighted MC vs. the unweighted one. In figure 1 the ratio panel also includes the ratio of the reweighted MC vs. an alternate MC sample created by changing the kernel in the MC to the quasi-collinear kernel. We see that this ratio is 1 with small variations.

4.1 Combining Kernel with Running Coupling

Another potential variation that may be of interest is to vary the kernel by a term proportional to the running coupling. Such a variation could be used to introduce some NLO effects into the kernel. If we consider only the lowest order in the variations, then

$$\delta F \approx \delta\alpha_S P_{qq}^{(1)} + \alpha_S \delta P_{qq}^{(1)} + \alpha_S^2 \delta P_{qq}^{(2)}. \tag{17}$$

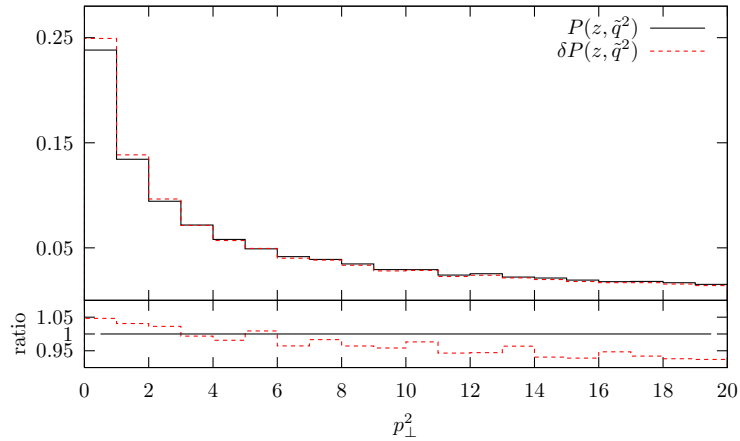

Fig. 2: The distribution of the $p_\perp^2$ of the outgoing quark for the collinear and quasi-collinear cases under the same conditions as figure 1.

We choose the form of $\delta P_{qq}^{(2)}(z)$ according to full NLO kernel [9, 10]. This is composed of two parts, the flavour singlet (S) and non-singlet (V) contributions

$$\delta P_{qq}^{(2)}(z,\tilde{q}^2) = P_{qq}^{S(2)}(z) + P_{qq}^{V(2)}(z), \tag{18}$$

We choose $\delta P^{(1)} = 0$ and $\delta\alpha = 0$ for these examples.

Figure 3 shows the effect on the number of emissions and figure 4 shows the effect on the $p_\perp^2$–spectrum of the outgoing quark line. We see that the number of emissions is slightly higher with a harder spectrum.

The construction of a next-to-leading log (NLL) parton shower has the problem of negative values for the splitting kernels. These destroy the probabilistic interpretation of the Sudakov form factors. Naively, one would assume that this will destroy any meaningful results for the NLL weights. In our case, this is not true. We are reweighting the total density according to the NLL corrections. These may introduce large or negative weights to the reweighted shower, but this is necessary as this correctly describes the density. In the inclusive picture, these negative weights are integrated over and pose no problem; exclusively, these negative weights must be treated correctly in the analysis.

5 Variation of Kinematics

We now consider another use of the alternate weights. Here we wish to use these weights to transform one parton shower into another. This, of course, is not an exact transformation. This requires additional knowledge about the structure of the alternate parton shower.

The idea is to use the variables generated by one shower and reshape the distribution to give the results if an alternate shower was used. In this section we discuss the intrinsic kinematical definitions.

Consider a new kinematics, similar to the one used in Pythia [4]. Here we wish to order the parton shower in virtuality (Q^2). This requires a mapping from $\tilde{q}^2$ into Q^2. Furthermore,

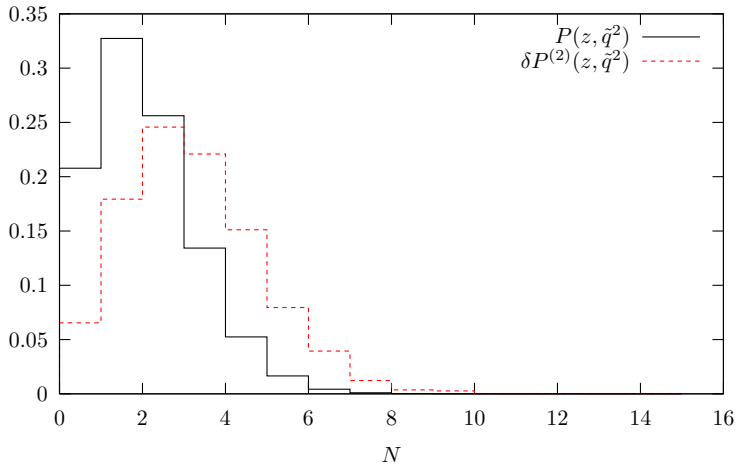

Fig. 3: The distribution of the number of emissions using the collinear kernel at $\mathcal{O}(\alpha_S)$ and applying the variation discusses in the text at $\mathcal{O}(\alpha_S^2)$.

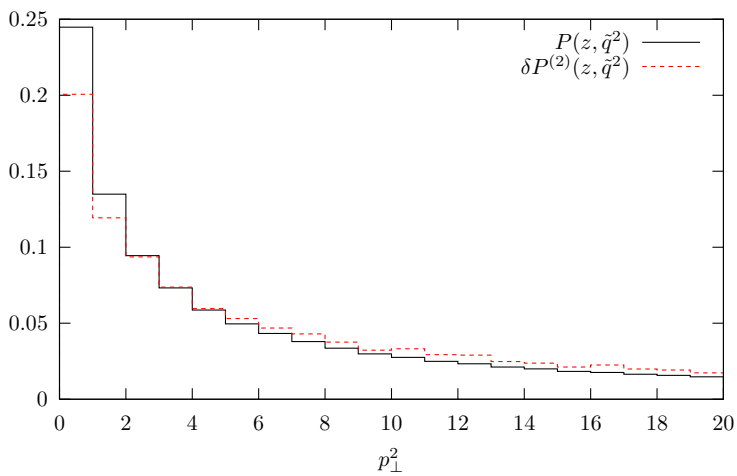

Fig. 4: The $p_\perp^2$ distribution of the outgoing quark under the same conditions as figure 3.

there is a different interpretation of the meaning of the momentum fraction z in the Pythia-like and Herwig-like shower; they have the same distribution, however. We compensate for this by constructing the full four-momentum from the Herwig-like shower and deconstructing the associated variables for each emission. The weights can then be computed from this. This method has the additional benefit that the four momentum configuration is identical in both cases; thus hadronization effects and hadron decays are identical. We define our variations such that

$$\bar{F}[(\alpha_S, P_{qq})(\bar{z}, Q^2)] = F[(\alpha_S, P_{qq})(z, \tilde{q}^2)] + \delta F, \tag{19}$$

where the left-hand side refers to the Pythia-like shower. From this we find

$$\delta F = \bar{F}[(\alpha_S, P_{qq})(\mathcal{T}(z, \tilde{q}^2))]\mathcal{J}(\bar{z}, Q^2) - F[(\alpha_S, P_{qq})(z, \tilde{q}^2)], \tag{20}$$

where $\mathcal{J}$ is the Jacobian factor for the coordinate transformation $\mathcal{T}(z, \tilde{q}^2)$ from the Herwig-variables to the Pythia variables. At this point we can exploit the analytic structure of the Sudakov form factor,

$$\Delta(t; t_0) = \Delta(t; t_1)\Delta(t_1; t_0). \tag{21}$$

This allows the seperation of the weights into the real and the Sudakov components and to calculate the Sudakov components over the full evolution scale, rather than just the scales between each emission. This gives

$$w_\Delta = \frac{\Delta_P(Q^2_{ini}; Q^2_0)}{\Delta_H(\tilde{q}^2_{ini}, \tilde{q}^2_0)}. \tag{22}$$

The total weight is given simply as

$$w = w_\Delta \prod_{i=1}^{N} w_i^{(R)}, \tag{23}$$

where the $w_i^{(R)}$ refer to the weights for the real emissions.

The question now is what does the weighted shower physically give us? This gives us the weight, relative to the unweighted original shower, of producing the kinematical configuration via the other shower. For our example here this means that it will weight our Herwig-like shower to be that of the Pythia-like construction. Our weighted shower will produce events that are both ordered in virtuality and in angle. Comparing the weighted results versus an independent implementation of the full Pythia-like shower would illustrate, for any observable ,the effect of the different limits in phase-space inherent in each implementation. Furthermore, it could be used to illustrate the effects of alternate choices of ordering; e.g. colour connections between jets.

To illustrate this technique we use as a model $e + e-$ annihilation into a $q\bar{q}$ pair. This pair then undergoes final state radiation, but the subsequent emissions do not. We reconstruct the kinematics of the event and, in order to conserve $\sqrt{s}$, we rescale each jet by a common factor, k, such that

$$\sqrt{s} = \sum_{i=1}^{N} \sqrt{q_i^2 + k\boldsymbol{p}_i^2}, \tag{24}$$

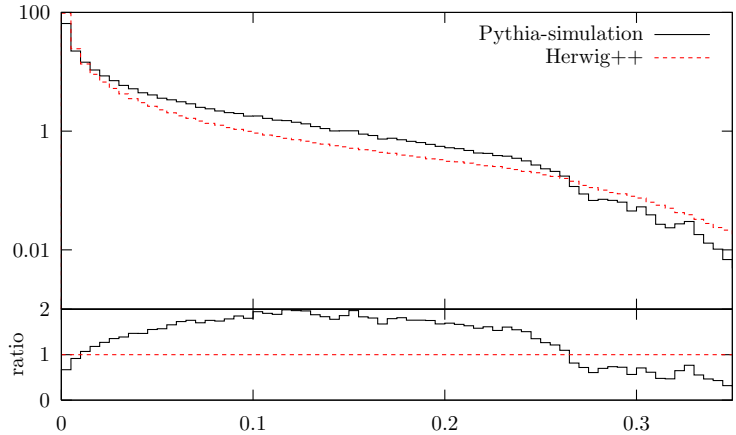

Fig. 5: $1 - T$ for the Herwig-like shower and reweighted to a Pythia-like shower, as described in the text. These differences are due to the different kinematics definitions used in each shower. The bottom panel shows the ratio of the Pythia-like vs. Herwig-like.

where q_i^2 is the virtuality of jet i. To illustrate the reweighting between the Herwig-like and Pythia-like shower we study the thrust observable. This is given by

$$T = \max_{\boldsymbol{n}} \frac{\sum_{i=1}^{N} |\boldsymbol{p}_i \cdot \boldsymbol{n}|}{\sum_{i=1}^{N} |\boldsymbol{p}_i|}. \tag{25}$$

This observable was chosen as the thrust has a strong correlation to the hardest emission, but also is effected by subsequent emissions. As we don't shower the emitted gluons, studying an observable which have a strong dependence on 2 or more emissions is not as illustrative.

Figure 5 shows the result for $\sqrt{s} = 1$ TeV. We can see the deviations, and as expected they are not too large. As these are not the result of a full event generation it is not useful to compare these to data.

6 Uncertainty in Unintegrated Parton Distribution Functions

In the last example we show how to apply the technique to compute the effect of uncertainties in the unintegrated parton distribution function (updf) for the backwards evolution algorithm of CASCADE [11]. In this algorithm the updfs are taken from the outputs of an alternate Monte Carlo algorithm, based on SMALLX [11–13]. This leads to large uncertainties in the updfs. Additionally, in order to fit the initial conditions of the updf MC, based on SMALLX, one must match the output of CASCADE to data. The ability to take the uncertainty of the updf MC into account will allow for better fits overall. Figure 6 shows a schematic of this procedure.

We present here the formula needed to compute the effect of the updf uncertainties in the CASCADE algorithm. We do not endeavor here to implement these weights in the CASCADE program, nor suggest the ideal treatment of this information. This is left as future exercises for the authors of CASCADE.

The CCFM equation describes the gluonic structure of the proton. The variables of this

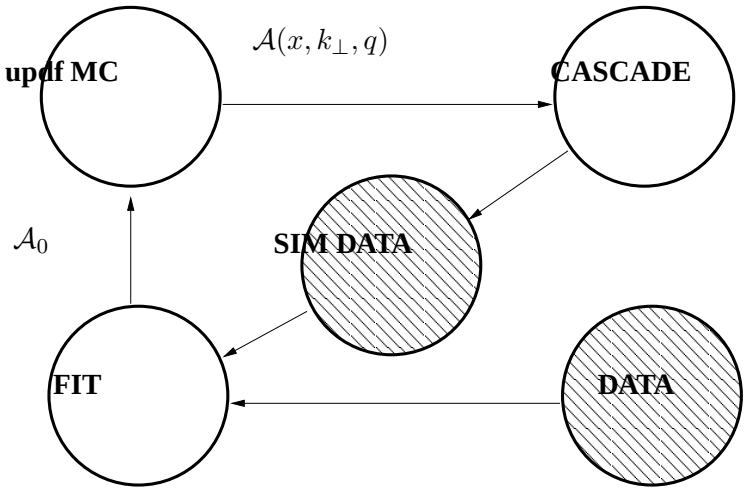

Fig. 6: Schematic of the flow of the fitting procedure using CASCADE and updf MC. As the output of the updf MC is not directly fitted, rather that of CASCADE, tracking uncertainties from the updf MC through CASCADE can prove useful in the fits.

evolution are a scale, q, the momentum fraction, x, and the transverse components, $k_\perp$. In CASCADE, given a step in the evolution terminates at q, x and $k_\perp$, the probability of evolving to a new $\bar{q}, x/z$ and $k'_\perp = |(1-z)/z\boldsymbol{q} + \boldsymbol{k}_\perp|$ is

$$\begin{aligned}\mathcal{P}(\bar{q}, z, \phi, k'_\perp; q, x, k_\perp) &= \frac{\tilde{P}(z, \bar{q}/z, k_\perp)}{2\pi z q^2}\mathcal{A}(x/z, k'_\perp, \bar{q}/z) \\ &\times \exp\left(-\int_q^{\bar{q}} \frac{dq'^2}{q'^2}\int \frac{dz}{z}\frac{d\phi}{2\pi}\tilde{P}(z, q'/z, k_\perp)\frac{\mathcal{A}(x/z, k'_\perp, q'/z)}{\mathcal{A}(x, k_\perp, q')}\right),\end{aligned} \tag{26}$$

where $\tilde{P}$ is the kernel including the non-sudakov form factor and $\mathcal{A}$ is the updf. In contrast to the previous examples, here the real and virtual contributions are clearly different. When we propogate the variance of the updf in the real function we find

$$\frac{\delta F_R[\boldsymbol{\varphi}]}{F_R[\boldsymbol{\varphi}]} = \frac{\delta\mathcal{A}(x/z, k'_\perp, q'/z)}{\mathcal{A}(x/z, k'_\perp, q'/z)}. \tag{27}$$

In the virtual case this is more complex. Here we find

$$\delta F_V[\boldsymbol{\varphi}] = \frac{\tilde{P}(z, q'/z, k_\perp)}{2\pi z q'^2}\left(\frac{B+\delta B}{A+\delta A} - \frac{B}{A}\right) \approx \frac{\tilde{P}(z, q'/z, k_\perp)}{2\pi z q'^2}\frac{1}{A}\left(\delta B - B\frac{\delta A}{A}\right), \tag{28}$$

where

$$A \equiv \mathcal{A}(x, k_\perp, q')\ ;\ B \equiv \mathcal{A}(x/z, k'_\perp, q'/z). \tag{29}$$

These formulae can be used to give the weight associated with the uncertainty due to the updf. Of course, implementation of this weight in the CASCADE framework requires still some work. Once complete, however, use of this alternate weight during the fitting procedure should help improve overall predictions of the model.

7 Conclusion

We have presented a new approach to understanding the errors associated with a MC prediction. This approach can be added to almost all currently existing MC programs without changing the physics or the behaviour of the code. Instead, we have provided a method to track alternate weights for events. These alternate weights provide the tool to reshape MC predictions to see what such a prediction would be if various pieces of the MC were altered.

Though this technique is quite successful, it cannot compensate for all possible alterations. As this algorithm provides an alternate weight for an event generated by a MC it cannot provide events which cannot be generated by the original MC. This means that some of the physical limitations of an already existing code cannot be overcome through this method. We don't see this as a drawback, however. The purpose of this technique is to understand the physics and the limitations inherent in a MC implementation. To this end, such limitations of this technique can provide valuable insight.

This paper has provided numerical examples of a toy parton shower model based on the real MC behaviour of Herwig++ [3, 8]. It may be quite illustrative to apply this method to a fully featured general purpose MC, including hadronization and hadron decay, to see how much variation exsists in such a parton shower implementation. With such an implementation one may be able to check the accuracy of many MC predictions and to understand the limitations of these predictions.

Acknowledgment

The authors would like to thank S. Jadach and Z. Wąs for many useful discussions.
Additionally, PS would like to thank H. Jung for suggesting the use of this method for the CASCADE fitting procedure.

References

[1] Grunewald, Martin W. and others (2000).

[2] Gieseke, Stefan, JHEP **01**, 058 (2005).

[3] Gieseke, S. and Ribon, A. and Seymour, M. H. and Stephens, P. and Webber, B., JHEP **02**, 005 (2004).

[4] Sjostrand, Torbjorn and others, Comput. Phys. Commun. **135**, 238 (2001).

[5] Jadach, S. and Skrzypek, M., Comput. Phys. Commun. **175**, 511 (2006).

[6] Gleisberg, Tanju and others, JHEP **02**, 056 (2004).

[7] Altarelli, G. and Parisi, G., Nucl. Phys. **B126**, 298 (1977).

[8] Gieseke, S. and Stephens, P. and Webber, B., JHEP **12**, 045 (2003).

[9] Furmanski, W. and Petronzio, R., Phys. Lett. **B97**, 437 (1980).

[10] Curci, G. and Furmanski, W. and Petronzio, R., Nucl. Phys. **B175**, 27 (1980).

[11] Jung, H. and Salam, G. P., Eur. Phys. J. **C19**, 351 (2001).

[12] Marchesini, G. and Webber, B. R., Nucl. Phys. **B386**, 215 (1992).

[13] Marchesini, G. and others, Comput. Phys. Commun. **67**, 465 (1992).

Perturbative description of inclusive single hadron production at HERA

S. Albino
II. Institute for Theoretical Physics, University of Hamburg,
Luruper Chaussee 149, 22761 Hamburg, Germany

Abstract
Light charged hadron production data in the current fragmentation region at HERA are calculated using next-to-leading order perturbative calculations and fragmentation functions obtained from similar data from e^+e^- reactions. General good agreement is found at large photon virtuality Q^2 and intermediate momentum fraction x_p, consistent with fragmentation function universality. The description of the small x_p and Q^2 region is improved by incorporating hadron mass effects.

1 Introduction

Unpolarized quark fragmentation functions (FFs) for charge-sign unidentified light charged hadrons $h^\pm = \pi^\pm$, $K^\pm$ and $p/\overline{p}$ have been well constrained by data from $e^+e^- \to h^\pm + X$ using calculations at next-to-leading order (NLO) accuracy. Due to universality in the factorization theorem, such FFs can be used to calculate the similar measurements of $ep \to e + h^\pm + X$. This contribution summarizes the main results of [1] comparing ep reaction data in the current fragmentation region from the H1 [2] and ZEUS [3] collaborations at HERA with calculations using FFs extracted from e^+e^- reactions.

The kinematic degrees of freedom are chosen to be the centre-of-mass energy $\sqrt{s}$ of the initial state ep system, the magnitude of the hard photon's virtuality $Q^2 = -q^2$, the Bjorken scaling variable $x = Q^2/(2P \cdot q)$ and the scaled detected hadron momentum $x_p = 2p_h \cdot q/q^2$. The normalized cross section (with the s dependence omitted for brevity) takes the form

$$F^{\text{proton } h^\pm}(\text{cuts}, x_{pA}, x_{pB}) = \frac{\int_{\text{cuts}} dQ^2 dx \int_{x_{pA}}^{x_{pB}} dx_p \frac{d\sigma^{\text{proton } h^\pm}}{dx_p dx dQ^2}(x, x_p, Q^2)}{\int_{\text{cuts}} dQ^2 dx \frac{d\sigma^{\text{proton}}}{dx dQ^2}(x, Q^2)}, \qquad (1)$$

where "cuts" refers to a specified region in the (x, Q^2) plane, and where $x_{pA(B)}$ is the lower (upper) edge of the x_p bin. The cross section and the kinematic variables are frame invariant, and are measured in the Breit frame, defined to be the frame where the photon energy vanishes. In this frame the target fragmentation region ($x_p < 0$) contains the proton remnants, while the struck parton fragments into the current fragmentation region ($x_p > 0$), and the latter process is equivalent to the fragmentation of a parton into an event hemisphere in e^+e^- reactions. The factorization theorem dictates that, at leading twist, the highly virtual photon undergoes hard scattering with a parton in the proton moving in the same direction and carrying away an energy / momentum fraction y. One of the partons produced in this scattering undergoes fragmentation to the observed hadron $h^\pm$ moving in the same direction and carrying away an energy / momentum

fraction z. In other words, after the change of integration variables $z \to x_p/z$ and $y \to x/y$, the factorized cross section in the numerator of Eq. (1) takes the form

$$\frac{d\sigma^{\text{proton } h^\pm}}{dx_p dx dQ^2}(x, x_p, Q^2) = \int_{x_p}^1 \frac{dz}{z} \int_x^1 \frac{dy}{y} \sum_{ij} \frac{d\sigma^{ij}}{dz dy dQ^2} \left(y, z, \frac{Q^2}{\mu^2}, a_s(\mu^2) \right) \times f_i^{\text{proton}} \left(\frac{x}{y}, \mu^2 \right) D_j^{h^\pm} \left(\frac{x_p}{z}, \mu^2 \right), \tag{2}$$

where f_i^{proton} is the parton distribution function (PDF) of parton i in the proton, $D_j^{h^\pm}$ the FF of parton j to $h^\pm$, $d\sigma^{ij}$ the equivalent factorized partonic observable given to NLO in Ref. [4], μ the factorization / renormalization scale which distinguishes the soft from the hard subprocesses and $a_s(\mu^2) = \alpha_s(\mu)/(2\pi)$.

2 Comparisons with data

At leading order in a_s, eq. (1) becomes

$$F^{\text{proton } h^\pm}(\text{cuts}, x_{pA}, x_{pB}) = \frac{\int_{x_{pA}}^{x_{pB}} dx_p \sum_I e_{q_I}^2(Q^2) G_I(Q^2) x_p D_I^{h^\pm}(x_p, Q^2)}{\sum_J e_{q_J}^2(Q^2) G_J(Q^2)}, \tag{3}$$

where the parton labels I, J are restricted to (anti)quarks q_I only, which have electric charges e_{q_I}, and $G_I(Q^2) = \int_{\text{cuts}} dx\, x f_I^{\text{proton}}(x, Q^2)$. In the limit that the G_I become independent of I, the numerator of Eq. (3) is equal to the equivalent LO result for $e^+e^- \to h^\pm + X$, and therefore the two types of observables are distinguished only by the G_I. If this discrepancy is small, a good description of HERA data is expected using FFs obtained from fits to e^+e^- data, such as the AKK [5], Kretzer [6] and KKP [7] FF sets [1] if universality and fixed order (FO) perturbation theory are reliable. Calculations using these sets for the H1 data are shown in Fig. 1, using the CTEQ6M PDF set [9] and the CYCLOPS program [10] here and throughout this work, unless otherwise stated. The strong disagreement between the FF sets at large x_p most likely arises from large experimental errors on the FFs due to poor constraints from e^+e^- reaction data at large momentum fraction. At high Q^2, the calculation for all 3 FF sets agrees well with the data. Therefore, the disagreements at large and small x_p values found with the lower Q^2 data may be due to effects beyond the FO approach at leading twist. For example, resummation of soft gluon emission logarithms that become large at small and large x_p may be necessary to improve the calculation here. This is illustrated in Fig. 2 (left) by the effect of scale variation on the calculation, being largest at small and large x_p. The effect of the observed hadron's mass m_h is also important at small x_p for low Q^2 values. For non-zero hadron mass, one has to distinguish between momentum, energy, light cone momentum etc., which are all equal when the hadron mass is negligible. According to the factorization theorem, the "momentum" fraction z appearing in eq. (2) is the fraction of light cone momentum carried away from the fragmenting parton by the observed hadron in a frame in which the spatial momenta of the virtual photon and the detected hadron are parallel, and $x_p = \xi_p(1 - m_h^2/(Q^2\xi_p^2))$ should be replaced by the ratio of

[1] Since this work was completed, 3 further sets [8] have been extracted using improved theoretical and experimental input.

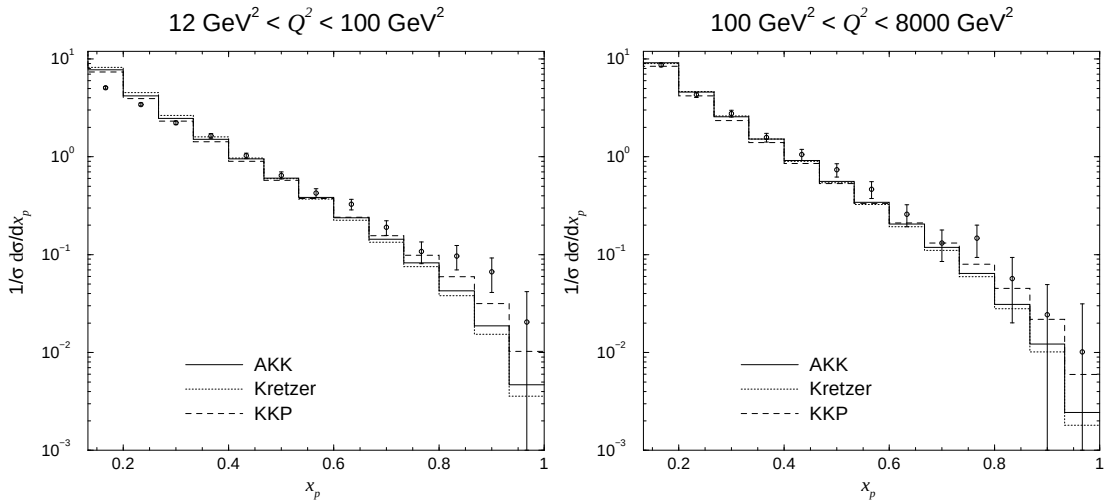

Fig. 1: Comparisons of theoretical predictions using the AKK, Kretzer and KKP FF sets with the x_p distributions from H1 [2].

the hadron's to the virtual photon's light cone momentum, ξ_p. Using this approach [1], one finds that the experimentally measured quantity $d\sigma^{\text{proton } h^\pm}/dx_p dx dQ^2$ is related to the calculated quantity $d\sigma^{\text{proton } h^\pm}/d\xi_p dx dQ^2$ by

$$\frac{d\sigma^{\text{proton } h^\pm}}{dx_p dx dQ^2}(x, x_p, Q^2) = \frac{1}{1 + \frac{m_h^2}{Q^2 \xi_p^2(x_p)}} \frac{d\sigma^{\text{proton } h^\pm}}{d\xi_p dx dQ^2}(x, \xi_p(x_p), Q^2), \tag{4}$$

which shows clearly that hadron mass effects become important at small x_p and low Q^2. According to Fig. 2, this correction improves the description in this region, if we compare the results of this figure with the low Q^2 results of Fig. 1. The choice $m_h = 0.5$ GeV represents an "average" mass for the light charged hadrons. We do not incorporate mass effects for the proton of the initial state, since this effect is expected to partially cancel between the numerator and denominator of eq. (1). By redoing the calculation with the MRST2001 PDF set [11], we see that the dependence on the choice of PDF set is small, particularly at small x_p, most likely because these quantities are well constrained but also because any variations in them are partially canceled between the numerator and denominator of eq. (1). As for e^+e^- reactions, the dependence on the gluon FF is small, particularly at large x_p.

To further verify these observations and inferences, we perform similar calculations for the ZEUS data. The different FF sets lead to similar results and good agreement with the data at large Q^2 and intermediate x_p (Fig. 3). The scale variation (Fig. 4, top) generally decreases with increasing Q^2, and is largest for small x_p. Both hadron mass effects and gluon fragmentation are most important at low Q^2 and small x_p (Fig. 4, bottom).

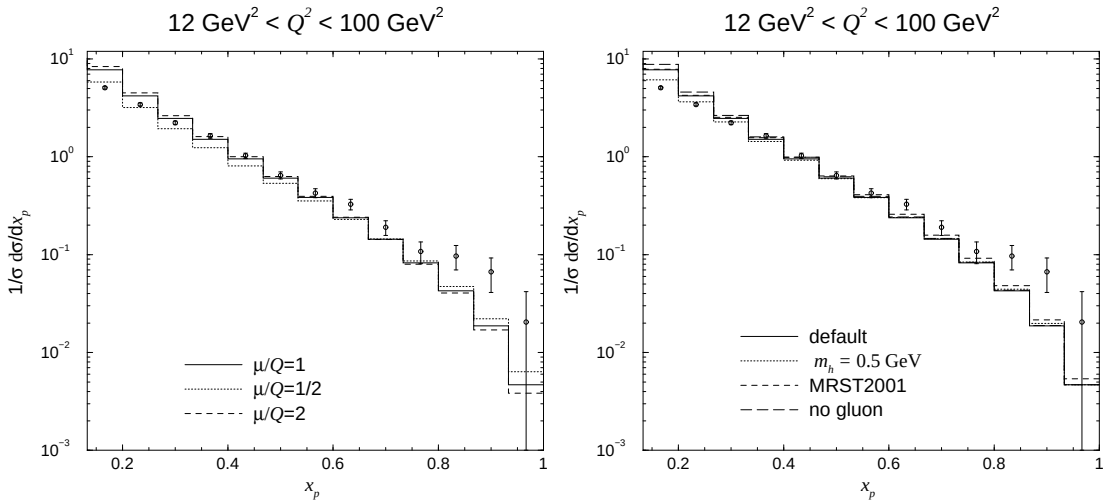

Fig. 2: As in Fig. 1, using only the AKK FF set. Left: The modifications arising from scale variation. Right: The modifications to the default predictions (solid line) arising from the replacement of the CTEQ6M PDF set by the MRST2001 PDF set of Ref. [11], from the removal of the evolved gluon, and from the incorporation of the hadron mass effect are shown.

3 Conclusions

High Q^2 measurements of inclusive single hadron production at HERA are well described by perturbative QCD in the framework of the factorization theorem using available FF sets. Although some disagreement is found with data at lower Q^2, we note that there is significant room for improvement in the theory in this region, such as hadron mass effects studied in this work, but also resummation of the FO series at small and large x_p, higher twist effects and quark mass effects. Whether such effects are in fact relevant can be better verified by the effect of incorporating such data into global fits of FFs. More importantly, such data may also provide valuable information on the FFs' quark flavour components not constrained by e^+e^- reaction data, particularly since these type of HERA measurements may now be made very precisely [12]. However, in order to constrain FFs for each hadron species individually, and to ensure that the data is not contaminated by light charged particles other than $\pi^\pm$, $K^\pm$ and $p/\overline{p}$, the hadron species of the HERA data need to be identified.

Acknowledgments

The author thanks Bernd A. Kniehl, Gustav Kramer and Carlos Sandoval for collaboration.

References

[1] S. Albino, B. A. Kniehl, G. Kramer and C. Sandoval, Phys. Rev. D **75**, 034018 (2007).

[2] C. Adloff *et al.* [H1 Collaboration], Nucl. Phys. B **504**, 3 (1997).

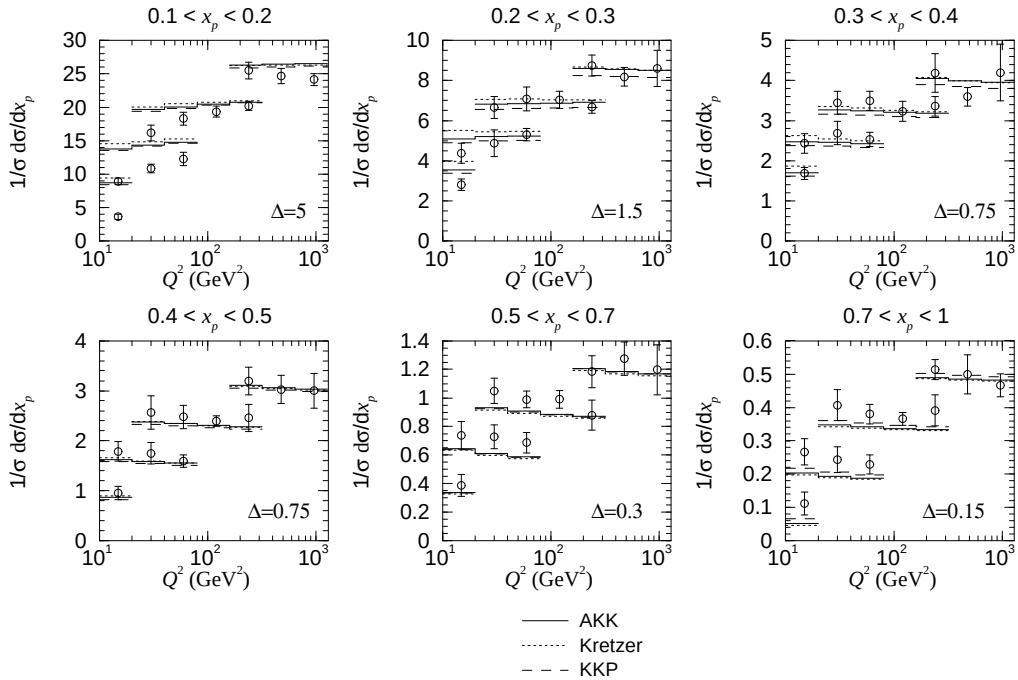

Fig. 3: As in Fig. 1, but for the ZEUS data [3]. Each data set is measured in a specific x_p-bin and, together with its predictions, is shifted upward relative to the one below by the indicated value for Δ.

[3] J. Breitweg *et al.* [ZEUS Collaboration], Phys. Lett. B **414**, 428 (1997).

[4] G. Altarelli, R. K. Ellis, G. Martinelli, and S. Y. Pi, Nucl. Phys. B **160**, 301 (1979).

[5] S. Albino, B. A. Kniehl, and G. Kramer, Nucl. Phys. B **725**, 181 (2005).

[6] S. Kretzer, Phys. Rev. D **62**, 054001 (2000).

[7] B.A. Kniehl, G. Kramer, and B. Pötter, Nucl. Phys. B **582**, 514 (2000).

[8] M. Hirai, S. Kumano, T. H. Nagai and K. Sudoh, Phys. Rev. D 75 (2007) 094009; D. de Florian, R. Sassot and M. Stratmann Phys. Rev. D 75 114010 (2007); Phys. Rev. D 76 074033 (2007); S. Albino, B. A. Kniehl and G. Kramer, Nucl. Phys. B **803** (2008) 42.

[9] J. Pumplin, D. R. Stump, J. Huston, H. L. Lai, P. Nadolsky, and W. K. Tung, JHEP **0207**, 012 (2002).

[10] D. Graudenz, Fortsch. Phys. **45**, 629 (1997).

[11] A. D. Martin, R. G. Roberts, W. J. Stirling, and R. S. Thorne, Eur. Phys. J. C **23**, 73 (2002).

[12] F. D. Aaron *et al.* [H1 Collaboration], Phys. Lett. B **654**, 148 (2007); B. Brzozowska [ZEUS Collaboration], prepared for the 15th International Workshop on Deep-Inelastic Scattering and Related Subjects (DIS2007), Munich, Germany, April 2007.

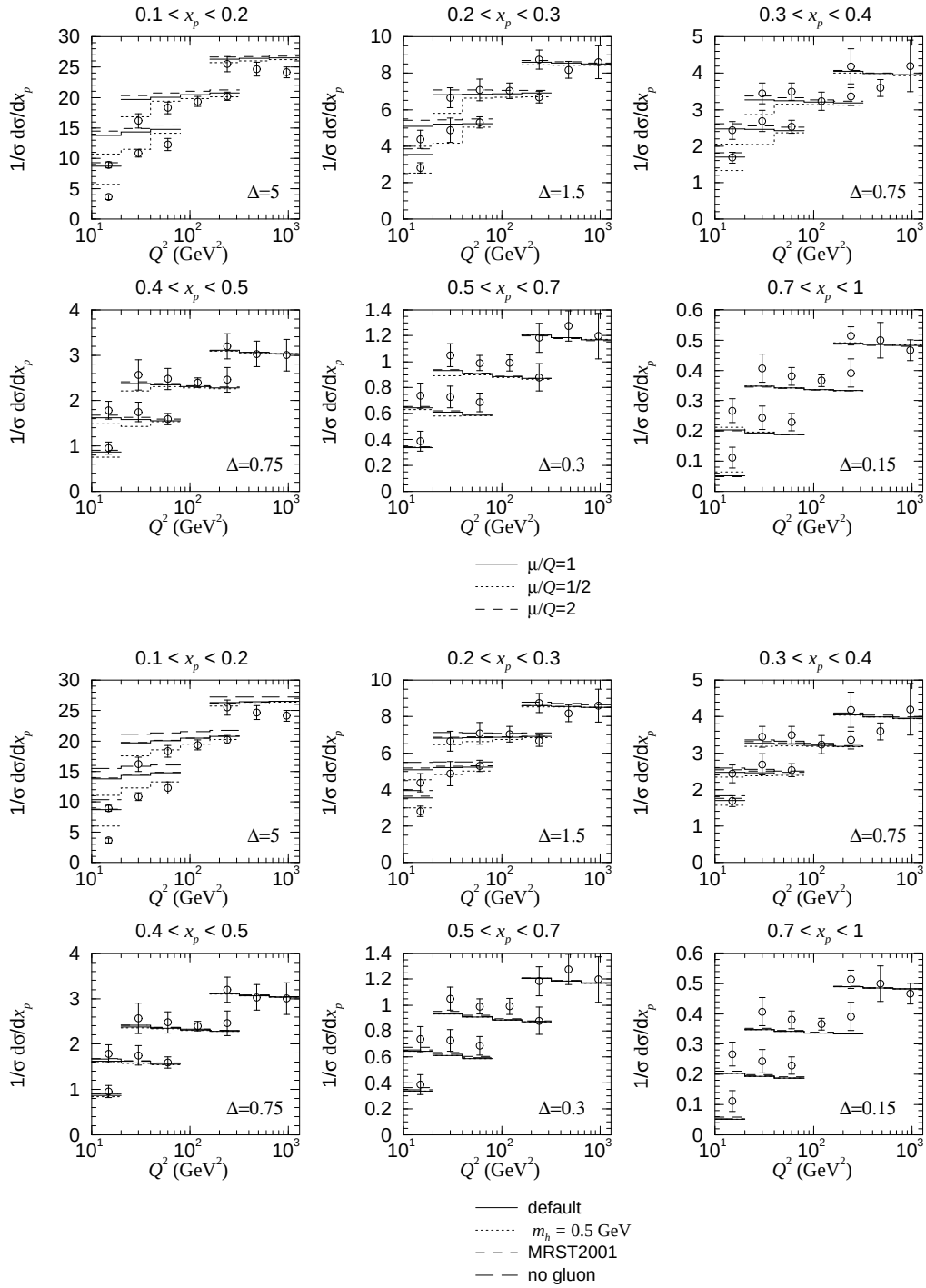

Fig. 4: As in Fig. 2, but for the ZEUS data [3].

Non-perturbative corrections from an s-channel approach

F. Hautmann
Department of Theoretical Physics, University of Oxford, Oxford OX1 3NP

Abstract
We report on studies of multi-parton corrections from nonlocal operator expansion. We discuss relations between eikonal-line matrix elements and parton distributions, and present an illustration for initial-state collinear evolution.

1 Introduction

Non-perturbative dynamics affects the structure of LHC events even for high momentum transfer, through hadronization, soft underlying scattering, multiple hard interactions. Models for these processes are necessary, for instance, for Monte Carlo generators to produce realistic event simulations.

The treatment of multiple parton interactions in QCD will require methods that go beyond the local operator expansion, and likely involve fully unintegrated parton correlation functions [1]. Besides the relevance for event generators, this should also provide a natural framework for the investigation at the LHC of possible new strong-interaction effects at very high energies, including parton saturation [2].

This report is based on the analysis [3] of nonlocal operator expansion, investigating corrections from graphs with multiple gluon exchange. The point of view in this study is to connect the treatment of multi-gluon contributions with formulations in terms of standard partonic operators, and in this respect it can be seen as deriving from the approach of [4]. We present an illustration for the case of structure functions. This case is also treated in the analyses of [5]. More discussion may be found in [6]. The formulation discussed below trades parton distribution functions for moments of eikonal-line correlators. We expect this formulation to be useful also for the treatment of the associated final-state distributions.

2 From parton distribution functions to eikonal-line matrix elements

The analysis [3] starts with the quark distribution function, defined as

$$f_q(x,\mu) = \frac{1}{4\pi}\int dy^- e^{ixP^+y^-}\,\langle P|\bar\psi(0)Q(0)\gamma^+Q^\dagger(y^-)\psi(0,y^-,\mathbf{0})|P\rangle_c \qquad (1)$$

where ψ is the quark field, Q is the gauge link, and the subscript c is the instruction to take connected graphs. The matrix element (1) can be rewritten as the real part of a forward scattering amplitude [3], in which we think of the operator $Q^\dagger\psi$ as creating an antiquark plus an eikonal line in the minus direction, starting at distance y^- from the position of the target.

Next, supposing that x is small, we treat the evolution of the antiquark-eikonal system in a hamiltonian framework (see [3] and references therein) which allows us to express the evolution operator in the high-energy approximation as an expansion in Wilson-line matrix elements. The leading term of this is ("dipole" term)

$$\Xi(\boldsymbol{z},\boldsymbol{b}) = \int [dP']\,\langle P'|\frac{1}{N_c}\,\mathrm{Tr}\{1 - F^\dagger(\boldsymbol{b}+\boldsymbol{z}/2)\,F(\boldsymbol{b}-\boldsymbol{z}/2)\}|P\rangle \quad , \tag{2}$$

where F is the eikonal operator

$$F(\boldsymbol{r}) = \mathcal{P}\exp\left\{-ig\int_{-\infty}^{+\infty} dz^-\mathcal{A}_a^+(0,z^-,\boldsymbol{r})\,t_a\right\}, \tag{3}$$

$\boldsymbol{z}$ is the transverse separation between the eikonals in (2), and $\boldsymbol{b}$ is the impact parameter.

In this representation the quark distribution (1) is given by the coordinate-space convolution

$$xf_q(x,\mu) = \int d\boldsymbol{b}\,d\boldsymbol{z}\,u(\mu,\boldsymbol{z})\,\Xi(\boldsymbol{z},\boldsymbol{b}) - UV \quad . \tag{4}$$

In [3] the explicit result is given for the function $u(\mu,\boldsymbol{z})$ at one loop in dimensional regularization and for the counterterm $-UV$ of $\overline{\mathrm{MS}}$ renormalization. The $\overline{\mathrm{MS}}$ result can also be recast in a physically more transparent form in terms of a cut-off on the $\boldsymbol{z}$ integration region, as long as the scale μ is sufficiently large compared to the inverse hadron radius:

$$xf_q(x,\mu) = \frac{N_c}{3\pi^4}\int d\boldsymbol{b}\,\frac{d\boldsymbol{z}}{\boldsymbol{z}^4}\,\theta(\boldsymbol{z}^2\mu^2 > a^2)\,\Xi(\boldsymbol{z},\boldsymbol{b}) \quad , \tag{5}$$

where a is a renormalization scheme dependent coefficient given in [3].

The Wilson-line matrix element $\Xi(\boldsymbol{z},\boldsymbol{b})$ receives contribution from both long distances and short distances. At small $\boldsymbol{z}$ it may be treated by a short distance expansion. At large $\boldsymbol{z}$ it should be parameterized consistently with bounds from unitarity and saturation [2] and determined from data.

3 An algebraic relation for eikonal operators

A general relation between fundamental and adjoint representation for Ξ, valid for any distance $\boldsymbol{z}$, is given in [3], based on the algebraic relation

$$\begin{aligned}\frac{1}{N_c^2-1}\mathrm{Tr}\left[1-U^\dagger(\boldsymbol{z})U(\boldsymbol{0})\right] &= \frac{C_A}{C_F}\frac{1}{N_c}\,\mathrm{Re\ Tr}\left[1-V^\dagger(\boldsymbol{z})V(\boldsymbol{0})\right] \\ &- \frac{1}{2}\frac{C_A}{C_F}\frac{1}{N_c^2}\,|\mathrm{Tr}\left[1-V^\dagger(\boldsymbol{z})V(\boldsymbol{0})\right]|^2\end{aligned} \tag{6}$$

with $V = F_{\mathrm{fund.}}$, $U = F_{\mathrm{adj.}}$.

From this one can obtain small-$\boldsymbol{z}$ relations connecting Ξ to the gluon distribution. For instance, for the fundamental representation at small $\boldsymbol{z}$ this yields

$$\Xi(\boldsymbol{b},\boldsymbol{z}) = \boldsymbol{z}^2\,\frac{\pi^2\alpha_s}{2N_c}\,xG(x,\mu)\,\phi(\boldsymbol{b}), \tag{7}$$

where by xG we denote the gluon distribution (either the x_c-scale or weighted-average expressions in [3]), and $\phi(\boldsymbol{b})$ obeys

$$\int d\boldsymbol{b}\, \phi(\boldsymbol{b}) = 1. \tag{8}$$

The result for Ξ in the fundamental representation corresponds directly to the one for the dipole cross section in the saturation model [2]. Results in the fundamental and adjoint cases are relevant to discuss quark saturation and gluon saturation.

4 Power-suppressed contributions

In the s-channel framework of [3] contributions to hard processes suppressed by powers of the hard scale are controlled by moments of Ξ,

$$\mathcal{M}_p = \frac{2^{2p}\, p}{\Gamma(1-p)} \int \frac{d\boldsymbol{z}}{\pi \boldsymbol{z}^2}\, (\boldsymbol{z}^2)^{-p} \int d\boldsymbol{b}\, \Xi(\boldsymbol{z}, \boldsymbol{b}) \ , \tag{9}$$

analytically continued for $p > 1$. Models for the dipole scattering function including saturation are reviewed in [2]. In this case the moments (9) are proportional to integrals over impact parameter of powers of the saturation scale. Higher moments are obtained from derivatives with respect to p,

$$\mathcal{M}_{p,0} \simeq \int d\boldsymbol{b}\, [Q_s^2(\boldsymbol{b})]^p \ , \quad \mathcal{M}_{p,k} \simeq (-1)^k\, \frac{d^k}{dp^k} \mathcal{M}_{p,0} \ . \tag{10}$$

As an illustration, we determine the C_A/x part of the coefficients of the first subleading power correction from the s-channel for transverse and longitudinal structure functions F_T, F_L. Denoting the Q^2 derivative by $\dot{F}_j = dF_j/d\ln Q^2$ for $j = T, L$, and its leading-power contribution by $\dot{F}_{j,lead.}$, one has

$$\dot{F}_j - \dot{F}_{j,lead.} = b_{j,0}\, \mathcal{M}_{2,0}/Q^2 + b_{j,1}\, \mathcal{M}_{2,1}/Q^2 + \cdots \tag{11}$$

Structure functions can be analyzed in the same way [3] as described in Sec. 2 for the quark distribution function. The main difference compared to the case of the quark distribution (1) is that the ultraviolet region of small $\boldsymbol{z}$ is now regulated by the physical scale Q^2 rather than requiring, e.g., $\overline{\rm MS}$ renormalization. Saturation is reobtained [3] within the dipole approximation [2]. By the analysis based on (6),(7) the saturation scale $Q_s(\boldsymbol{b})$ for a dipole in the fundamental representation is

$$Q_s^2(\boldsymbol{b}) = \frac{2\pi^2 \alpha_s}{N_c}\, xG(x,\mu)\, \phi(\boldsymbol{b}). \tag{12}$$

To study the expansion in powers of $1/Q^2$ it is convenient to go to Mellin moment space by representing Ξ via the Mellin transform

$$\Xi(\boldsymbol{z}, \boldsymbol{b}) = \boldsymbol{z}^2 \int_{a-i\infty}^{a+i\infty} \frac{du}{2\pi i}\, (\boldsymbol{z}^2)^{-u}\, \widetilde{\Xi}(u, \mathbf{b}) \ , \tag{13}$$

$0 < a < 1$. Then the structure functions $F_{T,L}$ have the representation

$$xF_{T,L} = \int d\boldsymbol{b} \int_{a-i\infty}^{a+i\infty} \frac{du}{2\pi i}\, \widetilde{\Xi}(u, \mathbf{b})\, \Phi_{T,L}(u) \ , \tag{14}$$

where $\Phi_{T,L}(u)$ can be read from [7] and are given by

$$\Phi_T(u) = \langle e_a^2\rangle \frac{N_c}{4^{u+2}\pi^2}(Q^2)^u \frac{\Gamma(3-u)\Gamma(2-u)\Gamma(1-u)}{\Gamma(5/2-u)\Gamma(3/2+u)}\,(1+u)\,\Gamma(u), \tag{15}$$

$$\Phi_L(u) = \langle e_a^2\rangle \frac{N_c}{4^{u+2}\pi^2}(Q^2)^u \frac{[\Gamma(2-u)]^3}{\Gamma(5/2-u)\Gamma(3/2+u)}\,2\,\Gamma(1+u), \tag{16}$$

with Γ the Euler gamma function. The expansion in $1/Q^2$ of (14) is controlled by the singularity structure of the integrand in the u-plane [3, 5, 6]. Eqs. (15),(16) show that longitudinal Φ_L has no pole at $u = 0$, so that the leading singularity is given by the $u = 0$ pole in $\widetilde{\Xi}$, while the first subleading pole $u = -1$ is absent in transverse Φ_T due to the numerator factor $(1 + u)$, so that the answer for the transverse case at next-to-leading level is determined by the singularity in $\widetilde{\Xi}$, with Φ contributing to the coefficient of the residue.

It can be verified that contributions to (14) in the lowest $p = 1$ moments in Eq. (10) correctly reproduce the small-x gluon part of renormalization-group evolution,

$$\begin{aligned}\dot{F}_{T,lead.} &= \langle e_a^2\rangle\,\frac{\alpha_s}{2\pi}\int_x^1 \frac{dz}{z}\,\frac{[z^2+(1-z)^2]}{2}\,f_g\Big(\frac{x}{z},Q\Big) + \text{quark term} \\ &\simeq \langle e_a^2\rangle\,\frac{\alpha_s}{2\pi}\,\frac{1}{3}\,G + \text{quark term}\ ,\end{aligned} \tag{17}$$

using (8),(12) and the gluon distribution G evaluated at the average [3] $x \simeq x_c$, with the lowest x-moment of the gluon $\to$ quark splitting function

$$\int_0^1 dz\,P_{qg}(z) = \int_0^1 dz\,[z^2+(1-z)^2]/2 = 1/3\ . \tag{18}$$

Beyond leading power, the first subleading corrections read

$$\dot{F}_T - \dot{F}_{T,lead.} = -\langle e_a^2\rangle \frac{C_A}{20\pi^3 x}\frac{1}{Q^2}\int d\boldsymbol{b}\,[Q_s^2(\boldsymbol{b})]^2 + \dots\ , \tag{19}$$

$$\begin{aligned}\dot{F}_L - \dot{F}_{L,lead.} &= -\langle e_a^2\rangle \frac{C_A}{15\pi^3 x}\Big[\frac{14}{15}+\psi(1)\Big]\frac{1}{Q^2}\int d\boldsymbol{b}\,[Q_s^2(\boldsymbol{b})]^2 \\ &+ \langle e_a^2\rangle \frac{C_A}{15\pi^3 x}\frac{1}{Q^2}\int d\boldsymbol{b}\,[Q_s^2(\boldsymbol{b})]^2\ln[Q^2/Q_s^2(\boldsymbol{b})] + \dots\ .\end{aligned} \tag{20}$$

That is, the b coefficients in (11) are given by

$$\begin{aligned} b_{T,0} = -\langle e_a^2\rangle\,C_A/(20\pi^3 x) \quad &, \quad b_{T,1} = 0\ , \\ b_{L,0} = -\langle e_a^2\rangle\,C_A\,[14/225+\psi(1)/15]/(\pi^3 x) \quad &, \quad b_{L,1} = \langle e_a^2\rangle\,C_A/(15\pi^3 x)\ ,\end{aligned} \tag{21}$$

with ψ the Euler psi function.

Via process-dependent coefficients analogous to those in (11), the eikonal-operator moments (9) will also control power-like contributions to the associated jet cross sections due to multi-parton interactions in the initial state. At present these processes are modeled by Monte Carlo, which point to their quantitative significance for the proper simulation of hard events at the LHC. The above discussion also suggests the potential usefulness in this context of analyzing jet and structure function data by trading parton distribution functions for s-channel correlators defined according to the method of Sec. 2.

References

[1] T.C. Rogers, Phys. Rev. **D78**, 074018 (2008);
T.C. Rogers, arXiv:0712.1195 [hep-ph] (2007).

[2] L. Motyka, K. Golec-Biernat and G. Watt, arXiv:0809.4191 [hep-ph] (2008).

[3] F. Hautmann and D.E. Soper, Phys. Rev. **D75**, 074020 (2007);
F. Hautmann, Phys. Lett. **B643**, 171 (2006).

[4] A.P. Bukhvostov, G.V. Frolov, L.N. Lipatov and E.A. Kuraev, Nucl. Phys. **B258**, 601 (1985).

[5] J. Bartels, C. Bontus and H. Spiesberger, arXiv:hep-ph/9908411 (1999);
J. Bartels and C. Bontus, Phys. Rev. **D61**, 034009 (2000);
J. Bartels, K. Golec-Biernat and K. Peters, Eur. Phys. J. **C17**, 121 (2000).

[6] F. Hautmann, arXiv:0802.1178 [hep-ph] (2008).

[7] S. Catani and F. Hautmann, Nucl. Phys. **B427**, 475 (1994);
S. Catani, M. Ciafaloni and F. Hautmann, Nucl. Phys. **B366**, 135 (1991);
S. Catani, M. Ciafaloni and F. Hautmann, Phys. Lett. **B242**, 97 (1990).

Single top production in the Wt mode with MC@NLO

Chris D. White
Nikhef, Kruislaan 409, 1058AG Amsterdam, The Netherlands

Abstract
We consider whether it is possible to isolate single top production in the Wt mode as a process at the LHC. A precise definition of this mode becomes problematic beyond leading order due to interference with $t\bar{t}$ production. We give two definitions of the Wt mode whose difference mainly measures this interference, and implement both in the MC@NLO program. Comparison of the results allows us to conclude that is indeed feasible to try to separate the $t\bar{t}$ and Wt processes, subject to adequate cuts.

1 Introduction

Single top physics is of great interest at the Tevatron and LHC both within and beyond the Standard Model. Firstly, it allows detailed scrutiny of the electroweak interactions of the top quark e.g. a direct measurement of V_{tb}. Secondly, the fact the mass of the top quark lies around the electroweak scale means that the top sector could be a sensitive probe of new physics. In the Standard Model, there are three ways to produce a single top quark. The least well understood of these is the Wt mode, in which the final state top quark is accompanied by a W boson. Although rather too small to be observed at the Tevatron, the cross-section is significant at the LHC (i.e. about 20% of the total single top cross-section).

At LO, the Wt mode has a well-defined cross-section, which is much smaller than that of $t\bar{t}$ production. At NLO, however, a problem arises due to the real emission contributions shown in Fig. 1. These essentially consist of $t\bar{t}$ production at LO, followed by the decay of the antitop, and result in a very large correction to the LO Wt cross-section. This large NLO contribution results from regions of the phase space where the invariant mass m_{bW} of the $W\bar{b}$ pair becomes equal to the top mass i.e. when the antitop propagator becomes resonant. The question then arises as to whether it is still possible to define the Wt mode in such a way that it can be measured independently of top pair production at the LHC. This issue can only be fully addressed in the MC@NLO framework, in which a NLO matrix element is matched with a parton shower, due

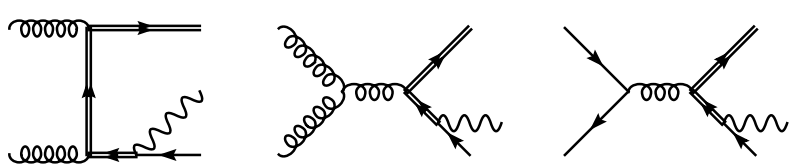

Fig. 1: Doubly resonant contributions to the Wt mode.

to the fact that the interference problem manifests itself at NLO and beyond. Furthermore, it is only in the presence of initial and final state showers that one has sufficiently realistic final states, which one may be reasonably confident of having an experimental applicable definition.

It could be argued that instead of isolating the Wt mode by itself, one should consider sums of processes with a given final state (in this case $W^+W^-b(\bar{b})$), as was done in the present context in [1]. However, such approaches are problematic given that NLO QCD corrections cannot be included. One knows, for example, that NLO corrections to $t\bar{t}$ production are large. This casts doubt on the accuracy of more inclusive approaches. Furthermore, it is unduly pessimistic to assume that interference with $t\bar{t}$ prevents the practical definition of the Wt mode. It is phenomenologically desirable to isolate this process, and if it can be done then this should be investigated fully. Furthermore, a suitable definition allows full NLO QCD corrections to be implemented, thus leads to the most accurate description.

The problem of isolating Wt production has been considered before in the literature, as it is necessary in any calculation beyond LO. Previous ideas for solving the interference problem include restricting m_{bW} directly so as to lie away from the top mass [2], or implementing a global subtraction term to remove the resonant $t\bar{t}$ contribution [3]. These methods were defined at the total cross-section level. A fully differential NLO definition was given in [4]. There, a transverse momentum veto was implemented on the b quark which did not originate from the top, if such a b was present. Harder b quarks tend to have originated from a $\bar{t}$ decay, thus such a veto can be used to filter out the $t\bar{t}$ contribution. Also in [4], some matrix elements with problematic initial states were removed ($\bar{q}q$ in all cases, and gg if the factorisation scale was equal to the transverse momentum veto).

Whilst these solutions work well at the purely NLO level, they are not immediately applicable beyond this e.g. in a real experiment it is not possible to ascertain which decay products originated from a given particle in the hard matrix element. The removal of particular initial states is also theoretically problematic. Firstly, it violates renormalisation group invariance - thus invalidating one of the main motivations for going to NLO (i.e. reduced scale dependence). Secondly, removal of particular initial states is not meaningful in the presence of initial state showers, which mix different partonic subchannels. Nevertheless, we will see that some of the preceding ideas can be generalised in order to suitably define the Wt mode at the MC@NLO level.

2 Two definitions of the Wt mode

We have given two independent definitions of the Wt mode, both of which are applicable locally in phase space and to all orders in the perturbation expansion. By comparing results from the two definitions, we can be confident that theoretical ambiguities in each definition are under control. Our two definitions are named as follows:

1. DIAGRAM REMOVAL (DR). Here one simply removes double resonant diagrams from the Wt amplitude.
2. DIAGRAM SUBTRACTION (DS). Here one modifies the naïve Wt cross-section with a subtraction term, which removes the $t\bar{t}$ resonant contribution locally in phase space.

The difference between the definitions arises from the fact that the subtraction is carried out at the amplitude and cross-section levels respectively. Thus, the difference between DR and DS mainly measures the interference term between the Wt and $t\bar{t}$ production modes.

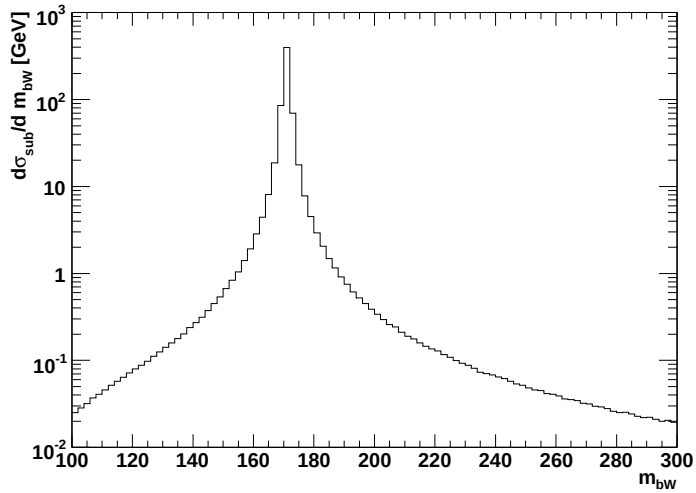

Fig. 2: The subtraction term used to form the DS cross-section, as a function of the invariant mass m_{bW} of the $W\bar{b}$ pair.

Each of the approaches has some theoretical difficulty. DR, for example, violates QCD gauge invariance. We performed detailed checks in a number of gauges to establish that this is not a problem in practice. In DS, there are some ambiguities in how one forms the subtraction term. All one ultimately requires is that it be strongly peaked when $m_{bW} \simeq m_t$, and that it falls away quickly as m_{bW} moves away from the top mass. We thus use a local subtraction term:

$$d\sigma_{sub} = |\tilde{A}(tW\bar{b})_{t\bar{t}}|^2 \times \frac{f_{BW}(m_{bW})}{f_{BW}(m_t)}. \tag{1}$$

Here $\tilde{A}(tW\bar{b})_{t\bar{t}}$ is the amplitude for $tW\bar{b}$ production coming from $t\bar{t}$-like diagrams, where the kinematics are reshuffled to place the $\bar{t}$ on-shell. This is then damped by a ratio of Breit-Wigner functions f_{BW} when the invariant mass m_{bW} lies away from the top mass m_t. For more details see [5]. A plot of our subtraction term is shown as a function of m_{bW} in Fig. 2. One can see that is indeed strongly peaked when $m_{bW} \to m_t$, and falls off quickly for other values of m_{bW}. It cannot be zero for $m_{bW} \neq m_t$ without violating gauge invariance, as happens in the DR definition. Having given two definitions of the Wt mode which are directly applicable in an all orders calculation, we have implemented both of them in the MC@NLO package of [6]. This required the recalculation of the Wt cross-section in the subtraction formalism of [7], and now completes the description of single top production modes in MC@NLO, as the s and t-channel modes have already been included [8]. Spin correlations of decay products were implemented for the DR cross-section using the method of [9].

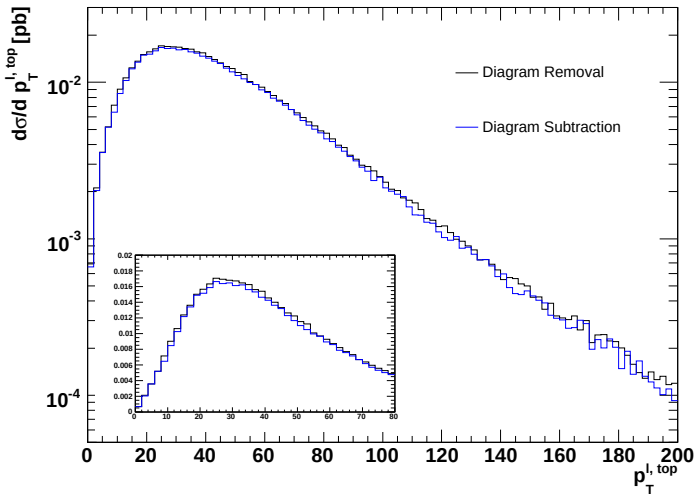

Fig. 3: Transverse momentum spectrum of the lepton from the top decay in both the DR and DS approaches, for $p_{t,veto} = 50$GeV.

3 Results

We considered example results in which all final state heavy particles decay leptonically. Furthermore, in order to address in more detail the issue of separation of the $t\bar{t}$ and Wt processes, we implemented a transverse momentum veto on the second hardest B hadron by analogy with [4]. That is, events are *not* accepted if they contain a second hardest B hadron whose pseudo-rapidity satisfies $|\eta| < 2.5$ and which has a transverse momentum $p_t^b < p_{t,veto}$. This then acts to reduce the interference term between Wt and $t\bar{t}$, due to the fact that harder b quarks tend to originate from a top decay.

We studied a number of observables, and compared the results from the DS and DR definitions of the Wt mode for various choices of $p_{t,veto}$. As a worst case scenario among the observables studied, we present results for the transverse momentum spectrum of the lepton from the top decay in Fig. 3. The results from the two definitions agree closely, except for at very high transverse momenta. However, the cross-section is small here. We also examined the effect of spin correlations, and of varying renormalisation and factorisation scales. These latter effects were larger than that arising from the difference between the DR and DS definitions in all cases.

4 Conclusion

QCD corrections threaten to undermine the definition of the Wt mode beyond LO due to interference with $t\bar{t}$ production. However, it is of clear phenomenological interest to be able to separate the former process in its own right. We have given two workable definitions of this process, implemented in the MC@NLO framework, such that the difference between the definitions mostly measures the interference between Wt and $t\bar{t}$ production.

Comparison of results obtained from the two definitions suggests that they agree closely subject to adequate cuts, and thus that it seems feasible to attempt to isolate Wt production at the LHC. Although further phenomenological analysis is needed to determine whether the $t\bar{t}$ background itself can be sufficiently reduced, the resulting MC@NLO codes nevertheless represent the state of the art description of the Wt mode.

Acknowledgements

This work was done in collaboration with S. Frixione, E. Laenen, P. Motylinski and B. Webber. CDW is supported by the Dutch National Foundation for Fundamental Physics Research (FOM).

References

[1] Kersevan, Borut Paul and Hinchliffe, Ian, JHEP **09**, 033 (2006).

[2] Belyaev, A. S. and Boos, E. E. and Dudko, L. V., Phys. Rev. **D59**, 075001 (1999).

[3] Tait, Tim M. P., Phys. Rev. **D61**, 034001 (2000).

[4] Campbell, John and Tramontano, Francesco, Nucl. Phys. **B726**, 109 (2005).

[5] Frixione, Stefano and Laenen, Eric and Motylinski, Patrick and Webber, Bryan R. and White, Chris D., JHEP **07**, 029 (2008).

[6] Frixione, Stefano and Webber, Bryan R., JHEP **06**, 029 (2002).

[7] Frixione, S. and Kunszt, Z. and Signer, A., Nucl. Phys. **B467**, 399 (1996).

[8] Frixione, Stefano and Laenen, Eric and Motylinski, Patrick and Webber, Bryan R., JHEP **03**, 092 (2006).

[9] Frixione, Stefano and Laenen, Eric and Motylinski, Patrick and Webber, Bryan R., JHEP **04**, 081 (2007).

PYTHIA 8 Status Report

Torbjörn Sjöstrand
Department of Theoretical Physics, Lund University

Abstract
PYTHIA 8, the C++ rewrite of the commonly-used PYTHIA event generator, is now available in a first full-fledged version 8.1. The older PYTHIA 6.4 generator in Fortran 77 is still maintained, for now, but users are strongly recommended to try out and move to the new version as soon as feasible.

1 Introduction

The "Lund Monte Carlo" family of event generators started in 1978 with the JETSET program. PYTHIA was begun a few years later, and the two eventually were joined under the PYTHIA label. Over the last 25 years the PYTHIA/JETSET program has been widely used to help understand the physics of high-energy collisions.

The program was from the onset written in Fortran 77, up to the current version 6.4 [1]. However, following the move of the experimental community to C++, a corresponding restart and rewrite was made for PYTHIA in 2004 – 2007, with most aspects cleaned up and modernized.

The first production quality release, PYTHIA 8.100, appeared towards the end of 2007 [2]. It was paced to arrive in time for LHC and therefore does not yet cover some physics topics. It has not yet caught on in the LHC experimental collaborations, however, and thus the older Fortran code is still maintained, even if at a reduced level.

2 Physics summary

Here follows a brief summary of the key physics aspects of PYTHIA 8.1, by topic.

Hard processes: The built-in library contains many leading-order processes, for the Standard Model almost all $2 \to 1$ and $2 \to 2$ ones and a few $2 \to 3$, beyond it a sprinkling of different processes, but not yet Supersymmetry or Technicolor. Parton-level events can also be input from external matrix-element-based generators, e.g. using Les Houches Event Files [3]. Also runtime interfaces are possible, and one such is provided to PYTHIA 6.4 for the generation of legacy processes. Resonance decays are included, often but not always with full angular correlations.

Parton showers: Transverse-momentum-ordered showers are used both for initial- and final-state radiation, the former based on backwards evolution. Implemented branchings are $q \to qg$, $g \to gg$, $g \to q\overline{q}$, $f \to f\gamma$ (f is a quark or lepton) and $\gamma \to f\overline{f}$. Recoils are handled in a dipole-style approach, but emissions are still associated with one emitting parton. Many processes include matching to matrix elements for the first (= hardest) emission; this especially concerns gluon emission in resonance decays.

Underlying events and minimum-bias events: PYTHIA implements a formalism with multiple parton–parton interactions, based on the standard QCD matrix elements for $2 \to 2$

processes, dampened in the $p_\perp \to 0$ limit. The collision rate is impact-parameter-dependent, and collisions are ordered in decreasing $p_\perp$. Multiple interactions (MI) are therefore combined with initial- and final-state radiation (ISR and FSR) in one common sequence of decreasing transverse momenta $p_{\perp 1} > p_{\perp 2} > p_{\perp 3} \ldots$,

$$\left.\frac{\mathrm{d}\mathcal{P}}{\mathrm{d}p_\perp}\right|_{p_\perp = p_{\perp i}} = \left(\frac{\mathrm{d}\mathcal{P}_{\mathrm{MI}}}{\mathrm{d}p_\perp} + \sum \frac{\mathrm{d}\mathcal{P}_{\mathrm{ISR}}}{\mathrm{d}p_\perp} + \sum \frac{\mathrm{d}\mathcal{P}_{\mathrm{FSR}}}{\mathrm{d}p_\perp}\right) \times \exp\left(-\int_{p_\perp}^{p_{\perp i-1}} \left(\frac{\mathrm{d}\mathcal{P}_{\mathrm{MI}}}{\mathrm{d}p'_\perp} + \sum \frac{\mathrm{d}\mathcal{P}_{\mathrm{ISR}}}{\mathrm{d}p'_\perp} + \sum \frac{\mathrm{d}\mathcal{P}_{\mathrm{FSR}}}{\mathrm{d}p'_\perp}\right) \mathrm{d}p'_\perp\right) ,$$

using the "winner takes all" Monte Carlo strategy. This leads to a competition, in particular between MI and ISR, for beam momentum. The beam remnants are colour-connected to the interacting subsystems, with a detailed modelling of the flavour and momentum structure, also for the parton densities to be used at each successive step. The framework also contains a model for colour reconnection, likely the least well understood aspect of this physics area, and therefore one that may require further development.

Hadronization: The Lund model for string fragmentation is used to describe the transition from coloured partons to colour singlet hadrons. Subsequent hadronic decays are usually described isotropic in phase space, but in some cases matrix-element information is inserted. It is also possible to link to external decay packages, e.g. for τ or B decays. A model for Bose–Einstein effects is included, but is off by default.

3 Program evolution

The above physics description largely also applies to PYTHIA 6.4. There are some differences to be noted, however.

Many old features have been definitely removed. Most notably this concerns the framework for independent fragmentation (a strawman alternative to string fragmentation) and the older mass-ordered showers (that still are in use in many collaborations, but do not fit so well with the new interleaved MI/ISR/FSR description).

Features that have been omitted so far, but should appear when time permits, include ep, γp and $\gamma\gamma$ beam configurations and a set of SUSY and Technicolor processes.

New features, relative to PYTHIA 6.4 include

- the interleaved MI/ISR/FSR evolution (6.4 only interleaved MI and ISR),
- a richer mix of underlying-event processes, no longer only QCD jets but also prompt photons, low-mass lepton pairs and J/ψ,
- possibility to select two hard processes in an event,
- possibility to use one PDF set for the hard process and another for MI/ISR, and
- updated decay data.

Major plans for the future include a new model for rescattering processes in the MI machinery, and new facilities to include matrix-element-to-parton-shower matching.

In addition minor improvements are introduced with each new subversion. Between the original 8.100 and the current 8.108 the list includes

- possibility to have acollinear beams, beam momentum spread and beam vertex spread,
- updated interfaces to several external packages,
- improved possibility to run several `Pythia` instances simultaneously,
- code modifications to compile under gcc 4.3.0 with the `-Wshadow` option, and
- some minor bug fixes.

4 Program structure

The structure of the PYTHIA 8 generator is illustrated in Fig. 1. The main class for all user interaction is called `Pythia`. It calls on the three classes

- `ProcessLevel`, for the generation of the hard process, by sampling of built-in matrix elements or input from an external program,
- `PartonLevel`, for the additional partonic activity by MI, ISR, FSR and beam remnants, and
- `HadronLevel`, for the transition from partons to hadrons and the subsequent decays.

Each of these, in their turn, call on further classes that perform the separate kinds of physics tasks.

Information is flowing between the different program elements in various ways, the most important being the event record, represented by the `Event` class. Actually, there are two objects of this class, one called `process`, that only covers the few partons of the hard process above, and another called `event`, that covers the full story from the incoming beams to the final hadrons. A small `Info` class keeps track of useful one-of-a-kind information, such as kinematical variables of the hard process.

There are also two incoming `BeamParticle`s, that keep track of the partonic content left in the beams after a number of interactions and initial-state radiations, and rescales parton distributions accordingly.

The process library, as well as parametrisations of total, elastic and diffractive cross sections, are used both by the hard-process selection machinery and the MI one.

The `Settings` database keeps track of all integer, double, boolean and string variables that can be changed by the user to steer the performance of PYTHIA, except that `ParticleDataTable` is its own separate database.

Finally, a number of utilities can be used just about anywhere, for Lorentz four-vectors, random numbers, jet finding, simple histograms, and for a number of other "minor" tasks.

5 Program usage

When you want to use PYTHIA 8 you are expected to provide the main program. At least the following commands should them be used:

- `#include "Pythia.h"` to gain access to all the relevant classes and methods,
- `using namespace Pythia8;` to simplify typing,
- `Pythia pythia;` to create an instance of the generator,

- `pythia.readString("command");` (repeated as required) to modify the default behaviour of the generator (see further below), or alternatively
- `pythia.readFile("filename");` to read in a whole file of commands, one per line,
- `pythia.init();` to initialize the generator, with different optional arguments to be used to set incoming beam particles and energies,
- `pythia.next();` to generate the next event, so this call would be placed inside the main event generation loop,
- `pythia.statistics();` to write out some summary information at the end of the run.

The `pythia.readString(...)` and `pythia.readFile(...)` methods are used to modify the values stored in the databases, and it is these that in turn govern the behaviour of the program. There are two main databases.

- `Settings` come in four kinds, boolean `flag`s, integer `mode`s, double-precision `parm`s, and string `word`s. In each case a change requires a statement of the form `task:property = value`, e.g. `TimeShower:pTmin = 1.0`.
- `ParticleDataTable` stores particle properties and decay tables. To change the former requires a statement of the form `id:property = value`, where `id` is the identity code of the particle, an integer. The latter instead requires the form `id:channel:property = value`, where `channel` is a consecutive numbering of the decay channels of a particle.

Commands to the two databases can be freely mixed. The structure with strings to be interpreted also allows some special tricks, like that one can write `on` instead of `true` and `off` instead of `false`, or that the matching to variable names in the databases is case-insensitive.

Information about all settings and particle data can be found in the online manual, which exists in three copies. The `xml` one is the master copy, which is read in when an instance of the generator is created, to set up the default values that subsequently can be modified. The same information is then also provided in a copy translated to more readable `html` format, and another copy in `php` format. The interactivity of the latter format allows a primitive graphical user interface, where a file of commands can be constructed by simple clicking and filling-in of boxes.

The online manual contains more than 60 interlinked webpages, from a program overview to some reference material, and in between extensive descriptions how to set up run tasks, how to study the output, and how to link to other programs. In particular, all possible settings are fully explained.

6 Trying it out

If you want to try out PYTHIA 8, here is how:

- Download `pythia8108.tgz` (or whatever is the current version when you read this) from
  `http://www.thep.lu.se/~torbjorn/Pythia.html`

- `tar xvfz pythia8108.tgz` to unzip and expand.
- `cd pythia8108` to move to the new directory.
- `./configure ...` is only needed to link to external libraries, or to use options for debug or shared libraries, so can be skipped in the first round.
- `make` will compile in $1-3$ minutes (for an archive library, same amount extra for a shared one).
- The `htmldoc/pythia8100.pdf` file contains A Brief Introduction [2].
- Open `htmldoc/Welcome.html` in a web browser for the full manual.
- Install the `phpdoc/` directory on a webserver and open `phpdoc/Welcome.php` in a web browser for an interactive manual.
- The `examples` subdirectory contains > 30 sample main programs: standalone, link to libraries, semi-internal processes, ...
- These can be run by `make mainNN` followed by `./mainNN.exe > outfile`.
- A `Worksheet` contains step-by-step instructions and exercises how to write and run main programs.

Note that PYTHIA is constructed so it can be run standalone, and this is the best way to learn how it works. For an experimental collaboration it would only be a piece in a larger software puzzle, and so a number of hooks has been prepared to allow various kinds of interfacing. The price to pay for using them is a more complex structure, where e.g. the origin of any errors is less easy to hunt down. Several aspects, such as the access to settings and particle data, should remain essentially unchanged, however.

7 Outlook

PYTHIA 6.4 is still maintained, with a current version 6.418 that weighs in at over 77,000 lines of code (including comments and blanks) and has a 580 page manual [1], plus update notes and sample main programs. No further major upgrades will occur with this program, however, and we intend to let it gradually die.

Instead PYTHIA 8.1 should be taking over. Currently it is smaller than its predecessor, with "only" 53,000 lines of code and a puny 27 page manual [2], but with much further online documentation and a big selection of sample main programs. It already contains several features not found in 6.4, and will gradually become the obvious version to use.

The LHC collaborations are strongly encouraged to accelerate the transition from 6.4 to 8.1, e.g. by serious tests with small production runs, to find any remaining flaws and limitations.

Acknowledgements

The PYTHIA 8 program was made possible by a three-year "sabbatical" with the SFT group at CERN/EP. This unwavering support is gratefully acknowledged. Mikhail Kirsanov and other members of the GENSER group has provided further help with Makefiles and other technical tasks. The work was supported in part by the European Union Marie Curie Research Training Network MCnet under contract MRTN-CT-2006-035606.

References

[1] Sjöstrand, T. and Mrenna, S. and Skands, P., JHEP **05**, 026 (2006).

[2] Sjöstrand, T. and Mrenna, S. and Skands, P., Comput. Phys. Commun. **178**, 852 (2008).

[3] Alwall, J. and others, Comput. Phys. Commun. **176**, 300 (2007).

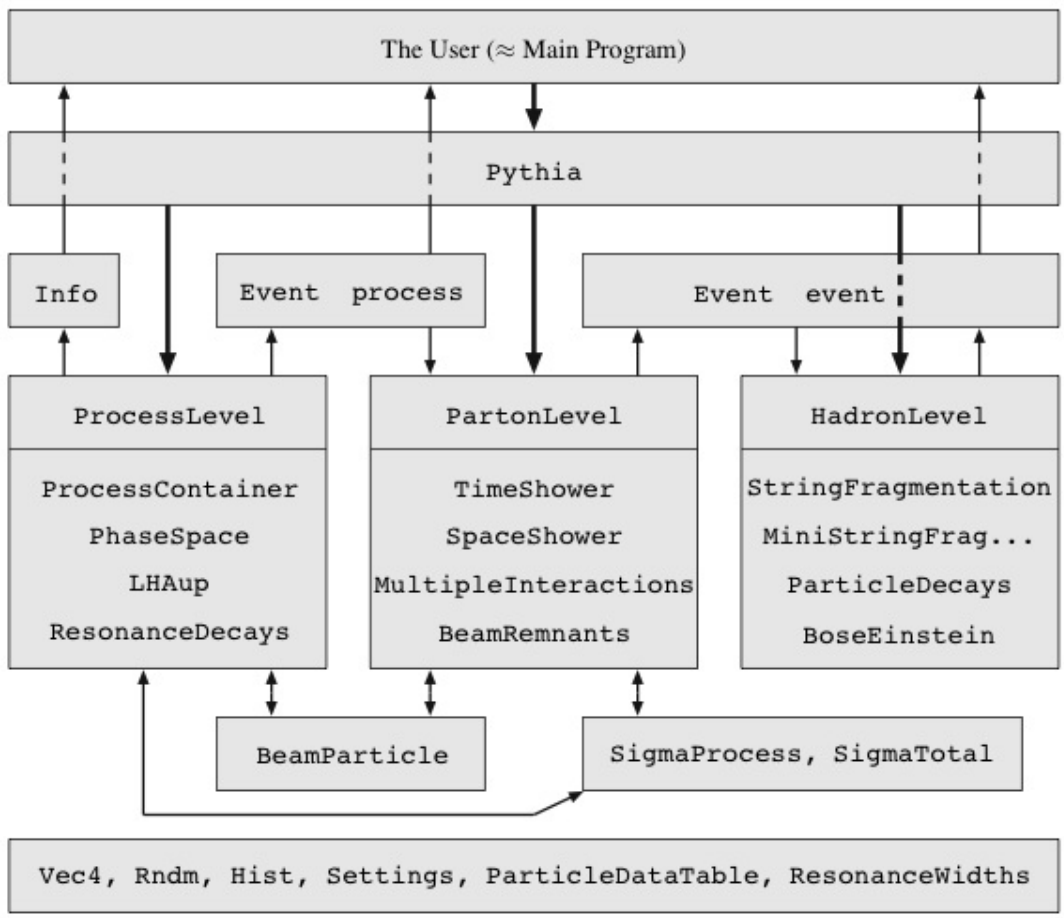

Fig. 1: The relationship between the main classes in PYTHIA 8. The thick arrows show the flow of commands to carry out different physics tasks, whereas the thinner show the flow of information between the tasks. The bottom box contains common utilities that may be used anywhere. Obviously the picture is strongly simplified.

THEPEG
Toolkit for High Energy Physics Event Generation

Leif Lönnblad
Department of Theoretical Physics, Lund University, Sweden

Abstract
I present the status of the THEPEG project for creating a common platform for implementing C++ event generators. I also describe briefly the status of the new version of ARIADNE implemented using this framework.

1 Introduction

Monte Carlo Event Generators have developed into essential tools in High Energy Physics. Without them it is questionable if it at all would be possible to embark on large scale experiments such as the LHC. Although the current event generators work satisfactorily, the next generation of experiments will substantially increase the demands both on the physics models implemented in the event generators and on the underlying software technology.

Below is a very brief description of the THEPEG [1] project for designing a general framework in `C++` for implementing event generator models, and also the ARIADNE program which uses THEPEG to implement the underlying dipole cascade model. Also HERWIG++ [2] is implemented in the THEPEG framework, but this program is described elsewhere in these proceedings.

2 Basic structure

THEPEG is a general platform written in `C++` for implementing models for event generation. It is made up from the basic model-independent parts of PYTHIA7 [3, 4], the original project of rewriting the Lund family of event generators in `C++`. When the corresponding rewrite of the HERWIG program [5] started it was decided to use the same basic infrastructure as PYTHIA7 and therefore the THEPEG was factorized out of PYTHIA7 and is now the base of both PYTHIA7 and HERWIG++ [2]. Also the coming `C++` version of ARIADNE [6] is using THEPEG. It should be noted, however, that the new `C++` version of PYTHIA, called PYTHIA8 is not built on THEPEG.

THEPEG implements a number of general utilities such as smart pointers, extended type information, persistent I/O, dynamic loading, a system for handling physical units and some extra utilities for kinematics, phase space generation etc.

The actual event generation is then performed by calling different *handler* classes for hard partonic sub-processes, parton densities, QCD cascades, hadronization etc. To implement a new model to be used by THEPEG, the procedure is then to write a new `C++` class inheriting from a corresponding handler class and implement a number of pre-defined virtual functions. Eg. a class for implementing a new hadronization model would inherit from the abstract `HandronizationHandler` class, and a new parton density parameterization would inherit

from the `PDFBase` class. These classes communicate with each other and with the underlying framework using pre-defined virtual function definitions and a highly structured `Event` object.

To generate events with THEPEG one first runs a setup program where an `EventGenerator` object is set up to use objects implementing different models for different steps of the generation procedure. All objects to be chosen from are stored in a *repository*, within which it is also possible to modify switches and parameters of the implemented models in a standardized fashion, using so called *interface* objects. Typically the user would choose from a number of pre-defined `EventGenerator` objects and only make minor changes for the specific simulation to be made. When an `EventGenerator` is properly set up, it is saved persistently to a file which can then be read into a special run program to perform the generation, in which case special `AnalysisHandler` objects may be specified to analyze the resulting events. Alternatively, the `EventGenerator` can be read into eg. a detector simulation program or a user supplied analysis program, where it can be used to generate events.

3 Status

THEPEG version 1.2 is available [1] and is working. As explained above, it contains the basic infrastructure for implementing and running event generation models. It also contains some simple physics models, such as some $2 \to 2$ matrix elements, a few parton density parameterizations (and an interface to LHAPDF [7]) and a near-complete set of particle decays. However, these are mainly in place for testing purposes, and to generate realistic events, the PYTHIA7 and/or HERWIG++ programs are needed.

Currently the program only works under Linux and MacOS using the `gcc` compiler. This is mainly due to the use of dynamic linking of shared object files, which is inherently platform-dependent. However, the build procedure uses the `libtool` facility [8], which will hopefully allow for easy porting to other platforms in the fututre.

Although THEPEG includes a general structure for implementing basic fixed-order matrix element generation to produce the initial hard subprocesses in the event generation, a general procedure for reading such parton level events from external programs using the Les Houches accord [9, 10] is included.

The documentation of THEPEG is currently quite poor. The code itself is documented using the Doxygen format [11], which provides some technical documentation. The lack of documentation means that there is currently a fairly high threshold for a beginner to start using and/or developing physics modules for THEPEG. However, THEPEG has a well worked through low-level interface to be able to set parameter and switches, etc. in classes introduced to the structure from the outside. This means that the running of THEPEG does not require a `C++` expert, but can be handled through a simple command-line facility or through a Java-based graphical user interface.

Among the recent developments in THEPEG one can note that there is now an option to do compile-time checking of units in all mathematical expressions. Also a number of helicity classes for construction of matrix elements has been imported from HERWIG++. Furthermore, the dependence on CLHEP [12] has been dropped and the only dependence on external packages is the GNU scientific library [13], which is a standard package in all Linux distributions.

3.1 ARIADNE

The reimplementation of the ARIADNE [6] program using the framework of THEPEG has started but is not yet publically available. Although this is mainly a pure rewrite of the fortran version of ARIADNE, it will contain some improvements, such as CKKW matching [14, 15]. In addition, an improved version of the LDCMC [16] is planned.

ARIADNE is supposed to be used together with Lund string fragmentation, and for that purpose an interface of relevant parts of the PYTHIA8 program to the THEPEG framework is planned. Meanwhile there is already a simplified implementation of string fragmentation in the PYTHIA7 program [4] which was the first attempt to reimplement PYTHIA into `C++`.

4 Conclusions

THEPEG can now be considered to be a stable piece of software. Several improvements can be expected in the future, but the basic structure is fixed and has been working well for all models which have been implemented so far.

References

[1] Leif Lönnblad and others, *THEPEG program*. `http://www.thep.lu.se/ThePEG`.

[2] Bahr, M. and others (2008).

[3] Bertini, Marc and Lönnblad, Leif and Sjöstrand, Torbjörn, Comput. Phys. Commun. **134**, 365 (2001).

[4] Leif Lönnblad and others, *PYTHIA7 program*. `http://www.thep.lu.se/Pythia7`.

[5] Corcella, G. and others, JHEP **01**, 010 (2001).

[6] Lönnblad, Leif, Comput. Phys. Commun. **71**, 15 (1992).

[7] Giele, W. and others (2002).

[8] Gord Matzigkeit and others, *The `libtool` program*. `http://www.gnu.org/software/libtool`.

[9] Boos, E. and others (2001).

[10] Alwall, J. and others, Comput. Phys. Commun. **176**, 300 (2007).

[11] Dimitri van Heesch, *The doxygen documentation system*. `http://www.doxygen.org`.

[12] Lönnblad, Leif, Comput. Phys. Commun. **84**, 307 (1994).

[13] M. Galassi and others, *The gnu scientific library*. `http://www.gnu.org/software/gsl`.

[14] Catani, S. and Krauss, F. and Kuhn, R. and Webber, B. R., JHEP **11**, 063 (2001).

[15] Lönnblad, Leif, JHEP **05**, 046 (2002).

[16] Kharraziha, Hamid and Lönnblad, Leif, JHEP **03**, 006 (1998).

CASCADE

Michal Deák[1], *Hannes Jung*[1,2], *Krzysztof Kutak*[1]
[1] Deutsches Elektronen-Synchroton DESY Hamburg, FRG
[2] University of Antwerp, Belgium

CASCADE is a full hadron level Monte Carlo event generator for ep, γp, pp and $p\bar{p}$ processes, which uses the unintegrated parton distribution functions convoluted with off - mass shell matrix elements for the hard scattering. The CCFM [1] evolution equation is an appropriate description valid for both small and moderate x which describes parton emission in the initial state in an angular ordered region of phase space. For inclusive quantities it is equivalent to the BFKL and DGLAP evolution in the appropriate asymptotic limits. The angular ordering of the CCFM description makes it directly applicable for Monte Carlo implementation.

A detailed description of CASCADE is given in [2], the source code of CASCADE and a manual can be found under: `http://www.desy.de/~jung/cascade/`. A description and discussion of the CCFM unintegrated gluon densities used in CASCADE can be found in [3, 4] The unintegrated gluon density $x\mathcal{A}_0(x, k_\perp, \bar{q})$ is a function of the longitudinal momentum fraction x the transverse momentum of the gluon $k_\perp$and the factorization scale $\bar{q}$. A general discussion of unintegrated gluon densities is given in [5–8].

The matrix elements for heavy quark [9, 10] and Higgs [11] production in k_t-factorization are available since long. The $k_\perp$-factorisation approach can be used all the way up to high transferred-momentum scales. As an illustration in Fig. 1 we present a numerical calculation for the transverse momentum spectrum of top-antitop pair production at the LHC [5]. Small-x effects are not large in this case. Rather, this process illustrates how $k_\perp$-factorisation works in the region of finite x and large virtualities of the order of the top quark mass. It is interesting to note that even at LHC energies the transverse momentum distribution of top quark pairs calculated from $k_\perp$-factorisation is similar to what is obtained from a full NLO calculation (including parton showers, MC@NLO [12]), with CASCADE giving a somewhat harder spectrum, Fig. 1.

However, to use CASCADE for standard processes at the LHC, $g^*g^* \rightarrow W/ZQ\bar{Q}$ production [13, 14] and quark induced processes [15] ($q^*g \rightarrow qg$) needed to be calculated in the k_t-factorization approach. First results from these calculations are given in [16].

The QCD-Compton process needs special attention: First, we are dealing with light partons, and collinear and soft regions have to be avoided. This is done by applying a cut on the transverse momentum p_t^{cm} of any of the outgoing q or g in the laboratory frame. Secondly, unintegrated quark distributions had to be determined. Since the aim is mainly to cover the forward or backward region at LHC, only the valence quarks are considered, avoiding any complication with double counting of sea-quarks and gluon contributions.The unintegrated quark density is obtained from a full CCFM evolution of valence quarks (taken at Q_0 from CTEQ 5 [17]) treating correctly the full kinematics during the evolution. Only the $q \rightarrow qg$ splitting functions were included, which are finite for small x.

For all processes, the initial state parton shower is obtained from a deconvolution of the CCFM unintegrated parton densities, obeying the angular ordering constraint. The angular ordering is essential for the x dependence of the unintegrated parton densities. However, during

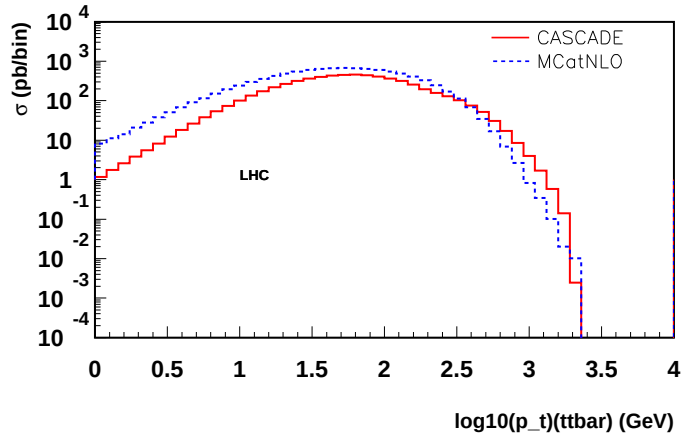

Fig. 1: Comparison of transverse momentum distribution of $t\bar{t}$ pairs calculated from CASCADE with the NLO calculation MC@NLO at LHC energies.

the initial state cascade, the emitted parton can also undergo a further time-like cascade. This time-like showering is now included, where the maximum virtuality of the showering partons is set by the transverse momentum of the parent parton. The time-like cascade follows again angular ordering, but it does not change (except from kinematics) the angular ordering of the initial state cascade, which is constrained by the unintegrated parton density.

New developments to properly model the dense partonic system have lead to the introduction of a absorptive boundary simulating effectively the saturation effect coming from non-linear evolution equations. The absorptive boundary at small x suppresses the small k_t region of the unintegrated gluon density. The initial parameters for these uPDFs have to be determined from fits to measurements [18] and yield a similarly good χ^2. These uPDFs are available in CASCADE (version 2.0.2), allowing the study of saturation effects with final state observables.

References

[1] M. Ciafaloni, Nucl. Phys. **B 296**, 49 (1988);
S. Catani, F. Fiorani, and G. Marchesini, Phys. Lett. **B 234**, 339 (1990);
S. Catani, F. Fiorani, and G. Marchesini, Nucl. Phys. **B 336**, 18 (1990);
G. Marchesini, Nucl. Phys. **B 445**, 49 (1995).

[2] H. Jung, Comp. Phys. Comm. **143**, 100 (2002).
`http://www.desy.de/~jung/cascade/`.

[3] M. Hansson and H. Jung, *Towards precision determination of uPDFs*, 2007.
`arXiv:0707.4276 [hep-ph]`.

[4] H. Jung, A. V. Kotikov, A. V. Lipatov, and N. P. Zotov, *Towards precision determination of unintegrated parton density functions*, 2006. `arXiv:hep-ph/0611093`.

[5] F. Hautmann and H. Jung, JHEP **10**, 113 (2008), `arXiv:0805.1049 [hep-ph]`.

[6] Small x Collaboration, J. R. Andersen *et al.*, Eur. Phys. J. **C48**, 53 (2006), arXiv:hep-ph/0604189.

[7] Small x Collaboration, J. R. Andersen *et al.*, Eur. Phys. J. **C35**, 67 (2004), hep-ph/0312333.

[8] Small x Collaboration, B. Andersson *et al.*, Eur. Phys. J. **C25**, 77 (2002), hep-ph/0204115.

[9] S. Catani, M. Ciafaloni, and F. Hautmann, Nucl. Phys. **B 366**, 135 (1991).

[10] A. V. Lipatov and N. P. Zotov, Eur. Phys. J. **C27**, 87 (2003); S. P. Baranov and N. P. Zotov, J. Phys. **G29**, 1395 (2003); S. P. Baranov, Phys. Rev. **D66**, 114003 (2002).

[11] F. Hautmann, Phys. Lett. **B535**, 159 (2002), hep-ph/0203140.

[12] S. Frixione, P. Nason, and B. R. Webber, JHEP **08**, 007 (2003), arXiv:hep-ph/0305252.

[13] M. Deak and F. Schwennsen, JHEP **09**, 035 (2008), arXiv:0805.3763 [hep-ph].

[14] S. P. Baranov, A. V. Lipatov, and N. P. Zotov, Phys. Rev. **D77**, 074024 (2008), arXiv:0708.3560 [hep-ph].

[15] M. Deak, H. Jung, and K. Kutak, *Valence quarks and k_T factorisation*, 2008. arXiv:0807.2403 [hep-ph].

[16] S. Baranov et al, *k_T-factorization and uPDFs at HERA and the LHC*, 2008. These proceedings.

[17] CTEQ Collaboration, H. L. Lai *et al.*, Eur. Phys. J. **C12**, 375 (2000), arXiv:hep-ph/9903282.

[18] K. Kutak and H. Jung (2008), arXiv:0812.4082 [hep-ph].

AlpGen and SHERPA in $Z/\gamma^* + jets$ at LHC

Piergiulio Lenzi
Università degli Studi di Firenze and INFN Sez. Firenze

Abstract
A study of **AlpGen** and **SHERPA** event generators in the production of $Z/\gamma^* + jets$ events at LHC is presented. Both generators implement a combined use of multi-parton tree level matrix element calculations and parton shower, but the prescriptions used to match the two approaches are different. We will show a collection of lepton and jet observables and how they change as the parameters that steer the matching prescription are altered. We will also show a comparison between the two algorithms when run with the default parameter choice. The study has been done using the Rivet analysis framework.

1 Introduction

The characterization of $Z/\gamma^* + jets$ production at LHC, with the vector boson decaying leptonically, will be one of the goals of the early LHC physics analyses; the rather clear leptonic signature will make these events easy to identify, and the vector boson kinematics will be reconstructed quite well even with a not perfectly calibrated/aligned detector: these signals will be very useful, for example, for the calibration of the calorimeter response using the balancing of the jets with the recoiling vector boson. Z bosons will be produced at the LHC with unprecedented rates, thus allowing a very precise determination of the vector boson mass and width; besides $Z/W + jets$ events represent a background for many new physics searches, such as SUSY.

For all these reasons it's extremely important to understand the different characteristics of the event generators that can produce these events, to understand the theoretical uncertainties connected to residual dependence on parameters such as the scale choice and to spot how the differences among the event generators on the market translate into the observables reconstructed in the experiments.

Several event generators exist that can produce $Z/\gamma^* + jets$ events. The **PYTHIA** [1] and **HERWIG** [2] event generators implement the LO calculation of the hard $2 \to 2$ process and then continue the evolution with the parton shower technique.

A different approach, which proved quite effective in describing Tevatron data, consists of the combination of matrix element (ME) tree level calculations for up to several partons in the final state and subsequent parton shower (PS), with care not to double count configurations that can be produced both from the matrix element and from the parton shower. **AlpGen** [3] and **SHERPA** [4] both implement this approach, but with significant differences.

2 Matching prescriptions

CKKW: The **SHERPA** event generator comes with its own ME calculator, called **AMEGIC++** [5] (A Matrix Element Generator In C++), and with its own PS, called **APACIC++** [6] (A Parton

CAscade in C++). In this event generator the CKKW prescription for matching ME and PS is implemented in full generality.

The CKKW prescription was originally proposed for e^+e^- collision [7], then it was extended to hadron collisions [8]. It's based on a separation of the phase space in a region for jet production, handled by the ME and a region for jet evolution, handled by the PS. The separation is determined using a $k_\perp$ measure; a configurable $k_\perp$ cutoff, $y_{cut} = Q^2_{cut}/E^2_{CM}$, is used to define the separation of the two regions; Q_{cut} is the only parameter of this matching prescription.

The first step of the CKKW matching prescription is the calculation of the ME cross sections for all the parton multiplicities we want to enter the final state. In this calculation y_{cut} is used to cutoff divergences: the cross section is calculated for parton configurations such that the minimum $k_\perp$ distance between two partons is above y_{cut}. In the ME cross section estimation a fixed value for α_S, ${\alpha_S}^{ME}$, is used.

The problem with ME calculation is that they are inclusive, so one cannot simply add ME cross sections for different final state parton multiplicities.

In the CKKW approach events produced according to the ME cross sections are reweighted with a Sudakov form factor weight. This makes ME cross sections exclusive. To calculate the Sudakov weight final state partons arising from the ME calculations are clustered back with a $k_\perp$ clustering till the core $2 \to 2$ process. In this way a series of splittings is reconstructed, that represent the splittings that would occur in a PS description of that final state. On this basis the Sudakov weight is calculated. An α_S correction is also applied to take into account that the splittings happened at scales different from Q_{cut}, as originally imposed in the ME calculation.

Below the scale y_{cut} the evolution is described by the PS alone, but with a veto to avoid emission above y_{cut}, that has been taken into account already in the ME.

MLM: The MLM prescription is implemented in **AlpGen**; it is similar to the CKKW prescription for what concerns the production of ME events and the reweighting of α_S but implements the Sudakov reweighting and the veto on the PS in a different way.

In the MLM approach a conventional PS program (**PYTHIA** or **HERWIG**) is used to shower events emerging from the ME. The shower is performed without any constraint. Partons resulting from the PS are clustered into jets with a cone algorithm. If all the jets match to all the partons generated from the ME the event is kept otherwise it is discarded. A special treatment is then needed for the events produced by the highest multiplicity ME, where additional jets, softer that the matched ones are allowed.

In this way the MLM prescription both reproduces the effect of the Sudakov reweighting and vetoes additional hard emission from the shower.

3 Analysis framework

Both programs were run with up to three additional partons from the matrix element. In order to better identify the effect of the different matching prescriptions we switched off the underlying event simulation.

We setup an analysis in the Rivet [9] analysis framework. Rivet is interfaced to a number

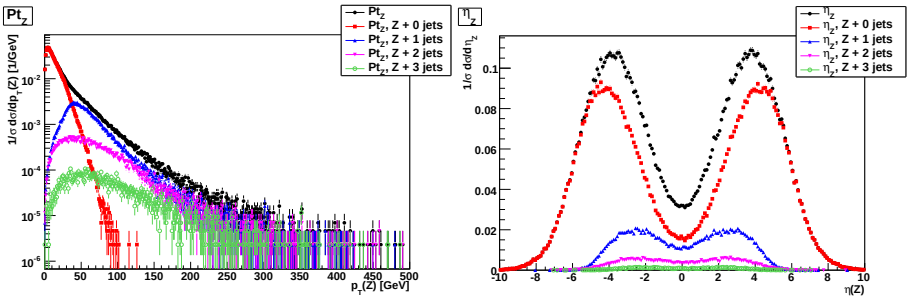

(a) (b)

Fig. 1: p_T spectrum (a) and η distribution (b) for events produced with **SHERPA**. The contribution from different jet multiplicities is put into evidence in color.

of event generators through the AGILe package; this means that one can run both **SHERPA** and **AlpGen** within Rivet and run exactly the same analysis code on them. Rivet analyses are actually run on the **HepMC** [10] record as it is produced from the generator.

We run the analysis at hadron level, selecting final state particles with pseudorapidity η such that $|\eta| < 5$. We selected lepton pairs with an invariant mass between $66\,\mathrm{GeV}$ and $116\,\mathrm{GeV}$. Jets were reconstructed with the longitudinally invariant $k_\perp$ algorithm [11], as implemented in the **FastJet** package [12]. We set the pseudo-radius parameter of the $k_\perp$ algorithm to 0.4 and we set a minimum p_T for jets of $30\,\mathrm{GeV}$.

4 Results for SHERPA

Fig. 1 shows the p_T (a) and η (b) distributions for the lepton pair produced in **SHERPA**. The contribution from different jet multiplicities is put into evidence in colour, while the overall contribution is in black. We observe that the high p_T tail of the distribution is due to the multiple jet contribution.

Fig. 2 shows differential jet rates in **SHERPA**. Differential jet rates are the distribution of the resolution parameter in the $k_\perp$ clustering, that makes an n jet event turn into an $n-1$ jet event. To compute differential jet rates one might think of running the $k_\perp$ clustering in exclusive mode with different values of the resolution parameter, looking for the parameter that makes on jet disappear, thus leading to the transition $n \to n-1$. Actually this is done more efficiently simply looking at the relevant recombinations in the clustering sequence when running $k_\perp$ clustering in inclusive mode. Those plots give a very detailed picture of how the phase space is filled. In particular one has to take care of what happens around the separation cut between the ME-filled region and the PS-filled region, marked with a vertical dashed line in the plots. The phase space above the line is filled by the ME, below by the PS. While the $1 \to 0$ transition looks quite smooth, some structure around the separation cut is present in the $2 \to 1$ and $3 \to 2$ plots. The effect is anyway moderate, and is due to mismatches that can occur close to the cut, due to the way the PS modifies the ME kinematics.

Fig. 3 shows how the p_T and η distribution of the lepton pair change if the value of the parameter Q_{cut} that steers the matching is changed. As Q_{cut} is increased the p_T spectrum tends

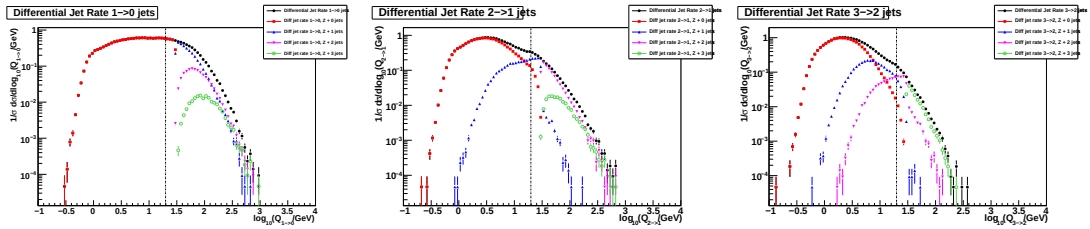

(a) (b) (c)

Fig. 2: Differential jet rates in **SHERPA**. (a) $1 \to 0$, (b) $2 \to 1$ (c), $3 \to 2$

to be softer and the η distribution less central. This is probably due to the reduced phase space available for the ME as Q_{cut} is increased. Since the ME is responsible for the hardest parton kinematics, an increase in Q_{cut} results in slightly softer spectra.

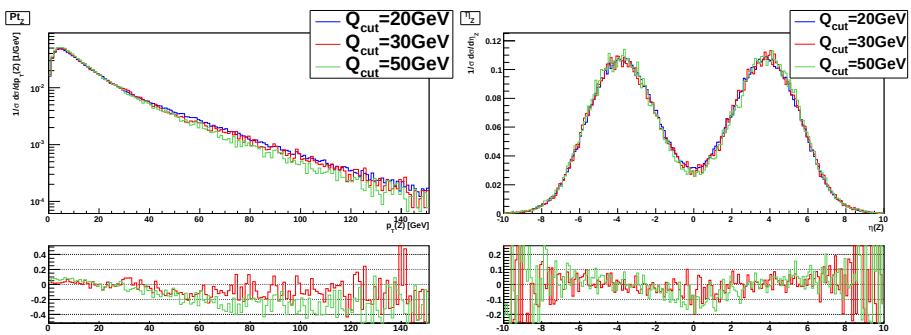

(a) (b)

Fig. 3: p_T distribution (a) and η distribution (b) for the lepton pair in **SHERPA** with three different values of Q_{cut}.

Fig. 4 shows the Q_{cut} dependency in differential jet rate plots. Differences are observed in the transition region around Q_{cut}. The difference with respect to the default $20\,\mathrm{GeV}$ is at most 40%.

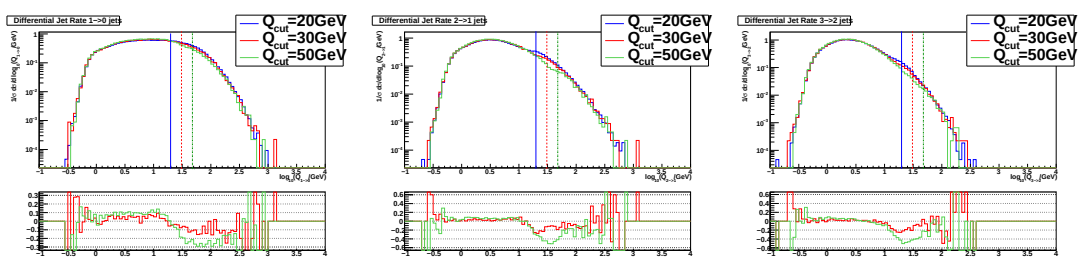

(a) (b) (c)

Fig. 4: Differential jet rates in **SHERPA** for three different values of Q_{cut}. (a) $1 \to 0$, (b) $2 \to 1$ (c), $3 \to 2$

5 Results for AlpGen

AlpGen sample has been showered using **PYTHIA**. We tried two different values for the minimum p_T in the cone algorithm that is used in **AlpGen** to steer the MLM matching: $25\,\mathrm{GeV}$ and $40\,\mathrm{GeV}$.

Fig. 5 shows the effect of this change on the lepton pair p_T and η spectra. The effect is almost negligible.

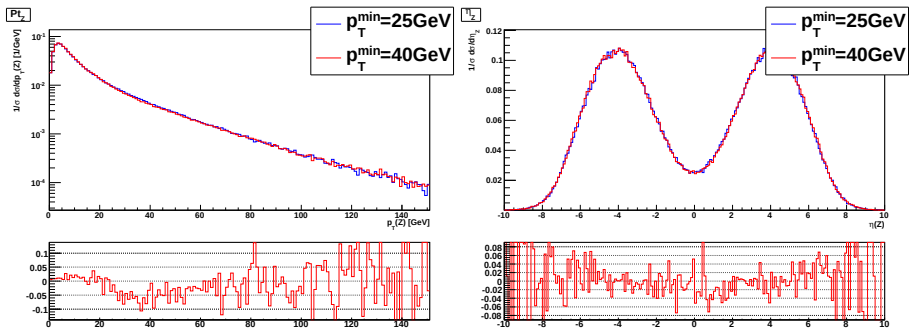

(a) (b)

Fig. 5: p_T distribution (a) and η distribution (b) for the lepton pair with three different values of p_T^{min} in **AlpGen**.

Fig. 6 shows differential jet rate plots for **AlpGen** for the two values of the minimum p_T in the internal cone algorithm. Also in this case the differences are concentrated in the region around p_T^{min}, that is effectively the value used in **AlpGen** to separate the ME and PS regions.

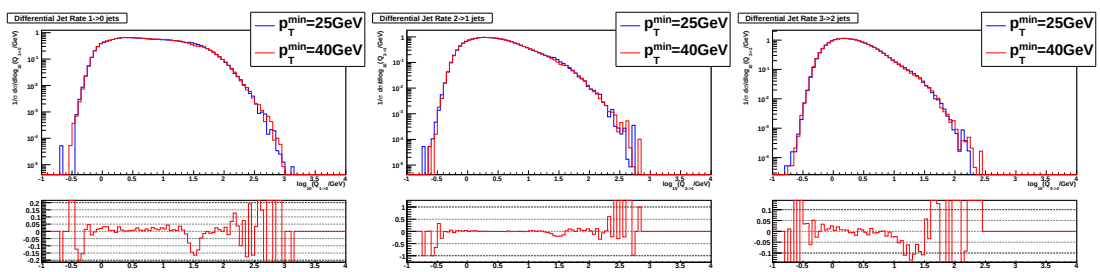

(a) (b) (c)

Fig. 6: Differential jet rates in **AlpGen**. (a) $1 \to 0$, (b) $2 \to 1$ (c), $3 \to 2$

6 A comparison between the two

We made a comparison between **AlpGen** and **SHERPA** when run with the default settings. For **AlpGen** we used both **PYTHIA** and **HERWIG** as parton showers. Fig. 7 shows the p_T spectrum and the η distribution of the lepton pair and the p_T spectrum of one of the two leptons. We observe that **SHERPA** shows the hardest spectrum both for the lepton pair and the single lepton, while **AlpGen**+**PYTHIA** is the softest. This translates into the η distribution, with **SHERPA** showing the most central boson, and **AlpGen**+**PYTHIA** the less central.

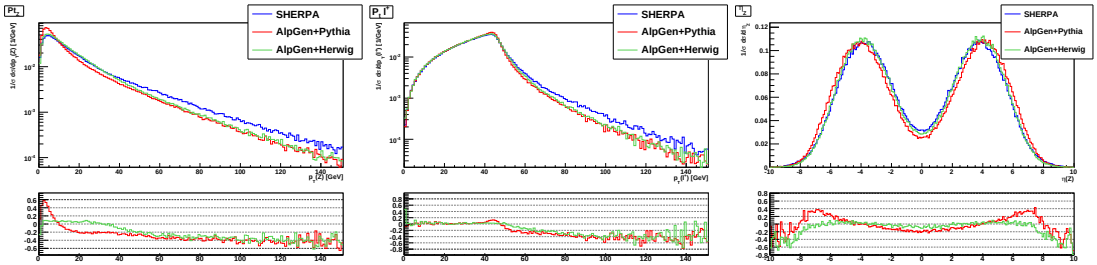

(a) (b) (c)

Fig. 7: p_T distribution of the lepton pair (a), of the positive lepton (b) and η distribution for the lepton pair (c) in **SHERPA**, **AlpGen**+**PYTHIA** and **AlpGen**+**HERWIG**. Relative difference plots are with respect to **SHERPA**.

Fig. 8 shows the jet multiplicity, the hardest and the second jet spectra. **SHERPA** shows a higher mean jet multiplicity; this is consistent with the harder leptonic spectra, given that the Z boson recoils against the jets. Also the leading jet p_T spectrum is harder in **SHERPA**, while the spectrum for the second jet is similar.

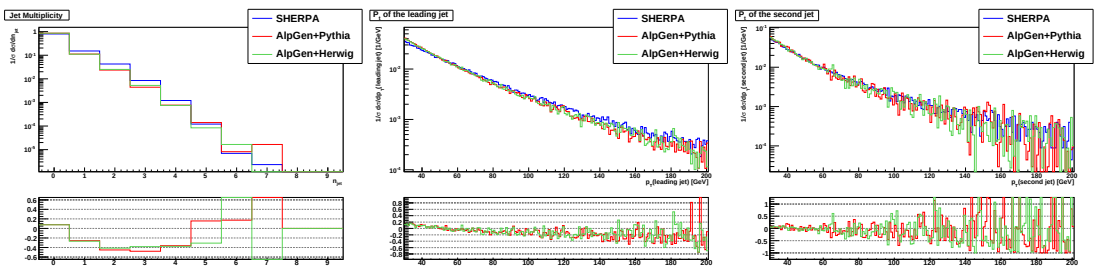

(a) (b) (c)

Fig. 8: Jet multiplicity (a) and p_T spectrum for the hardest (a) and second (b) jet in **SHERPA**, **AlpGen**+**PYTHIA** and **AlpGen**+**HERWIG**. Relative difference plots are with respect to **SHERPA**.

7 Conclusion

A study **AlpGen** and **SHERPA** for the production of $Z/\gamma^* + jets$ has been done. A series of consistency checks have been performed with both generators to check the sensitivity to parameters that steer the matching prescription. No big dependencies were spotted. The two generators were compared when run with default settings. Some not negligible differences were spotted, both in the lepton and jet observables. **SHERPA** shows in general harder spectra, and also a higher mean jet multiplicity.

The analyses shown in this paper were performed with the Rivet Analysis framework.

References

[1] Sjostrand, Torbjorn and Mrenna, Stephen and Skands, Peter, JHEP **05**, 026 (2006).

[2] Corcella, G. and others (2002).

[3] Mangano, Michelangelo L. and Moretti, Mauro and Piccinini, Fulvio and Pittau, Roberto and Polosa, Antonio D., JHEP **07**, 1 (2003).

[4] Gleisberg, Tanju and others, JHEP **02**, 56 (2004).

[5] Krauss, F. and Kuhn, R. and Soff, G., JHEP **02**, 044 (2002).

[6] Krauss, F. and Schalicke, A. and Soff, G., Comput. Phys. Commun. **174**, 876 (2006).

[7] Catani, S. and Krauss, F. and Kuhn, R. and Webber, B. R., JHEP **11**, 63 (2001).

[8] Krauss, F., JHEP **08**, 015 (2002).

[9] Waugh, B. M. and others (2006).

[10] Dobbs, Matt and Hansen, Jorgen Beck, Comput. Phys. Commun. **134**, 41 (2001).

[11] Catani, S. and Dokshitzer, Yuri L. and Webber, B. R., Phys. Lett. **B285**, 291 (1992).

[12] Cacciari, Matteo and Salam, Gavin P., Phys. Lett. **B641**, 57 (2006).

Generator comparison for top-pair production at CMS

Roberto Chierici
Institut de Physique Nucleaire de Lyon, IN2P3-CNRS, Université Claude Bernard Lyon 1, Villeurbanne, France

Abstract
This work presents a throughout comparison of some of the most popular generators for top-pair production at the LHC in the frame of the CMS software. The aim is to validate the physics contents after their integration in the experimental software and to give indications for the best possible choices of the generator set-up.

1 Introduction

The description of top-pair production at the LHC can be handled by different kind of generation tools. The most traditional approach, via leading order (LO) calculations (examples are generators like PYTHIA [1], TopRex [2]), is now accompanied by more modern tools allowing the inclusion of higher leading order (HLO) QCD terms, via the so-called matrix elements (ME) - parton shower (PS) matching [3] (examples are ALPGEN [4] or the recent version of MadGraph [5]). Also available are now next-to-leading-order (NLO) QCD generators like MC@NLO [6].

The aim of this work is to test the physics contents of the different generators in the domain of top physics and in the framework of the CMS software. This also allows a common environment for the comparisons. Studies at pure generator level are documented by several articles already [7]. This work should not be intended as a generator review.

2 Set-up and event reconstruction

In the following comparisons of event generators, performed for pp collisions at a centre-of-mass energy of 14 TeV, the pure PS part is described in a uniform way by the use of PYTHIA, with care to have the same input parameter settings in all conditions. Exception is MC@NLO, currently only interfaced to HERWIG. The scales and PDFs are also chosen to be as much as possible the same: exception to this is a slight difference in the scale definition in ALPGEN and MadGraph. The details of the input settings, as well as the numbers of events generated for this study, are reported in table 1. The validity of the choice of the tuning with new approaches for the description of the radiation goes beyond the scope of the present note; it is, on the contrary, relevant to maintain the input settings as uniform as possible.

The comparisons are made at the generator level, after radiation from PS. The variables are reconstructed from the quarks and leptons before their final state radiation, the shown variables are therefore sensitive to the description of initial or intermediate (from top) state radiation (ISR). All the plots shown in the following are normalised to unity for the sake of clarity.

Parameter	TopRex	MadGraph	ALPGEN	MC@NLO
PDFs	CTEQ5L	CTEQ5L	CTEQ5L	CTEQ5L
Renormalization scale	m_T	m_t	m_T	m_T
Factorization scale	m_T	m_t	m_T	m_T
Λ_{QCD} in PYTHIA (PARP(61), PARP(62)) (GeV)	0.25	0.25	0.25	-
Q^2_{max} PYTHIA switch (PARP(67))	2.5	2.5	2.5	-
Generated events	$1,5 \times 10^6$	3×10^6	2×10^5	1×10^6

Table 1: Main generator input parameter settings, and total number of generated events for this study. The transverse mass m_T is defined as $\sum_{tops}(m^2+p_T^2)$. The MC@NLO generator is only interfaced with the HERWIG hadronisation, so no direct comparison in the parameter settings can be made.

3 The importance of ME-PS matching

At the energy scale of the LHC the description of gluon radiation becomes crucial. Recent techniques for PS-ME matching allow to describe much better the hard gluon radiation, maintaining the parton shower approximation for low p_T emissions. In the following we have used TopReX as the LO reference, ALPGEN and MadGraph as examples of matched $t\bar{t}$ event generations and MC@NLO as a NLO QCD description of the $t\bar{t}$ process.

Differences in gluon radiation may manifest themselves in distortions of the top quark angular distributions and transverse variables. The most spectacular effect can be appreciated in the transverse momentum of the radiation itself, which equals the transverse momentum of the $t\bar{t}$ system.

This is what is shown in figure 1 for two standard generations in comparison to the newly available matching scheme [8] of MadGraph: all the different contributions to a fixed ME order, ie tt+0jets, tt+1jets, tt+2jets and tt+3jets, are explicitly indicated. The matching scheme is such that there is no phase space double counting in the different samples: no matching is performed for the last sample to let the PS predict configurations at higher jet multiplicities. The samples are mixed together according to the respective cross-sections. In the same figure also the azimuthal difference between the two tops is shown.

From the picture it is evident that gluon production via ME predicts a much harder transverse spectrum. The difference in shape is impressive, reaching orders of magnitude in the ratio at very high p_T. The increased activity in hard gluon emission for the matched case also explains a decreased azimuthal distance between the two tops, as shown in the right-hand plot. The predicted average p_T of the radiation by MadGraph is 62 GeV/c (72 GeV/c with ALPGEN), with a 40% probability of having more than 50 GeV/c as gluon p_T in $t\bar{t}$ events. This large gluon activity will have an impact in the capability of correctly reconstructing top quark events at the LHC, and in correctly interpreting radiation as a background for new physics searches.

Difference in differential distributions are visible not only in the transverse plane: having more radiation tends to increase the event transverse activity. Moreover, the two top quarks and the resulting decay products are more central and generally closer to each other. We believe the difference we see are important enough to motivate the choice of a matching generation for

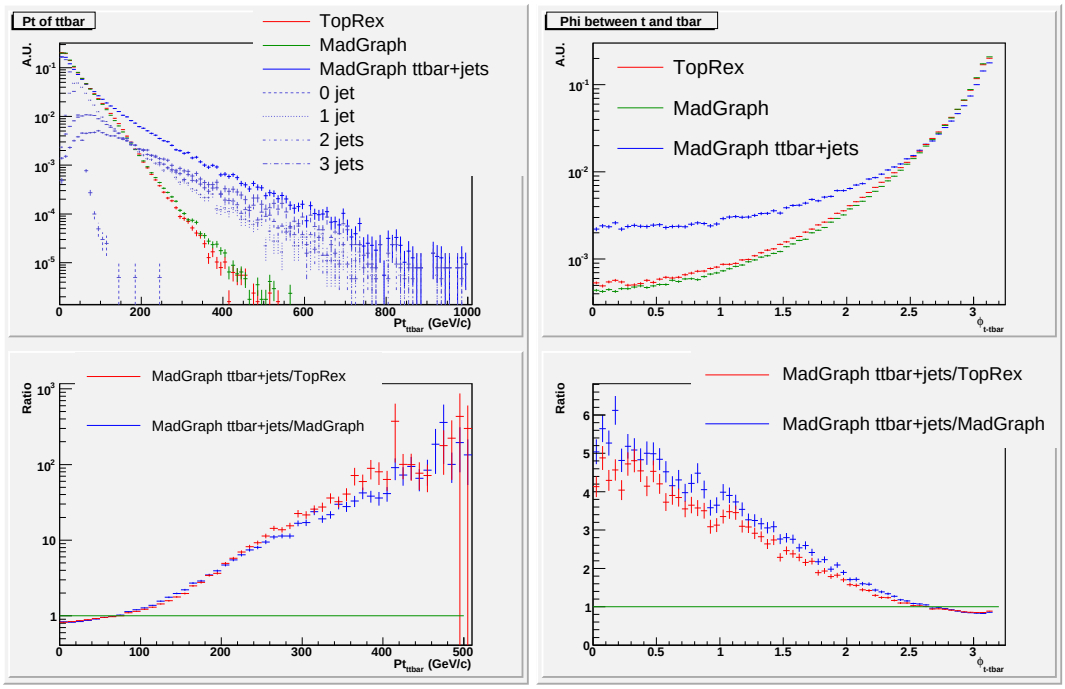

Fig. 1: Transverse momentum of the $t\bar{t}$ system (left) and azimuthal difference between the top quarks (right) for TopRex, standard MadGraph and MadGraph with matching. The individual components tt+njets are explicitly plotted in the left plot. The lower plots show the ratios of the histograms.

the description of any sufficiently hard SM process: this is particularly important when such processes are background to higher jet multiplicity configurations.

One important step in the validation of the physics contents of the matching in CMSSW is to compare two different approaches in the top sector. In figure 2 we present the ALPGEN predictions compared to MadGraph with ME-PS matching.

The blue and red curves represent the distributions for the matched samples of ALPGEN and MadGraph, respectively. For the p_T of the $t\bar{t}$ system also the individual components are shown. The agreement is more than acceptable for the p_T and remarkable for the azimuthal difference between the top quarks. Especially in the tails of the distributions, corresponding to high radiation conditions, the disagreement reduces to a maximum discrepancy of 50%. To properly appreciate the difference between the two predictions we should, however, account for the theory errors as well. These errors come, mainly, from scale definitions, PDFs, PS tunings; a detailed study on the dependence of the results on these effects is desirable before any conclusion on residual discrepancies between the generators can be drawn.

The comparison showed very good agreement in many other distributions that are not shown here. We observed a slight difference in shape for the transverse momentum and an excellent agreement for angular variables, with difference typically below 5%. We believe that the two generators can equally well be used to describe environments with hard gluon emission

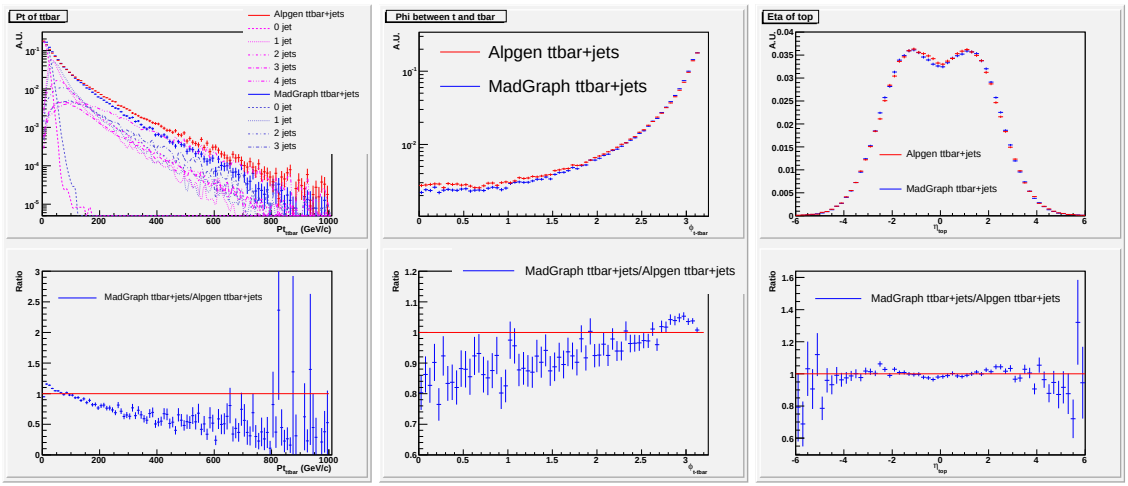

Fig. 2: Transverse momentum of the $t\bar{t}$ system (left), azimuthal difference between the tops (center) and pseudo-rapidity of the tops (right) for ALPGEN matched and MadGraph matched. The individual components tt+njets are explicitly plotted in the left plot. The lower plots show the ratios of the histograms.

in the final state.

4 Matched calculations versus NLO predictions

Another extremely important test comes by comparing ME-PS matched calculations with NLO QCD tools, especially for what concerns transverse variables. With the availability of MC@NLO as event generator this is now possible. Such comparison must be looked at with a grain of salt, since the hadronisation is performed with different tools and since inclusive NLO variables are compared with matched HLO quantities, typically at orders greater than the first. Nonetheless, in a throughout comparison of the kinematics of final state fermions and intermediate tops, a very good agreement was always found. Figure 3 shows the transverse momentum of the system, and excellent agreement in the high radiation tails is visible.

In this case discrepancies appear in the soft regime, where indeed the hadronisation with the PS plays an important role. There, a complete tuning of the PS models (with the respective externals MEs) needs to be made before performing a trustable comparison.

5 Summary and outlook

We presented a throughout comparison, at parton level, of generator predictions in the top sector at the LHC energy. The tests were performed in the framework of the CMS software. A generation with matching PS-ME gives important differences in the description of the radiation and should be chosen as currently the best way to describe SM processes where the description of QCD radiation is important. This is even more relevant when such process is background to something else (SM or new physics). Matched calculations have also been tested versus NLO generators, with very good agreement in the prediction of transverse variables.

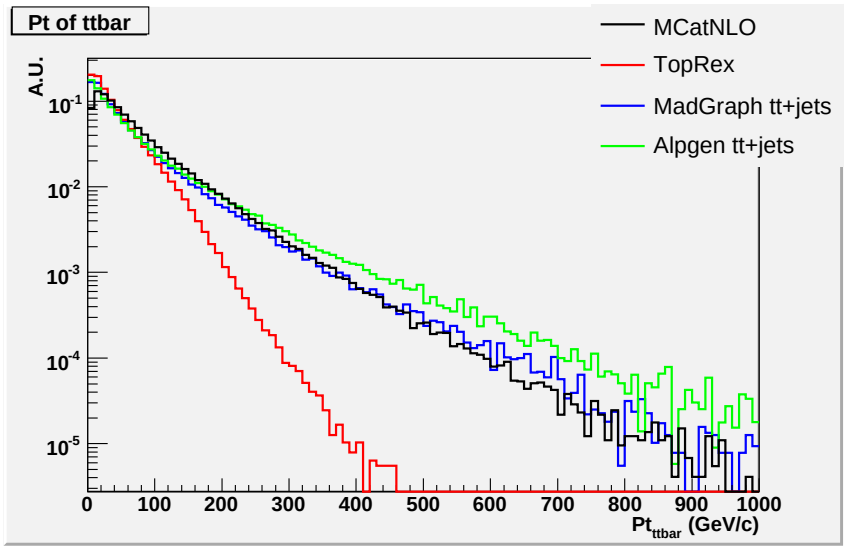

Fig. 3: Transverse momentum of the $t\bar{t}$ system for ME-PS matched predictions and MC@NLO.

References

[1] T. Sjöstrand et al., Comput. Phys. Commun. 135 (2001) 238.

[2] S.R. Slabospitsky, Comput. Phys. Commun. 148 (2002) 87.

[3] S.Hoche et al., hep-ph/0602031.

[4] M.L. Mangano et al., Journal of High Energy Physics **0307** (2003) 001.

[5] F. Maltoni and T. Stelzer, hep-ph/0208156.

[6] S. Frixione and B.R. Webber, Journal of High Energy Physics JHEP06 (2002) 029.

[7] M. Mangano et al., CERN-PH-TH-2006-232
J.Alwall et al., CERN-PH-TH-2007-066.

[8] J.Alwall et al., CERN-PH-TH-2007-066.

Herwig++ Status Report

M. Bähr[a], *S. Gieseke*[a], *M.A. Gigg*[b], *D. Grellscheid*[b], *K. Hamilton*[c], *O. Latunde-Dada*[d], *S. Plätzer*[a], *P. Richardson*[b,e], *M.H. Seymour*[e,f], *A. Sherstnev*[d], *J. Tully*[b], *B.R. Webber*[d]
[a] Institut für Theoretische Physik, Universität Karlsruhe,
[b] IPPP, Department of Physics, Durham University,
[c] Centre for Particle Physics and Phenomenology, Université Catholique de Louvain,
[d] Cavendish Laboratory, University of Cambridge,
[e] Physics Department, CERN,
[f] School of Physics and Astronomy, University of Manchester. *

Abstract
Herwig++ is the successor of the event generator HERWIG. In its present version 2.2.1 it provides a program for full LHC event generation which is superior to the previous program in many respects. We briefly summarize its features and describe present work and some future plans.

1 Introduction

With the advent of the LHC era it was decided to completely rewrite the general purpose event generator HERWIG [1,2] in C++ under the name Herwig++, based on the package ThePEG [3,4]. The goal is not only to provide a simple replacement of HERWIG but to incorporate physics improvements as well [5]. From 2001 until now Herwig++ has been continuously developed and extended [6–10]. The current version is 2.2.1, cf. [11]. The physics simulation of the current version is more sophisticated than the one of Fortran HERWIG in many respects. In this report we will briefly summarize the status of the different aspects of the simulation. These are the hard matrix elements available, initial and final state parton showers, the hadronization, hadronic decays and the underlying event. We conclude with an outlook to planned future improvements.

2 Physics simulation steps

2.1 Matrix elements

The event generation begins with the hard scattering of incoming particles or partons in the case of hadronic collisions. We have included a relatively small number of hard matrix elements. These include e^+e^- annihilation to $q\bar{q}$ pairs or simply to Z^0 bosons and deep inelastic scattering. In addition there is the Higgsstrahlung process $e^+e^- \to h^0 Z^0$. For hadron–hadron collisions we have the QCD $2 \to 2$ processes including heavy quark production. For colourless final states we have the following matrix elements,

$$hh \to (\gamma, Z^0) \to \ell^+\ell^- \,, \quad hh \to W^\pm \to \ell^\pm\nu_\ell(\bar{\nu}_\ell) \,, \quad hh \to h^0 \,, \quad hh \to h^0 Z^0 \,, \quad hh \to \gamma\gamma \,.$$

*herwig@projects.hepforge.org

We also provide matrix elements for processes with additional jets in the final state, like

$$hh \to (\gamma, Z^0, W^\pm) + \text{jet}\,, \quad hh \to h^0 + \text{jet}\,.$$

In addition, there are matrix elements for perturbative decays of the top quark, which will be simulated including spin correlations (see below). There will be some more matrix elements added in future versions, e.g. for $hh \to qqh^0$. Despite the rather small number of matrix elements, there is no real limitation to the processes that may be simulated with Herwig++. In practice, one may use any matrix element generator to generate a standard event file [12] which in turn can be read and processed by Herwig++.

For processes with many legs in the final state we follow a different strategy. When the number of legs becomes large — typically larger than 6–8 particles in the final state — it will be increasingly difficult to achieve an efficient event generation of the full matrix element. For these situations we have a generic framework to build up matrix elements for production and decays of particles in order to approximate any tree level matrix element as a simple production process with subsequent two or three body decays. This is a good approximation whenever the widths of the intermediate particles are small. The spin correlations among these particles can be restored with the algorithm described in [13]. Also finite width effects are taken into account [14]. The full simulation of several processes of many models for physics beyond the standard model (MSSM, UED, Randall–Sunrum model) is thus possible in Herwig++ [15]. Here, all necessary matrix elements for production and decay processes are constructed automatically from a model file.

2.2 Parton Showers and matching with matrix elements

After the hard process has been generated, typically at a large scale $\sim 100\,\text{GeV}$–$1\,\text{TeV}$, the coloured particles in the process radiate a large number of additional partons, predominantly gluons. As long as these are resolved by a hard scale of $\sim 1\,\text{GeV}$ this is simulated with a coherent branching algorithm, as outlined in [16] which generalizes the original algorithm [17–19] used in HERWIG. The main improvements with respect to the old algorithm are boost invariance along the jet axis, due to a covariant formulation, and the improved treatment of radiation off heavy quarks. We are using mass–dependent splitting functions and a description of the kinematics that allows us to dynamically generate the dead–cone effect. In addition to initial and final state parton showers there are also parton showers in the decay of heavy particles, the top quark in our case.

When extrapolating to hard, wide–angle emissions, the parton shower description is not sufficiently accurate in situations where observables depend on large transverse momenta in the process. In these cases we supply so–called hard matrix element corrections that describe the hardest parton emission, usually a hard gluon, with the full matrix element for the process that includes that extra parton. In order to consistently describe the whole phase space one has to apply soft matrix element corrections. Matrix element corrections are available for Drell–Yan type processes, Higgs production in gg fusion and e^+e^- annihilation to $q\bar{q}$–pairs. In addition, we apply a matrix element correction in top–quark decays [20].

From the point of view of perturbation theory, the hard matrix element correction is only one part of the next–to–leading order (NLO) correction to the Born matrix element. The full NLO

calculation also includes the virtual part with the same final state as the Born approximation. When trying to match NLO calculations and parton shower algorithms systematically, we have to avoid double counting of the real emission contributions. Two systematic approaches are being successfully discussed and applied in event generators: MC@NLO [21–23] and the POWHEG approach [24, 25]. In Herwig++ we have included working examples of matching in both approaches. The MC@NLO method, adopted to Herwig++ is described in [26]. Whereas the POWHEG method has already been applied for several processes in e^+e^- annihilation [27, 28] and also for Drell–Yan production [29]. Parts of these implementations will become available in future releases.

Another viable possibility to improve the description of QCD radiation in the event generation is the matching to multiple tree–level matrix elements, that describe the radiation of n additional jets with respect to the Born level. Theoretically most consistent is the CKKW approach [30] which has been studied in the context of an angular ordered parton shower in [31].

2.3 Hadronization and decays

The hadronization model in Herwig++ is the cluster hadronization model which has not been changed much from its predecessor in HERWIG. After the parton shower, all gluons are split nonperturbatively into $q\bar{q}$ pairs. Then, following the colour history of the parton cascade, all colour triplet–antitriplet pairs are paired up in colourless clusters which still carry all flavour and momentum information of the original partons. While these are heavier than some threshold mass they will fission into lighter clusters until all clusters are sufficiently light. These light clusters will then decay into pairs of hadrons.

The hadrons thus obtained are often heavy resonances that will eventually decay on timescales that are still irrelevant for the experiment. These hadronic decays have been largely rewritten and are modeled in much greater detail in Herwig++. While in HERWIG they were often simply decayed according to the available phase space only, we now take into account more experimental information, like form factors, that allow for a realistic modeling of decay matrix elements [32,33]. In a major effort, a large fraction of the decay channels described in the particle data book [34] have been included into Herwig++.

2.4 Underlying event

The underlying event model of Herwig++ is a model for multiple hard partonic interactions, based on an eikonal model, similar to JIMMY [35]. In addition to the signal process there are a number of additional QCD scatters, including full parton showers, that contribute to the overall hadronic activity in the final state and eventually also give rise to a (relatively soft) jet substructure in the underlying event. The model has two important parameters, one parameter μ, describing the spatial density of partonic matter in the colliding protons. Secondly, there is one cut off parameter $p_{\perp,\min}$ that gives a lower bound on the differential cross section for QCD $2 \to 2$ jet production. The model has been carefully tuned to Tevatron data [36]. Further possible bounds on the model parameters have been studied in [37]. An alternative modeling of the underlying event on the basis of the UA5 model [38] is also available for historic reasons.

Currently, the multiple partonic interaction model is limited to hard scattering while a soft

component is simply not present. For a realistic simulation of minimum bias events a soft component is, however, very important. An extension into the soft region, allowing us the simulation of minimum bias events is currently being studied and is likely to be included in the next release of Herwig++.

3 Availability

The latest version of Herwig++ is always available from hepforge:

```
http://projects.hepforge.org/herwig
```

There one can also find wiki pages to help with questions concerning installation, changing particular parameters and other frequently asked questions. The installation process is straightforward on any modern variant of linux. The physics details of the program are now documented in great detail in our manual [33]. The pdf version of the manual contains addional links to the online documentation of the code. All important parameters have been carefully tuned to a wealth of available data and the code is shipped with default paramters that give the best overall description of the data that we have tuned to. Details of the tune can also be found in the manual [33].

Acknowledgments

This work has been supported in part by the EU Marie Curie Research and Training Network MCnet under contract MRTN-CT-2006-035606.

References

[1] G. Corcella *et. al.*, *HERWIG 6: An event generator for hadron emission reactions with interfering gluons (including supersymmetric processes)*, *JHEP* **01** (2001) 010, [hep-ph/0011363].

[2] G. Corcella *et. al.*, *HERWIG 6.5 release note*, hep-ph/0210213.

[3] L. Lönnblad, *ThePEG, Pythia7, Herwig++ and Ariadne*, *Nucl. Instrum. Meth.* **A559** (2006) 246–248.

[4] M. Bertini, L. Lönnblad, and T. Sjöstrand, *Pythia version 7-0.0: A proof-of-concept version*, *Comput. Phys. Commun.* **134** (2001) 365–391, [hep-ph/0006152].

[5] S. Gieseke, *Event generators: New developments*, hep-ph/0210294.

[6] S. Gieseke, A. Ribon, M. H. Seymour, P. Stephens, and B. Webber, *Herwig++ 1.0: An event generator for e+ e- annihilation*, *JHEP* **02** (2004) 005, [hep-ph/0311208].

[7] S. Gieseke *et. al.*, *Herwig++ 2.0 beta release note*, hep-ph/0602069.

[8] S. Gieseke *et. al.*, *Herwig++ 2.0 release note*, hep-ph/0609306.

[9] M. Bähr *et. al.*, *Herwig++ 2.1 Release Note*, arXiv:0711.3137.

[10] M. Bähr *et. al.*, *Herwig++ 2.2 Release Note*, arXiv:0804.3053.

[11] http://projects.hepforge.org/herwig.

[12] J. Alwall *et. al.*, *A standard format for Les Houches event files*, *Comput. Phys. Commun.* **176** (2007) 300–304, [hep-ph/0609017].

[13] P. Richardson, *Spin correlations in Monte Carlo simulations*, *JHEP* **11** (2001) 029, [hep-ph/0110108].

[14] M. A. Gigg and P. Richardson, *Simulation of Finite Width Effects in Physics Beyond the Standard Model*, arXiv:0805.3037.

[15] M. Gigg and P. Richardson, *Simulation of beyond standard model physics in Herwig++*, *Eur. Phys. J.* **C51** (2007) 989–1008, [hep-ph/0703199].

[16] S. Gieseke, P. Stephens, and B. Webber, *New formalism for QCD parton showers*, *JHEP* **12** (2003) 045, [hep-ph/0310083].

[17] G. Marchesini and B. R. Webber, *Simulation of QCD Jets Including Soft Gluon Interference*, *Nucl. Phys.* **B238** (1984) 1.

[18] B. R. Webber, *A QCD Model for Jet Fragmentation Including Soft Gluon Interference*, *Nucl. Phys.* **B238** (1984) 492.

[19] G. Marchesini and B. R. Webber, *Monte Carlo Simulation of General Hard Processes with Coherent QCD Radiation*, *Nucl. Phys.* **B310** (1988) 461.

[20] K. Hamilton and P. Richardson, *A simulation of QCD radiation in top quark decays*, *JHEP* **02** (2007) 069, [hep-ph/0612236].

[21] S. Frixione and B. R. Webber, *Matching NLO QCD computations and parton shower simulations*, *JHEP* **06** (2002) 029, [hep-ph/0204244].

[22] S. Frixione, P. Nason, and B. R. Webber, *Matching NLO QCD and parton showers in heavy flavour production*, *JHEP* **08** (2003) 007, [hep-ph/0305252].

[23] S. Frixione and B. R. Webber, *The MC@NLO 3.3 event generator*, hep-ph/0612272.

[24] P. Nason, *A new method for combining NLO QCD with shower Monte Carlo algorithms*, *JHEP* **11** (2004) 040, [hep-ph/0409146].

[25] S. Frixione, P. Nason, and C. Oleari, *Matching NLO QCD computations with Parton Shower simulations: the POWHEG method*, *JHEP* **11** (2007) 070, [arXiv:0709.2092].

[26] O. Latunde-Dada, *Herwig++ Monte Carlo At Next-To-Leading Order for e+e- annihilation and lepton pair production*, *JHEP* **11** (2007) 040, [arXiv:0708.4390].

[27] O. Latunde-Dada, S. Gieseke, and B. Webber, *A positive-weight next-to-leading-order Monte Carlo for e+ e- annihilation to hadrons*, *JHEP* **02** (2007) 051, [hep-ph/0612281].

[28] O. Latunde-Dada, *Applying the POWHEG method to top pair production and decays at the ILC*, arXiv:0806.4560.

[29] K. Hamilton, P. Richardson, and J. Tully, *A Positive-Weight Next-to-Leading Order Monte Carlo Simulation of Drell-Yan Vector Boson Production*, arXiv:0806.0290.

[30] S. Catani, F. Krauss, R. Kuhn, and B. R. Webber, *QCD matrix elements + parton showers*, *JHEP* **11** (2001) 063, [hep-ph/0109231].

[31] S. Plätzer, *Diploma Thesis* , . Universität Karlsruhe, 2006.

[32] D. Grellscheid and P. Richardson, *Simulation of Tau Decays in the Herwig++ Event Generator*, arXiv:0710.1951.

[33] M. Bähr *et. al.*, *Herwig++ Physics and Manual*, arXiv:0803.0883.

[34] **Particle Data Group** Collaboration, C. Amsler *et. al.*, *Review of particle physics*, *Phys. Lett.* **B667** (2008) 1.

[35] J. M. Butterworth, J. R. Forshaw, and M. H. Seymour, *Multiparton interactions in photoproduction at HERA*, *Z. Phys.* **C72** (1996) 637–646, [hep-ph/9601371].

[36] M. Bähr, S. Gieseke, and M. H. Seymour, *Simulation of multiple partonic interactions in Herwig++*, *JHEP* **07** (2008) 076, [arXiv:0803.3633].

[37] M. Bähr, J. M. Butterworth, and M. H. Seymour, *The Underlying Event and the Total Cross Section from Tevatron to the LHC*, arXiv:0806.2949.

[38] **UA5** Collaboration, G. J. Alner *et. al.*, *The UA5 High-Energy anti-p p Simulation Program*, *Nucl. Phys.* **B291** (1987) 445.

Forward Physics Monte Carlo

M. Boonekamp[1]*,V. Juránek*[2]*, O. Kepka*[1,2,3]*, C. Royon*[1]
[1] CEA/IRFU/Service de physique des particules, 91191 Gif-sur-Yvette cedex, France
[2] Center for Particle Physics, Institute of Physics, Academy of Science, Prague
[3] IPNP, Faculty of Mathematics and Physics, Charles University, Prague

Abstract
We give a short description of the Forward Physics Monte Carlo (FPMC) which is intended for studies of diffractive physics and two-photon exchanges at the LHC.

The Forward Physics Monte Carlo (FPMC) was developed to cover a variety of physics processes that can be detected with very forward proton spectrometers. The detectors are currently being proposed to ATLAS and CMS collaborations and soon will enable studies of single and double diffractive production, central exclusive production (CEP), two-photon exchange etc. Implementing all of these processes into a single FPMC program has the advantage of a quick data-to-model comparison and easier interfacing with the detector simulation framework. The latest version of the generator is available at `www.cern.ch/project-fpmc.`

In this report we shortly summarize the structure and usage of the FPMC program before presenting a few results coming directly from the generator.

1 The FPMC program

The FPMC is a stand-alone generator which generates events, treats particle decays and hadronization as in HERWIG. The forward physics processes are based on an exchange of pomerons, photons, or gluons in case of double pomeron exchange, two-photon production and central exclusive production, respectively. In FPMC, the radiation of a mediating particle of the incoming proton is described in terms of fluxes, probabilities that the incoming proton emits a mediating particle of a given energy. A selection of a specific flux therefore leads to a generation of a particular physics processes. In the following we briefly mention the most important switches of the program which are tabulated in Table 1. The detailed description of the program can be found in the complete manual [1].

- TYPEPR - switches between exclusive (“EXC”) and inclusive processes (“INC”), for example between the Higgs diffractive production in completely exclusive mode or in the inclusive one when there are pomeron remnants present.
- TYPINT - selects the QCD (“QCD”) or photon (“QED”) processes.
- NFLUX - as mentioned above, it specifies the mechanism of the exchange: 9 (factorized model, double pomeron exchange), 10 (factorized model, double reggeon exchange), 15 (two-photon exchange based Budnev photon flux [2]), 16 (exclusive KMR model, two gluon exchange [3]). Other non-default fluxes like Papageorgiou photon flux [4] or photon flux for heavy ions [5] are also present.

- IPROC - the process number, specifies what final state will be produced of the exchanged particles, some possible values are listed in Table 2. For illustration: IPROC=19999, NFLUX=16, TYPEPR="QCD" generates exclusive Higgs production with all decay channels open following the KMR prediction or IPROC=16010, NFLUX=15, TYPEPR="QED" produces exclusive WW two-photon production.
- ISOFTM - with this parameter, the survival probability factor [6] can be turned on (1) and off (0). It is of the order of of 0.03 for LHC (0.1 for Tevatron) for QCD (double pomeron exchange, CEP) and 0.9 for QED two-photon exchange processes.
- IFITPDF - specifies a set of the parton density functions in the pomeron/reggeon. The common parameters are 10 or 20 which correspond to the most recent H1 and ZEUS fits of the densities, respectively [7].

Parameter	**Description**	**Default**
TYPEPR	Select exclusive 'EXC' or inclusive 'INC' production	'EXC'
TYPINT	Switch between QED and QCD process	'QCD'
NFLUX	Select flux	9
IPROC	Type of process to generate	11500
MAXEV	Number of events to generate	1000
ISOFTM	Turn survival probability factor on (1), off(0)	1
ECMS	CMS energy (in GeV)	14000
HMASS	Higgs mass (GeV/c^2)	115
PTMIN	Minimum p_T in hadronic jet production	0
YJMIN	Minimum jet rapidity	-6
YJMAX	Maximum jet rapidity	+6
EEMIN	Minimum dilepton mass in Drell-Yan	10.0
IFITPDF	Diffractive PDF	10
NTNAME	Output ntuple name	'tmpntuple.ntp'

Table 1: Main FPMC parameters.

2 Examples of processes produced in FPMC

2.1 Inclusive diffraction

The first example we discuss is the inclusive diffraction. The starting point to predict inclusive diffraction at the LHC (or the Tevatron) is the measurement of gluon and quark densities in the pomeron performed at HERA [7]. Once these parton densities are known, it is straightforward to compute the diffractive production at the Tevatron or the LHC. The only assumption is that the factorization breaking between ep and hadron collisions is a soft process, independent of the hard process and it can be applied as a multiplicative factor to the cross section. In that sense, we call this model "factorized" model. In FPMC, we assume the survival probability to be 0.1 at the Tevatron and 0.03 for the LHC.

It will be important to remeasure the structure of the pomeron at the LHC and to study the factorization breaking of the cross section at high energies because inclusive diffraction also represents an important background for most of the processes to be studied at the LHC using forward detectors like exclusive Higgs production, studies of the photon anomalous coupling, SUSY particle production in two-photon exchange, etc.

In Figure 1, we give the dijet cross section as a function of minimum transverse jet momentum p_T^{min} for inclusive dijets, light quark jets and b-jets only. These cross sections were obtained using the process numbers IPROC=11500, 11701 and 11705 for gg, light quark and b jets processes, respectively. Other parameters were set NFLUX=9, TYPEPR='QCD', IFITPDF=10.

2.2 Central exclusive production / exclusive double pomeron exchange

In exclusive production, the full energy of the exchanged particles (pomerons, gluons) is used to produce a heavy object (Higgs boson, dijets, diphotons, etc.) in the central detector and no energy is lost in pomeron remnants as in inclusive case. There is an important kinematic consequence that the mass of the produced object can be computed using the proton momentum losses ξ_1, ξ_2 measured in the forward detectors as $M = \sqrt{\xi_1 \xi_2 s}$ (with s being the total center of mass energy of colliding protons). We can benefit from the good forward detector resolution on ξ to measure the mass of the produced object precisely. Moreover, since the CEP fulfill certain selection rules also other kinematic properties (spin and parity) of the produced object can be easily determined.

In Fig. 2 (left), we display the CEP cross sections of Higgs boson with its direct background of b-jet production as they are obtained directly from FPMC generator using the process numbers IPROC=19999 and 16005, respectively. Other parameters were set to NFLUX=16, TYPEPR='QCD'.

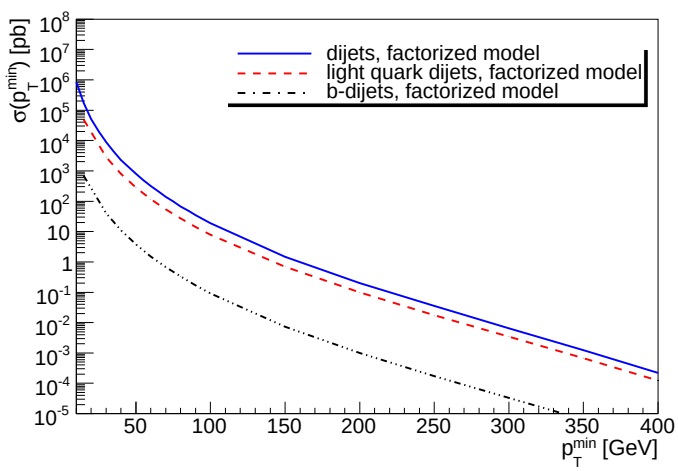

Fig. 1: Dijet cross section for inclusive dijets, light quark jets and b-jets only as a function of minimum transverse momentum of the two leading jets with $p_T^{jet1}, p_T^{jet2} > p_T^{min}$ at $\sqrt{s} = 14\,\text{TeV}$.

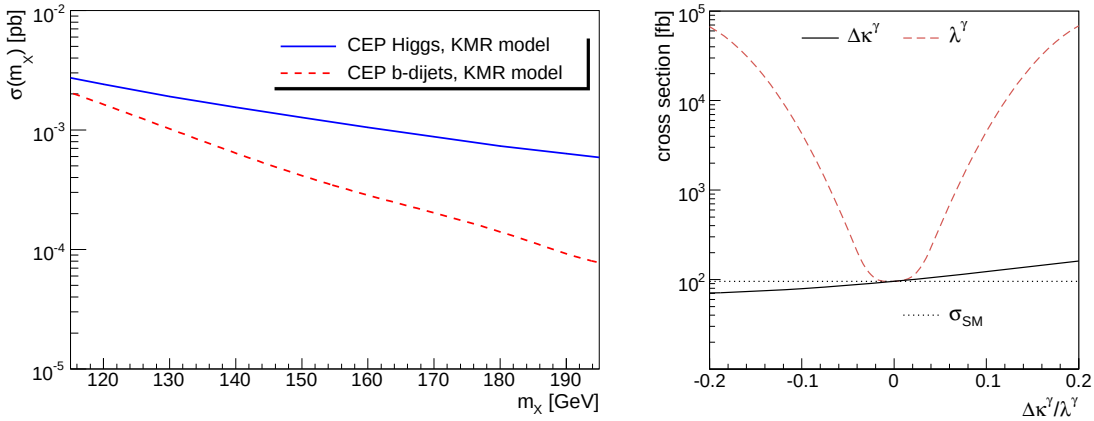

Fig. 2: *Left:* Higgs boson central exclusive production cross section for various masses of the Higgs boson m_X and b-jet production cross section as a function of the $b\bar{b}$ invariant mass. *Right:* Cross section of the SM WW production through two-photon exchange as well as the effect of the $\Delta\kappa^\gamma$ and λ^γ anomalous parameters.

2.3 WW two-photon production

The two-photon production is described in terms of the photon flux. In FPMC one can study the dilepton, diboson, diphoton, and Higgs production. In the following we will discuss as an example the W pair production. The process number and other parameters for this process are IPROC=16010, TYPEPR='EXC', TYPINC='QED'.

Besides the SM production, FPMC was interfaced with O'Mega matrix element generator [8] to allow anomalous coupling studies [9]. Currently, the triple gauge boson $WW\gamma$ effective Lagrangian is included which is parametrized with two anomalous parameters $\Delta\kappa^\gamma$, λ^γ. The dependence of the total diboson production cross section in two-photon exchanges as a function of the two anomalous parameters is depicted in Fig. 2 on the right.

3 Conclusion

In this short report, we described the new Forward Physics Monte Carlo generator which allows to produce single and double pomeron exchanges, two-photon induced processes and Central Exclusive Production at hadron colliders. These processes are a heart of the forward physics program at the LHC. The main aim is to combine various available models into one interface to allow easy data-to-model comparisons.

References

[1] M. Boonekamp, V. Juranek, O. Kepka, M. Rangel. C. Royon, to appear; see `http://cern.ch/project-fpmc/`

[2] V. M. Budnev, I. F. Ginzburg, G. V. Meledin and V. G. Serbo, Phys. Rept. **15** (1974) 181.

Process	IPROC	TYPEPR	TYPINC	NFLUX
Incl. H	11600+ID	INC	QCD	9,10,11
Excl. H	19900+ID	EXC	QCD	16
Excl. H	19900+ID	EXC	QED	12,13,14,15
Incl. $q\bar{q}$	11500	INC	QCD	9,10,11
Incl. $q\bar{q}$	11700+ID	INC	QCD	9,10,11
Excl. $q\bar{q}$	16000+ID	EXC	QCD	16
Incl. W^+W^-	12800	INC	QCD	9,10,11
Excl. W^+W^-	16010	EXC	QED	15
Incl. $\gamma\gamma$	12200	INC	QCD	9,10,11
Excl. $\gamma\gamma$	19800	INC	QCD	16
Excl. $\gamma\gamma$	19800	EXC	QED	12,13,14,15
Excl. ll	16006+IL	EXC	QED	12,13,14,15
Incl. ll	11350+IL	INC	QCD	9,10,11

Table 2: Setting of the FPMC for a number of physics processes. ID specif the decay products of a Higgs boson or a type of quarks produced. IL denote type of leptons in the final state. See manual for details [1].

[3] V.A. Khoze, A.D. Martin, M.G. Ryskin, Eur. Phys. J. **C19** (2001) 477; Eur. Phys. J. **C24** (2002) 581; arXiv:0802.0177; Phys. Lett. B650 (2007) 41; A.B. Kaidalov, V.A. Khoze, A.D. Martin, M.G. Ryskin, Eur. Phys. J. **C33** (2004) 261; Eur. Phys. J. **C31** (2003) 387

[4] E. Papageorgiu, Phys. Lett. B**250** (1990) 155 Phys. Lett. B **352** (1995) 394.

[5] M. Drees, J. Ellis, D. Zeppenfeld, Phys. Lett. **B223** (1989) 454.

[6] V. A. Khoze, A. D. Martin and M. G. Ryskin, Eur. Phys. J. C **23** (2002) 311.

[7] H1 Collaboration, Eur. Phys. J. C**48** (2006) 715;
C. Royon, L. Schoeffel, R. Peschanski, E. Sauvan, Nucl. Phys. B**746** (2006) 15;
C. Royon, L. Schoeffel, S. Sapeta, R. Peschanski, E. Sauvan, Nucl. Phys. B**781** (2007) 1.

[8] M. Moretti, T. Ohl and J. Reuter, arXiv:hep-ph/0102195.

[9] O. Kepka, C. Royon, arXiv:0808.0322, in press in Phys. Rev. D.

HEP data analysis using jHepWork and Java

S. Chekanov
HEP Division, Argonne National Laboratory, 9700 S.Cass Avenue, Argonne, IL 60439 USA

Abstract
A role of Java in high-energy physics (HEP) and recent progress in development of a platform-independent data-analysis framework, jHepWork, is discussed. The framework produces professional graphics and has many libraries for data manipulation.

1 Introduction

Nowadays, the advantages of Java over C++ seem overwhelming. Being the most popular open-source programing language[1], Java retains the C++ syntax, but significantly simplifies the language. This is (incomplete) list of advantages of Java over C++: 1) Java is multiplatform with the philosophy of "write once, run anywhere"; 2) Better structured, clean, efficient, simpler (no pointers); 3) Stable, robust and well supported: Java programs written (or compiled) many years from now can be compiled (or executed) without modifications even today. This is true even for JAVA source code with graphic widgets. In contrast, C++ programs always require continues time-consuming maintenance in order to follow the development of C++ compilers and graphic desktop environment; 4) Java has reflection technology, which is not present in C++. The reflection allows an application to discover information about created objects, thus a program can design itself at runtime. In particular, this is considered to be essential for building "intelligent" programs making decisions at runtime; 5) Free intelligent integrated-development environments (IDE), which are absolutely necessary for large software projects[2]; 6) Automatic garbage collection, i.e. a programmer does not need to perform memory management; 7) Extensive compile-time and run-time checking; 8) Programs written in Java can be embedded to the Web. This is important for distributed analysis environment (Java webstart, plugins, applets), especially when HEP data analysis tools are not localized in one single laboratory but scattered over the Web.

The importance of Java in HEP data analysis has been recognized since establishing the FreeHEP Java library and producing a first version of JAS (Java analysis studio) [1]. Presently, many elements of the grid software are written in Java. At LHC, Java is used for event displays and several other areas. While C++ language is remaining to be the main programming language at LHC, it lacks many features existing in Java, which makes the entire LHC software environment tremendously complicated. The lack of robustness and backward compatibility of C++ free compilers leads to various HEP-supported "scientific" flavors of Linux, with different architecture (32 bit or 64), which are all tightened to particular libraries and hardware. For example, the main computational platform for ATLAS is Scientific Linux 4.6. It will be used for future

[1] According to SourceForge.net and Freshmeat.net statistics, the number of open-source applications written in Java exceeds those written in C++.

[2] For example, the total number of lines of source code in ATLAS software is far higher than hundreds of thousands lines.

data taking, however, even now it is several generations behind the main-stream Linux modern distributions (Fedora, Ubuntu, Suse etc) and cannot be easily installed on modern laptops. Currently, the HEP community is required to support the entire computing chain, from hardware and operating systems, to the end-user programs, rather than concentrating on HEP-specific computational tasks. This is a significant difference from the initial concept, when HEP software could be run essentially on any platform and a vendor-supported operating system.

It should be pointed out that C+ has been chosen as the main programming language at LHC at the time when Java was still behind C++, lacking Just-in-time (JIT) compilers to convert parts of the bytecode to native code in order to improve execution time. At that time, Python [2], another portable programming language, also did not have enough power to be widely used in HEP. As Java, Python has also become increasingly popular programming language in science and engineering [3], since it is interactive, object-oriented, high-level, dynamic and portable. It has simple and easy to learn syntax which reduces the cost of program maintenance. While being portable, Python implemented in C (CPython) requires user-specific C/C++ libraries for high-performance computing, thus it cannot be considered a basis for a multiplatform data-analysis environment.

Jython [4] is an implementation of Python in Java and, as any Java application, is truly multiplatform. In contrast to CPython, Jython is fully integrated with the Java platform, thus Jython programs can make full use of extensive built-in and third-party Java libraries. Therefore, Jython programs have even more power than the standard Python implemented in C. Finally, the Jython interpreter is freely available for both commercial and non-commercial use.

jHepWork [5] is a full-featured object-oriented data analysis framework for scientists that takes advantage of the Jython language and Java. Jython macros are used for data manipulation, data visualization (plotting 1D and 2D histograms), statistical analysis, fits, etc. Data structures and data manipulation methods integrated with Java and JAIDA FreeHEP libraries [6] combine remarkable power with a very clear syntax. jHepWork Java libraries can also be used to develop programs using the standard JAVA, without Jython macros.

Programs written using jHepWork are usually rather short due the simple Python syntax and high-level constructs implemented in the core jHepWork libraries. As a front-end data-analysis environment, jHepWork helps to concentrate on interactive experimentation, debugging, rapid script development and finally on workflow of scientific tasks, rather than on low-level programming.

jHepWork is an open source product which is implemented 100 percent in Java. Since it is fully multiplatform, it does not require installation and can be run on any platform where Java is installed. It can be used to develop a range of data-analysis applications focusing on analysis of complicated data sets, histograms, statistical analysis of data, fitting. It offers a full-featured, extensible multiplatform IDE implemented in Java.

jHepWork is seamlessly integrated with Java-based Linear Collider Detector (LCD) software concept and it has the core based using FreeHEP libraries and other GNU-licensed packages. While jHepWork is mainly designed to be used in high-energy physics, it can also be used in any field, since all methods and classes are rather common in science and engineering.

Below we will discuss only the key features of jHepWork, without the coverage of all

available methods, which can easily be found using an extensive help system and the code completion feature of jHepWork. The main web page of jHepWork [5] contains the package itself, user manuals and about 50 examples with various macros. jHepWork consists of two major libraries: jeHEP (jHepWork IDE) and jHPlot (jHepWork data-analysis library). Both are licensed by the GNU General Public License (GPL).

2 Main differences with other data-analysis tools

Below we will compare jHepWork with two popular object-oriented packages currently used in high-energy physics: 1) JAS package [1], based on Java and FreeHEP libraries [6] and 2) C++ ROOT package [7].

2.1 Main differences with JAS

Compare to JAS, jHepWork:

- has a full-featured integrated development environment (IDE) with syntax highlighting, syntax checker, code completion, code analyser, an Jython shell and a file manager.
- contains powerful libraries to display data (including 3D plots) with a large choice for interactive labels and text attributes (subscripts, superscripts, overlines, arrows, Greek symbols etc.). jHepWork plots are more interactive than those written using FreeHEP JAIDA libraries linked with JAS. The plotting part is based on the jHPlot library developed for the jHepWork project and JaxoDraw Java application [8]. The latter can be used to draw Feynman diagrams in addition to standard plots;
- is designed to write short programs due to several enhancements and simpler class names. The classes written for jHepWork were designed keeping in mind simplicity of numerous high-level constructs enabling the user to write programs that are significantly shorter than programs written using JAS;
- includes high-level constructions for data manipulations, data presentations in form of tables, data input and output, calculations of systematical errors and visualization (plots, tables, spreadsheet, neural networks) which have no analogy in JAS;
- Essentially all jHepWok objects, including histograms, can be saved into files and restored using Java serialization mechanism. One can store collections of objects as well by using Jython maps or lists.
- includes an advanced help system with the code completion. For the core jHplot package, the code completion feature is complimented with a detailed API information on each method associated with certain class.

2.2 Main differences with the ROOT package

Compare to ROOT, jHepWork:

- is seamlessly integrated with Java-based Linear Collider Detector (LCD) software concept;
- is a Java-based program, thus it is fully multiplatform and does not require installation. This is especially useful for plugins distributed via the Internet in form of bytecode jar libraries;

- Java is very robust. Java source codes developed many years from now can easily be compiled without any changes even today. Even class libraries compiled many years from now can run on modern Java Virtual Machines. Therefore, the maintenance of jHepWork package is much less serious issue compared to ROOT;
- since jHepWork is 100% Java, it has automatic garbage collection, which is significant advantage over C++/C;
- has a full-featured IDE with syntax highlighting, syntax checker, code completion and analyser;
- can be integrated with the Web in form of applets, thus it is better suited for distributed analysis environment via the Internet. This is essential feature for modern large collaborations in high-energy physics and in other scientific fields;
- calculations based on Jython/Python scripts are typically 4-5 times shorter than equivalent C++ programs. Several examples are discussed in Ref. [5];
- calculations based on Jython scripts can be compiled to Java bytecode files and packed to jar class libraries without modifications of Jython scripts. In contrast, ROOT/CINT scripts have to be written using a proper C++ syntax, without CINT shortcuts, if they will be compiled into shared libraries;
- can access high-level Python and Java data structures;
- includes an advanced help system with a code completion based on the Java reflection technology. With increasingly large number of classes and methods in ROOT, it is difficult to understand which method belongs to which particular class. Using the jHepWork IDE, it is possible to access the full description of all classes and methods during editing Jython scripts;
- automatic updates which does not depend on particular platform. For ROOT, every new version has to be compiled from scratch;
- powerful and intelligent external IDEs (Eclipse, NetBean etc) can be used productivity in developing HEP analysis.

2.3 How fast it is?

Jython scripts are about 4-8 times slower than equivalent Java programs and about a factor five slower than the equivalent ROOT/CINT codes for operations on primitive data types (remember, all Jython data types are objects). This means that CPU extensive tasks should be moved to Java jar libraries.

jHepWork was designed for a data analysis in which program speed is not essential, as it is assumed that JHepWork scripts are used for operations with data and objects (like histograms) which have alredy been created by C++, Fortran or Java code. For such front-end data analysis, the bottleneck is mainly user input speed, interaction with a graphical object using mouse or network latency.

In practice, final results obtained with Jython programs can be obtained much faster than those designed in C++/Java, because development is so much easier in jHepWork that a user often winds up with a much better algorithm based on Jython syntax and jHepWork high-level objects

than he/she would in C++ or Java. In case of CPU extensive tasks, like large loops over primitive data types, reading files etc. one should use high-level structures of Jython and jHepWork or user-specific libraries which can be developed using the jHepWork IDE. Many examples are discussed in the jHepWork manual [5].

Acknowledgments. I would like to thanks many people for support, ideas and debugging of the current jHepWork version. This work supported in part by the U.S. Department of Energy, Division of High Energy Physics, under Contract DE-AC02-06CH11357.

References

[1] Java analysis studio.
URL http://jas.freehep.org/jas3/

[2] Python programming language – official website.
URL http://www.python.org/

[3] H. P. Langtangen, Python Scripting for Computational Science (Texts in Computational Science and Engineering), Springer-Verlag New York, Inc., Secaucus, NJ, USA, 2005.

[4] The jython project.
URL http://www.jython.org/

[5] S. Chekanov, JHEPWORK - JAVA object-oriented data analysis framework.
URL http://projects.hepforge.org/jhepwork/

[6] FreeHEP java libraries.
URL http://java.freehep.org/

[7] R. Brun, F. Rademakers, P. Canal, M. Goto, ROOT status and future developments, ECONF C0303241 (2003) MOJT001.

R. Brun, F. Rademakers, ROOT: An object oriented data analysis framework, Nucl. Instrum. Meth. A389 (1997) 81.
URL http://root.cern.ch/

[8] D. Binosi, L. Theussl, JaxoDraw: A graphical user interface for drawing feynman diagrams, Comp. Phys. Commun. 161 (2004) 76.
URL http://jaxodraw.sourceforge.net/

Tools for event generator tuning and validation

Andy Buckley
Institute for Particle Physics Phenomenology,
Durham University, UK

Abstract

I describe the current status of MCnet tools for validating the performance of event generator simulations against data, and for tuning their phenomenological free parameters. For validation, the Rivet toolkit is now a mature and complete system, with a large library of prominent benchmark analyses. For tuning, the Professor system has recently completed its first tunes of Pythia 6, with substantial improvements on the existing default tune and potential to greatly aid the setup of new generators for LHC studies.

1 Introduction

It is an inevitable consequence of the physics approximations in Monte Carlo event generators that there will be a number of relatively free parameters which must be tweaked if the generator is to describe experimental data. Such parameters may be found in most aspects of generator codes, from choices of Λ_{QCD} and $p_\perp$ cutoff in the perturbative parton cascade, to the non-perturbative hadronisation process. These latter account for the majority of parameters, since the models are deeply phenomenological, typically invoking a slew of numbers to describe not only the kinematic distribution of $p_\perp$ in hadron fragmentation, but also baryon/meson ratios, strangeness and $\{\eta, \eta'\}$ suppression, and distribution of orbital angular momentum [1–4]. The result is a proliferation of parameters — of which between $\mathcal{O}(10)$ and $\mathcal{O}(30)$ may be of particular importance for physics studies.

Apart from rough arguments about their typical scale, these parameters are freely-floating: they must be matched to experimental data for the generator to perform well. Additionally, it is important that this tuning is performed against a wide range of experimental analyses, since otherwise parameters to which the selective analyses are insensitive will wander freely and may drive unconsidered observables to bad or even unphysical places. This requires a systematic and global approach to generator tuning: accordingly, I will summarise the current state of tools for systematically validating and tuning event generator parameters, and the first results of such systematic tunings.

2 Validation tools: Rivet

The Rivet library is a successor to the successful HERA-oriented generator analysis library, HZTool [5]. Like its predecessor, the one library contains both a library of experimental analyses and tools for calculating physical observables. It is written in object-oriented C++ and there is strong emphasis on the following features:

- strict generator-independence: analyses are strictly performed on HepMC [6] event record objects with no knowledge of or ability to influence the generator behaviour;

- experimental reference data files are included for each standard analysis, and are used to ensure that analysis data binnings match their experimental counterparts as well as for fit comparisons;
- computational results are automatically cached for use between different analyses, using an infrastructure mechanism based on *projection* classes;
- clean, transparent and flexible programming interface: while much of the complexity is hidden, analyses retain a clear algorithmic structure rather than attempting to hide everything behind "magic" configuration files.

The "projection" objects used to compute complex observables are now a fairly complete set:

- various ways to obtain final state particles: all, charged only, excluding certain particles, with $p_\perp$ and rapidity cuts, etc.;
- event shapes: sphericity, thrust, Parisi C & D parameters, jet hemispheres;
- jet algorithms: CDF and DØ legacy cones, Durham/JADE, and $k_\perp$, anti-$k_\perp$, SISCONE, CDF "JETCLU" etc. from FastJet [7];
- miscellaneous: jet shapes, isolation calculators, primary and secondary vertex finders, DIS kinematics transforms, hadron decay finder, etc.

The set of standard analyses has also grown with time and is now particularly well-populated with analyses from the LEP and Tevatron experiments:

- LEP: ALEPH and DELPHI event shape analyses; ALEPH, DELPHI and PDG hadron multiplicities, strange baryons; DELPHI and OPAL b-fragmentation analyses;
- Tevatron: CDF underlying event analyses (from 2001, 2004 & 2008); CDF and DØ EW boson $p_\perp$ analyses; CDF and DØ QCD colour coherence, jet decorrelation, jet shapes, Z+jets, inclusive jet cross-section;
- HERA: H1 energy flow and charged particle spectra; ZEUS dijet photoproduction.

In addition, users can write their own analyses using the Rivet projections without needing to modify the Rivet source, by using Rivet's plugin system. We encourage such privately-implemented analyses to be submitted for inclusion in the main Rivet distribution, and would particularly welcome QCD analyses from HERA, b-factory and RHIC p-p experiments.

While Rivet is primarily a library which can be used from within any analysis framework (for example, it is integrated into the Atlas experiment's framework), the primary usage method is via a small executable called rivetgun. This provides a frontend for reading in HepMC events from ASCII dump files and also for running generators "on the fly" via the AGILe interface library. This latter approach is particularly nice because there is no need to store large HepMC dump files and the corresponding lack of file I/O speeds up the analysis by a factor $\sim \mathcal{O}(10)$. In this mode, Rivet is ideal for parameter space scans, since generator parameters can be specified by name on the rivetgun command line and applied without recompilation. AGILe currently supports API-level interfaces to the Fortran HERWIG 6 [2] and Pythia 6 [1] generators (combined with the AlpGen [8] MLM multi-jet merging generator, the CHARYBDIS black hole generator [9], and the JIMMY hard underlying event generator [10] for HERWIG), plus the C++ generators Herwig++ [3], Sherpa [4] and Pythia 8 [11].

At the time of writing, the current version of Rivet is 1.1.0, with a 1.1.1 patch release pending. The main framework benefits of the 1.1.x series over 1.0.x are a safer and simpler mechanism for handling projection objects (massively simplifying many analyses), better compatibility of the AGILe loader with the standard LCG Genser packaging and a large number of new and improved analyses and projections. A "bootstrap" script is provided for easy setup. Anyone interested in using Rivet for generator validation should first visit the website http://projects.hepforge.org/rivet/.

Rivet is now a stable and powerful framework for generator analysis and we are looking forward to its increasing rôle in constraining generator tunings for background modelling in LHC high-$p_\perp$ physics. Future versions will see improvements aimed at high-statistics validation simulations, such as histogramming where statistical error merging is automatically correct, as well as the addition of more validation analyses.

3 Tuning tools: Professor

While Rivet provides a framework for comparing a given generator tuning to a wide range of experimental data, it provides no intrinsic mechanism for improving the quality of that tune. Historically, the uninspiring task of tuning generator parameters to data "by eye" has been the unhappy lot of experimental researchers, with the unsystematic nature of the study reflecting that significant improvements in quality of both life and tuning would have been possible. This call for an automated and systematic approach to tuning is taken up by a second new tool: Professor. This is written in Python code as a set of factorised scripts, using the SciPy numerical library [12] and an interface to rivetgun.

The rough formalism of systematic generator tuning is to define a goodness of fit function between the generated and reference data, and then to minimise that function. The intrinsic problem is that the true fit function is certainly not analytic and any iterative approach to minimisation will be doomed by the expense of evaluating the fit function at a new parameter-space point: this may well involve ten or more runs of the generator with 200k–2M events per run. Even assuming that such runs can be parallelised to the extent that only the longest determines the critical path, an intrinsically serial minimisation of $\mathcal{O}(1000)$ steps will still take many months. This is clearly not a realistic strategy!

The Professor approach, which is the latest in a lengthy but vague history of such efforts [13, 14], is to parameterise the fit function with a polynomial. In fact, since the fit function itself is expected to be complex and not readily parameterisable, there is a layer of indirection: the polynomial is actually fitted to the generator response of each observable bin, MC_b to the changes in the n-element parameter vector, $\vec{p}$. To account for lowest-order parameter correlations, a second-order polynomial is used,

$$\mathrm{MC}_b(\vec{p}) \approx f^{(b)}(\vec{p}) = \alpha_0^{(b)} + \sum_i \beta_i^{(b)}\, p'_i + \sum_{i \le j} \gamma_{ij}^{(b)}\, p'_i\, p'_j, \tag{1}$$

where the shifted parameter vector $\vec{p}' \equiv \vec{p} - \vec{p}_0$, with $\vec{p}_0$ chosen as the centre of the parameter hypercube. A nice feature of using a polynomial fit function, other than its general-purpose robustness, is that the actual choice of the $\vec{p}_0$ is irrelevant: the result of a shift in central value is simply to redefine the coefficients, rather than change the functional form, but choosing a central value is numerically sensible.

The coefficients are determined by randomly sampling the generator from N parameter space points in an n-dimensional parameter hypercube defined by the user. Each sampled point may actually consist of many generator runs, which are then merged into a single collection of simulation histograms. A simultaneous equations solution is possible if the number of runs is the same as the number of coefficients between the n parameters, i.e. $N = N_{\text{min}}^{(n)} = (2 + 3n + n^2)/2$. However, using this minimum number of runs introduces a systematic uncertainty, as we certainly do not expect the bin MC response to be a perfect polynomial. Here we are helped by the existence of the Moore–Penrose pseudoinverse: a generalisation of the normal matrix inverse to non-square matrices with the desirable feature that an over-constrained matrix will be inverted in a way which gives a least-squares best fit to the target vector. Even more helpful is that a standard singular value decomposition (SVD) procedure can be used to deterministically implement the pseudoinverse computation. Hence, we phrase the mapping on a bin-by-bin basis from coefficients C to generator values V as $PC = V$, where P is the parameter matrix to be pseudo-inverted. For a two parameter case, parameters $\in \{x, y\}$, the above may be explicitly written as

$$\underbrace{\begin{pmatrix} 1 & x_1 & y_1 & x_1^2 & x_1 y_1 & y_1^2 \\ 1 & x_2 & y_2 & x_2^2 & x_2 y_2 & y_2^2 \\ & & & \vdots & & \end{pmatrix}}_{P \text{ (sampled param sets)}} \underbrace{\begin{pmatrix} \alpha_0 \\ \beta_x \\ \beta_y \\ \gamma_{xx} \\ \gamma_{xy} \\ \gamma_{yy} \end{pmatrix}}_{C \text{ (coeffs)}} = \underbrace{\begin{pmatrix} v_1 \\ v_2 \\ \vdots \end{pmatrix}}_{V \text{ (values)}} \tag{2}$$

where the numerical subscripts indicate the N generator runs. Note that the columns of P include all $N_{\text{min}}^{(2)} = 6$ combinations of parameters in the polynomial, and that P is square (i.e. minimally pseudo-invertible) when $N = N_{\text{min}}^{(n)}$. Then $C = \tilde{\mathcal{I}}[P]\, V$, where $\tilde{\mathcal{I}}$ is the pseudoinverse operator.

Now that we have, in principle, a good parameterisation of the generator response to the parameters, $\vec{p}$, for each observable bin, b, it remains to construct a goodness of fit (GoF) function and minimise it. We choose the χ^2 function, but other GoF measures can certainly be used. Since the relative importance of various distributions in the observable set is a subjective thing — given 20 event shape distributions and one charged multiplicity, it is certainly sensible to weight up the multiplicity by a factor of at least 10 or so to maintain its relevance to the GoF measure — we include weights, $w_{\mathcal{O}}$, for each observable, $\mathcal{O}$, in our χ^2 definition:

$$\chi^2(\vec{p}) = \sum_{\mathcal{O}} w_{\mathcal{O}} \sum_{b \in \mathcal{O}} \frac{(f_b(\vec{p}) - \mathcal{R}_b)^2}{\Delta_b^2}, \tag{3}$$

where $\mathcal{R}_b$ is the reference value for bin b and the total error Δ_b is the sum in quadrature of the reference error and the statistical generator errors for bin b — in practise we attempt to generate enough data that the MC error is much smaller than the reference error for all bins.

The final stage of our procedure is to minimise this parameterised χ^2 function. It is tempting to think that there is scope for an analytic global minimisation at this order of polynomial, but not enough Hessian matrix elements may be calculated to constrain all the parameters and

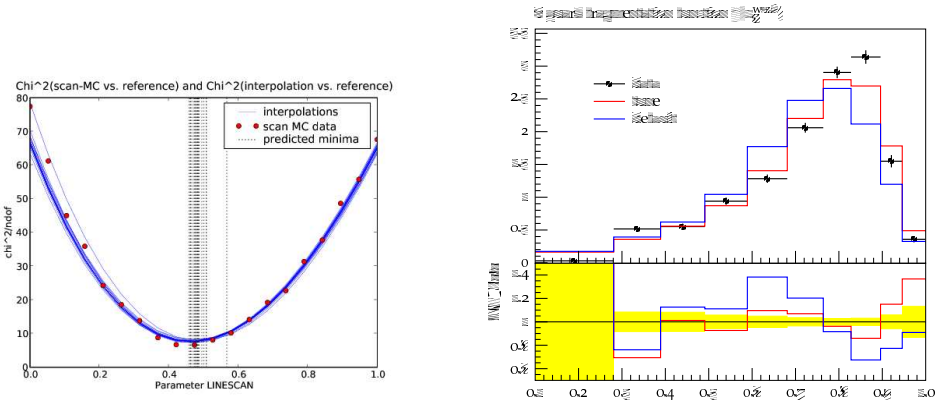

Fig. 1: (a) Parameter space line scan in χ^2, showing the agreement between Professor's predicted values (blue lines) and the true values (red dots). (b) Pythia 6 b-fragmentation functions, showing the improvements obtained using Professor (red) to tune the Bowler parameterisation against the default (blue).

hence we must finally resort to a numerical minimisation. We have implemented this in terms of minimisers from SciPy and also PyMinuit [15], with the latter's initial parameter space grid scan making it our preferred choice.

Finally, on obtaining a predicted best tune point from Professor, it is prudent to check the result. This can be done directly with rivetgun, and Professor also has a line scan feature which allows scans along arbitrary straight lines in parameter space, which is useful to verify that the χ^2 behaves as interpolated and to explicitly compare default tunes to predicted tunes. Such a line scan can be seen in Fig. 1(a). We have explicitly checked the robustness of the polynomial and the random distribution of sampling points against various skewed test distributions and the behaviour is robust. We have also found it to be useful to over-sample by a considerable fraction, and then to perform the χ^2 minimisation for a large number of distinct run-combinations, $N_{\text{min}}^{(n)} < N_{\text{tune}} \leq N$, which gives a systematic control on interpolation errors and usually a better performance than just using $N_{\text{tune}} = N$.[1]

The focus in testing and commissioning the Professor system has until recently been focused on Pythia 6 tunes against LEP data [16]. Here we were able to interpolate and minimise up to 10 parameters at a time for roughly 100 distributions, but beyond this the minimisation time became large and we were less happy with the minima. Eventually we decided to split the tuning into a two-stage procedure where flavour-sensitive fragmentation parameters were tuned first to provide a base on which to tune the semi-factorised kinematic parameters of the shower and hadronisation. The result has been a dramatic improvement of the Pythia 6 identified particle multiplicity spectra, without losing the event shape descriptions (originally tuned by DELPHI's version of the same procedure), and a major improvement of the b-fragmentation function as seen in Fig. 1(b).[2] This tune will be adopted as the default parameter set for the next release of

[1]Note that the tuning runs need a significant degree of variation, i.e. $N_{\text{tune}} \ll N$ for most of the tune run-combinations.

[2]Note that interpolation methods cannot deal with discrete settings such as the choice of functional form of b-fragmentation function. This required several parallel tunes with different values of the discrete parameter.

Pythia 6.

4 Conclusions

To conclude, the situation is looking positive for MC generator tuning at present: the Rivet and Professor tools are now in a state where they can be used to achieve real physics goals and the Pythia 6 tune described here (using both tools) has been a significant success. Development plans in the near future are very much aimed at getting the same tuning machinery to work for hadron collider studies, in particular initial state radiation (ISR) and underlying event (UE) physics. We aim to present tunes of C++ generators to LEP data shortly, along with first studies of interpolation-based tunes to CDF underlying event data. Finally, we are keen to constrain fragmentation and UE hadron physics for the LHC, using b-factory, RHIC and early LHC data.

References

[1] T. Sjostrand and S. Mrenna and P. Skands, JHEP **05**, 026 (2006), hep-ph/0603175.

[2] B. Webber and others, JHEP **01**, 010 (2001), hep-ph/0011363, HERWIG Collaboration.

[3] P. Richardson *et al.*, (2008), 0803.0883, Herwig++ Collaboration.

[4] F. Krauss and others, JHEP **02**, 056 (2004), hep-ph/0311263, Sherpa Collaboration.

[5] J. Bromley *et al.*, (1995), ZEUS and H1 Collaborations.

[6] M. Dobbs and J. B. Hansen, Comput. Phys. Commun. **134**, 41 (2001).

[7] M. Cacciari and G. Salam and G.Soyez, (2006), hep-ph/0607071.

[8] M. Mangano *et al.*, JHEP **07**, 001 (2003), hep-ph/0206293.

[9] C. Harris, P. Richardson, and B. Webber, JHEP **08**, 033 (2003), hep-ph/0307305.

[10] J. Butterworth, J. Forshaw, and M. Seymour, Z. Phys. **C72**, 637 (1996), hep-ph/9601371.

[11] T. Sjostrand, S. Mrenna, and P. Skands, Comput. Phys. Commun. **178**, 852 (2008), 0710.3820.

[12] SciPy website: http://www.scipy.org.

[13] DELPHI Collaboration, K. Hamacher *et al.*, Z. Phys. **C73**, 11 (1996).

[14] K. Hamacher and M. Weierstall, (1995), hep-ex/9511011.

[15] PyMinuit website: http://code.google.com/p/pyminuit/.

[16] A. Buckley *et al.*, Professor Collaboration, in preparation.

Prerequisites for the Validation of Experiment and Theory

Lars Sonnenschein
CERN and LPNHE Paris, Universités Paris VI, VII

Abstract
In physics a better understanding of nature is achieved by a recursive interplay between experiment and theory. This requires a validation of both. On the theory side Monte-Carlo event generators can be validated by means of data from experiment. This data has to be corrected for detector effects to render an immediate comparison to event generators meaningful. A HepData database is available to retrieve published measurements including error correlation matrices from authors. Furthermore a validation framework Rivet is available in which authors are supposed to implement the necessary code to reproduce their published measurement exactly. To prevent any ambiguities this implementation should be accomplished at the time of publication. The constraints from published measurements are needed for further event generator development, of which experiments in turn will benefit in the next iteration.

1 Introduction

In high energy physics the ultimate goal of experiment and theory is a better understanding of nature. While the theory needs input from experiment for the verification or falsification of concurrent models the experiment needs input from theory for the prediction of observables, the understanding of scattering processes/production rates and the discrimination of instrumental effects and background processes from (new) physics. A recursive interplay takes place between experiment and theory where the experiment probes the description of nature provided by the theory, as schematically depicted in fig. 1. The intersection point where experiment and theory meet is the cross section. But before measurements can be compared to theory, the measurements have to be corrected for detector effects on the one hand and the models in which the theory is embedded have to be simulated on the other hand. To render the comparison between theory

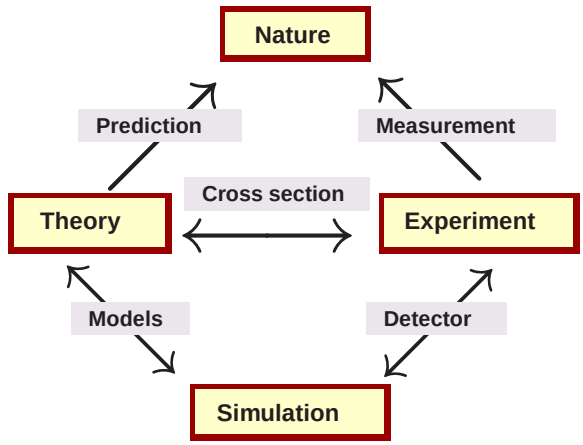

Fig. 1: Relations between theory, experiment, simulation and nature. The intersection point where experiment and theory meet is the cross section. While the theory makes predictions of nature and interfaces via models to the simulation the experiment measures nature and interfaces via the detector simulation or corrections obtained from data to the models.

and measurement meaningful the understanding (verification, validation and optimization) of Monte-Carlo event generation, simulation and experiment is crucial.

The need for the validation of experiment and theory is also documented by Sir Arthur Eddington's statement: "It is a good rule not to put overmuch confidence in a theory until it has been confirmed by observation. I hope I shall not shock the experimental physicists too much if I add that it is also a good rule not to put overmuch confidence in the observational results that are put forward *until they have been confirmed by theory*" (his italics).

2 Need for corrected data from experiment

The theory makes predictions to very few fixed orders (LO, NLO) plus resummation of radiation. More or less phenomenological models are needed for comparison with measurements. The models are implemented in Monte-Carlo event generators. They contain phenomenological parameters like e.g.:

- Parton shower termination parameters $p_\perp \min, m_{\min}$
- Lund string and cluster fragmentation parameters: string function parameters, mass
- Underlying event: primordial $k_\perp$, color reconnection parameters,
- Parton Distribution Functions (PDF's).

Therefore the models need to be validated and adjusted using real data from experiment. The data is coming form the HepData database [1] which is an archive of published HEP data from the last 30 years. It contains almost exclusively data which has been corrected for detector effects. Its focus is on cross section and similar measurements which makes the archive complementary to the Particle Data Group.

Authors who are publishing a measurement should remember to send their data to the HepData database. This data has to be corrected for detector effects (i.e. acceptance, efficiency

and instrumental background) which corresponds to a correction to the hadronic final state or particle level. It is important that the data is not corrected any further to prevent the introduction of model dependencies since the models are supposed to be tested with the data among others. Only if corrected in this way the data can be always compared to Monte-Carlo event generators and it will be useful any time in the future. Otherwise the published measurement will be obsolete sooner or later (typically rather soon).

3 Reproducibility of published analyses

Before a comparison of the theory and models via simulation to data can be accomplished the published analyses have to be implemented and they have to match the publications exactly. Phenomenologists spend an enormous amount of time to reproduce published data analysis in all details, e.g. jet algorithm details and how the algorithm has been applied exactly. The publication might seem unambiguous at the time of writing. Experience shows, that this is no longer the case later on. The solution is the validation tool Rivet [2] which contains the analysis code and provides the real data for comparison. Rivet can be directly interfaced by means of the standardised event record format HepMC [3] to various Monte-Carlo event generators, e.g. via the interface package AGILe [4]. Authors of published corrected measurements (see last section for details on the correction) should implement their analysis into the Rivet framework and this at the time of publication to prevent any ambiguities. Only in this way an exact reproduction is guaranteed.

Present and past collider centre-of-mass energies provide unique points of operation. Event generator authors (of Herwig++, Pythia8, Sherpa, etc.) appreciate very much corrected analyses form the electron positron collider LEP where the hadronisation corrections turned out to be larger than the detector corrections. Important constraints on fragmentation models have been provided by LEP analyses. The most important ones have already been implemented into the Rivet validation framework.

Another important item to be mentioned within the context of reproducibility is the correlation between errors in the measurement. The matrices of correlated errors are typically only provided by analyses accomplished in the QCD group of experiments. This information has to be obtained on an event by event basis and can therefore not be recovered from published plots containing measured distributions. Thus it is extremely important to document this information, too.

Constraints from new published data corrected for detector effects are needed for further Monte-Carlo event generator development, the more the better. Experiments will benefit from it in the next iteration.

4 Summary

An important prerequisite for the validation of experiment and theory is that experiments correct their data for detector effects. In this way the data can be used at a later time point, when different or new models and/or Monte-Carlo event generators have to be validated and optimised. In the case of correlated errors it is also important that the experiment provides the covariance matrix, since this information can not be recovered from published plots containing measured

distributions. Once a measurement is being published, the results should be send to the HepData database. The authors of the analysis should implement their analysis into the validation framework Rivet at the time of publication. In this way the usefulness of their measurement is guaranteed any time in the future. Experiments will benefit from the additional constraints imposed by their published analyses in the next iteration of event generator validation.

Acknowledgements

This work has been supported by the Marie Curie Program, in part under contract number MRTN-CT-2006-035606 and the HEPtools EU Marie Curie Research Training Network under contract number MRTN-CT-2006-035505.

References

[1] HepData database, `http://projects.hepforge.org/hepdata`.

[2] Validation framework Rivet, `http://projects.hepforge.org/rivet`.

[3] M. Dobbs, J. B. Hansen, L. Garren, and L. Sonnenschein, `http://lcgapp.cern.ch/project/simu/HepMC/20400/HepMC2_user_manual.pdf`.

[4] A Generator Interface Library, `http://projects.hepforge.org/agile`.

Chapter 7

List of Authors

List of Authors

Österberg, K., 527

Ajaltouni, Z.J., 331
Albino, S., 710
Altarelli, G., 8
Ambroglini, F., 663
Anderson, J., 105
Antchev, G. , 527
Arneodo, M., 397
Aspell, P., 527
Avati, V. , 527

Bähr, M., 641, 752
Bacchetta, A., 129
Bagliesi, M.G, 527
Ball, R.D., 8, 53
Banfi, A., 129, 155, 331
Baranov, S., 129, 205, 331
Bartalini, P., 631, 663
Bartels, J., 129, 205
Bechtel, F., 663, 670
Berardi, V., 527
Berretti, M., 527
Beuf, G., 8
Biasini, M., 296
Bierenbaum, I., 331
Blümlein, J., 331
Blair, R.E., 681
Bombonati, C., 296
Boonekamp, M., 105, 758
Bottigli, U., 527
Boutle, S., 274
Bozzo, M., 527
Brücken, E., 527
Bracinik, J., 274
Bruni, A., 427
Bruno, G.E., 296
Buckley, A., 768
Bunyatyan, A., 129, 421, 567, 675
Burkhardt, H., 105
Bussey, P., 557
Buzzo, A., 527

Cacciari, M., 272
Cafagna, F., 527
Calicchio, M., 527
Caola, F., 8
Catanesi, M.G., 527
Catastini, P.L., 527
Cecchi, R., 527
Ceccopieri, F.A., 458
Cerci, S., 516
Chekanov, S., 631, 681, 763
Chierici, R., 747
Ciafaloni, M., 8
Ciocci, M.A., 527
Coco, V., 129, 182
Colferai, D., 8
Cooper-Sarkar, A., 74, 567
Corcella, G., 129, 155, 331
Czakon, M., 331

Dainese, A., 272
Dasgupta, M., 129, 155
Deák, M., 129, 205, 737
Deile, M., 527
Delsart, P.A., 129, 182
Del Debbio, L., 53
De Roeck, A., 125
Diaconu, C., 567
Diehl, M., 397
Dimovasili, E., 527
Dittmar, M., 105
Dremin, I.M., 129, 257

Eggert, K., 527
Engel, R., 567
Eremin, V., 527
Erhan, S., 516
Ewerz, C., 510

Fanò, L., 663
Feltesse, J., 53
Ferrera, G., 331
Ferro, F., 527
Field, R., 663
Forte, S., 53

Garcia, F., 527
Geiser, A., 274

Geiser. A., 272
Gelis, F., 8
Giani, S., 527
Gieseke, S., 631, 641, 752
Gigg, M.A., 752
Glazov, A., 53, 74
Golec-Biernat, K., 471
Goulianos, K., 440
Grebenyuk, J., 74
Greco, V., 527
Grellscheid, D., 752
Grindhammer, G., 274
Grothe, M., 516
Guffanti, A., 53
Gwenlan, C., 129

Halyo, V., 105
Hamilton, K., 752
Hautmann, F., 129, 205, 716
Heino, J., 527
Heinrich, G., 681
Hildén, T., 527
Hiller, K., 540
Hollar, J., 516

Janssen, X., 427
Joseph, S., 129, 155
Jung, A.W., 274
Jung, H., 129, 205, 646, 737
Juránek, V., 758

Kašpar, J., 527
Kepka, O., 758
Khoze, V.A., 397, 482, 488
Kiesling, Ch., 567
Klasen, M., 448
Klein, S., 331
Kniehl, B.A., 331
Knutsson, A., 129, 205
Kopal, J., 527
Kramer, G., 331, 448
Krauss, F., 631
Kundrát, V., 527
Kurvinen, K., 527
Kutak, K., 129, 205, 567, 737

Lönnblad, L., 129, 733
Lami, S., 527
Latino, G., 527
Latorre, J.I., 53
Latunde-Dada, O., 752
Lauhakangas, R., 527
Lendermann, V., 74
Lenzi, P., 740
Li, G., 74
Likhoded, A., 331
Lipatov, A., 129, 205, 681
Lippmaa, E., 527
Lokajíček, M., 527
Lo Vetere, M., 527
Lucas Rodriguez, F., 527
Luisoni, G., 129, 155
Lytken, E., 296

Müller, K., 129, 240
Macrí, M., 527
Magazzù, G., 527
Majhi, A., 129
Majhi, S., 155
Marage, P., 427
Marti, L., 129, 646
Martin, A.D., 482, 488
Meucci, M., 527
Milstead, D.A., 331
Minutoli, S., 527
Mischke, A., 296
Moares, A., 656
Moch, S., 8
Motyka, L., 8, 471

Namsoo, T., 129, 646
Newman, P., 397, 401
Niewiadomski, H., 527
Nockles, C., 464
Noschis, E., 527
Notarnicola, G., 527
Nystrand, J., 503

Oliveri, E., 527
Oljemark, F., 527
Orava, R., 527
Oriunno, M., 527
Osman, S., 129, 646
Ostapchenko, S., 567

Palazzi, P., 527
Pedreschi, E., 527
Pereira, A.V., 516
Perrey, H., 129, 240
Petäjäjärvi, J., 527
Petersen, T., 105
Piccione, A., 53
Pierog, T., 567
Pinfold, J.L., 440
Piskounova, O.I., 331
Plätzer, S., 752

Quinto, M., 527

Rúriková, Z., 129, 274, 675
Radermacher, E., 527
Radescu, V., 53
Radicioni, E., 527
Ravotti, F., 527
Rella, G., 527
Richardson, P., 752
Robutti, E., 527
Rodrigo, G., 129
Rodrigues, E., 129
Rogal, M., 8
Rogers, T.C., 567
Rojo, J., 53, 129, 182
Roloff, P., 274
Ropelewski, L., 527
Rosemann, C., 296
Royon, Ch., 8, 205, 758
Ruggiero, G., 527
Rummel,A., 527
Ruspa, M., 401
Ryskin, M.G., 482, 488

Sálek, D., 8
Słomiński, W., 412
Saarikko, H., 527
Sabio Vera, A., 129, 205
Sako, T., 567
Salam, G.P., 8
Saleev, V.A., 331
Sander, C., 129, 182
Sanguinetti, G., 527
Santroni, A., 527
Schörner-Sadenius, Th., 129, 240
Schicker, R., 548
Schienbein, I., 331
Schmidke, W.B., 421
Schwennsen, F., 129, 205
Scribano, A., 527
Sette, G., 527
Seymour, M.H., 641, 752
Sherstnev, A., 752
Sjöstrand, T., 726
Snoeys, W., 527
Somogyi, G., 129
Sonnenschein, L., 774
Soyez, G., 129, 182
Spiesberger, H., 272, 331
Spinella, F., 527
Squillacioti, P., 527
Staśto, A.M., 8
Starodumov, A., 296
Stenzel, H., 540
Stephens, Ph., 699
Ster, A., 527
Stocco, D., 296
Strikman, M., 129, 257, 495, 567

Taylor, C., 527
Teubner, T., 464
Thorne, R.S., 8, 53, 331
Trócsányi, Z., 129
Treccani, M., 129
Treleani, D., 129, 635
Trentadue, L., 458
Trummal, A., 527
Tully, J., 752
Tung, W.K., 331
Turcato, M., 274
Turini, N., 527

Ubiali, M., 53

Valkárová, A., 412
van Hameren, A., 699
Van Mechelen, P., 557
Vermaseren, J.A.M., 8
Vogt, A., 8

Ward, B.F.L., 129, 155
Watt, G., 53, 471
Webber, B.R., 752
Weiss, Ch., 495
White, Ch., 8, 721
Whitmore, J., 527
Wolf, R., 296
Wu, J., 527

Yagües-Molina, A., 274
Yost, S.A., 129, 155

Zanderighi, G., 129, 331
Zotov, N., 129, 205, 331, 681
zur Nedden, M., 296

Chapter 8

List of Participants

List of Participants

Adamczyk Leszek AGH- University of Science and Technology Cracow
Adelodun Tesleem Alade University of Ibadan
Adorisio Cristina Universita' della Calabria
Ahmad, Ayaz Mohammad Aligarh Muslim University, Aligarh, India
Ahmed Ijaz National Centre for Physics Islamabad
Ajaltouni Ziad LHCB
Akcay Ali Riza TFI
Akhundov Arif University of Valencia, Spain
Albino Simon Hamburg University
Alcaraz Maestre Juan CIEMAT - Madrid
Alekhin Sergey Inst. for High Energy Physics (Protvino, Russia)
Alessandro Bertolin INFN - Sez. di Padova
Amelung Christoph CERN
Anastasiou Anastasiou ETH
Andersen Jeppe R. University of Cambridge
Andreev Valeri UCLA
Andreev Vladimir LPI, Moscow
Anjos, Nuno LIP
Antonio Zoccoli University and INFN - Bologna
Arneodo Michele Universita' del Piemonte Orientale, Novara, Italy
Arturo, Fernandez Tellez Universidad Autonoma de Puebla
Asghar, Muhammad Irfan National Centre for Physics
Aushev Vladimir KINR,Kiev/DESY
Avati Valentina Helsinki University
Avsar Emil Lund University
Aybat, Mert ETH
Bähr, Manuel University Karlsruhe
Bacchetta Alessandro DESY
Badelek Barbara Warsaw University
Baghdasaryan Artem DESY/Yerevan
Baines John RAL
Ball Richard Edinburgh
Bamberger Andreas University Freiburg
Banerjee Sunanda Tata Institute of Fundamental Research
Banfi Andrea Universita' degli Studi di Milano-Bicocca
Baranov Sergey Lebedev Institute of Physics, Moscow
Barbagli Giuseppe INFN - Firenze
Bargiotti Marianne CERN
Bartalini Paolo NTU
Bartels Joachim Universitaet Hamburg
Bechtel Florian Hamburg University
Behera, Prafulla University of Iowa

Behnke Olaf Uni Heidelberg
Bel'kov Alexander Joint Institute for Nuclear Research, Dubna, Russia
Bellagamba Lorenzo INFN Bologna
Bellan Paolo Padova University - INFN
Bellan Riccardo Universita' degli Studi di Torino - INFN
Belov Sergey Join Institute for Nuclear Research, Dubna, Russia
Bennaoum Malika theoritical physics
Beuf, Guillaume CEA / IPhT
Bierenbaum Isabella DESY, Zeuthen
Bluemlein Johannes DESY
Boettcher Helmut DESY Zeuthen
Bolzoni, Paolo DESY
Bombonati Carlo INFN & University of Padova
Bonato Alessio DESY / Hamburg University
Bondarenko Sergey Santiago de Compostela University
Boonekamp Maarten CEA/DAPNIA-Saclay
Boreskov Konstantin ITEP, Moscow
Bornheim Adolf CALTECH / CMS
Borras Kerstin DESY
Botje Michiel NIKHEF
Bourilkov Dimitri University of Florida
Boutle, Sarah University College London
Bozzi, Giuseppe ITP Karlsruhe
Bozzo Marco CERN and INFN Genova
Bracinik Juraj MPI Munchen
Brock Ian University of Bonn
Brona, Grzegorz University of Warsaw
Bruni Alessia INFN Bologna
Bruno Giuseppe Universita' di Bari
Buchmueller Oliver CERN
Buckley Andy IPPP, Durham
Bunyatyan Armen MPI-Heidelberg / YerPhI
Buran, Torleiv dpt.of phys., univ.of oslo
Bussey , Peter University of Glasgow
Buttar Craig Sheffield University
Butterworth Jonathan UCL
Cacciari Matteo LPTHE, UPMC Paris
Cafarella, Alessandro NCSR Demokritos
Cakir, Orhan Ankara University
Caldwell Allen Max-Planck-Institut
Caola, Fabrizio Universita' di Milano and INFN-Milano
Capua Marcella University of Calabria and INFN
Carli Tancredi CERN
Caron Sascha NIKHEF
Catmore James Lancaster University, ATLAS
Ceccopieri, Federico Alberto Universita' di Parma
Cerminara Gianluca INFN - Universita' degli Studi di Torino
Chachamis Grigorios University of Hamburg
Chekanov Sergei ANL/DESY
Chekelian Vladimir MPI Munich
Chierici Roberto CNRS/IPNL
Chiochia Vincenzo University of Zurich
Cholewa Axel DESY

Coca Cornelia National Institute of Physics and Nuclear Engineering IFIN-HH, Bucharest
Coco, Victor LAPP-IN2P3-CNRS
Cole Jo University of Bristol
Colferai Dimitri Universita' di Firenze e INFN (Italy)
Collins John Penn State Univ
Collins-Tooth Christopher University of Glasgow, ATLAS
Cooper-Sarkar Amanda (Mandy) Oxford University, UK
Corcella Gennaro CERN
Corradi Massimo INFN Bologna
Corriveau Francois IPP / McGill University
Costa Marco University of Turin
Coughlin Tim The University of Manchester
Cox Brian University of Manchester
Czakon, Michal University of Wuerzburg
Czyczula Zofia Jagiellonian University
d'Enterria David CERN
D'Orazio, Alessia Max-Planck-Institut f. Physik
Dainese Andrea INFN Legnaro
Daleo Alejandro ETH Zurich
Dasgupta Mrinal Manchester University
Daum Karin DESY/Uni Wuppertal
Davatz Giovanna CERN, EP
De Jesus Damiao, Dilson Universidade do Estado do Rio de Janeiro
De Roeck Albert CERN
Deak Michal DESY
Delenda Yazid University of Manchester
Delsart, Pierre-Antoine L.A.P.P (Annecy)
Derkach Denis DESY
Diaconu Cristinel CPPM/DESY
Dianna, Giovanni University of Milan - INFN
Diehl Markus DESY
Diez Carmen DESY
Dittmar Michael ETH Zurich
Dobur Didar INFN-Pisa
Drescher Hans-Joachim Frankfurt Institute for Advanced Studies
Drohan Janice UCL
Drozdetskiy Alexey University of Florida, Gainesvile, USA
Eggert Karsten CERN
Eisele Franz Physikalisches Institut heidelberg
Eisenberg Yehuda Weizmann Institute
Ellis Keith Fermilab
Emelyanov, Valery MEPHI
Enberg Rikard Ecole Polytechnique
Engel Ralph Forschungszentrum Karlsruhe
Ewerz Carlo ECT* Trento
Fabbri Fabrizio INFN Bologna - Italy
Fabris Daniela INFN Sezione di Padova - Italy
Falter Thomas Institut f. Theoretische Physik, Universitaet Giessen
Fano' Livio INFN - Perugia
Fawe Adewale Heritage international
Feltesse Joel DESY/HAMBURG/SACLAY
Felzmann Ulrich Institut für Experimentelle Kernphysik, University Karlsruhe
Ferrag Samir University of Oslo

Ferrera Giancarlo Univ. de Barcelona & Univ. de Granada, Spain
Ferro Fabrizio INFN Genova
Field Rick Florida/CDF
Filippo Ambroglini University of Perugia & INFN
Flossdorf Alexander DESY
Flucke Gero DESY
Forshaw Jeff Manchester University
Forte Stefano Milan University
Fuks Benjamin LPSC Grenoble
Gallinaro, Michele LIP
Gallo Elisabetta INFN Firenze
Gehrmann Aude ETH Zuerich
Geiser Achim DESY Hamburg
Geist Walter IReS/Strasbourg
Gelis, Francois CERN PH-TH
Ghazaryan Samvel Yerevan Physics Institute
Gieseke Stefan CERN/Uni Karlsruhe
Ginzburg Jonatan CERN
Gladilin Leonid Moscow State University
Glazov Alexandre DESY
Glover Nigel Durham U., IPPP
Gogitidze Nelly LPI, Moscow / DESY, Hamburg
Golec-Biernat, Krzysztof Institute of Nuclear Physics
Golutvin Igor JINR, CMS
Gotsman Error Tel Aviv University
Goulianos Konstantin Rockefeller University
Gouzevitch, Maxime Laboratoire LLR, Ecole Polytechnique
Grab Christoph ETH Zurich
Grebenyuk, Julia DESY, Hamburg
Greco Mario Univ. Rome III
Grindhammer Guenter Max-Planck-Institute for Physics, Munich
Grothe Monika Wisconsin/Turin
Groys Michael Tel Aviv university
Grzelinska, Agnieszka IFJ PAN, Cracow
Guernane Rachid LPC Clermont-Ferrand CNRS/IN2P3
Guffanti Alberto University of Edinburgh
Gustafson Gosta Lund University
Gutsche Oliver DESY / University of Hamburg
Guzey Vadim Ruhr-Universitaet Bochum
Gwenlan Claire UCL
Halyo, Valerie Princeton
Hansson Magnus Lund University
Harris Oliver UCL/ATLAS
Harrison Karl University of Cambridge
Hegner Benedikt DESY
Heinemann Beate University of California, Berkeley
Heister, Arno Boston University
Hinchliffe Ian Lawrence Berkeley National Lab
Hoeche Stefan TU Dresden
Hoepfner Kerstin RWTH Aachen, III.Phys.Inst.A
Hoeth Hendrik Lund University
Hoeth, Hendrik Lund University
Hollar, Jonathan Jason Lawrence Livermore Nat. Laboratory (LLNL)

Holzner Andre ETH Zuerich
Huston Joey Michigan State University
Iacobucci Giuseppe INFN Bologna
Illarionov Alexei INFN, Pisa & JINR, Dubna
Ingelman Gunnar Uppsala University
Ishikawa Akimasa KEK-IPNS
Jadach Stanislaw IFJ-PAN, Krakow
Janssen Xavier DESY
Javadi Khasraghi Atefeh Physics group of Alzahra university
Jechow Mirko Humbold-University zu Berlin Dep. of Physiscs
Jung Hannes DESY
Jung, Andreas W. University of Heidelberg, KIP
Kahle Benjamin DESY
Kaidalov Alexei ITEP, Moscow
Kapishin Mikhail JINR, Dubna
Karshon Uri Weizmann Institute, Rehovot, Israel
Kaspar Jan Physical Instute, Czech Academy of Sciences, Prague
Kataoka Mayuko KEK, Nara Women's University
Katkov, Igor DESY
Kepka Oldrich Dapnia SPP, CEA, Saclay
Kharzeev Dmitri BNL
Khein Lev Moscow State University
Khoze Valeri IPPP, University of Durham
Kiesling Christian Max-Planck-Institut für Physik
Kirsanov Mikhail INR Moscow
Klanner Robert University of Hamburg
Klasen Michael LPSC Grenoble
Klein Max University of Liverpool
Klein Sebastian DESY Zeuthen
Kluge Thomas DESY
Knutsson Albert DESY
Kolhinen Vesa Univ. of Jyvoskylo, Dept. of Physics
Kollar, Daniel MPI for Physics Munich
Korotkov, Vladislav IHEP
Kostka, Peter DESY
Kotanski Andrzej Jagellonian University, Cracow,Poland
Kotikov Anatoly Joint Institute for Nuclear Research
Kowalski Henri DESY
Kraan Aafke INFN Pisa
Kramer Gustav Hamburg University
Krastev Kaloyan DESY
Krauss Frank TU Dresden
Kretzer Stefan BNL / RBRC
Krueger Katja KIP, Uni Heidelberg
Kuhr Thomas CERN
Kulesza Anna DESY Theory
Kundrat Vojtech Institute of Physics ASCR, Prague, Czech Republic
Kurepin Alexey Institute for Nuclear Research, Moscow
Kusina, Aleksander Institute of Nuclear Physics PAN
Kutak Krzysztof DESY
Kyrieleis Albrecht University of Manchester
Lönnblad, Leif Lund University
Laenen Eric NIKHEF

Lagouri Theodota Aristotle University of Thessaloniki
Lami Stefano INFN Pisa
Latino Giuseppe Siena Univ. & Pisa INFN
Lavesson Nils Lund University
Lebedev Andrey LPI
Lehner Frank DESY
Lendermann Victor University of Heidelberg
Lenzi, Piergiulio Dipartimento di Fisica
Lessnoff Kenneth University of Bristol
Levchenko Boris SINP MSU
Levin Eugene Tel Aviv University
Levonian Sergey DESY
LI, Gang LAL
Likhoded Anatoly IHEP, Protvino, Russia
Lilley, Joseph University of Birmingham
Lipatov Artem SINP MSU
Lipatov Lev Hamburg University
Lipka Katerina University of Hamburg
Lippmaa Endel Estonian Academy of Sciences
Lippmaa Jaak HIP, Helsinki University
Livio Fano INFN Perugia
Loizides John University College London
Lola, Magda Univ. of Patras
Lublinsky Michael University of Connecticut
Luisoni, Gionata ITP University Zurich
Lukasik Jaroslaw DESY / AGH-UST Cracow
Lukina Olga Skobeltsyn Institute of Nuclear Physics, Moscow State University
Lunardon Marcello University and INFN Padova
Luszczak Agnieszka INF PAN KRAKOW
Lytken, Else CERN
Lytkin Leonid Dubna
Macri, Mario INFN Genova
Magill Stephen Argonne National Laboratory
Magnea Lorenzo University of Torino
Mangano Michelangelo CERN TH
Maor Uri Tel Aviv University
Marage, Pierre ULB - Universite Libre de Bruxelles
Marquet Cyrille CEA-Saclay SPhT
Marti-Magro Lluis Desy
Martin Alan IPPP, Durham
Martyn Hans-Ulrich RWTH Aachen & DESY
Martynov, Yevgen Bogolyubov Institute for Theoretical Physics
Marzani, Simone School of Physics
Mastroberardino Anna Calabria University
Matteuzzi Clara INFN and Universita Milano-Bicocca
Maxfield Stephen University of Liverpool
Mazumdar Kajari Tata Institute, Mumbai, India
Melzer-Pellmann Isabell-A. DESY Hamburg
Meyer Andreas Hamburg University
Michele Pioppi Univ. of Perugia
Miglioranzi Silvia DESY
Milcewicz Izabela Institute of Nuclear Physics, Cracow
Milstead David Stockholm University

Mischke Andre Utrecht University
Mitov Alexander DESY
Moch Sven-Olaf DESY
Moenig Klaus DESY
Monk James University College London
Monteno, Marco INFN
Moraes Arthur University of Sheffield
Morando Maurizio University of Padova
Morsch Andreas CERN
Motyka Leszek DESY
Mozer Matthias IIHE
Mrenna Stephen Fermilab
Mueller Katharina Universitaet Zuerich
Munier Stephane Ecole polytechnique
Murray Michael University of Kansas
Nachtmann Otto Universitaet Heidelberg
Nadolsky, Pavel Michigan State University
Naftali Eran Tel Aviv University
Nagano Kunihiro KEK
Nagy, Zoltan DESY
Namsoo Tim Bristol
Naumann Sebastian Univ. Hamburg
Newman Paul University of Birmingham
Nick Brook Brook University of Bristol
Niewiadomski Hubert CERN
Nuncio Quiroz Elizabeth Hamburg University / DESY
Nystrand Joakim University of Bergen
Olivier, Bob Max Planck Institute for Physics
Olness, Fredrick SMU / CERN
Orava Risto University of Helsinki & Helsinki Institute of Physics
Osman Sakar Lund University
Ostapchenko Sergey University of Karlsruhe
Osterberg Kenneth University of Helsinki
Ozerov, Dmitry ITEP
Padhi Sanjay DESY
Panagiotou Apostolos UNIV. OF ATHENS, HELLAS
Panikashvili Natalia Technion , Israel
Passaleva Giovanni INFN-Firenze
Pavel Nikolaj Humboldt-University Berlin, Inst. for Physics
Perez Emmanuelle CERN
Peschanski Robi Service de Physique Theorique (Saclay)
Peters Krisztian DESY H1
Petersen, Troels CERN
Petrov Vladimir IHEP. Protvino
Petrov, Vladimir Institute for High Energy Physics
Petrucci Fabrizio INFN Roma III
Petrukhin, Alexey DESY/ITEP
Piccinini Fulvio INFN Sezione di Pavia
Piccione Andrea INFN Torino
Pierog Tanguy FZK,IK
Pilkington Andrew University of Manchester
Pinfold, James University of Alberta
Piotrzkowski Krzysztof Louvain University

Pire Bernard CPhT Polytechnique, Palaiseau
Pirner Hans-Juergen Theoretical Physics, Heidelberg University
Pisano Cristian Vrije Universiteit Amsterdam
Piskounova Olga LPI, Moscow
Piskounova, Olga LPI
Plaätzer, Simon ITP, U Karlsruhe
Placzek Wieslaw Institute of Physics, Jagiellonian University, ul. Reymonta 4, 30-059 Cracow, Poland
Pokorski Witold CERN
Polesello Giacomo CERN/INFN Pavia
Price, Darren Lancaster University
Pukhaeva Nelli INFN Milano
Pumplin Jon Michigan State University
Qin Zhonghua DESY ATLAS GROUP
Rabbertz Klaus University of Karlsruhe
Radescu Voica DESY
Radescu Voica DESY
Ranieri Riccardo University of Firenze / INFN Firenze
Rathsman Johan Uppsala University
Ravindran Vajravelu Visitor, DESY-Zeuthen, Associate Prof at Harish-Chandra Research Institute, India
Rebuzzi, Daniela MPI - Munich
Reisert Burkard Max-Planck-Institute for Physics, Munich
Renner, Dru DESY Zeuthen
Rezaeian, Amir Universidad Tocnica Federico Santa Marra
Reznicek, Pavel IPNP, Charles University
Richardson Peter IPPP, Durham
Richter-Was Elzbieta Jagellonian University & Institute of Nuclear Physics IFJ PAN, Cracow, Poland
Rioutine, Roman IHEP
Risler Christiane DESY
Rizvi Eram QMUL
Robbe Patrick LAL Orsay
Rodrigo German CERN & IFIC Valencia
Rodrigues Eduardo NIKHEF
Rogal, Mikhail DESY, Zeuthen
Rojo-Chacon Juan LPTHE, Paris
Rolandi Gigi CERN
Roloff Philipp DESY
Roosen Robert Bruxelles
Rouby Xavier UC Louvain
Royon Christophe DAPNIA-SPP, CEA Saclay
Ruiz Hugo CERN
Ruiz Morales Ester UPM - Madrid
Rurikova, Zuzana DESY
Ruspa Marta Univ Piemonte Orientale
Ryan Patrick University of Wisconsin
Saarikko Heimo University of Helsinki
Sabio Vera Agustin CERN
Sacchi Roberto University of Torino
Sako, Takashi STE Labo. Nagoya University
Salam Gavin LPTHE, Univ Paris VI and VII and CNRS
Saleev Vladimir Samara State University
Saleh Rahimi Keshari MSc. student of Particle Physics, from Semnan Uni. ,Iran
Salek, David IPNP, Charles University, Prague
Salgado Carlos a Cern

Sander, Christian Institut fuer Experimentalphysik - Universitaet Hamburg
Savin Alexander University of Wisconsin-Madison
Sawicki Pawel Institute of Nuclear Physics, Krakow
Sbrizzi Antonio University of Bologna
Schicker Rainer Phys. Inst. Uni Heidelberg
Schienbein Ingo DESY
Schilling Frank-Peter CERN
Schmelling, Michael MPI for Nuclear Physics
Schmidke William MPI Munich
Schneider Anna Novgorod State University
Schneider Olivier EPFL, Lausanne (LHCb)
Schoerner-Sadenius Thomas Hamburg University
Schrempp Fridger DESY
Schultz-Coulon Hans-Christian Universitaet Heidelberg
Schumann Steffen ITP TU Dresden
Schwennsen Florian University Hamburg
Seymour Michael CERN
Sharafiddinov Rasulkhozha Institute of Nuclear Physics of Uzbekistan Academy of Sciences
Shaw Graham University of Manchester
Shcherbakova Elena II Inst. fr Theor. Phys. Hamburg UniversitŁt
Shears, Tara University of Liverpool
Shirmohammad Maryam Physics group, Alzahra University
Shulha Siarhei Joint Institute for Nuclear Research, Dubna, Russia
Siddiqui Rehan NCP/CERN
Siegert, Frank IPPP, University of Durham
Sigl Guenter Uni Hamburg
Sjöstrand Torbjörn CERN and Lund University
Skrzypek Maciej ifj-pan
Slabospitsky Sergey CMS Collaboration, IHEP
Sloan Terry Lancaster University
Smith John SUNY at Stony Brook, USA
Smizanska Maria Lancaster
Sobol Andrei IHEP, Protvino
Solano Ada Univ. of Torino and INFN Torino
Somogyi Gabor Institute of Nuclear Research of the Hungarian Academy of Sciences
Sonnenschein Lars CERN
Soper, Davison CERN/University of Oregon
Soyez Gregory University of Liege
Spiesberger Hubert Mainz University
Spiropulu Maria CERN
Sridhar Krishnamoorthy TIFR, Mumbai, India
Stamerra Antonio Universita' di Siena
Stanco Luca INFN Padova
Starodumov Andrey ETH Zurich
Starovoitov Pavel NC PHEP
Stasto Anna DESY
Staykova Zlatka DESY
Steinbrueck Georg Hamburg University
Stenzel Hasko University of Giessen
Stephens Philip IFJ-PAN
Stirling James University of Durham
Stocco Diego Universita' di Torino
Stockton, Mark University of Birmingham

Stoesslein Uta DESY Hamburg
Stopa Piotr Institute of Nuclear Physics Krakow Poland
Strikman Mark Penn State University
Sunar Deniz University of Antwerp
Sutton Mark University College London
Sykora Tomas UA Antwerp, MFF UK Prague
Szczypka Saul University of Bristol
Tapprogge Stefan Johannes Gutenberg Universitaet Mainz
Targett-Adams Christopher UCL
Tasevsky Marek Physics Institute, Prague
Tassi Enrico Universidad Autonoma de Madrid
Terron Juan Universidad Autonoma de Madrid
Teryaev Oleg JINR
Teubert Frederic CERN-PH
Teubner Thomas University of Liverpool
Thaeder, Jochen KIP Uni Heidelberg
Thompson Paul Birmingham University
Thorne Robert University College London
Todorova Sharka ASCR Prague
Tokushuku Katsuo KEK, IPNS
Toll Tobias DESY
Tonazzo Alessandra University Roma Tre and INFN
Traynor Daniel Queen Mary, University of London
Treleani Daniele University of Trieste
Trentadue, Luca Universita' di Parma and INFN Milano - Gr. Pr
Tsirova, Natalia Samara State University
Tuning Niels NIKHEF LHCb
Turcato Monica Hamburg University
Turnau Jacek Institue of Nuclear Physics, PAN, Krakow
Turrisi Rosario University and INFN - Padova
Uwe Ulrich Physikalisches Institut Heidelberg
Vajravelu Ravindran Associate Professor
Valkarova, Alice Charles University, Insitute of Particle and Nuclear Physics
Vallee Claude CPPM Marseille / DESY
van Hameren Andreas IFJ-PAN Krakow
Van Mechelen Pierre Universiteit Antwerpen
Vasin Dmitry Samara State University / Hamburg University
Vazdik Iakov Lebedev Physical Institute, Moscow
Vazquez Acosta Monica CERN
Venugopalan Raju Brookhaven National Laboratory USA
Verducci Monica CERN
Vervink Kim EPFL
Vilela Pereira, Antonio University degli Studi di Torino/INFN Torino
Villa Mauro INFN Bologna
von Manteuffel Andreas Heidelberg
Voss Kai-Cristian Bonn University
Vulpescu Bogdan Physics Institute, University Heidelberg, Germany
Walsh Roberval McGill University
Ward Bennie Baylor University
Was Zbigniew IFJ PAN
Watt Graeme University College London
Waugh Ben University College London
Weinzierl Stefan University of Mainz

Weiser Christian University of Karlsruhe
Weng Joanna CERN/University of Karlsruhe
Whalley Mike IPPP, Durham
White Chris NIKHEF
Whitmore Jim Penn State Univ. and U.S. National Science Foundation
Wing Matthew DESY/UCL
Winter Jan CERN TH and TU Dresden
Wobisch Markus Fermilab
Wolf Roger Uni-Heidelberg
Yagues Ana Humboldt University Berlin/ DESY
Yamazaki Yuji KEK-IPNS
Yokoya, Hiroshi CERN
Yoshida Rik Argonne National Laboratory
Yost Scott Baylor University
Zanderighi Giulia University of Oxford
Zapp Korinna Physikalisches Institut, Universit?t Heidelberg
Zarubin Anatoly JINR, CMS
Zenin Oleg IHEP, Russia
Zotov Nikolai Skobeltsyn Institute of Nuclear Physics, MSU
zur Nedden Martin Humboldt-Universitaet zu Berlin